



Advanced modelling for sheet metal forming under high temperature

Weijie Liu

► To cite this version:

Weijie Liu. Advanced modelling for sheet metal forming under high temperature. Mechanics of materials [physics.class-ph]. Université de Technologie de Troyes; Dalian University of Technology (Chine), 2017. English. NNT : 2017TROY0019 . tel-02414328

HAL Id: tel-02414328

<https://theses.hal.science/tel-02414328>

Submitted on 16 Dec 2019

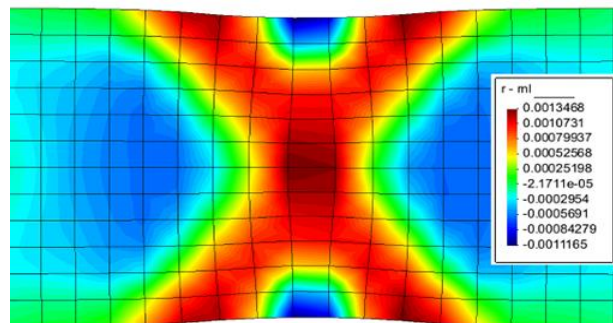
HAL is a multi-disciplinary open access archive for the deposit and dissemination of scientific research documents, whether they are published or not. The documents may come from teaching and research institutions in France or abroad, or from public or private research centers.

L'archive ouverte pluridisciplinaire **HAL**, est destinée au dépôt et à la diffusion de documents scientifiques de niveau recherche, publiés ou non, émanant des établissements d'enseignement et de recherche français ou étrangers, des laboratoires publics ou privés.

Thèse
de doctorat
de l'UTT

Weijie LIU

Advanced Modelling for Sheet Metal Forming under High Temperature



Spécialité :
Matériaux, Mécanique, Optique et Nanotechnologie

2017TROY0019

Année 2017

Thèse en cotutelle avec Dalian University of Technology
Dalian - Chine



大连理工大学
Dalian University of Technology



THESE

pour l'obtention du grade de

DOCTEUR de l'UNIVERSITE DE TECHNOLOGIE DE TROYES

Spécialité : MATERIAUX, MECANIQUE, OPTIQUE ET NANOTECHNOLOGIE

présentée et soutenue par

Weijie LIU

le 14 septembre 2017

Advanced Modelling for Sheet Metal Forming under High Temperature

JURY

M. J. ZHAO	PROFESSOR	Président
M. S. FOREST	DIRECTEUR DE RECHERCHE CNRS	Examinateur
M. J.-F. GANGHOFFER	PROFESSEUR DES UNIVERSITES	Rapporteur
M. P. HU	PROFESSOR	Directeur de thèse
M. C. LABERGÈRE	PROFESSEUR DES UNIVERSITES	Examinateur
M. K. SAANOUNI	PROFESSEUR DES UNIVERSITES	Directeur de thèse
M. S. ZHANG	PROFESSOR	Rapporteur
M. Y. ZHOU	PROFESSOR	Examinateur

Acknowledgement

First and foremost, I would like to express my sincere gratitude to my supervisors, Prof. Ping Hu and Prof. Khemais Saanouni, for giving me the opportunity to study under your guidance, for your great supports in academic and personal affairs and for the fruitful discussions and formulations that contributed to the achievement of this work. My grateful appreciation is extended to Prof. Yingqiao Guo, for his recommendation in my doctoral career.

Acknowledgement is due to China Scholarship Council (CSC) and National Research Agency (ANR) for their financial support of this research.

Next, I wish to thank all my colleagues from both DUT and UTT for the pleasant working conditions, the selfless aids and their friendship. In particular, I would like to convey my gratitude to Prof. Samuel Forest, Prof. Carl Labergere, Prof. Houssem Badreddine, Prof. Xiangkui Zhang, Dr. Zhenming Yue, Dr. Evangelia Diamantopoulou, Dr. Mohamed Ali Dhifallah and Dr. Kai Zhang, for their support and discussions in theoretical, numerical and experimental aspects respectively.

Finally, I am truly grateful to my parents, my sisters and their families, and my beloved wife for their everlasting love, patience, encouragement and support.

Table of Contents

ABSTRACT	IV
RESUME	V
GENERAL INTRODUCTION	1
PART I SIMPLIFIED INVERSE APPROACHES FOR SHEET METAL FORMING	6
INTRODUCTION	7
I. THE STATIC IMPLICIT ONE-STEP INVERSE APPROACH.....	9
I.1 INTRODUCTION	9
I.2 KINEMATIC FORMULATIONS OF TOTAL STRAIN	9
I.3 CONSTITUTIVE EQUATIONS USING THE DEFORMATION THEORY	11
I.4 SIMPLIFIED TOOLS' ACTIONS	12
II. THE STATIC IMPLICIT MULTI-STEP APPROACH	15
II.1 INTRODUCTION	15
II.2 KINEMATIC FORMULATIONS OF INCREMENTAL STRAIN.....	15
II.3 LOCAL INTEGRATIONS BASED ON FLOW THEORY	18
II.3.1 <i>Classical elastoplastic local integration</i>	18
II.3.2 <i>Examination of scalar return mapping method</i>	19
II.4 CONSTRUCTION OF INTERMEDIATE CONFIGURATIONS	22
II.4.1 <i>Resolution of the sliding surface</i>	22
II.4.2 <i>Initial solutions of the middle configuration</i>	25
II.4.3 <i>Equilibrium of the middle configurations.</i>	27
III. NUMERICAL APPLICATIONS	30
III.1 S-RAIL PART OF NUMISHEET 96.....	30
III.1.1 <i>Verification and estimation of the derived kinematic formulations</i>	31
III.1.2 <i>Errors in accumulated total strain of different layers</i>	34
III.1.3 <i>The constructed intermediate configurations</i>	34
III.2 APPLICATION TO B-PILLAR COMPONENT OF NUMISHEET 08	35
III.3 THE BOX SHAPED HOLDER PART	37
III.3.1 <i>The middle configurations using enhanced PMA method</i>	38
III.3.2 <i>The updated stress state</i>	39
IV. CONCLUSIONS	41
PART II ADVANCED MICROMORPHIC MODELING APPROACH FOR SHEET METAL FORMING SIMULATIONS .	42
V. INTRODUCTION	44
V.1 THE LOCAL CONTINUUM DAMAGE MODEL	45
V.2 THE GENERALIZED CONTINUUM DAMAGE MODEL.....	46
V.3 THE GENERALIZED HEAT EQUATIONS	51
VI. THEORETICAL FORMULATIONS	58
VI.1 INTRODUCTION	58

VI.2 GENERALIZED PRINCIPLE OF VIRTUAL POWER (BALANCE EQUATIONS).....	59
VI.2.1 <i>New degree of freedoms (dofs)</i>	59
VI.2.2 <i>Principle of virtual power for a micromorphic medium</i>	59
VI.2.3 <i>Generalized balance equations</i>	61
VI.3 THERMODYNAMIC FORMULATIONS	62
VI.3.1 <i>State variables</i>	62
VI.3.2 <i>Thermodynamic consistency and state potential (State relations)</i>	66
VI.3.3 <i>The generalized heat equation</i>	75
VI.3.4 <i>Dissipation analysis (Evolution equations)</i>	79
VI.4 TRANSFORMATION OF THE MICROMORPHIC BALANCE EQUATIONS.....	86
VI.5 DISCUSSIONS OF SPECIAL CASES.....	88
VI.5.1 <i>Classical local damage model</i>	89
VI.5.2 <i>Simplified classical elastoplastic model</i>	92
VI.5.3 <i>The existent generalized heat equations</i>	93
VI.5.4 <i>Discussions of the generalized heat equation</i>	112
VI.6 CONCLUSIONS	123
VI.7 APPENDIX.....	124
VI.7.1 <i>Formulations of plastic multiplier</i>	124
VI.7.2 <i>Formulations of elastoplastic tangent operator</i>	127
VII. NUMERICAL ASPECTS	130
VII.1 INTRODUCTION.....	130
VII.2 WEAK FORMS OF THE IBVP	130
VII.3 TIME AND SPACE DISCRETIZATION.....	131
VII.3.1 <i>Time discretization</i>	131
VII.3.2 <i>Space discretization</i>	131
VII.4 GLOBAL RESOLUTION SCHEME	140
VII.4.1 <i>Dynamic explicit analysis</i>	140
VII.4.2 <i>Contact problems</i>	143
VII.5 LOCAL INTEGRATION SCHEME	143
VII.5.1 <i>Local integration of time-dependent plasticity</i>	145
VII.6 APPENDICES.....	152
VII.6.1 <i>Appendix I – Q4r24 element for thick shell</i>	152
VII.6.2 <i>Appendix II – The standard hexahedral element</i>	154
VIII. PARAMETRIC STUDY OF THE MODEL	157
VIII.1 EFFECT OF THE LOCAL DAMAGE PARAMETERS.....	157
VIII.2 THE VISCOPLASTIC EFFECTS.....	161
VIII.3 EFFECT OF THE MICROMORPHIC MODULI.....	162
VIII.3.1 <i>Effect of the micromorphic damage moduli</i>	162
VIII.3.2 <i>Effect of the micromorphic isotropic hardening moduli</i>	167
VIII.3.3 <i>Summary</i>	168
VIII.4 ANISOTHERMAL MICROMORPHIC DAMAGE MODEL.....	169
VIII.4.1 <i>Anisothermal viscoplasticity with local damage for a material point</i>	170
VIII.4.2 <i>Biaxial tension for local damage with FE</i>	171
VIII.4.3 <i>Choices of micromorphic parameters with FE</i>	172

VIII.4.4 Biaxial tension for micromorphic damage with FE	174
VIII.4.5 Summary.....	176
IX. APPLICATIONS	177
IX.1 UNIAXIAL TENSILE TEST OF DP1000	177
IX.1.1 <i>The local damage behavior</i>	177
IX.1.2 <i>The micromorphic damage behavior</i>	179
IX.1.3 <i>Solutions with micromorphic damage and micromorphic isotropic hardening</i>	181
IX.2 CROSS SECTION DEEP DRAWING PROCESS	192
IX.2.1 <i>CSDD processes using the local damage model</i>	193
IX.2.2 <i>CSDD processes using the micromorphic damage model</i>	194
IX.3 PRESSURE VESSEL	200
X. CONLCUSIONS.....	206
XI. GLOBAL CONCLUSIONS AND PERSPECTIVES.....	207
RESUME EXTENSIF EN FRANÇAIS	210
中文扩展摘要	236
REFERENCES.....	259

Abstract

The objective of this work is to propose new advanced nonlocal constitutive equations for the modelling and numerical simulation of the sheet metal forming processes under high temperature. The general framework of micromorfing continua is used and the following aspects are investigated:

- 1). Development of a simplified static-implicit FEM multi-steps inverse approach, to efficiently providing formability analysis of the pre-designed metal forming components. The approach adopts the classical isothermal elastoplastic model based on the simplified incremental flow theory to updating stress states. Several middle configurations are constructed to representing specific loading histories and simplifying the contact behavior;
- 2). Formulations of a complete set of advanced micromorphic constitutive equations under the framework of irreversible thermodynamics and generalized continuum mechanics, to capture the strongly interactive nonlocal effects in the material strain-softening induced localization regions. The new extra micromorphic dofs lead to additional balance equations taking into account the nonlocal effects (e.g. the ductile damage, thermal effect and mixed hardening effects) and involving characteristic length scales as representative of the materials' microstructure;
- 3). A thorough discussion of existing extended heat equations is presented. Five types of the generalized heat equations: (i) the classical Fourier model, (ii) the Hyperbolic type with relaxation time, (iii) the Double temperature model, (iv) the Temperature (Entropy) gradient theory and (v) the Micro-temperature model, are classified according to the used different theoretical frameworks;
- 4). The micromorphic approach is applied to heat transfers and is shown to deliver new generalized heat equations as well as the nonlocal effects. The latter are compared to existing extended heat equations. A new pair of thermodynamically-consistent micromorphic heat equations are derived from appropriate Helmholtz free energy potentials depending on an additional micromorphic temperature and its first gradient. The introduction of the additional micromorphic temperature associated with the classical local temperature leads to a new thermal balance equation taking into account the nonlocal thermal effects and involving an internal length scale which represents the characteristic size of the system. Several existing extended generalized heat equations could be retrieved from constrained micromorphic heat equations with suitable selections of the Helmholtz free energy and heat flux expressions. As an example the propagation of plane thermal waves is investigated according to the various generalized heat equations. Possible applications to fast surface processes, nanostructured media and nanosystems are also discussed.

The simplified inverse approaches and the advanced micromorphic constitutive equations have been implemented in the platforms of KMAS and ABAQUS finite element code respectively. Parametric study of the micromorphic constitutive models as well as various applications in uniaxial tensile test of DP1000 and in sheet metal forming processes, e.g. S-Rail, Box supporter, B-Pillar and Cross section deep drawing, have been performed and compared with experimental results when available.

Résumé

L'objectif de ce travail est de proposer de nouvelles équations constitutives non-locales avancées pour la modélisation et la simulation numérique des procédés de mise en forme de tôles minces sous haute température. Le cadre général de la théorie des milieux micromorphes est utilisé et les aspects suivants sont traités en détail :

- 1). Développement d'une approche numérique simplifiée inverse statique-implicite multi-pas, pour analyser rapidement et efficacement la formabilité de composants mécanique en tôles minces de formes finales connues. Les approches adoptent le modèle classique élastoplastique isotherme basée sur la théorie simplifiée de la déformation totale et des incrémentations intermédiaires nécessaire à une meilleure mise à jour des états de contrainte. Plusieurs configurations intermédiaires sont construites pour mieux représenter les histoires de chargement spécifiques et simplifier la modélisation du contact pièce/outils;
- 2). Formulations d'un ensemble complet d'équations constitutives micromorphiques avancées dans le cadre de la thermodynamique des processus irréversibles avec variables d'état et de la mécanique des milieux continus généralisés, pour capturer les effets non locaux fortement couplés dans les zones de localisation. L'application du principe des puissances virtuelles en présence de nouvelles variables cinématiques (micromorphiques) conduit à des équations d'équilibre supplémentaires prenant en compte les effets non locaux (par exemple, l'endommagement ductile, les effets thermiques, les phénomènes d'écrouissage) et aboutissant à des longueurs internes caractéristiques de la microstructure des matériaux;
- 3). Une discussion approfondie des équations étendues de la chaleur proposées dans la littérature est présentée. Cinq types d'équations thermiques généralisées : (i) le modèle classique de Fourier, (ii) le modèle hyperbolique avec temps de relaxation, (iii) le modèle Double température, (iv) le modèle en gradient d'entropy et (v) - et le modèle de micro-température, sont classés selon les différents cadres théoriques utilisés;
- 4). L'approche micromorphe est appliquée aux transferts de chaleur et est présentée comme étant un cas général duquel sont déduits tous les autres modèles. Une nouvelle paire d'équations de chaleur micromorphes thermodynamiquement cohérentes est dérivée à partir de potentiels d'énergie libre de Helmholtz appropriés en fonction d'une température micromorphe supplémentaire et de son premier gradient. L'introduction de la température micromorphe supplémentaire associée à la température locale classique conduit à une nouvelle équation d'équilibre thermique prenant en compte les effets thermiques non locaux et impliquant une échelle de longueur interne qui représente la taille caractéristique du système. Plusieurs équations de chaleur généralisées étendues existantes pourraient être extraites d'équations de chaleur micromorphe contraintes avec des sélections appropriées des expressions d'énergie libre et de flux thermique de Helmholtz. A titre d'exemple, la propagation des ondes thermiques planes est étudiée en fonction des différentes équations de la chaleur généralisée. Les applications possibles aux procédés de surface rapides, aux milieux nanostructurés et aux nanosystèmes sont également discutées.

RESUME

Les approches inverse simplifiées et les équations constitutives micromorphes avancées ont été mises en œuvre dans des plateformes de code éléments finis KMAS et ABAQUS respectivement. Etude paramétrique des équations constitutives micromorphes ainsi que diverses applications comme l'essai de traction uniaxial en DP1000 et les procédés de formage de tôle, p.ex. S-Rail, Box supporter, B-Pillar et Cross section deep drawing, ont été réalisés et comparés aux résultats expérimentaux quand ils sont disponibles.

General Introduction

According to the International Organization of Motor Vehicle Manufacturers, a total of 90.1 million vehicles were produced globally in 2015, a 1.1% increase compared to 2014. On average, 900kg of steel is used per vehicle, while a typical passenger vehicle emits about 4.7 metric tons of carbon dioxide per year. The international Energy Agency estimates that the transportation sector accounts for approximately 19% of global energy consumption and 23% of energy-related carbon dioxide (CO₂) emissions (IEA, 2015), e.g. about 26% of the US's total greenhouse gas emissions, approximate one-fifth in the EU and around 10% of China's overall CO₂ emissions in 2008.

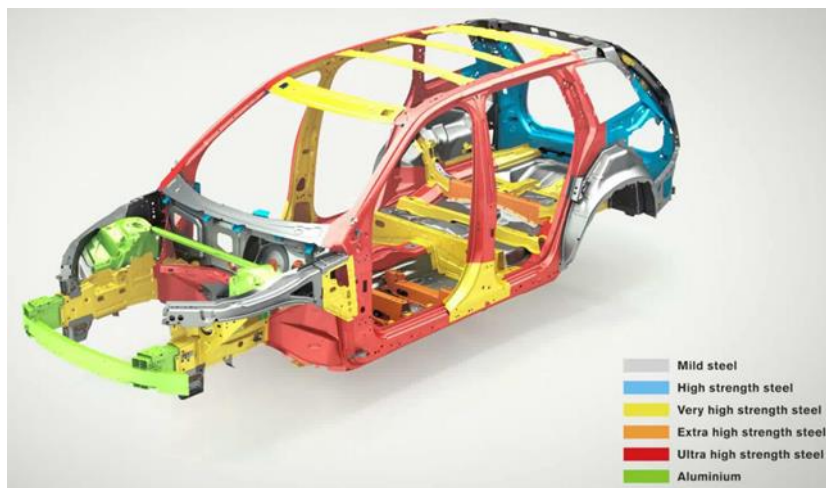


Fig. 0-1 Body Structure of Volvo XC90 2016

In order to meet the new requirements of economy and environment protection, material selection for mass reduction will continue to play an important role. New grades the Advanced High-Strength Steels (AHSS) enable the vehicle manufacturers to reduce weight by 25-39% compared to conventional steel. When applied to a typical five passenger car, the overall weight of the vehicle is reduced by 170 to 270Kg, which corresponds to a lifetime saving of 3 to 4.5 tonnes of greenhouse gases over the vehicle's total life cycle. This saving in emissions represents more than the total amount of CO₂ emitted during the production of all the steel in the vehicle, as shown by the body structure of Volvo XC90 in Fig. 0-1. However, increasing the strength of the as-received steel reduces the stretching capability of the steel because the work hardening exponent decrease with increasing strength for each type of steel (WORLDAUTOSTEEL, 2014). The hot-forming process (Karbasian and Tekkaya, 2010) is a proper way to improve the formability and avoid the large springback of AHSS. In the process, the blank material exhibiting a ferritic-pearlitic microstructure is heated to be austenitized in a furnace at least 5 min at 950°C, afterwards, the blank is formed and quenched simultaneously by the water-cooled die for 5-10s. During the forming process, the metallic material is subjected to large irreversible deformation leading to some macro-defects (local softening, cracking) supposed resulting from the ductile defects (micro-voids and micro-cracks) initiation, growth and propagation in some zones where the plastic strain is highly localized (Fig. 0-2). The fracture of metallic components during their manufacture or during their industrial use is a consequence of the strong localization of thermomechanical fields inside more or less narrow zones. The strong interactions

GENERAL INTRODUCTION

(or coupling) between the intensive thermomechanical fields (stress, strain, hardening, heat, damage ...) inside these localization zones, resulting in some induced softening due to the damage effect and/or to the temperature increase.

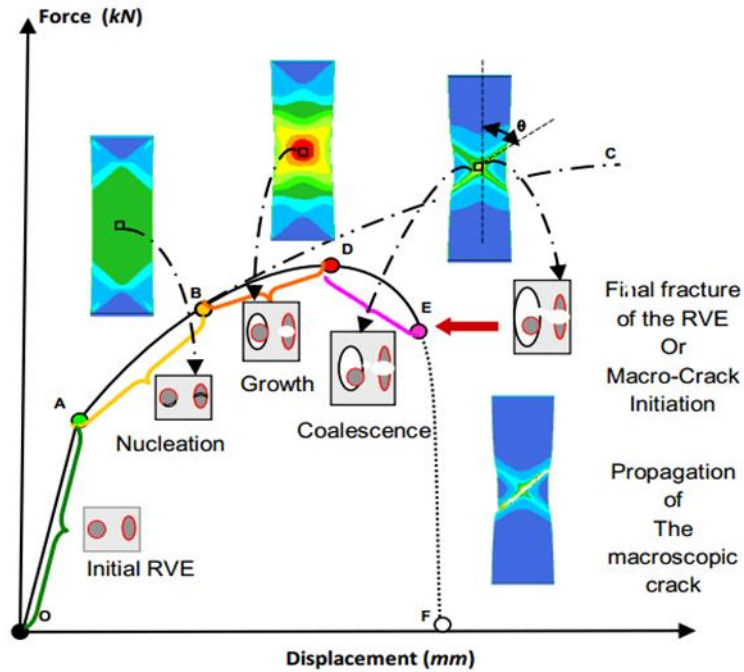


Fig. 0-2 Scheme of the ductile damage effects on the system response of a tension specimen (Saanouni, 2012)

Numerical simulation using the finite element method (FEM) is a considerable asset for the mechanical engineering industries. It takes an increasing and dominant place in certain fields of automotive industry. To simulate numerically a given forming process, a 3D model describing the main physical phenomena characterizing the thermomechanical behavior of the sheet is required. Because of the need for taking into account the interactions (or coupling) between the various thermo-mechanical phenomena exhibited inside the deformed metal, advanced (with high predictive capabilities) constitutive equations are crucial for the numerical simulation of forming processes. This can be done by using two kinds of modelling approach namely: the macroscopic phenomenological and monoscale approach and the micro-macro or multi-scale approach. The multi-scale approach in metal forming of metallic materials, based on the polycrystalline plasticity theory, is mainly used to describe the effects of the initial microstructure of the polycrystalline materials and its evolution during large plastic deformation (textural evolution) as can be found in works (Abdul-Latif and Saanouni, 1994; Boudifa et al., 2009; Franciosi et al., 1980) among many others. The macroscopic approach, which is the widely used one in metal forming, concerns the conventional plasticity with isotropic hardening based on a yield function using an anisotropic equivalent stress (quadratic or non-quadratic) together with a scalar hardening function (power function of the accumulated plastic strain). However, when the inelastic strains are very large they tend to localize inside narrow bands (shear bands) during the inelastic flow giving rise to the initiation, growth and coalescence of some micro-voids and micro-cracks. To describe this strong interactions between the inelastic (plastic or viscoplastic) flow and the ductile damage occurrence, several theories have been proposed. Firstly, the

GENERAL INTRODUCTION

most widely used approach in metal forming is based on the Gurson's type ductile damage modelling (Gurson, 1977) in order to describe as accurately as possible the ductile damage occurrence (Bontcheva and Iankov, 1991; Pardoen et al., 2004). In these approaches, the damage is mainly described by the volume fraction of the spherical or elliptical voids. This scalar variable is introduced in the plastic potential affecting the plastic flow through the normality rule and gives a decrease on the stresses when the void volume fraction increases under the applied external loading. Secondly, another kind of approaches, based on the continuum damage mechanics (CDM), represents the ductile damage by a scalar or tensor variable (Kachanov, 1986; Lemaitre, 1992; Lemaitre et al., 1985; Murakami, 2012; Saanouni, 2012) and its effect on the material behavior is accounted for thanks to the hypothesis of the strain equivalence, stress equivalence or energy equivalence (Boudifa et al., 2009; Chaboche et al., 2006; Chaboche, 1988a, b; Saanouni, 2008; Saanouni, 2012). This kind of fully coupled CDM approach has been used for damage prediction in metal forming assuming various types of coupling in some published works (Bezzina and Saanouni, 1996; Khelifa et al., 2005; Lee et al., 1985; Mathur and Dawson, 1987).

However, the well-established initial and boundary value problems based on fully local formulations of continuum damage mechanics exhibiting strong damage-induced softening due to thermal, damage or any other microstructure-dependent phenomena, lead to the numerical solutions highly sensitive to the space and time discretization and giving a physically meaningless solution. In mathematically, this results from the strain softening induced loss of ellipticity of the governing equations. The nature way to avoid this drawback is to considering nonlocal effects contributed from an approximate neighborhood of each material point within some characteristic lengths. The mechanics of generalized continua, which enables the introduction of the characteristic lengths into the constitutive equations of material with microstructure, is an adequate way to regularize the associated initial and boundary value problem (IBVP). Various generalized continuum theories, proposed mainly in 1890th (Cosserat and Cosserat, 1896, 1909) and during the 1960th (Eringen, 1966b; Eringen and Suhubi, 1964; Mindlin, 1965; Mindlin and Tiersten, 1962; Suhubi and Eringen, 1964; Toupin, 1962), have been used during the last decades (mainly since the 1980s) in order to accounting for some effects of characteristic lengths related to the material's microstructure and leading to a wide range of models. As summarized by Forest (2009), all these generalized continuum theories, which are still based on the assumption of local action, can be classified into two classes: (i) the higher grade continua and (ii) the higher order continua. Higher grade continua are those based on higher order spatial derivatives of the displacement field as originally proposed in literatures (Mindlin, 1965). On the other hand, higher order continua are based on the introduction of additional degrees of freedom as pioneered by the Cosserat brothers (Cosserat and Cosserat, 1896, 1909) and extensively developed by Eringen and his co-workers in 1960s (Eringen, 1966a, c, 1999; Eringen and Suhubi, 1964). A third class of generalized continuum theories is the so-called strictly nonlocal continuum field theories, initially introduced by Kröner, Krumhansl and others (Beran and McCoy, 1970; Kröner, 1967, 1968; Krumhansl, 1968; Kunin, 1968; Levin, 1971) as well as well-developed and summarized by Eringen et al. (Eringen, 2002; Eringen and Edelen, 1972) where a unified foundation of the basic field equations is presented and various main contributing works in the field are referenced. This class of nonlocal theories, which are not based on the principle of the local action, is 'concerned with the physics of material bodies whose behavior at a material point is influenced by the state of all points of the body'.

GENERAL INTRODUCTION

This work aims to develop an advanced generalized constitutive model of thermomechanical coupling in the framework of the generalized continuum mechanics (micromorphic theory) to introduce the concept of internal lengths that are representative of the material microstructures while accounting for the initial anisotropy under finite deformations. The structure of the thesis is organized as follows:

In **Part I**, the simplified static-implicit FEM Inverse approaches are initially developed to providing efficient formability analysis of the pre-designed forming component.

- 1). In Chapter I, the widely used one-step inverse approach is briefly revisited for the nonlinear kinematic formulations and total deformation based constitutive equations;
- 2). In Chapter II, the multi-step approach is developed by considering several intermediate deformable configurations, which are constructed through solving a quadratic optimal program and equilibrium iterations with generated initial solutions, to improve the history of the stress field. Accordingly, the measurement of finite logarithmic strain between successive middle configurations is reformulated; the local integration is performed using the elastoplastic model as well as the associated flow theory;
- 3). In Chapter III, numerical validations and applications are performed to various metal forming components.

In **Part II**, we concentrate on the development of a complete set of thermodynamically consistent generalized nonlocal constitutive model to capture the strong coupling between the intensive thermomechanical fields inside the strain-softening regime which results in the macro crack.

- 1). In Chapter VI, a complete set of micromorphic constitutive equations, strongly coupled with elasto-visco-plasticity, thermal effect, mixed hardening and ductile damage, as well as the associated micromorphic state variables characterizing size effects, is formulated under the framework of thermodynamics of irreversible processes. The introduction of the micromorphic degrees of freedom (dofs) related to the targeted micromorphic phenomena, leads to new additional balance equations involving some material internal lengths. Focusing on thermal aspects, a thorough discussion of existing extended and generalized heat equations derived from the micromorphic approach to heat transfer are well presented. Several existing extended heat equations could be retrieved from constrained micromorphic heat equations with appropriate selections of Helmholtz free energy and heat flux models;
- 2). Chapter VII presents the numerical aspects: the weak forms of the IBVP, the space discretization using shell and solid-shell finite element, the global resolution scheme as well as the fully implicit local integration scheme of the viscoplastic model;
- 3). In Chapter VIII, the parametric study of the local damage parameters, the viscoplastic moduli, the micromorphic moduli of damage and isotropic hardening, as well as the temperature dependent parameters in the micromorphic constitutive model and the impact on the solution of the associated IBVP are analyzed;
- 4). In Chapter IX, the material parameters of DP1000 are identified and applied to the uniaxial tension test with the micromorphic damage and isotropic hardening models respectively. The application of the micromorphic damage model to a cross section deep drawing process is performed and compared with the experimental results;

Finally, the main conclusions and perspectives of the present work are presented.

GENERAL INTRODUCTION

Part I Simplified inverse approaches for sheet metal forming

Content

PART I SIMPLIFIED INVERSE APPROACHES FOR SHEET METAL FORMING	6
INTRODUCTION	7
I. THE STATIC IMPLICIT ONE-STEP INVERSE APPROACH.....	9
I.1 INTRODUCTION	9
I.2 KINEMATIC FORMULATIONS OF TOTAL STRAIN	9
I.3 CONSTITUTIVE EQUATIONS USING THE DEFORMATION THEORY	11
I.4 SIMPLIFIED TOOLS' ACTIONS	12
II. THE STATIC IMPLICIT MULTI-STEP APPROACH	15
II.1 INTRODUCTION	15
II.2 KINEMATIC FORMULATIONS OF INCREMENTAL STRAIN.....	15
II.3 LOCAL INTEGRATIONS BASED ON FLOW THEORY	18
II.3.1 <i>Classical elastoplastic local integration</i>	18
II.3.2 <i>Examination of scalar return mapping method</i>	19
II.4 CONSTRUCTION OF INTERMEDIATE CONFIGURATIONS	22
II.4.1 <i>Resolution of the sliding surface</i>	22
II.4.2 <i>Initial solutions of the middle configuration</i>	25
II.4.3 <i>Equilibrium of the middle configurations</i>	27
III. NUMERICAL APPLICATIONS	30
III.1 S-RAIL PART OF NUMISHEET 96.....	30
III.1.1 <i>Verification and estimation of the derived kinematic formulations</i>	31
III.1.2 <i>Errors in accumulated total strain of different layers</i>	34
III.1.3 <i>The constructed intermediate configurations</i>	34
III.2 APPLICATION TO B-PILLAR COMPONENT OF NUMISHEET 08.....	35
III.3 THE BOX SHAPED HOLDER PART	37
III.3.1 <i>The middle configurations using enhanced PMA method</i>	38
III.3.2 <i>The updated stress state</i>	39
IV. CONCLUSIONS	41

Introduction

The inverse approach, originally proposed by Guo et al. (1990) to predict the deformation of forming parts with a geometrical knowledge of the designed workpiece, is widely used in the initial design stage of sheet metal forming due to its high efficiency. It costs much less computation than the incremental algorithm, mainly benefited from the simple constitutive equations of total stress and total strain derived from the Henchy deformation theory and the simplified tools' actions instead of the complex contact search processes. Numerous examinations shows that the inverse approach provides fairly well estimations in strain but poor accuracy of stress due to lacking in deformation histories.

The multi-step or multi-stage approach, initially proposed by Majlessi and Lee (1987, 1988), assumed that the forming processes were able to be decomposed into several steps, which retained proportional loading assumption and the principle of minimum potential energy from one to the next configuration, with intermediate configurations constructed from the geometric proportional method. The membrane element was implemented to analyze the axisymmetric problems. Lee and Huh (1998) followed this methodology and extended the inverse analysis to the general 3D multi-step analysis with developed three coordinates systems. The square cup drawing and oil-pan drawing were performed to optimize the initial blank shape with given geometrically generated sliding surfaces. Lee and Cao (2001) developed an axisymmetric shell element for the multi-step inverse analysis to improve the accuracy of the calculated initial blank shape and the strain distribution in deep drawing processes. Kim and Huh (2002) proposed the concept of constrained sliding surface which could be constructed directly by connecting the contact nodes obtained from the contact search processes. A direct mesh mapping method was developed to generate initial solutions of the section lines and was applied to the multi-stage rectangular cup and S-Rail forming processes. Guo et al. (2004) proposed the Pseudo-Inverse Approach (PIA) to improve stress estimation with elastoplastic isotropic damage model. The "True" intermediate configurations were generated by the method of minimization of the sheet profile's length in the view of geometrical calculation. The initial solution was generated by mapping blank's mesh onto the sliding surface retained same curvilinear length and angular position with respect to a reference center. The efficient scalar-prediction return mapping method was developed to implement the local integrations. However, the strain increments were calculated from the subtraction of the total strains between two successive configurations. Huang et al. (2006) proposed a modified arc-length search method to obtain the initial solutions on the intermediate three-dimensional configurations and introduced an sliding strategy forcing the nodes to retain on constrained sliding surface during Newton-Raphson iterations. Li et al. (2007) proposed an efficient algorithm (the direct scalar algorithm) for local integration. The direct scalar algorithm, introducing an elastic unloading-reloading factor, was taken as the initial solution of return mapping method to stable the iterative scheme. Tang et al. (2010) followed the PIA approach and extended it to the general three dimensional case. An approach of minimization of area solved by the sequential quadratic programming, was developed to generate the constrained intermediate surfaces. And a walk-through strategy was proposed to control the sliding of material points on the sliding surfaces. Halouani et al. (2012) applied the PIA to axisymmetric cold forging processes. The geometric proportional approach and the method of correctional free surface were proposed to generate the initial solutions of

PART I INTRODUCTION

the intermediate configurations. For the incremental deformation theory, the deformation path was assumed to be the minimum plastic work path in homogeneous deformation. Chung and Richmond (1993) presented this theory in which the increment of total strain is proportional to the fixed strain increment. A mathematical description of the constitutive law of deformation plasticity is developed based upon this path for rigid-plastic and for elastoplastic materials. Ramakrishnan et al. (1998) proposed a simple constitutive equation relating Cauchy stress tensor to a total-elastic-incremental-plastic strain (TEIP). A special form of the constitutive relation in the context of J₂ plasticity is presented that ensures that the proposed constitutive equation naturally obeys the normality and associative flow rules. Robert et al. (2012) presented a comparison between this theory and the flow theory with the Nakazima test and cylindrical cup of incremental sheet forming processes.

In this part, concentrating on the isothermal elastoplasticity coupled with isotropic hardening, the simple inverse approach is briefly reviewed and the multi-step approach is formulated in detail.

I. The static implicit one-step inverse approach

I.1 Introduction

The basic idea of the inverse approach is to perform a non-linear analysis to determine the positions of the material points in the initial flat blank and the strains in the final (known) drawn workpiece without considering the incremental processes of plasticity and contact. It takes the following assumptions: (i) planar stress state; (ii) finite elastoplastic strain with full incompressibility; (iii) deformation theory of plasticity; (iv) isotropic hardening law; (v) simplified tools' actions of pressure and friction forces;

In this section, the basic static implicit one-step inverse approach is reviewed. The purpose is not to go with details, but to represent the original work where the author's research starts from. Detailed formulations and discussions can be found in literatures (Batoz et al., 1998; Guo et al., 1990; Guo et al., 2002; Guo et al., 2003; Guo et al., 2000), among many others.

I.2 Kinematic formulations of total strain

In the inverse approach, only two configurations: the unknown initial flat blank (reference configuration) C^0 with given thickness distributions, and the final deformed workpiece (current configuration) C , are considered with simplified contact and friction conditions.

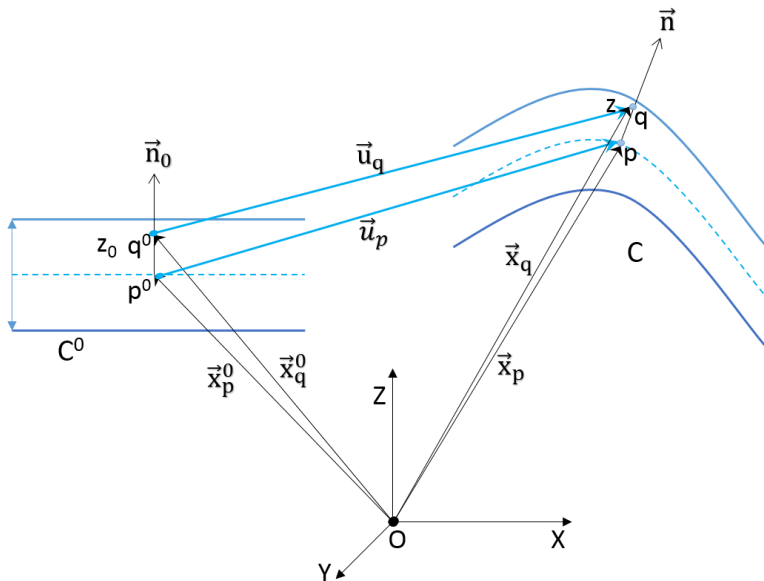


Fig. I-1 Kinematic relations of material point

Considering the movement of a material point from C^0 to C , leads to:

$$\{dx^0\} = \left([I] - \left[\frac{\partial u}{\partial x} \right] \right) \{dx\} = [F]^{-1} \{dx\} \quad (I.1)$$

The left Cauchy-Green tensor which describes the length and angle variations is defined as:

$$\langle dx^0 \rangle \{ dx^0 \} = \langle dx \rangle [F]^{-T} [F]^{-1} \{ dx \} = \langle dx \rangle [B]^{-1} \{ dx \} \quad (I.2)$$

The deformation at a point can be described by three principal stretches λ_i :

$$\lambda_i^{-2} = \frac{(dS_i^0)^2}{(dS_i)^2} = \frac{\langle dS_i \rangle [B]^{-1} \{ dS_i \}}{\langle dS_i \rangle \{ dS_i \}} = \langle n_i \rangle [B]^{-1} \{ n_i \} \quad (i=1,2,3) \quad (I.3)$$

or

$$[\lambda]^{-2} = [M][B]^{-1}[M] \quad (I.4)$$

with

$$[\lambda] = \begin{bmatrix} \lambda_1 & & \\ & \lambda_2 & \\ & & \lambda_3 \end{bmatrix} \quad [M] = \begin{bmatrix} \{n_1\} & \{n_2\} & \{n_3\} \end{bmatrix} \quad (I.5)$$

λ_i^{-2} and $\{n_i\}$ are the eigenvalues and eigenvectors of $[B]^{-1}$. $[M]$ defines the transformation between the local coordinates and the principal strain coordinates.

Considering the two material points q and q^0 along the thickness directions, as shown in Fig. I-1, which are placed on the reference and current configurations respectively, as shown in Fig., their position vectors can be expressed as:

$$\vec{x}_q = \vec{x}_p + z \vec{n} \quad \vec{x}_q^0 = \vec{x}_p^0 + z_0 \vec{n}_0 = \vec{x}_p - \vec{u}_p + z_0 \vec{n}_0 \quad (I.6)$$

where \vec{n} and \vec{n}_0 are the normal of the mid-surface at material points p and p^0 respectively. \vec{u}_p is the displacement vector of the point p with respect to its initial position p^0 .

Introducing two unit orthogonal tangent vectors \vec{t}_1 and \vec{t}_2 on C , leads to the following relations:

$$\{dx_q\} = [F_x]\{dx\} \quad \{dx_q^0\} = [F_x^0]^{-1}\{dx\} \quad (I.7)$$

where,

$$[F_x] = [T]([I] + z [b]) \quad [F_x^0]^{-1} = \begin{bmatrix} \vec{t}_1 - \vec{u}_{p,x} & \vec{t}_2 - \vec{u}_{p,y} & \frac{1}{\lambda_3} \vec{n}_0 \end{bmatrix} \quad (I.8)$$

In which, $[T] = [\vec{t}_1 \quad \vec{t}_2 \quad \vec{n}]$, $[b]$ is the curvature tensor of the configuration C :

$$[b] = \begin{bmatrix} \vec{t}_1 \cdot \vec{n}_{,x} & \vec{t}_1 \cdot \vec{n}_{,y} & 0 \\ \vec{t}_2 \cdot \vec{n}_{,x} & \vec{t}_2 \cdot \vec{n}_{,y} & 0 \\ 0 & 0 & 0 \end{bmatrix} = \begin{bmatrix} -r & -s & 0 \\ -s & -t & 0 \\ 0 & 0 & 0 \end{bmatrix} \quad (I.9)$$

r, s, t are the components of the curvature tensor of the deformed shell.

By assuming that the sheet is thin enough, the deformation gradient tensor from q^0 to q can be approximately expressed as:

$$[F]^{-1} = [F_x^0]^{-1} [F_x]^{-1} \approx [F_x^0]^{-1} ([I] - z [b]) [T]^T \quad (I.10)$$

and the inverse of left Cauchy-Green deformation tensor is given by:

$$[B]^{-1} = [F]^{-T} [F]^{-1} \approx \begin{bmatrix} a & b & 0 \\ b & c & 0 \\ 0 & 0 & (\lambda_3)^{-2} \end{bmatrix} \quad (I.11)$$

where,

$$\begin{aligned} a &= a_0(1+zr)^2 + 2b_0sz(1+rz) + c_0(sz)^2 \\ b &= a_0(1+rz)sz + b_0(1+rz)(1+zt) + b_0(sz)^2 + c_0sz(1+zt) \\ c &= a_0(sz)^2 + 2b_0sz(1+zt) + c_0(1+zt)^2 \end{aligned} \quad (I.12)$$

with

$$\begin{aligned} a_0 &= 1 - 2\vec{t}_1 \cdot \vec{u}_{p,x} - (\vec{u}_{p,x})^2 \\ b_0 &= -\vec{t}_1 \cdot \vec{u}_{p,y} - \vec{t}_2 \cdot \vec{u}_{p,x} + \vec{u}_{p,y} \cdot \vec{u}_{p,x} \\ c_0 &= 1 - 2\vec{t}_2 \cdot \vec{u}_{p,y} - (\vec{u}_{p,y})^2 \end{aligned} \quad (I.13)$$

Then, the planar principle stretches λ_1 and λ_2 are obtained from the eigenvalues of $[B]^{-1}$:

$$\lambda_i = \left[\frac{1}{2}(a+c) \pm \frac{1}{2}\sqrt{(a-c)^2 + 4b^2} \right]^{-1/2} \quad (I.14)$$

If the incompressibility is assumed, the thickness stretch is given by:

$$\lambda_3 = \frac{1}{\lambda_1 \lambda_2} = \frac{h}{h_0} \quad (I.15)$$

Finally, the logarithmic strain tensor expressed in the local coordinate is obtained:

$$[\varepsilon] = \begin{bmatrix} \varepsilon_x & \varepsilon_{xy} & 0 \\ \varepsilon_{xy} & \varepsilon_y & 0 \\ 0 & 0 & \varepsilon_z \end{bmatrix} = [M] \begin{bmatrix} \ln \lambda_1 & & \\ & \ln \lambda_2 & \\ & & \ln \lambda_3 \end{bmatrix} [M]^T \quad (I.16)$$

I.3 Constitutive equations using the deformation theory

Considering the heterogeneity of rolling sheet, the Hill's anisotropic yield function is defined as:

$$f(\sigma, q) = (\langle \sigma \rangle [P] \{\sigma\})^{1/2} - \bar{\sigma}_s(\bar{\varepsilon}^p) = 0 \quad (I.17)$$

with

$$[P] = \begin{bmatrix} 1 & -\frac{r}{1+r} & 0 \\ -\frac{r}{1+r} & 1 & 0 \\ 0 & 0 & \frac{2(1+2r)}{1+r} \end{bmatrix} \quad (I.18)$$

where, $r = \frac{1}{4}(r_0 + 2r_{45} + r_{90})$ is the normal anisotropic coefficient. r_0 , r_{45} and r_{90} are the anisotropic coefficients of degree 0, 45 and 90 with respect to the rolling direction, respectively.

The Henchy deformation theory declared that the stress tensor at every point is proportional to a tensor independent of time, is adopted. If we assume that the (small) elastic strains have the same anisotropic directions as the plastic ones, the following total constitutive equation is obtained:

$$\{\sigma\} = \frac{\bar{\sigma}}{\bar{\varepsilon}} [P]^{-1} \{\varepsilon\} \quad (I.19)$$

where, $\bar{\sigma}$ and $\bar{\varepsilon}$ are the equivalent stress and equivalent strain respectively.

I.4 Simplified tools' actions

The contact conditions between the sheet and the tools are simply replaced by some external forces on the sheet. The unknown contact force of punch \vec{F} is decomposed into normal pressure force \vec{F}_N and friction force \vec{F}_t , as shown in Fig. I-2:

$$\begin{aligned} \vec{F}\vec{n}^f &= \vec{F}_N\vec{n} + \vec{F}_t(-\vec{t}) \\ \tan\theta &= \frac{F_t}{F_N} = \mu \\ \vec{n}^f &= \frac{1}{\sqrt{1+\mu^2}}(\vec{n} - \mu\vec{t}) \end{aligned} \quad (I.20)$$

where \vec{n}^f is the direction of punch force, \vec{n} is the normal vector of the sheet tangent plane, $\vec{t} = \vec{u}_t / \|\vec{u}_t\|$ is a unit vector given by the projection on the sheet tangent plane of the relative movement between the sheet and the punch, μ is the friction coefficient, $\vec{u}_t = \vec{u} - (\vec{u}_h \cdot \vec{n})\vec{n}$ is the component of the displacement vector \vec{u} of the node along the tangent direction \vec{t} , and \vec{u}_h is the horizontal component of the displacement which is given at each iteration.

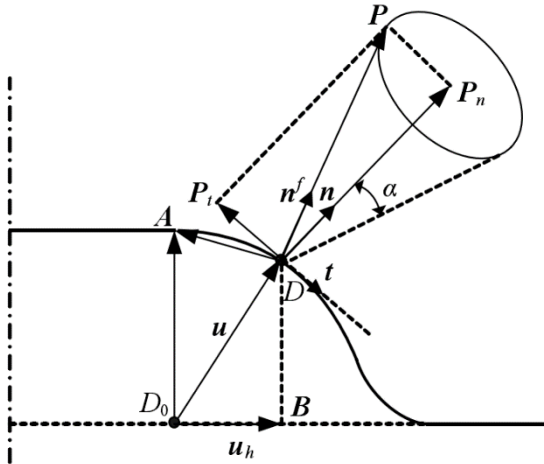


Fig. I-2 Friction forces of the punch

Considering the known constrained vertical displacement of each node, the punch force can be evaluated by:

$$F = \frac{F_{\text{int}}^z}{n_z^f} \quad (\text{I.21})$$

where, F_{int}^z and n_z^f are components of the internal force and the punch load normal along the Z axial.

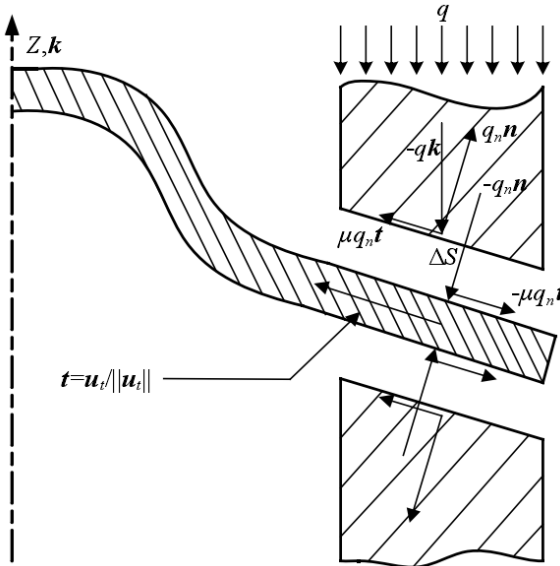


Fig. I-3 Friction forces of the blankholder

Under the blankholders, only the friction force is considered as the external force (Fig. I-3):

$$\vec{f} = -2\mu q_n \vec{t} \quad (\text{I.22})$$

where q_n is the known normal pressure.

PART I CHAPTER I INVERSE APPROACH

II. The static implicit multi-step approach

II.1 Introduction

Due to the nature defects of the inverse approach, several intermediate configurations reflecting the loading paths are introduced to improve the stress estimations. In this section, the multi-step approach introducing several constructed intermediate configurations is formulated. The constrained sliding surfaces are generated using the efficient geometric method and the mechanical initial solutions are obtained by the mapping technique. The finite forward strain increment is reformulated due to the successive deformed reference configurations. The local integration of the normal anisotropic elastoplastic model is performed by the classical return mapping algorithm and the scalar mapping method is examined to show its limitation. The main procedures in the multi-step approach can be summarized as follows:

- 1). Constructions of the intermediate configurations. Commonly, it needs two steps: constrained sliding surface and its initial solutions, to generate a proper intermediate configuration. The sliding surface of the blank sheet is supposed to be a deformed tensional membrane subjected to the Punch and Die at each interval, and can be constructed from the contact processes or geometric approaches. After that, the initial solutions, to position all the material points of the blank sheet on the sliding surface, are generated from the mapping approach.
- 2). Nonlinear kinematic formulations - the measurement of the strain increment between two successive configurations. The detailed kinematic formulations are derived in Section 2 for both flatten (case of one-step approach) and curved reference configurations. For the curved references, the upward formulations, instead of the subtraction of the total strains, of the measurement in strain increments are derived.
- 3). Constitutive local integrations. Due to the large finite strain increments, the classical Return Mapping method with an iterative scheme is considered to update the stress state.

II.2 Kinematic formulations of incremental strain

Now, concerning the curved reference configuration C^1 , the vectors of material points q and q^1 , shown in Fig. II-1, are expressed as:

$$\vec{x}_q = \vec{x}_p + z\vec{n} \quad \vec{x}_q^1 = \vec{x}_p^1 + z_1\vec{n}_1 = \vec{x}_p - \vec{u}_p + z_1\vec{n}_1 \quad (I.23)$$

where \vec{n} is the normal of the material point p positioned on the mid-surface, \vec{u}_p is the displacement vector of point p with respect to the reference configuration C^1 . Considering a material point q infinitely closed to the material point p along the normal direction, leads to:

$$d\vec{x}_q = d\vec{x}_p + zd\vec{n} + \vec{n} \cdot dz \quad d\vec{x}_q^1 = d\vec{x}_p^1 + z_1d\vec{n}_1 + \vec{n}_1 \cdot dz_1 \quad (I.24)$$

clearly, $d\vec{n}_1 \neq 0$ describes the curvature of the reference configuration C^1 .

Two unit orthogonal tangent vectors \vec{o}_1 and \vec{o}_2 are introduced on the mid-surface of final configuration C . Let x and y be the physical orthogonal curvilinear coordinates:

$$\vec{o}_1 = \vec{x}_{p,x} \quad \vec{o}_2 = \vec{x}_{p,y} \quad [\mathcal{T}] = [\vec{o}_1 \quad \vec{o}_2 \quad \vec{n}] \quad (I.25)$$

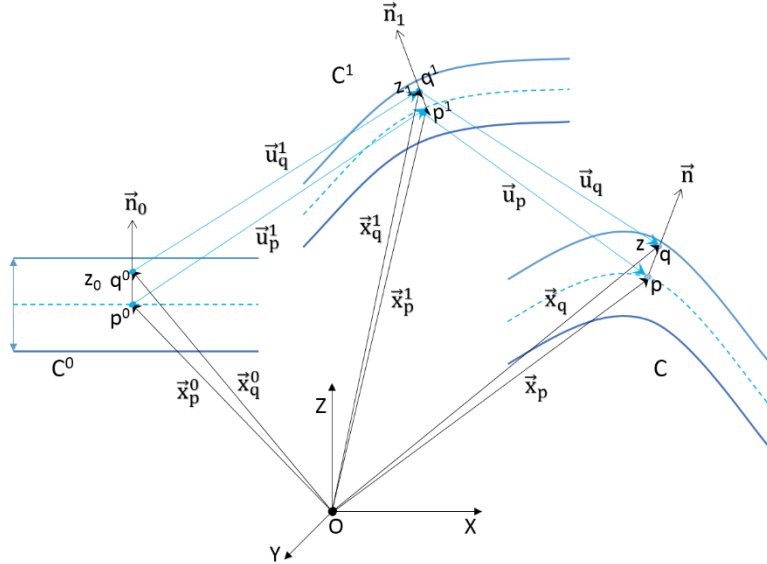


Fig. II-1 Kinematical relations of material point in three configurations

The first equation in Eq.(I.24) can be rewrite as:

$$d\vec{x}_q = (\vec{o}_1 + z\vec{n}_{,x})dx + (\vec{o}_2 + z\vec{n}_{,y})dy + \vec{n} \cdot dz \quad (I.26)$$

or in matrix form:

$$\{dx_q\} = [F_x] \{dx\} \quad (I.27)$$

with

$$[F_x] = [\vec{o}_1 + z\vec{n}_{,x} \quad \vec{o}_2 + z\vec{n}_{,y} \quad \vec{n}] = [\mathcal{T}] ([I] + z[b]) \quad (I.28)$$

and

$$[b] = \begin{bmatrix} \vec{o}_1 \cdot \vec{n}_{,x} & \vec{o}_1 \cdot \vec{n}_{,y} & 0 \\ \vec{o}_2 \cdot \vec{n}_{,x} & \vec{o}_2 \cdot \vec{n}_{,y} & 0 \\ 0 & 0 & 0 \end{bmatrix} = \begin{bmatrix} -r & -s & 0 \\ -s & -t & 0 \\ 0 & 0 & 0 \end{bmatrix} \quad (I.29)$$

r , s and t are the components of the curvature tensor of the configuration C .

Recall the Eq.(I.24), the second equation can be expressed as:

$$d\vec{x}_q^1 = (\vec{o}_1 - u_{p,x} + z_1 \vec{n}_{1,x})dx + (\vec{o}_2 - u_{p,y} + z_1 \vec{n}_{1,y})dy + \left(\frac{1}{\lambda_3} \vec{n}_1 + z_1 \vec{n}_{1,z} \right)dz \quad (I.30)$$

or in matrix form:

$$\{dx_q^1\} = [F_x^1]^{-1} \{dx\} \quad (I.31)$$

where,

$$[F_x^1]^{-1} = \begin{bmatrix} \vec{o}_1 - \vec{u}_{p,x} & \vec{o}_2 - \vec{u}_{p,y} & \frac{1}{\lambda_3} \vec{n}_1 \end{bmatrix} + \begin{bmatrix} z_1 \vec{n}_{1,x} & z_1 \vec{n}_{1,y} & 0 \end{bmatrix} \quad (I.32)$$

Clearly, the deformation gradient tensor of Eq.(I.32) is quite different from the Eq.(I.8), which referenced the initial configuration C^1 .

Using the Eqs.(I.24), (I.26) and (I.30), the inverse of deformation gradient tensor $[F]^{-1}$ between configurations C^1 and C is expressed as:

$$[F]^{-1} = [F_x^1]^{-1} [F_x]^{-1} \approx [F_x^1]^{-1} ([I] - z[b]) [T]^T \quad (I.33)$$

The inverse of left Cauchy-Green deformation tensor $[B]^{-1}$ is defined as:

$$[B]^{-1} = [F]^{-T} [F]^{-1} \approx \begin{bmatrix} a & b & 0 \\ b & c & 0 \\ 0 & 0 & (\lambda_3)^{-2} \end{bmatrix} \quad (I.34)$$

where,

$$\begin{aligned} a &= A_0(1+sr)^2 + 2B_0sz(1+sr) + C_0(sz)^2 \\ b &= A_0(1+sr)sz + B_0(1+sr)(1+zt) + B_0(sz)^2 + C_0sz(1+zt) \\ c &= A_0(sz)^2 + 2B_0sz(1+zt) + C_0(1+zt)^2 \end{aligned} \quad (I.35)$$

with

$$\begin{aligned} A_0 &= a_0 - z_1 \vec{n}_{1,x} (2(\vec{o}_1 - \vec{u}_{p,x}) + z_1(\vec{n}_{1,x})) \\ B_0 &= b_0 - z_1 ((\vec{o}_2 - \vec{u}_{p,y}) \vec{n}_{1,x} + (\vec{o}_1 - \vec{u}_{p,x}) \vec{n}_{1,y} + z_1 \vec{n}_{1,x} \vec{n}_{1,y}) \\ C_0 &= c_0 - z_1 \vec{n}_{1,y} (2(\vec{o}_2 - \vec{u}_{p,y}) + z_1(\vec{n}_{1,y})) \end{aligned} \quad (I.36)$$

It's worth to note that, if the material points are placed on the mid-surface ($z=0$), the Eq.(I.36) will descend to the Eq.(I.13). Consequently, the logarithmic strain increment obtained from Eq.(I.34) and the one given by Eq.(I.11) will be the same; for material points outside of the mid-surface, the strain increment estimated from the equation Eq.(I.35) provides apparently differences compared with the strain increment measured from Eq.(I.12), due to the curved reference configuration, which has severe effects on the left Cauchy-Green deformation tensor for material points along the thickness.

In summary, the measurement of strain increment from the inverse (one-step) approach (Eq.(I.11)) is only valid for the measurement on the mid-surface in the multi-step approach. In order to obtain the logarithmic strain increment and the accumulated strain, the left Cauchy-Green deformation tensor should be revised by Eq.(I.34), due to the bending effects from the deformed intermediate configurations. The differences of the accumulated strains are also examined from the numerical aspects in the following sections.

II.3 Local integrations based on flow theory

In this section, the classical anisotropic elastoplasticity coupled with isotropic hardening (Power-Law hardening) is chosen to perform the material responses in sheet metal forming processes. The associated normality rule as well as the quadratic plastic potential of Hill48 are restored to govern the evolution equations. In order to update the stress state for given strain increment, the classical Return Mapping algorithm (Ortiz and Simo, 1986; Simo and Hughes, 1998) with the Newton-Raphson iterative scheme is considered as an efficient method. On the other hand, the widely applied Scalar Return Mapping method (Guo et al., 2004; Halouani et al., 2012; Li et al., 2007; Titeux et al., 2004), which was initially proposed to overcome the convergence difficulties induced by the large strain increments, is also carefully examined to show its limitations.

II.3.1 Classical elastoplastic local integration

The quadratic plastic potential is defined as:

$$f(\sigma, q) = (\langle \sigma \rangle [P] \{ \sigma \})^{1/2} - \bar{\sigma}_s(q) = (\langle \sigma \rangle [P] \{ \sigma \})^{1/2} - \bar{\sigma}_s(\bar{\varepsilon}^p) \quad (I.37)$$

where, σ represents the Cauchy stress, q indicates the internal variables for isotropic hardening and usually takes to the equivalent plastic strain $\bar{\varepsilon}^p$, $\bar{\sigma}_s$ is the equivalent uniaxial yield stress, $[P]$ represents the anisotropic tensor (in plane stress state) as given in Eq.(I.18).

In this work, the classical multiplicative decomposition of the total gradient $[F]$ into elastic $[F^e]$ and plastic $[F^p]$ parts. In order to ensure fulfilment of the objectivity all the constitutive equations will be written with respect to the rotating frame defined by the rotation tensor $[Q]$. The evolution of this rotation tensor is defined in kinematical way based on the corotational framework. It leads to $[\dot{\varepsilon}] = [\dot{\varepsilon}^{el}] + [D^p]$ which is the additive decomposition of the total strain rate tensor into elastic part $[\dot{\varepsilon}^{el}]$ (Jaumann rate) and plastic part $[D^p]$. According to the normality rule, the rate of the plastic strain is given by:

$$\{D^p\} = \dot{\lambda} \left\{ \frac{\partial f}{\partial \{\sigma\}} \right\} = \dot{\lambda} \frac{[P] \{ \sigma \}}{(\langle \sigma \rangle [P] \{ \sigma \})^{1/2}} \quad (I.38)$$

where, λ indicates the Lagrange plastic multiplier.

The rate of stress can be expressed as:

$$\{\dot{\sigma}\} = [C]\{\dot{\varepsilon}\} - \lambda [C] \left\{ \frac{\partial f}{\partial \{\sigma\}} \right\} \quad (I.39)$$

where, $[C]$ represents the elastic modulus tensor.

The plastic multiplier λ is obtained from the constraint of the plastic consistency condition ($\dot{f} = 0$):

$$\lambda = \frac{\left\langle \frac{\partial f}{\partial \{\sigma\}} \right\rangle [C]\{\dot{\varepsilon}\}}{\left\langle \frac{\partial f}{\partial \{\sigma\}} \right\rangle [C] \left\{ \frac{\partial f}{\partial \{\sigma\}} \right\} - \frac{\partial f}{\partial q}} \quad (I.40)$$

Substituting the above plastic multiplier into Eq.(I.39), leads to the elastoplastic module tensor C^{ep} :

$$\dot{\sigma} = [C^{ep}]\{\dot{\varepsilon}\} = \left([C] - \frac{[C] \left\{ \frac{\partial f}{\partial \{\sigma\}} \right\} \left\langle \frac{\partial f}{\partial \{\sigma\}} \right\rangle [C]}{\left\langle \frac{\partial f}{\partial \{\sigma\}} \right\rangle [C] \left\{ \frac{\partial f}{\partial \{\sigma\}} \right\} - \frac{\partial f}{\partial q}} \right) \{\dot{\varepsilon}\} \quad (I.41)$$

The numerical implicit form of the updated stress is expressed as:

$$\{\sigma_{n+1}\} = \{\sigma_{n+1}^{trial}\} - \Delta\lambda [C] \left\{ \frac{\partial f}{\partial \{\sigma\}} \right\}_{n+1} \quad (I.42)$$

where, the elastic prediction of stress $\{\sigma_{n+1}^{trial}\} = \{\sigma_n\} + [C]\{\Delta\varepsilon_{n+1}\}$.

II.3.2 Examination of scalar return mapping method

The classical Simo's return mapping algorithm with Newton-Raphson iterative scheme is restored to update the stress. However, it meets convergence difficulties mainly caused by the large strain increment between the successive configurations. The scalar return mapping method, gives a direct resolution instead of the iteration algorithm, was developed to overcome the convergence difficulties. In this section, we'll examine and show the stable conditions of the scalar return mapping method in applications.

Concerning the implicit form of updated stress in Eq.(I.42), leads to the following iterative forms:

$$\begin{cases} \{\sigma_{n+1}^{(1)}\} = \{\sigma_{n+1}^{trial}\} - \frac{\Delta\lambda_1}{\bar{\sigma}_{n+1}^{trial}} [C][P]\{\sigma_{n+1}^{trial}\} & i=1 \\ \{\sigma_{n+1}^{(i)}\} = \{\sigma_{n+1}^{(i-1)}\} - \frac{\Delta\lambda_i}{\bar{\sigma}_{n+1}^{(i-1)}} [C][P]\{\sigma_{n+1}^{(i-1)}\} & i>1 \end{cases} \quad (I.43)$$

where, the superscript number indicates the i th iteration and the equivalent stress

$$\bar{\sigma}_{n+1}^{(i-1)} = \left(\left\langle \sigma_{n+1}^{(i-1)} \right\rangle [P] \left\{ \sigma_{n+1}^{(i-1)} \right\} \right)^{1/2}.$$

For cases of $i=2$ and $i=3$, the updated stresses are detailed expressed as:

$$\begin{aligned}\{\sigma_{n+1}^{(2)}\} &= \{\sigma_{n+1}^{(1)}\} - \frac{\Delta\lambda_2}{\bar{\sigma}_{n+1}^{(1)}} [C][P]\{\sigma_{n+1}^{(1)}\} \\ &= \{\sigma_{n+1}^{trial}\} - \left(\frac{\Delta\lambda_1}{\bar{\sigma}_{n+1}^{trial}} + \frac{\Delta\lambda_2}{\bar{\sigma}_{n+1}^{(1)}} \right) [C][P]\{\sigma_{n+1}^{trial}\} + \left(\frac{\Delta\lambda_1\Delta\lambda_2}{\bar{\sigma}_{n+1}^{(1)}\bar{\sigma}_{n+1}^{trial}} \right) ([C][P])^2 \{\sigma_{n+1}^{trial}\}\end{aligned}\quad (I.44)$$

and

$$\begin{aligned}\{\sigma_{n+1}^{(3)}\} &= \{\sigma_{n+1}^{(2)}\} - \frac{\Delta\lambda_3}{\bar{\sigma}_{n+1}^{(2)}} [C][P]\{\sigma_{n+1}^{(2)}\} \\ &= \{\sigma_{n+1}^{trial}\} - \left(\frac{\Delta\lambda_1}{\bar{\sigma}_{n+1}^{trial}} + \frac{\Delta\lambda_2}{\bar{\sigma}_{n+1}^{(1)}} + \frac{\Delta\lambda_3}{\bar{\sigma}_{n+1}^{(2)}} \right) ([C][P])\{\sigma_{n+1}^{trial}\} \\ &\quad + \left(\frac{\Delta\lambda_1\Delta\lambda_2}{\bar{\sigma}_{n+1}^{trial}\bar{\sigma}_{n+1}^{(1)}} + \frac{\Delta\lambda_1\Delta\lambda_3}{\bar{\sigma}_{n+1}^{trial}\bar{\sigma}_{n+1}^{(2)}} + \frac{\Delta\lambda_2\Delta\lambda_3}{\bar{\sigma}_{n+1}^{(1)}\bar{\sigma}_{n+1}^{(2)}} \right) ([C][P])^2 \{\sigma_{n+1}^{trial}\} \\ &\quad - \left(\frac{\Delta\lambda_1\Delta\lambda_2\Delta\lambda_3}{\bar{\sigma}_{n+1}^{trial}\bar{\sigma}_{n+1}^{(1)}\bar{\sigma}_{n+1}^{(2)}} \right) ([C][P])^3 \{\sigma_{n+1}^{trial}\}\end{aligned}\quad (I.45)$$

Then, the updated stress can be rewritten as:

$$\{\sigma_{n+1}^{(i)}\} = \{\sigma_{n+1}^{trial}\} - \sum_{j=1}^i A_j ([C][P])^j \{\sigma_{n+1}^{trial}\} \quad (i > 1) \quad (I.46)$$

Clearly, the stress state depends on the scalar A_j and matrix $([C][P])^j$.

Now, considering the widely adopted assumption in the works of sheet metal forming processes (Batoz et al., 1998; Guo et al., 1990; Guo et al., 2002; Guo et al., 2004; Guo et al., 2000; Halouani et al., 2012; Kankarani Farahani et al., 2014; Robert et al., 2012), it declares that: if we assume the same anisotropy (planar isotropy) for the elastic and plastic behavior and if we consider incompressibility for the elastic deformation, then the Poisson coefficient is related to the mean anisotropy coefficient r :

$$v = \frac{r}{1+r} \quad (I.47)$$

For the planar stress state, using the above relation, the multiplication of $([C][P])$ can be expressed as:

$$[C][P] = \begin{bmatrix} -\frac{E(r^3 - r - 1)}{(1+r)(1+2r)} & \frac{Er(r^2 + r - 1)}{(1+r)(1+2r)} & 0 \\ \frac{Er(r^2 + r - 1)}{(1+r)(1+2r)} & -\frac{E(r^3 - r - 1)}{(1+r)(1+2r)} & 0 \\ 0 & 0 & E \end{bmatrix} \quad (I.48)$$

The eigenvalue analysis of the matrix $([C][P])$ gives three different eigenvalues and eigenvectors respectively:

$$\left[\frac{E(r^2 + 1)}{2r^2 + 3r + 1}, \left\{ \left[\frac{\sqrt{2}}{2}, \frac{\sqrt{2}}{2}, 0 \right] \right\} \right] \left[E, \{[0, 0, 1]\} \right] \left[-Er + E, \left\{ \left[-\frac{\sqrt{2}}{2}, \frac{\sqrt{2}}{2}, 0 \right] \right\} \right] \quad (I.49)$$

which means the matrix $([C][P])$ is diagonalizable:

$$[C][P] = [Q][\Lambda][Q]^{-1} \quad (I.50)$$

$$\text{where } [Q] = \begin{bmatrix} \frac{\sqrt{2}}{2} & 0 & -\frac{\sqrt{2}}{2} \\ \frac{\sqrt{2}}{2} & 0 & \frac{\sqrt{2}}{2} \\ 0 & 1 & 0 \end{bmatrix} \text{ and } [\Lambda] = \begin{bmatrix} \frac{E(r^2 + 1)}{2r^2 + 3r + 1} & & \\ & E & \\ & & -Er + E \end{bmatrix}.$$

Accordingly, the matrix $([C][P])^j$ is also diagonalizable:

$$([C][P])^j = [Q](\Lambda)^j [Q]^{-1} \quad (I.51)$$

It means that the return-mapping directions $\{([C][P])^j \{\sigma_{n+1}^{trial}\}\}$ are parallel to each other. And this yields radius mapping method without the need of iteration scheme.

In summary, the scalar return mapping method is an approximation of the classical return mapping method, under the assumption that the elastic and plastic behavior have the same anisotropic property and incompressibility. Consequently, the errors on updated stress may appear when the relation Eq.(I.47) broke down. As shown in the work (Li et al., 2007), the scalar mapping method is very fast but may lead to certain errors. However, it could be regarded as a better initial solution for the classical return mapping algorithm to stable the convergence.

II.4 Construction of intermediate configurations

Let's recall the inverse approach, which only uses the pre-designed final formed part (final configuration) to evaluate the formability with completely ignoring the loading paths, and consequently results in the roughly evaluations of the stress state. In order to overcome these defects, several intermediate configurations are high efficiently constructed to introducing the deformation histories for general three dimensional part, with the following steps:

- 1). Resolution of the sliding surface.
 - a. Compute the elemental matrix of the area using (I.55).
 - b. Assemble the structural area matrix to form the Quadratic Programming (QP) optimization model using (I.56).
 - c. Solve the QP problem (e.g. Matlab/quadprog() subroutine).
- 2). Position overall material points on the sliding surface with the assumption of the equivalent initial blank reference for the final and middle configurations.
 - a. Compute the initial blank reference of the final part using the inverse approach.
 - b. Compute the initial blank of the middle sliding surface using the inverse approach.
 - c. Iteratively update the middle configuration by mapping the initial blank of final part to the middle sliding surface.
- 3). Go to the next iteration of step(2) with the updated middle configuration.

II.4.1 Resolution of the sliding surface

II.4.1.1 The pseudo minimum area method

In the general 3D case, the pseudo minimum area (PMA) method is proposed to efficiently generate the sliding surfaces, comparing with the work of minimization of area of the surface (Guo et al., 2004; Tang et al., 2010) which is hard to be solved.

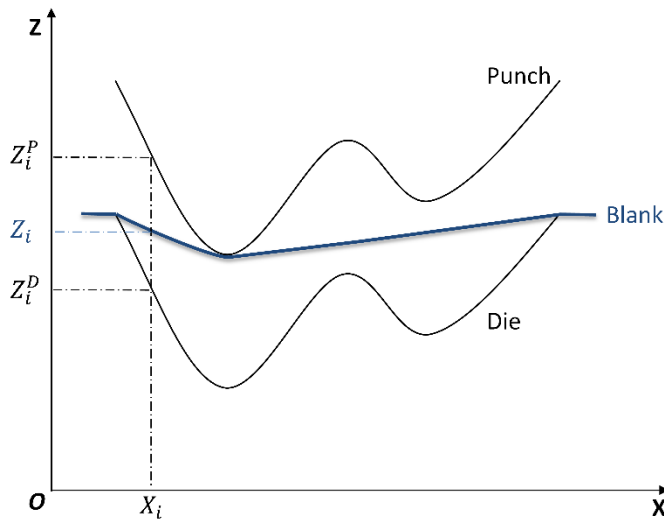


Fig. II-2 Blank sliding surface constrained by Punch and Die

The blank sheet is supposed to be a tensional membrane under the constraints of the tools, as shown in Fig. II-2. Then the shape of the deformed blank can be determined by minimizing the area of the surface.

However, this optimal model is solved inefficiently by the sequence quadratic program solver, due to the strongly nonlinear characteristics. In order to overcome this defect, the objective function in PMA is modified as the minimization of the sum of the elements' areas in square:

$$\begin{aligned} \min: f(\xi) &= \sum_{e=1}^n A_e^2(\xi) \\ \text{s.t. } & 0 \leq \xi_i \leq 1 (i=1,2,3..m) \end{aligned} \quad (I.52)$$

where, $A_e(\xi)$ is the area of element in number e , ξ_i represents the proportional coefficient of coordinate on each node, n and m represent the number of element and node respectively.

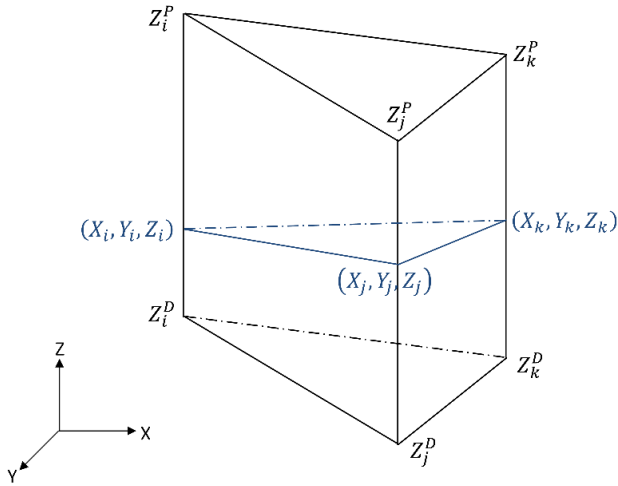


Fig. II-3 The coordinates of a triangle element on Punch, Blank and Die meshes

In Fig. II-3, it shows three triangular elements: up (Punch), down (Die) and middle (Blank). (x_i, y_i) , (x_j, y_j) and (x_k, y_k) are the coordinates of x and y in nodes i, j and k respectively. Superscripts 'P' and 'D' indicate the coordinates of Punch and Die. z_i, z_j and z_k are the design variables and can be expressed by the basic variables ξ_i, ξ_j and ξ_k as follows:

$$\begin{aligned} z_m &= \xi_m z_m^P + (1 - \xi_m) z_m^D \quad (m = i, j, k) \\ 0 \leq \xi_m &\leq 1 \end{aligned} \quad (I.53)$$

clearly, when $\xi_p = 0$, the node p is positioned on the Die mesh, and if $\xi_p = 1$, the node is located on the Punch mesh.

Concerning a triangular element e , the square of the element's area is given by:

$$A_e^2(\xi_i, \xi_j, \xi_k) = \frac{1}{4} \left\| \begin{vmatrix} \vec{i} & \vec{j} & \vec{k} \\ x_k - x_i & y_k - y_i & z_k - z_i \\ x_j - x_i & y_j - y_i & z_j - z_i \end{vmatrix} \right\|^2 \quad (I.54)$$

Supposing that $\{\xi_e\} = \begin{pmatrix} \xi_i & \xi_j & \xi_k \end{pmatrix}^T$ is the vector of the basic variables of element e , the square of the area can be rewritten in the matrix form:

$$A_e^2 = \frac{1}{4} \left(\frac{1}{2} \langle \xi_e \rangle [H_e] \{\xi_e\} + \langle C_e \rangle \{\xi_e\} + D_e \right) \quad (I.55)$$

where, $[H_e]$ is the symmetric square area matrix of the element, $\langle C_e \rangle$ and D_e are the vector and scalar of the square area in element e respectively. These variables can be easily obtained with some algebraic operations.

Supposing that $\{\xi\} = \begin{pmatrix} \xi_1 & \xi_2 & \dots & \xi_m \end{pmatrix}^T$ is the vector of the basic variables of the structure, $[H]$, $\{C\}$ and D are the matrix, vector and scalar of the structure assembled like the structural stiffness matrix and external force vector in FEM, then the square area of the structure can be expressed as:

$$f(\xi) = \sum_{e=1}^n A_e^2(\xi) = \frac{1}{4} \left(\frac{1}{2} \langle \xi \rangle [H] \{\xi\} + \langle C \rangle \{\xi\} + D \right) \quad (I.56)$$

Clearly, it's a quadratic programming model which can be solved (e.g. quadprog() subroutine from Matlab) very efficiently in polynomial time. In special cases to improve the quality of sliding surface, the PMA method could also be regarded as an efficient approach to search the contact nodes as shown in the work (Liu et al., 2013).

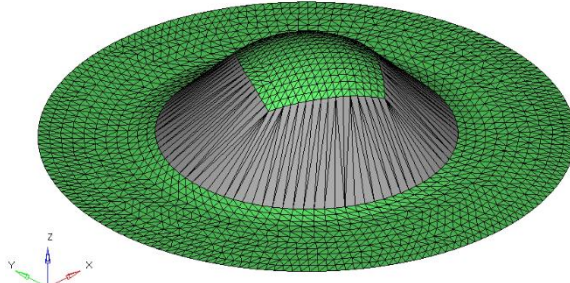


Fig. II-4 Construction of middle sliding surface using enhanced PMA method

II.4.1.2 The enhanced PMA method

Considering the design variables in (I.53) of PMA, the basic variable $\xi_m = 0$ indicates that the node m of the middle surface is in contact with the Punch, and $\xi_m = 1$ means the node m contacting the Die.

$$\begin{aligned} z_m &= \xi_m z_m^D + (1 - \xi_m) z_m^P \quad (m=i, j, k) \\ 0 &\leq \xi_m \leq 1 \end{aligned} \quad (I.57)$$

If we define a proper threshold tol , any nodes of the middle surface which satisfies the conditions $\xi_m < tol$ or $(1 - \xi_m) < tol$ are in contact with the tools. With this idea, the contact nodes are able to be efficiently obtained in time complexity $O(n)$. By directly connecting the contact nodes or using the

Delaunay triangulation algorithm (Shewchuk, 2002), the wall part of the middle surface can be generated. This idea is useful for the part with sloping wall.

As shown in Fig. II-4, the green part indicates the contact nodes with the tools and the gray part is the generated wall mesh by directly connecting the contact nodes.

II.4.2 Initial solutions of the middle configuration

From the previous section, the middle sliding surface is obtained by using the PMA approach. It is nothing but a geometric surface which indicates the possible deformed shape of the initial blank material. In order to make it represents the realistic deformation paths, overall material points of the pre-designed final configuration need to be properly positioned on the middle surface, the so-called initial solutions of the middle configuration.

The basic idea works like this: the constructed middle configuration can be regarded a state of the possible deformations with a given time in the forming processes, then the blank meshes with respect to the middle configuration and the known final part should be equivalent. By keeping the two blank meshes equivalent, we are able to find a group of proper distributions of overall material points on the middle configuration. As shown in Fig. II-5, the following steps have been carried out:

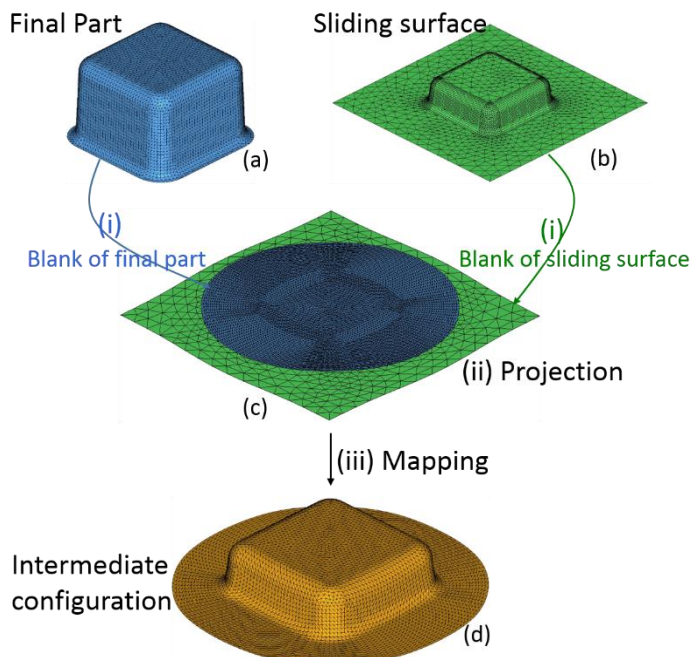


Fig. II-5 Scheme of initial solutions of the intermediate configuration

- 1). Solve the initial blank for the known pre-designed final part ($\text{blue } C_0$), with the help of the inverse approach. Since the initial blank is flat, the strain is measured with the equation Eq.(I.11), and the stress is updated with the total constitutive law (Eq.(I.19)). The simplified tools' actions are regarded as the external forces which are used to balance the commutated internal forces according to the integration of stress.
- 2). Estimate the initial blank mesh for the middle sliding surface ($\text{green } C_0^i$) using the inverse approach. The measurements of strain and stress are obtained also from Eq.(I.11) and Eq.(I.19). The difference

is on the computation of punch load, which is assumed to be proportional to the total punch force with a damping coefficient ($c_f = u_{cur} / u_{tal}$) which is the ratio of the current and total punch travel u_{cur} and u_{tal} .

- 3). Build the node-element relations between the two initial blank configurations. As shown in Fig. II-6(a), each material point (node P) of the blank C_0 is projected upon the blank C_0^i of the middle configuration, and can be uniquely identified with a specified element and a group of area coordinates (or linear shape functions) $P(A_i, A_j, A_k)$ in it. The unique identification will be used to locate the node on the middle sliding surface.
- 4). Position the material points for the middle configuration. The projected material point P of the final part's blank (C_0) are located on the 3D middle sliding surface (P') using the linear interpolation shape function while maintaining its unique identification $P'(A_i, A_j, A_k)$: the specified element and its area coordinates. Using the same scheme, the middle configuration (C_{iter+1}^i) is able to be constructed after locating overall material points of the final part's blank.
- 5). Check if the updated middle configuration is converged. The differences are measured between the two successive iterative updated middle configurations C_{iter}^i and C_{iter+1}^i . If the difference is converged, C_{iter+1}^i is the constructed initial solution of the middle configuration, as in Fig. II-5(d); otherwise, the configuration C_{iter+1}^i is regarded as the middle sliding surface, and go to step (ii).

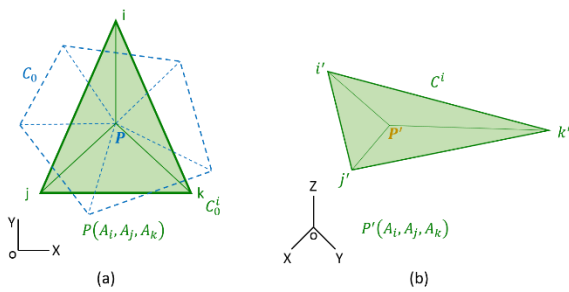


Fig. II-6 Scheme of node-element relations of the two initial blank configurations

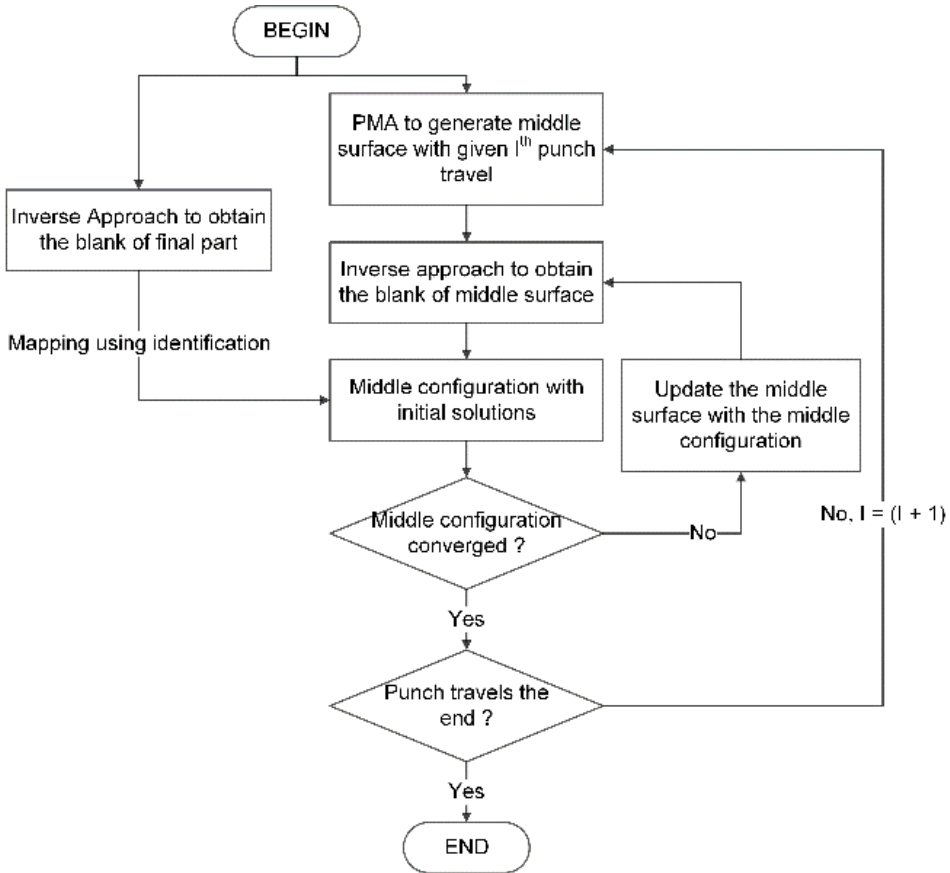


Fig. II-7 Flow diagram for the middle configurations

Fig. II-7 indicates the flowchart of constructions of the intermediate configurations.

II.4.3 Equilibrium of the middle configurations

With the help of the above procedures, several intermediate configurations with initial solutions are able to be efficiently constructed. However, it is worth to note that the total constitutive law (deformation theory) is used to provide initial solutions for the middle configurations. In this section, the nonlinear balance equations governing the displacement fields are solved with Newton-Raphson method to update the middle configurations.

Considering the triangular element, the elemental stiffness matrix is expressed in its local coordinate:

$$[K_e] = [B]^T [C^{ep}] [B] h_e A_e \quad (I.58)$$

in where, h_e and A_e are the thickness and area of the element, C^{ep} is the elastoplastic module tensor as derived in Eq.(I.41), $[B]$ is the strain operator of the triangular element:

$$[B] = \frac{1}{2A_e} \begin{bmatrix} b_i & 0 & b_j & 0 & b_m & 0 \\ 0 & c_i & 0 & c_j & 0 & c_m \\ c_i & b_i & c_j & b_j & c_m & b_m \end{bmatrix} \quad (I.59)$$

with $b_i = y_j - y_m$ and $c_i = -x_j + x_m$. The subscripts (i, j, m) follow the order $i \rightarrow j$, $j \rightarrow m$ and $m \rightarrow i$. x_i and y_i are the local nodal coordinates.

For the update of middle configuration, all the material points (nodes) are constrained to move on the middle surface. The elemental stiffness is enhanced by applying a penalty function to constrain the nodal movements:

$$[K_e] = [B]^T [C^{ep}] [B] h_e A_e + \gamma [N]^T [N] \quad (I.60)$$

where, γ is a penalty factor to be determined with the trial-error procedure and $[N]$ is the elemental matrix of the normal of all nodes.

The internal forces of this triangular element are given by:

$$\{f_{int}^e\} = [B]^T \{\sigma\} h_e A_e \quad (I.61)$$

in which, $\{\sigma\}$ is the updated stress state with evaluated finite logarithmic strain increment using the return-mapping algorithm.

With the help of the transformation matrix $[T]$ relating the global dof to the local one, the elemental stiffness matrix and internal forces are transferred to the global coordinate:

$$[K_e]_G = [T]^T [K_e] [T] \quad \{f_{int}^e\}_G = [T]^T \{f_{int}^e\} \quad (I.62)$$

Finally, the structural stiffness matrix, internal and external forces are assembled to obtain a nonlinear system which is solved with the Newton-Raphson iteration:

$$\{R(U^i)\} = \{F_{ext}(U^i) - F_{int}(U^i)\} = [K]\{\Delta U\} \neq 0 \quad (I.63)$$

and the displacement fields for the next iteration is updated by:

$$\{U^{(i+1)}\} = \{U^i\} + \{\Delta U\} \quad (I.64)$$

Fig. II-8 shows the flowchart of the procedure of balancing the middle configurations. In the common case, the update of the initial blank C_0 is negligible thanks to the reliable inverse approach.

PART I CHAPTER II MULTI-STEP APPROACH

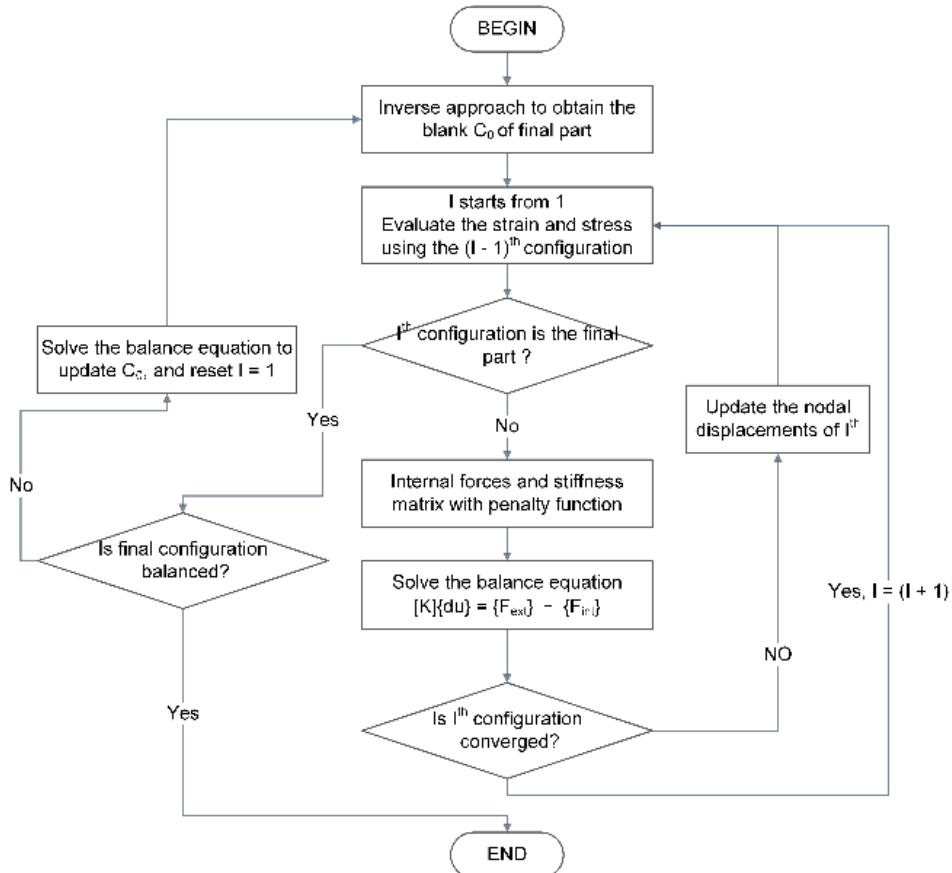


Fig. II-8 Flow diagram for the equilibrium procedure

III. Numerical applications

The numerical verifications and applications are presented in this section. In order to validate the derived kinematical formulations and improvements in stress estimations, the multi-step approach (MSTP - static implicit solver) is examined and is compared with the numerical results of the S-Rail, B-Pillar and box shaped holder forming components obtained from the commercial FE code LS-DYNA (INC - dynamic explicit solver).

III.1 S-Rail part of NUMISHEET 96

The CAD model and geometry of S-Rail are the same with Numisheet 96. The material properties of Draw Quality Mild Steel (IF) and forming parameters are shown in the below: Thickness $t = 1.0\text{mm}$, Young's Modulus $E = 206\text{GPa}$, Poisson's Ratio $\nu = 0.3$, Blank Holder Force 200KN , Friction Coefficient 0.11. In Table III-1, Dir means the angle measured from the rolling direction, YS gives 0.2% offset engineering Yield stress, TS indicates the engineering tensile stress, n and K are the parameters of stress-strain curve $\sigma = K\varepsilon^n$ and r is the anisotropic coefficient.

Dir	YS (MPa)	TS (MPa)	n	K (MPa)	r
0	152	294	0.239	526	1.85
45	159	301	0.231	530	1.52
90	163	292	0.231	516	2.37
AVE	158	297	0.233	526	1.82

Table III-1 Material's anisotropic parameters

In simulations with the INC, the triangular shell element without refining meshes is used to discrete the initial blank (20468 elements). Fig. III-1 shows the distributions of thickness on three different intermediate configurations(15mm, 25mm and 40mm) which were estimated by LS-DYNA and multi-step approach respectively. Clearly, both contour distributions of thickness obtained from INC and MSTP on the three configurations are very close, the maximum differences of thickest and thinnest for INC and MSTP are 0.00063mm (..) and 0.0096mm (0.11%) respectively.

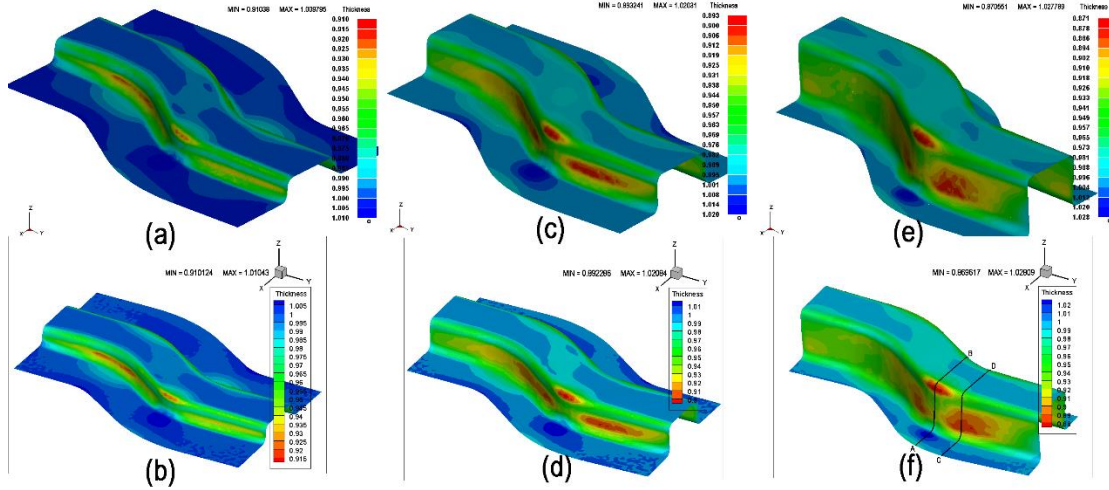


Fig. III-1 Comparisons of thickness distributions on three intermediate configurations simulated by LS-DYNA and Multi-step approach: (a) Depth 15mm of INC. (b) Depth 15mm of MSTP. (c) Depth 25mm of INC. (d) Depth 25mm of MSTP. (e) Depth 40mm of INC. (f) Depth 40mm of MSTP.

III.1.1 Verification and estimation of the derived kinematic formulations

In order to make clearer comparisons, two sections AB and CD , positioned on XZ plane with coordinates $Y=153.34\text{mm}$ and $Y=178.94\text{mm}$, are chosen to show the differences of the physical variables. Fig. III-2 shows the thickness evolutions of section AB and section CD from depth 5.5mm to 40mm calculated by INC and MSTP respectively. In general tendency, both the two section curves obtained from MSTP are in consistent with these calculated by INC at each configuration. However, there is still some differences between the two curves of INC and MSTP. In section AB , the maximum difference occurred around 40mm is 0.0014mm which is 0.15% and negligible compared with its absolute value; in section CD , the maximum difference 0.002mm (0.22%), is also negligible to its absolute value, appears around 130mm .

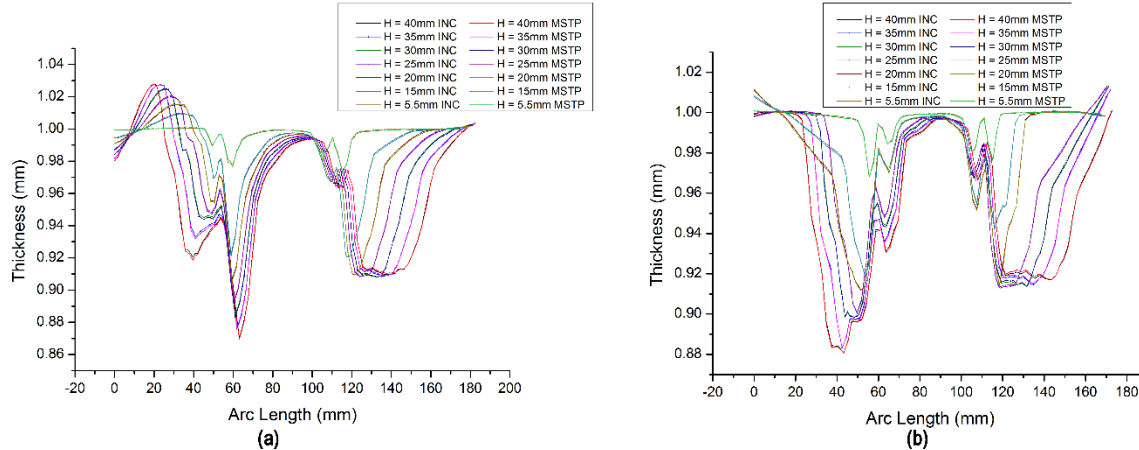


Fig. III-2 Comparisons of thickness distributions of two section curves on different depth obtained by LS-DYNA and Multi-step approach: (a) Section AB. (b) Section CD.

However, the thickness isn't a direct physical variable that derived from the kinematic formulations. Let's recall the processes of multi-step approach: Firstly, the logarithmic strains with respect to

displacements are derived from the kinematic formulation Eq.(I.34), which is a function of displacements and gives two planar strain through the two principle stretches (λ_1^1, λ_2^1). Secondly, the components of logarithmic strain tensor will be obtained from the principle strain tensor and their directions. The obtained components will be accumulated to the total strain during different configurations. And last, we'll use the constitutive equations to update stress, plastic strain, elastoplastic tensor etc.. It's clear that the consistency of thickness distribution (Fig. III-1 and Fig. III-2) certifies the correction of thickness strain which is calculated from the results of kinematic formulations with the assumption of plastic incompressibility. Here we still need more verifications of direct variables from kinematic formulations.

The evolutions of planar principle strains of section *AB* and *CD* are shown in Fig. III-3 respectively. From the processes of multi-step approach, we know that thickness strain equals to planar major strain adds minor strain.

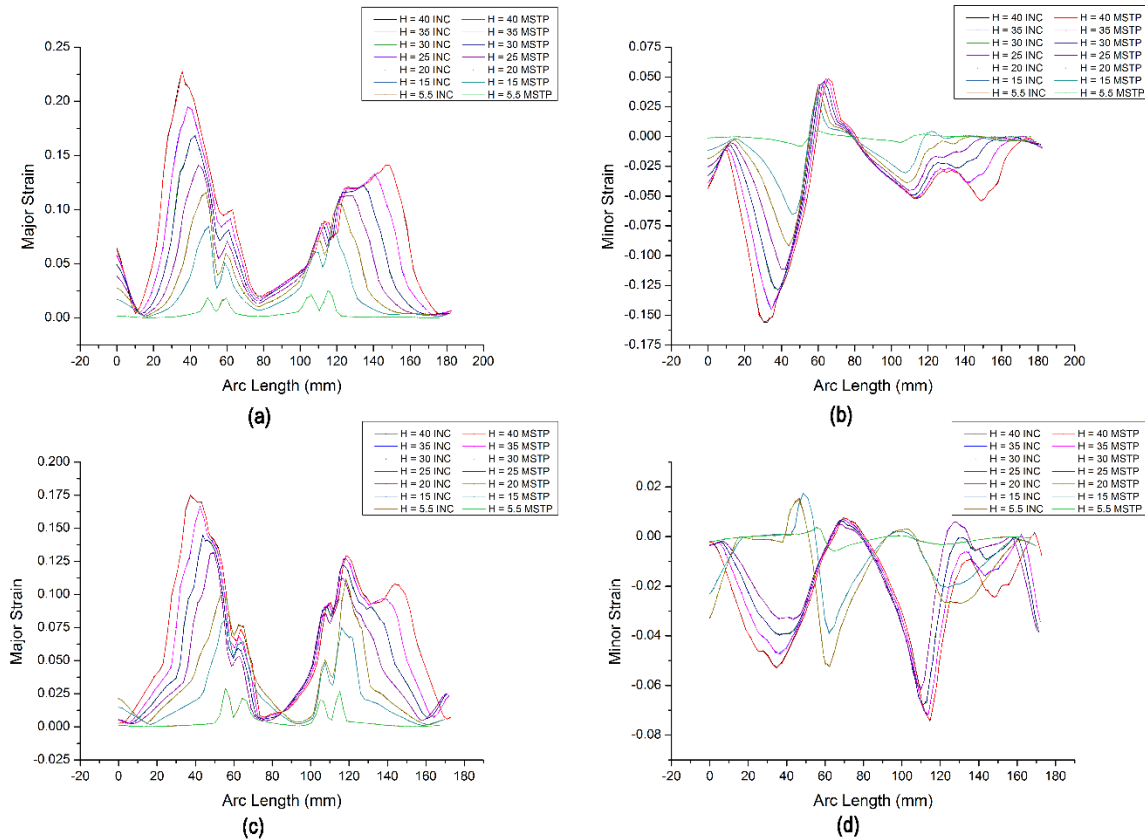


Fig. III-3 Comparisons of principle strain distributions of two section curves on different depth obtained by LS-DYNA and Multi-step approach: (a) Major strain of section AB. (b) Minor strain of section AB. (c) Major strain of section CD. (d) Minor strain of section CD.

For section *AB*, the positions of positive minor strain in Fig. III-3(b), which indicates the biaxial tension status and reduction in thickness, range from arc length around 58mm to about 80mm corresponding to the range of significant reduction in thickness shown in Fig. III-2(a). We can see that the maximum major strain (approximate 0.225) and minimum minor strain (approximate -0.150) locate around 35mm and indicate the state of a primary tension and a secondary compression consistent with the thickness thinning

around 35mm in Fig. III-2(a). From arc length about 120mm to 140mm, the major strain keeping increasing slowly and the minor strain firstly increasing and decreasing from 130mm, predict the local maximum thickness at about 130mm shown in Fig. III-2(a). For section CD, the maximum positive minor strain (about 0.01) appears at around 70mm. Although it's biaxial tension state, however, the corresponding major strain remains very small, which produces the small thinning in thickness. The maximum thinning takes place at approximate 40mm in Fig. III-2(b), because we have the maximum major strain (around 0.175 in Fig. III-3(c)) at this point while the minor strain is relatively small (only about -0.05) shown in Fig. III-3(d), even smaller than ($v * Major\ Strain$). The two values of principle strain give also the result of a state of biaxial tension at approximate 40mm. In Fig. III-3(d), the minor strain increasing slowly starts from about 40mm until around 70mm, then it keeps decreasing to arc length approximate 115mm. During these two periods, the major strain has the same general tendency but with two local extreme values which are also indicated at around 65mm and 110mm in Fig. III-2(b).

It can be concluded that the nonlinear geometric relations between strains and displacements, which provides the planar principle strains and their components, are well predicted from the kinematic formulations. And next, we can obtain the updated stresses according to the predicted incremental strains by using the return mapping method.

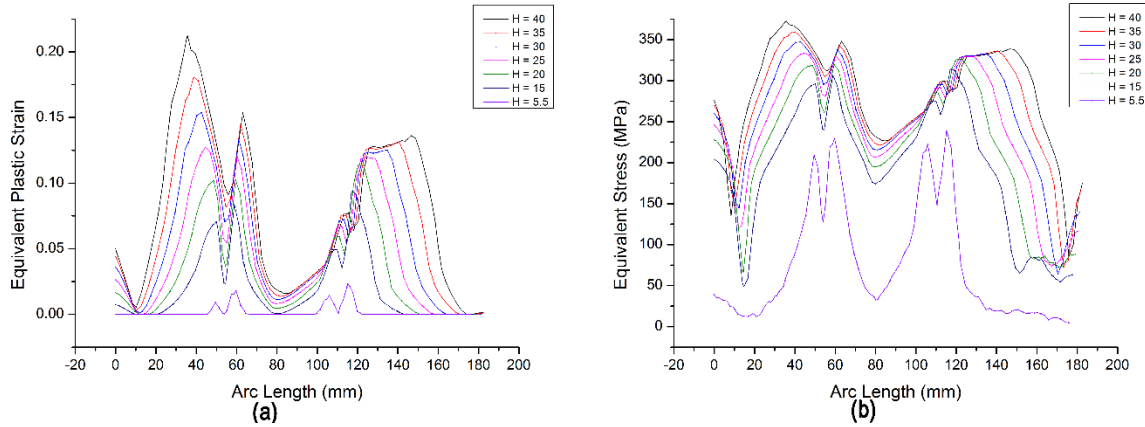


Fig. III-4 Estimations of equivalent values of section AB on different configurations obtained by multi-step approach: (a) Equivalent plastic strain. (b) Hill's equivalent Stress.

Fig. III-4 shows the evolutions of the equivalent plastic strain ($(\langle \varepsilon^p \rangle [P]^{-1} \{ \varepsilon^p \})^{1/2}$) and equivalent stress of Hill ($(\langle \sigma \rangle [P] \{ \sigma \})^{1/2}$) for section AB from depth 5.5mm to 40mm. It clearly shows both the equivalent plastic strain and equivalent stress in general tendency towards keeps increasing. However, in Fig. III-4(a), there is a small decrease in equivalent plastic strain appeared around arc length 120mm, which resulting from the state transformations of material points (from the state of biaxial tension to the state of primary tension and secondary compression). During the transformations, the material points still yield compressed plastic strains. It's also reflected in the planar principle strains Fig. III-3(a) and (b).

III.1.2 Errors in accumulated total strain of different layers

In the above section, we validate the effectiveness and the accuracy of the kinematic formulations. In this part, we'll implement the formulations derived from Eq.(I.34) to calculate the physical values of top and bottom layer by the accumulated method.

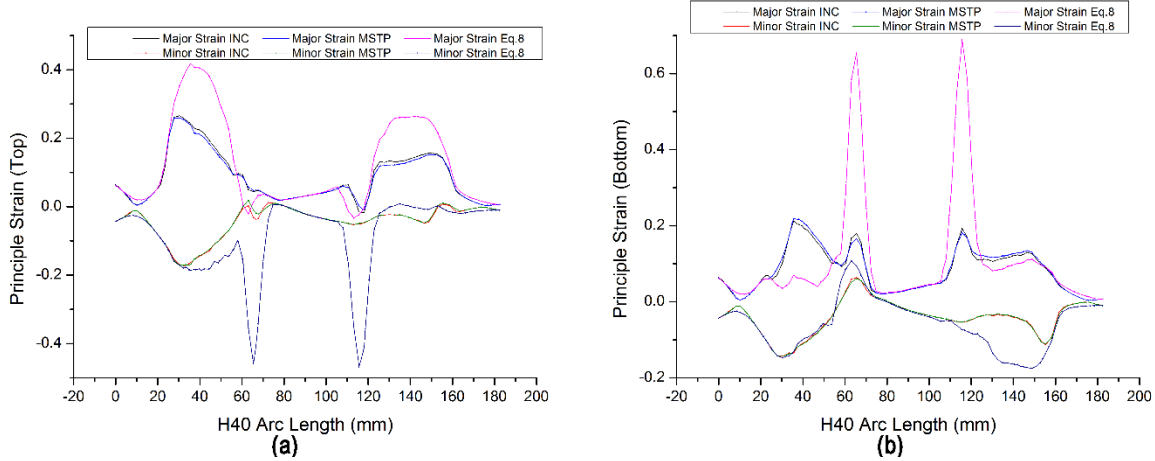


Fig. III-5 Comparisons of accumulated principle strains of section AB on configuration of depth 40mm obtained by LS-DYNA, Multi-step approach and Eq.8: (a) Top Layer. (b) Bottom Layer.

Fig. III-5 shows the accumulated total planar principle (major and minor) strains of section *AB* at depth 40mm, estimated from INC, MSTP and Eq.(I.11), respectively. Clearly, both the two top layer's major strains of INC and MSTP are very close, shown in Fig. III-5(a). However, the contour curve of predicted major strain from Eq.(I.11) up to 0.418, significantly departs from the other two curves. The same situation appears at the minor strain and the planar principle strains of section *CD* (Fig. III-5(b)). The differences of the planar principle strain imply the effects of the bending normal.

From this verification, it's clear to conclude that the total logarithmic strain estimated from Eq.(I.11) can be only valid for flat reference configuration, otherwise, the total strain should be accumulated from Eq.(I.34) which considering the bending effects.

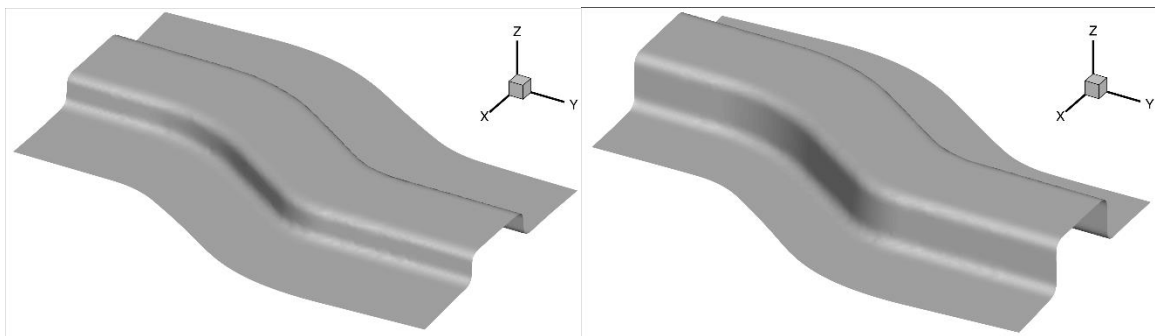


Fig. III-6 The constructed middle configurations: (a) Depth 15mm (b) Depth 25mm

III.1.3 The constructed intermediate configurations

Several intermediate configurations of the S-Rail part are efficiently constructed with the help of the PMA method which solves the QP problem with only 16 iterations. As shown in Fig. III-6, two middle configurations are presented for punch travel 15mm and 25mm.

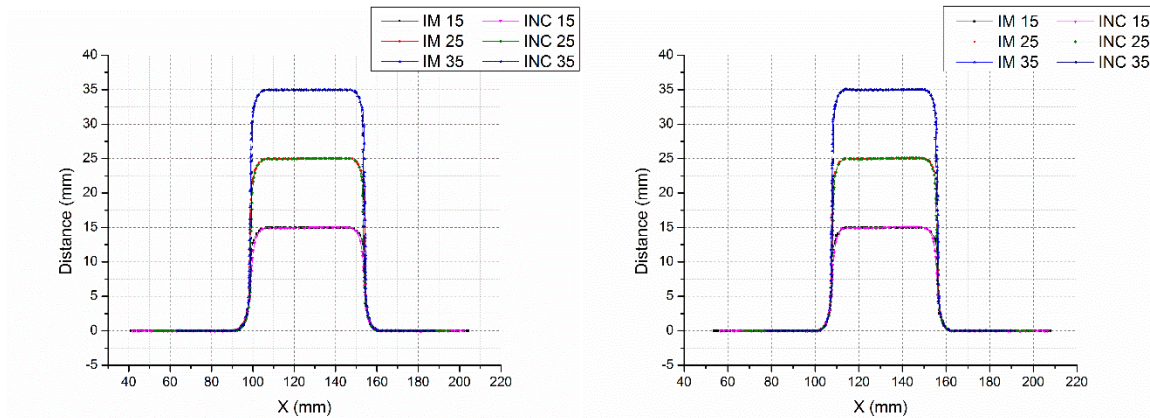


Fig. III-7 Sections of the generated middle configurations using LS-DYNA and PMA method: (a) Section AB
(b) Section CD

In Fig. III-7, the sections AB and CD are extracted to show the agreement with the intermediate states computed from the incremental approach, for three middle configurations (depth 15mm, 25mm and 35mm). It's obvious that the section curves of PMA coincide with the curves of INC.

Clearly, the middle configurations constructed by PMA method are in good agreements with the intermediate states computed from the incremental approach.

III.2 Application to B-Pillar component of NUMISHEET 08

To validate the improvement in stress estimations of the multi-step approach, by using intermediate configurations generated by the LS-DYNA (INC), is the main objective of this benchmark analysis. For simplicity, the material of high strength steel 22MnB5 is limited to the isothermal elastoplastic model with the following properties (interpolated based on the material response at 800°C and strain rate 1s^{-1}): Young's Modulus $E = 100\text{GPa}$, Poisson's Ratio $\nu = 0.3$, strain hardening modulus $K = 230\text{MPa}$, strain hardening exponent $n = 0.12$ and thickness $t = 1.95\text{mm}$. Two sections are defined in Fig. III-8 to analyze the simulation results: section 1 ($P1[538.189, -39.491]$ and normal $[1.0, 0.83078, 0.0]$) and section 2 ($P2[-25.0, 0.0]$) in plane YZ .

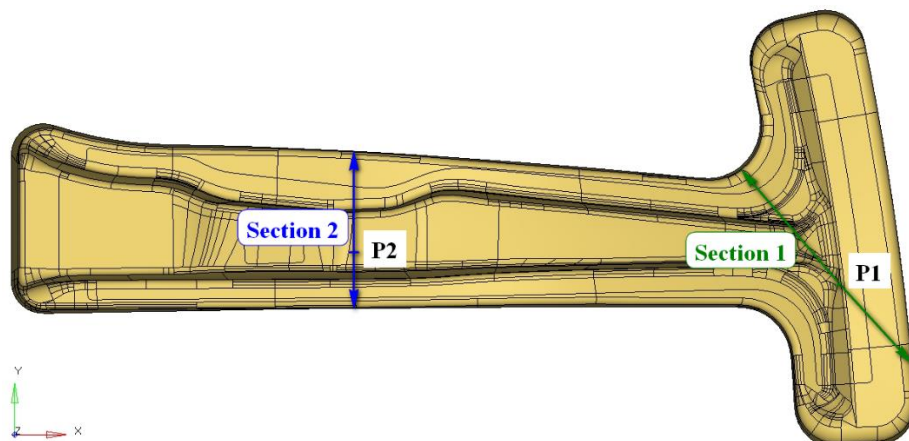


Fig. III-8 The geometry of B-Pillar

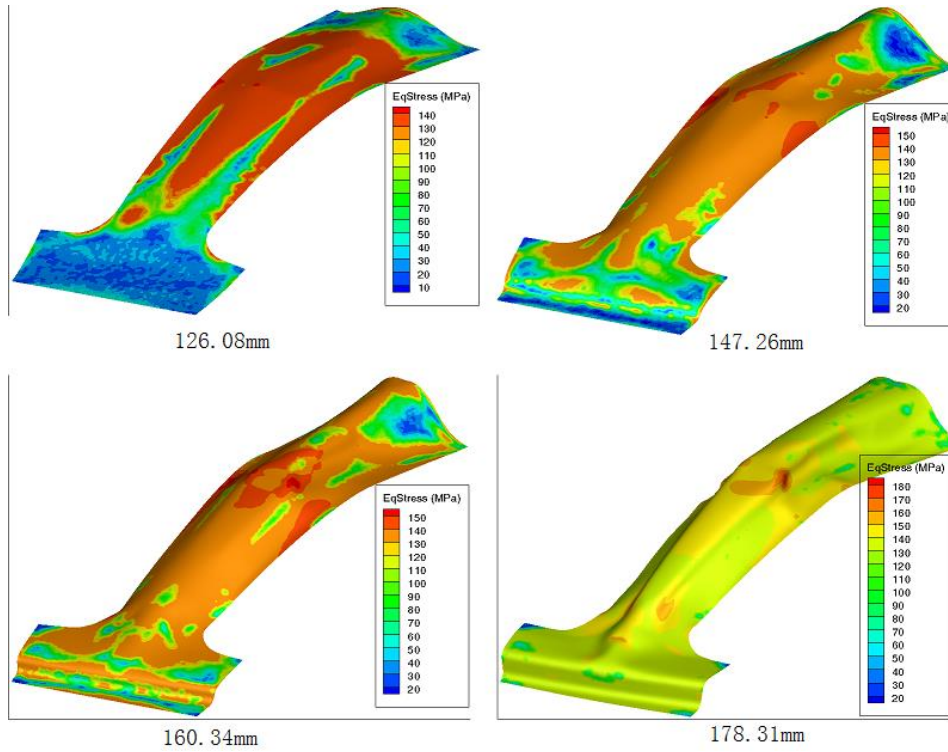


Fig. III-9 Equivalent stress of four intermediate configurations of B-Pillar

Fig. III-10 presents the distributions of stress components (σ_x and σ_y) of the two sections obtained from four different solvers: INC, One-step approach (OSTP), Multi-step approach using 4 intermediate configurations (MSTP 04IMs, as shown in Fig. III-9), and using 17 intermediate configurations (MSTP 17IMs), respectively. Let's examine the results obtained from the multi-step method with 4 intermediate configurations and from one-step approach at first, in section 1 (Fig. III-10 (a) and (b)), both the two approaches provide very close distributions of stress components, while around arc length 250mm, MSTP 04IMs gives a better prediction of stress X (82.32MPa) than the stress state obtained from OSTP (11.08MPa), compared with the stress X given by INC (128.99MPa). The same tendency and improvements on stress state of MSTP 04IMs with respect to the OSTP can be found in section 2 ranged from arc length 50mm to 100mm. In general, the multi-step method with 4 intermediate configurations gives equal or closer predictions compared with the OSTP approach. However, it's worth to note that both the MSTP 04IMs and OSTP predict incorrect stress state around arc length 200mm of section 1 ($\sigma_x = -136.26\text{MPa}$ and $\sigma_y = -200.19\text{MPa}$) and the beginning of section 2 ($\sigma_x = -131.46\text{MPa}$), with respect to the stress state updated from INC ($\sigma_x = 77.43\text{MPa}$ and $\sigma_y = 73.87\text{MPa}$ in section 1 and $\sigma_x = 138.88\text{MPa}$ in section 2) respectively.

Concerning the multi-step method with 17 intermediate configurations, from the distributions of stress state of the two sections in Fig. III-10, it clearly shows a tendency that the MSTP 17IMs predicts more accurate stress state than the stresses obtained from OSTP and MSTP 04IMs approaches, since the red curves (MSTP 17IMs) are mainly positioned between the curve obtained from the INC and the others two curves of MSTP 04IMs and OSTP methods. More particularly, the MSTP 17IMs method provides more

consistent evaluations on the stress state ($\sigma_x = 116.49 \text{ MPa}$ and $\sigma_y = 46.76 \text{ MPa}$ around arc length 200mm of section 1 and $\sigma_x = 140.93 \text{ MPa}$ at the beginning of section 2) with the INC method, for the material points incorrectly estimated by MSTP 04IMs and OSTP.

From this application, it's clear to note that with the increasing intermediate configurations, the multi-step approach shows more and more consistent distributions of stress state to the INC method.

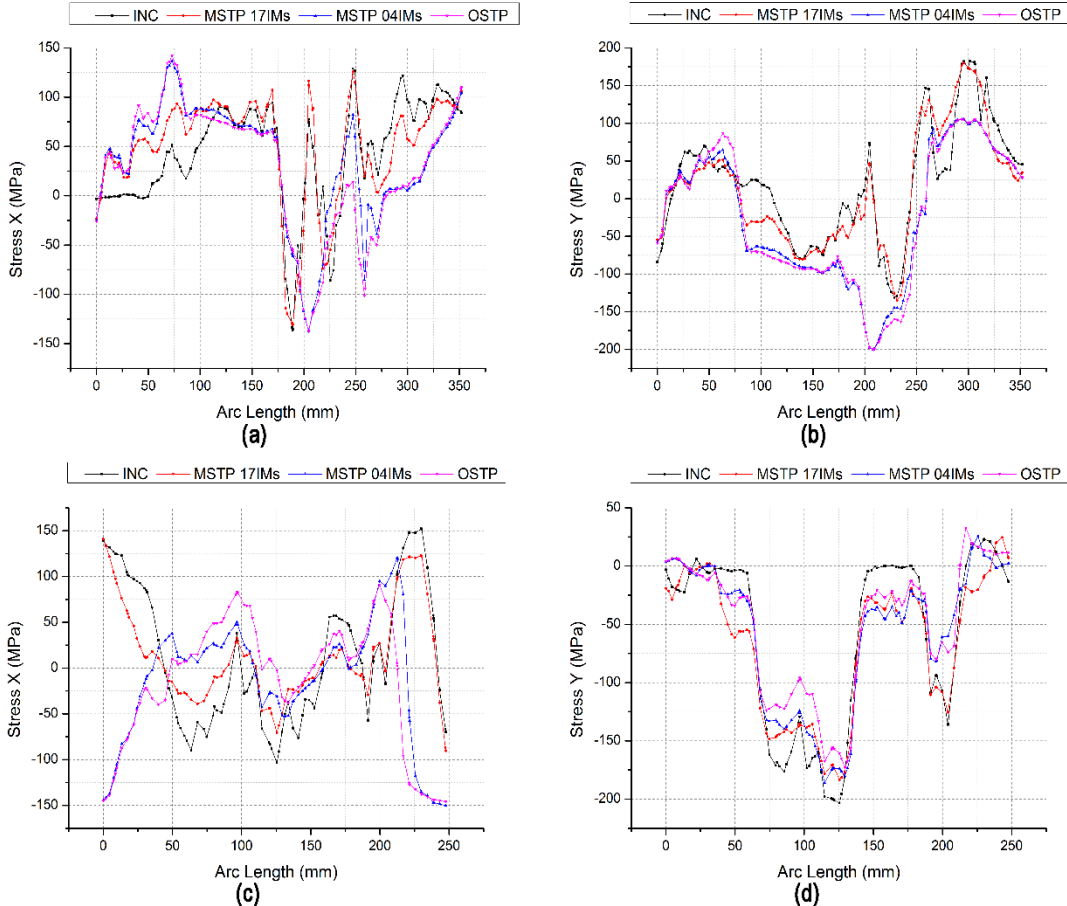


Fig. III-10 Comparisons of stress distributions on three sections updated by INC, MSTP approach (with two different schemes of intermediate configurations) and One-step approach (OSTP): (a) Stress X of Section 1. (b) Stress Y of Section 1. (c) Stress X of Section 2. (d) Stress Y of Section 2.

III.3 The box shaped holder part

The CAD model of the die of the box holder part is given in Fig. III-11. The blank material parameters and forming processes are: thickness $t = 1.0 \text{ mm}$, Young's modulus $E = 207.0 \text{ GPa}$, Poisson's ratio $\nu = 0.28$, yield stress 154.31 MPa , the hardening moduli $k = 520.4 \text{ MPa}$ and $n = 0.232$, average anisotropic coefficient 1.653, blank holder force 15KN and friction coefficient 0.15.

As is shown the PMA method works well for the S-Rail part, however, in practice, the PMA method may yield some errors for the special part which possesses sloping walls. The enhanced PMA method will be used to improve the shapes of the middle configurations.

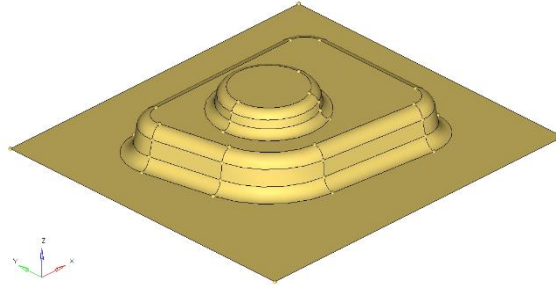


Fig. III-11 The CAD model of the Box shaped holder

III.3.1 The middle configurations using enhanced PMA method

The basic variables ξ_i of three middle configurations, constructed by the PMA method in punch travel 15mm, 25mm and 35mm, are shown in Fig. III-12. The gray color indicates the nodes satisfying the conditions ($\xi_m < 0.02$ or $(1 - \xi_m) < 0.01$) which are in contact with the punch or die.

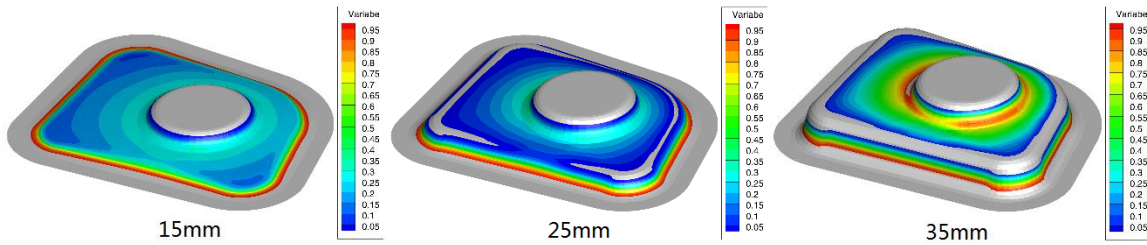


Fig. III-12 Basic variables of the constructed middle configurations using the PMA method

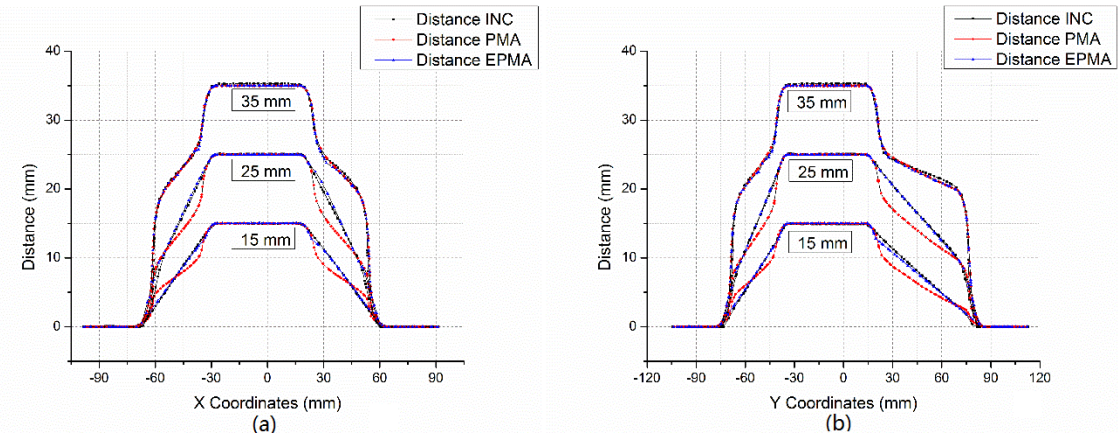


Fig. III-13 Section curves of the constructed middle configurations: (a) Section AB (b) Section CD

In Fig. III-13, the z coordinates (distance) of the section curves AB and CD, in three generated middle configurations which are obtained from the INC approach, the PMA method and the enhanced PMA method respectively, are shown. For the middle configuration of depth 15mm, the section curve of PMA provides smaller distances in a range of x coordinate -50 ~ -30mm (20~45mm), and larger distances in a range of -70~50mm (45~60mm), to the intermediate state of INC. Considering the die model of the part in Fig. III-11, there are two sloping walls named bottom and top respectively along the z axis. In depth 15mm, none of the nodes of the two sloping walls are actually in contact with the tools, as is shown in Fig.

III-12(a), the gray color appears only at the bottom and top surface. Using the selected contact nodes and the enhanced PMA method leads to consistent middle configuration with the one of INC.

For the 25mm middle configuration, the distance provided by the PMA method is lower in the range - 55~30mm (20~45mm), and in consistent with the result of INC for other regions. This can be explained from Fig. III-12(b), the gray color appears in the upper surface of the bottom sloping wall besides the top and bottom surfaces which results in the contact of the bottom sloping wall with the tools. Consequently, in the range -70~50mm (45~60mm) which lies on the bottom sloping wall, it is consistent with the INC's result. On the other hand, using the enhanced PMA method provides a full consistent middle configuration with the one of INC.

Considering the generated middle configuration of 35mm, both the PMA and enhanced PMA give well agreement with the intermediate state obtained from INC. That is because, the further the punch travels, the more contact nodes observed in sloping walls, as shown in Fig. III-12(c), both of the bottom and top sloping walls are in contact. In this case, it leads to no difference of the middle configurations between the PMA, the enhanced PMA and the INC method.

III.3.2 The updated stress state

The distributions of equivalent stress for two of the constructed middle configurations with depth 15mm and 25mm are shown in Fig. III-14.

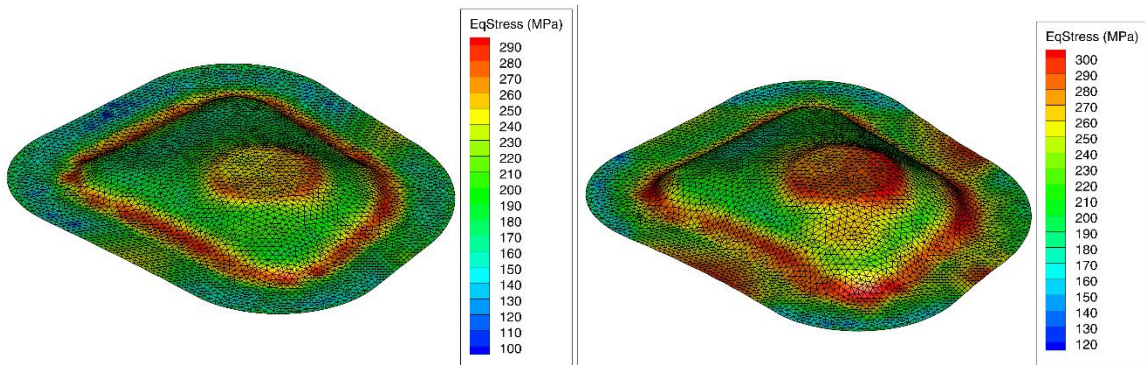


Fig. III-14 Equivalent stress of the constructed middle configurations depth 15mm and 25mm

The comparisons of stress components of section AB are shown in Fig. III-15. Clearly, the multi-step approach provides a significant improvement of the stress state compared with one-step approach, by using 8 constructed middle configurations. Especially for x coordinate close to 50mm and 200mm, the x component of stress is corrected from tensional state to compression with the help of the introduced intermediate configurations.

PART I CHAPTER III NUMERICAL APPLICATIONS

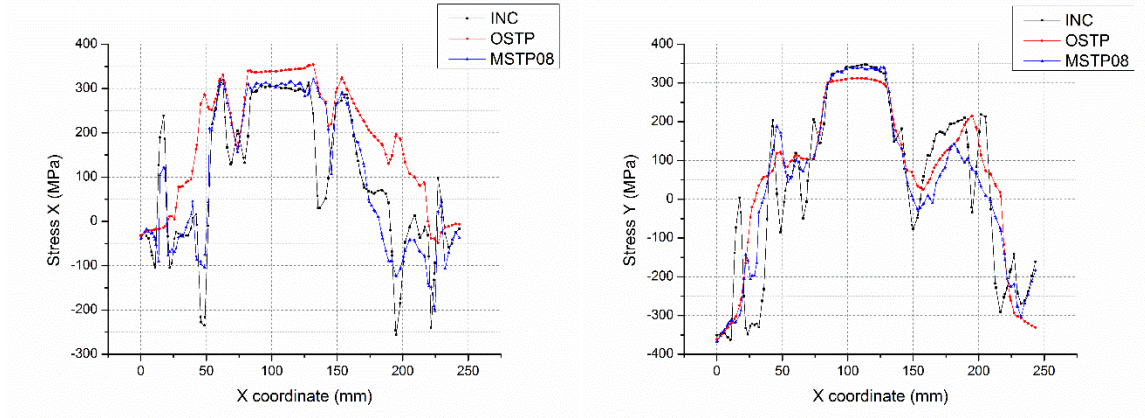


Fig. III-15 Stress components of section AB of the Box shaped holder part

IV. Conclusions

In this part, the efficient one-step inverse approach to roughly predict the formability of the final workpiece is briefly reviewed. In order to improve the stress estimations, the multi-step approach is formulated with constructed several intermediate configurations:

- 1). The finite logarithmic strain increment measurement (the kinematic formulations), between the two successive intermediate configurations, is derived and validated in the numerical simulation.
- 2). The elastoplasticity coupled with isotropic hardening is performed and the local integration is updated by the classical return mapping method. On the other hand, the scalar mapping algorithm is reexamined to clear its limitation in applications, while it could be regarded as a better initial solution for the iterative local integration scheme due to the convergence difficulties induced by the finite strain increments.
- 3). The efficient geometric approach to generate the sliding surfaces, and the mechanical initial solution are proposed to construct the proper intermediate configurations. The sliding surface is obtained by solving a QP program which can be efficiently worked out in polynomial time, and the direct mapping method is applied to construct the initial solutions of the intermediate configuration.

However, these simplified inverse approaches have some difficulties in using the sophisticated constitutive equations, such as considering the strain-softening phenomena induced by the damage or high temperature, the nonlocal effects, the viscos effects, etc. In the next part, we will concentrate on the more advanced numerical modeling combined with incremental approach for sheet metal forming processes.

Part II Advanced micromorphic modeling approach for sheet metal forming simulations

Content

PART II ADVANCED MICROMORPHIC MODELING APPROACH FOR SHEET METAL FORMING SIMULATIONS ..	42
V. INTRODUCTION	44
V.1 THE LOCAL CONTINUUM DAMAGE MODEL	45
V.2 THE GENERALIZED CONTINUUM DAMAGE MODEL.....	46
V.3 THE GENERALIZED HEAT EQUATIONS.....	51
VI. THEORETICAL FORMULATIONS	58
VI.1 INTRODUCTION.....	58
VI.2 GENERALIZED PRINCIPLE OF VIRTUAL POWER (BALANCE EQUATIONS).....	59
VI.2.1 <i>New degree of freedoms (dofs)</i>	59
VI.2.2 <i>Principle of virtual power for a micromorphic medium</i>	59
VI.2.3 <i>Generalized balance equations</i>	61
VI.3 THERMODYNAMIC FORMULATIONS	62
VI.3.1 <i>State variables</i>	62
VI.3.2 <i>Thermodynamic consistency and state potential (State relations)</i>	66
VI.3.3 <i>The generalized heat equation</i>	75
VI.3.4 <i>Dissipation analysis (Evolution equations)</i>	79
VI.4 TRANSFORMATION OF THE MICROMORPHIC BALANCE EQUATIONS.....	86
VI.5 DISCUSSIONS OF SPECIAL CASES.....	88
VI.5.1 <i>Classical local damage model</i>	89
VI.5.2 <i>Simplified classical elastoplastic model</i>	92
VI.5.3 <i>The existent generalized heat equations</i>	93
VI.5.4 <i>Discussions of the generalized heat equation</i>	112
VI.6 CONCLUSIONS	123
VI.7 APPENDIX.....	124
VI.7.1 <i>Formulations of plastic multiplier</i>	124
VI.7.2 <i>Formulations of elastoplastic tangent operator</i>	127
VII. NUMERICAL ASPECTS.....	130
VII.1 INTRODUCTION.....	130
VII.2 WEAK FORMS OF THE IBVP	130
VII.3 TIME AND SPACE DISCRETIZATION	131
VII.3.1 <i>Time discretization</i>	131
VII.3.2 <i>Space discretization</i>	131
VII.4 GLOBAL RESOLUTION SCHEME.....	140

VII.4.1 Dynamic explicit analysis	140
VII.4.2 Contact problems.....	143
VII.5 LOCAL INTEGRATION SCHEME	143
VII.5.1 Local integration of time-dependent plasticity.....	145
VII.6 APPENDICES.....	152
VII.6.1 Appendix I – Q4r24 element for thick shell.....	152
VII.6.2 Appendix II – The standard hexahedral element	154
VIII. PARAMETRIC STUDY OF THE MODEL	157
VIII.1 EFFECT OF THE LOCAL DAMAGE PARAMETERS	157
VIII.2 THE VISCOPLASTIC EFFECTS.....	161
VIII.3 EFFECT OF THE MICROMORPHIC MODULI.....	162
VIII.3.1 Effect of the micromorphic damage moduli	162
VIII.3.2 Effect of the micromorphic isotropic hardening moduli	167
VIII.3.3 Summary.....	168
VIII.4 ANISOTHERMAL MICROMORPHIC DAMAGE MODEL.....	169
VIII.4.1 Anisothermal viscoplasticity with local damage for a material point	170
VIII.4.2 Biaxial tension for local damage with FE.....	171
VIII.4.3 Choices of micromorphic parameters with FE	172
VIII.4.4 Biaxial tension for micromorphic damage with FE	174
VIII.4.5 Summary.....	176
IX. APPLICATIONS	177
IX.1 UNIAXIAL TENSILE TEST OF DP1000	177
IX.1.1 The local damage behavior.....	177
IX.1.2 The micromorphic damage behavior	179
IX.1.3 Solutions with micromorphic damage and micromorphic isotropic hardening	181
IX.2 CROSS SECTION DEEP DRAWING PROCESS	192
IX.2.1 CSDD processes using the local damage model.....	193
IX.2.2 CSDD processes using the micromorphic damage model	194
IX.3 PRESSURE VESSEL	200
X. CONLCUSIONS.....	206

V. Introduction

The mechanics of materially simple continua, explored in Part I, supposes that the mechanical state at any material point $P(\vec{x})$, of coordinates \vec{x} , from the actual deformed configuration is completely determined by the history of state variables in an arbitrarily small neighborhood surrounding this point (principle of determinism and principle of local action). In this framework, the knowledge of the first transformation gradient E (or first displacement gradient) suffices amply to determine the mechanical state (kinematic, behavior) of this material point.

In metal forming, the components are mainly performed using hot or cold forming processes under fairly extreme conditions, such as complex multiaxial loading, high temperatures, high strain rates, etc. Under such conditions, the material strain is governed by complex physical mechanisms, which are largely influenced by the microstructures and their textures during large plastic deformation. These complex physical phenomena should be taken into account to precise the numerical simulations. The continuum damage mechanics (CDM) approach enables the inclusion of thermal, damage and many other physical effects into the well-known constitutive equations, which are widely used in metal forming simulations, based on the local action assumption. Through large elastoplastic deformation, the intense shear bands are often observed in metal forming processes, which are generally the consequence of the strain-softening behavior of the material mainly induced by thermal or microscopic defects, and lead to formation of the macroscopic cracks. However, the CDM approach is limited in its applicability for strain-softening behavior, and reveals a pathological dependence on the direction and the fineness of the finite element mesh, and converges to a physically meaningless solution. The problem is now well-known and is the consequence of the mathematically ill-posed initial and boundary problem (IBVP), which loses ellipticity in statics or hyperbolicity in dynamics. The CDM approach is mathematically unstable when strain-softening behavior is introduced. In literature many enhanced physical or phenomenological models are proposed to overcome this dependency, which has led to various numerical simulation strategies, e.g. the nonlocal plastic models, the gradient-enhanced models, the viscoplastic models.

In this part, a complete set of constitutive equations, strongly coupled, anisothermal, anisotropic for elasto-visco-plasticity with isotropic ductile damage, isotropic and kinematic hardening, micromorphic ductile damage, micromorphic isotropic and kinematic hardening and micromorphic temperature, is derived from the state and dissipation potentials, under the framework of the extended irreversible thermodynamics, to overcome the mesh-dependency problem.

Throughout this thesis the following notions are used: x , \vec{x} , \underline{x} , $\vec{\underline{x}}$, $\underline{\underline{x}}$, $\vec{\underline{\underline{x}}}$ and $\underline{\underline{\underline{x}}}$ indicate the zero (scalar), first (vector), second, third, fourth, fifth and sixth rank tensors respectively. The usual tensorial product is indicated by the symbol \otimes , while the contracted (or inner) product is indicated by \cdot , $: \cdot$, \therefore and $::$ for the simple, double, triple and quadruple contractions respectively.

V.1 The local continuum damage model

Fracture of engineering components is often preceded by flow localization inducing considerable changes in the microstructure of the material, like microcracking in concrete, fibre pull-out or delamination in composites and the formation of voids in ductile metals. Considerable effort has been expended by the scientific community in order to solve crack propagation problem in a manner that is computationally as light as possible and that gives the same results for the crack path and propagation rate whichever mesh is used.

The discrete and smeared crack approaches (De Borst et al., 2004; De Borst et al., 1993; Ngo and Scordelis, 1967; Rashid, 1968; Saouma and Ingraffea, 1981; Suidan and Schnobrich, 1973), are appropriate for modeling one or more dominant cracks and the diffuse cracking patterns that arise due to the heterogeneity of concrete and the presence of reinforcement respectively, were initially proposed by introducing the crack as a geometric entity, which was implemented by triggering a crack grow when the nodal force exceeded a tensile strength criterion as well as splitting the node into two. This original form has the inherent disadvantages of pre-assumed mesh bias and the continuous change in topology, which are largely alleviated by using the meshless methods (e.g. element-free Galerkin method (Belytschko et al., 1994)) or the finite element method (X-FEM) using the partition-of-unity property of shame functions (Belytschko and Black, 1999; Dolbow and Belytschko, 1999). The Cracks within the original structures can be modelled either through the insertion of special types elements whose boundaries lie along the faces of the advancing crack (e.g. cohesive zone element method (Barenblatt, 1962; Dugdale, 1960; Hillerborg et al., 1976; Hutchinson and Evans, 2000; Needleman, 1987)) or by the introduction of elements with enriched nodal degree of freedom (e.g. extended finite element method X-FEM (Dolbow and Belytschko, 1999; Sukumar et al., 2000)). The later method allows crack propagation without remeshing and the enrichment of the existing degrees of freedom accounts for the displacement jump along the crack and the singular stress field at the tip of the propagating crack.

On dealing with large plastic deformation, the plastic strains tend to localize inside narrow bands during the metal deformation giving rise to the initiation, growth and coalescence of some micro-voids and micro-cracks usually called ductile damage. In order to take this phenomenon into account, several theories have been proposed to describe this damage occurrence as well as its effect on the material behavior. The most widely used approach in metal forming is based on the Gurson's type ductile damage modelling (Gurson, 1977) in order to describe as accurately as possible the ductile damage occurrence (Aravas, 1986; Bennani and Oudin, 1995; Bontcheva and Iankov, 1991; Boudeau and Gelin, 1994; Brunet et al., 1996; Gelin and Moisan, 1990; Gelin et al., 1985; Oñate et al., 1988; Pardoen et al., 2004). In these approaches, the damage is mainly described by the volume fraction of the spherical or elliptical voids. This scalar variable is introduced in the plastic potential affecting the plastic flow through the normality rule and gives a decrease on the stresses when the void volume fraction increases under the applied external loading. Another kind of approaches, based on the continuum damage mechanics (CDM) since the early works of Kachanov (1958) and Rabotnov (1969), represents the ductile damage by a scalar or tensorial variable Suidan and Schnobrich, 1973Suidan and Schnobrich, 1973(Kachanov, 1986; Lemaitre, 1992; Lemaitre et al., 2009; Murakami, 1988; Voyiadjis and Kattan, 1992a, b; Voyiadjis et al., 1999) and its effect on the material behavior is accounted for thanks to the hypothesis of the strain equivalence, stress equivalence or energy equivalence (Chaboche, 1988a, b; Saanouni and Chaboche, 2003a). A comparative study of different

ductile damage models can be found in (Pardoen et al., 1998). This kind of CDM approach has been used for damage prediction in metal forming assuming various types of coupling in some published works (Badreddine et al., 2016; Badreddine et al., 2010; Badreddine et al., 2015; Issa, 2010; Issa et al., 2012; Labergere et al., 2014; Lestriez et al., 2004; SAANOUNI et al., 1996; Saanouni, 2008; Saanouni, 2012; Saanouni et al., 2010; Saanouni and Chaboche, 2003b; Yue, 2014).

V.2 The generalized continuum damage model

As is now well accepted, the classical local continuum models do not incorporate an internal length scale and is inappropriate for progressive deformation of materials exhibiting strong localization or strain softening (Bažant, 1976; Rice, 1976) after reaching a peak strength value. Theoretically, when the tangent stiffness matrix of the material ceases to be positive definite, the governing equations of motion lose ellipticity under quasi-static loading conditions, while under dynamic loading conditions wave speed becomes imaginary (Hill, 1962; Rice, 1976; Thomas, 1961), which renders the boundary value problem ill-posed. From the numerical point of view, this situation manifests itself by spurious mesh-dependency of finite element computations: strain localizes into a narrow band whose width depends on the element size and tends to zero as the mesh is refined (Belytschko et al., 1986; Pietruszczak and Mróz, 1981; Tvergaard, 1982; Tvergaard et al., 1981). The corresponding load-displacement curves of system responses always exhibit earlier drop for a sufficiently fine mesh, and the total energy dissipated by fracture goes to zero!

The simplest but crude remedy, popular in engineering applications, is to adjust the post-peak slope of the stress-strain diagram as a function of the element size. When this is done properly, the energy dissipated in a band of cracking elements does not depend on the width of the band (Bažant, 1976; Bažant and Cedolin, 1983; Bažant and Oh, 1983; Pietruszczak and Mróz, 1981). A more general and fundamental approach, to avoid strain localization to a zero volume and to overcome spurious mesh sensitivity, is the nonlocal continuum theory, which states that “the physics of material bodies whose behavior at a material point is influenced by the state of all points of the body”. Following the classical notions, material points of a body are considered to be continuous and are assigned some physically independent objects (variables) (e.g., mass, charge, electric field, magnetic field) (Eringen, 2002). Numerous researches not suffering from loss of ellipticity of the field equations in localization zone, e.g. high grade continua (Aifantis, 1984, 1992; Bennett et al., 2012; De Borst and Mühlhaus, 1992; Forest et al., 2000; Mindlin, 1965; Mindlin and Eshel, 1968; Nguyen, 2011; Rodríguez-Ferran et al., 2011), Cosserat continua (Aslan et al., 2011; Cordero et al., 2013; Cosserat and Cosserat, 1896, 1909, 2009; Diamantopoulou et al., 2017; Dillard et al., 2006; Eringen, 1966a, c; Eringen, 1970; Eringen, 1999; Eringen and Suhubi, 1964; Forest, 2009; Forest, 2016; Forest and Aifantis, 2010; Forest and Sievert, 2006; Saanouni and Hamed, 2013), strictly nonlocal continuum field theory (Bažant, 1984; Bažant et al., 1984; Eringen, 1966d; Eringen, 2002; Eringen and Edelen, 1972; Jirásek, 1998; Kröner, 1967; Krumhansl, 1968; Kunin, 1968) or viscoplastic regularization (Needleman, 1988, 2015; Pijaudier-Cabot et al., 1988), are capable to provide the well-posed initial and boundary value problems.

1). The nonlocal continuum theory

The nonlocal continuum theory was introduced by Kröner, Krumhansl and others (Beran and McCoy, 1970; Kröner, 1967, 1968; Krumhansl, 1968; Kunin, 1968; Levin, 1971) and developed in detail by Eringen et al. (Ari and Eringen, 1983; Eringen, 1972; Eringen and Edelen, 1972). In this theory, the macroscopic strain and stress may be regarded as certain averages of the microscopic strains and

stresses taken over volume. If the strain field is nearly macroscopic homogeneous, the constitutive equations may be formulated as a relation between strain and stress at same location. However, if high gradients of strain exist, the whole macroscopic stress distribution over the volume should be related to the whole macroscopic strain distribution over the volume. Bažant et al. (1984) presented an imbricate continuum based on the hypothesis that the stress depends on the change of distance between two points lying a finite distance apart, and obtained stable strain-softening distributed over finite size region in one-dimensional analysis. The principle difference from the classical nonlocal continuum theory is that the equation of motion involves not only the averaging of strain but also the averaging of stress gradients. Later, Bažant (1984) extended the imbricate continuum theory to two or three dimensions to model strain-softening within zones of finite size. The proper variational method for the imbricate continuum is developed and the continuum equations of motion are derived from the principle of virtual power. The continuum equations involving both the average of stress and strain by displacement gradient ensures the symmetric finite element stiffness matrices. The original formulation of the nonlocal theory for strain-softening regime is studied in detail by Pijaudier-Cabot and Bažant (1987) for elastic behavior. Unlike the imbricate nonlocal continuum theory in which all the behavior is formulated as nonlocal including the elastic part of strain, the new nonlocal damage theory subjects nonlocal treatment only to those variables that control strain softening and remains the elastic strain as local. The spatial average of the local damage energy release rate, over the representative volume of the material whose size is a characteristic of the material, is adopted to replace the local one. Avoidance of spurious mesh sensitivity and proper convergence are demonstrated by numerical examples, including the static strain softening in a bar, longitudinal wave propagation in strain softening material and static layered finite element analysis of a beam. Later, Bažant and Pijaudier-Cabot (1988) extended the previous work to a more general form in which the strain remains local yielding the standard equilibrium equation as well as the boundary condition, while the local damage is replaced by its nonlocal damage defined by a spatial averaging of local damage for the elastic behavior. The previous work of using the nonlocal damage energy release rate can be regarded as a simplified approximation of the nonlocal damage formulation. The analysis of the strain localization instability in a bar shows that the size of the localization zone is found to be approximately proportional to the characteristic length of the nonlocal continuum in the ratio of 1.88. Pijaudier-Cabot et al. (1988) presented a comparison of various models for strain-softening due to damage such as cracking or void growth. It concludes that despite the rate-dependent model prevents the differential equation of motion from becoming elliptic and ensures the mesh-dependent problem is well posed, however, the results are not quite satisfactory. At localization the strains are finite but the localization zone tends to an infinitely small size, similar to the rate-independent continuum model. The use of high-order spatial derivatives implies high-order partial differential equations of the motion and additional boundary conditions, can be regarded as a special case of the nonlocal model with the help of the Taylor series. The nonlocal continuum with local strain applies the averaging only to those variables that control strain-softening, e.g. the local damage energy release rate. The significant size effect due to the strain-softening portion of the uniaxial response is adequately modelled by this model and in agreement with experimental evidence. Bažant and Jirásek (2002) presented a detailed review of the progress in nonlocal models

of integral type which has emerged as an effective means for regularizing the boundary value problem with strain softening, capturing the size effects and avoiding spurious localization that gives rise to pathological mesh sensitivity in numerical computations, and discussed their physical justifications, advantages and numerical applications, during the last two decades. Many recent work in applications based on the nonlocal continuum can be found in literatures (Abiri and Lindgren, 2015; Alam et al., 2013; Andrade et al., 2011; Balieu et al., 2014; Belnoue et al., 2010; Belnoue et al., 2007; Grassl and Jirásek, 2006; Havlásek et al., 2016; He et al., 2015; Jirásek and Rolshoven, 2003; Nguyen et al., 2015; Toti et al., 2015; Xenos and Grassl, 2016).

2). The gradient-dependent model

By employing the methods developed in the theory of fluid interfaces (Aifantis and Serrin, 1983a, b) which introduces second density gradients in the dependence of interfacial stress, Triantafyllidis and Aifantis (1986) proposed a new framework for considering the strain induced localization and the loss of ellipticity in the governing equilibrium equations for hyperelastic material at finite strains. In this theory, an additional second deformation gradient dependent term is introduced into the expression of the strain energy density, which leads to equilibrium equations remain elliptic. The analytical solutions of the Blatz-Ko material is obtained in the particular case. In the work of Lasry and Belytschko (1988), a simple approach based on introducing additional high order terms in the governing equations in the strain-softening portions of the domain was proposed. With the help of the Taylor expansion of the nonlocal strain model, the addition of a second order derivative term to the strain formulation leads to an efficient localization limiter (explicit gradient form), which ensures the energy dissipation remains finite at arbitrary mesh refinement, for strain-softening materials. Mühlhaus et al. (De Borst and Mühlhaus, 1992; Mühlhaus and Alfantis, 1991) developed a generalized plasticity model, which belongs to the class of gradient models and is accomplished by introducing higher-order spatial gradients of the equivalent plastic strain into the yield function while the flow rule and the elasticity law remain unaltered. Additional boundary conditions and the smoothness C^1 continuity of the interpolation functions of the plastic multiplier are required for the equilibrium conditions, due to the presence of the strain gradients in the constitutive laws. De Borst et al. (De Borst and Mühlhaus, 1992; De Borst et al., 1993) provided an overview of three different approaches, the addition of higher-order deformation gradients, the use of micropolar continuum and the addition of rate dependence, in the finite element analysis of localization phenomena, and developed two families of finite elements for the implementation of gradient-dependent plasticity. De Borst et al. (1999) proposed a combination model coupling the gradient plasticity and gradient damage for localization analysis. It concludes that coupling the theory to damage suffers from two drawbacks: the results are excessively sensitive to the damage threshold, and it's difficult to find physical grounds for a combination of two softening mechanisms. Peerlings et al. (2001) made a critical comparison of the nonlocal damage model based on the work of Pijaudier-Cabot and Bažant (1987) and the two gradient-enhanced damage formulations: explicit and implicit gradient approximations derived by (Engelen et al., 2003; Peerlings et al., 1995, 1996; Peerlings, 1999) and clarified some of the similarities and intrinsic differences. Gradient terms of order higher than two have been rigorously neglected in the explicit model, whereas these terms have indirectly been preserved in the implicit formulation. As a result, spatial interactions span the

entire domain in the implicit model, similarly to the nonlocal model. The explicit model shows a response which is entirely different and which is even nonphysical in several aspects. In particular, the wave velocity is unbounded and the predicted crack growth may be instantaneous. In the implicit gradient formulation the wave velocity and crack growth rate remain finite, as in the nonlocal model. Peerlings et al. (2004) presented a new gradient damage model derived from thermodynamics statements in elastic regime. Nonstandard terms of nonlocal strain are added to the free energy potential. The stress is enhanced by the differences of local and nonlocal strain. The damage evolution is replaced by the nonlocal equivalent strain. Abu Al-Rub and Voyatzis (2006) presented a physically motivated mathematical form for the gradient plasticity theory, which is based on the Taylor's dislocation hardening model that incorporates evolution equations of SSD and GND densities and assumes a simple addition of the densities from SSDs and GNDs, and bridges the gap between continuum and dislocation-based theories. A different expression for the material length scale parameter is obtained which indicates that the length scale is not fixed and varies with the course of plastic deformation and grain size. Mediavilla et al. (2006b) used a combined continuous-discontinuous approach, in which the continuous damage mechanics describes the material degeneration (strain-softening response), and the discontinuous approach typically used in fracture mechanics captures the crack growth, to describe the complete failure process including the crack initiation and crack propagation in sheet metal forming, initially proposed by Mediavilla et al. (2006a). The damage evolution, governed by a nonlocal internal variable which is averaged from a second order partial differential equation associated to its local values to avoid the pathological localization and mesh dependence, and a remeshing strategy, devised to capture the localization zone and accommodate the crack propagation, are performed on the platform of MSC.Marc using linear quadrilateral element with assumed strain to prevent locking. The simulations of blanking, fine-blanking and score-forming processes are in agreement with experimental observations. Many recent researches can be found in literatures (Abu Al-Rub et al., 2007; Jirásek and Rolshoven, 2009a, b).

3). The viscoplastic regularization

The viscoplastic framework (strain rate hardening/softening) can be used for regularization of local damage models. The basic idea of viscoplastic regularization is that when the deformation rate starts to increase in the softer element, the increase in strain rate makes the element stiffer again. Needleman (1988) initially presented the role of material rate dependence in setting the character of governing equations, which ensures the ellipticity of incremental equilibrium equations for quasi-static problems and real wave speeds for dynamic problems, with a simple one-dimensional problem. The pathological mesh sensitivity associated with numerical solutions of localization problems is eliminated. It concludes that material rate dependence implicitly introduces a length scale into the governing equations. However, it experienced numerical instability problems when the rate-independent limit is approached. Sluys and De Borst (1992) proposed a smeared-crack model in which the stress after cracking is not only a function of the crack strain, but also of the crack strain rate. The essential features of the rate-dependent model are the implicit presence of an internal length scale and the dispersive character of wave propagation. Inspired from the viscoplastic regularization, Dubé et al. (1996) presented a rate dependent continuum damage

model which is defined by modifying the evolution law for damage and more specifically the expression of the damage multiplier, and applied it to an isotropic damage model with crack closure. Upon softening, the rate-dependent damage model yields a second-order partial differential equation governing motion, which is unconditionally hyperbolic, instead of a third-order equation in viscoplasticity. Wang et al. (1996) derived a closed-form solution for a strain-softening viscoplastic medium in combination with an imperfection which is used to trigger the localization zone. It shows that the two length scales are coupled, namely the size of the imperfection and the material length scale implicitly introduced by the viscoplasticity theory. The width of the shear band is dominated by the smallest value of these two length scales. The influence of the imperfection decreases when the shear band is some distance away from the imperfect zone. Niazi et al. (2013) revisited the viscoplastic regularization for quasi-static problems with two different types of strain rate hardening models, and identified two length scales: a primary length scale relating to the diffuse neck length scale and a secondary length scale which relates to the localized neck length scale. It shows that the primary viscoplastic length scale is a function of the hardening and damage parameters and does not depend upon the prescribed strain rate whereas the secondary length scale is a function of the strain rate. As damage grows, the effective regularization length gradually decreases. When the effective regularization length gets shorter than the element length numerical results become mesh dependent again.

4). The high order continua

The high order continua are based on the introduction of additional degree of freedoms, such as Cosserat continua (Cosserat and Cosserat, 1896, 1909, 2009) and the micromorphic model. The micromorphic theory was proposed simultaneously by Eringen and Suhubi (1964) and Mindlin (1964). It consists of introducing a general incompatible full field of micro-deformation as an extra degree of freedom, in addition to the classical displacement field. Several available approaches can be reconciled based on Eringen's general micromorphic framework and its extension to viscoplasticity (Forest, 2009; Hirschberger, 2009; Kirchner and Steinmann, 2005). The micromorphic approach can be applied to single/poly-crystal damage plasticity (Aslan et al., 2011; Cordero et al., 2013; Forest et al., 2014) and any macroscopic quantity in order to introduce a characteristic length scale in the original classical continuum model in a systematic way, as presented in literatures (Forest, 2009; Saanouni, 2012). Nedjar et al. (Frémond and Nedjar, 1995, 1996; Nedjar, 2001) derived a nonlocal damage theory within the framework of the principle of virtual power to avoid the mesh-dependence problem. The damage velocity and its gradient are introduced into the power of internal forces, which yields additional balance equations associated with the counterparts of damage rate and its gradient, to take the interactions of microscopic movements into account. From the comparison between nonlocal and micromorphic theories (Forest and Aifantis, 2010), it concludes that: when the microstrain remains as close as possible to the plastic strain, the micromorphic model reduces to the gradient plastic model (Aifantis, 1984, 1987; Forest et al., 2002) which can be constructed from a gradient type of internal variable model (Forest and Sievert, 2003; Forest et al., 2002; Gurtin, 1996) and is used for strain localization simulations (De Borst and Pamin, 1996; De Borst et al., 1999; De Borst et al., 1993). Later, the micromorphic and strain/damage gradient models are extended to the nonlinear relations between

generalized stresses and strains by Forest (2016). Saanouni and Hamed (Hamed, 2012) proposed a thermodynamically consistent fully coupled micromorphic formulation using the appropriate micromorphic state variables and their first gradients within the framework of generalized nonlocal continua. Numerical implementation of the micromorphic damage model shows the capability to converge to a mesh-independent solution. Diamantopoulou et al. (2017) applied the micromorphic damage model to the uniaxial tensile test and air bending test which are both in agreement with the experimental results and reduce the dependence of the responses against the refinement of the mesh.

V.3 The generalized heat equations

In the analysis of conduction heat transfer, the Fourier model (Fourier, 1822, 1878), indicating that the heat flux vector is proportional to the temperature gradient, is the most widely employed model in solving engineering problems. Such a heat conduction equation combined with the energy conservation law leads to a parabolic equation predicting an infinite propagation speed of thermal pulses (Bai and Lavine, 1995; Barletta and Zanchini, 1997; Cattaneo, 1948, 1958; Coleman et al., 1982; Coleman et al., 1985; Jou et al., 1988; Müller and Ruggeri, 1993; Swenson, 1978; Vernotte, 1958; Zanchini, 1999). From the experimental standpoint, this result is inaccurate for thermal conduction problems at cryogenic temperature or in the presence of strong temperature gradients during material surface processing by laser treatment or fast machining. For instance, the propagation speed of thermal signals has been measured in liquid helium (Peshkov, 1944, 1946), in NaF at about 10°K (Jackson and Walker, 1971) and in Bi at 3.4°K (Narayananamurti and Dynes, 1972). A thermal Mach number has also been reported for heat conduction through solids (Da Yu, 1989). On the other side, several experiments or simulations on heat transport of materials with structure at nanometer length scale (e.g. semiconductor quantum dots and superlattices, Carbon nanotubes, polymer nanocomposites, multilayer coatings, microelectronic and optoelectronic devices, and microelectromechanical sensors) (Cahill et al., 2014; Cahill et al., 2003; Jou and Cimmelli Vito, 2016; Tzou, 2014; Wang and Wang, 2006) which involves high frequencies and small length scales, show significantly different results from those of the classical Fourier model. For instance, the heat flux obtained by applying a temperature gradient in nanometer-scale silicon samples, is found to be significantly lower than that predicted by Fourier's model (Larson et al., 1986), which is suggested as the result of a reduction in the conductivity of the material. Considering the heat carriers' mean-free-path ℓ and a relevant characteristic length L of the system expressed by the Knudsen number $Kn = \ell/L$, the Fourier model is valid in the limit of very small Knudsen number (i.e. $\ell/L \ll 1$). When the Knudsen number becomes comparable to or higher than 1, due to an increase of mean-free-path (as in rarefied gases and in aerospace engineering or in miniaturization/nano technologies), the heat transport is no longer diffusive but ballistic. The nonlocal effects are especially important in the nanoscale structures (Alvarez and Jou, 2007; Kaiser et al., 2017; Sellitto et al., 2016). A review of the current micro-, meso- and macroscopic methods in micro- and nanoscale heat transport has been presented in the literature (Guo and Wang, 2015).

To overcome the paradox of an infinite propagation speed of thermal signals, and to describe the heat transport behavior of nanoscale devices, many works have been done in the literature. They are briefly reviewed in what follows classified into four classes depending in the used theoretical framework:

1) Class I – modifications of the classical Fourier model

The original work was proposed by Cattaneo (Cattaneo, 1948, 1958) and Vernotte (Vernotte, 1958), which used an approximate version of kinetic theory of gases and suggested a modification of the constitutive equation of heat flux with a relaxation term. When combined with the first law of thermodynamics (energy conservation), this leads to a hyperbolic heat conduction equation, which removes the paradox of infinite temperature propagation speed and gives a solution more consistent with the experimental evidence. However, many works (Bai and Lavine, 1995; Barletta and Zanchini, 1997; Coleman et al., 1982; Coleman et al., 1985; Körner and Bergmann, 1998; Zanchini, 1999) raise the question whether Cattaneo's hyperbolic heat equation is compatible with the second law of thermodynamics. They show that the modification of the Fourier model may yield a non-positive entropy production per unit volume, clearly in conflict with the second law of thermodynamics. Later, Müller (Müller, 1966; Muller, 1967; Müller and Ruggeri, 1993), motivated by the work of Cattaneo, has tried to derive the modifications of the Fourier model of heat flux and Navier-Stokes equations from the thermodynamics of irreversible processes (TIP). He noticed that the argument of TIP could be used to derive the Cattaneo's equation from the generalized Gibbs equation. He proposed a so called "extended thermodynamics of irreversible processes" based on the assumption that the generalized specific entropy is function of the heat flux. In this framework, he obtained a generalized heat equation predicting a finite speed while the second law of thermodynamics is fulfilled. Afterwards, a large number of papers have appeared, based on the Müller's methodology and mainly devoted to gases. A relatively complete review of this type of generalized irreversible thermodynamics can be found in Jou et al. (Jou et al., 1988; Jou et al., 2010; Jou et al., 1993). In the framework of the rational thermodynamics, Coleman et al. (Coleman et al., 1982; Coleman et al., 1985) extended the specific internal energy to a quadratic function of the heat flux. Consequently, the specific entropy and specific Helmholtz free energy were also extended by the heat flux, due to the relationship between internal energy and free energy. The evolution of temperature was governed by a pair of equations. Temizer et al. (Temizer and Wriggers, 2010) derived a high order continuum formulations of linearized thermal conduction similar to the strain-gradient elasticity theory. In particular, a thermal dissipation potential that depends on the gradients of the temperature up to second-order was assumed. Accordingly, the constitutive equations associated with heat flux, derived from the dissipation potential, leads to extended Onsager-Casimir symmetry relationships. The Guyer-Krumhansl (GK) equation (Both et al., 2016; Guyer and Krumhansl, 1966), using the linearized Boltzmann equation of phonon kinetic theory in which heat transport is described by momentum and energy exchanges between colliding massless particles called phonons, emphasizes the role of nonlocal effects in heat transport. A new coefficient associated to nonlocality and higher spatial order of heat flux is introduced into the evolution equation of the heat flux. It has been successfully used to describe a heat pulse experiment at room temperature in a macroscopic, heterogeneous specimen, that cannot be modelled properly either by the Fourier model or the Cattaneo equation (Both et al., 2016). In the references (Jou et al., 2010; Lebon, 2014; Ván and Fülöp, 2012), the GK equation applied to model heat conduction at micro and nanoscales, has also been rigorously derived within the framework of extended irreversible thermodynamics (EIT). The other two enhanced heat fluxes: the Jeffreys type (lagging heat equation) and the Green-Naghdi equation can be also derived under the

framework of EIT (Ván and Fülöp, 2012). Similar to the Fourier model, the GK equation also predicts that thermal signals propagate at infinite velocity. In order to account for the nonlocal effects in metals irradiated by ultrashort laser pulses inducing large temperature gradient, Sobolev (Sergei, 1997; Sobolev, 1993; Sobolev, 1995, 2014, 2016) proposed an extension of Cattaneo's equation with an additional contribution from the second-order space derivative of heat flux, which can be regarded as an special case of the GK equation, and applied it to the double temperature model. In order to be satisfactory for high-frequency processes, all the higher-order fluxes must be incorporated into the formalism. The kinetic theory points out the fact that the relaxation times of higher-order fluxes are not always shorter than the collision time. When the frequency becomes comparable to the inverse of the relaxation time of the first-order flux, they will behave like independent variables (Sellitto et al., 2016). This yields the Ballistic heat transport model, in which the effective thermal conductivity is expressed in terms of the classical bulk thermal conductivity, the relaxation time and the Knudsen number. The dual-phase-lag model (Tzou, 1995, 2014) evolving from the Fourier model introduces two phase lags: the phase lag of the heat flux captures the small-scale response in time and the phase lag of the temperature gradient captures the small-scale response in space, into the constitutive equation of heat flux. Combining these constitutive models with the energy balance law leads to a fourth-order partial differential heat equation as well as third-order time derivative. The Boltzmann equation being hard to solve, Chen (Chen, 2001) established the ballistic-diffusive heat-conduction equations, which are applicable to transient heat conduction and are derived from the Boltzmann equation under the relaxation approximation and from the splitting of the distribution function into a diffusive and a ballistic parts, as required in small structures. Computational results suggest that it is a much better alternative to the Fourier and the Cattaneo equations at scales where the mean free path is comparable to the system size and the time is comparable to the carrier relaxation time. In fact, to obtain a finite velocity for the propagation of thermal signals it is not necessary to assume relaxation terms in heat equation. This result can be also obtained if one assumes a non-linear diffusion equation with the thermal conductivity depending on the temperature in an appropriate way (Luikov et al. (Luikov et al., 1976), Bubnov (Bubnov, 1976) and Swenson (Swenson, 1978)).

- 2) Class II – considering the temperature gradient as an argument of the Helmholtz free energy
There are essentially three ways to comply with the second law of thermodynamics when introducing the gradient of temperature or gradient of entropy:
 - a). by introducing an extra entropy flux: Ireman et al. (Ireman and Nguyen, 2004), based on the idea of Maugin's (Maugin, 1990; Maugin and Muschik, 1994a; Maugin and Muschik, 1994b) work on gradients of internal variables, discuss several ways of introducing the gradient of temperature in continuum thermodynamics; the gradient theory assumes additional entropy production;
 - b). modification with extra energy production: Forest et al. (Forest et al., 2000) made an attempt to incorporate temperature and temperature gradient into the second grade theory, with extra energy production (extra power) by extending the method of virtual power and continuum thermodynamics. An extra entropy production from the divergence of the generalized thermodynamic forces associated with the temperature gradient was derived.

Later, Forest et al. (Forest and Amestoy, 2008) developed the entropy gradient theory and derived an enhanced heat equation which has the structure of the Cahn-Hilliard equation in mass transport theory. He also showed that the entropy gradient theory and temperature gradient theory are not equivalent. The generalized heat equation derived from the temperature gradient theory can be regarded as an approximation of the reference gradient of entropy theory;

- c). modification with additional entropy production. Nguyen (Nguyen, 2010) proposed an additional entropy production and a new relationship between internal energy and free energy to introduce the gradient of temperature in the set of state variables. The deduced generalized heat equation predicts a finite propagation of thermal pulses.
- 3) Class III – double temperature model
- Aifantis (Aifantis, 1980a, b; Forest and Aifantis, 2010) derived the double temperature model, from electron-phonon collisions during the ultra-short pulsed laser heating of metals, based on the mixture theory of Müller (Müller, 2001). Sobolev (Sobolev, 2016) showed that the two temperature model using Fourier's model is a parabolic heat equation. He also derived an extended hyperbolic two temperature model by using the Cattaneo's equation.
- 4) Class IV – the micro-temperature or micro-entropy theory
- The micro-temperature, that depends on the micro-coordinates of the micro-elements, was initially considered by Wozniak (Wozniak, 1967) assuming known functions of temperature and temperature gradients. Based on the work on kinematics and dynamics of a continuum with microstructure by Eringen and Suhubi (Eringen and Suhubi, 1964; Suhubl and Eringen, 1964), Grot (Grot, 1969) proposed a theory of thermodynamics for elastic materials with microstructure which possessed micro-deformations and micro-temperatures. The micro-temperatures were determined by a balance law. The second law of thermodynamics is modified to include micro-temperature, and the first moment of the energy equation is added to the usual balance laws of a continuum with microstructure. From the linear approximation, the temperature and micro-temperature are determined by a pair of equations. Later, Iesan (Iesan, 2002) also deduced the same pair of governing heat equations using homogeneous and isotropic micromorphic continua (Eringen, 1966b; Eringen, 1970, 1992; Eringen, 1999; Eringen and Suhubi, 1964; Suhubl and Eringen, 1964). The theory of micromorphic fluids with microstructures has been studied in various papers (Koh, 1973; Riha, 1977; Říha, 1975; Verma et al., 1979). A study of the problem of heat conduction in micromorphic continua was presented by Riha (Říha, 1976) and an agreement was obtained between theoretical results and experimental data for the silicone rubber containing spherical aluminum particles and for the human body blood. Green et al. (Green and Naghdi, 1991) illustrated in details of the thermal propagation in a rigid solid at finite speed, based on the established thermomechanical theory with the introduction of a balance of entropy and the use of energy equation as an identity for all motions and all temperature fields after the elimination of external fields (Green and Naghdi, 1977). Later, a thermoelasticity theory without energy dissipation for nonpolar bodies, based on the new thermomechanical theory, has been presented in (Green and Naghdi, 1993). It permits the transmission of heat as thermal waves at finite speed. Iesan et al. (Iesan and Nappa, 2005) used the procedure proposed by Green et al. (Green and Naghdi, 1977)

and extended it to the micromorphic continua. In the linearized theory, it predicts the thermal propagation with finite speed. In the previous theories, the micro-temperature is a vector quantity akin to a temperature gradient. In contrast, Forest et al. (Forest and Aifantis, 2010) present theories involving scalar micro-temperature or micro-entropy, by applying the micromorphic approach (Forest, 2009; Saanouni and Hamed, 2013) extending the local model to the micromorphic framework, to the temperature and entropy, respectively. They showed that the gradient entropy theory and gradient temperature theory can be regarded as a limit case of the micro-entropy and micro-temperature theories.

Model	Authors	Heat equations
Classical heat equation with Fourier's model	Fourier, 1878	$\rho C_e \dot{T} = \kappa \Delta T$
Hyperbolic type with relaxation time	Cattaneo I, 1948	$\rho C_e \dot{T} + \tau \kappa \Delta \dot{T} = \kappa \Delta T$
	Cattaneo II, 1948	$\rho C_e \dot{T} + \tau \rho C_e \ddot{T} = \kappa \Delta T$
Coleman et al., 1982		$\begin{cases} \left(\rho C_e + \vec{q} \cdot \frac{dA}{dT} \cdot \vec{q} \right) \dot{T} + 2\vec{q} \cdot \underline{A} \cdot \dot{\vec{q}} = -\text{div}(\vec{q}) \\ \vec{q} + \underline{\tau} \cdot \dot{\vec{q}} = -\underline{\kappa} \cdot \vec{\nabla} T \end{cases}$
Temperature (or Entropy) gradient model	Nguyen, 2010	$\rho C_e \dot{T} + M \vec{\nabla} \dot{T} \cdot \vec{\nabla} T = \kappa \Delta T$
	Forest, 2008	$\rho C_e \dot{T} + T_0 A_T \Delta \dot{T} = \kappa \Delta T$
	Forest, 2008	$\rho C_e \dot{T} + T_0 A_T \Delta \dot{T} + \frac{A_s^2 C_e^2}{\rho T_0} \Delta^2 \dot{s} = \kappa \Delta T$
	Forest, 2010	$\rho C_e \dot{T} - \alpha T_0 \ddot{T} + M T_0 \Delta \dot{T} = \kappa \Delta T$
Double temperature model	Aifantis, 1980	$\dot{T} + \alpha \ddot{T} - \beta \Delta \dot{T} + \gamma \Delta^2 T = \lambda \Delta T$
	Sobolev, 2016	$\begin{aligned} \dot{T}_i + (\tau + \tau_{12}) \ddot{T}_i + \tau \tau_{12} \ddot{T}_i - l^2 \Delta \dot{T}_i &= \bar{\kappa} \Delta T_i \\ \dot{T}_i + (\tau + \tau_{12}) \ddot{T}_i + \tau \tau_{12} \ddot{T}_i - (l^2 + l_e^2) \Delta \dot{T}_i - l_e^2 \tau_{12} \Delta^2 T_i &= \bar{\kappa} \Delta T_i \end{aligned}$
Micro-temperature model	Iesan, 2002	$\begin{cases} c \dot{T} = k \Delta T + k_1 \text{div}(\vec{T}) \\ b \dot{\vec{T}} = k_6 \Delta \vec{T} + (k_4 + k_5) \vec{\nabla} (\text{div}(\vec{T})) - k_2 \vec{T} - k_3 \vec{\nabla} T \end{cases}$
	Iesan, 2005	$\begin{cases} a \ddot{T} + m \text{div}(\dot{\vec{T}}) = k \Delta T \\ b \ddot{\vec{T}} = d_2 \Delta \vec{T} + (d_1 + d_3) \vec{\nabla} (\text{div}(\vec{T})) - m \vec{\nabla} \dot{T} \end{cases}$

	Microtemperature type	$\rho T(\zeta_2 \ddot{\bar{T}} + \zeta_1 \ddot{T}) - T \bar{M}^g \Delta \dot{\bar{T}}$ $-T \left[\frac{1}{2} \rho C_e \left(\frac{\dot{\bar{T}}}{\bar{T}} - \frac{\dot{T}}{T} \right) + 2 \bar{M} (\dot{\bar{T}} - \dot{T}) \right] = \kappa \Delta T$
Micromorphic temperature model	Two-temperature type	$\rho C_e \dot{T} + \rho T(\zeta_2 \ddot{\bar{T}} + \zeta_1 \ddot{T}) - 2T \bar{M} (\dot{\bar{T}} - \dot{T})$ $-T \bar{M}^g \Delta \dot{\bar{T}} = \kappa \Delta T$
		$\rho C_e \dot{T} + \rho (\tau C_e + T_0 \zeta_1) \ddot{T} + \rho T_0 (\tau \zeta_1 + \zeta_2) \ddot{\bar{T}}$ $+ \tau \rho T_0 \zeta_2 \ddot{\bar{T}} - T_0 \bar{M}^g \Delta \dot{\bar{T}} - T_0 \bar{M}^g \Delta \dot{T} = \kappa \Delta T$

Table V-1 Various generalized heat equations

In the second part of thesis, we focus on the theoretical formulations and numerical implementations of the proposed micromorphic constitutive equations. The main work are summarized as following:

- 1). Theoretical formulations of the thermodynamically consistent nonlocal constitutive equations of elasto-visco-plasticity, coupling with isotropic ductile damage, temperature, mixed hardening as well as associated micromorphic state variables, in finite deformation. The new balance equations are obtained due to the introduction of the additional micromorphic state variables. The state relations and evolution equations are derived according to proper selections of the Helmholtz free energy and the dissipation potentials;
- 2). For the heat transfers, an intensive review of the current extended heat equations are studied, which could be classified into five types according to the used different theoretical frameworks. The micromorphic heat equations are derived by introducing the new micromorphic temperature and its first gradient, which yields a new thermal balance equation coupling with the classical local heat conduction equation. A pair of generalized heat equations governs the evolution of temperature and allows the introduction of nonlocal thermal effects and an internal length scale. The propagation of thermal plane waves is investigated according to various generalized heat equations. Several extended heat equations could be retrieved from the constrained micromorphic heat equations;
- 3). Three types of first-order finite element: a planar quadrangular element of plane stress, a quadrangular shell element and a solid-shell element, are developed in Abaqus to adapt the new micromorphic state variables;
- 4). The local integration of the strongly coupled micromorphic constitutive equations is performed using the well-known return-mapping algorithm based on the elastic prediction and plastic correction method for general non-associative elasto-visco-plasticity model in the presence of nonlinear isotropic and kinematic hardenings;
- 5). Parametric study of the local damage parameters, the coefficients of viscoplastic effects, the micromorphic damage and isotropic hardening parameters as well as the anisothermal micromorphic damage model, are well performed. With the identified parameters of material

PART II CHAPTER V INTRODUCTION

DP1000, the proposed nonlocal constitutive equations are applied to the uniaxial tensile test and cross section deep drawing processes respectively.

VI. Theoretical formulations

VI.1 Introduction

In several situations as for continuum with scale effects, continuum with heterogeneous microstructure, continuum with strong micro discontinuities, etc., the displacement vector and its first gradient are not sufficient to define the mechanical state in a material point. It is then necessary to add other variables as well as their gradients of the first, second, or higher orders, in the principle of virtual power and as new arguments in state and dissipation potentials. This defines the so-called mechanics of generalized continua or of materially non-simple continua. All these theories seek to define the mechanical state at a material point in terms of a more or less vast domain surrounding the point, or even of the whole domain. Finally, this introduces a kind of length scale effect in terms of the morphology of the spatial distribution of the different phases inside the representative volume element (RVE) and of the size of the various constitutive elements, or the effects of the gradients of physical fields. Commonly, the theory of the generalized continuum mechanics is classified, as schematized in Fig. VI-1, in three distinct theories(Diamantopoulou et al., 2017; Forest, 2009; Labergère, 2015; Saanouni, 2012; Saanouni and Hamed, 2013):

- 1). High grade continua, which is based on the introduction of the high order spatial gradients of the displacement vector \vec{u} in addition to the first displacement vector into the principle of virtual power, as initially proposed by (Mindlin, 1965; Mindlin and Eshel, 1968; Toupin, 1964; Toupin, 1962);
- 2). High order continua, which was initially proposed by the Cosserat brothers (Cosserat and Cosserat, 1896, 1909) and subsequently developed by Eringen and his co-workers in 1960s (Eringen, 1966a, c; Eringen, 1970; Eringen, 1999; Eringen and Suhubi, 1964; Mindlin, 1964), supports the additional degree of freedoms (dof) which are generally new kinematic variables and their high order gradients in the principle of virtual power;
- 3). Strictly nonlocal continuum field theory well summarized in the recent work by Eringen (Eringen, 2002).

As suggested by Forest (Forest, 2006; Forest, 2009), all these generalized continuum theories are still based on the assumption of local action (Truesdell and Noll, 2004a). The class of nonlocal theories are “concerned with the physics of material bodies whose behavior at a material point is influenced by the state of all points of the body” as stated by Eringen in his introduction (Eringen, 2002).

The constitutive equations presented in this part, is based on the macroscopic phenomenological approach in the context of the thermodynamics of irreversible processes with state variables (Germain et al., 1983; Lemaitre et al., 1985; Saanouni, 2012; Truesdell and Noll, 1965). Each selected physical phenomenon is associated with a state variable defined in the deformation space, whose relation with its dual variables in the stress space is conditioned by the construction of a state potential and its evolution is based on the choice of an adequate dissipation potential.

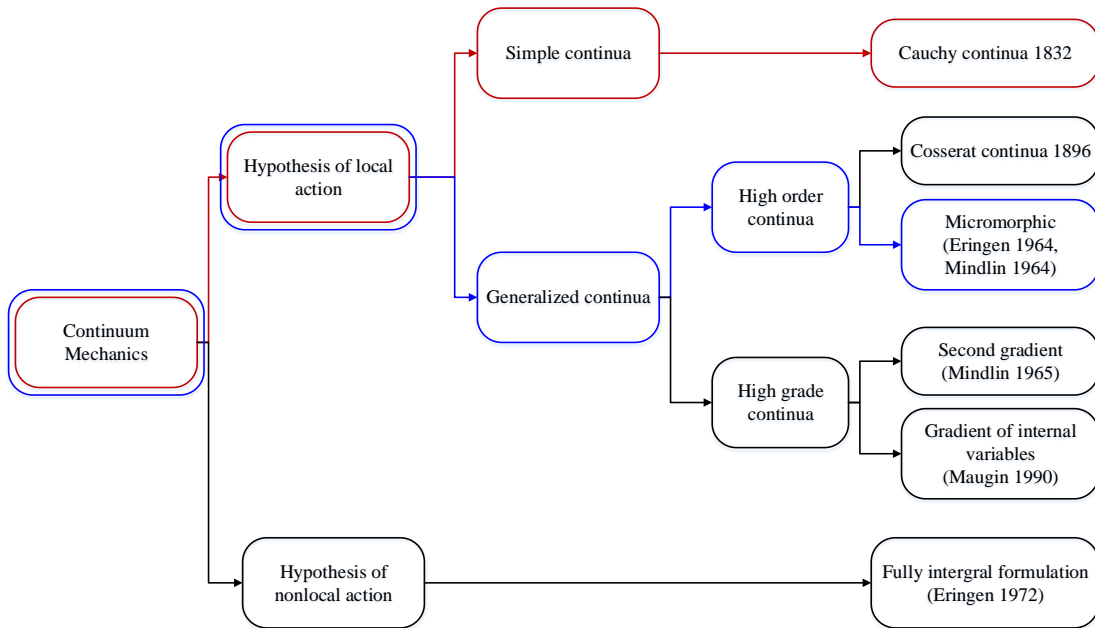


Fig. VI-1 Scheme of different theories in continuum mechanics

VI.2 Generalized principle of virtual power (Balance equations)

VI.2.1 New degree of freedoms (dofs)

In order to account for the material's softening phenomena, which results from the evolution of ductile damage or the thermal effects and yields the high sensitive mesh-dependency in the numerical simulations, four new pairs of micromorphic variables associated with their local state variables are introduced as additional internal degree of freedoms, i.e. (\bar{d}, \bar{Y}) for micromorphic damage, (\bar{r}, \bar{R}) for micromorphic isotropic hardening, $(\bar{\alpha}, \bar{X})$ for micromorphic kinematic hardening and (\bar{T}, \bar{s}) for micromorphic temperature, besides the classical degree of freedoms of displacement field, to represent the respective related nonlocal effects.

VI.2.2 Principle of virtual power for a micromorphic medium

The generalized virtual power of internal forces δP_{int} is extended by the new micromorphic variables and their first gradients:

$$\delta P_{int} = - \int_{\Omega} \left(\underline{\sigma} : \vec{\nabla} \delta \vec{u} + \vec{Y} \delta \vec{d} + \vec{R} \delta \vec{r} + \underline{X} : \delta \underline{\alpha} + \vec{s} \delta \vec{T} + \vec{Y} \cdot \vec{\nabla} \delta \vec{d} + \vec{R} \cdot \vec{\nabla} \delta \vec{r} + \vec{X} : \vec{\nabla} \delta \underline{\alpha} + \vec{s} \cdot \vec{\nabla} \delta \vec{T} \right) dV \quad (\text{II.1})$$

where, $\underline{\sigma}$ indicates the Cauchy stress tensor, \vec{Y} , \vec{R} , \vec{X} and \vec{s} are the generalized stress-like variables with respect to the first gradients of the new micromorphic dofs. The superimposed symbol (*) indicates the kinematically admissible virtual fields.

Similarly, the virtual power of external body and contact forces δP_{ext} are enriched by:

$$\delta P_{ext} = \int_{\Omega} \rho \left[\left(\vec{f}^u \cdot \delta \dot{\vec{u}} \right) + \left(f^d \cdot \delta \dot{\vec{d}} + \vec{f}^{gd} \cdot \vec{\nabla} \delta \dot{\vec{d}} \right) + \left(f^r \cdot \delta \dot{\vec{r}} + \vec{f}^{gr} \cdot \vec{\nabla} \delta \dot{\vec{r}} \right) \right] dV \\ + \left[\left(f^{\bar{a}} : \delta \dot{\vec{\alpha}} + \vec{f}^{g\bar{a}} : \vec{\nabla} \delta \dot{\vec{\alpha}} \right) + \left(f^{\bar{T}} \cdot \delta \dot{\vec{T}} + \vec{f}^{g\bar{T}} \cdot \vec{\nabla} \delta \dot{\vec{T}} \right) \right] dS \\ + \int_{\Gamma} \left[\left(\vec{F}^u \cdot \delta \dot{\vec{u}} \right) + \left(F^d \cdot \delta \dot{\vec{d}} \right) + \left(F^r \cdot \delta \dot{\vec{r}} \right) + \left(F^{\bar{a}} : \delta \dot{\vec{\alpha}} \right) + \left(F^{\bar{T}} \cdot \delta \dot{\vec{T}} \right) \right] dS \quad (II.2)$$

where, \vec{f}^u , f^d , \vec{f}^{gd} , f^r , \vec{f}^{gr} , $f^{\bar{a}}$, $\vec{f}^{g\bar{a}}$, $f^{\bar{T}}$ and $\vec{f}^{g\bar{T}}$ are the simple and generalized body forces associated with the displacement, the micromorphic variables and their respective first gradient. Also \vec{F}^u , F^d , F^r , $F^{\bar{a}}$ and $F^{\bar{T}}$ are the simple and generalized micromorphic contact forces acting on the appropriate parts of the boundary Γ .

Finally, the virtual power of inertia forces can be expressed as:

$$\delta P_a = \int_V \rho \left(\ddot{\vec{u}} \cdot \delta \dot{\vec{u}} + \zeta_d \ddot{\vec{d}} \cdot \delta \dot{\vec{d}} + \zeta_r \ddot{\vec{r}} \cdot \delta \dot{\vec{r}} + \zeta_{\bar{a}} \ddot{\vec{\alpha}} : \delta \dot{\vec{\alpha}} + \zeta_{\bar{T}} \ddot{\vec{T}} \delta \dot{\vec{T}} + \zeta_{\bar{T}_2} \ddot{\vec{T}} \delta \dot{\vec{T}} \right) dV \quad (II.3)$$

where, $\ddot{\vec{d}}$, $\ddot{\vec{r}}$, $\ddot{\vec{\alpha}}$, $\ddot{\vec{T}}$ and $\ddot{\vec{T}}$ are the generalized acceleration terms associated with micromorphic damage, micromorphic isotropic hardening, micromorphic kinematic hardening and micromorphic temperature, respectively. ζ_d , ζ_r , $\zeta_{\bar{a}}$ and $\zeta_{\bar{T}}$ are scale factors which map the local density of the material to the micromorphic level (Nedjar, 2001). Two thermal contributions are introduced for the sake of generality. The first one mimics the mechanical acceleration and introduces the second time derivative of the micromorphic temperature. The second one involves only the first time derivative of the micromorphic temperature based on the idea of micro-kinetic energy in the spirit of the kinetic theory of gas.

It should be noticed that there are two kinds of inertia contributions (first and second time derivatives) from micromorphic temperature. The first inertia term (second time derivative) is similar to the inertia of displacement. The second inertia term (the first time derivative) is based on some justifications from kinetic theory of gas, where the kinetic energy is proportional to temperature. In (Mandl, 2008) it is recalled that Maxwell and Boltzmann have developed a kinetic theory that yields a fundamental understanding of temperature in gases. The kinetic theory assumes that pressure is caused by the force associated with individual atoms striking the walls, and that this energy is translational kinetic energy. Using a sophisticated symmetry argument, Boltzmann deduced what is now called the Maxwell–Boltzmann probability distribution function for the velocity of particles in an ideal gas (Swendsen, 2006). From that probability distribution function, the average kinetic energy, E_k (per particle), of a monatomic ideal gas is:

$$E_k = \frac{1}{2} m v_{rms}^2 = \frac{3}{2} k_B T \quad (II.4)$$

where k_B is the Boltzmann constant, and v_{rms} is the root-mean-square speed. It is reasonable to assume that the temperature is function of particles velocity. Then, the first time derivative of temperature will result in an acceleration term, which is a kind of generalized force. That is why we postulate that the

generalized thermal inertia (Holba and Šesták, 2015; Šesták and Holba, 2013) (inertia of temperature) is proportional to the first and second time derivatives of temperature.

The generalized principle of virtual power stipulates that the sum of the virtual powers of internal and external forces balances the power of acceleration forces for all admissible virtual velocity and micromorphic fields (K.A. stands for kinematically admissible fields in the usual sense):

$$\delta P_{\text{int}} + \delta P_{\text{ext}} = \delta P_a \quad \forall \delta \dot{\vec{u}}, \delta \dot{\vec{d}}, \delta \dot{\vec{r}}, \delta \dot{\underline{\alpha}}, \delta \dot{\vec{T}} \text{ K.A.} \quad (\text{II.5})$$

VI.2.3 Generalized balance equations

Substituting Eqs. (II.1)-(II.3) into Eq. (II.5), the consequences are the classical equilibrium equation as well as four additional balance equations associated with the micromorphic variables together with their Neumann-type boundary conditions:

- The classical equilibrium equations:

$$\begin{cases} \vec{\nabla} \cdot \underline{\sigma} + \rho \vec{f}^u = \rho \ddot{\vec{u}} & \text{in } \Omega \\ \underline{\sigma} \cdot \vec{n} = \vec{F}^u & \text{on } \Gamma \end{cases} \quad (\text{II.6})$$

- The micromorphic temperature balance equations:

$$\begin{cases} (\vec{\nabla} \cdot \vec{s} - \vec{s}) + \rho (f^{\tau} - \vec{\nabla} \cdot \vec{f}^{g\tau}) = \rho (\zeta_{\tau_2} \ddot{\vec{T}} + \zeta_{\tau_1} \dot{\vec{T}}) & \text{in } \Omega \\ (\vec{s} - \rho \vec{f}^{g\tau}) \cdot \vec{n} = F^{\tau} & \text{on } \Gamma \end{cases} \quad (\text{II.7})$$

- The micromorphic damage balance equations:

$$\begin{cases} (\vec{\nabla} \cdot \vec{Y} - \vec{Y}) + \rho (f^d - \vec{\nabla} \cdot \vec{f}^{gd}) = \rho \zeta_d \ddot{\vec{d}} & \text{in } \Omega \\ (\vec{Y} - \rho \vec{f}^{gd}) \cdot \vec{n} = F^d & \text{on } \Gamma \end{cases} \quad (\text{II.8})$$

- The micromorphic isotropic hardening equations:

$$\begin{cases} (\vec{\nabla} \cdot \vec{R} - \vec{R}) + \rho (f^r - \vec{\nabla} \cdot \vec{f}^{gr}) = \rho \zeta_r \ddot{\vec{r}} & \text{in } \Omega \\ (\vec{R} - \rho \vec{f}^{gr}) \cdot \vec{n} = F^r & \text{on } \Gamma \end{cases} \quad (\text{II.9})$$

- The micromorphic kinematic hardening equations:

$$\begin{cases} (\vec{\nabla} \cdot \vec{\underline{X}} - \vec{\underline{X}}) + \rho (\underline{f}^{\bar{\alpha}} - \vec{\nabla} \cdot \vec{\underline{f}}^{g\bar{\alpha}}) = \rho \zeta_{\bar{\alpha}} \ddot{\underline{\alpha}} & \text{in } \Omega \\ (\vec{\underline{X}} - \rho \vec{\underline{f}}^{g\bar{\alpha}}) \cdot \vec{n} = \underline{F}^{\bar{\alpha}} & \text{on } \Gamma \end{cases} \quad (\text{II.10})$$

These balance equations with their associated Neumann-type boundary conditions will be used, with other equations, to solve the initial and boundary value problem (IBVP) in order to determine all the local and micromorphic unknown dofs.

VI.3 Thermodynamic formulations

The balance equations (II.6)~(II.10) extracted from the generalized principle of virtual power are not sufficient, by themselves, to solve the IBVP. Additional equations are then required to complete the number of equations necessary to solve the problems. These missing equations are nothing but the so called constitutive equations relating the local and micromorphic stress-like variables to their conjugated strain-like variables.

This paragraph is dedicated to the formulation of these constitutive equations for deformable solids under finite thermomechanical transformation. This will be performed in the framework of the thermodynamics of irreversible processes with state variables (see for example Saanouni (2012)). This consists in:

- Selecting the convenient pairs of local and micromorphic state variables (strain-like, stress-like) associated with the selected thermomechanical phenomena under concern
- Defining the required effective state variables on the “undamaged” or “safe” deformed configuration in order to perform, systematically, the strong effect of the ductile damage on the other thermodynamical phenomena
- Constructing a convenient state potential, a scalar valued convex function of the strain-like variables, from which the stress-like variables (or the state relationships) will be extracted
- Constructing the convenient yield functions as well as the dissipation potentials, a scalar-valued convex function of the stress-like variables, from which the evolution equations governing all the dissipative phenomena have to be extracted based on the generalized normality rules.

This formulation methodology will be followed to formulate the required local and micromorphic constitutive equations.

VI.3.1 State variables

The local state method, in the context of the thermodynamics of irreversible processes with state variables, is adopted to formulate a wide class of thermo-elasto-inelastic constitutive equations accounting for many physical phenomena including ductile damage.

VI.3.1.1 Choice of state variables

The pairs of state variables are presented in Table VI-1. Each pair is composed of a strain-like variable together with its dual force or stress-like variable (Saanouni, 2012).

Phenomenon	Internal Variable	Dual Variable
Observable state variables		
Mechanical variables	$\underline{\varepsilon}$	$\underline{\sigma}$
Thermal variables	T	s
Non observable state variables		
Thermal exchanges	$\frac{\vec{q}}{T}$	$\vec{g} = \vec{\nabla}T$

Reversible strains	$\underline{\varepsilon}^e$	$\underline{\sigma}$
Kinematic hardenings	$\underline{\alpha}$	\underline{X}
Isotropic hardening	r	R
Isotropic ductile damage	d	Y
Micromorphic kinematic hardening	$\begin{cases} \underline{\alpha} \\ \vec{\nabla} \underline{\alpha} \end{cases}$	$\begin{cases} \underline{X} \\ \vec{\underline{X}} \\ \underline{\dot{X}} \end{cases}$
Micromorphic isotropic hardening	$\begin{cases} \check{r} \\ \vec{\nabla} \check{r} \end{cases}$	$\begin{cases} \check{R} \\ \vec{\check{R}} \end{cases}$
Micromorphic isotropic damage	$\begin{cases} \check{d} \\ \vec{\nabla} \check{d} \end{cases}$	$\begin{cases} \check{Y} \\ \vec{\check{Y}} \\ \underline{\check{Y}} \end{cases}$
Micromorphic temperature	$\begin{cases} \check{T} \\ \vec{\nabla} \check{T} \end{cases}$	$\begin{cases} \check{s} \\ \vec{\check{s}} \\ \underline{\check{s}} \end{cases}$

Table VI-1 State variables associated with physical phenomena

- a) Any total strain tensor, associated with an adequate stress tensor according to the stress-strain conjugacy principle. These pairs can be: $(\underline{\varepsilon}, \underline{\sigma})$, $(\underline{\varepsilon}, \underline{\tau})$, $(\underline{E}, \underline{S})$, or $(\underline{E}, \underline{\pi})$, where $\underline{\varepsilon} = \int \underline{D} dt$ is the Eulerian total strain tensor, \underline{D} is the Eulerian strain rate tensor, $\underline{\sigma}$ is the Eulerian Cauchy stress tensor, $\underline{\tau}$ is the Eulerian Kirchhoff stress tensor, $\underline{E} = \int \underline{\dot{E}} dt$ is the Lagrangian total strain tensor, $\underline{S} = J \underline{F}^{-1} \underline{\sigma} (\underline{F}^{-1})^T$ is the Lagrangian Piola-Kirchhoff stress tensor, $\underline{F} = \int \underline{\dot{F}} dt$ is the total transformation gradient as well as the Boussinesq or Piola-Lagrange stress tensor $\underline{\pi} = J \underline{\sigma} (\underline{F}^{-1})^T$;
- b) The absolute temperature associated with the specific entropy (T, s) ;
- c) Thermal exchanges are governed by the heat flux vector (normalized by the temperature) associated with the temperature gradient $\left(\frac{\vec{q}}{T}, \vec{g} \right)$;
- d) Thermo-elastic strain $\underline{\varepsilon}^e$ is associated with the Cauchy stress if total incompressibility is accepted (Saanouni, 2012);
- e) Kinematic hardening is represented by a purely deviator tensor $\underline{\alpha}$, associated with its dual variable \underline{X} , which measures the translation of the yield surface center in stress space.

- f) Isotropic hardening is characterized by the scalar variable r associated with its dual variable R , which measures the variation in stress space of the elastic domain radius.
- g) Damage is naturally fairly anisotropic on a microscopic level. There are various mathematical representations, fourth-order tensor, second-order tensor or scalar, of damage in literatures (Krajcinovic, 1996; Lemaitre, 1992; Lemaitre et al., 1985; Lemaitre et al., 2009; Lemaitre and Desmorat, 2005; Murakami, 2012; Voyiadjis et al., 1999). In this thesis, we use a scalar d associated with a thermodynamics force Y in order to represent isotropic ductile damage.
- h) Localized effects of kinematic and isotropic hardening are represented by the micromorphic kinematic or isotropic hardening strain-like variable $\underline{\alpha}$ and \check{r} , which are supposed to carry the targeted gradient effects and have the same nature as the local kinematic or isotropic hardening state variable $\underline{\alpha}$ and r , and their first gradients $\vec{\nabla}\underline{\alpha}$ and $\vec{\nabla}\check{r}$ associated with their dual stress-like variables \check{X} , \check{R} , $\vec{\underline{X}}$ and $\vec{\check{R}}$, respectively.
- i) Due to the high sensitivity to the localization, the nonlocal damage effect is characterized by the micromorphic isotropic damage \check{d} and its first gradient $\vec{\nabla}\check{d}$. \check{Y} and $\check{\check{Y}}$ are their generalized dual forces.
- j) The thermal gradient effects are represented by the state variable of micromorphic temperature \check{T} and its first gradient $\vec{\nabla}\check{T}$ (their dual stress-like forces \check{s} and $\check{\check{s}}$). The micromorphic temperature is associated with the local temperature T .

VI.3.1.2 Damaged effective state variables

In the local state method, in order to formulate the constitutive equations for materially simple continuous media, the assumption that the medium concerned is perfectly continuous and not containing any surface or volume discontinuities is adopted. However, the presence of the local damage, in the form of a fairly random distribution of microvoids and/or microcracks, rightly introduces micro-discontinuities in the representative volume element (RVE) which is unrealistic to search for the exact topology. An exhaustive discussion on the different ways of defining this equivalent fictive RVE can be found in literature (Besson et al., 2001; Murakami, 2012; Saanouni, 2012). Here, the fictive configuration is defined by using the total energy equivalence hypothesis (a generalization of the elastic energy equivalence hypothesis), which states that at any time, an RVE in its real deformed and damaged (rotated) configuration, and where the thermomechanical state, at this time, is defined by the set of state variable pairs from Table VI-1; we associate a safe (i.e. undamaged) equivalent fictive configuration, the thermomechanical state of which is described by the effective state variables listed in Table VI-2, in such a manner that the total energy defined over the two real and fictive configurations is the same (Saanouni, 2012).

The Helmholtz energy is assumed to be the sum of elastic energy W_{ela} , energy dissipated in the kinematic hardening W_{kin} , and energy dissipated in isotropic hardening W_{iso} . By extending these definition to the micromorphic state variables, the application of this energy equivalence principle leads to:

$$\begin{aligned} \left\{ \begin{array}{l} W_{ela} = \frac{1}{2} \underline{\sigma} : \underline{\varepsilon}^e = \frac{1}{2} \tilde{\underline{\sigma}} : \tilde{\underline{\varepsilon}}^e \\ W_{kin} = \frac{1}{2} \underline{X} : \underline{\alpha} = \frac{1}{2} \tilde{\underline{X}} : \tilde{\underline{\alpha}} \\ W_{iso} = \frac{1}{2} Rr = \frac{1}{2} \tilde{R}\tilde{r} \end{array} \right. & \text{and} \quad \left\{ \begin{array}{l} \check{W}_{kin} = \frac{1}{2} \check{\underline{X}} : \check{\underline{\alpha}} = \frac{1}{2} \check{\tilde{\underline{X}}} : \check{\tilde{\underline{\alpha}}} \\ \check{W}_{kin}^g = \frac{1}{2} \check{\underline{X}} : \vec{\nabla} \check{\underline{\alpha}} = \frac{1}{2} \check{\tilde{\underline{X}}} : \vec{\nabla} \check{\tilde{\underline{\alpha}}} \end{array} \right. & \text{and} \quad \left\{ \begin{array}{l} \check{W}_{iso} = \frac{1}{2} \check{R} \check{r} = \frac{1}{2} \check{\tilde{R}} \check{\tilde{r}} \\ \check{W}_{iso}^g = \frac{1}{2} \check{R} \cdot \vec{\nabla} \check{r} = \frac{1}{2} \check{\tilde{R}} \cdot \vec{\nabla} \check{\tilde{r}} \end{array} \right. \quad (\text{II.11}) \end{aligned}$$

	Deformed and damaged real RVE	Undamaged fictive RVE
Rotated configurations (RVE)		
	$(T, s), \left(\frac{\vec{q}}{T}, \vec{g} \right)$	$(T, s), \left(\frac{\vec{q}}{T}, \vec{g} \right)$
	$\left\{ \begin{array}{l} (\check{T}, \check{s}) \\ (\vec{\nabla} \check{T}, \check{s}) \end{array} \right.$	$\left\{ \begin{array}{l} (\check{T}, \check{s}) \\ (\vec{\nabla} \check{T}, \check{s}) \end{array} \right.$
	$(\underline{\varepsilon}^e, \underline{\sigma})$	$(\tilde{\underline{\varepsilon}}^e, \tilde{\underline{\sigma}})$
Internal state variables	$(\underline{\alpha}, \underline{X}), \left\{ \begin{array}{l} (\underline{\alpha}, \underline{X}) \\ (\vec{\nabla} \underline{\alpha}, \underline{X}) \end{array} \right.$	$(\tilde{\underline{\alpha}}, \tilde{\underline{X}}), \left\{ \begin{array}{l} (\tilde{\underline{\alpha}}, \tilde{\underline{X}}) \\ (\vec{\nabla} \tilde{\underline{\alpha}}, \tilde{\underline{X}}) \end{array} \right.$
	$(r, R), \left\{ \begin{array}{l} (\check{r}, \check{R}) \\ (\vec{\nabla} \check{r}, \check{R}) \end{array} \right.$	$(\tilde{r}, \tilde{R}), \left\{ \begin{array}{l} (\tilde{r}, \tilde{R}) \\ (\vec{\nabla} \tilde{r}, \tilde{R}) \end{array} \right.$
	$(d, Y), \left\{ \begin{array}{l} (\check{d}, \check{Y}) \\ (\vec{\nabla} \check{d}, \check{Y}) \end{array} \right.$	$(\tilde{d}, \tilde{Y}), \left\{ \begin{array}{l} (\tilde{d}, \tilde{Y}) \\ (\vec{\nabla} \tilde{d}, \tilde{Y}) \end{array} \right.$
Total energy	$W_{Total}(\underline{\varepsilon}^e, \underline{\alpha}, r, d, T, \check{T}, \vec{\nabla} \check{T}, \check{d}, \vec{\nabla} \check{d}, \check{\underline{\alpha}}, \vec{\nabla} \check{\underline{\alpha}}, \check{r}, \vec{\nabla} \check{r})$ $W_{Total} = W_{ela} + W_{kin} + W_{iso}$	$=$ $\tilde{W}_{Total}(\tilde{\underline{\varepsilon}}^e, \tilde{\underline{\alpha}}, \tilde{r}, T, \check{T}, \vec{\nabla} \check{T}, \check{d}, \vec{\nabla} \check{d}, \tilde{\check{\underline{\alpha}}}, \vec{\nabla} \tilde{\check{\underline{\alpha}}}, \tilde{r}, \vec{\nabla} \tilde{r})$

Table VI-2 Definition of the total energy equivalence hypothesis in strain space (Helmholtz energy)

A general solution that satisfies the equations Eq.(II.11) may take the following form in the case of the simple isotropic ductile damage:

$$\begin{cases} \tilde{\underline{\sigma}} = \frac{\underline{\sigma}}{g_{ela}(d)} & \tilde{\underline{\varepsilon}}^e = (g_{ela}(d))\underline{\varepsilon}^e \\ \tilde{\underline{X}} = \frac{\underline{X}}{g_{kin}(d)} & \tilde{\underline{\alpha}} = (g_{kin}(d))\underline{\alpha} \\ \tilde{R} = \frac{R}{g_{iso}(d)} & \tilde{r} = (g_{iso}(d))r \end{cases} \quad \text{and} \quad \begin{cases} \tilde{\underline{\check{R}}} = \frac{\check{R}}{\check{g}_{iso}(d)} & , \quad \tilde{\check{r}} = (\check{g}_{iso}(d))\check{r} \\ \tilde{\underline{\check{R}}} = \frac{\check{R}}{\check{g}_{iso}^g(d)} & , \quad \vec{\nabla} \tilde{\check{r}} = (\check{g}_{iso}^g(d))\vec{\nabla} \check{r} \\ \tilde{\underline{\check{X}}} = \frac{\check{X}}{\check{g}_{kin}(d)} & , \quad \tilde{\underline{\check{\alpha}}} = (\check{g}_{kin}(d))\check{\underline{\alpha}} \\ \tilde{\underline{\check{X}}} = \frac{\check{X}}{\check{g}_{kin}^g(d)} & , \quad \vec{\nabla} \tilde{\underline{\check{\alpha}}} = (\check{g}_{kin}^g(d))\vec{\nabla} \check{\underline{\alpha}} \end{cases} \quad (II.12)$$

where, the damage effect functions ($g_{ela}(d)$, $g_{kin}(d)$, $g_{iso}(d)$, $\check{g}_{iso}(d)$, $\check{g}_{iso}^g(d)$, $\check{g}_{kin}(d)$, $\check{g}_{kin}^g(d)$) are scalar, positive, and decreasing functions of the scalar isotropic damage variable d . They take value of unity in the total absence of damage and tend toward zero when damage approaches unity, resulting in the final fracture of the RVE.

Here, for the sake of simplicity, the following choices have been made:

$$\begin{cases} g_{ela}(d) = g_{kin}(d) = \check{g}_{kin}(d) = \check{g}_{kin}^g(d) = \sqrt{1-d} \\ \text{and} \\ g_{iso}(d) = \check{g}_{iso}(d) = \check{g}_{iso}^g(d) = \sqrt{1-d^\gamma} \end{cases} \quad (II.13)$$

where, γ is a scalar parameter characterizing the coupling between the ductile local damage and the isotropic local and micromorphic hardenings.

VI.3.2 Thermodynamic consistency and state potential (State relations)

VI.3.2.1 The principles of the irreversible thermodynamics

VI.3.2.1.1 First law of thermodynamics: Energy conservation

The energy conservation principle postulates the existence of a state function called internal energy E homogeneous to an amount of work, so that at any time in the area \wp_t , the sum of the material time derivative of internal energy and the kinetic energy K is equal to the sum of the power of external forces applied to \wp_t and the heat quantity Q received by \wp_t :

$$\frac{d}{dt}(E+K) = P_{ext} + Q \quad (II.14)$$

Moreover, using the kinetic energy theorem, which stipulates that the material time derivative of kinetic energy is the sum of the real power of external and internal forces:

$$\frac{dK}{dt} = P_{ext} + P_{int} \quad (II.15)$$

Then, Eq.(II.14) becomes to:

$$\frac{dE}{dt} + P_{\text{int}} = Q \quad (\text{II.16})$$

In the current deformed configuration C_t , this is expressed by the following integral equations:

$$\frac{d}{dt} \int_{\Omega_t} (\rho e) dv = \int_{\Omega_t} \left(\underline{\sigma} : \underline{D} + \dot{\underline{Y}} \underline{d} + \dot{\underline{R}} \underline{r} + \dot{\underline{X}} : \dot{\underline{\alpha}} + \dot{\underline{s}} \dot{\underline{T}} + \dot{\underline{Y}} \cdot \vec{\nabla} \underline{d} + \dot{\underline{R}} \cdot \vec{\nabla} \underline{r} + \dot{\underline{X}} : \vec{\nabla} \dot{\underline{\alpha}} + \dot{\underline{s}} \cdot \vec{\nabla} \dot{\underline{T}} \right) dv + \int_{\Omega_t} (\rho \zeta) dv - \int_{\Gamma_t} (\vec{q} \cdot \vec{n}) ds \quad (\text{II.17})$$

where, e is the specific internal energy (per unit mass), ζ is the internal (or volume) heat source, and \vec{q} is the heat flux vector received across the boundary surface Γ_t having the vector \vec{n} as an outward normal (i.e. the direction of the heat flow).

By using the material time derivative of a volume integral together with the divergence theorem in order to transform surface integrals into volume integrals, and by applying the spatial localization theorem (or local action theorem) for materially simple continua, we obtain the generalized localized (differential) form of the first principle of thermodynamics as:

$$\rho \dot{e} = \left(\underline{\sigma} : \underline{D} + \dot{\underline{Y}} \underline{d} + \dot{\underline{R}} \underline{r} + \dot{\underline{X}} : \dot{\underline{\alpha}} + \dot{\underline{s}} \dot{\underline{T}} + \dot{\underline{Y}} \cdot \vec{\nabla} \underline{d} + \dot{\underline{R}} \cdot \vec{\nabla} \underline{r} + \dot{\underline{X}} : \vec{\nabla} \dot{\underline{\alpha}} + \dot{\underline{s}} \cdot \vec{\nabla} \dot{\underline{T}} \right) + \rho \zeta - \text{div}(\vec{q}) \quad (\text{II.18})$$

VI.3.2.1.2 Second law of thermodynamics: Inequality of entropy

The first law of thermodynamics can be regarded as an expression of the inter-convertibility of heat and work, maintaining an energy balance; as such it places no restriction on the direction of the process. The direction of physical processes can be expressed as a constraint on the way entropy can change during any process. This is what the second law of thermodynamics is about. It states that the rate of entropy production is always greater than or equal to the amount of heat received divided by the absolute temperature.

$$\frac{dS}{dt} \geq \frac{Q}{T} \quad (\text{II.19})$$

where, $S = \rho s$ is the entropy and T is the absolute temperature and s being the specific entropy (per unit mass).

In the current deformed configuration C_t , it can be expressed by the following integral equations:

$$\frac{d}{dt} \int_{\Omega_t} (\rho s) dv - \int_{\Omega_t} \left(\rho \frac{\zeta}{T} \right) dv + \int_{\Gamma_t} \left(\frac{\vec{q}}{T} \cdot \vec{n} \right) ds \geq 0 \quad (\text{II.20})$$

The use of the divergence theorem together with the principle of space localization for materially simple continua leads to the local (differential) form of the second principle of thermodynamics in the current configuration:

$$\rho\dot{s} - \rho\frac{\zeta}{T} + \text{div}\left(\frac{\vec{q}}{T}\right) \geq 0 \quad (\text{II.21})$$

The extended localized forms of the first and second law of thermodynamics can be combined, via the elimination of the internal heat quantity ζ , in order to give a single inequality called the fundamental inequality of thermodynamics:

$$\rho(T\dot{s} - \dot{e}) + \left(\frac{\underline{\sigma} : \underline{D} + \vec{Y} \cdot \vec{d} + \vec{R} \cdot \vec{r} + \vec{X} : \vec{\alpha} + \vec{s} \cdot \vec{T}}{+ \vec{Y} \cdot \vec{\nabla} \vec{d} + \vec{R} \cdot \vec{\nabla} \vec{r} + \vec{X} : \vec{\nabla} \vec{\alpha} + \vec{s} \cdot \vec{\nabla} \vec{T}} \right) - \frac{\vec{q}}{T} \cdot \vec{g} \geq 0 \quad (\text{II.22})$$

where, \vec{g} is the first gradient of absolute temperature.

Considering the specific Helmholtz free energy ($\psi = e - Ts$), gives us the generalized so-called Clausius-Duhem inequality:

$$-\rho(s\dot{T} + \dot{\psi}) + \left(\frac{\underline{\sigma} : \underline{D} + \vec{Y} \cdot \vec{d} + \vec{R} \cdot \vec{r} + \vec{X} : \vec{\alpha} + \vec{s} \cdot \vec{T}}{+ \vec{Y} \cdot \vec{\nabla} \vec{d} + \vec{R} \cdot \vec{\nabla} \vec{r} + \vec{X} : \vec{\nabla} \vec{\alpha} + \vec{s} \cdot \vec{\nabla} \vec{T}} \right) - \frac{\vec{q}}{T} \cdot \vec{g} \geq 0 \quad (\text{II.23})$$

We postulate that the state potential here taken as the Helmholtz free energy in the current deformed configuration, is a closed convex function of the all effective strain-like state variables, including the classical local state variables $\underline{\varepsilon}^{re}$, d , r and $\underline{\alpha}$ as well as the micromorphic variables \vec{d} , \vec{r} , $\vec{\alpha}$ and \vec{T} , and also their respective first gradients $\vec{\nabla} \vec{d}$, $\vec{\nabla} \vec{r}$, $\vec{\nabla} \vec{\alpha}$ and $\vec{\nabla} \vec{T}$, and a concave function of the temperature. Accordingly, the time derivative of the specific Helmholtz free energy $\psi(\underline{\varepsilon}^{re}, T, d, r, \underline{\alpha}, \vec{d}, \vec{r}, \vec{\alpha}, \vec{T}, \vec{\nabla} \vec{d}, \vec{\nabla} \vec{r}, \vec{\nabla} \vec{\alpha}, \vec{\nabla} \vec{T})$ is then given by:

$$\begin{aligned} \dot{\psi} &= \frac{\partial \psi}{\partial \underline{\varepsilon}^{re}} : \dot{\underline{\varepsilon}}^{re} \\ &+ \frac{\partial \psi}{\partial d} \dot{d} + \frac{\partial \psi}{\partial r} \dot{r} + \frac{\partial \psi}{\partial \underline{\alpha}} : \dot{\underline{\alpha}} + \frac{\partial \psi}{\partial T} \dot{T} \\ &+ \frac{\partial \psi}{\partial \vec{d}} \cdot \vec{\dot{d}} + \frac{\partial \psi}{\partial \vec{r}} \cdot \vec{\dot{r}} + \frac{\partial \psi}{\partial \vec{\alpha}} : \vec{\dot{\alpha}} + \frac{\partial \psi}{\partial \vec{T}} \cdot \vec{\dot{T}} \\ &+ \frac{\partial \psi}{\partial \vec{\nabla} \vec{d}} \cdot \vec{\nabla} \vec{\dot{d}} + \frac{\partial \psi}{\partial \vec{\nabla} \vec{r}} \cdot \vec{\nabla} \vec{\dot{r}} + \frac{\partial \psi}{\partial \vec{\nabla} \vec{\alpha}} : \vec{\nabla} \vec{\dot{\alpha}} + \frac{\partial \psi}{\partial \vec{\nabla} \vec{T}} \cdot \vec{\nabla} \vec{\dot{T}} \end{aligned} \quad (\text{II.24})$$

Substituting Eq.(II.24) into Eq.(II.23) and assuming the additive decomposition of total strain rate into small reversible and large irreversible parts $\underline{D} = \dot{\underline{\varepsilon}}^{re} + \underline{D}^{ir}$, it gives the following expression of the inequality:

$$\begin{aligned}
 & \left(\underline{\sigma} - \rho \frac{\partial \psi}{\partial \underline{\varepsilon}^{re}} \right) : \dot{\underline{\varepsilon}}^{re} - \rho \left(s + \frac{\partial \psi}{\partial T} \right) \dot{T} \\
 & + \left(\bar{Y} - \rho \frac{\partial \psi}{\partial d} \right) \dot{\bar{d}} + \left(\bar{R} - \rho \frac{\partial \psi}{\partial r} \right) \dot{\bar{r}} + \left(\bar{X} - \rho \frac{\partial \psi}{\partial \underline{\alpha}} \right) : \dot{\underline{\alpha}} + \left(\bar{s} - \rho \frac{\partial \psi}{\partial \bar{T}} \right) \dot{\bar{T}} \\
 & + \left(\bar{\bar{Y}} - \rho \frac{\partial \psi}{\partial \bar{\nabla} \bar{d}} \right) \cdot \vec{\nabla} \dot{\bar{d}} + \left(\bar{\bar{R}} - \rho \frac{\partial \psi}{\partial \bar{\nabla} \bar{r}} \right) \cdot \vec{\nabla} \dot{\bar{r}} + \left(\bar{\bar{X}} - \rho \frac{\partial \psi}{\partial \bar{\nabla} \bar{\alpha}} \right) : \vec{\nabla} \dot{\underline{\alpha}} + \left(\bar{\bar{s}} - \rho \frac{\partial \psi}{\partial \bar{\nabla} \bar{T}} \right) \cdot \vec{\nabla} \dot{\bar{T}} \\
 & + \underline{\sigma} : \underline{D}^{ir} - \left(\rho \frac{\partial \psi}{\partial d} \dot{d} + \rho \frac{\partial \psi}{\partial r} \dot{r} + \rho \frac{\partial \psi}{\partial \underline{\alpha}} : \dot{\underline{\alpha}} \right) - \frac{\vec{q}}{T} \cdot \vec{\nabla} T \geq 0
 \end{aligned} \tag{II.25}$$

Without loss of generality, we assume that the items $\left(\underline{\sigma} - \rho \frac{\partial \psi}{\partial \underline{\varepsilon}^{re}} \right)$, $\left(s + \frac{\partial \psi}{\partial T} \right)$, $\left(\bar{Y} - \rho \frac{\partial \psi}{\partial d} \right)$, $\left(\bar{R} - \rho \frac{\partial \psi}{\partial r} \right)$, $\left(\bar{X} - \rho \frac{\partial \psi}{\partial \underline{\alpha}} \right)$, $\left(\bar{s} - \rho \frac{\partial \psi}{\partial \bar{T}} \right)$, $\left(\bar{\bar{Y}} - \rho \frac{\partial \psi}{\partial \bar{\nabla} \bar{d}} \right)$, $\left(\bar{\bar{R}} - \rho \frac{\partial \psi}{\partial \bar{\nabla} \bar{r}} \right)$, $\left(\bar{\bar{X}} - \rho \frac{\partial \psi}{\partial \bar{\nabla} \bar{\alpha}} \right)$ and $\left(\bar{\bar{s}} - \rho \frac{\partial \psi}{\partial \bar{\nabla} \bar{T}} \right)$ do not depend on their rates respectively, as well as the micromorphic variables do not dissipate, then following standard arguments (Truesdell and Noll (Truesdell and Noll, 2004b)), we may have the following state relations:

$$\begin{aligned}
 \underline{\sigma} &= \rho \frac{\partial \psi}{\partial \underline{\varepsilon}^{re}} & s &= -\frac{\partial \psi}{\partial T} \\
 Y &= -\rho \frac{\partial \psi}{\partial d} & R &= \rho \frac{\partial \psi}{\partial r} & X &= \rho \frac{\partial \psi}{\partial \underline{\alpha}} \\
 \bar{Y} &= \rho \frac{\partial \psi}{\partial \bar{d}} & \bar{R} &= \rho \frac{\partial \psi}{\partial \bar{r}} & \bar{X} &= \rho \frac{\partial \psi}{\partial \bar{\underline{\alpha}}} \\
 \bar{\bar{Y}} &= \rho \frac{\partial \psi}{\partial \bar{\nabla} \bar{d}} & \bar{\bar{R}} &= \rho \frac{\partial \psi}{\partial \bar{\nabla} \bar{r}} & \bar{\bar{X}} &= \rho \frac{\partial \psi}{\partial \bar{\nabla} \bar{\alpha}} \\
 \bar{s} &= \rho \frac{\partial \psi}{\partial \bar{T}} & \bar{\bar{s}} &= \rho \frac{\partial \psi}{\partial \bar{\nabla} \bar{T}}
 \end{aligned} \tag{II.26}$$

and the classical local dissipation: including the intrinsic dissipation and thermal dissipation:

$$\phi = \phi_{in} + \phi_{th} = \underline{\sigma} : \underline{D}^{ir} + Y \dot{d} - R \dot{r} - X : \dot{\underline{\alpha}} - \frac{\vec{q}}{T} \cdot \vec{g} \geq 0 \tag{II.27}$$

with, intrinsic dissipation $\phi_{in} = \underline{\sigma} : \underline{D}^{ir} + Y \dot{d} - R \dot{r} - X : \dot{\underline{\alpha}}$, and the thermal dissipation $\phi_{th} = -\frac{\vec{q}}{T} \cdot \vec{g}$. In the following the reversible strains will be noted as elastic $\underline{\varepsilon}^e$ and the irreversible (or inelastic) strains can be either viscoplastic noted $\underline{\varepsilon}^{vp}$ for time-dependent inelasticity or plastic noted $\underline{\varepsilon}^p$ for time-independent inelastic flow.

VI.3.2.2 Choice of strongly coupled state potential: Helmholtz free energy

In this thesis, the micromorphic state variables and their first gradients are assumed to be not directly affected by the micromorphic damage. On the other hand, the micromorphic state variables are assumed to contribute to the Helmholtz free energy in terms of the relative difference with respect to the local variables of the same nature. The Helmholtz free energy is supposed to be divided into two terms by an additive decomposition: thermo-elastic damageable potential $\rho\psi_{tel}(\underline{\varepsilon}^e, d, T, \bar{T}, \vec{\nabla}\bar{T})$ and thermo-inelastic damageable potential $\rho\psi_{inel}(d, r, \underline{\alpha}, \bar{d}, \bar{r}, \bar{\alpha}, \vec{\nabla}\bar{d}, \vec{\nabla}\bar{r}, \vec{\nabla}\bar{\alpha})$, according to:

$$\rho\psi = \rho\psi_{tel}(\underline{\varepsilon}^e, d, T, \bar{T}, \vec{\nabla}\bar{T}) + \rho\psi_{inel}(d, r, \underline{\alpha}, \bar{d}, \bar{r}, \bar{\alpha}, \vec{\nabla}\bar{d}, \vec{\nabla}\bar{r}, \vec{\nabla}\bar{\alpha}) \quad (\text{II.28})$$

Keeping in mind the definition of the effective local and micromorphic state variables defined by Eq.(II.13), these state potentials can be chosen as:

$$\begin{aligned} \rho\psi_{tel} &= \frac{1}{2}\underline{\tilde{\varepsilon}}^e : \underline{\underline{\Lambda}}(T) : \underline{\tilde{\varepsilon}}^e - (T - T_0)\underline{P}(T) : \underline{\tilde{\varepsilon}}^e - (T - \bar{T})\bar{P}(T) : \underline{\tilde{\varepsilon}}^e \\ &\quad - \rho \frac{C_\varepsilon}{2T_0} (T - T_0)^2 + \frac{1}{2} (\bar{M}(T)(T - \bar{T})^2) + \frac{1}{2} (\bar{M}^g(T) \vec{\nabla}\bar{T} \cdot \vec{\nabla}\bar{T}) \\ &= (1-d) \frac{1}{2} \underline{\varepsilon}^e : \underline{\underline{\Lambda}}(T) : \underline{\varepsilon}^e - \sqrt{1-d} [(T - T_0)\underline{P}(T) + (T - \bar{T})\bar{P}(T)] : \underline{\varepsilon}^e \\ &\quad - \rho \frac{C_\varepsilon}{2T_0} (T - T_0)^2 + \frac{1}{2} (\bar{M}(T)(T - \bar{T})^2) + \frac{1}{2} (\bar{M}^g(T) \vec{\nabla}\bar{T} \cdot \vec{\nabla}\bar{T}) \end{aligned} \quad (\text{II.29})$$

and,

$$\begin{aligned} \rho\psi_{inel} &= \frac{1}{2} (\underline{\tilde{\alpha}} : \underline{\underline{C}}(T) : \underline{\tilde{\alpha}}) + \frac{1}{2} [(\underline{\tilde{\alpha}} - \bar{\underline{\alpha}}) : \bar{\underline{\underline{C}}}(T) : (\underline{\tilde{\alpha}} - \bar{\underline{\alpha}})] + \frac{1}{2} (\vec{\nabla}\bar{\underline{\alpha}} : \bar{\underline{\underline{C}}}^g(T) : \vec{\nabla}\bar{\underline{\alpha}}) \\ &\quad + \frac{1}{2} (Q(T)\tilde{r}^2) + \frac{1}{2} [\bar{Q}(T)(\tilde{r} - \bar{r})^2] + \frac{1}{2} (\bar{Q}^g(T) \vec{\nabla}\bar{r} \cdot \vec{\nabla}\bar{r}) \\ &\quad + \frac{1}{2} [\bar{H}(T)(d - \bar{d})^2] + \frac{1}{2} (\bar{H}^g(T) \vec{\nabla}\bar{d} \cdot \vec{\nabla}\bar{d}) \\ &= (1-d) \left[\frac{1}{2} (\underline{\alpha} : \underline{\underline{C}}(T) : \underline{\alpha}) + \frac{1}{2} [(\underline{\alpha} - \bar{\underline{\alpha}}) : \bar{\underline{\underline{C}}}(T) : (\underline{\alpha} - \bar{\underline{\alpha}})] + \frac{1}{2} (\vec{\nabla}\bar{\underline{\alpha}} : \bar{\underline{\underline{C}}}^g(T) : \vec{\nabla}\bar{\underline{\alpha}}) \right] \\ &\quad + (1-d^\gamma) \left[\frac{1}{2} (Q(T)r^2) + \frac{1}{2} [\bar{Q}(T)(r - \bar{r})^2] + \frac{1}{2} (\bar{Q}^g(T) \vec{\nabla}\bar{r} \cdot \vec{\nabla}\bar{r}) \right] \\ &\quad + \frac{1}{2} [\bar{H}(T)(d - \bar{d})^2] + \frac{1}{2} (\bar{H}^g(T) \vec{\nabla}\bar{d} \cdot \vec{\nabla}\bar{d}) \end{aligned} \quad (\text{II.30})$$

where, $\underline{\underline{\Lambda}}$ is the positive definite and symmetric fourth-rank tensor of the elastic moduli, \underline{P} is the positive definite and symmetric second-rank tensor of thermal expansion, \bar{P} is the positive definite and symmetric second-tensor of micromorphic thermal expansion, C_ε is the (scalar) specific heat capacity at constant volume, \bar{M} is the (scalar) coupling modulus with respect to temperature, \bar{M}^g is the (scalar) modulus of

gradient of micromorphic temperature, $\underline{\underline{C}}$ (fourth-rank symmetric tensor) and Q (scalar) are the kinematic and isotropic hardening macro moduli, $\breve{\underline{\underline{C}}}$ (fourth-rank symmetric tensor), \breve{Q} and \breve{H} (scalars) are the coupling moduli with respect to the kinematic hardening, isotropic hardening and damage respectively, $\breve{\underline{\underline{C}}}^g$ (sixth-rank symmetric tensor), \breve{Q}^g and \breve{H}^g (scalars) are the micromorphic moduli relative to the first gradients of micromorphic kinematic hardening, isotropic hardening and damage respectively, the subscript (T) indicates that the material properties are function of the local temperature (no dependence with respect to the micromorphic temperature).

In this choice, we note that temperature only plays the simple role of parameter in inelastic potential through dependence of some physical properties versus temperature. For which temperature performs the role of simple parameter except in the case of thermoelastic coupling, is consistent with the hypothesis H7 stated by Saanouni (2012):

- H7: Except the case of a thermoelastic behavior, for which experimental data have completely defined the thermoelastic coupling, we assume the widely used assumption, which is to use temperature as a simple parameter in the state potential and yield functions. This is done by assuming that the material parameters are functions of temperature. These functions must be determined, *a posteriori*, by simply smoothing parameter values previously “measured” at different temperatures between the reference temperature and the maximum operating temperature of each material. So these functions are not explicitly known at the time of the choice of potentials and yield functions.

Using the state relations in Eq.(II.26), the stress-like variables that are associated with all strain-like variables used in the state potential are obtained:

- Cauchy stress tensor:

$$\begin{aligned}\underline{\sigma} &= \rho \frac{\partial \psi}{\partial \underline{\varepsilon}^e} = \breve{\underline{\Lambda}}(T) : \underline{\underline{\varepsilon}}^e - (T - T_0) \breve{P}(T) - (T - \breve{T}) \breve{\tilde{P}}(T) \\ &= (1-d) \breve{\underline{\Lambda}}(T) : \underline{\underline{\varepsilon}}^e - \sqrt{1-d} (T - T_0) \breve{P}(T) - \sqrt{1-d} (T - \breve{T}) \breve{\tilde{P}}(T)\end{aligned}\quad (\text{II.31})$$

- Specific entropy:

$$s = -\frac{\partial \psi}{\partial T} = \frac{1}{\rho} \left\{ \left(\breve{P}(T) + \breve{\tilde{P}}(T) \right) : \underline{\underline{\varepsilon}}^e + \rho \frac{C_e}{T_0} (T - T_0) - \breve{M}(T) (T - \breve{T}) \right\} \quad (\text{II.32})$$

- Damage stress:

$$Y = -\rho \frac{\partial \psi}{\partial d} = Y_E + Y_A + Y_R + Y_d \quad (\text{II.33})$$

with,

$$\begin{cases} Y_E = \frac{1}{2} \underline{\varepsilon}^e : \underline{\underline{\Lambda}}(\tau) : \underline{\varepsilon}^e - \frac{1}{2\sqrt{1-d}} [(\tau - \tau_0) \underline{P}(\tau) : \underline{\varepsilon}^e + (\tau - \bar{\tau}) \bar{\underline{P}}(\tau) : \underline{\varepsilon}^e] \\ Y_A = \frac{1}{2} \underline{\alpha} : \underline{\underline{C}}(\tau) : \underline{\alpha} + \frac{1}{2} (\underline{\alpha} - \bar{\underline{\alpha}}) : \underline{\underline{C}}(\tau) : (\underline{\alpha} - \bar{\underline{\alpha}}) + \frac{1}{2} \vec{\nabla} \underline{\alpha} : \underline{\underline{C}}^g(\tau) : \vec{\nabla} \underline{\alpha} \\ Y_R = \frac{1}{2} \gamma d^{\gamma-1} Q(\tau) r^2 + \frac{1}{2} \gamma d^{\gamma-1} \bar{Q}(\tau) (r - \bar{r})^2 + \frac{1}{2} \gamma d^{\gamma-1} \bar{Q}^g(\tau) \vec{\nabla} \bar{r} \cdot \vec{\nabla} \bar{r} \\ Y_d = -\bar{H}(\tau)(d - \bar{d}) \end{cases} \quad (II.34)$$

- Isotropic hardening stress:

$$\begin{aligned} R &= \rho \frac{\partial \psi}{\partial r} = \tilde{Q}(\tau) r + \tilde{\bar{Q}}(\tau) (r - \bar{r}) \\ &= (1 - d^\gamma) [Q(\tau) r + \bar{Q}(\tau) (r - \bar{r})] \end{aligned} \quad (II.35)$$

- Kinematic hardening stress:

$$\begin{aligned} X &= \rho \frac{\partial \psi}{\partial \underline{\alpha}} = \underline{\underline{C}}(\tau) : \underline{\alpha} + \underline{\underline{\tilde{C}}}(\tau) : (\underline{\alpha} - \bar{\underline{\alpha}}) \\ &= (1 - d) [\underline{\underline{C}}(\tau) : \underline{\alpha} + \underline{\underline{\tilde{C}}}(\tau) : (\underline{\alpha} - \bar{\underline{\alpha}})] \end{aligned} \quad (II.36)$$

- Stress-like variables of micromorphic damage and its first gradient:

$$\begin{aligned} \bar{Y} &= \rho \frac{\partial \psi}{\partial d} = -\bar{H}(\tau)(d - \bar{d}) \\ \bar{\bar{Y}} &= \rho \frac{\partial \psi}{\partial \vec{\nabla} d} = \bar{H}^g(\tau) \vec{\nabla} \bar{d} \end{aligned} \quad (II.37)$$

- Stress-like variables with respect to micromorphic isotropic hardening and its first gradient:

$$\begin{aligned} \bar{R} &= \rho \frac{\partial \psi}{\partial \bar{r}} = -\tilde{\bar{Q}}(\tau)(r - \bar{r}) = -(1 - d^\gamma) \bar{Q}(\tau)(r - \bar{r}) \\ \bar{\bar{R}} &= \rho \frac{\partial \psi}{\partial \vec{\nabla} \bar{r}} = \tilde{\bar{Q}}^g(\tau) \vec{\nabla} \bar{r} = (1 - d^\gamma) \bar{Q}^g(\tau) \vec{\nabla} \bar{r} \end{aligned} \quad (II.38)$$

- Stress-like variables of micromorphic kinematic hardening and its first gradient:

$$\begin{aligned} \bar{X} &= \rho \frac{\partial \psi}{\partial \bar{\underline{\alpha}}} = -\underline{\underline{\tilde{C}}}(\tau) : (\underline{\alpha} - \bar{\underline{\alpha}}) = -(1 - d) \underline{\underline{\tilde{C}}}(\tau) : (\underline{\alpha} - \bar{\underline{\alpha}}) \\ \bar{\bar{X}} &= \rho \frac{\partial \psi}{\partial \vec{\nabla} \bar{\underline{\alpha}}} = \underline{\underline{\tilde{C}}}^g(\tau) : \vec{\nabla} \bar{\underline{\alpha}} = (1 - d) \underline{\underline{\tilde{C}}}^g(\tau) : \vec{\nabla} \bar{\underline{\alpha}} \end{aligned} \quad (II.39)$$

- Stress-like variables with respect to micromorphic temperature and its first gradient:

$$\begin{aligned} \bar{s} &= \rho \frac{\partial \psi}{\partial \bar{T}} = \tilde{\bar{P}}(\tau) : \underline{\varepsilon}^e - \bar{M}(\tau)(\tau - \bar{T}) = \sqrt{1-d} \bar{P}(\tau) : \underline{\varepsilon}^e - \bar{M}(\tau)(\tau - \bar{T}) \\ \bar{\bar{s}} &= \rho \frac{\partial \psi}{\partial \vec{\nabla} \bar{T}} = \bar{M}^g(\tau) \vec{\nabla} \bar{T} \end{aligned} \quad (II.40)$$

It is worth noting, that the state relations Eq.(II.31) – Eq.(II.36) can be decomposed into classical local contribution and the extended nonlocal partial with the help of the micromorphic state relations :

$$\begin{cases} \underline{\sigma} = \underline{\sigma}_{loc} + \underline{\sigma}_{nloc} \\ \underline{\sigma}_{loc} = (1-d)\underline{\Lambda}(\tau):\underline{\varepsilon}^e - \sqrt{1-d}(T-T_0)\underline{P}(\tau) \\ \underline{\sigma}_{nloc} = -\sqrt{1-d}(T-\bar{T})\bar{P}(\tau) \end{cases} \quad (\text{II.41})$$

$$\begin{cases} s = s_{loc} + s_{nloc} \\ s_{loc} = \frac{1}{\rho}\tilde{P}(\tau):\underline{\varepsilon}^e + \frac{C_\varepsilon}{T_0}(T-T_0) \\ s_{nloc} = \frac{1}{\rho}\tilde{\bar{P}}(\tau):\underline{\varepsilon}^e - \frac{1}{\rho}\bar{M}(\tau)(T-\bar{T}) \end{cases} \quad (\text{II.42})$$

$$\begin{cases} Y = Y_{loc} + Y_{nloc} \\ Y_{loc} = \frac{1}{2}\underline{\varepsilon}^e:\underline{\Lambda}(\tau):\underline{\varepsilon}^e + \frac{1}{2}\underline{\alpha}:\underline{C}(\tau):\underline{\alpha} + \frac{1}{2}\gamma d^{\gamma-1}Q(\tau)r^2 - \frac{1}{2\sqrt{1-d}}(T-T_0)\underline{P}(\tau):\underline{\varepsilon}^e \\ Y_{nloc} = \bar{Y} - \frac{1}{2\sqrt{1-d}}(T-\bar{T})\bar{P}(\tau):\underline{\varepsilon}^e \\ \quad + \frac{1}{2}(\underline{\alpha}-\bar{\underline{\alpha}}):\underline{\bar{C}}(\tau):(\underline{\alpha}-\bar{\underline{\alpha}}) + \frac{1}{2}\vec{\nabla}\underline{\alpha}:\underline{\bar{C}}^g(\tau):\vec{\nabla}\bar{\underline{\alpha}} \\ \quad + \frac{1}{2}\gamma d^{\gamma-1}\bar{Q}(\tau)(r-\bar{r})^2 + \frac{1}{2}\gamma d^{\gamma-1}\bar{Q}^g(\tau)\vec{\nabla}\bar{r}\cdot\vec{\nabla}\bar{r} \end{cases} \quad (\text{II.43})$$

$$\begin{cases} R = R_{loc} + R_{nloc} \\ R_{loc} = (1-d^\gamma)Q(\tau)r \\ R_{nloc} = (1-d^\gamma)\bar{Q}(\tau)(r-\bar{r}) = -\bar{R} \end{cases} \quad (\text{II.44})$$

$$\begin{cases} X = X_{loc} + X_{nloc} \\ X_{loc} = (1-d)\underline{C}(\tau):\underline{\alpha} \\ X_{nloc} = (1-d)\underline{\bar{C}}(\tau):(\underline{\alpha}-\bar{\underline{\alpha}}) = -\bar{X} \end{cases} \quad (\text{II.45})$$

For the sake of simplicity of formulations, the subsequent subscript (τ) of material property is neglected in most cases.

VI.3.2.3 Micro-cracks closure effects

Concerning a representative volume element (RVE) undergoing tension loading, the creation of open micro-defects results in lower moduli. However, during the unloading and progressive transformation into

the compressive phase, the micro-cracks close progressively until complete closure if the compression force is sufficient. In this case, the moduli of elasticity and hardening must be able to restore to gradually return to their initial values before damage when all the created micro-cracks are fully closed. This change of the material physical properties depending on the sign of the imposed loading related to the progressive closure of the open micro-cracks and vice-versa, called the quasi-unilateral effect, is not an easy task since it is the origin of loss of continuity and even convexity of the state and dissipation potential, mainly when the damage is anisotropic (Besson et al., 2001; Lemaître et al., 2009; Lemaître and Desmorat, 2005).

A simple way to account for this effect while avoiding any loss of continuity or convexity of the state functions, consists of decomposing the effective state variables into positive and negative parts with the help of the spectral decomposition of any symmetric second-rank tensors \underline{Z} in the form:

$$\begin{aligned}\underline{Z} &= \langle \underline{Z} \rangle_+ + \langle \underline{Z} \rangle_- \\ \langle \underline{Z} \rangle_+ &= \sum_{i=1}^3 \langle Z_i \rangle \vec{e}_i \otimes \vec{e}_i\end{aligned}\quad (\text{II.46})$$

where, Z_i and \vec{e}_i are the three eigenvalues and corresponding eigenvectors of the tensor \underline{Z} and $\langle Z_i \rangle$ is the positive part of Z_i defined by: $\langle Z_i \rangle = \max(0, Z_i)$. These two positive and negative parts of the tensor verify the following orthogonality and differentiability properties:

$$\begin{aligned}\langle \underline{Z} \rangle_- : \langle \underline{Z} \rangle_+ &= \langle \underline{Z} \rangle_+ : \langle \underline{Z} \rangle_- = 0 \\ d(\langle \underline{Z} \rangle_+ : \langle \underline{Z} \rangle_+) &= 2 \langle \underline{Z} \rangle_+ : d\underline{Z} \\ d(\langle \underline{Z} \rangle_- : \langle \underline{Z} \rangle_-) &= 2 \langle \underline{Z} \rangle_- : d\underline{Z}\end{aligned}\quad (\text{II.47})$$

Then the following derivatives of the positive and negative parts of the tensor \underline{Z} can easily be established:

$$\begin{aligned}\frac{\partial \langle \underline{Z} \rangle_+}{\partial \underline{Z}} &= \frac{\partial \langle Z_{ij} \rangle_+}{\partial Z_{kl}} = \begin{cases} \delta_{ik} \delta_{jl} & \text{if } Z_{ij} > 0 \\ 0 & \text{if } Z_{ij} < 0 \end{cases} = \langle \underline{1} \rangle_+ \\ \frac{\partial \langle \underline{Z} \rangle_-}{\partial \underline{Z}} &= \frac{\partial \langle Z_{ij} \rangle_-}{\partial Z_{kl}} = \begin{cases} \delta_{ik} \delta_{jl} & \text{if } Z_{ij} < 0 \\ 0 & \text{if } Z_{ij} > 0 \end{cases} = \langle \underline{1} \rangle_- \\ \frac{\partial \langle \underline{Z} : \underline{1} \rangle_+}{\partial \underline{Z}} &= \frac{\partial \langle Z_{ij} \delta_{ij} \rangle_+}{\partial Z_{kl}} = \begin{cases} (\delta_{ik} \delta_{jl}) \delta_{ij} & \text{if } Z_{ij} > 0 \\ 0 & \text{if } Z_{ij} < 0 \end{cases} = \langle \underline{1} \rangle_+ \\ \frac{\partial \langle \underline{Z} : \underline{1} \rangle_-}{\partial \underline{Z}} &= \frac{\partial \langle Z_{ij} \delta_{ij} \rangle_-}{\partial Z_{kl}} = \begin{cases} (\delta_{ik} \delta_{jl}) \delta_{ij} & \text{if } Z_{ij} < 0 \\ 0 & \text{if } Z_{ij} > 0 \end{cases} = \langle \underline{1} \rangle_-\end{aligned}\quad (\text{II.48})$$

For the sake of simplification, the above decomposition is only applied to the thermo-elastic damageable potential $\rho \psi_{tel}(\underline{\varepsilon}^e, d, T, \bar{T}, \bar{\nabla} \bar{T})$. More complex formulation can be found in literature (Issa, 2010; Issa et al., 2012; Saanouni, 2012; Yue, 2014). The Eq.(II.29) is modified as:

$$\begin{aligned}
 \rho\psi_{tel} = & \frac{1}{2}\tilde{\underline{\varepsilon}}^e : \underline{\underline{\Lambda}}(\boldsymbol{\tau}) : \tilde{\underline{\varepsilon}}^e - (\boldsymbol{\tau} - \boldsymbol{\tau}_0)P(\boldsymbol{\tau}) : \tilde{\underline{\varepsilon}}^e - (\boldsymbol{\tau} - \bar{\boldsymbol{\tau}})\bar{P}(\boldsymbol{\tau}) : \tilde{\underline{\varepsilon}}^e \\
 & - \rho \frac{C_e}{2T_0} (\boldsymbol{\tau} - \boldsymbol{\tau}_0)^2 + \frac{1}{2} (\bar{M}(\boldsymbol{\tau})(\boldsymbol{\tau} - \bar{\boldsymbol{\tau}})^2) + \frac{1}{2} (\bar{M}^g(\boldsymbol{\tau}) \vec{\nabla} \bar{\boldsymbol{\tau}} \cdot \vec{\nabla} \bar{\boldsymbol{\tau}}) \\
 = & \frac{1}{2}(1-d)(\underline{\varepsilon}_+^e : \underline{\underline{\Lambda}}(\boldsymbol{\tau}) : \underline{\varepsilon}_+^e) + \frac{1}{2}(1-hd)(\underline{\varepsilon}_-^e : \underline{\underline{\Lambda}}(\boldsymbol{\tau}) : \underline{\varepsilon}_-^e) \\
 & - (\boldsymbol{\tau} - \boldsymbol{\tau}_0)P(\boldsymbol{\tau}) : (\sqrt{1-d}\underline{\varepsilon}_+^e + \sqrt{1-hd}\underline{\varepsilon}_-^e) - (\boldsymbol{\tau} - \bar{\boldsymbol{\tau}})\bar{P}(\boldsymbol{\tau}) : (\sqrt{1-d}\underline{\varepsilon}_+^e + \sqrt{1-hd}\underline{\varepsilon}_-^e) \\
 & - \rho \frac{C_e}{2T_0} (\boldsymbol{\tau} - \boldsymbol{\tau}_0)^2 + \frac{1}{2} (\bar{M}(\boldsymbol{\tau})(\boldsymbol{\tau} - \bar{\boldsymbol{\tau}})^2) + \frac{1}{2} (\bar{M}^g(\boldsymbol{\tau}) \vec{\nabla} \bar{\boldsymbol{\tau}} \cdot \vec{\nabla} \bar{\boldsymbol{\tau}})
 \end{aligned} \tag{II.49}$$

where, the tensor $\underline{\varepsilon}_+^e$ and $\underline{\varepsilon}_-^e$ are the positive and negative parts of the elastic strain tensor. The parameter h ($0 \leq h \leq 1$) is related to the micro-cracks closure effect and allows reducing the damage growth under the negative parts of the applied loading, with two extreme cases: (a) $h=0$ makes no difference of the damage growth between positive and negative loads; (b) $h=1$ for which the damage growth takes places only under the positive part of the applied loading path.

According to the state relation in Eq.(II.26), the stress-like variable of damage is replaced by:

$$Y = -\rho \frac{\partial \psi}{\partial d} = \left\{
 \begin{aligned}
 & \frac{1}{2}(\underline{\varepsilon}_+^e : \underline{\underline{\Lambda}}(\boldsymbol{\tau}) : \underline{\varepsilon}_+^e) + \frac{1}{2}h(\underline{\varepsilon}_-^e : \underline{\underline{\Lambda}}(\boldsymbol{\tau}) : \underline{\varepsilon}_-^e) \\
 & - \frac{1}{2\sqrt{1-d}} [(\boldsymbol{\tau} - \boldsymbol{\tau}_0)P(\boldsymbol{\tau}) + (\boldsymbol{\tau} - \bar{\boldsymbol{\tau}})\bar{P}(\boldsymbol{\tau})] : \underline{\varepsilon}_+^e \\
 & - \frac{h}{2\sqrt{1-hd}} [(\boldsymbol{\tau} - \boldsymbol{\tau}_0)P(\boldsymbol{\tau}) + (\boldsymbol{\tau} - \bar{\boldsymbol{\tau}})\bar{P}(\boldsymbol{\tau})] : \underline{\varepsilon}_-^e \\
 & + \frac{1}{2}\underline{\alpha} : \underline{\underline{C}}(\boldsymbol{\tau}) : \underline{\alpha} + \frac{1}{2}(\underline{\alpha} - \bar{\underline{\alpha}}) : \bar{\underline{\alpha}}(\boldsymbol{\tau}) : (\underline{\alpha} - \bar{\underline{\alpha}}) + \frac{1}{2}\vec{\nabla} \bar{\underline{\alpha}} : \bar{\underline{\alpha}}(\boldsymbol{\tau}) : \vec{\nabla} \bar{\underline{\alpha}} \\
 & + \frac{1}{2}\gamma d^{\gamma-1}Q(\boldsymbol{\tau})r^2 + \frac{1}{2}\gamma d^{\gamma-1}\bar{Q}(\boldsymbol{\tau})(r - \bar{r})^2 + \frac{1}{2}\gamma d^{\gamma-1}\bar{Q}^g(\boldsymbol{\tau})\vec{\nabla} \bar{r} \cdot \vec{\nabla} \bar{r} - \bar{H}(\boldsymbol{\tau})(d - \bar{d})
 \end{aligned}
 \right\} \tag{II.50}$$

VI.3.3 The generalized heat equation

Considering the nonlocal thermal effects, the new micromorphic temperature associated with the local temperature is introduced into this theory, and the generalized heat equations governing the evolution of temperature is well presented. There are also many other possibilities to consider the nonlocality of temperature, and will be discussed in Sec. VI.5.4.

VI.3.3.1 Formulations of the heat equation

Just as the principle of virtual power leads to the momentum balance equations, the first law of thermodynamics can lead to the differential heat equation governing the evolution of temperature, with the help of the Helmholtz free energy and the above deduced state relations.

The local form of the generalized first law of thermodynamics is given by:

$$-\rho \dot{e} + \left(\underline{\sigma} : \underline{D} + \vec{Y} \dot{\vec{d}} + \vec{R} \dot{\vec{r}} + \vec{X} : \dot{\underline{\alpha}} + \vec{s} \dot{\vec{T}} \right) + (\rho \zeta - \text{div}(\vec{q})) = 0 \quad (\text{II.51})$$

Let us introduce the classical relations between the internal energy and the Helmholtz free energy:

$$\psi = e + sT \quad (\text{II.52})$$

Substituting Eq.(II.52) into Eq.(II.51) leads to the following equation:

$$-\rho(\psi - sT - s\dot{T}) + \left(\underline{\sigma} : \underline{D} + \vec{Y} \dot{\vec{d}} + \vec{R} \dot{\vec{r}} + \vec{X} : \dot{\underline{\alpha}} + \vec{s} \dot{\vec{T}} \right) + (\rho \zeta - \text{div}(\vec{q})) = 0 \quad (\text{II.53})$$

By using the material time derivative of free energy Eq.(II.24) and the state relations in Eq.(II.26), it leads to the form of the heat equation:

$$\underline{\sigma} : \underline{D}'^r + Y \dot{d} - R \dot{r} - X : \dot{\underline{\alpha}} + (\rho \zeta - \vec{\nabla} \cdot \vec{q}) - \rho s \dot{T} = 0 \quad (\text{II.54})$$

Considering the state relation of entropy in Eq.(II.26), the material time derivative of entropy is:

$$\begin{aligned} \dot{s} &= -\frac{\partial}{\partial T}(\psi) \\ &= -\frac{1}{\rho} \left(\frac{\partial \underline{\sigma}}{\partial T} : \dot{\underline{\varepsilon}}^e - \rho \frac{\partial(s)}{\partial T} \dot{T} - \frac{\partial Y}{\partial T} \dot{d} + \frac{\partial R}{\partial T} \dot{r} + \frac{\partial X}{\partial T} : \dot{\underline{\alpha}} + \frac{\partial \vec{Y}}{\partial T} \dot{\vec{d}} + \frac{\partial \vec{R}}{\partial T} \dot{\vec{r}} + \frac{\partial \vec{X}}{\partial T} : \dot{\underline{\alpha}} + \frac{\partial \vec{s}}{\partial T} \dot{\vec{T}} \right. \\ &\quad \left. + \frac{\partial \vec{Y}}{\partial T} \cdot \vec{\nabla} \dot{\vec{d}} + \frac{\partial \vec{R}}{\partial T} \cdot \vec{\nabla} \dot{\vec{r}} + \frac{\partial \vec{X}}{\partial T} : \vec{\nabla} \dot{\underline{\alpha}} + \frac{\partial \vec{s}}{\partial T} \cdot \vec{\nabla} \dot{\vec{T}} \right) \end{aligned} \quad (\text{II.55})$$

Substituting the above equation into the heat equation Eq.(II.54) gives the detailed expressions of the form of the heat equation:

$$\begin{aligned} &\underline{\sigma} : \underline{D}'^r - \rho T \frac{\partial(s)}{\partial T} \dot{T} + Y \dot{d} - R \dot{r} - X : \dot{\underline{\alpha}} + (\rho \zeta - \vec{\nabla} \cdot \vec{q}) \\ &+ T \left(\frac{\partial \underline{\sigma}}{\partial T} : \dot{\underline{\varepsilon}}^e - \frac{\partial Y}{\partial T} \dot{d} + \frac{\partial R}{\partial T} \dot{r} + \frac{\partial X}{\partial T} : \dot{\underline{\alpha}} + \frac{\partial \vec{Y}}{\partial T} \dot{\vec{d}} + \frac{\partial \vec{R}}{\partial T} \dot{\vec{r}} + \frac{\partial \vec{X}}{\partial T} : \dot{\underline{\alpha}} + \frac{\partial \vec{s}}{\partial T} \dot{\vec{T}} \right. \\ &\quad \left. + \frac{\partial \vec{Y}}{\partial T} \cdot \vec{\nabla} \dot{\vec{d}} + \frac{\partial \vec{R}}{\partial T} \cdot \vec{\nabla} \dot{\vec{r}} + \frac{\partial \vec{X}}{\partial T} : \vec{\nabla} \dot{\underline{\alpha}} + \frac{\partial \vec{s}}{\partial T} \cdot \vec{\nabla} \dot{\vec{T}} \right) = 0 \end{aligned} \quad (\text{II.56})$$

If we pose:

$$R_{pl} = \left(\frac{\partial \underline{\sigma}}{\partial T} : \dot{\underline{\varepsilon}}^e - \frac{\partial Y}{\partial T} \dot{d} + \frac{\partial R}{\partial T} \dot{r} + \frac{\partial X}{\partial T} : \dot{\underline{\alpha}} + \frac{\partial \vec{Y}}{\partial T} \dot{\vec{d}} + \frac{\partial \vec{R}}{\partial T} \dot{\vec{r}} + \frac{\partial \vec{X}}{\partial T} : \dot{\underline{\alpha}} + \frac{\partial \vec{s}}{\partial T} \dot{\vec{T}} \right. \\ \left. + \frac{\partial \vec{Y}}{\partial T} \cdot \vec{\nabla} \dot{\vec{d}} + \frac{\partial \vec{R}}{\partial T} \cdot \vec{\nabla} \dot{\vec{r}} + \frac{\partial \vec{X}}{\partial T} : \vec{\nabla} \dot{\underline{\alpha}} + \frac{\partial \vec{s}}{\partial T} \cdot \vec{\nabla} \dot{\vec{T}} \right) \quad (\text{II.57})$$

defining the isentropic comes from the variations of stress or temperature term of the heat equation. Finally, the heat equation takes the following simple form:

$$-\rho T \frac{\partial(s)}{\partial T} \dot{T} + (\rho \varsigma - \vec{\nabla} \cdot \vec{q}) + \phi_{in} + R_{pl} T = 0 \quad (\text{II.58})$$

With the definition of the specific heat capacity for constant volume:

$$T \left(\frac{\partial s}{\partial T} \right)_{V=const} = C_e \quad (\text{II.59})$$

The heat equation becomes to:

$$-\rho C_e \dot{T} + (\rho \varsigma - \vec{\nabla} \cdot \vec{q}) + \phi_{in} + R_{pl} T = 0 \quad (\text{II.60})$$

Clearly, the generalized heat equation keeps its classical form, the only difference is on the R_{pl} which obtains the contributions from the micromorphic variables. If all micromorphic variables vanish, the R_{pl} will degenerate to the classical contribution, then the heat equations will be the classical local heat equations (Saanouni, 2012).

VI.3.3.2 Detailed expressions of the generalized heat equation

For the sake of simplicity, the explicit dependence of the material parameters on the temperature is omitted in this section. For deformable solids, it's clear that the evolution of the temperature depends on the partial derivatives of stress-like variables with respect to temperature and the material time derivatives of strain-like variables (i.e. the isentropic term R_{pl} defined in Eq.(II.57)). By using the deduced state relations Eq.(II.31) – Eq.(II.40), the partial derivatives of stress-like variables with respect to temperature are given:

- Cauchy stress:

$$\frac{\partial \underline{\sigma}}{\partial T} = (1-d) \frac{\partial \underline{\Lambda}}{\partial T} : \underline{\varepsilon}^e - \sqrt{1-d} \left(\underline{P} + (T-T_0) \frac{\partial \underline{P}}{\partial T} + \underline{\check{P}} + (T-\check{T}) \frac{\partial \underline{\check{P}}}{\partial T} \right) \quad (\text{II.61})$$

- Damage stress:

$$\frac{\partial \underline{\gamma}}{\partial T} = \begin{cases} \frac{1}{2} \underline{\varepsilon}^e : \frac{\partial \underline{\Lambda}}{\partial T} : \underline{\varepsilon}^e - \frac{\underline{P}}{2\sqrt{1-d}} : \underline{\varepsilon}^e - \frac{(T-T_0)}{2\sqrt{1-d}} \frac{\partial \underline{P}}{\partial T} : \underline{\varepsilon}^e - \frac{\underline{\check{P}}}{2\sqrt{1-d}} : \underline{\varepsilon}^e - \frac{(T-\check{T})}{2\sqrt{1-d}} \frac{\partial \underline{\check{P}}}{\partial T} : \underline{\varepsilon}^e \\ + \frac{1}{2} \underline{\alpha} : \frac{\partial \underline{C}}{\partial T} : \underline{\alpha} + \frac{1}{2} (\underline{\alpha} - \check{\underline{\alpha}}) : \frac{\partial \underline{\check{C}}}{\partial T} : (\underline{\alpha} - \check{\underline{\alpha}}) + \frac{1}{2} \vec{\nabla} \check{\underline{\alpha}} : \frac{\partial \underline{\check{C}}^g}{\partial T} : \vec{\nabla} \underline{\alpha} \\ + \frac{1}{2} \gamma d^{\gamma-1} \frac{\partial Q}{\partial T} r^2 + \frac{1}{2} \gamma d^{\gamma-1} \frac{\partial \check{Q}}{\partial T} (r - \check{r})^2 + \frac{1}{2} \gamma d^{\gamma-1} \frac{\partial \check{Q}^g}{\partial T} \vec{\nabla} \check{r} \cdot \vec{\nabla} r \\ - \frac{\partial \check{H}}{\partial T} (d - \check{d}) \end{cases} \quad (\text{II.62})$$

- Isotropic hardening stress:

$$\frac{\partial R}{\partial T} = (1-d^r) \frac{\partial Q}{\partial T} r + (1-d^r) \frac{\partial \check{Q}}{\partial T} (r - \check{r}) \quad (\text{II.63})$$

- Kinematic hardening stress:

$$\frac{\partial \underline{X}}{\partial T} = (1-d) \frac{\partial \underline{C}}{\partial T} : \underline{\alpha} + (1-d) \frac{\partial \check{C}}{\partial T} : (\underline{\alpha} - \check{\alpha}) \quad (\text{II.64})$$

- Stress-like variables with respect to micromorphic damage:

$$\begin{aligned} \frac{\partial \check{Y}}{\partial T} &= -\frac{\partial \check{H}}{\partial T} (d - \check{d}) \\ \frac{\partial \vec{\check{Y}}}{\partial T} &= \frac{\partial \check{H}^g}{\partial T} \vec{\nabla} \check{d} \end{aligned} \quad (\text{II.65})$$

- Stress-like variables of micromorphic isotropic hardening:

$$\begin{aligned} \frac{\partial \check{R}}{\partial T} &= -(1-d^r) \frac{\partial \check{Q}}{\partial T} (r - \check{r}) \\ \frac{\partial \vec{\check{R}}}{\partial T} &= (1-d^r) \frac{\partial \check{Q}^g}{\partial T} \vec{\nabla} \check{r} \end{aligned} \quad (\text{II.66})$$

- Stress-like variables with respect to micromorphic kinematic hardening:

$$\begin{aligned} \frac{\partial \underline{\check{X}}}{\partial T} &= -(1-d) \frac{\partial \underline{\check{C}}}{\partial T} : (\underline{\alpha} - \check{\alpha}) \\ \frac{\partial \vec{\underline{\check{X}}}}{\partial T} &= (1-d) \frac{\partial \vec{\check{C}}^g}{\partial T} : \vec{\nabla} \check{\alpha} \end{aligned} \quad (\text{II.67})$$

- Stress-like variables of micromorphic temperature:

$$\begin{aligned} \frac{\partial \check{s}}{\partial T} &= \sqrt{1-d} \frac{\partial \check{P}}{\partial T} : \underline{\varepsilon}^e - \check{M} - \frac{\partial \check{M}}{\partial T} (T - \check{T}) \\ \frac{\partial \vec{\check{s}}}{\partial T} &= \frac{\partial \check{M}^g}{\partial T} \vec{\nabla} \check{T} \end{aligned} \quad (\text{II.68})$$

Using the state relations Eq.(II.31) – Eq.(II.40), and the above partial derivatives Eq.(II.61) – Eq.(II.68), the final heat equation can be expressed as:

$$\left. \begin{aligned}
 & -\rho C_e \dot{T} + (\rho \varsigma - \vec{\nabla} \cdot \vec{q}) \\
 & + \sqrt{1-d} \left[\sqrt{1-d} \underline{\underline{\Delta}} : \underline{\underline{\varepsilon}}^e - (T - T_0) \underline{\underline{P}} - (T - \bar{T}) \underline{\underline{\bar{P}}} \right] : \underline{\underline{D}}^{ir} \\
 & + \gamma \dot{d} \\
 & - (1-d^\gamma) [Qr + \bar{Q}(r - \bar{r})] \dot{r} \\
 & - (1-d) [\underline{\underline{C}} : \underline{\underline{\alpha}} + \underline{\underline{\bar{C}}} : (\underline{\underline{\alpha}} - \underline{\underline{\bar{\alpha}}})] : \dot{\underline{\underline{\alpha}}}
 \end{aligned} \right\} \\
 + T \left. \begin{aligned}
 & \sqrt{1-d} \left[\sqrt{1-d} \frac{\partial \underline{\underline{\Delta}}}{\partial T} : \underline{\underline{\varepsilon}}^e - (T - T_0) \frac{\partial \underline{\underline{P}}}{\partial T} - \underline{\underline{P}} - (T - \bar{T}) \frac{\partial \underline{\underline{\bar{P}}}}{\partial T} - \underline{\underline{\bar{P}}} \right] : \dot{\underline{\underline{\varepsilon}}}^e \\
 & - \frac{\partial \gamma}{\partial T} \dot{d} - \frac{\partial \bar{H}}{\partial T} (d - \bar{d}) \dot{d} + \frac{\partial \bar{H}^g}{\partial T} \vec{\nabla} \bar{d} \cdot \vec{\nabla} \dot{d} \\
 & + (1-d^\gamma) \left[\frac{\partial Q}{\partial T} r \dot{r} + \frac{\partial \bar{Q}}{\partial T} (r - \bar{r}) \dot{r} - \frac{\partial \bar{Q}}{\partial T} (r - \bar{r}) \dot{\bar{r}} + \frac{\partial \bar{Q}^g}{\partial T} \vec{\nabla} \bar{r} \cdot \vec{\nabla} \dot{\bar{r}} \right] \\
 & + (1-d) \left[\left[\frac{\partial \underline{\underline{C}}}{\partial T} : \underline{\underline{\alpha}} + \frac{\partial \underline{\underline{\bar{C}}}}{\partial T} : (\underline{\underline{\alpha}} - \underline{\underline{\bar{\alpha}}}) \right] : \dot{\underline{\underline{\alpha}}} - \left[\frac{\partial \underline{\underline{\bar{C}}}}{\partial T} : (\underline{\underline{\alpha}} - \underline{\underline{\bar{\alpha}}}) \right] : \dot{\underline{\underline{\bar{\alpha}}}} + \left(\frac{\partial \underline{\underline{\bar{C}}}^g}{\partial T} : \vec{\nabla} \underline{\underline{\bar{\alpha}}} \right) : \vec{\nabla} \dot{\underline{\underline{\bar{\alpha}}}} \right] \\
 & + \left[\sqrt{1-d} \frac{\partial \underline{\underline{\bar{P}}}}{\partial T} : \underline{\underline{\varepsilon}}^e - \bar{M} - \frac{\partial \bar{M}}{\partial T} (T - \bar{T}) \right] \dot{\bar{T}} + \left[\frac{\partial \bar{M}^g}{\partial T} \vec{\nabla} \bar{T} \right] \cdot \vec{\nabla} \dot{\bar{T}}
 \end{aligned} \right\} = 0 \quad (II.69)$$

VI.3.4 Dissipation analysis (Evolution equations)

By assuming the hypothesis of thermal and intrinsic dissipations uncoupling, we are able to analyze thermal and intrinsic dissipations separately, in order to deduce the heat flux vector and the rate of strain-like variables in damageable inelastic solids. There are many possibilities to account for the micromorphic dissipations, coupling of thermal mechanics and plastic potentials. For simplification, we limit ourselves to the quadratic plastic potential, no dissipations from micromorphic variables and assume that the moduli are functions of temperature and indirectly affected by nonlocal temperature.

VI.3.4.1 Thermal dissipation analysis

The diffusion of heat in a deformable continuous medium is a phenomenon which is naturally time dependent. Thus, in order to define the heat flux vector \vec{q} , Fourier's dual potential of thermal dissipation is used in stress space in the form of a closed convex function of the temperature gradient:

$$\varphi_{th}^*(\vec{g}; T) = \frac{1}{2} \vec{g} \cdot \underline{k}(T) \cdot \vec{g} \geq 0 \quad (II.70)$$

where, \underline{k} is the positive definite second-rank symmetric tensor of thermal conductivities. Due to the hypothesis of normal dissipation, the heat flux variable is obtained:

$$\frac{\vec{q}}{T} = - \frac{\partial \varphi_{th}^*(\vec{g}; T)}{\partial \vec{g}} = - \underline{k}(T) \cdot \vec{g} \quad (II.71)$$

If we assume the isotropy of the thermal conductivity $\underline{k}(T) = k(T)\underline{1}$, and the (scalar) coefficient of thermal conductivity is inversely proportional to temperature, so that $Tk(T) = k$ is a constant, then the well-known Fourier linear thermal conductivity relationship is obtained from Eq.(II.71):

$$\vec{q} = -k\vec{g} \quad (\text{II.72})$$

Let us verify the positivity conditions for thermal dissipation in Eq.(II.27):

$$\phi_{th} = -\frac{\vec{q}}{T} \cdot \vec{g} = -(-k(T) \cdot \vec{g}) \cdot \vec{g} = k(T) \cdot \vec{g} \cdot \vec{g} \geq 0 \quad (\text{II.73})$$

As \underline{k} is positive definite symmetric second-rank tensor in Eq.(II.70), this thermal inequality is identically verified, thus ensuring an unconditional thermodynamic admissibility for the Fourier linear model of heat flow.

VI.3.4.2 The intrinsic dissipations analysis

VI.3.4.2.1 Time – independent plasticity

In time-independent inelastic flow, we have $\underline{D}^{ir} = \underline{D}^p$ or $\underline{\varepsilon}^{ir} = \underline{\varepsilon}^p$ where $\underline{\varepsilon}^{ir} = \int_t \underline{D}^{ir} dt$ and $\underline{\varepsilon}^p = \int_t \underline{D}^p dt$. The stress-like variables have been derived from the Helmholtz free energy written in effective strain space through Section VI.3.2.2 above. In this section, we will analyze the different dissipative phenomena, in order to define their evolution equations with the appropriate yield functions and dissipation potentials following the local state method. For case of time-independent plasticity, the generalized normality rule and maximum volumetric dissipation will be used to deduce the evolution equations. Here we limit ourselves to the single yield surface for both plasticity and damage (choice of two yield surfaces is possible in literature (Saanouni, 2012)).

VI.3.4.2.1.1 Plastic potential and evolution equations

In this section, we focus on the analysis of anisotropic plastic dissipations with isotropic damage, kinematical hardening and isotropic hardening. The plastic potential is defined, in the effective stress space, under the following form:

$$F_p(\tilde{\underline{\sigma}}, \tilde{\underline{X}}, \tilde{R}; T) = f_p + \frac{a(T)}{2} \tilde{\underline{X}} : \underline{\underline{C}}^{-1}(T) : \tilde{\underline{X}} + \frac{b(T)}{2} \frac{\tilde{R}^2}{Q(T)} + F_d(Y; d) \quad (\text{II.74})$$

where, f_p is the plastic yield criterion:

$$f_p(\tilde{\underline{\sigma}}, \tilde{\underline{X}}, \tilde{R}; T) = \|\tilde{\underline{\sigma}} - \tilde{\underline{X}}\| - \tilde{R} - \sigma_{yp}(T) = \frac{\|\tilde{\underline{\sigma}} - \tilde{\underline{X}}\|}{\sqrt{1-d}} - \frac{R}{\sqrt{1-d'}} - \sigma_{yp}(T) \quad (\text{II.75})$$

with the norm $\|\tilde{\underline{\sigma}} - \tilde{\underline{X}}\| = \sqrt{(\tilde{\underline{\sigma}} - \tilde{\underline{X}}) : \underline{\underline{H}}(T) : (\tilde{\underline{\sigma}} - \tilde{\underline{X}})}$ defines the effective stress with the fourth-rank operator $\underline{\underline{H}}(T)$ governing the anisotropic of the plasticity, $\sigma_{yp}(T)$ is the initial size of the plastic yield

surface, b and a are the nonlinear parameters of isotropic and kinematic hardening respectively. The isotropic ductile damage potential $F_d(Y; d)$ is defined as:

$$F_d(Y; d) = \frac{S(T)}{(s(T)+1)} \left\langle \frac{Y - Y_0(T, d)}{S(T)} \right\rangle^{(s(T)+1)} \frac{1}{(1-d)^{\beta(T)}} \quad (\text{II.76})$$

where, the parameters S , s , Y_0 and β characterize the nonlinear evolution of ductile damage.

Considering the generalized normality rule, the evolution equations for strain-like variables are obtained in the below:

- Plastic strain rate

$$\underline{D}^p = \dot{\lambda} \frac{\partial F_p}{\partial \underline{\sigma}} = \dot{\lambda} \left(\frac{1}{\sqrt{1-d}} \frac{H(T) : (\underline{\sigma} - \underline{X})}{\|\underline{\sigma} - \underline{X}\|} \right) = \dot{\lambda} \frac{\underline{n}_f}{\sqrt{1-d}} = \dot{\lambda} \tilde{\underline{n}}_f \quad (\text{II.77})$$

with λ is the so-called Lagrange plastic multiplier.

- Kinematic hardening strain rate

$$\dot{\underline{\alpha}} = -\dot{\lambda} \frac{\partial F_p}{\partial \underline{X}} = \dot{\lambda} (\tilde{\underline{n}}_f - a(T) \tilde{\underline{C}}^{-1}(T) : \underline{X}) = \dot{\lambda} (\tilde{\underline{n}}_f - \underline{m}_f) \quad (\text{II.78})$$

with $\underline{m}_f = a(T) \left[(\underline{1} + \underline{\underline{C}}^{-1}(T) : \underline{\underline{C}}(T)) \underline{\alpha} - \underline{\underline{C}}^{-1}(T) : \underline{\underline{C}}(T) : \underline{\alpha} \right]$.

- Isotropic hardening strain rate

$$\dot{r} = -\dot{\lambda} \frac{\partial F_p}{\partial R} = \dot{\lambda} \left(\frac{1}{\sqrt{1-d^\gamma}} - b(T) \frac{R}{\tilde{Q}(T)} \right) = \dot{\lambda} \left(\frac{1}{\sqrt{1-d^\gamma}} - o \right) \quad (\text{II.79})$$

with $o = b(T) \left[\left(1 + \frac{\tilde{Q}(T)}{Q(T)} \right) r - \left(\frac{\tilde{Q}(T)}{Q(T)} \right) \tilde{r} \right]$.

- Isotropic damage rate

$$\dot{d} = \dot{\lambda} \frac{\partial F_p}{\partial Y} = \dot{\lambda} \left\langle \frac{Y - Y_0(T, d)}{S(T)} \right\rangle^{(s(T))} \frac{1}{(1-d)^{\beta(T)}} = \dot{\lambda} \hat{Y} \quad (\text{II.80})$$

It's worth to note that if the scalar factors $a(T)$ and $b(T)$ vanish, the evolution equations of kinematic and isotropic hardening Eq.(II.78) and Eq.(II.79) will degenerate to their linear forms respectively.

VI.3.4.2.1.2 Formulations of plastic multiplier

The evolutions of dissipative phenomena under given applied loading conditions maximize the volumetric dissipation (Eq.(II.27)) under the condition $f_p \leq 0$. Due to the Kuhn-Tucker conditions ($\dot{\lambda} \geq 0$,

$f_p \leq 0$ and $\dot{\lambda} f_p = 0$), we obtain the above evolution equations, in which $\dot{\lambda}$ is a Lagrange multiplier also called plastic multiplier, which is positive or null, and fulfill the Kuhn-Tucker (or loading/unloading) conditions as well as the consistency conditions:

$$\begin{cases} \dot{\lambda} \geq 0, f_p \leq 0 \text{ and } \dot{\lambda} f_p = 0 & \text{Kuhn-Tucker conditions} \\ \dot{\lambda} \dot{f}_p = 0 \text{ if } f_p = 0 & \text{Consistency conditions} \end{cases} \quad (\text{II.81})$$

If $\dot{\lambda} = 0$, it will not produce new plastic strain; if $\dot{\lambda} > 0$, in order to fulfill the consistency conditions, $\dot{f}_p = 0$ must be satisfied:

$$\dot{f}_p = \frac{\partial f_p}{\partial \underline{\sigma}} : \dot{\underline{\sigma}} + \frac{\partial f_p}{\partial \underline{X}} : \dot{\underline{X}} + \frac{\partial f_p}{\partial R} \dot{R} + \frac{\partial f_p}{\partial d} \dot{d} + \frac{\partial f_p}{\partial T} \dot{T} = 0 \quad (\text{II.82})$$

In this case, the plastic multiplier is given by (detailed formulations are listed in Appendix VI.7.1):

$$\dot{\lambda} = \frac{1}{H_p} \left[(1-d) \tilde{n}_f : \underline{\underline{\Lambda}} : \underline{\underline{D}} + H_T \dot{T} + \left(\tilde{n}_f : \underline{\underline{\tilde{P}}} \right) \dot{\underline{\underline{T}}} + \left(\tilde{n}_f : \underline{\underline{\tilde{C}}} \right) : \dot{\underline{\underline{\alpha}}} + \left(\frac{\underline{\underline{\tilde{Q}}}}{\sqrt{(1-d^\gamma)}} \right) \dot{\underline{\underline{r}}} \right] \quad (\text{II.83})$$

where,

$$\left\{ \begin{array}{l} H_T = \tilde{n}_f : \left[\begin{array}{l} \sqrt{1-d} \left(\sqrt{1-d} \frac{\partial \underline{\underline{\Lambda}}}{\partial T} : \underline{\underline{\varepsilon}_e} - \underline{\underline{P}} - \underline{\underline{\check{P}}} - (\underline{T} - \underline{T}_0) \frac{\partial \underline{\underline{P}}}{\partial T} - (\underline{T} - \underline{\check{T}}) \frac{\partial \underline{\underline{\check{P}}}}{\partial T} \right) \\ -(1-d) \left(\frac{\partial \underline{\underline{C}}}{\partial T} : \underline{\underline{\alpha}} + \frac{\partial \underline{\underline{\check{C}}}}{\partial T} : (\underline{\underline{\alpha}} - \underline{\underline{\check{\alpha}}}) \right) \end{array} \right] \\ - \sqrt{(1-d^\gamma)} \left(\frac{\partial Q}{\partial T} r + \frac{\partial \underline{\underline{Q}}}{\partial T} (r - \underline{\underline{r}}) \right) - \frac{\partial \sigma_{yp}}{\partial T} \\ H_p = (1-d) \left(\tilde{n}_f : \left[\begin{array}{l} \underline{\underline{\Lambda}} : \tilde{n}_f + (\underline{\underline{C}} + \underline{\underline{\check{C}}}) : (\tilde{n}_f - a(\underline{\underline{1}} + \underline{\underline{C}}^{-1} : \underline{\underline{\check{C}}}) \underline{\underline{\alpha}} + a(\underline{\underline{C}}^{-1} : \underline{\underline{\check{C}}}) : \underline{\underline{\check{\alpha}}}) \end{array} \right] \right. \\ \left. + \left(1-b \left(\frac{Q+\underline{\underline{Q}}}{Q} \right) \tilde{r} + b \left(\frac{\underline{\underline{Q}}}{Q} \right) \tilde{\underline{\underline{r}}} \right) (Q + \underline{\underline{Q}}) \right. \\ \left. - \left[\begin{array}{l} \tilde{n}_f : \left[\begin{array}{l} -\underline{\underline{\Lambda}} : \underline{\underline{\varepsilon}_e} + \frac{(\underline{T} - \underline{T}_0)}{2\sqrt{1-d}} (\underline{\underline{P}} + \underline{\underline{\check{P}}}) \end{array} \right] + \tilde{n}_f : (\underline{\underline{C}} : \underline{\underline{\alpha}} + \underline{\underline{\check{C}}} : (\underline{\underline{\alpha}} - \underline{\underline{\check{\alpha}}})) \\ + \frac{1}{\sqrt{(1-d^\gamma)}} \left(\gamma d^{\gamma-1} [Qr + \underline{\underline{Q}}(r - \underline{\underline{r}})] \right) + \left(\frac{\|\underline{\sigma} - \underline{X}\|}{2\sqrt{(1-d)^3}} - \frac{\gamma d^{\gamma-1} R}{2\sqrt{(1-d^\gamma)^3}} \right) \hat{\gamma} \end{array} \right] \right) \end{array} \right\} \quad (\text{II.84})$$

VI.3.4.2.1.3 Elastoplastic tangent operator

The numerical resolution of equilibrium problems in elastoplastic solids often requires the tangent elastoplastic operator which links stress rates to total strain rates. In the present case, this operator is

obtained by deriving the Cauchy stress tensor with respect to time (detailed formulations are listed in Appendix VI.7.2):

$$\dot{\underline{\sigma}} = \underline{\underline{L}} : \underline{\underline{D}} + \underline{\underline{L}} \dot{\underline{T}} + \underline{\underline{L}} \dot{\underline{T}} + \underline{\underline{L}} : \dot{\underline{\alpha}} + \underline{\underline{L}} \dot{\underline{r}} \quad (\text{II.85})$$

where,

$$\begin{cases} \underline{\underline{L}} = \tilde{\underline{\Lambda}} - \frac{1}{H_p} \left((\tilde{\underline{n}}_f : \tilde{\underline{\Lambda}}) \otimes (\tilde{\underline{\Lambda}} : \tilde{\underline{n}}_f) + \left(\underline{\underline{\Lambda}} : \underline{\varepsilon}_e - \frac{(T - T_0)}{2\sqrt{1-d}} (\underline{P} + \underline{\check{P}}) \right) \otimes (\tilde{\underline{n}}_f : \tilde{\underline{\Lambda}}) \hat{Y} \right) \\ \underline{\underline{L}} = \tilde{\underline{\Lambda}}' : \underline{\varepsilon}_e - \underline{\check{P}} - \underline{\check{P}} - (T - T_0) \underline{\check{P}}' - (T - \check{T}) \underline{\check{P}}' - \frac{H_T}{H_p} \left(\tilde{\underline{\Lambda}} : \tilde{\underline{n}}_f + \left(\underline{\underline{\Lambda}} : \underline{\varepsilon}_e - \frac{(T - T_0)}{2\sqrt{1-d}} (\underline{P} + \underline{\check{P}}) \right) \hat{Y} \right) \\ \underline{\underline{L}} = \underline{\check{P}} - \frac{\tilde{\underline{n}}_f : \tilde{\underline{\check{P}}}}{H_p} \left(\tilde{\underline{\Lambda}} : \tilde{\underline{n}}_f + \left(\underline{\underline{\Lambda}} : \underline{\varepsilon}_e - \frac{(T - T_0)}{2\sqrt{1-d}} (\underline{P} + \underline{\check{P}}) \right) \hat{Y} \right) \\ \underline{\underline{L}} = -\frac{\tilde{\underline{n}}_f : \tilde{\underline{\check{C}}}}{H_p} \otimes \left(\tilde{\underline{\Lambda}} : \tilde{\underline{n}}_f + \left(\underline{\underline{\Lambda}} : \underline{\varepsilon}_e - \frac{(T - T_0)}{2\sqrt{1-d}} (\underline{P} + \underline{\check{P}}) \right) \hat{Y} \right) \\ \underline{\underline{L}} = -\frac{\tilde{\underline{Q}}}{H_p \sqrt{(1-d^\gamma)}} \left(\tilde{\underline{\Lambda}} : \tilde{\underline{n}}_f + \left(\underline{\underline{\Lambda}} : \underline{\varepsilon}_e - \frac{(T - T_0)}{2\sqrt{1-d}} (\underline{P} + \underline{\check{P}}) \right) \hat{Y} \right) \end{cases} \quad (\text{II.86})$$

VI.3.4.2.1.4 Thermodynamic admissibility

In order to satisfy the Clausius-Duhem inequality, the intrinsic volumic dissipation Eq.(II.27) must be either positive or null:

$$\phi_{in} = \underline{\sigma} : \underline{\underline{D}}^p - \underline{\underline{X}} : \dot{\underline{\alpha}} - R\dot{r} + Y\dot{d} \geq 0 \quad (\text{II.87})$$

By using the evolution equations Eq.(II.77) – Eq.(II.80) together with the state relations Eq.(II.31) to Eq.(II.40), the intrinsic dissipation can be expressed as:

$$\begin{aligned} \dot{\phi}_{in} &= \underline{\sigma} : \underline{\underline{D}}^p - \underline{\underline{X}} : \dot{\underline{\alpha}} - R\dot{r} + Y\dot{d} \\ &= \dot{\lambda} \underline{\sigma} : \tilde{\underline{n}}_f - \dot{\lambda} \underline{\underline{X}} : (\tilde{\underline{n}}_f - m_f) - \dot{\lambda} R \left(\frac{1}{\sqrt{(1-d^\gamma)}} - o \right) + \dot{\lambda} Y \hat{Y} \\ &= \dot{\lambda} \left[\left\| \tilde{\underline{\sigma}} - \tilde{\underline{X}} \right\| - \tilde{R} - \sigma_{yp}(T) + a \underline{\underline{X}} : \tilde{\underline{\underline{C}}}^{-1}(T) : \underline{\underline{X}} \right. \\ &\quad \left. + b(T) \frac{R^2}{\tilde{Q}(T)} + Y \left\langle \frac{Y - Y_0(T, d)}{S(T)} \right\rangle^{s(T)} \frac{1}{(1-d)^{\beta(T)}} + \sigma_{yp}(T) \right] \geq 0 \end{aligned} \quad (\text{II.88})$$

Since $\dot{\lambda} > 0$ and $f_p(\tilde{\underline{\sigma}}, \tilde{\underline{X}}, \tilde{R}; T) = 0$ for plastic flow with damage, this inequality becomes:

$$a(T) \underline{\underline{X}} : \tilde{\underline{\underline{C}}}^{-1}(T) : \underline{\underline{X}} + b(T) \frac{R^2}{\tilde{Q}(T)} + Y \left\langle \frac{Y - Y_0(T, d)}{S(T)} \right\rangle^{s(T)} \frac{1}{(1-d)^{\beta(T)}} + \sigma_{yp}(T) \geq 0 \quad (\text{II.89})$$

This inequality is fulfilled if $\sigma_{yp}(T) \geq 0$, $\frac{b(T)}{Q(T)} \geq 0$ and $a(T)\tilde{\underline{C}}^{-1}(T)$ is semi-positive definite tensor,

by virtue of positivity of all of the other quantities.

VI.3.4.2.2 Time - dependent plasticity (viscoplasticity)

Further to the thermal dissipation and time-independent plastic dissipation, the analysis of time-dependent plastic dissipation, commonly called viscoplasticity, is presented. Now we have $\underline{D}^{ir} = \underline{D}^{vp}$ or $\underline{\varepsilon}^{ir} = \underline{\varepsilon}^{vp}$. The phenomena linked to the time-dependent inelastic flow are described with yield criterion: it assumes, as in terms of time-independent plasticity, the existence in stress or strain space of a limit yield surface from which there is no inelastic flow. However, for time-dependent plasticity, the stress state is not forced to remain on the yield surface $f_p(\tilde{\underline{\sigma}}, \tilde{\underline{X}}, \tilde{R}; T) = 0$. This turns out to be a kind of generalization of the multi-surfaces plasticity theory so that the inelastic flow takes place even if $f_p(\tilde{\underline{\sigma}}, \tilde{\underline{X}}, \tilde{R}; T) > 0$. Indeed, this condition expresses the distance between the current stress state at a given point and the resulting surface defined by $f_p(\tilde{\underline{\sigma}}, \tilde{\underline{X}}, \tilde{R}; T) = 0$. This distance directly defines, in the stress space, the so-called viscous stress σ^{vp} .

VI.3.4.2.2.1 Viscoplastic potential and restoration

In this section, we focus on the single potential, fully anisotropic damageable thermo-elasto-viscoplasticity with ductile damage. We postulate that the overall viscoplastic potential $\varphi(\tilde{\underline{\sigma}}, \tilde{R}, \tilde{\underline{X}}, T)$ is additively decomposed into three contributions representing respectively: the viscoplastic flow $\varphi_{vp}(\tilde{\underline{\sigma}}, \tilde{R}, \tilde{\underline{X}}, T)$, restoration by the kinematic hardening and isotropic hardening $\varphi_{rxr}(\tilde{R}, \tilde{\underline{X}}, T)$ and the damage $\varphi_d(R, \underline{X}, T, Y; d)$.

The Norton-Hoff potential for the viscoplastic part is defined as (many other choices are available in the literature (Saanouni, 2012)):

$$\varphi_{vp}(\tilde{\underline{\sigma}}, \tilde{R}, \tilde{\underline{X}}, T) = \frac{K^{vp}(T)}{m_{vp}(T)+1} \left\langle \frac{F_p(\tilde{\underline{\sigma}}, \tilde{R}, \tilde{\underline{X}}, T)}{K^{vp}(T)} \right\rangle^{m_{vp}(T)+1} \quad (\text{II.90})$$

where, K^{vp} and m_{vp} are two constants which are characteristic of material viscosity and $F_p(\tilde{\underline{\sigma}}, \tilde{R}, \tilde{\underline{X}}, T)$ is given as below:

$$F_p(\tilde{\underline{\sigma}}, \tilde{R}, \tilde{\underline{X}}, T) = f_p + \left(\frac{a(T)}{2} \tilde{\underline{X}} : \underline{\underline{C}}^{-1}(T) : \tilde{\underline{X}} + \frac{b(T)}{2} \frac{\tilde{R}^2}{Q(T)} - \frac{a(T)}{2} \tilde{\underline{\alpha}} : \underline{\underline{C}}(T) : \tilde{\underline{\alpha}} - \frac{b(T)}{2} Q(T) \tilde{r}^2 \right) \quad (\text{II.91})$$

$$f_p(\tilde{\underline{\sigma}}, \tilde{R}, \tilde{\underline{X}}, T) = \|\tilde{\underline{\sigma}} - \tilde{\underline{X}}\| - \tilde{R} - \sigma_{yp}(T)$$

For the restoration potential, we also assume an additive contribution from restoration over kinematic and isotropic hardenings:

$$\varphi_{rxr} = \frac{K^{rr}(T)}{m_{rr}(T)+1} \left\langle \frac{\tilde{R}}{K^{rr}(T)} \right\rangle^{m_{rr}(T)+1} + \frac{K^{rx}(T)}{m_{rx}(T)+1} \left\langle \frac{\|\tilde{X}\|}{K^{rx}(T)} \right\rangle^{m_{rx}(T)+1} \quad (\text{II.92})$$

where, K^{rr} and m_{rr} are the parameters characteristic of isotropic hardening restoration, K^{rx} and m_{rx} are parameters characteristic of kinematic strain hardening restoration. The norm $\|\tilde{X}\| = \sqrt{\tilde{X} : H_x(T) : \tilde{X}}$ is the anisotropic equivalent stress from the kinematic stress tensor.

Finally, the ductile damage potential, into which we introduce the accumulated viscoplastic strain rate, is defined by:

$$\varphi_d = \frac{S(T)}{(s(T)+1)(1-d)^{\beta(T)}} \left\langle \frac{Y - Y_0(T, d)}{S(T)} \right\rangle^{(s(T)+1)} \dot{p} \quad (\text{II.93})$$

with \dot{p} is the accumulated viscoplastic strain rate and is supposed purely ductile without creep damage.

VI.3.4.2.2 Evolution equations

Using the generalized normality rule, the evolution equations deduced from theses potentials are:

- Viscoplastic strain rate

$$\underline{D}^{vp} = \frac{\partial \varphi}{\partial \underline{\sigma}} = \left\langle \frac{f_p}{K^{vp}} \right\rangle^{m_{vp}} \frac{1}{\sqrt{1-d}} \frac{H_\sigma(T) : (\underline{\sigma} - \underline{X})}{\|\underline{\sigma} - \underline{X}\|} = \dot{\lambda}_{vp} \tilde{n}_f \quad (\text{II.94})$$

where, the multiplier $\dot{\lambda}_{vp}$, depending on the form of the potential, is defined as follows:

$$\dot{\lambda}_{vp} = \left\langle \frac{f_p}{K^{vp}(T)} \right\rangle^{m_{vp}(T)} \quad (\text{II.95})$$

- Kinematic hardening strain rate

$$\begin{aligned} \dot{\underline{\alpha}} &= -\frac{\partial \varphi}{\partial \underline{X}} = - \left[\left\langle \frac{f_p}{K^{vp}(T)} \right\rangle^{m_{vp}(T)} \left(\frac{\partial f_p}{\partial \underline{X}} + a(T) \underline{C}^{-1}(T) : \underline{X} \right) \right] - \left\langle \frac{\|\tilde{X}\|}{K^{rx}(T)} \right\rangle^{m_{rx}(T)} \frac{H_x(T) : \tilde{X}}{\|\underline{X}\|} \\ &= \dot{\lambda}_{vp} \left[\tilde{n}_f - a(T) \underline{1} : \underline{\alpha} - a(T) (\underline{C}^{-1}(T) : \underline{C}(T)) : (\underline{\alpha} + \underline{\alpha}) \right] - \left\langle \frac{\|\tilde{X}\|}{K^{rx}(T)} \right\rangle^{m_{rx}(T)} \frac{\tilde{H}_x(T) : \underline{X}}{\|\tilde{X}\|} \end{aligned} \quad (\text{II.96})$$

- Isotropic hardening strain rate

$$\begin{aligned} \dot{r} &= -\frac{\partial \varphi}{\partial R} = - \left[\left\langle \frac{f_p}{K^{vp}(T)} \right\rangle^{m_{vp}(T)} \left(\frac{\partial f_p}{\partial R} + \frac{b(T)}{\tilde{Q}(T)} R \right) \right] - \left\langle \frac{\tilde{R}}{K^{rr}(T)} \right\rangle^{m_{rr}(T)} \\ &= \frac{\dot{\lambda}_{vp}}{\sqrt{1-d^\gamma}} \left[1 - \left(1 + \frac{\tilde{Q}(T)}{Q(T)} \right) b(T) \tilde{r} + \frac{\tilde{Q}(T)}{Q(T)} b(T) \tilde{r} \right] - \left\langle \frac{\tilde{R}}{K^{rr}(T)} \right\rangle^{m_{rr}(T)} \end{aligned} \quad (\text{II.97})$$

- Isotropic ductile damage rate

$$\dot{d} = \frac{\partial \varphi}{\partial Y} = \frac{\dot{p}}{(1-d)^{\beta(\tau)}} \left\langle \frac{Y - Y_0(T, d)}{S(T)} \right\rangle^{s(\tau)} = \dot{p} \hat{\gamma} \quad (\text{II.98})$$

The accumulated viscoplastic strain rate is expressed as:

$$\dot{p} = \sqrt{\underline{D}^{vp} : \underline{H}_{\underline{\sigma}}^{-1}(T) : \underline{D}^{vp}} = \frac{\dot{\lambda}_{vp}}{\sqrt{1-d}} \quad (\text{II.99})$$

We can easily define the equation for the actual viscoplastic yield surface from Eq.(II.95):

$$f_{vp} = f_p - K^{vp}(T) \left(\dot{\lambda}_{vp} \right)^{\frac{1}{m_{vp}(T)}} = f_p - K^{vp}(T) \left(\dot{p} \sqrt{1-d} \right)^{\frac{1}{m_{vp}(T)}} = f_p - \sigma^{vp} = 0 \quad (\text{II.100})$$

As expected, the viscous stress is very dependent on the form of the viscoplastic potential and is defined as:

$$\sigma^{vp} = K^{vp}(T) \left(\dot{\lambda}_{vp} \right)^{\frac{1}{m_{vp}(T)}} = K^{vp}(T) \left(\dot{p} \sqrt{1-d} \right)^{\frac{1}{m_{vp}(T)}} \quad (\text{II.101})$$

VI.3.4.2.2.3 Thermodynamic admissibility

Intrinsic volumic dissipation takes the form:

$$\phi_{in}^{vp} = \underline{\sigma} : \underline{D}^{vp} - \underline{X} : \dot{\underline{\alpha}} - R\dot{r} + Y\dot{d} \geq 0 \quad (\text{II.102})$$

By using the evolution equations Eq.(II.94) to Eq.(II.98), as well as Eq.(II.100) which define the actual viscoplastic yield surface, the intrinsic dissipation can be expressed in the form:

$$\dot{\lambda}_{vp} \left[f_{vp} + a(T) \tilde{X} : \underline{\underline{C}}^{-1}(T) : \tilde{X} + \left\langle \frac{\|\tilde{X}\|}{K^{rx}(T)} \right\rangle^{m_{rx}(T)} \frac{\underline{X} : \tilde{H}_x(T) : \underline{X}}{\|\tilde{X}\|} \right. \\ \left. + b(T) \frac{\tilde{R}^2}{Q(T)} + \tilde{R} \left\langle \frac{\tilde{R}}{K^{rr}(T)} \right\rangle^{m_{rr}(T)} + \sigma^{vp} + \sigma_{yp}(T) + \frac{Y\hat{Y}}{\sqrt{1-d}} \right] \geq 0 \quad (\text{II.103})$$

Since $\dot{\lambda} > 0$ and $f_{vp}(\tilde{\sigma}, \tilde{X}, \tilde{R}; T) = 0$, this inequality is fulfilled if $\sigma_{yp}(T) \geq 0$, $\frac{b(T)}{Q(T)} \geq 0$, $K^{rx}(T) \geq 0$,

$K^{rr}(T) \geq 0$ and $a(T) \underline{\underline{C}}^{-1}(T)$ is semi-positive definite tensor, according to the positivity of all the other quantities.

VI.4 Transformation of the micromorphic balance equations

Recall the generalized balance equations as well as their Neumann boundary conditions in Eqs.(II.6) ~ (II.10), they can be transformed to the strain-like spaces, with the help of the state relations in Eq.(II.31) ~ Eq.(II.40), under the following forms ($\text{Lap}(X)$ being the Laplacian of X):

- The classical equilibrium equation

$$\begin{cases} \left[(1-d)\underline{\Delta}(T) : \vec{\nabla}\underline{\varepsilon}^e + (1-d)\vec{\nabla} \cdot \underline{\Delta}(T) : \underline{\varepsilon}^e \right. \\ \left. - \sqrt{1-d}(\vec{\nabla}(T-T_0)) \cdot \underline{P}(T) - \sqrt{1-d}(T-T_0)\vec{\nabla} \cdot \underline{P}(T) \right] = \rho\ddot{u} & \text{in } \Omega \\ \left. - \sqrt{1-d}(\vec{\nabla}(T-\bar{T})) \cdot \underline{P}(T) - \sqrt{1-d}(T-\bar{T})\vec{\nabla} \cdot \underline{P}(T) + \rho\vec{f}^u \right] \\ \left[(1-d)\underline{\Delta}(T) : \underline{\varepsilon}^e - \sqrt{1-d}(T-T_0)\underline{P}(T) - \sqrt{1-d}(T-\bar{T})\underline{P}(T) \right] \cdot \vec{n} = \vec{F}^u & \text{on } \Gamma \end{cases} \quad (\text{II.104})$$

- The balance equation of the micromorphic damage

$$\begin{cases} \left[\check{H}^g(T) Lap(\check{d}) + \vec{\nabla} \check{H}^g(T) \cdot \vec{\nabla} \check{d} \right] + \check{H}(T)(d - \check{d}) + \rho(f^{\check{d}} - \vec{\nabla} \cdot \vec{f}^{g\check{d}}) = \rho\zeta_{\check{d}}\ddot{\check{d}} & \text{in } \Omega \\ \left[\check{H}^g(T)(\vec{\nabla} \check{d}) - \rho\vec{f}^{g\check{d}} \right] \cdot \vec{n} = F^{\check{d}} & \text{on } \Gamma \end{cases} \quad (\text{II.105})$$

- The balance equation of the micromorphic isotropic hardening

$$\begin{cases} \left[(1-d^\gamma)[Q^g(T) Lap(\check{r}) + \vec{\nabla} Q^g(T) \cdot \vec{\nabla} \check{r} + \check{Q}(T)(r - \check{r})] + \rho(f^{\check{r}} - \vec{\nabla} \cdot \vec{f}^{g\check{r}}) = \rho\zeta_{\check{r}}\ddot{\check{r}} \right. & \text{in } \Omega \\ \left. \left[(1-d^\gamma)\check{Q}^g(T)(\vec{\nabla} \check{r}) - \rho\vec{f}^{g\check{r}} \right] \cdot \vec{n} = F^{\check{r}} \right. & \text{on } \Gamma \end{cases} \quad (\text{II.106})$$

- The balance equation of the micromorphic kinematic hardening (assuming the fully isotropy in kinematic hardening phenomena)

$$\begin{cases} \left[(1-d)[\check{C}^g(T) : Lap(\check{\alpha}) + \vec{\nabla} \cdot \check{C}^g(T) : \vec{\nabla} \check{\alpha} + \check{C}(T) : (\underline{\alpha} - \check{\alpha})] + \rho(f^{\check{\alpha}} - \vec{\nabla} \cdot \vec{f}^{g\check{\alpha}}) = \rho\zeta_{\check{\alpha}}\ddot{\check{\alpha}} \right. & \text{in } \Omega \\ \left. \left[(1-d)\check{C}^g(T) : \vec{\nabla} \check{\alpha} - \rho\vec{f}^{g\check{\alpha}} \right] \cdot \vec{n} = E^{\check{\alpha}} \right. & \text{on } \Gamma \end{cases} \quad (\text{II.107})$$

or for the special case of isotropy kinematic hardening (Saanouni, 2012):

$$\begin{cases} \left[(1-d)[\check{C}^g(T) Lap(\check{\alpha}) + \vec{\nabla} \check{C}^g(T) \cdot \vec{\nabla} \check{\alpha} + \check{C}(T)(\underline{\alpha} - \check{\alpha})] + \rho(f^{\check{\alpha}} - \vec{\nabla} \cdot \vec{f}^{g\check{\alpha}}) = \rho\zeta_{\check{\alpha}}\ddot{\check{\alpha}} \right. & \text{in } \Omega \\ \left. \left[(1-d)\check{C}^g(T) \vec{\nabla} \check{\alpha} - \rho\vec{f}^{g\check{\alpha}} \right] \cdot \vec{n} = E^{\check{\alpha}} \right. & \text{on } \Gamma \end{cases} \quad (\text{II.108})$$

- The balance equation of the micromorphic temperature

$$\begin{cases} \left[\check{M}^g(T) Lap(\bar{T}) + \vec{\nabla} \check{M}^g(T) \cdot \vec{\nabla} \bar{T} \right] + \rho(f^{\bar{T}} - \vec{\nabla} \cdot \vec{f}^{g\bar{T}}) = \rho(\zeta_{\bar{T}_1}\dot{\bar{T}} + \zeta_{\bar{T}_2}\ddot{\bar{T}}) & \text{in } \Omega \\ \left[+\check{M}(T)(T - \bar{T}) - \sqrt{1-d}\underline{P}(T) : \underline{\varepsilon}^e \right] \\ \left[\check{M}^g(T)(\vec{\nabla} \bar{T}) - \rho\vec{f}^{g\bar{T}} \right] \cdot \vec{n} = F^{\bar{T}} & \text{on } \Gamma \end{cases} \quad (\text{II.109})$$

For the sake of simplicity and without any experimental information, if the overall micromorphic body and contact forces are neglected:

$$\begin{aligned} F^{\check{d}} &= F^{\check{r}} = F^{\bar{T}} = 0 & E^{\check{\alpha}} &= 0 \\ f^{\check{d}} &= f^{\check{r}} = f^{\bar{T}} = 0 & f^{\check{\alpha}} &= 0 \\ \vec{f}^{g\check{d}} &= \vec{f}^{g\check{r}} = \vec{f}^{g\bar{T}} = \vec{0} & \vec{f}^{g\check{\alpha}} &= \vec{0} \end{aligned} \quad (\text{II.110})$$

The above balance equations (Eqs.(II.105) ~ (II.109)) can be rewrite as:

$$\begin{cases} \left[I_{\bar{d}}^2 \text{Lap}(\bar{d}) + \frac{\vec{\nabla} \bar{H}^g(T)}{\bar{H}(T)} \cdot \vec{\nabla} \bar{d} \right] + (d - \bar{d}) = \rho \frac{\zeta_{\bar{d}} \ddot{d}}{\bar{H}(T)} \\ \bar{H}^g(T) \vec{\nabla} \bar{d} \cdot \vec{n} = 0 \end{cases} \quad (\text{II.111})$$

$$\begin{cases} (1-d') \left[I_{\bar{r}}^2 \text{Lap}(\bar{r}) + \frac{\vec{\nabla} \bar{Q}^g(T)}{\bar{Q}(T)} \cdot \vec{\nabla} \bar{r} + (r - \bar{r}) \right] = \rho \frac{\zeta_{\bar{r}} \ddot{r}}{\bar{Q}(T)} \\ [(1-d') \bar{Q}^g(T) (\vec{\nabla} \bar{r})] \cdot \vec{n} = 0 \end{cases} \quad (\text{II.112})$$

$$\begin{cases} (1-d) \left[I_{\bar{\alpha}}^2 \text{Lap}(\bar{\alpha}) + \frac{\vec{\nabla} \bar{C}^g(T)}{\bar{C}(T)} \cdot \vec{\nabla} \bar{\alpha} + (\alpha - \bar{\alpha}) \right] = \rho \frac{\zeta_{\bar{\alpha}} \ddot{\alpha}}{\bar{C}(T)} \\ [(1-d) \bar{C}^g(T) (\vec{\nabla} \bar{\alpha})] \cdot \vec{n} = 0 \end{cases} \quad (\text{II.113})$$

$$\begin{cases} \left[I_{\bar{T}}^2 \text{Lap}(\bar{T}) + \frac{\vec{\nabla} \bar{M}^g(T)}{\bar{M}(T)} \cdot \vec{\nabla} \bar{T} \right] + \left[(T - \bar{T}) - \frac{\sqrt{1-d}}{\bar{M}(T)} \bar{P}(T) : \varepsilon^e \right] = \rho \left(\frac{\zeta_{\bar{T}_1}}{\bar{M}(T)} \dot{\bar{T}} + \frac{\zeta_{\bar{T}_2}}{\bar{M}(T)} \ddot{\bar{T}} \right) \\ (\bar{M}^g(T) \vec{\nabla} \bar{T}) \cdot \vec{n} = 0 \end{cases} \quad (\text{II.114})$$

where, $I_{\bar{d}}$, $I_{\bar{r}}$, $I_{\bar{\alpha}}$ and $I_{\bar{T}}$ are the internal length scale parameters relative to the micromorphic damage, isotropic hardening, kinematic hardening and temperature, and defined by the ratio of the micromorphic moduli:

$$I_{\bar{d}}^2 = \frac{\bar{H}^g(T)}{\bar{H}(T)} \quad I_{\bar{r}}^2 = \frac{\bar{Q}^g(T)}{\bar{Q}(T)} \quad I_{\bar{\alpha}}^2 = \frac{\bar{C}^g(T)}{\bar{C}(T)} \quad I_{\bar{T}}^2 = \frac{\bar{M}^g(T)}{\bar{M}(T)} \quad (\text{II.115})$$

It is worth noting that if the micromorphic moduli are independent of the local temperature, it leads to the same micromorphic balance equations given in literature (Saanouni and Hamed, 2013). If the micromorphic inertia terms vanish, it leads to the implicit form of the well-known Helmholtz equation proposed in the framework of the so-called gradient-enhanced models (Engelen et al., 2003; Peerlings, 1999; Peerlings et al., 2001; Peerlings et al., 2004).

VI.5 Discussions of special cases

The generalized micromorphic model strongly coupled thermo-elasto-visco-plasticity and ductile damage is presented in the previous chapters. Here we'll present that how this micromorphic model will degenerate to the classical local damage model, and the classical elasto-plastic model which is used in the first part of thesis. After, concerning that the generalized heat equation (Eq.(II.69)) is too complicated, the thermo-elastic micromorphic heat equation is presented for simplification. The work on the exist work on the nonlocal heat equations are also briefly reviewed.

VI.5.1 Classical local damage model

In this section, we'll perform the required formulations to obtain the degenerated classical local damage model from the above extended micromorphic (nonlocal) model.

VI.5.1.1 The local balance equation

If we neglect the introduced additional micromorphic dofs: micromorphic damage, micromorphic isotropic and kinematic hardening, micromorphic temperature, the virtual power of internal forces will be reduced to the classical form:

$$\delta P_{\text{int}} = - \int_{\Omega} (\underline{\sigma} : \dot{\underline{\varepsilon}}^*) dV \quad (\text{II.116})$$

Accordingly, the virtual power of external forces will degenerate to the classical form, if the generalized body and contact forces associated with micromorphic fields:

$$\delta P_{\text{ext}} = \rho \int_{\Omega} (\vec{f}^u \cdot \dot{\vec{u}}^*) dV + \int_{\Gamma} (\vec{F}^u \cdot \dot{\vec{u}}^*) dS \quad (\text{II.117})$$

and the virtual power of inertia forces also reduces to:

$$\delta P_a = \rho \int_V (\ddot{\vec{u}} \cdot \dot{\vec{u}}^*) dV \quad (\text{II.118})$$

With the help of principle of virtual power, we may obtain the classic equilibrium equation associated with the dofs of displacements:

$$\begin{cases} \vec{\nabla} \cdot \underline{\sigma} + \rho \vec{f}^u = \rho \ddot{\vec{u}} & \text{in } \Omega \\ \underline{\sigma} \cdot \vec{n} = \vec{F}^u & \text{on } \Gamma \end{cases} \quad (\text{II.119})$$

VI.5.1.2 The local state relations

In the absence of micromorphic fields, the differential form first law of thermodynamics becomes to the traditional one:

$$-\rho \dot{e} + (\underline{\sigma} : \dot{\underline{\varepsilon}}) + (\rho \varsigma - \text{div}(\vec{q})) = 0 \quad (\text{II.120})$$

Consequently, the Helmholtz free energy $\psi(\underline{\varepsilon}^e, T, d, r, \underline{\alpha})$ reduces to a closed convex function of the classical local state variables: $\underline{\varepsilon}^e$, d , r and $\underline{\alpha}$, and a concave function of the temperature.

Using the second law of thermodynamics and the above equations, the following classical state relations are obtained:

$$\begin{aligned} \underline{\sigma} &= \rho \frac{\partial \psi}{\partial \underline{\varepsilon}^e} & s &= -\frac{\partial \psi}{\partial T} \\ Y &= -\rho \frac{\partial \psi}{\partial d} & R &= \rho \frac{\partial \psi}{\partial r} & \underline{X} &= \rho \frac{\partial \psi}{\partial \underline{\alpha}} \end{aligned} \quad (\text{II.121})$$

and the local dissipations:

$$\phi = \phi_{in} + \phi_{th} = \underline{\sigma} : \underline{D}^{\text{ir}} - \underline{X} : \dot{\underline{\alpha}} - R\dot{r} + Y\dot{d} - \frac{\vec{q}}{T} \cdot \vec{g} \geq 0 \quad (\text{II.122})$$

Accordingly, if we let the micromorphic moduli equal to zero ($\check{M} = \check{M}^g = \check{Q} = \check{H} = \check{Q}^g = \check{H}^g = 0$, $\check{P} = 0$, $\check{C} = 0$, $\check{C}^g = 0$), then the generalized Helmholtz free energy Eq.(II.28) will reduce to the local form:

$$\rho\psi = \rho\psi_{tel}(\underline{\varepsilon}^e, d, T) + \rho\psi_{intel}(d, r, \underline{\alpha}) \quad (\text{II.123})$$

with,

$$\begin{aligned} \rho\psi_{tel} &= \frac{1}{2} \tilde{\underline{\varepsilon}}^e : \underline{\Lambda}(T) : \tilde{\underline{\varepsilon}}^e - (T - T_0) \underline{P}(T) : \tilde{\underline{\varepsilon}}^e - \rho \frac{C_\varepsilon}{2T_0} (T - T_0)^2 \\ &= \sqrt{1-d} \left[\sqrt{1-d} \frac{1}{2} \underline{\varepsilon}^e : \underline{\Lambda}(T) : \underline{\varepsilon}^e - (T - T_0) \underline{P}(T) : \underline{\varepsilon}^e \right] - \rho \frac{C_\varepsilon}{2T_0} (T - T_0)^2 \end{aligned} \quad (\text{II.124})$$

and,

$$\begin{aligned} \rho\psi_{intel} &= \frac{1}{2} (\underline{\tilde{\alpha}} : \underline{\underline{C}}(T) : \underline{\tilde{\alpha}}) + \frac{1}{2} (Q(T) \tilde{r}^2) \\ &= \frac{1}{2} (1-d) (\underline{\alpha} : \underline{\underline{C}}(T) : \underline{\alpha}) + \frac{1}{2} (1-d^\gamma) (Q(T) r^2) \end{aligned} \quad (\text{II.125})$$

Using the state relations in Eq.(II.121), the classical local stress-like variables are obtained:

- Cauchy stress tensor:

$$\begin{aligned} \underline{\sigma} &= \rho \frac{\partial \psi}{\partial \underline{\varepsilon}^e} = \tilde{\underline{\Lambda}}(T) : \underline{\varepsilon}^e - (T - T_0) \tilde{\underline{P}}(T) \\ &= (1-d) \underline{\underline{\Lambda}}(T) : \underline{\varepsilon}^e - \sqrt{1-d} (T - T_0) \underline{P}(T) \end{aligned} \quad (\text{II.126})$$

- Specific entropy:

$$s = -\frac{\partial \psi}{\partial T} = \frac{1}{\rho} \left[\tilde{\underline{P}}(T) : \underline{\varepsilon}^e + \rho \frac{C_\varepsilon}{T_0} (T - T_0) \right] \quad (\text{II.127})$$

- Damage stress:

$$Y = -\rho \frac{\partial \psi}{\partial d} = \frac{1}{2} \underline{\varepsilon}^e : \underline{\Lambda}(T) : \underline{\varepsilon}^e - \frac{1}{2\sqrt{1-d}} (T - T_0) \underline{P}(T) : \underline{\varepsilon}^e + \frac{1}{2} \underline{\alpha} : \underline{\underline{C}}(T) : \underline{\alpha} + \frac{1}{2} \gamma d^{\gamma-1} Q(T) r^2 \quad (\text{II.128})$$

- Isotropic hardening stress:

$$R = \rho \frac{\partial \psi}{\partial r} = \tilde{Q}(T) r = (1-d^\gamma) Q(T) r \quad (\text{II.129})$$

- Kinematic hardening stress:

$$\underline{X} = \rho \frac{\partial \psi}{\partial \underline{\alpha}} = \tilde{\underline{C}}(T) : \underline{\alpha} = (1-d) \underline{\underline{C}}(T) : \underline{\alpha} \quad (\text{II.130})$$

VI.5.1.3 The local evolution equations

As indicated in the extension of micromorphic fields, no dissipations from micromorphic variables are assumed, it leads to pure local dissipations (intrinsic and thermal dissipations). Therefore, the thermal dissipation analysis for heat flux vector and the plastic potential and yield function remain unchanged. However, the evolution equations will be modified to the followings, because of the degeneration on the state relations Eq.(II.126) to Eq.(II.130):

- Plastic strain rate

$$\underline{D}^p = \dot{\lambda} \frac{\partial F_p}{\partial \underline{\sigma}} = \dot{\lambda} \left(\frac{1}{\sqrt{(1-d)}} \frac{\underline{H}(T) : (\underline{\sigma} - \underline{X})}{\|\underline{\sigma} - \underline{X}\|} \right) = \dot{\lambda} \frac{\underline{n}_f}{\sqrt{(1-d)}} = \dot{\lambda} \underline{\tilde{n}}_f \quad (\text{II.131})$$

- Kinematic hardening strain rate

$$\dot{\underline{\alpha}} = -\dot{\lambda} \frac{\partial F_p}{\partial \underline{X}} = \dot{\lambda} (\underline{\tilde{n}}_f - \underline{m}_f) \quad (\text{II.132})$$

with $\underline{m}_f = a(T) \underline{\alpha}$.

- Isotropic hardening strain rate

$$\dot{r} = -\dot{\lambda} \frac{\partial F_p}{\partial R} = \dot{\lambda} \left(\frac{1}{\sqrt{(1-d')}} - o \right) \quad (\text{II.133})$$

with $o = b(T)r$.

- Isotropic damage rate

$$\dot{d} = \dot{\lambda} \frac{\partial F_p}{\partial Y} = \dot{\lambda} \left(\frac{Y - Y_0(T, d)}{S(T)} \right)^{s(T)} \frac{1}{(1-d)^{\beta(T)}} = \dot{\lambda} \hat{Y} \quad (\text{II.134})$$

Clearly, the differences in evolution equations of isotropic and kinematic hardening strains can be given by:

$$\begin{cases} o = b(T) \left(1 + \frac{\bar{Q}(T)}{Q(T)} \right) r - b(T) \left(\frac{\bar{Q}(T)}{Q(T)} \right) \bar{r} & \text{micromorphic} \\ o = b(T)r & \text{local} \end{cases} \quad (\text{II.135})$$

$$\begin{cases} \underline{m}_f = a(T) \left(\underline{1} + \underline{C}^{-1}(T) : \underline{\bar{C}}(T) \right) \underline{\alpha} - a(T) \left(\underline{C}^{-1}(T) : \underline{\bar{C}}(T) \right) : \underline{\alpha} & \text{micromorphic} \\ \underline{m}_f = a(T) \underline{\alpha} & \text{local} \end{cases} \quad (\text{II.136})$$

For the formulations on plastic multiplier and tangent operators, we just need to replace the micromorphic expressions of o and \underline{m}_f by the local formulas respectively. It's also the same case for viscoplastic evolution equations.

VI.5.2 Simplified classical elastoplastic model

In section VI.5.1, we demonstrate that with certain processes, ignoring the micromorphic dofs and vanishing the coupling moduli, the generalized micromorphic damaged model will reduce to the local damaged model. Here, we'll present the degenerations from the above local damage model to the classical elasto-plastic or elasto-visco-plastic model.

If we ignore the internal variable – local damage, the Helmholtz free energy $\psi(\underline{\varepsilon}^e, T, r, \underline{\alpha})$ will be a closed convex function of the classical local state variables: $\underline{\varepsilon}^e$, r and $\underline{\alpha}$, and a concave function of the temperature.

With the help from the first and second laws of thermodynamics, the following classical state relations are obtained:

$$\underline{\sigma} = \rho \frac{\partial \psi}{\partial \underline{\varepsilon}^e} \quad s = -\frac{\partial \psi}{\partial T} \quad R = \rho \frac{\partial \psi}{\partial r} \quad \underline{X} = \rho \frac{\partial \psi}{\partial \underline{\alpha}} \quad (\text{II.137})$$

And the local dissipations:

$$\phi = \phi_{in} + \phi_{th} = \underline{\sigma} : \underline{D}^{ir} - \underline{X} : \dot{\underline{\alpha}} - R \dot{r} - \frac{\vec{q}}{T} \cdot \vec{g} \geq 0 \quad (\text{II.138})$$

If we let the local damage equal to zero ($d=0$), which means no damage effects, we'll obtain the classical local state relations and elasto-plastic or elasto-visco-plastic evolution equations.

The Helmholtz free energy Eq.(II.123) will reduce to:

$$\rho \psi = \rho \psi_{tel}(\underline{\varepsilon}^e, d, T) + \rho \psi_{intel}(d, r, \underline{\alpha}) \quad (\text{II.139})$$

with,

$$\rho \psi_{tel} = \frac{1}{2} \underline{\varepsilon}^e : \underline{\Lambda}(T) : \underline{\varepsilon}^e - (T - T_0) \underline{P}(T) : \underline{\varepsilon}^e - \rho \frac{C_\varepsilon}{2T_0} (T - T_0)^2 \quad (\text{II.140})$$

and,

$$\rho \psi_{intel} = \frac{1}{2} (\underline{\alpha} : \underline{C}(T) : \underline{\alpha}) + \frac{1}{2} (Q(T)r^2) \quad (\text{II.141})$$

Accordingly, the classical local stress-like variables are obtained:

- Cauchy stress tensor:

$$\underline{\sigma} = \rho \frac{\partial \psi}{\partial \underline{\varepsilon}^e} = \underline{\Lambda}(T) : \underline{\varepsilon}^e - (T - T_0) \underline{P}(T) \quad (\text{II.142})$$

- Specific entropy (neglecting the micromorphic terms compared with the generalized specific entropy in Eq.(II.42)):

$$s = -\frac{\partial \psi}{\partial T} = \frac{1}{\rho} \left[\underline{P}(T) : \underline{\varepsilon}^e + \rho \frac{C_\varepsilon}{T_0} (T - T_0) \right] \quad (\text{II.143})$$

- Isotropic hardening stress:

$$R = \rho \frac{\partial \psi}{\partial r} = Q(T)r \quad (\text{II.144})$$

- Kinematic hardening stress:

$$\underline{X} = \rho \frac{\partial \psi}{\partial \underline{\alpha}} = \underline{\underline{C}}(T) : \underline{\underline{\alpha}} \quad (\text{II.145})$$

With the condition $d=0$, the plastic potential and yield function are given by:

$$\begin{cases} F_p(\underline{\sigma}, \underline{X}, R; T) = f_p + \frac{a(T)}{2} \underline{X} : \underline{\underline{C}}^{-1}(T) : \underline{X} + \frac{b(T)}{2} \frac{R^2}{Q(T)} \\ f_p(\underline{\sigma}, \underline{X}, R; T) = \|\underline{\sigma} - \underline{X}\| - R - \sigma_y(T) \end{cases} \quad (\text{II.146})$$

Using the normality rule, the evolutions of elasto-plastic model are given by:

- Plastic strain rate

$$\underline{D}^p = \dot{\lambda} \frac{\partial F_p}{\partial \underline{\sigma}} = \dot{\lambda} \left(\frac{\underline{\underline{H}}(T) : (\underline{\sigma} - \underline{X})}{\|\underline{\sigma} - \underline{X}\|} \right) = \dot{\lambda} \underline{n}_f \quad (\text{II.147})$$

- Kinematic hardening strain rate

$$\dot{\underline{\alpha}} = -\dot{\lambda} \frac{\partial F_p}{\partial \underline{X}} = \dot{\lambda} (\underline{n}_f - a(T) \underline{\alpha}) \quad (\text{II.148})$$

- Isotropic hardening strain rate

$$\dot{r} = -\dot{\lambda} \frac{\partial F_p}{\partial R} = \dot{\lambda} (1 - b(T)r) \quad (\text{II.149})$$

Clearly, if the coefficient a and b vanish, the kinematic and isotropic hardening strains will become to linear. It's the same as the model we used in Part I.

VI.5.3 The existent generalized heat equations

VI.5.3.1 Classical heat equation with internal variables

In the classical thermodynamics, for any material volume V , the global form of the first law (energy conservation) can be written as:

$$\frac{dE}{dt} + \frac{dK}{dt} = W + Q \quad (\text{II.150})$$

where E denotes the internal energy, K is the kinetic energy, W is the mechanical power input, and Q is the heat quantity input to the system.

By using the material time derivatives of a volume integral together with the divergence theorem in order to transform surface integrals into volume integrals, and by applying the spatial localization lemma (or local action theorem) for materially simple continua, the localized (differential) form of the first principle of thermodynamics is obtained as:

$$\rho \dot{e} = \underline{\sigma} : \dot{\underline{\varepsilon}} - \text{div}(\vec{q}) + \xi \quad (\text{II.151})$$

where ρ denotes the mass density of the body, e is the (specific) internal energy per unit mass, $\underline{\sigma}$ is the Cauchy stress tensor, $\dot{\underline{\varepsilon}}$ is the strain rate tensor, \vec{q} indicates the heat flux vector received across the boundaries of the body and ξ is the body heat source.

The integral form of the second law (inequality of entropy) of thermodynamics is given by:

$$\frac{d}{dt} \int_V (\rho s) dV - \int_V \left(\frac{\xi}{T} \right) dV + \int_{\Gamma} \left(\frac{\vec{q} \cdot \vec{n}}{T} \right) dS \geq 0 \quad (\text{II.152})$$

where s is the specific entropy, T is the absolute temperature and \vec{n} is the outward normal to the boundary surface. The use of the divergence theorem together with the principle of space localization for materially simple continua, leads to the local (differential) form of the second principle of thermodynamics in the current configuration:

$$\rho \dot{s} + \text{div} \left(\frac{\vec{q}}{T} \right) - \frac{\xi}{T} \geq 0 \quad (\text{II.153})$$

The relationship between internal energy and the Helmholtz free energy is assumed as:

$$\psi(\underline{\varepsilon}^e, \underline{\alpha}_n, T) = e - Ts \quad (\text{II.154})$$

where ψ is the specific Helmholtz free energy, $\underline{\varepsilon}^e$ is the reversible part of the strain tensor and $\underline{\alpha}_n$ are the (n) internal state variables associated with intrinsic dissipative phenomena (i.e. kinematic hardening or isotropic hardening). The dual stress-like variables associated with these internal state variables are denoted by \underline{A}_n .

Substituting Eq.(II.151) and Eq.(II.154) into Eq.(II.153) to eliminate the body heat source ξ and the specific internal energy, leads to the so-called Clausius-Duhem inequality under its local form:

$$\underline{\sigma} : \dot{\underline{\varepsilon}} - \rho(\dot{\psi} + s\dot{T}) - \frac{\vec{q}}{T} \cdot \vec{\nabla} T \geq 0 \quad (\text{II.155})$$

Here, the Helmholtz free energy is assumed to be a positive, close and convex function of the reversible strain $\underline{\varepsilon}^e$ and the overall strain-like internal state variables $\underline{\alpha}_n$, and is a concave function of temperature T . By assuming the additive decomposition of the total strain rate into elastic part and irreversible part ($\dot{\underline{\varepsilon}} = \dot{\underline{\varepsilon}}^e + \dot{\underline{\varepsilon}}^{ir}$), the Clausius-Duhem inequality Eq.(II.155) can be expressed as:

$$\left(\underline{\sigma} - \rho \frac{\partial \psi}{\partial \underline{\varepsilon}^e} \right) : \dot{\underline{\varepsilon}}^e - \rho \left(\frac{\partial \psi}{\partial T} + s \right) \dot{T} + \underline{\sigma} : \dot{\underline{\varepsilon}}^{ir} - \frac{\partial \psi}{\partial \underline{\alpha}_n} : \dot{\underline{\alpha}}_n - \frac{\vec{q}}{T} \cdot \vec{\nabla} T \geq 0 \quad (\text{II.156})$$

For simplicity, we assume that the terms $\left(\underline{\sigma} - \rho \frac{\partial \psi}{\partial \underline{\varepsilon}^e}\right)$ and $\left(\frac{\partial \psi}{\partial T} + s\right)$ do not depend on the rates of the state variables respectively, then following standard arguments (Truesdell and Noll (Truesdell and Noll, 2004a)), we obtain the state relations:

$$\underline{\sigma} = \rho \frac{\partial \psi}{\partial \underline{\varepsilon}^e} \quad s = -\frac{\partial \psi}{\partial T} \quad (\text{II.157})$$

and the residual dissipation:

$$\varphi_v = \varphi_{in} + \varphi_{th} = \underline{\sigma} : \dot{\underline{\varepsilon}}^{ir} - \underline{A}_n : \dot{\underline{\alpha}}_n - \frac{\vec{q}}{T} \cdot \vec{\nabla} T \geq 0 \quad (\text{II.158})$$

where, $\varphi_{in} = \underline{\sigma} : \dot{\underline{\varepsilon}}^{ir} - \underline{A}_n : \dot{\underline{\alpha}}_n$ is the intrinsic dissipation with $\underline{A}_n = \frac{\partial \psi}{\partial \underline{\alpha}_n}$, and $\varphi_{th} = -\frac{\vec{q}}{T} \cdot \vec{\nabla} T$ is the thermal dissipation.

Using the deduced state relations Eq.(II.157), and substituting Eq.(II.154) into the first law of thermodynamics Eq.(II.151), lead to the classical local form of the heat equation:

$$\rho \dot{s} T + \operatorname{div}(\vec{q}) - \xi - \varphi_{in} = 0 \quad (\text{II.159})$$

Considering the rigid body heat conduction ($\varphi_{in} = 0$) in the absence of body heat source, the above heat equation reduces to:

$$\rho C_e \dot{T} + \operatorname{div}(\vec{q}) = 0 \quad (\text{II.160})$$

where, $C_e = T \frac{\partial s}{\partial T}$ denotes the specific heat capacity at constant volume. In particular, if the Fourier law (Fourier, 1822) of heat flux is assumed:

$$\vec{q} = -\kappa \vec{\nabla} T \quad (\text{II.161})$$

with $\kappa > 0$ is the thermal conductivity coefficient for isotropic materials, then, the equation (Eq.(II.160)) leads to the following classical parabolic heat equation:

$$\rho C_e \dot{T} = \kappa \Delta T \quad (\text{II.162})$$

where, Δ stands for the Laplacian operator.

As shown in (Cattaneo, 1948, 1958; Jou et al., 1993; Vernotte, 1958), the parabolic heat equation results in a paradox of propagation of thermal signals with infinite speed. In the linear approximation, this implies that the influence of such a signal is felt immediately throughout the whole system(Jou et al., 1993). However, from the experimental point of view, Peshkov (Peshkov, 1944) found that in liquid Helium II, the thermal wave velocity is one order of magnitude smaller than the speed of sound and is called the speed of second sound. Recent measurements of the propagation speed of thermal signals at room temperature,

in inhomogeneous materials, have been performed by Kaminski (Kaminski, 1990) showing clearly that the parabolic heat model is inaccurate to describe these phenomena.

VI.5.3.2 Hyperbolic heat equation with relaxation time

VI.5.3.2.1 The heat equation of Cattaneo I

Cattaneo (Cattaneo, 1948) addressed the question of the paradox of heat conduction in 1948. He modified the (stationary) Fourier law based on the elementary kinetic theory of gases. He focused upon a small volume element of linear dimensions of the mean free path of the molecules in which a temperature gradient prevails, to review the Maxwell's molecular interpretation to heat conduction. After, he changed this argument slightly and argued that there is a time-lag between the start of the particles at their point of departure and the time of passing through the middle layer (Müller and Ruggeri, 1993). If the temperature changes in time, it is thus clear that the heat flux at a certain time depends on the temperature gradient at an earlier time. It therefore seemed reasonable to formulate the transient Fourier model as:

$$q_i = -\kappa \left(\frac{\partial T}{\partial x_i} - \tau \frac{d}{dt} \left(\frac{\partial T}{\partial x_i} \right) \right) \quad (\text{II.163})$$

where τ is a positive scalar called thermal relaxation time of the heat conducting medium (free electrons in the case of metals).

By substituting the above modified transient Fourier model into the heat equation Eq.(II.160), the following partial differential heat equation of rigid body is obtained:

$$\rho C_e \dot{T} + \tau \kappa \Delta \dot{T} = \kappa \Delta T \quad (\text{II.164})$$

Clearly, the above deduced heat equation Eq.(II.164) is not a hyperbolic type, and therefore predicts infinite speed for the temperature propagation.

VI.5.3.2.2 The heat equation of Cattaneo II

Later, Cattaneo proceeded to modify the equation (Eq.(II.163)) by assuming that the operator $\tau(d/dt)$ is small such that:

$$\left(1 - \tau \frac{d}{dt} \right)^{-1} \approx 1 + \tau \frac{d}{dt} \quad (\text{II.165})$$

By using this approximation, the transient Fourier model Eq.(II.163) transforms into the so-called Cattaneo equation:

$$q_i + \tau \dot{q}_i = -\kappa \frac{\partial T}{\partial x_i} \quad (\text{II.166})$$

Combining the above equations (Eqs.(II.151), (II.159)) and the state relations Eq.(II.157), we can easily obtain the following relationship:

$$\rho\dot{e} = \rho C_e \dot{T} + \underline{\sigma} : \dot{\underline{\epsilon}} - \varphi_{in} - T \left(\frac{\partial \underline{\sigma}}{\partial T} : \dot{\underline{\epsilon}}^e + \frac{\partial \underline{A}_n}{\partial T} : \dot{\underline{\alpha}}_n \right) \quad (\text{II.167})$$

Substituting Cattaneo's equation Eq.(II.166) into Eq.(II.151) and using the above relation Eq.(II.167), leads to the following generalized heat equation with internal variables:

$$\left[\rho C_e \dot{T} - \varphi_{in} - T \left(\frac{\partial \underline{\sigma}}{\partial T} : \dot{\underline{\epsilon}}^e + \frac{\partial \underline{A}_n}{\partial T} : \dot{\underline{\alpha}}_n \right) \right] + \tau \frac{\partial}{\partial t} \left(\rho C_e \dot{T} - \varphi_{in} - T \left(\frac{\partial \underline{\sigma}}{\partial T} : \dot{\underline{\epsilon}}^e + \frac{\partial \underline{A}_n}{\partial T} : \dot{\underline{\alpha}}_n \right) \right) = \kappa \Delta T + \xi + \tau \dot{\xi} \quad (\text{II.168})$$

Concerning the rigid body heat conduction (with neither intrinsic dissipation nor deformations), the heat equation will transform to the often called Cattaneo's hyperbolic heat equation:

$$\rho C_e \dot{T} + \tau \rho C_e \ddot{T} = \kappa \Delta T \quad (\text{II.169})$$

This is the telegraph equation. It is hyperbolic, if $\tau > 0$ holds.

Let us assume the plane thermal wave (Jou et al., 1993):

$$T(x,t) = T_0 \exp[i(kx - \omega t)] \quad (\text{II.170})$$

where T_0 indicates the amplitude, k is the (complex) wave number, w is the (real) frequency. The dispersion relation obtained by substituting Eq.(II.170) into Eq.(II.169) is:

$$-i\omega - \tau\omega^2 + \frac{\kappa}{\rho C_e} k^2 = 0 \quad (\text{II.171})$$

By solving the above equation with k a complex number, the nonlinear dispersion equation of the thermal waves and the attenuation distance α are obtained as:

$$v_p = \frac{\omega}{\operatorname{Re}(k)} = \frac{\sqrt{2 \frac{\kappa}{\rho C_e} \omega}}{\sqrt{\tau\omega + \sqrt{1 + \tau^2 \omega^2}}} \quad (\text{II.172})$$

$$\alpha = \frac{1}{\operatorname{Im}(k)} = 2 \frac{\kappa}{\rho C_e v_p} \quad (\text{II.173})$$

For low frequencies ($\tau\omega \ll 1$), the velocity $v_p \approx \sqrt{2\kappa\omega/\rho C_e}$ and $\alpha = \sqrt{2\kappa/\rho C_e \omega}$, which are the results predicted by the classical heat equation using Fourier's Law. In high frequency limit ($\tau\omega \gg 1$), the first-order term in Eq.(II.169) is small compared with the two other terms, and Eq.(II.169) becomes a wave equation whose solution is known in the literature as second sound. The quantities v_p and α tend to the

limiting values: $v_p \approx \sqrt{\frac{\kappa}{\rho C_e \tau}}$ and $\alpha \approx 2 \sqrt{\frac{\kappa \tau}{\rho C_e}}$.

However, the most critical argument on Cattaneo's hyperbolic heat equation is its inconsistency with the second law of thermodynamics (Bai and Lavine, 1995; Barletta and Zanchini, 1997; Coleman et al.,

1982; Coleman et al., 1985; Körner and Bergmann, 1998; Zanchini, 1999). Cattaneo's hyperbolic heat equation may yields negative values of the entropy production rate per unit volume.

Combing the local forms of first and second principles (Eq.(II.151) and Eq.(II.153)), the relation $de = Tds$ holds locally leading to the following expression of the entropy production rate (Barletta and Zanchini, 1997):

$$s_p = -\frac{\vec{q}}{T^2} \cdot \vec{\nabla} T \quad (\text{II.174})$$

Substituting the generalized heat flux Eq.(II.166) into the above entropy production rate equation, leads to:

$$s_p = \frac{1}{\kappa T^2} \left(\vec{q} \cdot \vec{q} + \tau \vec{q} \cdot \frac{\partial \vec{q}}{\partial t} \right) \quad (\text{II.175})$$

whenever the heat flux \vec{q} has a constant direction and decreases at some point so deeply that $|\partial \vec{q} / \partial t| > |\vec{q}|/\tau$, the right hand side of Eq.(II.175), becomes negative and the local equilibrium scheme cannot be applied.

VI.5.3.2.3 The model of Müller from extended TIP

Motivated by the work of Cattaneo, Müller (Müller, 1966; Muller, 1967; Müller and Ruggeri, 1993) tried to derive the modifications of the Fourier law of heat flux from the principle of thermodynamics of irreversible processes (TIP). He noticed that the argument of TIP could be used to derive the Cattaneo equation. All what we need is to assume that the specific entropy depends not only on the classical variables but also on the heat flux. The generalized Gibbs equation is given by:

$$\dot{s} = \frac{1}{T} \left(\dot{e} - \frac{p}{\rho^2} \dot{\rho} + 2aT\vec{q} \cdot \dot{\vec{q}} + 2bT\underline{\sigma}^{dev} : \dot{\underline{\sigma}}^{dev} + 2cT\pi\dot{\pi} \right) \quad (\text{II.176})$$

where, p is the pressure, $\underline{\sigma}^{dev}$ is the deviatoric part of stress tensor, $\pi = (tr(\underline{\sigma})/3 + p)$ is the dynamic pressure, and the negative coefficients a , b and c enable s to have a maximum in equilibrium, when \vec{q} , $\underline{\sigma}^{dev}$ and π all vanish.

By using the mass conservation law, momentum conservation and energy conservation, Eq.(II.176) becomes the following equation of entropy balance (Müller and Ruggeri, 1993):

$$\rho\dot{s} + \vec{\nabla} \cdot \left(\frac{\vec{q}}{T} \right) = \vec{q} \cdot \left(\vec{\nabla} \left(\frac{1}{T} \right) + 2\rho a \dot{\vec{q}} \right) + \underline{\sigma}^{dev} : \left(\frac{1}{T} (\vec{\nabla} \vec{v})^{dev} + 2\rho b \dot{\underline{\sigma}}^{dev} \right) + \pi \left(\frac{1}{T} \vec{\nabla} \cdot \vec{v} + 2\rho c \dot{\pi} \right) \quad (\text{II.177})$$

Müller interpreted \vec{q}/T as the entropy flux and the right side of Eq.(II.177) as the entropy production, which is a sum of products of the thermodynamic fluxes and modified thermodynamics forces. However, because the definition of the entropy flux is ambiguous, it is possible to add the term $K\underline{\sigma}^{dev} \cdot \vec{q} + L\pi\vec{q}$ with arbitrary coefficients K and L , to the usual entropy flux without upsetting the structure of the entropy production as a sum of products of forces and fluxes:

$$\begin{aligned} \rho\dot{s} + \vec{\nabla} \cdot \vec{\phi} &= \vec{q} \cdot \left(\vec{\nabla} \left(\frac{1}{T} \right) + 2\rho a \dot{\vec{q}} + K \vec{\nabla} \cdot \underline{\sigma}^{dev} + L \vec{\nabla} \pi \right) \\ &\quad + \underline{\sigma}^{dev} : \left(\frac{1}{T} \left(\vec{\nabla} \vec{v} \right)^{dev} + 2\rho b \dot{\underline{\sigma}}^{dev} + K \vec{\nabla} \vec{q} \right) + \pi \left(\frac{1}{T} \vec{\nabla} \cdot \vec{v} + 2\rho c \dot{\pi} + L \vec{\nabla} \cdot \vec{q} \right) \end{aligned} \quad (\text{II.178})$$

where, the generalized entropy flux is $\vec{\phi} = \left(\frac{\vec{q}}{T} + K \underline{\sigma}^{dev} \cdot \vec{q} + L \pi \vec{q} \right)$. The entropy production must be non-negative. For simplification, linear phenomenological relations between the fluxes and the forces are assumed:

$$\begin{aligned} \vec{q} &= -\kappa \left(\vec{\nabla} T - 2\rho a T^2 \dot{\vec{q}} - K T^2 \vec{\nabla} \cdot \underline{\sigma}^{dev} - L T^2 \vec{\nabla} \pi \right) \\ \underline{\sigma}^{dev} &= 2\mu \left(\left(\vec{\nabla} \vec{v} \right)^{dev} + 2\rho b T \dot{\underline{\sigma}}^{dev} + K T \vec{\nabla} \vec{q} \right) \\ \pi &= \lambda \left(\vec{\nabla} \cdot \vec{v} + 2\rho c T \dot{\pi} + L T \vec{\nabla} \cdot \vec{q} \right) \end{aligned} \quad (\text{II.179})$$

It is worth noting that the heat flux in Eq.(II.179) is equivalent to Cattaneo's equation Eq.(II.166), if the coefficients K and L vanish and $\tau = -2\rho a T^2$ holds. And from Eq.(II.178), it clearly shows that Eq.(II.179) is compatible with the second law of thermodynamics.

This theory is called extended TIP, because it has extended the list of state variables on which the specific entropy and the entropy flux can depend. After this modification of ordinary TIP, a large number of papers have appeared, using the Müller's methodology and devoted in particular to gases. An exhaustive review of this type of irreversible thermodynamics is given by Jou et al. (Jou et al., 1988; Jou et al., 1993).

VI.5.3.2.4 The model of Coleman from rational thermodynamics

Coleman et al. (Coleman et al., 1982; Coleman et al., 1985) derived the restrictions that the second law of thermodynamics imposes on constitutive equations of the type proposed by Cattaneo. For generalization, Cattaneo's equation (Eq.(II.166)) is equivalent to:

$$\vec{q} + \underline{\tau}(T) \cdot \dot{\vec{q}} = -\underline{\kappa}(T) \cdot \vec{\nabla} T \quad (\text{II.180})$$

with $\underline{\tau}(T)$ and $\underline{\kappa}(T)$ non-singular second-order tensors that, as function of temperature, depend on the material under consideration. Clearly, in the isotropic case, it will be the same as Eq.(II.166).

The authors showed that the relation Eq.(II.180) with the tensors $\underline{\tau}(T)$ and $\underline{\kappa}(T)$ non-singular is compatible with the thermodynamics only if $\underline{\kappa}(T)$ is positive definite, the tensor $Z(T) = \underline{\kappa}(T)^{-1} \underline{\tau}(T)$ is symmetric, and the specific internal energy e , the specific entropy s and the specific Helmholtz free energy $\psi = e - Ts$ are not functions of T only, but are instead given by functions \tilde{e} , \tilde{s} and $\tilde{\psi}$ of the form:

$$\begin{aligned}\rho e &= \rho \tilde{e}(T, \vec{q}) = \rho e_0(T) + \vec{q} \cdot \underline{A}(T) \cdot \vec{q} \\ \rho s &= \rho \tilde{s}(T, \vec{q}) = \rho s_0(T) + \vec{q} \cdot \underline{B}(T) \cdot \vec{q} \\ \rho \psi &= \rho \tilde{\psi}(T, \vec{q}) = \rho \psi_0(T) + \frac{1}{2T} \vec{q} \cdot \underline{Z}(T) \cdot \vec{q}\end{aligned}\quad (\text{II.181})$$

with

$$\underline{A}(T) = -\frac{T^2}{2} \frac{d}{dT} \left(\frac{\underline{Z}(T)}{T^2} \right) \quad \underline{B}(T) = -\frac{1}{2} \frac{d}{dT} \left(\frac{\underline{Z}(T)}{T} \right) \quad (\text{II.182})$$

here, e_0 , s_0 and ψ_0 are the specific internal energy, specific entropy and specific Helmholtz free energy at equilibrium. In the absence of both deformation and a supply of heat by radiation, clearly, \dot{e} is not given by the classical formula Eq.(II.167) $\dot{e} = C_e(T)\dot{T}$ ($C_e(T)$ being the equilibrium heat capacity), but is instead given by:

$$\rho \dot{e} = \left[\rho C_e(T) + \vec{q} \cdot \frac{d}{dT} \underline{A}(T) \cdot \vec{q} \right] \dot{T} + 2\vec{q} \cdot \underline{A}(T) \cdot \dot{\vec{q}} \quad (\text{II.183})$$

Thus, the evolution of the heat flux and temperature field is governed by a pair of nonlinear partial differential equations:

$$\begin{cases} \vec{q} + \underline{\tau}(T) \cdot \dot{\vec{q}} + \underline{\kappa}(T) \cdot \vec{\nabla} T = \vec{0} \\ \text{div}(\vec{q}) + \left(\rho C_e(T) + \vec{q} \cdot \frac{d}{dT} \underline{A}(T) \cdot \vec{q} \right) \dot{T} + 2\vec{q} \cdot \underline{A}(T) \cdot \dot{\vec{q}} = 0 \end{cases} \quad (\text{II.184})$$

It is worth noting that if the parameter $\underline{Z}(T)$ is isotropic and equals to $Z(T) = DT^2$ (where D is constant) (Bai and Lavine, 1995), the general result from Eq.(II.181) reduces to $\rho \tilde{e}(T, \vec{q}) = \rho e_0(T)$ and $\rho \tilde{s}(T, \vec{q}) = \rho s_0(T) - \frac{D}{2} \vec{q} \cdot \vec{q}$, which is similar to the relationship given by Jou et al. (Jou et al., 1988).

By comparing the two non-equilibrium thermodynamics theories, it is clear that: (i) the extended TIP theory modifies the entropy (entropy flux and entropy production) from the generalized Gibbs equation; (ii) the rational thermodynamics theory starts from the extension of the specific internal energy, and consequently, (iii) the specific entropy and specific Helmholtz free energy are enhanced automatically due to the dual relation $\psi = e - Ts$. In summary, both theories contain Cattaneo's equation and make it compatible with the second law of thermodynamics.

VI.5.3.3 Temperature or entropy gradient dependent free energy potential

VI.5.3.3.1 Temperature gradient model from Nguyen

Nguyen et al. (Iremen and Nguyen, 2004; Nguyen, 2010; Nguyen and Andrieux, 2005) assumed an extra entropy supply and modified the relationship between internal energy and Helmholtz free energy, to

account for the temperature gradient effects. The dual relationship is given under the following modified form:

$$e(s, \vec{s}, \vec{\nabla} \vec{u}, r) = \psi(T, \vec{\nabla} T, \vec{\nabla} \vec{u}, r) + sT + \vec{s} \cdot \vec{\nabla} T \quad (\text{II.185})$$

with the introduction of a new specific entropy vector \vec{s} .

The first principle (energy conservation) of thermodynamics remains unchanged, while an additional entropy source is assumed in the second law, the local forms being given by:

$$\begin{cases} \rho \dot{e} = \underline{\sigma} : \dot{\underline{\varepsilon}} - \operatorname{div}(\vec{q}) + \xi \\ \rho \left(\dot{s} + \frac{\dot{\vec{s}}}{T} \cdot \vec{\nabla} T \right) - \left(\frac{\xi}{T} \right) + \operatorname{div} \left(\frac{\vec{q}}{T} \right) \geq 0 \end{cases} \quad (\text{II.186})$$

Combining the above equations (Eq.(II.185) and Eq.(II.186)), leads to the following local form of the Clausius-Duhem inequality:

$$\left(\underline{\sigma} - \rho \frac{\partial \psi}{\partial \underline{\varepsilon}^e} \right) : \dot{\underline{\varepsilon}}^e - \rho \left(\frac{\partial \psi}{\partial T} + s \right) \dot{T} - \rho \left(\frac{\partial \psi}{\partial \vec{\nabla} T} + \vec{s} \right) \cdot \vec{\nabla} \dot{T} + \underline{\sigma} : \dot{\underline{\varepsilon}}^{ir} - \frac{\partial \psi}{\partial \alpha_n} : \dot{\alpha}_n - \frac{\vec{q}}{T} \cdot \vec{\nabla} T \geq 0 \quad (\text{II.187})$$

For simplicity, we assume that the terms $\left(\underline{\sigma} - \rho \frac{\partial \psi}{\partial \underline{\varepsilon}^e} \right)$, $\left(\frac{\partial \psi}{\partial T} + s \right)$ and $\left(\frac{\partial \psi}{\partial \vec{\nabla} T} + \vec{s} \right)$ do not depend on

the rates of the state variables respectively, then following standard arguments (Truesdell and Noll (Truesdell and Noll, 2004a)), we obtain the following state relations:

$$\underline{\sigma} = \rho \frac{\partial \psi}{\partial \underline{\varepsilon}^e} \quad s = -\frac{\partial \psi}{\partial T} \quad \vec{s} = -\frac{\partial \psi}{\partial \vec{\nabla} T} \quad (\text{II.188})$$

and the classical residual dissipation:

$$\varphi_V = \varphi_{in} + \varphi_{th} = \underline{\sigma} : \dot{\underline{\varepsilon}}^{ir} - A_n : \dot{\alpha}_n - \frac{\vec{q}}{T} \cdot \vec{\nabla} T \geq 0 \quad (\text{II.189})$$

Substituting the new dual relations into the first principle of thermodynamics yields the following form of the heat equation:

$$\rho T \dot{s} + \rho \vec{s} \cdot \vec{\nabla} T - \xi + \operatorname{div}(\vec{q}) - \varphi_{in} = 0 \quad (\text{II.190})$$

In the case of rigid body conduction (no intrinsic dissipation), the free energy can be defined as follows:

$$\rho \psi(T, \vec{\nabla} T) = -\rho C_\varepsilon T \left(\ln \frac{T}{T_0} - 1 \right) - \frac{M}{2} \vec{\nabla} T \cdot \vec{\nabla} T \quad (\text{II.191})$$

where, $C_\varepsilon > 0$ and $M > 0$ are two positive material coefficients (Nguyen, 2010). Using the state relations Eq.(II.188), the generalized heat equation is given by:

$$\rho C_e \dot{T} + M \vec{\nabla} \dot{T} \cdot \vec{\nabla} T + \operatorname{div}(\vec{q}) = 0 \quad (\text{II.192})$$

Taking into account the Fourier law of heat flux, the heat equation just becomes:

$$\rho C_e \dot{T} + M \vec{\nabla} \dot{T} \cdot \vec{\nabla} T = \kappa \Delta T \quad (\text{II.193})$$

Nguyen (Nguyen, 2010), considers the example of the small perturbation of a stationary temperature $T_0(x) = T_0 + gx/L$, in a 1D rigid rod $[0, L]$.

The associated linearized heat equation, using Fourier's law of heat flux, can be expressed as:

$$\rho C_e T_{,t} + \frac{Mg}{L} T_{,xt} = \kappa T_{,xx} \quad (\text{II.194})$$

An elementary solution given in the work (Nguyen, 2010), shows that the thermal pulses propagate at finite velocity given by $-Mg\kappa L / (\rho^2 C_e^2 I^2 L^2 + M^2 g^2)$ with damping coefficient defined by $\rho C_e \kappa L^2 / (\rho^2 C_e^2 I^2 L^2 + M^2 g^2)$.

VI.5.3.3.2 Hyper-temperature (entropy gradient) model

In 2008, Forest and Amestoy (Forest and Amestoy, 2008) extended the classical thermodynamics of solids to incorporate a non-trivial dependence of the internal energy density function on the gradient of entropy. The generalized heat equation derived from this theory is shown to be different from existing models including gradient of temperature effects in the free energy. In this theory, the additional contributions to the power of internal and external forces are assumed, in the form:

$$\begin{aligned} P_{\text{int}} &= - \int_V (\underline{\sigma} : \vec{\nabla} \vec{v}^* + \sigma_s \dot{s}^* + \vec{\sigma}_s \cdot \vec{\nabla} \dot{s}^*) dV \quad P_a = \rho \int_V (\dot{\vec{v}} \cdot \vec{v}^*) dV \\ P_{\text{ext}} &= \int_V (\rho \vec{f}^u \cdot \dot{\vec{u}}^* + f^s \dot{s}^* + \vec{f}^s \cdot \vec{\nabla} \dot{s}^*) dV + \int_{\Gamma} (\vec{F}^u \cdot \dot{\vec{u}}^* + F^s \dot{s}^*) ds \end{aligned} \quad (\text{II.195})$$

with, σ_s and $\vec{\sigma}_s$ (called hyper-temperature vector (Forest and Amestoy, 2008)) denotes micro-stresses. \vec{f}^u , f^s , \vec{f}^s and \vec{F}^u , F^s are the simple and generalized body forces and contact forces respectively associated with \vec{u} and s , and no micro-inertia effects are attached to entropy.

Applying the principle of virtual power results in the following balance equations and associated boundary conditions:

$$\begin{cases} \vec{\nabla} \cdot \underline{\sigma} + \rho \vec{f}^u = 0 & \text{in } \Omega \\ \underline{\sigma} \cdot \vec{n} = \vec{F}^u & \text{on } \Gamma \end{cases} \quad \begin{cases} \vec{\nabla} \cdot (\vec{\sigma}_s - \vec{f}^s) - \sigma_a + f^s = 0 & \text{in } \Omega \\ (\vec{\sigma}_s - \vec{f}^s) \cdot \vec{n} = F^s & \text{on } \Gamma \end{cases} \quad (\text{II.196})$$

Consequently, using the kinetic energy theorem, the local form of the energy balance follows:

$$\rho \dot{e} = \underline{\sigma} : \dot{\underline{\epsilon}} + \sigma_s \dot{s} + \vec{\sigma}_s \cdot \vec{\nabla} \dot{s} - \operatorname{div}(\vec{q}) + \xi \quad (\text{II.197})$$

Substituting the above extended rate of specific internal energy Eq.(II.197) into the classical second law of thermodynamics (Eq.(II.153)), leads to the generalized Clausius-Duhem inequality:

$$\rho(T\dot{s} - \dot{e}) + \underline{\sigma} : \dot{\underline{\varepsilon}} + \sigma_s \dot{s} + \vec{\sigma}_s \cdot \vec{\nabla} \dot{s} - \frac{\vec{q}}{T} \cdot \vec{\nabla} T \geq 0 \quad (\text{II.198})$$

Considering thermoelastic solids and the set of state variables $(\underline{\varepsilon}, s, \vec{\nabla} s)$, the inequality eq.(II.198) becomes:

$$\rho \left(T - \frac{\partial e}{\partial s} + \frac{\sigma_s}{\rho} \right) \dot{s} + \left(\underline{\sigma} - \rho \frac{\partial e}{\partial \underline{\varepsilon}} \right) : \dot{\underline{\varepsilon}} + \left(\vec{\sigma}_s - \rho \frac{\partial e}{\partial \vec{\nabla} s} \right) \cdot \vec{\nabla} \dot{s} - \frac{\vec{q}}{T} \cdot \vec{\nabla} T \geq 0 \quad (\text{II.199})$$

from which the state relations are derived based on the Coleman-Noll standard arguments:

$$\underline{\sigma} = \rho \frac{\partial e}{\partial \underline{\varepsilon}} \quad T = \frac{\partial e}{\partial s} - \frac{\sigma_s}{\rho} \quad \vec{\sigma}_s = \rho \frac{\partial e}{\partial \vec{\nabla} s} \quad (\text{II.200})$$

and the residual thermal dissipation:

$$\varphi_v = \varphi_{th} = -\frac{\vec{q}}{T} \cdot \vec{\nabla} T \geq 0 \quad (\text{II.201})$$

Substituting the state laws Eq.(II.200) into the local energy balance equation (Eq.(II.197)), leads to the classical form of the heat equation:

$$\rho T \dot{s} = -\operatorname{div}(\vec{q}) + \xi \quad (\text{II.202})$$

Concerning the following internal energy density function, linearized around the reference entropy s_0 in rigid heat conduction:

$$\rho e(s, \vec{\nabla} s) = \rho s T_0 + \rho^2 \frac{(s - s_0)^2}{4\beta} + \frac{1}{2} A_s \vec{\nabla} s \cdot \vec{\nabla} s \quad (\text{II.203})$$

where, β and A_s are two positive material parameters. Using the derived state laws in Eq.(II.200) and the Fourier law Eq.(II.161), the heat equation is derived as:

$$\rho T_0 \dot{s} = \kappa \Delta T = \frac{\rho \kappa}{2\beta} (\Delta s - l_s^2 \Delta^2 s) \quad (\text{II.204})$$

where, $l_s^2 = \frac{2\beta A_s}{\rho^2}$ is a characteristic length related to material parameters.

It is worth noting that this enhanced heat equation (Eq.(II.204)) has the structure of the Cahn-Hilliard equation in mass transport theory (Cahn and Hilliard, 1958; Gurtin, 1996). The classical heat equation is retrieved for a vanishing intrinsic length scale $l_s = 0$, or equivalently $A_s = 0$, in the absence of prescribed external micro-forces. The additional contribution in Eq.(II.204) accounts for the size effects in heat conduction in micro-heterogeneous bodies.

By using the expressions of internal energy density function, the free energy density is given by:

$$\begin{aligned}\rho\psi(T, \vec{\nabla}T, \Delta s) = & -\rho(T-T_0)s_0 - \beta(T-T_0)^2 + \frac{2A_s\beta^2}{\rho^2}\vec{\nabla}T \cdot \vec{\nabla}T \\ & + \frac{4A_s^2\beta^2}{\rho^3}\vec{\nabla}T \cdot \vec{\nabla}(\Delta s) + \frac{\beta A_s^2}{\rho^2}(\Delta s)^2 + \frac{2\beta^2 A_s^3}{\rho^4}\vec{\nabla}(\Delta s) \cdot \vec{\nabla}(\Delta s)\end{aligned}\quad (\text{II.205})$$

The first line of the expression corresponds to the quadratic form in a linearized theory of rigid heat conduction including the temperature gradient as state variables:

$$\rho\psi_T(T, \vec{\nabla}T) = -\rho(T-T_0)s_0 - \frac{1}{2}\frac{\rho C_\varepsilon}{T_0}(T-T_0)^2 + \frac{1}{2}A_T\vec{\nabla}T \cdot \vec{\nabla}T \quad (\text{II.206})$$

with $\beta = \rho C_\varepsilon / 2T_0$ and $A_T T_0^2 = A_s C_\varepsilon^2$. The second line of the expression shows that the gradient of entropy and gradient of temperature theories are not equivalent. If the parameter A_s is sufficiently small, the gradient of temperature model Eq.(II.206) can be regarded as an approximation of the gradient of entropy theory.

The generalized heat equation derived from the gradient entropy theory can be rewritten as:

$$\rho C_\varepsilon \dot{T} + \frac{A_s C_\varepsilon^2}{T_0} \Delta \dot{T} + \frac{A_s^2 C_\varepsilon^2}{\rho T_0} \Delta^2 \dot{s} = \kappa \Delta T \quad (\text{II.207})$$

If one considers a sufficiently small value of A_s , the last term in the left hand of Eq.(II.207) can be neglected, the heat equation becomes:

$$\rho C_\varepsilon \dot{T} + T_0 A_T \Delta \dot{T} = \kappa \Delta T \quad (\text{II.208})$$

which is exactly the heat equation derived from the temperature gradient theory Eq.(II.206). Note that the heat equation (Eq.(II.208)), derived from the gradient temperature theory, has the same form as the heat equation of Cattaneo I (Eq.(II.164)) taking $\tau = T_0 A_T / \kappa$.

VI.5.3.4 Double temperature model

VI.5.3.4.1 Aifantis' double temperature model

A generalized heat equation has also been phenomenologically derived by Aifantis (Aifantis, 1980a, b; Forest and Aifantis, 2010) based on a double temperature mixture type theory. For the sake of brevity, we limit ourselves to the rigid body assumption. In the case of a heat conducting two components system (indicated by 1 and 2), the following two energy balance equations must be fulfilled:

$$\rho_1 \dot{e}_1 = -\operatorname{div}(\vec{q}_1) + \xi_1 \quad \rho_2 \dot{e}_2 = -\operatorname{div}(\vec{q}_2) + \xi_2 \quad (\text{II.209})$$

In a mixture for which the particle densities are $\rho_1 = \rho_2 = \rho/2$, the macroscopic internal energy, heat flux and effective temperature are defined as:

$$2e = e_1 + e_2 \quad 2\vec{q} = \vec{q}_1 + \vec{q}_2 \quad 2T = T_1 + T_2 \quad (\text{II.210})$$

In the absence of chemical reactions, the source terms are assumed to compensate $\xi_1 + \xi_2 = 0$. The entropy production due to each constituent is assumed to take the form:

$$\rho \dot{s}_1 + \text{div} \left(\frac{\vec{q}_1}{T_1} \right) = \pi_1 \quad \rho \dot{s}_2 + \text{div} \left(\frac{\vec{q}_2}{T_2} \right) = \pi_2 \quad 2\pi = \pi_1 + \pi_2 \geq 0 \quad (\text{II.211})$$

Combining the balance equations of energy Eq.(II.209) and the entropy inequality Eq.(II.211), the reduced Clausius-Duhem inequality is derived:

$$\rho \left(1 - \frac{1}{T_1} \frac{\partial e_1}{\partial s_1} \right) \dot{s}_1 + \rho \left(1 - \frac{1}{T_2} \frac{\partial e_2}{\partial s_2} \right) \dot{s}_2 + \rho \left(\frac{\xi_1}{T_1} + \frac{\xi_2}{T_2} \right) - \frac{\vec{q}_1}{T_1} \cdot \vec{\nabla T}_1 - \frac{\vec{q}_2}{T_2} \cdot \vec{\nabla T}_2 \geq 0 \quad (\text{II.212})$$

Then, the state relationships linking partial temperature and entropies are derived based on the Coleman-Noll arguments:

$$T_1 = \frac{\partial e_1}{\partial s_1} \quad T_2 = \frac{\partial e_2}{\partial s_2} \quad (\text{II.213})$$

The residual dissipation:

$$\varphi_V = \varphi_{th} = \rho \left(\frac{\xi_1}{T_1} + \frac{\xi_2}{T_2} \right) - \frac{\vec{q}_1}{T_1} \cdot \vec{\nabla T}_1 - \frac{\vec{q}_2}{T_2} \cdot \vec{\nabla T}_2 \geq 0 \quad (\text{II.214})$$

If the temperature variations remain sufficiently small, the generalized Fourier law are assumed to take the form:

$$\begin{Bmatrix} \vec{q}_1 \\ \vec{q}_2 \end{Bmatrix} = - \begin{bmatrix} \kappa_{11} & \kappa_{12} \\ \kappa_{21} & \kappa_{22} \end{bmatrix} \begin{Bmatrix} \vec{\nabla T}_1 \\ \vec{\nabla T}_2 \end{Bmatrix} \quad (\text{II.215})$$

and the generalized specific heat capacities (C_{ij}) are also introduced in the form:

$$\rho_1 e_1 = C_{11} T_1 + C_{12} T_2 \quad \rho_2 e_2 = C_{21} T_1 + C_{22} T_2 \quad (\text{II.216})$$

Within the assumption of linear framework, the coupling term may be taken as proportional to the temperature gap:

$$\xi_1 = -\xi_2 = h(T_2 - T_1) \quad (\text{II.217})$$

where, h is a coupling parameter (microscopic heat transfer).

Substituting the above state constitutive equations into the corresponding balance equations, the following partial differential equations are obtained:

$$\begin{bmatrix} C_{11} \frac{d}{dt} - \kappa_{11} \Delta + h & C_{12} \frac{d}{dt} - \kappa_{12} \Delta - h \\ C_{21} \frac{d}{dt} - \kappa_{21} \Delta - h & C_{22} \frac{d}{dt} - \kappa_{22} \Delta + h \end{bmatrix} \begin{Bmatrix} T_1 \\ T_2 \end{Bmatrix} = \begin{Bmatrix} 0 \\ 0 \end{Bmatrix} \quad (\text{II.218})$$

Elimination of T_1 and T_2 leads to the following higher order heat equation for the effective (global) temperature:

$$\dot{T} + \alpha \ddot{T} - \beta \Delta \dot{T} + \gamma \Delta^2 T = \lambda \Delta T \quad (\text{II.219})$$

where,

$$\begin{aligned} \alpha &= \frac{C_{11}C_{22} - C_{12}C_{21}}{h(C_{11} + C_{22} + C_{12} + C_{21})} & \beta &= \frac{\kappa_{11}C_{22} + \kappa_{22}C_{11} + \kappa_{12}C_{21} + \kappa_{21}C_{12}}{h(C_{11} + C_{22} + C_{12} + C_{21})} \\ \gamma &= \frac{\kappa_{11}\kappa_{22} - \kappa_{12}\kappa_{21}}{h(C_{11} + C_{22} + C_{12} + C_{21})} & \lambda &= \frac{\kappa_{11} + \kappa_{22} + \kappa_{12} + \kappa_{21}}{(C_{11} + C_{22} + C_{12} + C_{21})} \end{aligned} \quad (\text{II.220})$$

It must be noted that Eq.(II.219) contains two more terms, the second time derivative and fourth space derivative of temperature, compared with the heat equation of Cattaneo I (Eq.(II.164)). The fourth order spatial derivative term can be neglected when the thermal conductivity of electron component κ_{11} is much larger than the lattice component κ_{22} , e.g. in pure metal (Sobolev, 2016). This equation also similar to Barenblatt's infiltration theory for the pore pressure in double porosity media (Aifantis, 1980a).

VI.5.3.4.2 Hyperbolic two-temperature model

As summarized by Sobolev (Sobolev, 2016), the double temperature model is still a parabolic heat equation. In order to obtain hyperbolic heat equations of the two-temperature model, he adopts the Cattaneo equation Eq.(II.166) as the extension of the heat flux model. It yields the heat conduction equation for the electron and lattice temperatures in the form:

$$\left\{ \begin{array}{l} \frac{\partial T_1}{\partial t} + (\tau + \tau_{12}) \frac{\partial^2 T_1}{\partial t^2} + \tau \tau_{12} \frac{\partial^3 T_1}{\partial t^3} = \bar{\kappa} \frac{\partial^2 T_1}{\partial x^2} + I^2 \frac{\partial^3 T_1}{\partial x^2 \partial t} + \bar{Q} + (\tau + \tau_2) \frac{\partial \bar{Q}}{\partial t} + \tau \tau_2 \frac{\partial^2 \bar{Q}}{\partial t^2} \\ \frac{\partial T_2}{\partial t} + (\tau + \tau_{12}) \frac{\partial^2 T_2}{\partial t^2} + \tau \tau_{12} \frac{\partial^3 T_2}{\partial t^3} = \bar{\kappa} \frac{\partial^2 T_2}{\partial x^2} + I^2 \frac{\partial^3 T_2}{\partial x^2 \partial t} + \bar{Q} + \tau \frac{\partial \bar{Q}}{\partial t} \end{array} \right. \quad (\text{II.221})$$

where τ is electron relaxation time, $\tau_{12} = C_1 C_2 / \alpha (C_1 + C_2)$ is characteristic time of energy exchange between electron and lattice, α is the electron-phonon coupling factor, C_1 and C_2 are the electron and lattice heat capacity, respectively, $\bar{\kappa} = \kappa / (C_1 + C_2)$ with κ is the electron thermal conductivity, $I = \sqrt{\kappa C_2 / \alpha (C_1 + C_2)}$ is the characteristic (internal) length scale, $\bar{Q} = Q / (C_1 + C_2)$ with Q is a heat source due to laser irradiation, $\tau_2 = C_2 / \alpha$ is a characteristic warm-up time of the lattice.

If the heat source is omitted, the heat conduction equation can be written as:

$$\dot{T}_i + (\tau + \tau_{12}) \ddot{T}_i + \tau \tau_{12} \ddot{T}_i - I^2 \Delta \dot{T}_i = \bar{\kappa} \Delta T_i \quad (\text{II.222})$$

In the work (Sobolev, 2016) a plane thermal wave $T(x, t) = T_0 \exp[i(\omega t - kx)]$ is considered to examine the properties of the heat equations. The dispersion relation for Eq.(II.221) takes the form:

$$i\omega^3\tau\tau_{12} + \omega^2(\tau + \tau_{12}) - i\omega(1 + \tau_2\bar{\kappa}k^2) - \bar{\kappa}k^2 = 0 \quad (\text{II.223})$$

At the high frequency limit, Eq.(II.223) implies that the temperature discontinuities propagate in the system with finite velocity $V_p = \sqrt{\kappa/C_1\tau}$, which depends only on the physical parameters of electron gas and is of the order of Fermi velocity. In the intermediate frequency, the local equilibrium in the electron gas is reached and energy is transferred into the bulk metal by diffusive transport of thermalized electrons and from the electron gas to the initially cold lattice by electron-phonon coupling. In the low frequency, the thermal equilibrium between electron and the lattice is reached, i.e. the energy exchange between the electron gas and the lattice is negligible and energy transfer in the system is described by classical heat conduction equation of parabolic type.

VI.5.3.4.3 Generalized two-temperature model with nonlocal effects

To account for the spatial nonlocal effects (when the characteristic length scale of the process becomes comparable with the mean free path of heat carriers) due to large temperature gradients, Sobolevs (Sobolev, 2016) extended Cattaneo's equation with additional second-order space derivatives:

$$\vec{q} + \tau\dot{\vec{q}} = -\kappa\vec{\nabla}T + I_e^2\Delta\vec{q} \quad (\text{II.224})$$

where I_e is the space non-locality of the heat transfer process (correlation length), which for metal is of the order of the mean free path of electrons.

For the sake of simplicity, the material parameters are assumed to be constant and the extended heat equation takes the form:

$$\dot{T}_i + (\tau + \tau_{12})\ddot{T}_i + \tau\tau_{12}\ddot{T}_i - (I^2 + I_e^2)\Delta\dot{T}_i - I_e^2\tau_{12}\Delta\ddot{T}_i = \bar{\kappa}\Delta T_i + Q_i^{eff} \quad (\text{II.225})$$

where, the index i refers to the two temperatures, Q_i^{eff} is the effective energy source, which is expressed as:

$$\begin{aligned} Q_1^{eff} &= \bar{Q} + (\tau + \tau_2)\dot{\bar{Q}} - I_e^2\Delta\bar{Q} + \tau\tau_2\ddot{\bar{Q}} - \tau_2I_e^2\Delta\dot{\bar{Q}} \\ Q_2^{eff} &= \bar{Q} + \tau\dot{\bar{Q}} - I_e^2\Delta\bar{Q} \end{aligned} \quad (\text{II.226})$$

Comparing with the hyperbolic two-temperature model Eq.(II.221), the extended second-order space derivatives of heat flux result in an additional fourth order derivative of the temperature $I_e^2\tau_{12}\Delta\ddot{T}$, and additional terms in the effective energy source. If $I_e = 0$, Eq.(II.225) reduces to Eq.(II.222), which implies a hyperbolic type with finite propagation of thermal waves. When $I_e > 0$, it is a parabolic function and discontinuities are smoothed by diffusion associated with the effective thermal diffusivity.

VI.5.3.5 Microtemperature models

VI.5.3.5.1 Continuum with micro-temperature vector

VI.5.3.5.1.1 Heat equation of linear micro-stretch thermoelastic body using Grot's theory

Based on the theory, established by Grot (Grot, 1969) dealing with thermodynamics of elastic bodies with microstructure whose microelements possess a micro-temperature vector, Iesan et al. (Iesan, 2002, 2007; Iesan and Nappa, 2005; Iesan and Quintanilla, 2009; Iesan and Scalia, 2010) derived a linear theory of micro-stretch thermo-elastic bodies with micro-temperatures. The second moment of the stress tensor and the average micro-stress moment are neglected in the balance laws since these functions appear only nonlinearly in the field equations. The local forms of balance of energy and the balance of first moment of energy can be expressed as:

$$\rho \dot{e} = \underline{\sigma} : \vec{\nabla} \vec{v} + (\underline{\sigma} - \underline{\sigma}_m) : \underline{v} + \underline{\sigma}_m : \vec{\nabla} \underline{v} + \text{div}(\vec{q}) + \xi \quad (\text{II.227})$$

and

$$\rho \dot{\vec{e}}_m = \underline{\sigma}_m : (\vec{\nabla} v - \underline{v}) + \text{div}(\underline{q}) + \vec{q} - \vec{Q} + \vec{\xi} \quad (\text{II.228})$$

with, \vec{v} is the velocity vector, $\underline{\sigma}$ is the micro-stress tensor, \underline{v} denotes the micro-gyration tensor, $\underline{\sigma}_m$ is the first stress moment third-rank tensor, \vec{e}_m represents the first moment of energy vector, \underline{q} is the first heat flux moment second-rank tensor, \vec{Q} is the micro-heat flux average, and $\vec{\xi}$ is the first heat supply moment tensor.

The local form of the second law of thermodynamics is modified to include the micro-temperature:

$$\rho \dot{s} - \text{div} \left(\frac{\vec{q}}{T} + \frac{\underline{q}}{T} \cdot \vec{T} \right) - \frac{1}{T} (\xi + \vec{\xi} \cdot \vec{T}) \geq 0 \quad (\text{II.229})$$

where, \vec{T} is the micro-temperature vector.

Concerning the linear micro-stretch elastic solid (see the work of Eringen (Eringen, 1999)), the above entropy inequality can be rewritten as:

$$\begin{aligned} & \rho (T \dot{s} - \dot{e} - \vec{T} \cdot \dot{\vec{e}}_m) + \underline{\sigma} : \underline{\dot{\varepsilon}} + \underline{\sigma}_c : \underline{k} + \vec{h} \cdot \dot{\vec{\zeta}} - g \dot{\varphi} + \underline{\sigma}_m : (\dot{\underline{\varepsilon}} - \dot{\varphi} \underline{I}) \cdot \vec{T} + \frac{\vec{q}}{T} \cdot \vec{\nabla} T \\ & + \frac{\vec{\nabla} T}{T} \cdot \underline{q} \cdot \vec{T} - \underline{q} : \vec{\nabla} \vec{T} + (\vec{q} - \vec{Q}) \cdot \vec{T} \geq 0 \end{aligned} \quad (\text{II.230})$$

with, $\underline{\varepsilon} = \vec{\nabla} \vec{u} + \vec{\alpha} \cdot \vec{\varphi}$, $\underline{k} = \vec{\nabla} \vec{\varphi}$ and $\vec{\zeta} = \vec{\nabla} \varphi$ indicate the generalized strain tensors in the linear theory of micro-stretch continua, $\vec{\alpha}$ denotes the alternating symbol, $\vec{\varphi}$ is the micro-rotation vector and φ denotes the micro-dilatation function, $\underline{\sigma}_c$ is the coupled stress tensor, \vec{h} indicates the micro-stretch vector, g is the internal body force, \underline{I} denotes the identity tensor. Considering the following form of free energy:

$$\psi = e - Ts + \vec{T} \cdot \vec{e}_m \quad (\text{II.231})$$

the inequality just becomes:

$$\begin{aligned} & -\rho \left(\dot{\psi} + \dot{T}s - \vec{T} \cdot \vec{e}_m \right) + (\underline{\sigma} + \vec{\sigma}_m \cdot \vec{T}) : \dot{\underline{\varepsilon}} + \underline{\sigma}_c : \underline{k} + \vec{h} \cdot \dot{\vec{\zeta}} - (g + \vec{\sigma}_m : \underline{L} \cdot \vec{T}) \dot{\varphi} + \frac{\vec{q}}{T} \cdot \vec{\nabla} T \\ & + \frac{\vec{\nabla} T}{T} \cdot \underline{q} \cdot \vec{T} - \underline{q} : \vec{\nabla} \vec{T} + (\vec{q} - \vec{Q}) \cdot \vec{T} \geq 0 \end{aligned} \quad (\text{II.232})$$

In the linear theory of thermodynamic materials with micro-temperature, the following constitutive equations (Iesan, 2007) are obtained:

$$\begin{aligned} \underline{\sigma} &= \rho \frac{\partial \psi}{\partial \underline{\varepsilon}} \quad \underline{\sigma}_c = \rho \frac{\partial \psi}{\partial \underline{k}} \quad \vec{h} = \rho \frac{\partial \psi}{\partial \vec{\zeta}} \\ g &= -\rho \frac{\partial \psi}{\partial \varphi} \quad s = -\frac{\partial \psi}{\partial T} \quad \vec{e}_m = \frac{\partial \psi}{\partial \vec{T}} \end{aligned} \quad (\text{II.233})$$

and residual thermal dissipation:

$$\varphi_V = \varphi_{th} = \vec{q} \cdot \vec{\nabla} T - T_0 \underline{q} : \vec{\nabla} \vec{T} + T_0 (\vec{q} - \vec{Q}) \cdot \vec{T} \geq 0 \quad (\text{II.234})$$

The linear approximations for the generalized heat fluxes are given by:

$$\vec{q} = \underline{\kappa} \cdot \vec{\nabla} T + \underline{H} \cdot \vec{T} \quad \underline{q} = -\underline{P} : \vec{\nabla} \vec{T} \quad \vec{Q} = (\underline{\kappa} - \underline{\kappa}) \cdot \vec{\nabla} T + (\underline{H} - \underline{\Lambda}) \cdot \vec{T} \quad (\text{II.235})$$

with, the constitutive coefficients $\underline{\kappa}$, \underline{H} , \underline{P} , $\underline{\kappa}$ and $\underline{\Lambda}$ satisfy the inequality equation (Eq.(II.234)).

By using the equations (Eqs.(II.227), (II.228), (II.231) and (II.233)), and in the framework of the linear theory (Iesan, 2007), the following field equations of temperature and micro-temperature are obtained:

$$\begin{cases} k \Delta T + k_1 \operatorname{div}(\vec{T}) - \beta_0 T_0 \operatorname{div}(\vec{v}) - \beta_1 T_0 \dot{\varphi} - c \dot{T} = -\xi \\ k_6 \Delta \vec{T} + (k_4 + k_5) \vec{\nabla}(\operatorname{div}(\vec{T})) + \mu_1 \vec{\alpha} : \vec{\nabla} \dot{\varphi} - \mu_2 \vec{\nabla} \dot{\varphi} - b \dot{\vec{T}} - k_2 \vec{T} - k_3 \vec{\nabla} T = \vec{\xi} \end{cases} \quad (\text{II.236})$$

where, k_i , β_i , c and b are material constants.

Concerning the rigid body heat conduction (without body heat sources), the above generalized heat equations become:

$$\begin{cases} c \dot{T} = k \Delta T + k_1 \operatorname{div}(\vec{T}) \\ b \dot{\vec{T}} = k_6 \Delta \vec{T} + (k_4 + k_5) \vec{\nabla}(\operatorname{div}(\vec{T})) - k_2 \vec{T} - k_3 \vec{\nabla} T \end{cases} \quad (\text{II.237})$$

Combining the above two heat equations and considering the internal constraint that $\vec{T} = \vec{\nabla} T$, the generalized heat equation becomes:

$$c \dot{T} = (k + k_1 - k_2 - k_3) \Delta T - b \Delta \dot{T} + (k_4 + k_5) \Delta^2 T \quad (\text{II.238})$$

If $\Delta^2 T$ is small enough, the above heat equation (Eq.(II.238)) is equivalent to the one derived from the hyper-temperature model (Eq.(II.208)).

VI.5.3.5.1.2 Heat equation in micromorphic continua using Green's theory

İeşan and Nappa (İeşan and Nappa, 2005) also deduced the heat equation in micromorphic continua, while using the thermomechanical theory established by Green et al. (Green and Naghdi, 1977). In particular, he showed that in the linearized theory according to this approach, heat can be transferred as thermal waves with finite speed. The heat equations of linear theory for temperature and micro-temperature are given by:

$$\begin{cases} a\ddot{T} + m \operatorname{div}(\dot{\vec{T}}) = k\Delta T \\ b\ddot{\vec{T}} = d_2\Delta\vec{T} + (d_1 + d_3)\vec{\nabla}(\operatorname{div}(\vec{T})) - m\vec{\nabla}T \end{cases} \quad (\text{II.239})$$

where, a , m , k , b and d_i are material constants.

Combining the above two heat equations and assuming that $\vec{T} = \vec{\nabla}T$, the generalized heat equation just becomes:

$$a\ddot{T} + 2m\Delta\dot{T} + b\Delta\ddot{T} - (d_1 + d_2 + d_3)\Delta^2T = k\Delta T \quad (\text{II.240})$$

Compared with the heat equations (Eqs.(II.237)) from Grot's theory, Eq.(II.239) predicts a finite propagation. For a hypothetical medium in which $m=0$, Eqs.(II.239) are uncoupled in the sense that the temperature is independent of micro-temperatures. In this case the temperature satisfies the classical wave equation. Moreover, it is interesting to note the similarity between the equations for micro-temperatures and the Navier's equations of motion.

VI.5.3.5.2 Scalar micro-temperature and micro-entropy

Forest and Aifantis (Forest and Aifantis, 2010) proposed theories based on scalar micro-temperature and micro-entropy model, by applying the micromorphic approach (Forest, 2009) to the temperature and entropy. They showed that the gradient of entropy theory and gradient temperature theories can be regarded as a limit case of the micro-entropy and micro-temperature theories. The formulations of micro-entropy model is now briefly reviewed in the purely thermal case. It assumes that there exist additional independent power of internal and external generalized forces due to the introduced micro-entropy variable \check{s} and $\vec{\nabla}\check{s}$. The virtual power of the generalized internal forces (Germain, 1973) is enhanced:

$$P_{\text{int}} = - \int_V \left(\check{\sigma}_a \dot{\check{s}}^* + \vec{\sigma}_b \cdot \vec{\nabla} \dot{\check{s}}^* \right) dV \quad (\text{II.241})$$

where $\check{\sigma}_a$ and $\vec{\sigma}_b$ are generalized stresses or micro-forces according to Gurin's (Gurin, 1996) terminology.

The virtual power of external generalized forces is expressed as:

$$P_{\text{ext}} = \int_{\Gamma} \left(F^{\check{s}} \dot{\check{s}}^* \right) dS \quad (\text{II.242})$$

where $F^{\check{s}}$ is the generalized contact forces.

In the quasi-static case, applying the generalized principle of virtual power results in the following balance equation and the associated Neumann-type boundary condition:

$$\begin{cases} \vec{\nabla} \cdot \vec{\sigma}_b - \check{\sigma}_a = 0 & \text{in } \Omega \\ \vec{\sigma}_b \cdot \vec{n} = F^s & \text{on } \Gamma \end{cases} \quad (\text{II.243})$$

Accordingly, the first principle of thermodynamics is extended with the micro-entropy variable. The local forms of the principles of thermodynamics are given by:

$$\begin{cases} \rho \dot{e} = \check{\sigma}_a \dot{s} + \vec{\sigma}_b \cdot \vec{\nabla} \dot{s} - \text{div}(\vec{q}) + \xi \\ \rho \dot{s} - \left(\frac{\xi}{T} \right) + \text{div} \left(\frac{\vec{q}}{T} \right) \geq 0 \end{cases} \quad (\text{II.244})$$

Using the classical relationship between internal energy and free energy (Eq.(II.154)), yields the following extended Clausius-Duhem inequality:

$$\rho \left(T - \frac{\partial e}{\partial s} \right) \dot{s} + \left(\check{\sigma}_a - \rho \frac{\partial e}{\partial \check{s}} \right) \dot{s} + \left(\vec{\sigma}_b - \rho \frac{\partial e}{\partial \vec{\nabla} \check{s}} \right) \cdot \vec{\nabla} \dot{s} - \frac{\vec{q}}{T} \vec{\nabla} T \geq 0 \quad (\text{II.245})$$

The following state relations are derived based on the Coleman-Noll arguments:

$$T = \frac{\partial e}{\partial s} \quad \check{\sigma}_a = \rho \frac{\partial e}{\partial \check{s}} \quad \vec{\sigma}_b = \rho \frac{\partial e}{\partial \vec{\nabla} \check{s}} \quad (\text{II.246})$$

and the residual dissipation:

$$\varphi_v = \varphi_{th} = -\frac{\vec{q}}{T} \cdot \vec{\nabla} T \geq 0 \quad (\text{II.247})$$

Substituting the state laws Eq.(II.246) into the local energy balance equation (Eq.(II.244)), leads to the classical form of the heat equation:

$$\rho T \dot{s} = -\text{div}(\vec{q}) + \xi \quad (\text{II.248})$$

Within a linear context, the following quadratic energy potential (Forest and Aifantis, 2010) is defined:

$$\rho e(s, \check{s}, \vec{\nabla} \check{s}) = \rho s T_0 + \rho^2 \frac{(s - s_0)^2}{4\beta} + \frac{1}{2} \check{H}(s - \check{s})^2 + \frac{1}{2} A_s \vec{\nabla} \check{s} \cdot \vec{\nabla} \check{s} \quad (\text{II.249})$$

where, β , \check{H} and A_s are material parameters. The state relations are obtained:

$$T = T_0 + \rho \frac{(s - s_0)}{2\beta} + \frac{\check{H}(s - \check{s})}{\rho} \quad \check{\sigma}_a = -\check{H}(s - \check{s}) \quad \vec{\sigma}_b = A_s \vec{\nabla} \check{s} \quad (\text{II.250})$$

Combining the Fourier law (Eq.(II.161)), the heat equation (Eq.(II.248)), the relevant state relations (Eq.(II.246)) and the balance equation (Eq.(II.243)), the following generalized heat equation is obtained:

$$\rho T_0 \dot{s} = \kappa \left(\frac{\rho}{2\beta} \vec{\nabla}^2 s - \frac{A_s}{\rho} \vec{\nabla}^4 \breve{s} \right) \quad (\text{II.251})$$

It should be noticed that this equation coincides with the heat equation (Eq.(II.204)) derived from the gradient of entropy theory, specialized for $\breve{\sigma}_a = 0$, when the following internal constraint is enforced:

$$\breve{s} = s \quad (\text{II.252})$$

As a result, the gradient of entropy theory can be regarded as a limit case of the micro-entropy model.

VI.5.4 Discussions of the generalized heat equation

With the purpose to focus on the heat equations, thermo-elasticity is assumed in this section to simplify the complex detailed generalized heat equation (Eq.(II.69)). On the discussions of nonlocal thermal effects, the existent heat equations have been briefly reviewed in Section VI.5.3. Following the approach of extended irreversible thermodynamics, some possible extended entropies are formulated to result a nonlocal heat equation while is consistent with the second law of the thermodynamics. For the sake of simplicity, the explicit dependence of the material parameters on the temperature is omitted.

VI.5.4.1 Simplified thermo-elastic micromorphic heat equation

In order to perform a clear analysis, the thermo-elasticity is adopted to avoid the intrinsic dissipations. Then, the generalized balance equations (Eq.(II.6) and Eq.(II.7)) reduce to:

$$\begin{cases} \vec{\nabla} \cdot \underline{\sigma} + \rho \vec{f}^u = \rho \ddot{u} & \text{in } \Omega \\ \underline{\sigma} \cdot \vec{n} = \vec{F}^u & \text{on } \Gamma \end{cases} \quad \begin{cases} \left(\vec{\nabla} \cdot \vec{s} - \breve{s} \right) + \rho \left(f^T - \vec{\nabla} \cdot \vec{f}^{gT} \right) = \rho \zeta_{\bar{T}_1} \dot{\bar{T}} + \rho \zeta_{\bar{T}_2} \ddot{\bar{T}} & \text{in } \Omega \\ \left(\breve{s} - \rho \vec{f}^{gT} \right) \cdot \vec{n} = F^T & \text{on } \Gamma \end{cases} \quad (\text{II.253})$$

The local forms of the first principle (Eq.(II.18)) and the second principle (Eq.(II.21)) of thermodynamics are given by:

$$\begin{cases} \rho \dot{e} = \underline{\sigma} : \underline{\dot{\epsilon}} + \left(\breve{s} \dot{\bar{T}} + \vec{s} \cdot \vec{\nabla} \dot{\bar{T}} \right) + \left(\rho \zeta - \text{div}(\vec{q}) \right) \\ \rho \dot{s} - \rho \frac{\zeta}{T} + \text{div} \left(\frac{\vec{q}}{T} \right) \geq 0 \end{cases} \quad (\text{II.254})$$

Considering the relationships between the internal energy and Helmholtz free energy $e = \psi + sT$, leads to the following Clausius-Duhem inequality:

$$\left(\underline{\sigma} - \rho \frac{\partial \psi}{\partial \underline{\epsilon}^e} \right) : \underline{\dot{\epsilon}}^e - \rho \left(s + \frac{\partial \psi}{\partial T} \right) \dot{T} + \left(\breve{s} - \rho \frac{\partial \psi}{\partial \breve{T}} \right) \dot{\bar{T}} + \left(\vec{s} - \rho \frac{\partial \psi}{\partial \vec{\nabla} \bar{T}} \right) \cdot \vec{\nabla} \dot{\bar{T}} - \frac{\vec{q}}{T} \vec{\nabla} T \geq 0 \quad (\text{II.255})$$

For the sake of simplicity, we assume that the micromorphic temperature doesn't dissipate and the terms $\left(\underline{\sigma} - \rho \frac{\partial \psi}{\partial \underline{\epsilon}^e} \right)$, $\left(s + \frac{\partial \psi}{\partial T} \right)$, $\left(\breve{s} - \rho \frac{\partial \psi}{\partial \breve{T}} \right)$ and $\left(\vec{s} - \rho \frac{\partial \psi}{\partial \vec{\nabla} \bar{T}} \right)$ do not depend on the rates of the state variables respectively, then following standard arguments (Truesdell and Noll (2004a)), the following state relations are obtained:

$$\underline{\sigma} = \rho \frac{\partial \psi}{\partial \underline{\varepsilon}^e} \quad s = -\frac{\partial \psi}{\partial T} \quad \bar{s} = \rho \frac{\partial \psi}{\partial \bar{T}} \quad \bar{\bar{s}} = \rho \frac{\partial \psi}{\partial \bar{\nabla} \bar{T}} \quad (\text{II.256})$$

and the classical thermal dissipations:

$$\phi = -\frac{\vec{q}}{T} \cdot \vec{g} \geq 0 \quad (\text{II.257})$$

The differential form of the generalized heat equation (Eq.(II.54)) reduces to:

$$\rho \dot{s} T - \rho \zeta + \operatorname{div}(\vec{q}) = 0 \quad (\text{II.258})$$

For the sake of simplifications, in the next we focus on the rigid body heat transfer (). Using the state relations in Eq.(II.256), the above classical form of heat equation becomes:

$$\rho T \frac{\partial s}{\partial T} \dot{T} - T \left(\frac{\partial \bar{s}}{\partial T} \dot{\bar{T}} + \frac{\partial \bar{\bar{s}}}{\partial T} \cdot \bar{\nabla} \dot{\bar{T}} \right) + \operatorname{div}(\vec{q}) - \rho \zeta = 0 \quad (\text{II.259})$$

or

$$-T \left(\rho \frac{\partial^2 \psi}{\partial T^2} \dot{T} + \rho \frac{\partial^2 \psi}{\partial \bar{T} \partial T} \dot{\bar{T}} + \rho \frac{\partial^2 \psi}{\partial \bar{\nabla} \bar{T} \partial T} \cdot \bar{\nabla} \dot{\bar{T}} \right) + \operatorname{div}(\vec{q}) - \rho \zeta = 0 \quad (\text{II.260})$$

After substituting the balance equation of micromorphic temperature and neglecting the external forces, the temperature and micromorphic temperature fields are found to be governed by a pair of equations:

$$\begin{cases} \rho T \frac{\partial s}{\partial T} \dot{T} - T \left(\frac{\partial \bar{s}}{\partial T} \dot{\bar{T}} + \frac{\partial \bar{\bar{s}}}{\partial T} \cdot \bar{\nabla} \dot{\bar{T}} \right) + \operatorname{div}(\vec{q}) - \rho \zeta = 0 \\ \bar{\nabla} \cdot \left(\rho \frac{\partial \psi}{\partial \bar{\nabla} \bar{T}} \right) - \rho \frac{\partial \psi}{\partial \bar{T}} = \rho \left(\zeta_{\bar{T}_1} \dot{\bar{T}}_1 + \zeta_{\bar{T}_2} \ddot{\bar{T}}_2 \right) \end{cases} \quad (\text{II.261})$$

Combining the two equations in Eq.(II.261), leads to the generalized partial differential micromorphic heat equation associated to the Helmholtz free energy:

$$\begin{aligned} & \rho T \left(\zeta_{\bar{T}_1} \ddot{\bar{T}}_1 + \zeta_{\bar{T}_2} \ddot{\bar{T}}_2 \right) - \rho T \left[\frac{\partial^2 \psi}{\partial T^2} \dot{T} + \frac{\partial^2 \psi}{\partial \bar{T} \partial T} \left(\dot{\bar{T}} - \dot{T} \right) - \frac{\partial^2 \psi}{\partial \bar{T}^2} \dot{\bar{T}} + \left(\frac{\partial^2 \psi}{\partial T \partial \bar{\nabla} \bar{T}} - \frac{\partial^2 \psi}{\partial \bar{\nabla} \bar{T} \partial T} \right) \cdot \bar{\nabla} \dot{\bar{T}} \right] \\ & - T \operatorname{div} \left(\rho \frac{\partial^2 \psi}{\partial T \partial \bar{\nabla} \bar{T}} \dot{T} + \rho \frac{\partial^2 \psi}{\partial \bar{T} \partial \bar{\nabla} \bar{T}} \dot{\bar{T}} + \rho \frac{\partial^2 \psi}{\partial \bar{\nabla} \bar{T}^2} \cdot \bar{\nabla} \dot{\bar{T}} \right) + \operatorname{div}(\vec{q}) - \rho \zeta = 0 \end{aligned} \quad (\text{II.262})$$

where the temperature and micro-temperature variables are both present.

VI.5.4.2 Special cases of the micromorphic heat equation

In this section specific constitutive expressions of the free energy and dissipation potentials are chosen in order to derive explicit generalized heat equations within the micromorphic framework.

VI.5.4.2.1 Wave type heat equation

If the Helmholtz free energy is defined as:

$$\rho\psi(T, \bar{T}, \vec{\nabla}\bar{T}) = -\rho CT \left(\ln \frac{T}{T_0} - 1 \right) - \rho \bar{C} \bar{T} \left(\ln \frac{\bar{T}}{T_0} - 1 \right) - \frac{1}{2} \bar{M} (T - \bar{T})^2 + \frac{1}{2} \bar{M}^g \vec{\nabla}\bar{T} \cdot \vec{\nabla}\bar{T} \quad (\text{II.263})$$

where, C and \bar{C} are the coefficients for local and micromorphic temperature, respectively. \bar{M} is the micromorphic temperature modulus coupling both the local and micromorphic temperature. \bar{M}^g denotes the micromorphic modulus related to the first gradient of the micromorphic temperature (for simplicity, the moduli are assumed to be independent of local temperature and the isotropic case only is considered).

According to the deduced state laws Eq.(II.256), the following stress-like variables are given by:

$$\begin{aligned} s &= -\frac{\partial \psi}{\partial T} = C \ln \frac{T}{T_0} + \frac{\bar{M}}{\rho} (T - \bar{T}) \\ \bar{s} &= \rho \frac{\partial \psi}{\partial \bar{T}} = -\rho \bar{C} \ln \frac{\bar{T}}{T_0} + \bar{M} (T - \bar{T}) \\ \vec{s} &= \rho \frac{\partial \psi}{\partial \vec{\nabla}\bar{T}} = \bar{M}^g \vec{\nabla}\bar{T} \end{aligned} \quad (\text{II.264})$$

Substituting the above free energy Eq.(II.263) into the generalized heat equation Eq.(II.262), leads to:

$$\rho T \left(\zeta_{\bar{T}_1} \ddot{\bar{T}} + \zeta_{\bar{T}_2} \ddot{\bar{T}} \right) - T \left[\rho \bar{C} \frac{\dot{\bar{T}}}{\bar{T}} - \rho C \frac{\dot{T}}{T} + 2\bar{M} (\dot{\bar{T}} - \dot{T}) \right] - T \bar{M}^g \Delta \dot{\bar{T}} + \operatorname{div}(\vec{q}) - \varsigma = 0 \quad (\text{II.265})$$

The heat equation can also be directly obtained from Eq.(II.258) which provides an equivalent but shorter expression of the heat equation (Eq.(II.265)):

$$\rho C \dot{T} + T \bar{M} (\dot{\bar{T}} - \dot{T}) + \operatorname{div}(\vec{q}) - \varsigma = 0 \quad (\text{II.266})$$

This equation can also be obtained from Eq.(II.265) after noting that:

$$\bar{M}^g \Delta \bar{T} + \rho \bar{C} \ln \frac{\bar{T}}{T_0} - \bar{M} (T - \bar{T}) = \rho (\zeta_1 \dot{\bar{T}} + \zeta_2 \ddot{\bar{T}}) \quad (\text{II.267})$$

which follows from the combination of the micromorphic balance equation Eq.(II.253) and the state laws Eq.(II.264).

If the Fourier model of heat flux vector is chosen and neglecting the body heat source, the above generalized heat equation will become to:

$$\rho T \left(\zeta_{\bar{T}_1} \ddot{\bar{T}} + \zeta_{\bar{T}_2} \ddot{\bar{T}} \right) - T \left[\rho \bar{C} \frac{\dot{\bar{T}}}{\bar{T}} - \rho C \frac{\dot{T}}{T} + 2\bar{M} (\dot{\bar{T}} - \dot{T}) \right] - T \bar{M}^g \Delta \dot{\bar{T}} = \kappa \Delta T \quad (\text{II.268})$$

It is interesting to consider the internal constraint which consists in forcing the difference between temperature and micromorphic temperature to be close to 0. After enforcing this constraint, the following generalized heat equation is obtained:

$$\rho T \left(\zeta_{\bar{\tau}_1} \ddot{\bar{T}} + \zeta_{\bar{\tau}_2} \ddot{\bar{T}} \right) + \rho (C - \bar{C}) \dot{T} - T \bar{M}^g \Delta \dot{T} = \kappa \Delta T \quad (\text{II.269})$$

We may note that:

- a) If $\zeta_{\bar{\tau}_2} = 0$ (implying that the inertia is only proportional to the first time derivative of temperature), the linearization of the heat equation (Eq.(II.269)) leads to:

$$\rho T_0 \zeta_{\bar{\tau}_1} \ddot{\bar{T}} + \rho (C - \bar{C}) \dot{T} - T_0 \bar{M}^g \Delta \dot{T} = \kappa \Delta T \quad (\text{II.270})$$

which has the same form as the generalized heat equations derived from the double temperature model in Eq.(II.219), provided that the four-order term in Eq.(II.219) is small enough to be neglected (e.g. in pure metal, the thermal conductivity of electron component is much larger than that of lattice component), if $C - \bar{C} = C_e$ holds.

- b) If the two generalized heat capacities are equivalent $C = \bar{C}$, the heat equation becomes:

$$\rho T_0 \zeta_{\bar{\tau}_1} \ddot{\bar{T}} - T_0 \bar{M}^g \Delta \dot{T} = \kappa \Delta T \quad (\text{II.271})$$

It is similar to the heat equation (Eq.(II.240)) derived by Iesan and Nappa (2005) in the absence of the fourth order derivatives, based on the balance laws of micromorphic continua established by (Eringen, 1970, 1992). It involves $\rho T_0 \zeta_{\bar{\tau}_1} = a$ and $\bar{M}^g = -m/T_0$.

- c) In Eq.(II.271), if $\bar{M}^g = 0$ for a hypothetical medium or if $\Delta \dot{T}$ is relatively small compared with other two terms, it indicates that the temperature satisfies the classical wave equation:

$$\ddot{\bar{T}} = \frac{\kappa}{\rho T_0 \zeta_{\bar{\tau}_1}} \Delta T \quad (\text{II.272})$$

This wave equation Eq.(II.272) indicates a finite propagation velocity $\sqrt{\frac{\kappa}{\rho T_0 \zeta_{\bar{\tau}_1}}}$.

VI.5.4.2.2 Double temperature type heat equation

Considering the following definition of the convex Helmholtz free energy:

$$\rho \psi(T, \bar{T}, \vec{\nabla} \bar{T}) = -\rho C_e T \left(\ln \frac{T}{T_0} - 1 \right) - \frac{1}{2} \bar{M}(T - \bar{T})^2 + \frac{1}{2} \bar{M}^g \vec{\nabla} \bar{T} \cdot \vec{\nabla} \bar{T} \quad (\text{II.273})$$

Substituting the free energy Eq.(II.273) into the generalized heat equation Eq.(II.262), leads to:

$$\rho T \left(\zeta_{\bar{\tau}_1} \ddot{\bar{T}} + \zeta_{\bar{\tau}_2} \ddot{\bar{T}} \right) + \rho C_e \dot{T} - 2T \bar{M} \left(\dot{\bar{T}} - \dot{T} \right) - T \bar{M}^g \Delta \dot{T} + \operatorname{div}(\vec{q}) - \varsigma = 0 \quad (\text{II.274})$$

The Fourier law and the Cattaneo equation for the heat flux are used to derive the classical parabolic, hyperbolic and generalized two-temperature heat equations respectively.

VI.5.4.2.2.1 Using the Fourier model

Considering the Fourier model of heat flux and neglecting the body heat source, the previous generalized heat equation will become:

$$\rho C_e \dot{T} + \rho T \left(\zeta_{\bar{\tau}_1} \ddot{\bar{T}} + \zeta_{\bar{\tau}_2} \ddot{\bar{T}} \right) - 2T \bar{M} \left(\dot{\bar{T}} - \dot{T} \right) - T \bar{M}^g \Delta \dot{\bar{T}} = \kappa \Delta T \quad (\text{II.275})$$

We now enforce the constraint that the temperature and microtemperature variables coincide. The linearized generalized heat equation Eq.(II.275), becomes:

$$\rho C_e \dot{T} + \rho T_0 \left(\zeta_{\bar{\tau}_1} \ddot{\bar{T}} + \zeta_{\bar{\tau}_2} \ddot{\bar{T}} \right) - T_0 \bar{M}^g \Delta \dot{\bar{T}} = \kappa \Delta T \quad (\text{II.276})$$

The following special cases are derived:

- a) If $\zeta_{\bar{\tau}_2} = 0$, the linearized heat equation (Eq.(II.276)) just becomes:

$$\rho C_e \dot{T} + \rho T_0 \zeta_{\bar{\tau}_1} \ddot{\bar{T}} - T_0 \bar{M}^g \Delta \dot{\bar{T}} = \kappa \Delta T \quad (\text{II.277})$$

which is the same with the classical two temperature model in Eq.(II.219), if $\alpha = T_0 \zeta_1 / C_e$, $\beta = T_0 \bar{M}^g / \rho C_e$, $\gamma = 0$ and $\lambda = \kappa / \rho C_e$ hold.

- b) If $\zeta_{\bar{\tau}_1} = 0$ (implying that the inertia is proportional to the second time derivative of temperature), the heat equation (Eq.(II.276)) is expressed as:

$$\rho C_e \dot{T} + \rho T_0 \zeta_{\bar{\tau}_2} \ddot{\bar{T}} - T_0 \bar{M}^g \Delta \dot{\bar{T}} = \kappa \Delta T \quad (\text{II.278})$$

which is a third-order partial differential equation.

VI.5.4.2.2.2 Using the Cattaneo model

If Cattaneo's model is adopted, the linearized Eq.(II.274) provides the following relationship:

$$\rho \dot{e} = \rho T_0 \left(\zeta_{\bar{\tau}_1} \ddot{\bar{T}} + \zeta_{\bar{\tau}_2} \ddot{\bar{T}} \right) + \rho C_e \dot{T} - 2T_0 \bar{M} \left(\dot{\bar{T}} - \dot{T} \right) - T_0 \bar{M}^g \Delta \dot{\bar{T}} + \left(\underline{\sigma} : \underline{\dot{\varepsilon}} + \xi \dot{\bar{T}} + \vec{\xi} \cdot \vec{\nabla} \dot{\bar{T}} \right) \quad (\text{II.279})$$

Substituting the Cattaneo equation (Eq.(II.166)) into Eq.(II.254), leads to:

$$\rho \dot{e} + \tau \rho \ddot{e} = \left(\underline{\sigma} : \underline{\dot{\varepsilon}} + \xi \dot{\bar{T}} + \vec{\xi} \cdot \vec{\nabla} \dot{\bar{T}} \right) + \rho \zeta + \kappa \Delta T + \tau \frac{\partial}{\partial t} \left(\underline{\sigma} : \underline{\dot{\varepsilon}} + \xi \dot{\bar{T}} + \vec{\xi} \cdot \vec{\nabla} \dot{\bar{T}} \right) + \tau \frac{\partial(\rho \zeta)}{\partial t} \quad (\text{II.280})$$

Using the relation Eq.(II.279), the above equation becomes:

$$\begin{aligned} & \rho C_e \dot{T} + \rho \left(\tau C_e + T_0 \zeta_{\bar{\tau}_1} \right) \ddot{\bar{T}} + \rho T_0 \left(\tau \zeta_{\bar{\tau}_1} + \zeta_{\bar{\tau}_2} \right) \ddot{\bar{T}} + \tau \rho T_0 \zeta_{\bar{\tau}_2} \ddot{\bar{T}} \\ &= \kappa \Delta T + T_0 \bar{M}^g \Delta \dot{\bar{T}} + T_0 \bar{M}^g \Delta \dot{\bar{T}} + \rho \zeta + \tau \frac{\partial(\rho \zeta)}{\partial t} \end{aligned} \quad (\text{II.281})$$

It is worth noting that, if $\zeta_{\bar{\tau}_2} = 0$ holds, we get

$$\rho C_e \dot{T} + \rho \left(\tau C_e + T_0 \zeta_{\bar{\tau}_1} \right) \ddot{\bar{T}} + \rho T_0 \tau \zeta_{\bar{\tau}_1} \ddot{\bar{T}} = \kappa \Delta T + T_0 \bar{M}^g \Delta \dot{\bar{T}} + T_0 \bar{M}^g \Delta \dot{\bar{T}} + \rho \zeta + \tau \frac{\partial(\rho \zeta)}{\partial t} \quad (\text{II.282})$$

which has the same form as the generalized two-temperature model with nonlocal effects Eq.(II.225).

If the term $\Delta\ddot{T}$ is relative small compared with other terms, Eq.(II.282) takes the same form as the heat equation derived from the hyperbolic two-temperature model (Eq.(II.221)):

$$\rho C_e \dot{T} + \rho(\tau C_e + T_0 \zeta_{\bar{\tau}_1}) \ddot{T} + \rho T_0 \tau \zeta_{\bar{\tau}_1} \ddot{\tilde{T}} = \kappa \Delta T + T_0 \tilde{M}^g \Delta \dot{T} + \rho \zeta + \tau \frac{\partial(\rho \zeta)}{\partial t} \quad (\text{II.283})$$

VI.5.4.2.3 Hyper-temperature type heat equation

Considering the constrained micromorphic heat equation (Eq.(II.276)), if we postulate that the inertia of temperature is sufficiently small compared with other terms, the generalized heat equation becomes:

$$\rho C_e \dot{T} - T_0 \tilde{M}^g \Delta \dot{T} = \kappa \Delta T \quad (\text{II.284})$$

which is exactly the heat equation derived from the temperature gradient theory (Eq.(II.206)). It can also be regarded as an approximation of the heat equation derived from the entropy gradient theory (Eq.(II.207)), if $\tilde{M}^g = -A_T$ holds.

VI.5.4.2.4 Hyperbolic type heat equation

Let us now focus on the linearized heat equation (Eq.(II.277)), for cases where the term $\Delta\dot{T}$ is sufficiently small compared with other terms. The heat equation then is the same as the hyperbolic heat equation with relaxation time:

$$\rho C_e \dot{T} + \rho T_0 \zeta_{\bar{\tau}_1} \ddot{T} = \kappa \Delta T \quad (\text{II.285})$$

by taking $\zeta_{\bar{\tau}_1} = \tau C_e / T_0$ holds.

VI.5.4.3 Solution analysis of nonlocal heat equations

In this section, the simple plane thermal wave Eq.(II.170), which is a solution of the hyperbolic heat equation with relaxation time, is adopted to examine the generalized heat equations derived above. Since the heat equations from the Cattaneo I model (Eq.(II.164)), the hyper-temperature (entropy gradient) model (Eq.(II.207) and Eq.(II.208)), the microtemperature model using Grot's theory (Eq.(II.238)) and the micro-temperature or the micro-entropy model (Eq.(II.251)), can be regarded as special cases of the heat equations from the classical two-temperature model of Aifantis (Eq.(II.219)), as well as the hyperbolic and generalized two-temperature heat equations have been analyzed by Sobolev (2016); Only the following three types of generalized heat equations will be analyzed:

$$\begin{cases} F_N(T) = T_{,t} + A_N T_{,xt} - B_N T_{,xx} = 0 \\ F_D(T) = T_{,t} + A_D T_{,tt} - B_D T_{,xx} - C_D T_{,xxt} = 0 \\ F_W(T) = A_W T_{,tt} - B_W T_{,xx} - C_W T_{,xxt} = 0 \end{cases} \quad (\text{II.286})$$

where, $F_N(T)$ is the generalized heat equation derived from Nguyen's gradient temperature model (Eq.(II.194)), $F_D(T)$ is the heat equation from the constrained micromorphic theory (Eq.(II.277)) in double temperature type with omitted fourth order derivative, $F_W(T)$ is the heat equation deduced from the

micromorphic theory which has the same structure as the micro-temperature model using Green's theory (Eq.(II.239)). These coefficients are given by: $A_N = \frac{Mg}{\rho C_\varepsilon L}$ and $B_N = \frac{\kappa}{\rho C_\varepsilon} > 0$, $A_D = \frac{T_0 \zeta \tau_1}{C_\varepsilon}$, $B_D = \frac{\kappa}{\rho C_\varepsilon} > 0$ and $C_D = \frac{T_0 \bar{M}^g}{\rho C_\varepsilon}$, $A_W = \rho T_0 \zeta \tau_1$, $B_W = \kappa > 0$ and $C_W = T_0 \bar{M}^g$.

Substituting the assumed plane thermal wave solution, $T(x,t) = T_0 \exp[i(kx - \omega t)]$ (Eq.(II.170)) with k is the (complex) wave number indicating the attenuation of the amplitude of the propagating wave, ω is the (real) frequency, into the above nonlocal heat equations, leads to the following dispersion relationships:

$$\begin{cases} -i\omega + A_N k \omega + B_N k^2 = 0 \\ -i\omega - A_D \omega^2 + B_D k^2 - iC_D \omega k^2 = 0 \\ -A_W \omega^2 + B_W k^2 - iC_W \omega k^2 = 0 \end{cases} \quad (\text{II.287})$$

VI.5.4.3.1 Solutions of Nguyen's generalized heat equation

Let us write $k = a + ib$ and substitute it into the dispersion relation (Eq.(II.287) a), leading to:

$$(-\omega + A_N b \omega + 2abB_N)i + (A_N a \omega + B_N(a^2 - b^2)) = 0 \quad (\text{II.288})$$

In order to satisfy the above equation, it requires:

$$\begin{cases} \omega = A_N b \omega + 2abB_N \\ A_N a \omega + B_N(a^2 - b^2) = 0 \end{cases} \quad (\text{II.289})$$

Solving the above nonlinear dispersion equations leads to the following velocity V_p and the attenuation coefficient α :

$$V_p = \frac{\omega}{\operatorname{Re} k} = \left[-\frac{1}{2} \frac{A_N}{B_N} + \frac{2}{\sqrt{-2\omega(A_N^2 \omega - \sqrt{A_N^4 \omega^2 + 16B_N^2})}} \right] \quad (\text{II.290})$$

$$\alpha = \frac{1}{\operatorname{Im}(k)} = \frac{1}{(A_N + 2B_N V_p)\omega} \quad (\text{II.291})$$

for lower frequencies $A_N^2 \omega \ll 4B_N$, the velocity is infinite; in high frequency $A_N^2 \omega \gg 4B_N$, the velocity approaches the limit $V_p \approx -2Mg/(\kappa L)$ and the attenuation distance is infinite.

Clearly, the heat equation provides a finite propagation speed of thermal waves in high frequency, while requiring the coefficient g to be a negative number in order to obtain a positive velocity V_p , due to the thermal conductivity coefficient $\kappa > 0$, material parameter $M > 0$ and the length $L > 0$ of the rod,

are all positive defined parameters in the literature(Nguyen, 2010). Consequently, $A_N = Mg/(\rho C_e L) < 0$ holds. It should be noticed that it predicts an infinite velocity of thermal propagation at low frequency, in the case of existence the attenuation of amplitude of thermal wave (k is complex), which differs from the classical Fourier model and the hyperbolic heat equation with relaxation time. However, as shown in literature (Nguyen, 2010), the heat equation gives a finite speed propagation of thermal wave with the help of $k = i/l$ and ω are both complex numbers.

VI.5.4.3.2 Solutions of the heat equation in the double temperature theory

Let us take $k = a + ib$ and substitute it into the dispersion relation (Eq.(II.287) b), leading to:

$$(-\omega + 2abB_D - C_D\omega(a^2 - b^2))i + (-A_D\omega^2 + B_D(a^2 - b^2) + 2abC_D\omega) = 0 \quad (\text{II.292})$$

In order to satisfy the above equation, it is required that:

$$\begin{cases} \omega = 2abB_D - C_D\omega(a^2 - b^2) \\ A_D\omega^2 = B_D(a^2 - b^2) + 2abC_D\omega \end{cases} \quad (\text{II.293})$$

Solving the above nonlinear dispersion equations results in the following velocity V_p and attenuation distance α :

$$V_p = \frac{\omega}{\operatorname{Re} k} = \sqrt{\frac{2(B_D^2 + C_D^2\omega^2)}{(A_D B_D - C_D) + \sqrt{(A_D B_D - C_D)^2 + \left(\frac{B_D}{\omega} + A_D C_D\omega\right)^2}}} \quad (\text{II.294})$$

$$\alpha = \frac{1}{\operatorname{Im}(k)} = \frac{2(B_D^2 + C_D^2\omega^2)}{(B_D + A_D C_D\omega^2)V_p} \quad (\text{II.295})$$

- a) At low frequency $C_D^2\omega^2 \ll B_D^2$, the velocity $V_p \approx \sqrt{2\kappa\omega/(\rho C_e)}$ and $\alpha \approx \sqrt{2\kappa/(\rho C_e\omega)}$ has the same form as predicted by the classical theory based on Fourier's model (Jou et al., 1993). In the high frequency limit $C_D^2\omega^2 \gg B_D^2$, the velocity $V_p \approx \sqrt{2\bar{M}^g\omega/(\rho\zeta_{\bar{T}_1})}$ and $\alpha \approx 2C_D/(A_D V_p) \approx \sqrt{2\bar{M}^g/(\rho\zeta_{\bar{T}_1}\omega)}$. Clearly, the factor $(\bar{M}^g/\zeta_{\bar{T}_1})$ should be positive ($A_D C_D > 0$) to have an infinite real velocity V_p of the propagation.
- b) If $A_D = 0$, it yields the hyper-temperature heat equation (Eq.(II.284)), or the heat equation from Cattaneo I (Eq.(II.164)), or the heat equation (Eq.(II.238)) derived by Iesan (Iesan, 2007) in the absence of the spatial fourth-order term. The velocity and attenuation distance are given by:

$$V_p = \frac{\omega}{\operatorname{Re} k} = \sqrt{\frac{2(B_D^2 + C_D^2 \omega^2)}{-C_D + \sqrt{C_D^2 + \left(\frac{B_D}{\omega}\right)^2}}} \quad (\text{II.296})$$

$$\alpha = \frac{1}{\operatorname{Im}(k)} = \frac{2(B_D^2 + C_D^2 \omega^2)}{B_D V_p} \quad (\text{II.297})$$

Clearly, for low frequency $C_D^2 \omega^2 \ll B_D^2$, the velocity $V_p \approx \sqrt{2\kappa\omega/(\rho C_\varepsilon)}$ and $\alpha \approx \sqrt{2\kappa/(\rho C_\varepsilon \omega)}$, in the high frequency limit $C_D^2 \omega^2 \gg B_D^2$, the velocity approaches $V_p \approx \sqrt{-2T_0 \bar{M}^g \omega/(\rho C_\varepsilon)}$ and $\alpha \approx \sqrt{-2(T_0 \bar{M}^g)^3 \omega^3 / (\rho C_\varepsilon \kappa^2)}$, by taking $\bar{M}^g < 0$. This type of heat equations also predicts propagation at infinite velocity.

- c) If $C_D = 0$ it yields the hyperbolic heat equation with relaxation time (Eq.(II.285)). The velocity and attenuation distance are obtained:

$$V_p = \frac{\omega}{\operatorname{Re} k} = \sqrt{\frac{2B_D^2}{A_D B_D + \sqrt{(A_D B_D)^2 + \left(\frac{B_D}{\omega}\right)^2}}} \quad (\text{II.298})$$

$$\alpha = \frac{1}{\operatorname{Im}(k)} = \frac{2B_D}{V_p} \quad (\text{II.299})$$

which are exactly the solutions given by the hyperbolic heat equation of Cattaneo II in Eq.(II.169), corresponding to the finite propagation of thermal waves: in low frequencies ($A_D \omega \ll 1$), the velocity $v_p \approx \sqrt{2\kappa\omega/\rho C_\varepsilon}$ and $\alpha = \sqrt{2\kappa/\rho C_\varepsilon \omega}$, in high frequency limit ($A_D \omega \gg 1$), the velocity $v_p \approx \sqrt{\kappa/(\rho T_0 \zeta_{\bar{T}_1})}$ and $\alpha \approx 2\sqrt{T_0 \zeta_{\bar{T}_1} \kappa / (\rho C_\varepsilon^2)}$, by taking $\zeta_{\bar{T}_1} = \tau C_\varepsilon / T_0$.

VI.5.4.3 Solutions of the heat equations in wave type

Taking $k = a + ib$ and substitute it into the dispersion relation (Eq.(II.286)c), gives:

$$(2abB_w - C_w \omega(a^2 - b^2))i + (-A_w \omega^2 + B_w(a^2 - b^2) + 2abC_w \omega) = 0 \quad (\text{II.300})$$

In order to satisfy the above equation, it is required that:

$$\begin{cases} -A_w \omega^2 + B_w(a^2 - b^2) + 2abC_w \omega = 0 \\ 2abB_w - C_w \omega(a^2 - b^2) = 0 \end{cases} \quad (\text{II.301})$$

Solving the above nonlinear dispersion equations, yields the velocity V_p :

$$V_p = \frac{\omega}{Re k} = \sqrt{\frac{2(B_w^2 + C_w^2 \omega^2)}{A_w B_w + A_w \sqrt{B_w^2 + C_w^2 \omega^2}}} \quad (II.302)$$

and the attenuation distance α :

$$\alpha = \frac{2(B_w^2 + C_w^2 \omega^2)}{(A_w C_w \omega^2) V_p} \quad (II.303)$$

for low frequencies ($C_w^2 \omega^2 \ll B_w^2$), the finite velocity $v_p \approx \sqrt{\kappa / (\rho T_0 \zeta_{\bar{T}_1})}$ and the attenuation distance is infinite; in high frequency limit ($C_w^2 \omega^2 \gg B_w^2$), the velocity approaches $v_p \approx \sqrt{2T_0 \bar{M}^g \omega}$ and $\alpha \approx \sqrt{2T_0 \bar{M}^g / \omega} / \rho T_0 \zeta_{\bar{T}_1}$, by taking the two parameters $\zeta_{\bar{T}_1}$ and \bar{M}^g being positive.

Clearly, the velocity given by Eq.(II.302) also predicts the infinite speed of thermal propagation, and this infinite propagation is caused by the term $\Delta \dot{T}$ in Eq.(II.270). If $C_w = 0$ for a hypothetical medium, or if the term $\Delta \dot{T}$ is sufficiently small compared with other two terms to be neglected, the velocity is finite:

$$V_p = \frac{\omega}{Re k} = \sqrt{\frac{B_w}{A_w}} = \sqrt{\frac{\kappa}{\rho T_0 \zeta_1}} \quad (II.304)$$

which is exactly the velocity of the wave equation Eq.(II.272). The attenuation distance is infinite.

VI.5.4.4 Summary

The micromorphic approach, initially developed by Mindlin and Eringen in the mechanical context, has been applied to the problem of heat transfer by means of a generalized principle of virtual power. For that purpose, an independent microtemperature field is introduced and its gradient is assumed to contribute to the free energy density function. The proposed phenomenological method has been shown to lead to a pair of coupled generalized heat equations. The model identically satisfies the local condition of positive dissipation rate. The constrained case for which the microtemperature coincides with the temperature itself is of particular interest because it can be compared to the various extensions of the heat equation available in the literature. The proposed equation is enhanced by essentially three new contributions which were illustrated in the linearized case. The three terms affect the transient thermal behavior of the material only. The first new term is related to the Laplacian of the temperature rate, a contribution which was proposed first by Cattaneo in an early version of his theory. A second contribution is proportional to the second time derivative of the temperature which changes the usual heat equation into a hyperbolic equation with a positive characteristic time. The last term associated with the third time derivative of temperature remains rather unexplored even though it is present in some generalized theories found in the literature.

The proposed theory was shown to differ from existing thermomechanical extensions of Eringen's micromorphic model that rely on the introduction of a microtemperature vector akin to a relaxed temperature gradient. It has also been compared to the effective heat equation arising from the double

PART II CHAPTER VI THEORETICAL FORMULATIONS

temperature model involving two coupled heat equations and leading also to fourth order spatial derivatives:

- The hyperbolic heat equation of Cattaneo II with relaxation time, can be obtained from the thermodynamically consistent micromorphic heat equation by neglecting the nonlocal effects of the temperature.
- The classical, hyperbolic and generalized two-temperature models can be also retrieved from the micromorphic heat equations.
- Both the micro-temperature heat equation using Green's theory and the micromorphic heat equation provide a pair of governing equations for local and micro/micromorphic temperature. And the classical wave equation can be obtained from their constrained heat equations.

The proposed theory allows for a direct coupling with the mechanics of materials and is thought to be useful for the simulation of fast heat and mechanical treatments of materials including metal forming at high speeds, laser surface treatments of materials, etc. The nonlocality in the proposed theory resulting from the introduction of the gradient of micromorphic temperature could be an alternative to the analysis of heat transport based on enhanced heat fluxes.

VI.6 Conclusions

In this chapter, the theoretical formulations of the thermomechanical micromorphic nonlocal model is systematically presented:

- 1). A complete set of generalized micromorphic constitutive equations is derived in the context of the thermodynamics of irreversible processes to capture the strongly nonlocal behavior of materials in the localization regions. It contains the formulations of the balance equations, the state relations and the evolution equations. The micromorphic model couples with elasto-visco-plasticity, ductile damage, temperature and mixed hardening as well as the nonlocal effects;
- 2). An intensive review of the existent generalized heat equations is recalled in five classifications: (i) the Fourier model, (ii) the hyperbolic type with relaxation time, (iii) the double temperature model, (iv) the temperature/entropy gradient theory as well as (v) the micro-temperature model. A simple plane wave function is chosen to examine the predicted thermal propagations;
- 3). A pair of micromorphic heat equations is simplified and compared with the existing extended heat equations taking appropriate selections of Helmholtz free energy. The additional micromorphic temperature leads to a new thermal balance equation taking into account the thermal nonlocal effects. Several existing generalized heat equations could be retrieved from the constrained micromorphic heat equations.

VI.7 Appendix

VI.7.1 Formulations of plastic multiplier

To lighten the notations in this appendix, the explicit dependence of the material parameters on the temperature is omitted. Due to the Kuhn-Tucker conditions ($\dot{\lambda} \geq 0$, $f_p \leq 0$ and $\dot{\lambda} f_p = 0$) and the consistency conditions, the yield criterion f_p must fulfill the condition:

$$\dot{f}_p = \frac{\partial f}{\partial \underline{\sigma}} : \dot{\underline{\sigma}} + \frac{\partial f}{\partial \underline{X}} : \dot{\underline{X}} + \frac{\partial f}{\partial R} \dot{R} + \frac{\partial f}{\partial d} \dot{d} + \frac{\partial f}{\partial T} \dot{T} = 0 \quad (\text{II.305})$$

Using the state relations Eq.(II.31), Eq.(II.35) and Eq.(II.36), the time derivatives of Cauchy stress, isotropic and kinematic hardening stresses, under the assumption of additive decompositions of total strain rate, are given by:

$$\begin{aligned} \dot{\underline{\sigma}} &= \frac{\partial \underline{\sigma}}{\partial \underline{\varepsilon}_e} : \dot{\underline{\varepsilon}_e} + \frac{\partial \underline{\sigma}}{\partial d} \dot{d} + \frac{\partial \underline{\sigma}}{\partial T} \dot{T} + \frac{\partial \underline{\sigma}}{\partial \bar{T}} \dot{\bar{T}} = \frac{\partial \underline{\sigma}}{\partial \underline{\varepsilon}_e} : (\underline{D} - \dot{\lambda} \tilde{n}_f) + \dot{\lambda} \frac{\partial \underline{\sigma}}{\partial d} \hat{Y} + \frac{\partial \underline{\sigma}}{\partial T} \dot{T} + \frac{\partial \underline{\sigma}}{\partial \bar{T}} \dot{\bar{T}} \\ \dot{\underline{X}} &= \frac{\partial \underline{X}}{\partial \underline{\alpha}} : \dot{\underline{\alpha}} + \frac{\partial \underline{X}}{\partial d} \dot{d} + \frac{\partial \underline{X}}{\partial T} \dot{T} + \frac{\partial \underline{X}}{\partial \bar{\alpha}} : \dot{\bar{\alpha}} = \frac{\partial \underline{X}}{\partial \underline{\alpha}} : \dot{\underline{\alpha}} (\tilde{n}_f - \underline{m}_f) + \dot{\lambda} \frac{\partial \underline{X}}{\partial d} \hat{Y} + \frac{\partial \underline{X}}{\partial T} \dot{T} + \frac{\partial \underline{X}}{\partial \bar{\alpha}} : \dot{\bar{\alpha}} \\ \dot{R} &= \frac{\partial R}{\partial r} \dot{r} + \frac{\partial R}{\partial d} \dot{d} + \frac{\partial R}{\partial T} \dot{T} + \frac{\partial R}{\partial \bar{r}} \dot{\bar{r}} = \frac{\partial R}{\partial r} \dot{r} \left(\frac{1}{\sqrt{(1-d')}} - o \right) + \dot{\lambda} \frac{\partial R}{\partial d} \hat{Y} + \frac{\partial R}{\partial T} \dot{T} + \frac{\partial R}{\partial \bar{r}} \dot{\bar{r}} \end{aligned} \quad (\text{II.306})$$

with the derivatives of Cauchy stress, isotropic and kinematic hardening stresses are deduced as below respectively:

$$\begin{cases} \frac{\partial \underline{\sigma}}{\partial \underline{\varepsilon}_e} = (1-d) \underline{\Lambda} \\ \frac{\partial \underline{\sigma}}{\partial d} = -\underline{\Lambda} : \underline{\varepsilon}_e + \frac{1}{2\sqrt{1-d}} (\underline{T} - \underline{T}_0) \underline{P} + \frac{1}{2\sqrt{1-d}} (\underline{T} - \underline{T}_0) \underline{\bar{P}} \\ \frac{\partial \underline{\sigma}}{\partial T} = \frac{\partial \underline{\Lambda}}{\partial T} : \underline{\varepsilon}_e - \underline{\tilde{P}} - \underline{\bar{\tilde{P}}} - (\underline{T} - \underline{T}_0) \frac{\partial \underline{\tilde{P}}}{\partial T} - (\underline{T} - \underline{\bar{T}}) \frac{\partial \underline{\bar{\tilde{P}}}}{\partial T} \\ \frac{\partial \underline{\sigma}}{\partial \bar{T}} = \underline{\tilde{P}} \end{cases} \quad (\text{II.307})$$

$$\begin{cases} \frac{\partial \underline{X}}{\partial \underline{\alpha}} = (1-d) (\underline{C} + \underline{\bar{C}}) \\ \frac{\partial \underline{X}}{\partial d} = -\underline{C} : \underline{\alpha} - \underline{\bar{C}} : (\underline{\alpha} - \underline{\bar{\alpha}}) = -\frac{\underline{X}}{(1-d)} \\ \frac{\partial \underline{X}}{\partial T} = (1-d) \frac{\partial \underline{C}}{\partial T} : \underline{\alpha} + (1-d) \frac{\partial \underline{\bar{C}}}{\partial T} : (\underline{\alpha} - \underline{\bar{\alpha}}) \\ \frac{\partial \underline{X}}{\partial \bar{\alpha}} = -(1-d) \underline{\bar{C}} \end{cases} \quad (\text{II.308})$$

$$\begin{cases} \frac{\partial R}{\partial r} = (1-d^\gamma)(Q + \bar{Q}) \\ \frac{\partial R}{\partial d} = -\gamma d^{\gamma-1} [Qr + \bar{Q}(r - \bar{r})] = -\gamma d^{\gamma-1} \frac{R}{(1-d^\gamma)} \\ \frac{\partial R}{\partial T} = (1-d^\gamma) \frac{\partial Q}{\partial T} r + (1-d^\gamma) \frac{\partial \bar{Q}}{\partial T} (r - \bar{r}) \\ \frac{\partial R}{\partial \bar{r}} = -(1-d^\gamma) \bar{Q} \end{cases} \quad (\text{II.309})$$

According to the evolution equations Eq.(II.77) – Eq.(II.80), the time rate of yield criterion can be expressed as:

$$\begin{aligned} \dot{f} = & \left[\tilde{n}_f : \left(\frac{\partial \underline{\sigma}}{\partial \underline{\varepsilon}_e} : (\underline{D} - \lambda \tilde{n}_f) + \lambda \frac{\partial \underline{\sigma}}{\partial d} \hat{Y} + \frac{\partial \underline{\sigma}}{\partial T} \dot{T} + \frac{\partial \underline{\sigma}}{\partial \bar{r}} \dot{\bar{r}} \right) \right]_{\underline{\sigma}} + \left[(-\tilde{n}_f) : \left(\frac{\partial \underline{X}}{\partial \underline{\alpha}} : \lambda (\tilde{n}_f - \underline{m}_f) + \lambda \frac{\partial \underline{X}}{\partial d} \hat{Y} + \frac{\partial \underline{X}}{\partial T} \dot{T} + \frac{\partial \underline{X}}{\partial \bar{r}} : \dot{\underline{\alpha}} \right) \right]_{\underline{X}} \\ & + \left[\left(-\frac{1}{\sqrt{(1-d^\gamma)}} \right) \left(\frac{\partial R}{\partial r} \dot{\lambda} \left(\frac{1}{\sqrt{1-d^\gamma}} - o \right) + \lambda \frac{\partial R}{\partial d} \hat{Y} + \frac{\partial R}{\partial T} \dot{T} + \frac{\partial R}{\partial \bar{r}} \dot{\bar{r}} \right) \right]_{\underline{R}} \\ & + \left[\left(\frac{\|\underline{\sigma} - \underline{X}\|}{2\sqrt{(1-d)^3}} - \frac{\gamma d^{\gamma-1} R}{2\sqrt{(1-d^\gamma)^3}} \right) \dot{\lambda} \hat{Y} \right]_d + \left[\left(-\frac{\partial \sigma_y}{\partial T} \right) \dot{T} \right]_{\underline{T}} \\ = & \left[\tilde{n}_f : \frac{\partial \underline{\sigma}}{\partial \underline{\varepsilon}_e} : \underline{D} + \left(\tilde{n}_f : \frac{\partial \underline{\sigma}}{\partial T} \right) \dot{T} - \dot{\lambda} \left(\tilde{n}_f : \frac{\partial \underline{\sigma}}{\partial \underline{\varepsilon}_e} : \tilde{n}_f \right) \right. \\ & \quad \left. + \dot{\lambda} \left(\tilde{n}_f : \frac{\partial \underline{\sigma}}{\partial d} \right) \hat{Y} + \left(\tilde{n}_f : \tilde{\underline{P}} \right) \dot{\underline{T}} \right]_{\underline{\sigma}} \\ & - \left[\left(\tilde{n}_f : \frac{\partial \underline{X}}{\partial T} \right) \dot{T} + \dot{\lambda} \left(\tilde{n}_f : \frac{\partial \underline{X}}{\partial \underline{\alpha}} : (\tilde{n}_f - \underline{m}_f) \right) \right. \\ & \quad \left. + \dot{\lambda} \left(\tilde{n}_f : \frac{\partial \underline{X}}{\partial d} \right) \hat{Y} - \left(\tilde{n}_f : \tilde{\underline{C}} \right) : \dot{\underline{\alpha}} \right]_{\underline{X}} \\ & - \left[\left(\frac{1}{\sqrt{(1-d^\gamma)}} \frac{\partial R}{\partial T} \right) \dot{T} + \dot{\lambda} \left(\frac{1}{1-d^\gamma} \frac{\partial R}{\partial r} - \frac{o}{\sqrt{(1-d^\gamma)}} \frac{\partial R}{\partial r} \right) + \dot{\lambda} \left(\frac{1}{\sqrt{(1-d^\gamma)}} \frac{\partial R}{\partial d} \right) \hat{Y} - \left(\frac{1}{\sqrt{(1-d^\gamma)}} \tilde{\bar{Q}} \right) \dot{\bar{r}} \right]_{\underline{R}} \\ & + \left[\left(-\frac{\partial \sigma_y}{\partial T} \right) \dot{T} \right]_{\underline{T}} + \left[\dot{\lambda} \left(\frac{\|\underline{\sigma} - \underline{X}\|}{2\sqrt{(1-d)^3}} - \frac{\gamma d^{\gamma-1} R}{2\sqrt{(1-d^\gamma)^3}} \right) \hat{Y} \right]_d \end{aligned} \quad (\text{II.310})$$

The items explicitly independent on the plastic multiplier are reorganized:

$$\begin{aligned}
 f_{\parallel} = & \tilde{\eta}_f : \frac{\partial \underline{\sigma}}{\partial \underline{\varepsilon}_e} : \underline{D} + \left(\tilde{\eta}_f : \tilde{\underline{P}} \right) \dot{\underline{T}} + \left(\tilde{\eta}_f : \tilde{\underline{C}} \right) : \dot{\underline{\alpha}} + \left(\frac{1}{\sqrt{(1-d^\gamma)}} \tilde{\underline{Q}} \right) \dot{\underline{r}} \\
 & + \left(\tilde{\eta}_f : \frac{\partial \underline{\sigma}}{\partial T} \right) \dot{T} - \left(\tilde{\eta}_f : \frac{\partial \underline{X}}{\partial T} \right) \dot{\underline{T}} - \left(\frac{1}{\sqrt{(1-d^\gamma)}} \frac{\partial R}{\partial T} \right) \dot{T} + \left(-\frac{\partial \sigma_y}{\partial T} \right) \dot{T}
 \end{aligned} \tag{II.311}$$

and the coefficient for the plastic multiplier is given by:

$$\begin{aligned}
 -H_p = & - \left(\tilde{\eta}_f : \frac{\partial \underline{\sigma}}{\partial \underline{\varepsilon}_e} : \tilde{\eta}_f \right) - \left(\tilde{\eta}_f : \frac{\partial \underline{X}}{\partial \underline{\alpha}} : (\tilde{\eta}_f - m_f) \right) - \left(\frac{1}{1-d^\gamma} \frac{\partial R}{\partial r} - \frac{o}{\sqrt{(1-d^\gamma)}} \frac{\partial R}{\partial r} \right) \\
 & + \left(\tilde{\eta}_f : \frac{\partial \underline{\sigma}}{\partial d} \right) \hat{Y} - \left(\tilde{\eta}_f : \frac{\partial \underline{X}}{\partial d} \right) \hat{Y} - \left(\frac{1}{\sqrt{(1-d^\gamma)}} \frac{\partial R}{\partial d} \right) \hat{Y} + \left(\frac{\|\underline{\sigma} - \underline{X}\|}{2\sqrt{(1-d)^3}} - \frac{\gamma d^{\gamma-1} R}{2\sqrt{(1-d^\gamma)^3}} \right) \hat{Y}
 \end{aligned} \tag{II.312}$$

Then, the Eq.(II.310) can be rewritten as:

$$\dot{f} = f_{\parallel} - H_p \dot{\lambda} = 0 \tag{II.313}$$

Using the deduced derivatives in Eq.(II.307) – Eq.(II.309), we may have the following expressions:

$$\begin{aligned}
 f_{\parallel} = & \tilde{\eta}_f : \frac{\partial \underline{\sigma}}{\partial \underline{\varepsilon}_e} : \underline{D} + \left(\tilde{\eta}_f : \frac{\partial \underline{\sigma}}{\partial T} \right) \dot{T} - \left(\tilde{\eta}_f : \frac{\partial \underline{X}}{\partial T} \right) \dot{\underline{T}} - \left(\frac{1}{\sqrt{(1-d^\gamma)}} \frac{\partial R}{\partial T} \right) \dot{T} + \left(-\frac{\partial \sigma_y}{\partial T} \right) \dot{T} \\
 & + \left(\tilde{\eta}_f : \tilde{\underline{P}} \right) \dot{\underline{T}} + \left(\tilde{\eta}_f : \tilde{\underline{C}} \right) : \dot{\underline{\alpha}} + \left(\frac{1}{\sqrt{(1-d^\gamma)}} \tilde{\underline{Q}} \right) \dot{\underline{r}} \\
 = & (1-d) \tilde{\eta}_f : \underline{\Delta} : \underline{D} + \left[\begin{array}{l} \tilde{\eta}_f : \left[\begin{array}{l} \sqrt{1-d} \left(\sqrt{1-d} \underline{\Delta}' : \underline{\varepsilon}_e - \underline{P} - \tilde{\underline{P}} - (T - T_0) \underline{P}' - (T - \bar{T}) \tilde{\underline{P}'} \right) \\ -(1-d) (\underline{C}' : \underline{\alpha} + \tilde{\underline{C}}' : (\underline{\alpha} - \bar{\underline{\alpha}})) \\ - \left(\sqrt{(1-d^\gamma)} (Q'r + \bar{Q}'(r - \bar{r})) \right) - \sigma'_y \end{array} \right] \end{array} \right] \dot{T} \\
 & + \left(\tilde{\eta}_f : \tilde{\underline{P}} \right) \dot{\bar{T}} + \left(\tilde{\eta}_f : \tilde{\underline{C}} \right) : \dot{\bar{\underline{\alpha}}} + \left(\frac{1}{\sqrt{(1-d^\gamma)}} \tilde{\underline{Q}} \right) \dot{\bar{r}} \\
 = & (1-d) \tilde{\eta}_f : \underline{\Delta} : \underline{D} + H_T \dot{T} + \left(\tilde{\eta}_f : \tilde{\underline{P}} \right) \dot{\bar{T}} + \left(\tilde{\eta}_f : \tilde{\underline{C}} \right) : \dot{\bar{\underline{\alpha}}} + \left(\frac{1}{\sqrt{(1-d^\gamma)}} \tilde{\underline{Q}} \right) \dot{\bar{r}}
 \end{aligned} \tag{II.314}$$

and

$$\begin{aligned}
 H_p = & (1-d) \left(\tilde{\eta}_f : \left[\underline{\Lambda} : \tilde{\eta}_f + (\underline{\underline{C}} + \underline{\underline{\check{C}}}) : (\tilde{\eta}_f - \underline{m}_f) \right] \right) + \left(1 - \sqrt{(1-d^\gamma)} o \right) (Q + \check{Q}) \\
 & - \left[\begin{aligned}
 & \tilde{\eta}_f : \left(-\underline{\Lambda} : \underline{\varepsilon}_e + \frac{(\underline{T} - \underline{T}_0)}{2\sqrt{1-d}} (\underline{P} + \underline{\check{P}}) \right) + \tilde{\eta}_f : (\underline{\underline{C}} : \underline{\alpha} + \underline{\underline{\check{C}}} : (\underline{\alpha} - \underline{\check{\alpha}})) \\
 & + \frac{1}{\sqrt{(1-d^\gamma)}} (\gamma d^{\gamma-1} [Qr + \check{Q}(r - \check{r})]) + \left(\frac{\|\underline{\sigma} - \underline{X}\|}{2\sqrt{(1-d)^3}} - \frac{\gamma d^{\gamma-1} R}{2\sqrt{(1-d^\gamma)^3}} \right)
 \end{aligned} \right] \hat{\gamma}
 \end{aligned} \tag{II.315}$$

Clearly, now we obtain the plastic multiplier:

$$\dot{\lambda} = \frac{1}{H_p} \left[(1-d) \tilde{\eta}_f : \underline{\Lambda} : \underline{D} + H_T \dot{T} + (\tilde{\eta}_f : \underline{\check{P}}) \dot{\check{T}} + (\tilde{\eta}_f : \underline{\underline{\check{C}}}) : \dot{\underline{\alpha}} + \left(\frac{\check{Q}}{\sqrt{(1-d^\gamma)}} \right) \dot{\check{r}} \right] \tag{II.316}$$

with

$$\begin{aligned}
 H_p = & \left[\tilde{\eta}_f : \underline{\Lambda} : \tilde{\eta}_f + (\underline{\underline{C}} + \underline{\underline{\check{C}}}) \tilde{\eta}_f : (\tilde{\eta}_f - \underline{m}_f) \right] + \left(1 - \sqrt{(1-d^\gamma)} \left(b \left(\frac{Q + \check{Q}}{Q} \right) r - b \left(\frac{\check{Q}}{Q} \right) \check{r} \right) \right) (Q + \check{Q}) \\
 & + \left[\begin{aligned}
 & \tilde{\eta}_f : \left(\underline{\Lambda} : \underline{\varepsilon}_e - \frac{1}{2\sqrt{1-d}} (\underline{T} - \underline{T}_0) \underline{P} - \frac{1}{2\sqrt{1-d}} (\underline{T} - \underline{T}_0) \underline{\check{P}} \right) \\
 & - \tilde{\eta}_f : \frac{\underline{X}}{(1-d)} - \frac{\gamma d^{\gamma-1}}{\sqrt{(1-d^\gamma)}} \frac{R}{(1-d^\gamma)} - \left(\frac{\|\underline{\sigma} - \underline{X}\|}{2\sqrt{(1-d)^3}} - \frac{\gamma d^{\gamma-1} R}{2\sqrt{(1-d^\gamma)^3}} \right)
 \end{aligned} \right] \hat{\gamma}
 \end{aligned} \tag{II.317}$$

VI.7.2 Formulations of elastoplastic tangent operator

Considering the state relation of Cauchy stress tensor Eq.(II.31), the rate of stress with respect to time is given by:

$$\dot{\underline{\sigma}} = \frac{\partial \underline{\sigma}}{\partial \underline{\varepsilon}_e} : \dot{\underline{\varepsilon}}_e + \frac{\partial \underline{\sigma}}{\partial d} \dot{d} + \frac{\partial \underline{\sigma}}{\partial T} \dot{T} + \frac{\partial \underline{\sigma}}{\partial \check{T}} \dot{\check{T}} \tag{II.318}$$

Considering the evolution equations of plastic strain and damage Eq.(II.77) and Eq.(II.80), and the plastic multiplier Eq.(II.83), with the help of the assumption of additive decomposition of total strain rate, we obtain the following expressions:

$$\begin{aligned}
 \dot{\underline{\sigma}} &= \frac{\partial \underline{\sigma}}{\partial \underline{\varepsilon}_e} : (\underline{D} - \lambda \underline{n}_f) + \lambda \frac{\partial \underline{\sigma}}{\partial d} \hat{Y} + \frac{\partial \underline{\sigma}}{\partial T} \dot{T} + \frac{\partial \underline{\sigma}}{\partial \bar{T}} \dot{\bar{T}} \\
 &= \left[\frac{\partial \underline{\sigma}}{\partial \underline{\varepsilon}_e} - \frac{1}{H_p} \left(\frac{\partial \underline{\sigma}}{\partial \underline{\varepsilon}_e} : \underline{n}_f - \frac{\partial \underline{\sigma}}{\partial d} \hat{Y} \right) \underline{n}_f : \underline{\Lambda} \right] : \underline{D} + \left[\frac{\partial \underline{\sigma}}{\partial T} - \frac{H_T}{H_p} \left(\frac{\partial \underline{\sigma}}{\partial \underline{\varepsilon}_e} : \underline{n}_f - \frac{\partial \underline{\sigma}}{\partial d} \hat{Y} \right) \right] \dot{T} \\
 &\quad + \left[\frac{\partial \underline{\sigma}}{\partial \bar{T}} - \frac{(\underline{n}_f : \bar{P})}{H_p} \left(\frac{\partial \underline{\sigma}}{\partial \underline{\varepsilon}_e} : \underline{n}_f - \frac{\partial \underline{\sigma}}{\partial d} \hat{Y} \right) \right] \dot{\bar{T}} - \left[\frac{(\underline{n}_f : \bar{C})}{H_p} \right] : \dot{\underline{\alpha}} \left(\frac{\partial \underline{\sigma}}{\partial \underline{\varepsilon}_e} : \underline{n}_f - \frac{\partial \underline{\sigma}}{\partial d} \hat{Y} \right) \\
 &\quad - \left[\frac{\check{Q}}{H_p \sqrt{(1-d^\gamma)}} \left(\frac{\partial \underline{\sigma}}{\partial \underline{\varepsilon}_e} : \underline{n}_f - \frac{\partial \underline{\sigma}}{\partial d} \hat{Y} \right) \right] \dot{r}
 \end{aligned} \tag{II.319}$$

The derivatives of Cauchy stress with respect to elastic strain, damage and temperature are deduced in the below:

$$\begin{cases} \frac{\partial \underline{\sigma}}{\partial \underline{\varepsilon}_e} = (1-d)\underline{\Lambda} \\ \frac{\partial \underline{\sigma}}{\partial d} = -\underline{\Lambda} : \underline{\varepsilon}_e + \frac{(T-T_0)}{2\sqrt{1-d}} (\underline{P} + \bar{\underline{P}}) \\ \frac{\partial \underline{\sigma}}{\partial T} = \frac{\partial \underline{\Lambda}}{\partial T} : \underline{\varepsilon}_e - \underline{P} - \bar{\underline{P}} - (T-T_0) \frac{\partial \underline{P}}{\partial T} - (T-\bar{T}) \frac{\partial \bar{\underline{P}}}{\partial T} \\ \frac{\partial \underline{\sigma}}{\partial \bar{T}} = \bar{\underline{P}} \end{cases} \tag{II.320}$$

Substituting the above derivatives into Eq.(II.319) leads to:

$$\begin{aligned}
 \dot{\underline{\sigma}} &= \left[\underline{\Lambda} - \frac{1}{H_p} \left((\underline{n}_f : \underline{\Lambda}) \otimes (\underline{\Lambda} : \underline{n}_f) + \left(\underline{\Lambda} : \underline{\varepsilon}_e - \frac{(T-T_0)}{2\sqrt{1-d}} (\underline{P} + \bar{\underline{P}}) \right) \otimes (\underline{n}_f : \underline{\Lambda}) \hat{Y} \right) \right] : \underline{D} \\
 &\quad + \left[\underline{\Lambda}' : \underline{\varepsilon}_e - \underline{P} - \bar{\underline{P}} - (T-T_0) \underline{P}' - (T-\bar{T}) \bar{\underline{P}}' - \frac{H_T}{H_p} \left(\underline{\Lambda} : \underline{n}_f + \left(\underline{\Lambda} : \underline{\varepsilon}_e - \frac{(T-T_0)}{2\sqrt{1-d}} (\underline{P} + \bar{\underline{P}}) \right) \hat{Y} \right) \right] \dot{T} \\
 &\quad + \left[\frac{\bar{\underline{P}}}{H_p} - \frac{(\underline{n}_f : \bar{P})}{H_p} \left(\frac{\partial \underline{\sigma}}{\partial \underline{\varepsilon}_e} : \underline{n}_f - \frac{\partial \underline{\sigma}}{\partial d} \hat{Y} \right) \right] \dot{\bar{T}} - \left[\frac{(\underline{n}_f : \bar{C})}{H_p} \otimes \left(\frac{\partial \underline{\sigma}}{\partial \underline{\varepsilon}_e} : \underline{n}_f - \frac{\partial \underline{\sigma}}{\partial d} \hat{Y} \right) \right] : \dot{\underline{\alpha}} - \left[\frac{\check{Q} \left(\frac{\partial \underline{\sigma}}{\partial \underline{\varepsilon}_e} : \underline{n}_f - \frac{\partial \underline{\sigma}}{\partial d} \hat{Y} \right)}{H_p \sqrt{(1-d^\gamma)}} \right] \dot{r}
 \end{aligned} \tag{II.321}$$

and it can be rewritten as:

$$\dot{\underline{\sigma}} = \underline{\mathcal{L}}_D : \underline{D} + \underline{\mathcal{L}}_T \dot{T} + \underline{\mathcal{L}}_{\bar{T}} \dot{\bar{T}} + \underline{\mathcal{L}}_{\underline{\alpha}} : \dot{\underline{\alpha}} + \underline{\mathcal{L}}_r \dot{r} \tag{II.322}$$

with:

$$\begin{cases}
 \underline{\underline{L}}_{\sigma} = \tilde{\underline{\Lambda}} - \frac{1}{H_p} \left((\tilde{\underline{n}}_f : \tilde{\underline{\Lambda}}) \otimes (\tilde{\underline{\Lambda}} : \tilde{\underline{n}}_f) + \left(\underline{\underline{\Lambda}} : \underline{\varepsilon}_e - \frac{(\underline{\tau} - \underline{\tau}_0)}{2\sqrt{1-d}} (\underline{P} + \underline{\check{P}}) \right) \otimes (\tilde{\underline{n}}_f : \tilde{\underline{\Lambda}}) \hat{Y} \right) \\
 \underline{\underline{L}}_{\tau} = \tilde{\underline{\Lambda}}' : \underline{\varepsilon}_e - \tilde{\underline{P}} - \tilde{\underline{\check{P}}} - (\underline{\tau} - \underline{\tau}_0) \tilde{\underline{P}}' - (\underline{\tau} - \underline{\check{\tau}}) \tilde{\underline{P}}' - \frac{H_{\tau}}{H_p} \left(\tilde{\underline{\Lambda}} : \tilde{\underline{n}}_f + \left(\underline{\underline{\Lambda}} : \underline{\varepsilon}_e - \frac{(\underline{\tau} - \underline{\tau}_0)}{2\sqrt{1-d}} (\underline{P} + \underline{\check{P}}) \right) \hat{Y} \right) \\
 \underline{\underline{L}}_{\tilde{\tau}} = \tilde{\underline{P}} - \frac{\tilde{\underline{n}}_f : \tilde{\underline{P}}}{H_p} \left(\tilde{\underline{\Lambda}} : \tilde{\underline{n}}_f + \left(\underline{\underline{\Lambda}} : \underline{\varepsilon}_e - \frac{(\underline{\tau} - \underline{\tau}_0)}{2\sqrt{1-d}} (\underline{P} + \underline{\check{P}}) \right) \hat{Y} \right) \\
 \underline{\underline{L}}_{\tilde{\alpha}} = -\frac{\tilde{\underline{n}}_f : \tilde{\underline{\tilde{C}}}}{H_p} \otimes \left(\tilde{\underline{\Lambda}} : \tilde{\underline{n}}_f + \left(\underline{\underline{\Lambda}} : \underline{\varepsilon}_e - \frac{(\underline{\tau} - \underline{\tau}_0)}{2\sqrt{1-d}} (\underline{P} + \underline{\check{P}}) \right) \hat{Y} \right) \\
 \underline{\underline{L}}_{\tilde{\omega}} = -\frac{\tilde{\underline{Q}}}{H_p \sqrt{(1-d^{\gamma})}} \left(\tilde{\underline{\Lambda}} : \tilde{\underline{n}}_f + \left(\underline{\underline{\Lambda}} : \underline{\varepsilon}_e - \frac{(\underline{\tau} - \underline{\tau}_0)}{2\sqrt{1-d}} (\underline{P} + \underline{\check{P}}) \right) \hat{Y} \right)
 \end{cases} \quad (II.323)$$

VII. Numerical aspects

VII.1 Introduction

This chapter is dedicated to the numerical aspects including the weak forms of the overall IBVP, time and space discretization, global resolution scheme of the dynamic explicit solver in ABAQUS and the local constitutive integration scheme. The quadrangular membrane element, the quadrangular shell element and the brick solid element based on assumed strain method are performed by using the subroutine VUEL from ABAQUS.

VII.2 Weak forms of the IBVP

The weak forms associated with the various strong forms of balance equations can be obtained using the weighted residual methods. Let Ω_t be the space occupied by the body at a typical time t , and Γ be its boundary relative to the actual deformed configuration. By applying the weighted residual method to the simplified strong forms of balance equations (Eqs.(II.111) ~ (II.114)), and integration by part and the use of Neumann boundary conditions, the weak forms take the following form:

$$\left\{ \begin{array}{l} J_u(\delta\vec{v}) = \int_{\Omega_t} (\sigma : \vec{\nabla} \delta\vec{v}) dV + \int_{\Omega_t} [\rho(\ddot{\vec{u}} - \vec{f}^u) \cdot \delta\vec{v}] dV - \int_{\Gamma_t} (\vec{F}^u \cdot \delta\vec{v}) dS = 0 \quad \forall \delta\vec{v} \text{ K.A.} \\ J_d(\delta\vec{d}) = - \int_{\Omega_t} l_r^2 \vec{\nabla} \vec{d} \cdot \vec{\nabla} \delta\vec{d} dV + \int_{\Omega_t} \frac{\vec{\nabla} \bar{H}^g(T)}{\bar{H}(T)} \cdot \vec{\nabla} \vec{d} \delta\vec{d} dV + \int_{\Omega_t} (d - \bar{d}) \delta\vec{d} dV - \int_{\Omega_t} \rho \frac{\zeta_d \ddot{d}}{\bar{H}(T)} \delta\vec{d} dV = 0 \quad \forall \delta\vec{d} \text{ K.A.} \\ J_r(\delta\vec{r}) = - \int_{\Omega_t} (1 - d^\gamma) l_r^2 \vec{\nabla} \vec{r} \cdot \vec{\nabla} \delta\vec{r} dV + \int_{\Omega_t} (1 - d^\gamma) \frac{\vec{\nabla} \bar{Q}^g(T)}{\bar{Q}(T)} \cdot \vec{\nabla} \vec{r} \delta\vec{r} dV + \int_{\Omega_t} (1 - d^\gamma) (r - \bar{r}) \delta\vec{r} dV - \int_{\Omega_t} \rho \frac{\zeta_r \ddot{r}}{\bar{Q}(T)} \delta\vec{r} dV = 0 \quad \forall \delta\vec{r} \text{ K.A.} \\ J_{\underline{\alpha}}(\delta\underline{\alpha}) = - \int_{\Omega_t} (1 - d) l_{\underline{\alpha}}^2 \vec{\nabla} \underline{\alpha} \cdot \vec{\nabla} \delta\underline{\alpha} dV + \int_{\Omega_t} (1 - d) \frac{\vec{\nabla} \bar{C}^g(T)}{\bar{C}(T)} \cdot \vec{\nabla} \underline{\alpha} \delta\underline{\alpha} dV + \int_{\Omega_t} (1 - d) (\underline{\alpha} - \bar{\alpha}) \delta\underline{\alpha} dV - \int_{\Omega_t} \rho \frac{\zeta_{\underline{\alpha}} \ddot{\underline{\alpha}}}{\bar{C}(T)} \delta\underline{\alpha} dV = 0 \quad \forall \delta\underline{\alpha} \text{ K.A.} \\ J_{\bar{T}}(\delta\bar{T}) = - \int_{\Omega_t} l_r^2 \vec{\nabla} \bar{T} \cdot \vec{\nabla} \delta\bar{T} dV + \int_{\Omega_t} \frac{\vec{\nabla} \bar{M}^g(T)}{\bar{M}(T)} \cdot \vec{\nabla} \bar{T} \delta\bar{T} dV - \int_{\Omega_t} \frac{\sqrt{1-d}}{\bar{M}(T)} \check{P} : \underline{\varepsilon}^e \delta\bar{T} dV + \int_{\Omega_t} (T - \bar{T}) \delta\bar{T} dV - \int_{\Omega_t} \rho \frac{\zeta_{\bar{T}_1} \dot{\bar{T}} + \zeta_{\bar{T}_2} \ddot{\bar{T}}}{\bar{M}(T)} \delta\bar{T} dV = 0 \quad \forall \delta\bar{T} \text{ K.A.} \\ J_T(\delta T) = - \kappa \int_{\Omega_t} \vec{\nabla} T \cdot \vec{\nabla} \delta T dV - \int_{\Omega_t} (\rho C_v \dot{T}) \delta T dV + \int_{\Omega_t} (R_{pl} T) \delta T dV + \int_{\Omega_t} \phi_{in} \delta T dV + \int_{\Omega_t} (\rho \varsigma) \delta T dV + \int_{\Gamma_t^q} q_T \delta T dS = 0 \quad \forall \delta T \text{ K.A.} \end{array} \right. \quad (II.324)$$

where, K.A. stands for kinematically admissible velocity fields, and $q_T = (-\kappa \vec{\nabla} T \cdot \vec{n}_t)_{\Gamma_t^q}$ is the given heat flux across the boundary Γ_t^q .

In the present work, only four of the above overall weak forms of the IBVP, associated with the following six degree of freedoms (dofs) are studied and implemented: the three displacement field (Eq. (II.324a)), one micromorphic damage (Eq. (II.324b)), one micromorphic isotropic hardening (Eq. (II.324c)) and one local temperature (Eq. (II.324f)). They will be solved simultaneously by Abaqus/Explicit solver using the explicit central-difference or forward-difference integration scheme as well as user developed finite elements with new micromorphic dofs.

VII.3 Time and space discretization

This section is dedicated to the discretization in the time domain $I_t = [t_0, t_f]$ and in the space domain Ω_t , of all the coupled weak forms defining the IBVP discussed above. The time discretization is based on the finite difference method (FDM), while the space discretization is based on the finite element method (FEM). The assumed strain element formulation is used for the nonlinear displacement field and the standard shape function are chosen to interpolate the micromorphic fields.

VII.3.1 Time discretization

The total time interval I_t is thus discretized into N_t subintervals with empty intersections, so that the approximation $I_t = [t_0, t_f] \equiv \bigcup_{n=0}^{N_t} [t_n, t_{n+1}] = t_n + \Delta t$ is valid with sufficient precision. For each of these subintervals of time, we are therefore solving a nonlinear problem to determine all the unknowns of the IBVP. In fact, since all of the unknowns of the IBVP are supposed to be known at time t_n , the problem is to compute these unknowns at the end of the subinterval under concern i.e. $t_{n+1} = t_n + \Delta t$, using the load increment prescribed over that time increment Δt .

VII.3.2 Space discretization

The standard displacement-based FEM is used to discretize the reference configuration Ω_{t_n} into a finite number N_e of subdomains or finite elements (FE) with simple geometric form called Ω_e , with empty intersections. The Hu-Washizu hybrid variational principle for nonlinear solid mechanics is given by Fish and Belytschko (1988):

$$\delta\pi(\vec{v}, \dot{\underline{\varepsilon}}^a, \underline{\sigma}^a) = \int_{\Omega_e} (\delta \dot{\underline{\varepsilon}}^a)^T : \underline{\sigma} d\Omega + \delta \int_{\Omega_e} (\underline{\sigma}^a)^T : (\vec{\nabla}_s \vec{v} - \dot{\underline{\varepsilon}}^a) d\Omega - \delta \dot{\vec{d}} \cdot \vec{f}^{ext} = 0 \quad (\text{II.325})$$

where, δ denotes the standard variation operator, \vec{v} the velocity field, $\dot{\underline{\varepsilon}}^a$ is the assumed (interpolated) strain rate, $\underline{\sigma}^a$ the interpolated stress, $\underline{\sigma}$ the stress evaluated by the constitutive law, $\dot{\vec{d}}$ the nodal velocities, \vec{f}^{ext} the external nodal forces, and $\vec{\nabla}_s \vec{v}$ the symmetric part of the gradient of the velocity.

The assumed strain elements here are based on a simplified form of the Hu-Washizu variational principle as described by Simo and Hughes (1986) in which the interpolated stress is assumed to be orthogonal to the difference between the symmetric part of the velocity gradient and the assumed strain rate. Consequently, the second term of Eq.(II.325) vanishes, yielding:

$$\delta\pi(\dot{\underline{\varepsilon}}^a) = \int_{\Omega_e} (\delta \dot{\underline{\varepsilon}}^a)^T : \underline{\sigma} d\Omega - \delta \dot{\vec{d}} \cdot \vec{f}^{ext} = 0 \quad (\text{II.326})$$

Under this assumption, the variational principle (II.326) is independent of the interpolated stress and doesn't need the definition of an assumed-stress field $\underline{\sigma}^a$.

The discrete equations then require only the interpolation of the velocity and the assumed strain rate within an element, for which we use standard finite element nomenclature:

$$\begin{aligned}\vec{v}(x,t) &= \underline{N}(x) \cdot \dot{\vec{d}}(t) \\ \underline{\dot{\epsilon}^a}(x,t) &= \underline{B}^a(x) \cdot \dot{\vec{d}}(t)\end{aligned}\quad (\text{II.327})$$

and the standard shape function is used to interpolate the micromorphic fields:

$$\begin{aligned}\bar{x}^e(\xi_i, t) &= \langle N_{\bar{x}}^e(\xi_i) \rangle \cdot \{ \bar{x}_n^e(\xi_i, t) \} \\ \vec{\nabla} \bar{x}^e(\xi_i, t) &= [B_{\bar{x}}^e(\xi_i)] \cdot \{ \bar{x}_n^e(\xi_i, t) \}\end{aligned}\quad (\text{II.328})$$

where, \bar{x}^e denotes the local temperature and the micromorphic fields: damage, isotropic hardening, kinematic hardening and temperature.

Substituting Eq.(II.327) - (II.328) into Eq.(II.324) and Eq.(II.326), the elementary discretized weak forms for a typical element take the form:

$$\left\{ \begin{array}{l} J_u(\delta \bar{v}) = \langle \delta \bar{u}_n^e \rangle \left([M_u^e] \{ \ddot{u}_n^e \} + \{ F_{\text{int}-u}^e \} - \{ F_{\text{ext}-u}^e \} \right) \\ J_{\bar{d}}(\delta \bar{d}) = -\langle \delta \bar{d}_n^e \rangle \left([M_{\bar{d}}^e] \{ \ddot{d}_n^e \} + \{ F_{\text{int}-\bar{d}}^e \} - \{ F_{\text{ext}-\bar{d}}^e \} \right) \\ J_{\bar{r}}(\delta \bar{r}) = -\langle \delta \bar{r}_n^e \rangle \left([M_{\bar{r}}^e] \{ \ddot{r}_n^e \} + \{ F_{\text{int}-\bar{r}}^e \} - \{ F_{\text{ext}-\bar{r}}^e \} \right) \\ J_{\bar{\alpha}}(\delta \bar{\alpha}) = -[\delta \bar{\alpha}_n^e]^T \left([M_{\bar{\alpha}}^e] [\ddot{\alpha}_n^e] + [F_{\text{int}-\bar{\alpha}}^e] - [F_{\text{ext}-\bar{\alpha}}^e] \right) \\ J_{\bar{T}}(\delta \bar{T}) = -\langle \delta \bar{T}_n^e \rangle \left([M_{\bar{T}}^e] \{ \ddot{T}_n^e \} + \{ F_{\text{int}-\bar{T}}^e \} - \{ F_{\text{ext}-\bar{T}}^e \} \right) \\ J_T(\delta T) = -\langle \delta T_n^e \rangle \left([M_T^e] \{ \dot{T}_n^e \} + \{ F_{\text{int}-T}^e \} - \{ F_{\text{ext}-T}^e \} \right) \end{array} \right. \quad (\text{II.329})$$

where, the consistent mass matrices, the internal and external forces vectors for a typical reference element are given in the reference frame by:

1). Displacement field

$$\begin{aligned}[M_u^e] &= \int_{\Omega_r^e} \rho [N_u^e]^T [N_u^e] J_v^e dV \\ \{F_{\text{int}-u}^e\} &= \int_{\Omega_r^e} [B_u^e]^T \{ \sigma^e \} J_v^e dV \\ \{F_{\text{ext}-u}^e\} &= \int_{\Omega_r^e} \rho [N_u^e]^T \{ f^u \} J_v^e dV + \int_{\Gamma_t^u} [N_u^e]^T \{ F^u \} J_s^e dS\end{aligned}\quad (\text{II.330})$$

with $[N_u^e]$ is the matrix of the shape functions of displacement field and $[B_u^e]$ its related derivatives matrix taking into account the assumed strain terms as given in Eq.(II.327), and $J_v^e = \det([J^e]) = \det([\partial \vec{x} / \partial \vec{\xi}])$ is the determinant of the Jacobian matrix if the volume mapping transformation between the real and the reference elements Ω_r^e while J_s^e is the Jacobian of the boundaries (or surface) transformation.

2). Micromorphic damage

$$\begin{aligned}
 [M_{\bar{d}}^e] &= \int_{\Omega_r^e} \rho \frac{\zeta_{\bar{d}}}{\bar{H}(T)} \langle N_{\bar{d}}^e \rangle \{N_{\bar{d}}^e\} J_v^e dV \\
 \{F_{\text{int}-\bar{d}}^e\} &= \int_{\Omega_r^e} \left(I_{\bar{d}}^2 [B_{\bar{d}}^e]^T [B_{\bar{d}}^e] + \{N_{\bar{d}}^e\} \langle N_{\bar{d}}^e \rangle \right. \\
 &\quad \left. - \frac{1}{\bar{H}(T)} \frac{\partial \bar{H}^g(T)}{\partial T} \{N_{\bar{d}}^e\} \langle T_n^e \rangle [B_T^e]^T [B_{\bar{d}}^e] \right) \{d_n^e\} J_v^e dV \\
 \{F_{\text{ext}-\bar{d}}^e\} &= \int_{\Omega_r^e} d^e \{N_{\bar{d}}^e\} J_v^e dV
 \end{aligned} \tag{II.331}$$

with d^e is the local damage of the element.

3). Micromorphic isotropic hardening

$$\begin{aligned}
 [M_{\bar{r}}^e] &= \int_{\Omega_r^e} \rho \frac{\zeta_{\bar{r}}}{\bar{Q}(T)} \{N_{\bar{r}}^e\} \langle N_{\bar{r}}^e \rangle J_v^e dV \\
 \{F_{\text{int}-\bar{r}}^e\} &= \int_{\Omega_r^e} \left(1 - (d^e)^\gamma \right) \left(I_{\bar{r}}^2 [B_{\bar{r}}^e]^T [B_{\bar{r}}^e] + \{N_{\bar{r}}^e\} \langle N_{\bar{r}}^e \rangle \right. \\
 &\quad \left. - \frac{1}{\bar{Q}(T)} \frac{\partial \bar{Q}^g(T)}{\partial T} \{N_{\bar{r}}^e\} \langle T_n^e \rangle [B_T^e]^T [B_{\bar{r}}^e] \right) \{\bar{r}_n^e\} J_v^e dV \\
 \{F_{\text{ext}-\bar{r}}^e\} &= \int_{\Omega_r^e} \left(1 - (d^e)^\gamma \right) r^e \{N_{\bar{r}}^e\} J_v^e dV
 \end{aligned} \tag{II.332}$$

with r^e indicates the classical isotropic hardening of the element.

4). Micromorphic kinematic hardening

$$\begin{aligned}
 [M_{\bar{\alpha}}^e] &= \int_{\Omega_r^e} \rho \frac{\zeta_{\bar{\alpha}}}{\bar{C}(T)} [N_{\bar{\alpha}}^e]^T : [N_{\bar{\alpha}}^e] J_v^e dV \\
 \{F_{\text{int}-\bar{\alpha}}^e\} &= \int_{\Omega_r^e} \left(1 - d^e \right) \left(I_{\bar{\alpha}}^2 [B_{\bar{\alpha}}^e]^T : [B_{\bar{\alpha}}^e] + [N_{\bar{\alpha}}^e]^T : [N_{\bar{\alpha}}^e] \right. \\
 &\quad \left. - \frac{1}{\bar{C}(T)} \frac{\partial \bar{C}^g(T)}{\partial T} \langle T_n^e \rangle [B_T^e]^T [N_{\bar{\alpha}}^e]^T : [B_{\bar{\alpha}}^e] \right) [\bar{\alpha}_n^e] J_v^e dV \\
 \{F_{\text{ext}-\bar{\alpha}}^e\} &= \int_{\Omega_r^e} \left(1 - d^e \right) [N_{\bar{\alpha}}^e]^T : \underline{\alpha}^e J_v^e dV
 \end{aligned} \tag{II.333}$$

with $\underline{\alpha}^e$ denotes the classical kinematic hardening of the element.

5). Micromorphic temperature

$$\begin{aligned}
 \left[M_{\bar{T}}^e \right] &= \int_{\Omega_r^e} \rho \frac{\zeta_{\bar{T}2}}{\bar{M}(T)} \{ N_{\bar{T}}^e \} \langle N_{\bar{T}}^e \rangle J_v^e dV \\
 \{ F_{int-\bar{T}}^e \} &= \int_{\Omega_r^e} \left(-\frac{1}{\bar{M}(T)} \frac{\partial \bar{M}^g(T)}{\partial T} \{ N_{\bar{T}}^e \} \langle T_n^e \rangle [B_{\bar{T}}^e]^T [B_{\bar{T}}^e] \right) \{ \bar{T}_n^e \} J_v^e dV + \int_{\Omega_r^e} \rho \frac{\zeta_{\bar{T}1}}{\bar{M}(T)} \{ N_{\bar{T}}^e \} \langle N_{\bar{T}}^e \rangle \{ \dot{\bar{T}}_n^e \} J_v^e dV \\
 \{ F_{ext-\bar{T}}^e \} &= - \int_{\Omega_r^e} \frac{\sqrt{1-d^e}}{\bar{M}(T)} \{ N_{\bar{T}}^e \} \bar{P} : \underline{\varepsilon}^e J_v^e dV + \int_{\Omega_t} T^e \{ N_{\bar{T}}^e \} J_v^e dV
 \end{aligned} \tag{II.334}$$

with T^e the local temperature evaluated in the element.

6). Local temperature

$$\begin{aligned}
 \left[M_T^e \right] &= \int_{\Omega_r^e} \rho C_v \{ N_T^e \} \langle N_T^e \rangle J_v^e dV \\
 \{ F_{int-T}^e \} &= \int_{\Omega_r^e} \left(\kappa [B_T^e]^T [B_T^e] - R_{pl}^e \{ N_T^e \} \langle N_T^e \rangle \right) \{ T_n^e \} J_v^e dV - \int_{\Omega_t} \phi_{in}^e \{ N_T^e \} J_v^e dV \\
 \{ F_{ext-T}^e \} &= \int_{\Omega_r^e} \rho \zeta^e \{ N_T^e \} J_v^e dV + \int_{\Gamma_t^q} q_T \{ N_T^e \} J_s^e ds
 \end{aligned} \tag{II.335}$$

with R_{pl}^e (see Eq.(II.57)) is a part contributions from the time derivative of the entropy in the element, and ϕ_{in}^e (see Eq.(II.87)) is the intrinsic dissipation of the element.

These consistent mass matrices are often favorably replaced by diagonal matrices called the lumped mass matrices, obtained by concentrating the constant mass of each element in its selected nodes. Several methods are used to diagonalize the mass matrix, as can be found in literature (Jürgen, 1996; T J R, 1987; Zienkiewicz and Taylor, 2005).

VII.3.2.1 Finite elements

In this work, overall three types of elements, containing the plane stress quadrangular element, the bilinear quadrangular shell element and the solid-shell element, are developed to implement the micromorphic model based on the assumed strain method (ASM). The planar quadrangular element (Jinyan et al., 2004) uses the reduced one-point integration and the assumed strain formulations based on the Hu-Washizu hybrid variational principle. Special care is given to avoiding hourglass modes and volumetric locking as well as shear locking. The assumed strain fields are constructed so that those portions of the fields which lead to volumetric and shear locking phenomena are eliminated by projection, while the implementation of the uniform reduced integration scheme is straightforward to suppress hourglass modes. Several numerical examples have been examined to validate the performance of this formulations, as can be found in literature (Jinyan et al., 2004). In the next sections, only the quadrangular shell element and the solid-shell element are presented.

VII.3.2.1.1 Q4r24 shell element

The bilinear quadrangular shell element, using full integration for membrane and bending effects and selective integration for the assumed transverse shear strain, is developed with the help of the theory of Mindlin (thick shell). It is extended to the elasto-plastic material model based on the previous work of Bassa (2011). A short review and the standard formulations can be found in the Appendix I (Section VII.6.1).

VII.3.2.1.1.1 The assumed transverse shear strain

The assumed strain method for transverse shear is usually adopted to replace the methods of selective or reduced integrations. The special case of the Q4r24 element is that the shear strain is not directly expressed in terms of the interpolation of the shear strains at the four nodes, but evaluated from the shear strains at four nodes positioned in the middle of each one of the four edges of the element.

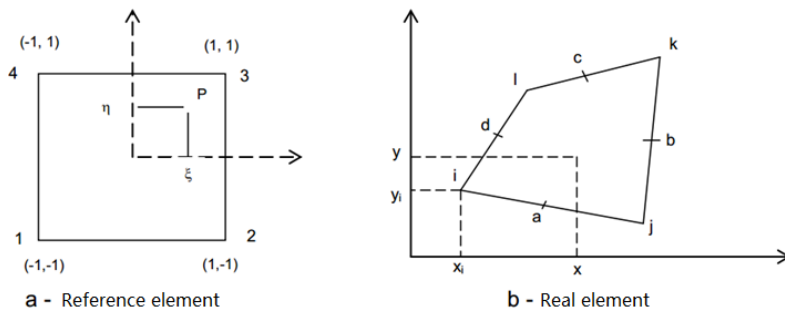


Figure VII-1 The reference element and real deformed element

As shown in Figure VII-1, the shear strain in the element is interpolated from the four middle nodes: $a(\xi=0, \eta=-1)$, $b(\xi=1, \eta=0)$, $c(\xi=0, \eta=1)$ and $d(\xi=-1, \eta=0)$, in the following form:

$$\begin{cases} \gamma_\xi = \frac{1}{2}(1-\eta)\gamma_{\xi a} + \frac{1}{2}(1+\eta)\gamma_{\xi c} \\ \gamma_\eta = \frac{1}{2}(1-\xi)\gamma_{\eta d} + \frac{1}{2}(1+\xi)\gamma_{\eta b} \end{cases} \quad (\text{II.336})$$

and the shear strains in local coordinates can be easily obtained under the transformation:

$$\begin{Bmatrix} \gamma_\xi \\ \gamma_\eta \end{Bmatrix} = [J] \begin{Bmatrix} \gamma_x \\ \gamma_y \end{Bmatrix} \quad (\text{II.337})$$

By using Eq.(II.405), the assumed shear strain is expressed as:

$$\{\gamma\} = [B^{as}] \{w_n^e\} \quad (\text{II.338})$$

where, the assumed B matrix is $[B^{as}] = [J_0]^{-1} [C^a] [J_e B_e]$ and $\{w_n^e\}$ is the vector of nodal displacement and rotations. The matrices $[C^a]$ and $[J_e B_e]$ are defined by:

$$[C^a] = \frac{1}{2} \begin{bmatrix} 1-\eta & 0 & 0 & 0 & 1+\eta & 0 & 0 & 0 \\ 0 & 0 & 0 & 1+\xi & 0 & 0 & 0 & 1-\xi \end{bmatrix} \quad [J_e B_e] = \begin{cases} [J_a] [B^s]_a \\ [J_b] [B^s]_b \\ [J_c] [B^s]_c \\ [J_d] [B^s]_d \end{cases} \quad (\text{II.339})$$

with

$$\begin{aligned} [J_a] &= [J(\xi=0, \eta=-1)] \quad [B^s]_a = [B^s(\xi=0, \eta=-1)] \\ [J_b] &= [J(\xi=1, \eta=0)] \quad [B^s]_b = [B^s(\xi=1, \eta=0)] \\ [J_c] &= [J(\xi=0, \eta=1)] \quad [B^s]_c = [B^s(\xi=0, \eta=1)] \\ [J_d] &= [J(\xi=-1, \eta=0)] \quad [B^s]_d = [B^s(\xi=-1, \eta=0)] \end{aligned} \quad (\text{II.340})$$

VII.3.2.1.1.2 Formulations of the reduced integration

In order to save the computation time especially in explicit finite element solver, the reduced integration with hourglass control is usually applied. The hourglass control is made by introducing parameters for “artificial damping” and “damping stiffness”. The anti-hourglass mode vector γ derived by orthogonal conditions plays an important role in the construction of a stabilization stiffness matrix and additional correction force vectors to avoid hourglass phenomena. The stabilization vector γ can be obtained simply by taking the partial derivatives of the generalized strain vector with respect to the natural coordinates:

$$\{\gamma\} = \frac{1}{4} (\{h\} - \langle h \rangle \cdot \{C_x^e\} \{b_x\} - \langle h \rangle \cdot \{C_y^e\} \{b_y\}) \quad (\text{II.341})$$

where, $\langle h \rangle = \langle 1 \ -1 \ 1 \ -1 \rangle$, the vector of nodal coordinates $\langle C_x^e \rangle = \langle x_i \ x_j \ x_k \ x_l \rangle$ and $\langle C_y^e \rangle = \langle y_i \ y_j \ y_k \ y_l \rangle$, and the vectors $\langle b_x \rangle = \langle N_{i,x} \rangle$ and $\langle b_y \rangle = \langle N_{i,y} \rangle$ are evaluated at the integration point $(\xi, \eta) = (0, 0)$.

In the local coordinates, the membrane deformation is rewritten as:

$$\{\varepsilon^m\} = \begin{bmatrix} \langle b_x \rangle + \langle \gamma \rangle h_{x,x} & | & \langle b_y \rangle + \langle \gamma \rangle h_{y,y} \\ \hline | & | \\ \langle b_y \rangle + \langle \gamma \rangle h_{y,y} & | & \langle b_x \rangle + \langle \gamma \rangle h_{x,x} \end{bmatrix} \begin{cases} \{U_x^e\} \\ \{U_y^e\} \end{cases} \quad (\text{II.342})$$

which can be regarded as a combination of standard B matrix and the anti-hourglass control part. The vectors $\langle U_x^e \rangle = \langle u_i \ u_j \ u_k \ u_l \rangle$ and $\langle U_y^e \rangle = \langle v_i \ v_j \ v_k \ v_l \rangle$.

For the bending strains, the curvature is modified as:

$$\{\kappa\} = \begin{bmatrix} & \langle b_x \rangle + \langle \gamma \rangle h_{,x} \\ -\langle b_y \rangle - \langle \gamma \rangle h_{,y} & \\ -\langle b_x \rangle - \langle \gamma \rangle h_{,x} & \langle b_y \rangle + \langle \gamma \rangle h_{,y} \end{bmatrix} \begin{Bmatrix} \{\theta_x^e\} \\ \{\theta_y^e\} \end{Bmatrix} \quad (\text{II.343})$$

where, the vectors $\langle \theta_x^e \rangle = \langle \theta_{xi} \quad \theta_{xj} \quad \theta_{xk} \quad \theta_{xl} \rangle$ and $\langle \theta_y^e \rangle = \langle \theta_{yi} \quad \theta_{yj} \quad \theta_{yk} \quad \theta_{yl} \rangle$.

The assumed transverse shear strain can be also reorganized under the following form:

$$\{\gamma\} = (\left[B_0^s \right] + \eta \left[B_{s1}^s \right] + \xi \left[B_{s2}^s \right]) \{w_n^e\} \quad (\text{II.344})$$

where, $\left[B_0^s \right]$ is the standard B matrix evaluated at the center, the stable matrix $\left[B_{s1}^s \right]$ and $\left[B_{s2}^s \right]$ are used to avoid the zero energy phenomena:

$$\begin{aligned} \left[B_{s1}^s \right] &= \frac{1}{2} \begin{bmatrix} -\bar{J}_{11} & \bar{J}_{11} \\ -\bar{J}_{21} & \bar{J}_{21} \end{bmatrix} \left[J_e B_e \right] \\ \left[B_{s2}^s \right] &= \frac{1}{2} \begin{bmatrix} \bar{J}_{12} & -\bar{J}_{12} \\ \bar{J}_{22} & -\bar{J}_{22} \end{bmatrix} \left[J_e B_e \right] \end{aligned} \quad (\text{II.345})$$

Consequently, the stiffness matrix is enhanced with the stable matrix of membrane:

$$\left[K_e^m \right] = \left[K_0^m \right] + \left[K_s^m \right] \quad (\text{II.346})$$

where, $\left[K_0^m \right]$ is the standard stiffness matrix measured at the center of the element and the stable stiffness matrix $\left[K_s^m \right] = \left[B^m \right]^T \left[D_s^m \right] \left[B^m \right]$ where:

$$\begin{aligned} \left[B^m \right] &= \begin{bmatrix} \langle \gamma \rangle & \\ & \langle \gamma \rangle \end{bmatrix} \quad H_{ij} = \iint h_i h_j (\det J) d\xi d\eta \quad (i, j = x, y) \\ \left[D_s^m \right] &= \begin{bmatrix} H_{xx} D_{11}^m + H_{yy} D_{33}^m & H_{xy} D_{12}^m + H_{xy} D_{33}^m \\ H_{xy} D_{12}^m + H_{xy} D_{33}^m & H_{yy} D_{22}^m + H_{xx} D_{33}^m \end{bmatrix} \end{aligned} \quad (\text{II.347})$$

D_{ij}^m is the component of the membrane matrix $\left[D^m \right]$ in Appendix VII.6.1.

The bending stiffness matrix is given by:

$$\left[K_e^b \right] = \left[K_0^b \right] + \left[K_s^b \right] \quad (\text{II.348})$$

where, $\left[K_0^b \right]$ is the standard stiffness matrix of bending, $\left[K_s^b \right] = \left[B^b \right]^T \left[D_s^b \right] \left[B^b \right]$ is the stable stiffness matrix with $\left[B^b \right] = \left[B^m \right]$:

$$\begin{bmatrix} D_s^b \end{bmatrix} = \begin{bmatrix} H_{yy}D_{22}^b + H_{xx}D_{33}^b & -H_{xy}D_{12}^b - H_{xy}D_{33}^b \\ -H_{xy}D_{12}^b - H_{xy}D_{33}^b & H_{xx}D_{11}^b + H_{yy}D_{33}^b \end{bmatrix} \quad (\text{II.349})$$

D_{ij}^b is the component of the integrated bending matrix $[D^b]$.

The stiffness matrix for the transverse shear becomes:

$$\begin{bmatrix} K_e^s \end{bmatrix} = \begin{bmatrix} K_0^s \end{bmatrix} + \begin{bmatrix} K_s^{s1} \end{bmatrix} + \begin{bmatrix} K_s^{s2} \end{bmatrix} \quad (\text{II.350})$$

where, $\begin{bmatrix} K_0^s \end{bmatrix}$ is the standard stiffness matrix measured at the center, $\begin{bmatrix} K_s^{s1} \end{bmatrix}$ and $\begin{bmatrix} K_s^{s2} \end{bmatrix}$ are the stable stiffness matrix:

$$\begin{bmatrix} K_s^{s1} \end{bmatrix} = \begin{bmatrix} B_{s1}^s \end{bmatrix}^T \begin{bmatrix} D_s^s \end{bmatrix} \begin{bmatrix} B_{s1}^s \end{bmatrix} \quad \begin{bmatrix} K_s^{s2} \end{bmatrix} = \begin{bmatrix} B_{s2}^s \end{bmatrix}^T \begin{bmatrix} D_s^s \end{bmatrix} \begin{bmatrix} B_{s2}^s \end{bmatrix} \quad (\text{II.351})$$

$\begin{bmatrix} D_s^s \end{bmatrix} = Ah/3 \begin{bmatrix} D^s \end{bmatrix}$ is the integrated moduli of transverse shear.

VII.3.2.1.2 Solid-shell element

The standard formulations of the first order solid element is presented in Appendix VII.6.2. It is well known that if the displacement gradient is used to construct a stiffness matrix, the element can lock for incompressible materials and will exhibit excessive shear stiffness in bending. It is therefore advantageous to project the displacement gradient onto an assumed strain field $\bar{\varepsilon}$ to eliminate these drawbacks (Belytschko and Bindeman, 1993). The discrete gradient operator is projected onto an appropriate subspace in order to eliminate shear and membrane locking. This projection technique can derived from the formalism of the assumed strain method (Abd-Meraiam and Combescure, 2009).

VII.3.2.1.2.1 The assumed strain field

The discrete equation only requires the interpolation of the velocity field and of the assumed strain field. The assumed strain rate $\dot{\varepsilon}$ is expressed in terms of a \bar{B} matrix, projected starting from the classical discrete gradient B defined by Eq.(II.411):

$$\{\dot{\varepsilon}\} = [\bar{B}] \{\dot{u}\} \quad (\text{II.352})$$

Here, the Hallquist form of the b_i vectors in Eq.(II.413) in Appendix VII.6.2 is replaced with the mean form \hat{b}_i from Flanagan and Belytschko (1981):

$$\hat{b}_i = \frac{1}{V_e} \int_{\Omega_e} N_{i,i}(\xi, \eta, \zeta) d\Omega \quad i=1,2,3 \quad (\text{II.353})$$

where, V_e is the element volume.

To define the projected \bar{B} operator, only the nonconstant part of the strain field is projected. Therefore, it is convenient to separate \bar{B} into its constant and nonconstant parts as follows:

$$\bar{B} = B_c + \bar{B}_n \quad (\text{II.354})$$

where,

$$[\bar{B}_n] = \begin{bmatrix} \hat{b}_x^T & & \\ & \hat{b}_y^T & \\ \cdots & \cdots & \hat{b}_z^T \\ \hat{b}_y^T & \hat{b}_x^T & \\ \cdots & \cdots & \hat{b}_z^T \\ \hat{b}_z^T & \hat{b}_x^T & \\ \hat{b}_z^T & \hat{b}_y^T & \end{bmatrix} \quad \begin{bmatrix} X_{1234}^T & -\bar{v}Y_{3}^T - vY_{24}^T & -\bar{v}Z_2^T - vZ_{34}^T \\ -\bar{v}X_3^T - vX_{14}^T & Y_{1234}^T & -\bar{v}Z_1^T - vZ_{34}^T \\ -\bar{v}X_2^T - vX_{14}^T & -\bar{v}Y_1^T - vY_{24}^T & Z_{1234}^T \\ Y_{12}^T & X_{12}^T & 0 \\ Z_{13}^T & 0 & X_{13}^T \\ 0 & Z_{23}^T & Y_{23}^T \end{bmatrix} \quad (\text{II.355})$$

with \bar{B}_n is the assumed strain quintessential bending incompressible or ASQBI field, which is able to avoid the volumetric locking as the Poisson's ratio v approaches 0.5 and capture the transverse shear strains which occur in a beam or plate in bending, and $\bar{v} = v/(1-v)$:

$$\begin{aligned} X_{1234} &= \sum_{a=1}^4 h_{a,x} \gamma_a & Y_{1234} &= \sum_{a=1}^4 h_{a,y} \gamma_a & Z_{1234} &= \sum_{a=1}^4 h_{a,z} \gamma_a \\ X_{24} &= h_{2,x} \gamma_2 + h_{4,x} \gamma_4 & X_2 &= h_{2,x} \gamma_2 \\ h_1 &= \eta \zeta & h_2 &= \zeta \xi & h_3 &= \xi \eta & h_4 &= \xi \eta \zeta \\ \gamma_a &= \frac{1}{8} \left[h_a - \sum_{j=1}^3 (h_a^T x_j) b_j \right] \end{aligned} \quad (\text{II.356})$$

The second form of the \bar{B}_n is the assumed deviatoric strain or ADS strain field as given by:

$$[\bar{B}_n] = \begin{bmatrix} \frac{2}{3}X_{1234}^T & -\frac{1}{3}Y_{1234}^T & -\frac{1}{3}Z_{1234}^T \\ -\frac{1}{3}X_{1234}^T & \frac{2}{3}Y_{1234}^T & -\frac{1}{3}Z_{1234}^T \\ -\frac{1}{3}X_{1234}^T & -\frac{1}{3}Y_{1234}^T & \frac{2}{3}Z_{1234}^T \\ Y_{12}^T & X_{12}^T & 0 \\ Z_{13}^T & 0 & X_{13}^T \\ 0 & Z_{23}^T & Y_{23}^T \end{bmatrix} \quad (\text{II.357})$$

The nonconstant part of the strain field is equivalent to the deviatoric part of the nonconstant part of the symmetric displacement gradient. Because the deviatoric strain field is isochoric, the volumetric strain associated with plastic deformation vanishes (Belytschko and Bindeman, 1993). For more details about the comparison of the two forms of \bar{B}_n can be found in literature (Belytschko and Bindeman, 1993).

VII.3.2.1.2.2 The constitutive model

For the standard 3D constitutive model, the elastic moduli is defined in Eq.(II.414) (Appendix VII.6.2) with Lamé constants. However, the solid-shell element, which has the ability to model thin, three-

dimensional structures uses only a single layer of elements along the thickness, while accurately describing the various through-thickness phenomena (e.g. bending and elasto-plasticity). It modifies the three-dimensional constitutive model to achieve a shell-like behavior and approach the plane-stress states (Abed-Meraim and Combescure, 2002; ABED-MERAIM and Combescure, 2007, 2009; Abed-Meraim et al., 2013; Bassa, 2011). The improved planar stress type constitutive model, which uncouples the response in terms of in-plane and transverse normal stresses versus normal strains, is adopted:

$$[D] = \begin{bmatrix} \bar{\lambda} + 2\mu & \bar{\lambda} & & \\ \bar{\lambda} & \bar{\lambda} + 2\mu & & \\ & & E & \\ & & & \mu \\ & & & \mu \\ & & & \mu \end{bmatrix} \quad (\text{II.358})$$

where, E is the Young's modulus, $\bar{\lambda}$ and μ are the classical Lamé constants.

VII.3.2.1.2.3 The stiffness matrix and internal forces

Normally, the reduced integration with stabilization control evaluated in a co-rotational coordinate system is used to integrate the stiffness matrix and internal forces. However, it is possible to use the ADS or ASQBI strain fields with multiple integration points, which can improve the solutions by improving the stress interpolation for the nonlinear material responses, without encountering locking since these strain fields maintain zero dilatation in the nonconstant part of the strain field (Belytschko and Bindeman, 1993). The eight-point integration scheme is adopted with doing $2 \times 2 \times 2$ Gauss integration to replace the classical stiffness matrix and internal forces in Eq.(II.415) (Appendix VII.6.2):

$$\begin{aligned} [K_e] &= \iiint [\bar{B}]^T [D] [\bar{B}] dv = \int_{-1}^1 \int_{-1}^1 \int_{-1}^1 [\bar{B}]^T [D] [\bar{B}] \det[J] d\xi d\eta d\zeta \\ &\approx \sum_{q=1}^2 \sum_{p=1}^2 \sum_{t=1}^2 [\bar{B}(\xi_q, \eta_p, \zeta_t)]^T [D] [\bar{B}(\xi_q, \eta_p, \zeta_t)] \det[J(\xi_q, \eta_p, \zeta_t)] \varpi_q \varpi_p \varpi_t \\ \{f^{\text{int}}\} &= \iiint [\bar{B}]^T \{\sigma\} dv = \int_{-1}^1 \int_{-1}^1 \int_{-1}^1 [\bar{B}]^T \{\sigma\} \det[J] d\xi d\eta d\zeta \\ &\approx \sum_{q=1}^2 \sum_{p=1}^2 \sum_{t=1}^2 [\bar{B}(\xi_q, \eta_p, \zeta_t)]^T \{\sigma(\xi_q, \eta_p, \zeta_t)\} \det[J(\xi_q, \eta_p, \zeta_t)] \varpi_q \varpi_p \varpi_t \end{aligned} \quad (\text{II.359})$$

VII.4 Global resolution scheme

VII.4.1 Dynamic explicit analysis

Considering the explicit dynamics analysis procedure in Abaqus/Explicit, the solutions of the IBVP with four weak forms presented above are obtained simultaneously by an explicit coupling, based upon the implementation of an explicit integration rule together with the use of diagonal or lumped mass matrices (see Abaqus Analysis User's Guide). The equations of motion for the body are integrated using the explicit central-difference integration scheme:

$$\begin{aligned}\{\ddot{u}\}^{(n+1/2)} &= \{\dot{u}\}^{(n-1/2)} + \frac{\Delta t^{(n+1)} + \Delta t^{(n)}}{2} \{\ddot{u}\}^{(n)} \\ \{u\}^{(n+1)} &= \{u\}^{(n)} + \Delta t^{(n+1)} \{\ddot{u}\}^{(n+1/2)}\end{aligned}\quad (\text{II.360})$$

and the acceleration $\{\ddot{u}\}^{(n)}$ at increment number n is evaluated from the discrete weak forms Eq.(II.329):

$$\{\ddot{u}\}^{(n)} = [M_u]^{-1} \left(\{F_{ext-u}^{(n)}\} - \{F_{int-u}^{(n)}\} \right) \quad (\text{II.361})$$

The solutions of the micromorphic damage and the micromorphic isotropic hardening are also integrated in time using the above explicit central-difference scheme presented by displacement fields. However, for coupled temperature-displacement fields problems, the temperature is integrated in time using the explicit forward-difference integration scheme:

$$\begin{aligned}\{\dot{T}\}^{(n)} &= [M_T]^{-1} \left(\{F_{ext-T}^{(n)}\} - \{F_{int-T}^{(n)}\} \right) \\ \{T\}^{(n+1)} &= \{T\}^{(n)} + \Delta t^{(n+1)} \{\dot{T}\}^{(n)}\end{aligned}\quad (\text{II.362})$$

At each time increment $[t_n, t_{n+1} = t_n + \Delta t]$, the overall state variables at t_n and the increments of all displacement-like variables are provided to compute the state variables at t_{n+1} , and the accelerations of the displacement-like variables by solving the weak forms of the IVP (Eq.(II.324)). The main steps of the dynamic explicit resolution scheme are summarized as following:

- 1). Resolution of the equation of displacement field in the Eq.(II.329)
 - a) Compute the lumped mass matrix $[M_u^e]$ for once, using the Eq.(II.330) at the beginning of the analysis step;
 - b) Estimate the new stable time increment Δt_u using the Eq.(II.364);
 - c) Update the displacement field $\vec{u}^{(n+1)}$ using the Eq.(II.360);
 - d) Compute the state variables, e.g. $\underline{\sigma}^{(n+1)}, \underline{\varepsilon}_p^{(n+1)}$, by the local integration scheme (Section VII.5);
 - e) Compute the internal forces $\{F_{int-u}^e\}$ and external $\{F_{ext-u}^e\}$ forces using the Eq.(II.330);
 - f) Compute the acceleration $\ddot{\vec{u}}^{(n+1)}$ and the velocity $\dot{\vec{u}}^{(n+3/2)}$ according to the Eq.(II.360) and Eq.(II.361).
- 2). Resolutions of the equations of micromorphic fields (damage and isotropic hardening) in Eq.(II.329)
 - a) Compute the lumped mass matrix of micromorphic fields $[M_d^e]$ (Eq.(II.331)) and $[M_r^e]$ (Eq.(II.332)) for once, at the beginning of the analysis step;
 - b) Estimate the stable time increment Δt_d and Δt_r ;
 - c) Update the micromorphic variables $\bar{d}^{(n+1)} = \bar{d}^{(n)} + \Delta t \dot{\bar{d}}^{(n+1/2)}$ and $\bar{r}^{(n+1)} = \bar{r}^{(n)} + \Delta t \dot{\bar{r}}^{(n+1/2)}$;

- d) Compute the internal forces $\{F_{\text{int}-\bar{d}}^e\}$ and $\{F_{\text{int}-\bar{r}}^e\}$, and external forces $\{F_{\text{ext}-\bar{d}}^e\}$ and $\{F_{\text{ext}-\bar{r}}^e\}$, using the Eq.(II.331) and Eq.(II.332);
 - e) Solve the accelerations $\ddot{\bar{d}}^{(n+1)}$ and $\ddot{\bar{r}}^{(n+1)}$, and the time rates of the micromorphic fields $\dot{\bar{d}}^{(n+3/2)}$ and $\dot{\bar{r}}^{(n+3/2)}$.
- 3). Resolution of the equation of local temperature in the Eq.(II.329)
- a) Compute the lumped capacitance matrix $[M_T^e]$ for once using the Eq.(II.335);
 - b) Estimate the stable time increment Δt_T ;
 - c) Update the local temperature $T^{(n+1)}$ using the Eq.(II.362);
 - d) Compute the internal flux vector $\{F_{\text{int}-T}^e\}$ by Eq.(II.335);
 - e) Solve the time rate of temperature $\dot{T}^{(n+1)}$ by Eq.(II.362);

4). Go to the next time step.

The explicit dynamic procedure requires no iterations and no tangent stiffness matrix. However, the explicit procedure, integrates through time by using many time increments, is conditional stable. The stable time increment with damping is given by:

$$\Delta t_u \leq \frac{2}{w_{\max}} \left(\sqrt{(1 + \zeta^2)} - \zeta \right) \quad (\text{II.363})$$

in which, w_{\max} is the elementary highest eigenvalue and $\zeta \leq 1$ is a damping parameter. A conservative estimate of the stable time increment is given by the minimum taken over all the elements. The above stability limit can be rewritten as:

$$\Delta t_u \leq \min \left(\frac{L_e}{C_d} \right) \quad (\text{II.364})$$

where, L_e is the characteristic element dimension and C_d is the current effective, dilatational wave speed of the material. The characteristic element dimension is derived from an analytic upper bound expression for the maximum element eigenvalue. And the dilatational wave speed of the material can be approximated by $C_d = \sqrt{(\lambda + 2\mu)/\rho}$.

Similarly, considering different values of the micromorphic density $\zeta_{\bar{d}}, \zeta_{\bar{r}}, \zeta_{\bar{\alpha}}, \zeta_{\bar{\tau}}$ (Eq.(II.324)), leads to the stability limits associated with each micromorphic field to define the associated stable time increments $(\Delta t_{\bar{d}}, \Delta t_{\bar{r}}, \Delta t_{\bar{\alpha}}, \Delta t_{\bar{\tau}}, \Delta t_T)$. Since each IBVP has a critical stable time increment, the global stability limit is governed by the minimum value of all the critical stable conditions:

$$\Delta t \leq \min(\Delta t_u, \Delta t_{\bar{d}}, \Delta t_{\bar{r}}, \Delta t_{\bar{\alpha}}, \Delta t_{\bar{\tau}}, \Delta t_T) \quad (\text{II.365})$$

VII.4.2 Contact problems

Contact and interactions with or without friction plays a fundamental role in the solution of metal forming processes. In order to impose the contact conditions that will be used to calculate contact forces, the penalty method, calculates the interpenetration distance between solids at a given contact interface point, and use this displacement and a penalty parameter to deduce the contact forces, is adopted as a standard way in Abaqus (see Abaqus Analysis User's Guide).

In this thesis, the contact pair algorithm for modeling contact and interaction problems in Abaqus/Explicit, which uses the penalty contact algorithm and the pure master-slave surface weighting formulations to ensure that proper contact conditions are enforced efficiently, is used. The contact forces are a function of the penetration distance are applied to the slave nodes to oppose the penetration, while equal and opposite forces act on the master surface distributed at the penetration point. The classical isotropic Coulomb friction model, representing the linear relationship between the transmit shear and the normal forces via the friction coefficient, is used to account for the friction between the contacting bodies.

VII.5 Local integration scheme

To solve the algebraic system given in Eq.(II.329), the computation of internal and external forces needs the evaluations of the local stress tensor $\underline{\sigma}_{n+1}$ Eq.(II.330), the local damage d_{n+1} Eq.(II.331), the isotropic hardening r_{n+1} Eq.(II.332), the kinematic hardening α_{n+1} Eq.(II.333) and the local temperature T_{n+1} Eq.(II.334) at each integration point at each element at time step ($t_{n+1} = t_n + \Delta t$), according to the known state variables at time t_n , the state relations Eqs.(II.31)~(II.40) and the evolution equations Eqs.(II.77)~(II.98). The mechanical state variables are updated by the local integration scheme, while the micromorphic damage \check{d}_{n+1} , micromorphic isotropic hardening \check{r}_{n+1} remain constant taking their values at the end of the current time increment t_{n+1} , which are obtained simultaneously by an explicit coupling in the Abaqus/Explicit dynamic analysis. When all the mechanical state variables as well as the micromorphic dofs (local as well as micromorphic ones) are known the local thermal problem is then solved to compute T_{n+1} .

Recall that the evolution equations of our constitutive equation are first-order ordinary partial differential evolution equations of two types formally written under the following form:

$$\begin{cases} \dot{y} = \varphi(y, t) \\ y(t) = y_n \quad t = t_n \end{cases} \quad \forall t \in [t_n, t_{n+1}] \quad (\text{II.366})$$

and

$$\begin{cases} \dot{y} = \varphi(y, t)[\phi(y, t) - y] \\ y(t) = y_n \quad t = t_n \end{cases} \quad \forall t \in [t_n, t_{n+1}] \quad (\text{II.367})$$

The solution of Eq.(II.366) obtained from the classical θ -method is:

$$y_{n+\theta} = y_n + \Delta t (\theta \dot{y}_{n+1} + (1-\theta) \dot{y}_n) \quad \text{for } 0 \leq \theta \leq 1 \quad (\text{II.368})$$

while the solution of Eq.(II.367) has the following form:

$$y_{n+\theta} = y_n \exp(-\theta \varphi(y_{n+\theta}) \Delta t) + [1 - \exp(-\theta \varphi(y_{n+\theta}) \Delta t)] \phi(y_{n+\theta}) \quad \text{for } 0 \leq \theta \leq 1 \quad (\text{II.369})$$

Applying the solutions Eq.(II.368) and Eq.(II.369) under the fully implicit assumption ($\theta=1$), allows rewriting the state variables, at the end of the time step t_{n+1} for the time-independent plasticity, under the following form:

1). The Cauchy stress and the plastic strain tensors:

$$\begin{cases} \underline{\varepsilon}_{n+1}^{vp} = \underline{\varepsilon}_n^{vp} + \Delta \lambda_{vp} \frac{1}{\sqrt{1-d_{n+1}}} \frac{H(T_n) : (\underline{\sigma}_{n+1} - \underline{X}_{n+1})}{\|\underline{\sigma}_{n+1} - \underline{X}_{n+1}\|} \\ \underline{\sigma}_{n+1} = (1-d_{n+1}) \underline{\Lambda}(T_n) : (\underline{\varepsilon}_n + \Delta \underline{\varepsilon} - \Delta \underline{\varepsilon}^{vp}) - \sqrt{1-d_{n+1}} (T_n - T_0) \underline{P}(T_n) - \sqrt{1-d_{n+1}} (T_n - \bar{T}_n) \bar{P}(T_n) \end{cases} \quad (\text{II.370})$$

2). The ductile damage:

$$\begin{cases} d_{n+1} = d_n + \frac{\Delta \lambda_{vp}}{(1-d_{n+1})^{\beta(T_n)}} \left\langle \frac{Y_{n+1} - Y_0(T_n)}{S(T_n)} \right\rangle^{s(T_n)} \\ Y_{n+1} = \frac{1}{2} (\underline{\varepsilon}_n + \Delta \underline{\varepsilon} - \Delta \underline{\varepsilon}^{vp}) : \underline{\Lambda}(T_n) : (\underline{\varepsilon}_n + \Delta \underline{\varepsilon} - \Delta \underline{\varepsilon}^{vp}) \\ - \frac{1}{2\sqrt{1-d_{n+1}}} [(T_n - T_0) \underline{P}(T_n) + (T_n - \bar{T}_n) \bar{P}(T_n)] : (\underline{\varepsilon}_n + \Delta \underline{\varepsilon} - \Delta \underline{\varepsilon}^{vp}) \\ + \frac{1}{2} C(T_n) \underline{\alpha}_{n+1} : \underline{\alpha}_{n+1} + \frac{1}{2} \bar{C}(T_n) (\underline{\alpha}_{n+1} - \bar{\alpha}_{n+1}) : (\underline{\alpha}_{n+1} - \bar{\alpha}_{n+1}) + \frac{1}{2} \bar{C}^g(T_n) \vec{\nabla} \bar{\alpha}_{n+1} : \vec{\nabla} \bar{\alpha}_{n+1} \\ + \frac{1}{2} \gamma d^{\gamma-1} (Q(T_n) r_{n+1}^2 + \bar{Q}(T_n) (r_{n+1} - \bar{r}_{n+1})^2 + \bar{Q}^g(T_n) \vec{\nabla} \bar{r}_{n+1} \cdot \vec{\nabla} \bar{r}_{n+1}) - H(T_n) (d_{n+1} - \bar{d}_{n+1}) \end{cases} \quad (\text{II.371})$$

3). The isotropic hardening:

$$\begin{cases} r_{n+1} = r_n e^{-\Delta \lambda_{vp} b(T_n) \left(1 + \frac{\bar{Q}(T_n)}{Q(T_n)} \right)} + \left[1 - e^{-\Delta \lambda_{vp} b(T_n) \left(1 + \frac{\bar{Q}(T_n)}{Q(T_n)} \right)} \right] \left[\frac{Q(T_n) + b(T_n) \bar{Q}(T_n) \tilde{r}_{n+1}}{b(T_n) \sqrt{1-d_{n+1}^\gamma} (Q(T_n) + \bar{Q}(T_n))} \right] \\ R_{n+1} = (1-d_{n+1}^\gamma) Q(T_n) r_{n+1} + (1-d_{n+1}^\gamma) \bar{Q}(T_n) (r_{n+1} - \bar{r}_{n+1}) \end{cases} \quad (\text{II.372})$$

4). The kinematic hardening:

$$\begin{cases} \underline{\alpha}_{n+1} = \underline{\alpha}_n e^{-\Delta \lambda_{vp} a(T_n) \left(1 + \frac{\bar{C}(T_n)}{C(T_n)} \right)} + \left[1 - e^{-\Delta \lambda_{vp} a(T_n) \left(1 + \frac{\bar{C}(T_n)}{C(T_n)} \right)} \right] \left[\frac{C(T_n) \tilde{n}_f + a(T_n) \bar{C}(T_n) \bar{\alpha}_{n+1}}{a(T_n) (C(T_n) + \bar{C}(T_n))} \right] \\ \underline{X}_{n+1} = (1-d_{n+1}) C(T_n) \underline{\alpha}_{n+1} + (1-d_{n+1}) \bar{C}(T_n) (\underline{\alpha}_{n+1} - \bar{\alpha}_{n+1}) \end{cases} \quad (\text{II.373})$$

And the viscoplastic "yield criterion":

$$f_{n+1}^{vp} = \|\tilde{\underline{\sigma}}_{n+1} - \tilde{\underline{X}}_{n+1}\| - \tilde{R}_{n+1} - K^{vp}(T_n) \left(\frac{\Delta \lambda_{vp}}{\Delta t} \right)^{\frac{1}{m_{vp}(T_n)}} - \sigma_{yp}(T_n) = 0 \quad (\text{II.374})$$

Remark: Since the time-independent plasticity is a special case of the viscoplasticity by vanishing the viscostress σ^{vp} defined by Eq.(II.101) of Section VI.3.4.2.2, here the local integration is performed only for the time-dependent plasticity (or viscoplasticity).

VII.5.1 Local integration of time-dependent plasticity

VII.5.1.1 Elastic prediction

Let us suppose that the total incremental strain ($\Delta\underline{\varepsilon}$) over the current time step is completely elastic which does not induce any plastic flow, hardening or damage i.e. $\Delta\lambda_{vp} = 0$. In this case, the elastic trial strain at time t_{n+1} is given by:

$$\underline{\varepsilon}_{n+1}^{e,trial} = \underline{\varepsilon}_n^e + \Delta\underline{\varepsilon} = \underline{\varepsilon}_n - \underline{\varepsilon}_n^{vp} + \Delta\underline{\varepsilon} \quad (\text{II.375})$$

It results the trial stress by using the state relation of Eq.(II.31):

$$\underline{\sigma}_{n+1}^{trial} = (1-d_n) \underline{\Delta}(T_n) : \underline{\varepsilon}_{n+1}^{e,trial} - \sqrt{1-d_n} (T_n - T_0) \underline{P}(T_n) - \sqrt{1-d_n} (T_n - \bar{T}_n) \bar{\underline{P}}(T_n) \quad (\text{II.376})$$

Since $\Delta\lambda_{vp} = 0$ is zero for this trial elastic loading increment, The viscoplastic yield criterion (Eq.(II.374)) corresponding to this trial stress is written as:

$$f_{n+1}^{vp,trial} = \frac{\|\underline{\sigma}_{n+1}^{trial} - \underline{X}_n\|}{\sqrt{1-d_n}} - \frac{R_n}{\sqrt{1-d_n^\gamma}} - \sigma_{yp}(T_n) \quad (\text{II.377})$$

If $f_{n+1}^{vp,trial} \leq 0$, then the solution is effectively elastic one meaning that the trial stress state $\underline{\sigma}_{n+1}^{trial}$ is lying inside the yield surface (e.g. elastic unloading), and the states variables are updated with the following solution:

$$\begin{cases} \underline{\sigma}_{n+1}^{vp} = \underline{\sigma}_n^{vp} & \underline{\alpha}_{n+1} = \underline{\alpha}_n & \underline{r}_{n+1} = \underline{r}_n & d_{n+1} = d_n \\ \underline{\sigma}_{n+1} = \underline{\sigma}_{n+1}^{trial} & \underline{X}_{n+1} = \underline{X}_n & \underline{R}_{n+1} = \underline{R}_n & Y_{n+1} = Y_n \end{cases} \quad (\text{II.378})$$

If $f_{n+1}^{vp,trial} > 0$, it means that the trial stress state lies outside of the viscoplastic yield surface. The solution is viscoplastic and the trial solution should be corrected to determine the final values of the state variables which ensure that viscoplastic yield condition is fulfilled:

$$f_{n+1}^{vp} = \frac{\|\underline{\sigma}_{n+1} - \underline{X}_{n+1}\|}{\sqrt{1-d_{n+1}}} - \frac{R_{n+1}}{\sqrt{1-d_{n+1}^\gamma}} - K^{vp}(T_n) \left(\frac{\Delta \lambda_{vp}}{\Delta t} \right)^{\frac{1}{m_{vp}(T_n)}} - \sigma_{yp}(T_n) = 0 \quad (\text{II.379})$$

VII.5.1.2 Plastic correction

To proceed with this viscoplastic correction, the discretized, nonlinear and fully coupled equations Eqs.(II.370) ~ (II.374) must be solved using the Newton-Raphson iterative scheme to determine the stress-like variables and the admissibility conditions at t_{n+1} , the so-called return mapping algorithm.

The stress-like variables at the end of the time increment are expressed as:

1). The Cauchy stress tensor:

$$\underline{\sigma}_{n+1} = (1 - d_{n+1}) \underline{\Lambda}(T_n) : \left(\underline{\varepsilon}_{n+1}^{e, trial} - \Delta \lambda_{vp} \frac{1}{\sqrt{1-d_{n+1}}} \frac{\underline{H}(T_n) : (\underline{\sigma}_{n+1} - \underline{X}_{n+1})}{\|\underline{\sigma}_{n+1} - \underline{X}_{n+1}\|} \right) - \sqrt{1-d_{n+1}} (T_n - T_0) \underline{P}(T_n) - \sqrt{1-d_{n+1}} (T_n - \bar{T}_n) \bar{P}(T_n)$$
(II.380)

2). The stress-like variable of isotropic hardening:

$$R_{n+1} = (1 - d_{n+1}^\gamma) \begin{bmatrix} (Q(T_n) + \bar{Q}(T_n)) \left(r_n e^{-\Delta \lambda_{vp} b(T_n) \left(1 + \frac{\bar{Q}(T_n)}{Q(T_n)} \right)} + \left(1 - e^{-\Delta \lambda_{vp} b(T_n) \left(1 + \frac{\bar{Q}(T_n)}{Q(T_n)} \right)} \right) \frac{Q(T_n) + b \bar{Q}(T_n) \tilde{r}_{n+1}}{b(T_n) \sqrt{1-d_{n+1}^\gamma} (Q(T_n) + \bar{Q}(T_n))} \right) \\ - \bar{Q}(T_n) \tilde{r}_{n+1} \end{bmatrix}$$
(II.381)

3). The stress-like variable of kinematic hardening:

$$X_{n+1} = (1 - d_{n+1}) \begin{bmatrix} (C(T_n) + \bar{C}(T_n)) \left(\underline{\alpha}_n e^{-\Delta \lambda_{vp} a(T_n) \left(1 + \frac{\bar{C}(T_n)}{C(T_n)} \right)} + \left[1 - e^{-\Delta \lambda_{vp} a(T_n) \left(1 + \frac{\bar{C}(T_n)}{C(T_n)} \right)} \right] \left[\frac{C(T_n)}{a(T_n)(C(T_n) + \bar{C}(T_n))} \tilde{n}_f + \frac{\bar{C}(T_n)}{C(T_n) + \bar{C}(T_n)} \bar{\alpha}_{n+1} \right] \right) \\ - \bar{C}(T_n) \bar{\alpha}_{n+1} \end{bmatrix}$$
(II.382)

4). The viscous stress:

$$\underline{\sigma}_{n+1}^{vp} = K^{vp}(T_n) \left(\frac{\Delta \lambda_{vp}}{\Delta t} \right)^{\frac{1}{m_{vp}(T_n)}}$$
(II.383)

5). The norm tensor:

$$\underline{Z}_{n+1} = \underline{\sigma}_{n+1} - \underline{X}_{n+1}$$
(II.384)

Considering the full anisotropic viscoplasticity, we obtain the following three high nonlinear equations with three independent variables $\Delta \lambda_{vp}$, d and \underline{n}_f :

$$\begin{cases} f_{n+1}^{vp} = \frac{\|\underline{Z}_{n+1}\|}{\sqrt{1-d_{n+1}}} - \frac{R_{n+1}}{\sqrt{1-d_{n+1}^\gamma}} - \sigma_{n+1}^{vp} - \sigma_{vp}(T_n) = 0 \\ g_{n+1} = d_{n+1} - d_n - \frac{\Delta \lambda_{vp}}{(1-d_{n+1})^{\beta(T_n)}} \left\langle \frac{Y_{n+1} - Y_0(T_n)}{S(T_n)} \right\rangle^{s(T_n)} = 0 \\ h_{n+1} = H(T_n) : \underline{Z}_{n+1} - \|\underline{Z}_{n+1}\| \underline{n}_{n+1}^f = 0 \end{cases} \quad (\text{II.385})$$

Using the Newton-Raphson scheme to linearize and solve the nonlinear equations:

$$\begin{bmatrix} f_{vp} \\ g \\ h \end{bmatrix}_{n+1} + \begin{bmatrix} \frac{\partial f_{vp}}{\partial \Delta \lambda_{vp}} & \frac{\partial f_{vp}}{\partial d_{n+1}} & \frac{\partial f_{vp}}{\partial \underline{n}_{n+1}^f} \\ \frac{\partial g}{\partial \Delta \lambda_{vp}} & \frac{\partial g}{\partial d_{n+1}} & \frac{\partial g}{\partial \underline{n}_{n+1}^f} \\ \frac{\partial h}{\partial \Delta \lambda_{vp}} & \frac{\partial h}{\partial d_{n+1}} & \frac{\partial h}{\partial \underline{n}_{n+1}^f} \end{bmatrix}_{n+1} \cdot \begin{bmatrix} \delta \Delta \lambda_{vp} \\ \delta d \\ \delta \underline{n}_f \end{bmatrix}_{n+1} = \{0\} \quad (\text{II.386})$$

and the update of the basic variables in the form:

$$\begin{cases} (\Delta \lambda_{vp}^{n+1})^{i+1} = (\Delta \lambda_{vp}^{n+1})^i + \delta \Delta \lambda_{vp} \\ d_{n+1}^{i+1} = d_{n+1}^i + \delta d \\ (\underline{n}_f^{n+1})^{i+1} = (\underline{n}_f^{n+1})^i + \delta \underline{n}_f \end{cases} \quad (\text{II.387})$$

VII.5.1.2.1 Prime derivatives

The derivatives in Eq.(II.386) are given by:

$$\begin{aligned} \frac{\partial f_{vp}}{\partial \Delta \lambda_{vp}} &= \frac{1}{2\sqrt{1-d_{n+1}}} \frac{H(T_n) : (\underline{\sigma}_{n+1} - \underline{X}_{n+1})}{\|\underline{\sigma}_{n+1} - \underline{X}_{n+1}\|} \frac{\partial}{\partial \Delta \lambda_{vp}} (\underline{\sigma}_{n+1} - \underline{X}_{n+1}) \\ &\quad - \frac{1}{\sqrt{1-d_{n+1}^\gamma}} \frac{\partial}{\partial \Delta \lambda_{vp}} (R_{n+1}) - \frac{\partial}{\partial \Delta \lambda_{vp}} (\sigma_{n+1}^{vp}) \\ \frac{\partial f_{vp}}{\partial d_{n+1}} &= \frac{\|\underline{\sigma}_{n+1} - \underline{X}_{n+1}\|}{2\sqrt{(1-d_{n+1})^3}} - \frac{\gamma d_{n+1}^{\gamma-1}}{2\sqrt{(1-d_{n+1}^\gamma)^3}} R_{n+1} \\ &\quad + \frac{1}{2\sqrt{1-d_{n+1}}} \frac{H(T_n) : (\underline{\sigma}_{n+1} - \underline{X}_{n+1})}{\|\underline{\sigma}_{n+1} - \underline{X}_{n+1}\|} \frac{\partial}{\partial d_{n+1}} (\underline{\sigma}_{n+1} - \underline{X}_{n+1}) - \frac{1}{\sqrt{1-d_{n+1}^\gamma}} \frac{\partial}{\partial d_{n+1}} (R_{n+1}) \\ \frac{\partial f_{vp}}{\partial \underline{n}_{n+1}^f} &= \frac{1}{2\sqrt{1-d_{n+1}}} \frac{H(T_n) : (\underline{\sigma}_{n+1} - \underline{X}_{n+1})}{\|\underline{\sigma}_{n+1} - \underline{X}_{n+1}\|} \frac{\partial}{\partial \underline{n}_f^{n+1}} (\underline{\sigma}_{n+1} - \underline{X}_{n+1}) - \frac{1}{\sqrt{1-d_{n+1}^\gamma}} \frac{\partial}{\partial \underline{n}_f^{n+1}} (R_{n+1}) \end{aligned} \quad (\text{II.388})$$

$$\begin{aligned}
 \frac{\partial g}{\partial \Delta \lambda_{vp}} &= -\frac{1}{(1-d_{n+1})^{\beta(\tau_n)}} \left\langle \frac{Y_{n+1} - Y_0(\tau_n)}{S(\tau_n)} \right\rangle^{s(\tau_n)} - \frac{\Delta \lambda_{vp} S(\tau_n)}{S(\tau_n)(1-d_{n+1})^{\beta(\tau_n)}} \left\langle \frac{Y_{n+1} - Y_0(\tau_n)}{S(\tau_n)} \right\rangle^{s(\tau_n)-1} \frac{\partial}{\partial \Delta \lambda_{vp}} (Y_{n+1}) \\
 \frac{\partial g}{\partial d_{n+1}} &= 1 - \frac{\Delta \lambda_{vp}}{(1-d_{n+1})^{\beta(\tau_n)}} \left\langle \frac{Y_{n+1} - Y_0(\tau_n)}{S(\tau_n)} \right\rangle^{s(\tau_n)-1} \left[-\frac{\beta(\tau_n)}{(1-d_{n+1})} \left\langle \frac{Y_{n+1} - Y_0(\tau_n)}{S(\tau_n)} \right\rangle + \frac{s(\tau_n)}{S(\tau_n)} \frac{\partial}{\partial d_{n+1}} (Y_{n+1}) \right] \\
 \frac{\partial g}{\partial n_f^{n+1}} &= -\frac{\Delta \lambda_{vp} S(\tau_n)}{S(\tau_n)(1-d_{n+1})^{\beta(\tau_n)}} \left\langle \frac{Y_{n+1} - Y_0(\tau_n)}{S(\tau_n)} \right\rangle^{s(\tau_n)-1} \frac{\partial}{\partial n_f} (Y_{n+1})
 \end{aligned} \tag{II.389}$$

$$\begin{aligned}
 \frac{\partial h}{\partial \Delta \lambda_{vp}} &= (\underline{H}(\tau_n) - \underline{n}_{n+1}^f \otimes \underline{n}_{n+1}^f) \frac{\partial}{\partial \Delta \lambda_{vp}} (\underline{\sigma}_{n+1} - \underline{X}_{n+1}) \\
 \frac{\partial h}{\partial d_{n+1}} &= (\underline{H}(\tau_n) - \underline{n}_{n+1}^f \otimes \underline{n}_{n+1}^f) \frac{\partial}{\partial d_{n+1}} (\underline{\sigma}_{n+1} - \underline{X}_{n+1}) \\
 \frac{\partial h}{\partial n_f^{n+1}} &= (\underline{H}(\tau_n) - \underline{n}_{n+1}^f \otimes \underline{n}_{n+1}^f) \frac{\partial}{\partial n_f^{n+1}} (\underline{\sigma}_{n+1} - \underline{X}_{n+1}) - \|\underline{Z}_{n+1}\| \underline{1}
 \end{aligned} \tag{II.390}$$

VII.5.1.2.2 Coefficients of state variables for the multiplier $\Delta \lambda_{vp}$

The partial derivatives of state variables with respect to the multiplier are given by:

$$\begin{aligned}
 \frac{\partial \underline{\sigma}_{n+1}}{\partial \Delta \lambda_{vp}} &= \sqrt{1-d_{n+1}} \underline{\Lambda}(\tau_n) : \frac{\partial}{\partial \Delta \lambda_{vp}} (\underline{\varepsilon}_{n+1}^e) \\
 \frac{\partial R_{n+1}}{\partial \Delta \lambda_p} &= (1-d_{n+1}^\gamma) (Q(\tau_n) + \bar{Q}(\tau_n)) \frac{\partial}{\partial \Delta \lambda_p} (r_{n+1}) \\
 \frac{\partial X_{n+1}}{\partial \Delta \lambda_{vp}} &= (1-d_{n+1}) (C(\tau_n) + \bar{C}(\tau_n)) \frac{\partial}{\partial \Delta \lambda_p} (\underline{\alpha}_{n+1}) \\
 \frac{\partial \underline{\sigma}_{n+1}^{vp}}{\partial \Delta \lambda_{vp}} &= \frac{\kappa^{vp}(\tau_n)}{m_{vp}(\tau_n)} \left(\frac{\Delta \lambda_{vp}}{\Delta t} \right)^{\frac{1}{m_{vp}(\tau_n)}-1} \frac{1}{\Delta t} \\
 \frac{\partial Y_{n+1}}{\partial \Delta \lambda_{vp}} &= \left[\begin{array}{l} \left(\underline{\Lambda}(\tau_n) : \langle \underline{\varepsilon}_{n+1}^e \rangle_+ \right) - \frac{1}{2\sqrt{1-d_{n+1}}} \left[(\tau_n - \tau_0) P(\tau_n) + (\tau_n - \bar{\tau}_n) \bar{P}(\tau_n) \right] \\ + h \left(\underline{\Lambda}(\tau_n) : \langle \underline{\varepsilon}_{n+1}^e \rangle_- \right) - \frac{h}{2\sqrt{1-hd_{n+1}}} \left[(\tau_n - \tau_0) P(\tau_n) + (\tau_n - \bar{\tau}_n) \bar{P}(\tau_n) \right] \end{array} \right] : \frac{\partial}{\partial \Delta \lambda_{vp}} \langle \underline{\varepsilon}_{n+1}^e \rangle \\
 &\quad + \left[(C(\tau_n) + \bar{C}(\tau_n)) \underline{\alpha}_{n+1} - \bar{C}(\tau_n) \underline{\alpha}_{n+1} \right] \frac{\partial}{\partial \Delta \lambda_p} (\underline{\alpha}_{n+1}) + \bar{C}^g(\tau_n) \vec{\nabla} \underline{\alpha}_{n+1} : \frac{\partial}{\partial \Delta \lambda_p} (\vec{\nabla} \underline{\alpha}_{n+1}) \\
 &\quad + \gamma d_{n+1}^{\gamma-1} \left[(Q(\tau_n) + \bar{Q}(\tau_n)) r_{n+1} - \bar{Q}(\tau_n) \bar{r}_{n+1} \right] \frac{\partial}{\partial \Delta \lambda_p} (r_{n+1}) + \gamma d_{n+1}^{\gamma-1} \bar{Q}^g(\tau_n) \vec{\nabla} \bar{r}_{n+1} : \frac{\partial}{\partial \Delta \lambda_p} (\vec{\nabla} \bar{r}_{n+1})
 \end{aligned} \tag{II.391}$$

and

$$\begin{aligned}
 \frac{\partial \underline{\varepsilon}_{n+1}^e}{\partial \Delta \lambda_{vp}} &= -\frac{1}{\sqrt{1-d_{n+1}}} n_{n+1}^f \\
 \frac{\partial r_{n+1}}{\partial \Delta \lambda_{vp}} &= b(T_n) \left(1 + \frac{\check{Q}(T_n)}{Q(T_n)} \right) e^{-\Delta \lambda_{vp} b(T_n) \left(1 + \frac{\check{Q}(T_n)}{Q(T_n)} \right)} \\
 &\quad \left(-r_n + \left[\frac{Q(T_n)}{b(T_n) \sqrt{1-d_{n+1}^\gamma} (Q(T_n) + \check{Q}(T_n))} + \frac{\check{Q}(T_n)}{Q(T_n) + \check{Q}(T_n)} \check{r}_{n+1} \right] \right) \\
 \frac{\partial \underline{\alpha}_{n+1}}{\partial \Delta \lambda_{vp}} &= a(T_n) \left(1 + \frac{\check{C}(T_n)}{C(T_n)} \right) e^{-\Delta \lambda_{vp} a(T_n) \left(1 + \frac{\check{C}(T_n)}{C(T_n)} \right)} \\
 &\quad \left(-\underline{\alpha}_n + \left[\frac{C(T_n)}{a(T_n) \sqrt{1-d_{n+1}} (C(T_n) + \check{C}(T_n))} n_{n+1}^f + \left(\frac{\check{C}(T_n)}{C(T_n) + \check{C}(T_n)} \right) \check{\underline{\alpha}}_{n+1} \right] \right)
 \end{aligned} \tag{II.392}$$

VII.5.1.2.3 Coefficients of state variables for the damage d

The partial derivatives of state variables with respect to the damage are given by:

$$\begin{aligned}
 \frac{\partial \underline{\sigma}_{n+1}}{\partial d_{n+1}} &= \left\{ \begin{array}{l} -\underline{\Lambda}(\tau_n) : \underline{\varepsilon}_{n+1}^e + (1-d_{n+1}) \underline{\Lambda}(\tau_n) : \frac{\partial}{\partial d_{n+1}} (\underline{\varepsilon}_{n+1}^e) \\ + \frac{1}{2\sqrt{1-d_{n+1}}} [(\tau_n - \tau_0) P(\tau_n) + (\tau_n - \bar{\tau}_n) \bar{P}(\tau_n)] \end{array} \right\} \\
 \frac{\partial R_{n+1}}{\partial d_{n+1}} &= \gamma d_{n+1}^{\gamma-1} [-(Q(\tau_n) + \bar{Q}(\tau_n)) r_{n+1} + \bar{Q}(\tau_n) \bar{r}_{n+1}] + (1-d_{n+1}^\gamma) (Q(\tau_n) + \bar{Q}(\tau_n)) \frac{\partial}{\partial d_{n+1}} (r_{n+1}) \\
 \frac{\partial \underline{x}_{n+1}}{\partial d_{n+1}} &= [-(C(\tau_n) + \bar{C}(\tau_n)) \underline{\alpha}_{n+1} + \bar{C}(\tau_n) \bar{\alpha}_{n+1}] + (1-d_{n+1}) (C(\tau_n) + \bar{C}(\tau_n)) \frac{\partial}{\partial d_{n+1}} (\underline{\alpha}_{n+1}) \\
 \frac{\partial \sigma_{n+1}^{vp}}{\partial d_{n+1}} &= 0 \\
 \frac{\partial Y_{n+1}}{\partial d_{n+1}} &= \left[\begin{array}{l} \left(\underline{\Lambda}(\tau_n) : \langle \underline{\varepsilon}_{n+1}^e \rangle_+ \right) - \frac{1}{2\sqrt{1-d_{n+1}}} [(\tau_n - \tau_0) P(\tau_n) + (\tau_n - \bar{\tau}_n) \bar{P}(\tau_n)] \\ + h \left(\underline{\Lambda}(\tau_n) : \langle \underline{\varepsilon}_{n+1}^e \rangle_- \right) - \frac{h}{2\sqrt{1-hd_{n+1}}} [(\tau_n - \tau_0) P(\tau_n) + (\tau_n - \bar{\tau}_n) \bar{P}(\tau_n)] \end{array} \right] : \frac{\partial}{\partial d_{n+1}} \langle \underline{\varepsilon}_{n+1}^e \rangle \\
 &\quad + [(C(\tau_n) + \bar{C}(\tau_n)) \underline{\alpha}_{n+1} - \bar{C}(\tau_n) \bar{\alpha}_{n+1}] : \frac{\partial}{\partial d_{n+1}} (\underline{\alpha}_{n+1}) + \bar{C}^g(\tau_n) \vec{\nabla} \bar{\alpha}_{n+1} : \frac{\partial}{\partial d_{n+1}} (\vec{\nabla} \bar{\alpha}_{n+1}) \\
 &\quad + \gamma d_{n+1}^{\gamma-1} [(Q(\tau_n) + \bar{Q}(\tau_n)) r_{n+1} - \bar{Q}(\tau_n) \bar{r}_{n+1}] \frac{\partial}{\partial d_{n+1}} (r_{n+1}) + \gamma d_{n+1}^{\gamma-1} \bar{Q}^g(\tau_n) \vec{\nabla} \bar{r}_{n+1} : \frac{\partial}{\partial d_{n+1}} (\vec{\nabla} \bar{r}_{n+1}) \\
 &\quad - \bar{H}(\tau_n) + \frac{1}{2} \gamma (\gamma-1) d_{n+1}^{\gamma-2} Q(\tau_n) {r_{n+1}}^2 + \frac{1}{2} \gamma (\gamma-1) d_{n+1}^{\gamma-2} \bar{Q}(\tau_n) ({r_{n+1}} - \bar{r}_{n+1})^2 \\
 &\quad - \frac{1}{4\sqrt{(1-d_{n+1})^3}} [(\tau_n - \tau_0) P(\tau_n) + (\tau_n - \bar{\tau}_n) \bar{P}(\tau_n)] : \langle \underline{\varepsilon}_{n+1}^e \rangle_+ \\
 &\quad - \frac{h^2}{4\sqrt{(1-hd_{n+1})^3}} [(\tau_n - \tau_0) P(\tau_n) + (\tau_n - \bar{\tau}_n) \bar{P}(\tau_n)] : \langle \underline{\varepsilon}_{n+1}^e \rangle_- \tag{II.393}
 \end{aligned}$$

and

$$\begin{aligned}
 \frac{\partial \underline{\varepsilon}_{n+1}^e}{\partial d_{n+1}} &= -\frac{\Delta \lambda_{vp}}{2\sqrt{(1-d_{n+1})^3}} n_{n+1}^f \\
 \frac{\partial r_{n+1}}{\partial d_{n+1}} &= \left(1 - e^{-\Delta \lambda_{vp} b(\tau_n) \left(1 + \frac{\bar{Q}(\tau_n)}{Q(\tau_n)} \right)} \right) \frac{\gamma d_{n+1}^{\gamma-1} Q(\tau_n)}{2b(\tau_n) \sqrt{(1-d_{n+1}^\gamma)^3} (Q(\tau_n) + \bar{Q}(\tau_n))} \\
 \frac{\partial \underline{\alpha}_{n+1}}{\partial d_{n+1}} &= \left(1 - e^{-\Delta \lambda_{vp} a(\tau_n) \left(1 + \frac{\bar{C}(\tau_n)}{C(\tau_n)} \right)} \right) \frac{C(\tau_n)}{2a(\tau_n) \sqrt{(1-d_{n+1})^3} (C(\tau_n) + \bar{C}(\tau_n))} n_{n+1}^f \tag{II.394}
 \end{aligned}$$

VII.5.1.2.4 Coefficients of state variables for the normal direction \underline{n}_f

The partial derivatives of state variables with respect to the normal direction are given by:

$$\begin{aligned}
 \frac{\partial \underline{\sigma}_{n+1}}{\partial \underline{n}_{n+1}^f} &= (1 - d_{n+1}) \underline{\Lambda}(\underline{T}_n) : \frac{\partial}{\partial \underline{n}_{n+1}^f} (\underline{\varepsilon}_{n+1}^e) \\
 \frac{\partial R_{n+1}}{\partial \underline{n}_{n+1}^f} &= (1 - d_{n+1}^\gamma) (Q(\underline{T}_n) + \check{Q}(\underline{T}_n)) \frac{\partial}{\partial \underline{n}_{n+1}^f} (r_{n+1}) \\
 \frac{\partial X_{n+1}}{\partial \underline{n}_{n+1}^f} &= (1 - d_{n+1}) (C(\underline{T}_n) + \check{C}(\underline{T}_n)) \frac{\partial}{\partial \underline{n}_{n+1}^f} (\alpha_{n+1}) \\
 \frac{\partial \sigma_{n+1}^{vp}}{\partial \underline{n}_{n+1}^f} &= 0 \\
 \frac{\partial Y_{n+1}}{\partial \underline{n}_{n+1}^f} &= \left[\begin{array}{l} \left(\underline{\Lambda}(\underline{T}_n) : \langle \underline{\varepsilon}_{n+1}^e \rangle_+ \right) - \frac{1}{2\sqrt{1-d_{n+1}}} \left[(\underline{T}_n - \underline{T}_0) P(\underline{T}_n) + (\underline{T}_n - \check{\underline{T}}_n) \check{P}(\underline{T}_n) \right] \\ + h \left(\underline{\Lambda}(\underline{T}_n) : \langle \underline{\varepsilon}_{n+1}^e \rangle_- \right) - \frac{h}{2\sqrt{1-hd_{n+1}}} \left[(\underline{T}_n - \underline{T}_0) P(\underline{T}_n) + (\underline{T}_n - \check{\underline{T}}_n) \check{P}(\underline{T}_n) \right] \end{array} \right] : \frac{\partial}{\partial \underline{n}_f} \langle \underline{\varepsilon}_{n+1}^e \rangle \\
 &\quad + \left[(C(\underline{T}_n) + \check{C}(\underline{T}_n)) \alpha_{n+1} - \check{C}(\underline{T}_n) \check{\alpha}_{n+1} \right] : \frac{\partial}{\partial \underline{n}_f} (\alpha_{n+1}) + \check{C}^g(\underline{T}_n) \vec{\nabla} \check{\alpha}_{n+1} : \frac{\partial}{\partial \underline{n}_f} (\vec{\nabla} \check{\alpha}_{n+1}) \\
 &\quad + \gamma d_{n+1}^{\gamma-1} \left[(Q(\underline{T}_n) + \check{Q}(\underline{T}_n)) r_{n+1} - \check{Q}(\underline{T}_n) \check{r}_{n+1} \right] \frac{\partial}{\partial \underline{n}_f} (r_{n+1}) + \gamma d_{n+1}^{\gamma-1} \check{Q}^g(\underline{T}_n) \vec{\nabla} \check{r}_{n+1} : \frac{\partial}{\partial \underline{n}_f} (\vec{\nabla} \check{r}_{n+1}) \\
 &\quad + \gamma d_{n+1}^{\gamma-1} \left[(Q(\underline{T}_n) + \check{Q}(\underline{T}_n)) r_{n+1} - \check{Q}(\underline{T}_n) \check{r}_{n+1} \right] \frac{\partial}{\partial \underline{n}_f} (r_{n+1}) + \gamma d_{n+1}^{\gamma-1} \check{Q}^g(\underline{T}_n) \vec{\nabla} \check{r}_{n+1} : \frac{\partial}{\partial \underline{n}_f} (\vec{\nabla} \check{r}_{n+1})
 \end{aligned} \tag{II.395}$$

and

$$\begin{aligned}
 \frac{\partial \underline{\varepsilon}_{n+1}^e}{\partial \underline{n}_{n+1}^f} &= - \frac{\Delta \lambda_{vp}}{\sqrt{1-d_{n+1}}} \frac{1}{2} \\
 \frac{\partial r_{n+1}}{\partial \underline{n}_{n+1}^f} &= 0 \\
 \frac{\partial \alpha_{n+1}}{\partial \underline{n}_{n+1}^f} &= \left(1 - e^{-\Delta \lambda_{vp} a(\underline{T}_n) \left(1 + \frac{C(\underline{T}_n)}{C(\underline{T}_n)} \right)} \right) \frac{C(\underline{T}_n)}{a \sqrt{1-d_{n+1}} (C(\underline{T}_n) + \check{C}(\underline{T}_n))} \frac{1}{2}
 \end{aligned} \tag{II.396}$$

VII.6 Appendices

VII.6.1 Appendix I – Q4r24 element for thick shell

In order to consider the plate theory and thick shell or the theory of Mindlin, the Q4r24 element is developed, which is a bilinear quadrangle and has six degrees of freedom each node including three translations and three rotations in the global coordinates. The planar translations u and v are used to define the membrane effects, the normal translation w and the rotations θ_x and θ_y serve the formation of shear effects, as well as the rotations θ_x and θ_y define the bending effects. The sixth dofs θ_z is used to avoid the singularity of the stiffness matrix. The formulations are briefly reviewed based on the previous work of Bassa (2011).

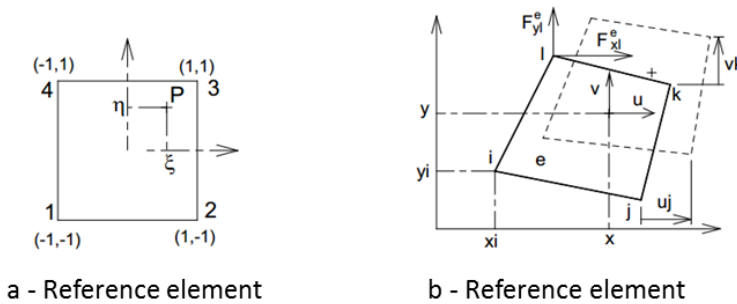


Figure VII-2 The reference element and real element

The shape function of the isoparametric bilinear quadrilateral element is expressed as:

$$N_i = \frac{1}{4}(1 + \xi_i \xi)(1 + \eta_i \eta) \quad (\text{II.397})$$

with the pair of nature coordinates (ξ_i, η_i) take the values $(-1, -1)$, $(1, -1)$, $(1, 1)$ and $(-1, 1)$.

Consequently, the Jacobian matrix is obtained:

$$[J] = \begin{bmatrix} x_{,\xi} & y_{,\xi} \\ x_{,\eta} & y_{,\eta} \end{bmatrix} = \begin{bmatrix} N_{i,\xi} & 0 \\ N_{i,\eta} & 0 \end{bmatrix} \begin{bmatrix} x_i^e & y_i^e \end{bmatrix} \quad (\text{II.398})$$

with x_i^e and y_i^e are the vectors of nodal coordinates in the real element respectively.

VII.6.1.1 Membrane

The membrane strain at the nature coordinate (ξ, η) of the element is given by:

$$\{\varepsilon^m\} = \begin{bmatrix} \varepsilon_{xx} \\ \varepsilon_{yy} \\ 2\varepsilon_{xy} \end{bmatrix} = \begin{bmatrix} 1 & 0 & 0 & 0 \\ 0 & 0 & 0 & 1 \\ 0 & 1 & 1 & 0 \end{bmatrix} \begin{bmatrix} [J]^{-1} & 0 \\ 0 & [J]^{-1} \end{bmatrix} \begin{bmatrix} N_{i,\xi} & 0 \\ N_{i,\eta} & 0 \\ 0 & N_{i,\xi} \\ 0 & N_{i,\eta} \end{bmatrix} \begin{bmatrix} u_i^e \\ v_i^e \end{bmatrix} = [B^m] \{u_n^e\} \quad (\text{II.399})$$

where, $[B^m]$ is the B matrix of the membrane and $\{u_n^e\}$ is the vector of the nodal displacements.

Considering the tangent operator $[D]$, and using the principle of virtual power, the elemental stiffness matrix of membrane part becomes:

$$[K_e^m] = \iiint_{V^e} [B^m]^T [D^m] [B^m] dV = \int_{-1}^1 \int_{-1}^1 [B^m]^T [D^m] [B^m] \det[J] d\xi d\eta = \sum_{q=1}^4 [H^m(\xi_q, \eta_q)] \varpi_q \quad (\text{II.400})$$

where, $[D^m] = \int_{-h/2}^{h/2} [D] dz$ and

$$[H^m(\xi, \eta)] = [B^m]^T [D^m] [B^m] \det[J]; \quad \varpi_q = 1; \quad \xi_q = \pm 1/\sqrt{3}; \quad \eta_q = \pm 1/\sqrt{3} \quad (\text{II.401})$$

VII.6.1.2 Bending

For the bending, the rotations θ_x and θ_y are used to evaluate the curvatures of bending:

$$\{\kappa\} = \begin{Bmatrix} \theta_{y,x} \\ -\theta_{x,y} \\ \theta_{y,y} - \theta_{x,x} \end{Bmatrix} = \begin{bmatrix} 0 & 0 & 1 & 0 \\ 0 & -1 & 0 & 0 \\ -1 & 0 & 0 & 1 \end{bmatrix} \begin{bmatrix} [J]^{-1} & 0 \\ 0 & [J]^{-1} \end{bmatrix} \begin{Bmatrix} N_{i,\xi} & 0 \\ N_{i,\eta} & 0 \\ 0 & N_{i,\xi} \\ 0 & N_{i,\eta} \end{Bmatrix} \begin{Bmatrix} \theta_{xi}^e \\ \theta_{yi}^e \end{Bmatrix} = [B^b] \{\theta_n^e\} \quad (\text{II.402})$$

where, the B matrix of bending $[B^b]$ and $\{\theta_n^e\}$ is the vector of the nodal rotations.

The elemental stiffness matrix of the bending is obtained with the help of tangent operator $[D]$ as well as the principle of virtual power:

$$[K^b] = \iiint_{V^e} [B^b]^T [D^b] [B^b] dV = \int_{-1}^1 \int_{-1}^1 [B^b]^T [D^b] [B^b] \det[J] d\xi d\eta = \sum_{q=1}^4 [H^b(\xi_q, \eta_q)] \varpi_q \quad (\text{II.403})$$

where, $[D^b] = \int_{-h/2}^{h/2} [D] z^2 dz$ and

$$[H^b(\xi, \eta)] = [B^b]^T [D^b] [B^b] \det[J]; \quad \varpi_q = 1; \quad \xi_q = \pm 1/\sqrt{3}; \quad \eta_q = \pm 1/\sqrt{3} \quad (\text{II.404})$$

VII.6.1.3 Transverse shear

The deformations of transverse shear are expressed by:

$$\{\gamma\} = \begin{Bmatrix} \frac{\partial \omega}{\partial x} + \theta_y \\ \frac{\partial \omega}{\partial y} - \theta_x \end{Bmatrix} = \begin{bmatrix} 1 & 0 & 0 & 1 \\ 0 & 1 & -1 & 0 \end{bmatrix} \begin{bmatrix} [J]^{-1} & [1] \\ [1] & [1] \end{bmatrix} \begin{Bmatrix} N_{i,\xi} & 0 & 0 \\ N_{i,\eta} & 0 & 0 \\ 0 & N_i & 0 \\ 0 & 0 & N_i \end{Bmatrix} \begin{Bmatrix} w_i^e \\ \theta_{xi}^e \\ \theta_{yi}^e \end{Bmatrix} = [B^s] \{w_n^e\} \quad (\text{II.405})$$

where, the B matrix of transverse shear $[B^s]$ and $\{w_n^e\}$ is the vector of the nodal displacement and rotations.

The stiffness matrix of the transverse shear can be expressed as:

$$[K^s] = \iiint_{V^e} [B^s]^T [D^s] [B^s] dV = \int_{-1}^1 \int_{-1}^1 [B^s]^T [D^s] [B^s] \det[J] d\xi d\eta = \sum_{q=1}^4 [H^s(\xi_q, \eta_q)] \varpi_q \quad (\text{II.406})$$

where,

$$\begin{aligned} [H^s(\xi, \eta)] &= [B^s]^T [D^s] [B^s] \det[J]; \quad \varpi_q = 1; \quad \xi_q = \pm 1/\sqrt{3}; \quad \eta_q = \pm 1/\sqrt{3} \\ [D^s] &= \frac{E}{2(1+\nu)} \begin{bmatrix} 5/6 & \\ & 5/6 \end{bmatrix} \end{aligned} \quad (\text{II.407})$$

It is worth noting that the full integrations are adopted for the membrane, bending and transverse shear, which usually causes incorrect results when the thickness of the plate becomes relative small compared with other two dimensions, the so-called shear locking problem. The selective integration with full integration for membrane and bending as well as reduced integration for transvers shear, or the fully reduced integration with hourglass control techniques are often chosen to avoid the shear locking problems.

VII.6.2 Appendix II – The standard hexahedral element

The standard 1st order solid element is a hexahedral, eight-node and isoparametric element with linear interpolation. It is provided with eight (full) integration points in the local coordinate frame. Figure VII-3 shows the reference geometry of the element, the nodal coordinates, as well as the geometry of the real element. The coordinates x_i , $i = 1, 2, 3$, of a point in the element are related to the nodal coordinates x_{ii} using the classical linear isoparametric shape functions N_i ($i = 1, \dots, 8$) and the relations:

$$x_i = x_{ii} N_i(\xi, \eta, \zeta) = \sum_{l=1}^8 x_{il} N_l(\xi, \eta, \zeta) \quad (\text{II.408})$$

where, the interpolation functions can be expressed as $N_i = \frac{1}{8} (1 + \xi \xi_i)(1 + \eta \eta_i)(1 + \zeta \zeta_i)$.

VII.6.2.1 Strain-displacement relationships

The interpolation of the displacement field u_i inside the element in terms of the nodal displacements u_{ii} is similar:

$$u_i = u_{ii} N_i(\xi, \eta, \zeta) \quad (\text{II.409})$$

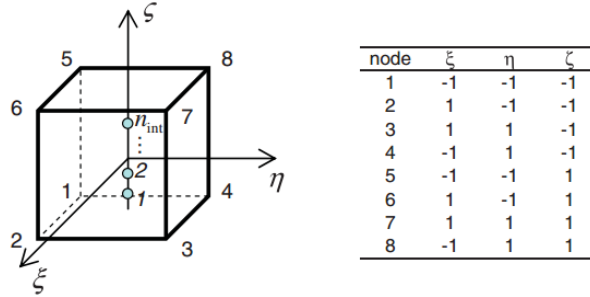


Figure VII-3 The reference and real hexahedral element

The displacement field interpolation allows the strain field to be related to the nodal displacements. The linear part of the strain tensor is given by:

$$\varepsilon_{ij} = \frac{1}{2}(u_{i,j} + u_{j,i}) = \frac{1}{2}(u_\eta N_{i,j} + u_\eta N_{j,i}) \quad (\text{II.410})$$

or in matrix form, the B matrix becomes:

$$[B] = [C][J_{\text{Inv}}][N_d] \quad (\text{II.411})$$

where,

$$[C] = \begin{bmatrix} 1 & & & & & & \\ & \ddots & & & & & \\ & & 1 & & & & \\ & & & \ddots & & & \\ & & & & 1 & & \\ & & & & & \ddots & \\ & & & & & & 1 \end{bmatrix} \quad [J_{\text{Inv}}] = \begin{bmatrix} [J]^{-1} & & & \\ & [J]^{-1} & & \\ & & [J]^{-1} & \\ & & & [J]^{-1} \end{bmatrix} \quad [N_d] = \begin{bmatrix} N_{I,\xi_1} & & & \\ & \ddots & & \\ & & N_{I,\xi_2} & \\ & & & \ddots \\ & & & & N_{I,\xi_I} \end{bmatrix}$$

(II.412)

and , here we introduce the b_i vectors from Hallquist (1983), defined as:

$$b_i = N_{I,i} = \frac{\partial N_I}{\partial x_i} \quad i=1,2,3 \quad (\text{II.413})$$

VII.6.2.2 The elastic constitutive model

For the linear isotropic elasticity, the elastic moduli tensor is given by:

$$[D] = \begin{bmatrix} \bar{\lambda} + 2\mu & \bar{\lambda} & \bar{\lambda} & & & \\ \bar{\lambda} & \bar{\lambda} + 2\mu & \bar{\lambda} & & & \\ \bar{\lambda} & \bar{\lambda} & \bar{\lambda} + 2\mu & & & \\ & & & \mu & & \\ & & & & \mu & \\ & & & & & \mu \end{bmatrix} \quad (\text{II.414})$$

where, $\bar{\lambda}$ and μ are Lame constant.

VII.6.2.3 Stiffness matrix and internal forces

Using the principle of virtual power and the discretization of strain field Eq.(II.410), the stiffness matrix and the internal forces are defined as:

$$\begin{aligned}
 [K_e] &= \iiint [B]^T [D][B] dv = \int_{-1}^1 \int_{-1}^1 \int_{-1}^1 [B]^T [D][B] \det[J] d\xi d\eta d\zeta \\
 &\approx \sum_{q=1}^{n_q} \sum_{p=1}^{n_p} \sum_{t=1}^{n_t} [B(\xi_q, \eta_p, \zeta_t)]^T [D][B(\xi_q, \eta_p, \zeta_t)] \det[J(\xi_q, \eta_p, \zeta_t)] \varpi_q \varpi_p \varpi_t \\
 \{f^{\text{int}}\} &= \iiint [B]^T \{\sigma\} dv = \int_{-1}^1 \int_{-1}^1 \int_{-1}^1 [B]^T \{\sigma\} \det[J] d\xi d\eta d\zeta \\
 &\approx \sum_{q=1}^{n_q} \sum_{p=1}^{n_p} \sum_{t=1}^{n_t} [B(\xi_q, \eta_p, \zeta_t)]^T \{\sigma(\xi_q, \eta_p, \zeta_t)\} \det[J(\xi_q, \eta_p, \zeta_t)] \varpi_q \varpi_p \varpi_t
 \end{aligned} \tag{II.415}$$

VIII. Parametric study of the model

As presented in Chapter VI, the micromorphic constitutive equations derived from the framework of the irreversible thermodynamics and the generalized principle of virtual power, are characterized by a group of specific material parameters which need to be determined from the experimental data. However, before doing the identifications, the parametric study of the micromorphic model should be performed and the results carefully analyzed to well understand the predictive possibilities of the proposed micromorphic fully coupled constitutive equations. The detailed study of the effect of the material parameters entering the fully coupled constitutive equations is well discussed in the literature (Saanouni, 2012). Furthermore, here we will only focus on the parametric study involving in the local damage parameters, the micromorphic moduli and the thermal effects.

VIII.1 Effect of the local damage parameters

Considering the material property of parametric study: $E = 208.0 \text{ GPa}$, $\nu = 0.3$, $\sigma_y = 809.0 \text{ MPa}$, $Q = 4.0 \text{ GPa}$, $b = 13.0$, $C = 32.0 \text{ GPa}$ and $a = 150.0$, a single integration point is chosen to undergo the uniaxial tension state with initial damage parameters: $S = 3.5$, $s = 1.2$, $\beta = 2.0$, $Y_0 = 0.0$ and $\gamma = 4.0$ which yields the plastic strain of final fracture $\varepsilon_f^p \approx 25.1\%$ and maximum equivalent stress $\sigma_m = 1196.3 \text{ MPa}$.

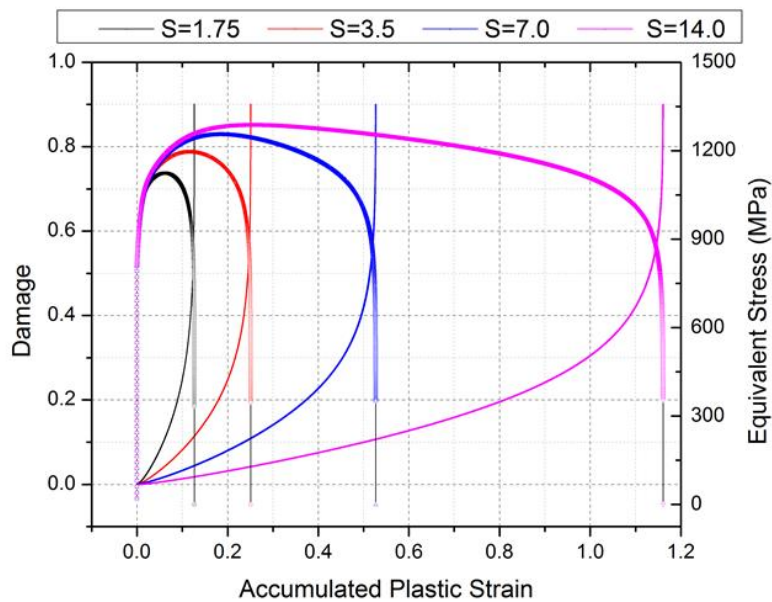


Fig. VIII-1 Influence of the parameter S on the evolution of damage and equivalent stress

In the following, only one damage parameter varies while keeping the other parameters fixed at each analysis.

Fig. VIII-1 shows the effect of the parameter S by taking four different values $S=1.75$, $S=3.5$, $S=7.0$ and $S=14.0$, on the damage evolution curves as well as the stress-plastic strain curves. As expected, the greater S the smaller damage rate is, the greater maximum equivalent stress is and later final fracture occurs: $\varepsilon_f^p \approx 12.7\%$ and $\sigma_m = 1123.7 \text{ MPa}$ for $S=1.75$, $\varepsilon_f^p \approx 52.7\%$ and $\sigma_m = 1253.9 \text{ MPa}$ for $S=7.0$, $\varepsilon_f^p \approx 116.1\%$ and $\sigma_m = 1289.8 \text{ MPa}$ for $S=14.0$. Note that the variation of S in a ratio of 2 causes a variation of the material ductility (plastic strain at fracture) substantially in the same ratio. The increase of the maximum stress results from the same effect of the damage on the other internal stresses.

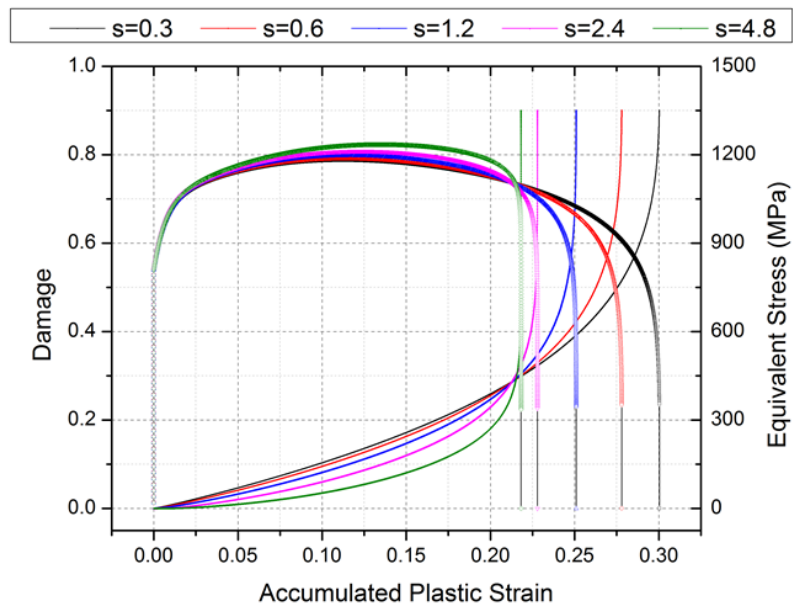


Fig. VIII-2 Influence of the parameter s on the evolution of damage and equivalent stress

In Fig. VIII-2, five different values of damage parameter $s=0.3$, $s=0.6$, $s=1.2$, $s=2.4$ and $s=4.8$ are presented to examine its effect on the damage evolution and stress-strain curves. It seems clearly that the parameter s governs the nonlinearity of the damage evolution: the higher value of s , the earlier final fracture time, the smaller plastic strain and the more brittle behavior of the material. Considering the formula of damage evolution in Eq.(II.98), when the parameter s approaches to zero, the damage rate will become approximately proportional to the plastic multiplier (effective plastic strain rate) $\dot{d} = \dot{\lambda}/(1-d)^\beta$, if the effect of the parameter β representing the nonlinearity of damage is negligible. As we can see this from Fig. VIII-2, focusing on the plastic strain smaller than 20%, it is worth noting that the differences of the damage become smaller and smaller as the decrease of the parameter s in a ratio of 2. Let us imagine that there would be a limit damage curve, which is in theoretically when $s=0.0$, however, for practical purpose, the damage evolution curves even for the parameter $s=0.3$ and $s=0.6$ are barely distinguishable. And in such case, this nonlinear relationship with the plastic strain is caused by the parameter β .

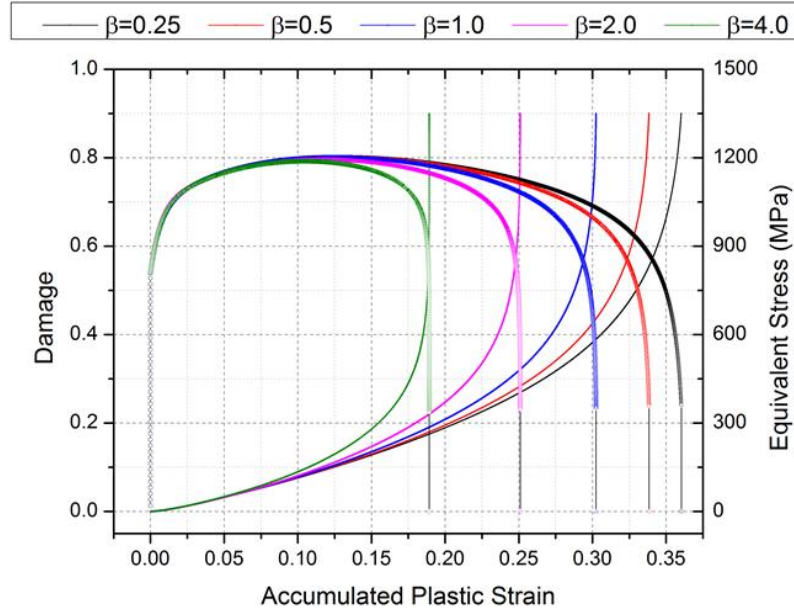


Fig. VIII-3 Influence of the parameter β on the evolution of damage and equivalent stress

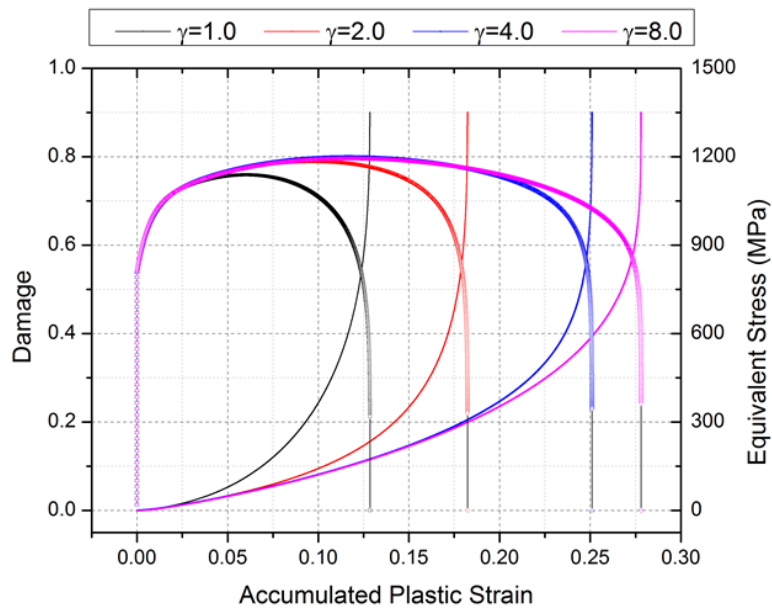


Fig. VIII-4 Influence of the parameter γ on the evolution of damage and equivalent stress

The influence of the parameter β taking five different values on the response of the model is illustrated in Fig. VIII-3 regarding to the damage evolution and strain-stress curves. We can see that the bigger value of the parameter β yields the earlier final fracture time, the smaller plastic strain and the larger damage rate. Meanwhile, it should be noticed that this effect is similar to the effect of the parameter S which only delays or accelerate the damage growth without modifying the shape of the damage evolution curves.

PART II CHAPTER VIII PARAMETRIC STUDY

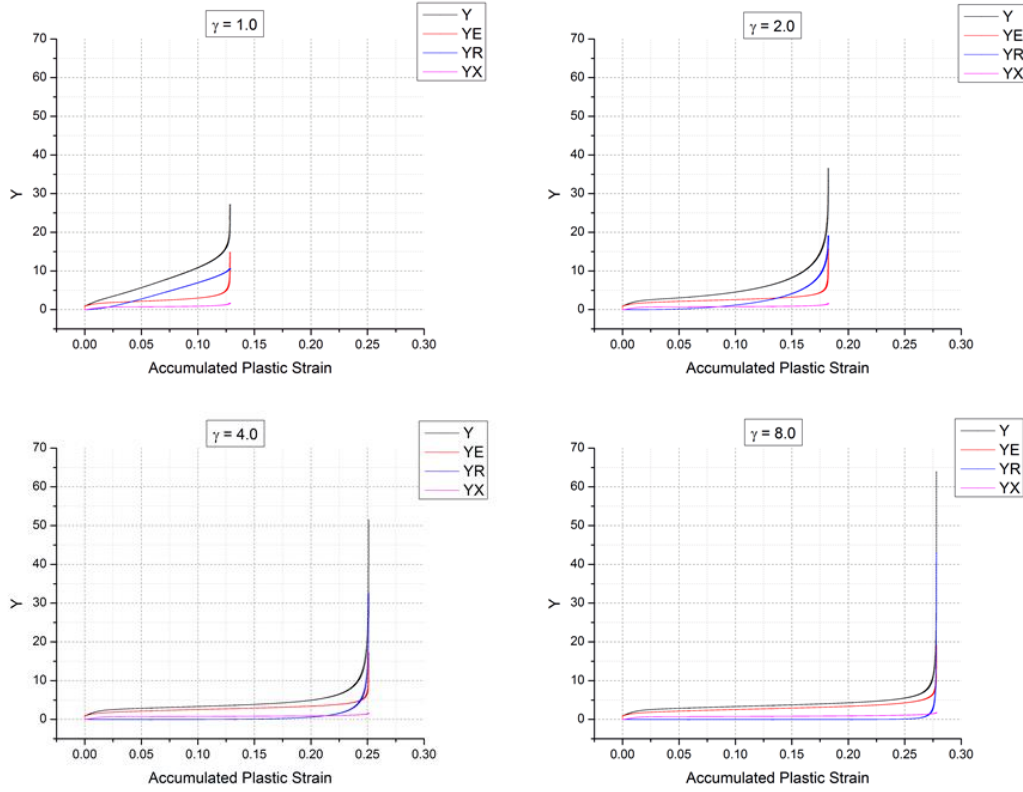


Fig. VIII-5 Influence of parameter γ on the evolution of damage energy release rate Y

In Fig. VIII-4, the effect the parameter γ indirectly affects the damage growth through the isotropic hardening is examined with four different values $\gamma=1.0$, $\gamma=2.0$, $\gamma=4.0$ and $\gamma=8.0$. It is clear that the greater values of γ results the latter final fracture time and the larger plastic strain, while without changing the shape of the damage evolution curves. Considering the formula of Y_R in Eq.(II.34), we can see that the higher value of γ provides a smaller value of Y_R for damage $d \ll 1$, and a larger Y_R when damage approaches to the criterion. In Fig. VIII-5, it is clear that the contribution from the isotropic hardening to the damage energy release rate grows rapidly and becomes dominant one when $\gamma=1.0$ and $\gamma=2.0$. On the other side, the damage energy release rate from isotropic hardening evolves slowly and behavior a sharply increase when the damage approaches its critical value for $\gamma=4.0$ and $\gamma=8.0$.

	$S=3.5$	$s=1.2$	$\beta=2.0$	$\gamma=4.0$
$\varepsilon_{f0.5x}^p$	0.127	0.278	0.302	0.182
$\varepsilon_{f1.0x}^p / \varepsilon_{f0.5x}^p$	1.976	0.903	0.831	1.379
$\varepsilon_{f2.0x}^p$	0.527	0.228	0.189	0.278
$\varepsilon_{f2.0x}^p / \varepsilon_{f1.0x}^p$	2.099	0.908	0.753	1.108

Table VIII-1 Summary of the plastic strain at final fracture for different damage parameters

In Table VIII-1, it summarizes the plastic strain at the final fracture for different times of the initial values of the damage parameters. We may notice that the increase of the parameters S and s in the ratio of 2 approximately provides an increase of the final fracture plastic strain with roughly proportional coefficients 2.0 and 0.9 respectively.

In summary, if we expect latter final fracture time or larger plastic strain, we should increase the parameters S and γ or decrease the parameters S and β , and vice versa. However, it is worth noting that it is only the parameter S which governs the more brittle or more ductile material behavior in the proposed model.

VIII.2 The viscoplastic effects

As described in Section VI.3.4.2.2, the Norton-Hoff viscoplastic flow is defined to govern the evolution equations and yields the Norton-Hoff type of viscous stress. Referencing the literature (Saanouni, 2012), the hyperbolic sine type of viscous stress resulting from the hyperbolic cosine viscous potential could be an alternative:

$$\sigma^{vp} = \begin{cases} K(\dot{\lambda}_{vp})^{1/m} & \text{Norton-hoff} \\ K_1 \operatorname{argsinh}(\dot{\lambda}_{vp}/K_2) & \text{Hyperbolic Sine} \end{cases} \quad (\text{II.416})$$

Considering the formula $\operatorname{argsinh}(x) = \ln(x + \sqrt{1+x^2})$, leads to the hyperbolic sine type viscous stress:

$$\sigma^{vp} = K_1 \left[\ln\left(\dot{\lambda}_{vp} + \sqrt{(K_2)^2 + (\dot{\lambda}_{vp})^2}\right) - \ln(K_2) \right] \quad (\text{II.417})$$

If the coefficient $K_2 = 1.0$, the hyperbolic sine type viscous stress becomes to:

$$\sigma^{vp} = K_1 \ln\left(\dot{\lambda}_{vp} + \sqrt{1 + (\dot{\lambda}_{vp})^2}\right) \quad (\text{II.418})$$

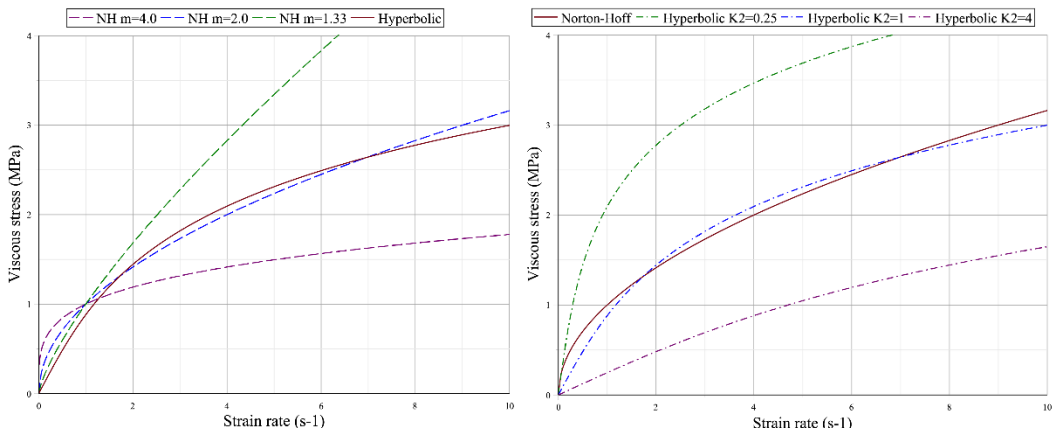


Fig. VIII-6 The viscous stress of the Norton-Hoff and Hyperbolic Sine

Fig. VIII-6 presents the Norton-Hoff viscous stress $(\dot{\lambda}_{vp})^{1/m}$ and the Hyperbolic sine type viscous stress $\ln\left(\dot{\lambda}_{vp} + \sqrt{(K_2)^2 + (\dot{\lambda}_{vp})^2}\right) - \ln(K_2)$ with three different values of parameters m and K_2 . In Fig. VIII-6(a), it shows the Norton-Hoff viscous stress taking three different values of the parameter $m = 4.0$, $m = 2.0$ and $m = 1.33$ as well as the hyperbolic sine type taking $K_2 = 1.0$. Note that the types of the Norton-Hoff and the Hyperbolic Sine are nearly equivalent when the parameters take $m = 2.0$ and $K_2 = 1.0$ in the range of the strain rate from 0.0s^{-1} to 10.0s^{-1} which approximately contains most of the forming processes. As the increase of the parameter m , the Norton-Hoff viscous stress grows rapidly for strain rate over than 1.0s^{-1} ; on the other hand, the viscostress evolves sharply for strain rate smaller than 1.0s^{-1} and slowly for high strain rate over than 1.0s^{-1} , as the decrease of the parameter m . In Fig. VIII-6(b), three choices of the parameter $K_2 = 0.25$, $K_2 = 1.0$ and $K_2 = 4.0$ are plotted as well as the Norton-Hoff curve taking $m = 2.0$. It is clear that in the range of strain rate $[0, 10]\text{s}^{-1}$, for high values of K_2 , the viscostress of the Hyperbolic sine becomes approximately linear to the strain rate; for small K_2 , the responses of the viscostress vary rapidly and smooth. It is worth noting the differences of the viscous stress for strain rate smaller than 1.0s^{-1} , not like the Norton-Hoff type varying only on the top the hyperbolic curve of $K_2 = 1.0$.

VIII.3 Effect of the micromorphic moduli

The uniaxial tensile test using the micromorphic damage model is chosen to make parametric study with the geometric information given in Section IX.1. Considering the simplified balance equation of the micromorphic damage in Eq.(II.111), the three independent variables: the micromorphic modulus \check{H} , the internal length l_d (or the micromorphic gradient modulus \check{H}^g) and the micromorphic density scalar ζ_d are performed parametric study.

VIII.3.1 Effect of the micromorphic damage moduli

As shown in Fig. VIII-7, the consistent force-displacement curves are obtained for two mesh sizes: 0.4mm and 0.8mm by taking the micromorphic damage parameters: $\check{H} = 37.5\text{N}\cdot\text{mm}^{-2}$, $\zeta_d = 1.0$, the internal length $l_d = 1.0\text{mm}$ and $S = 3.0$.

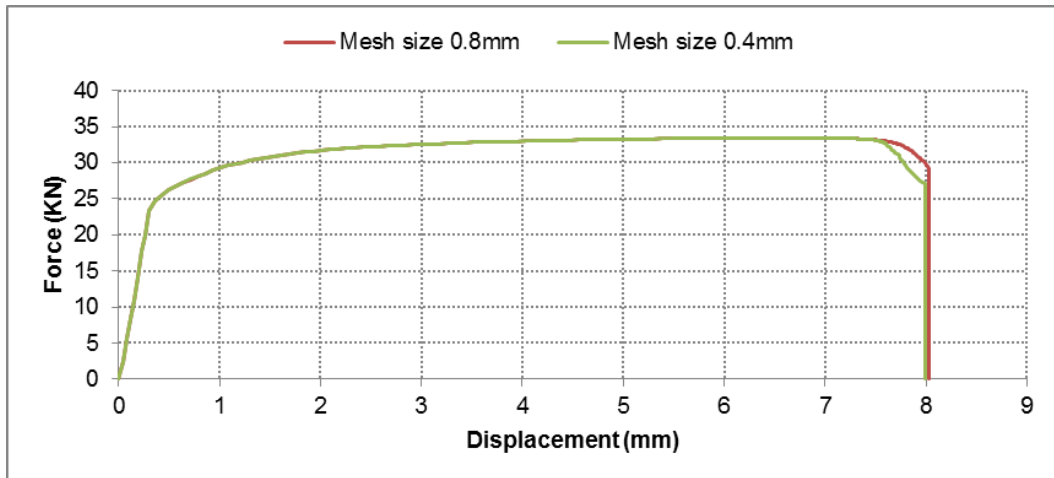


Fig. VIII-7 Consistent Force-displacement curves

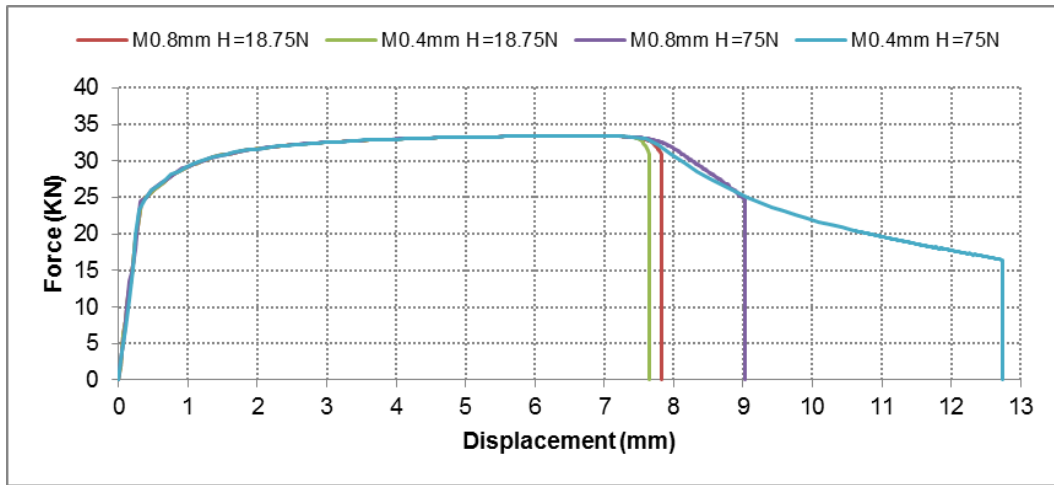


Fig. VIII-8 Force-Displacement curves for different values of micromorphic parameter \bar{H}

1). Variation of the micromorphic modulus \bar{H}

Fig. VIII-8 shows two groups of the force-displacement curves taking the parameter $0.5\bar{H}$ and $2.0\bar{H}$ while maintaining the internal length $l_d = 1.0\text{mm}$ for two mesh sizes 0.4mm and 0.8mm.

Clearly, for the parameter $\bar{H} = 18.75\text{N}\cdot\text{mm}^{-2}$, the nonlocal effect induced by the micromorphic damage is insufficient to converge the difference of the system responses between the two mesh sizes; for the parameter $\bar{H} = 75\text{N}\cdot\text{mm}^{-2}$, the nonlocal effect to the smaller mesh size 0.4mm is too excessive yielding the final fracture around 12.7mm while the final fracture displacement of mesh size 0.8mm remains close to 9.0mm.

2). Effects of the internal length l_d

In Fig. VIII-9, it presents the system responses of different values of the internal length: $\sqrt{0.1}\text{mm}$ and $\sqrt{10}\text{mm}$ for two mesh sizes respectively, while the micromorphic damage modulus \bar{H} remains $37.5\text{N}\cdot\text{mm}^{-2}$. For the case of small internal length $\sqrt{0.1}\text{mm}$, the force-displacement

curves of mesh sizes 0.4mm and 0.8mm are similar to the responses of the model which take the micromorphic damage parameter $\check{H}=18.75N\cdot mm^{-2}$ in Fig. VIII-8. In such cases, the micromorphic damage effects induced by the small internal length or the slight micromorphic damage parameter from Eq.(II.111), are too small to negligible which yields the system responses close to the local damage model. For high value of the internal length $\sqrt{10}mm$, the final fracture displacement of mesh size 0.8mm approaches to 10.0mm, while the response of mesh size 0.4mm clearly shows that the micromorphic damage effect is excessively strong and yields no appearance of rupture although the displacement reaches up to 13.0mm.

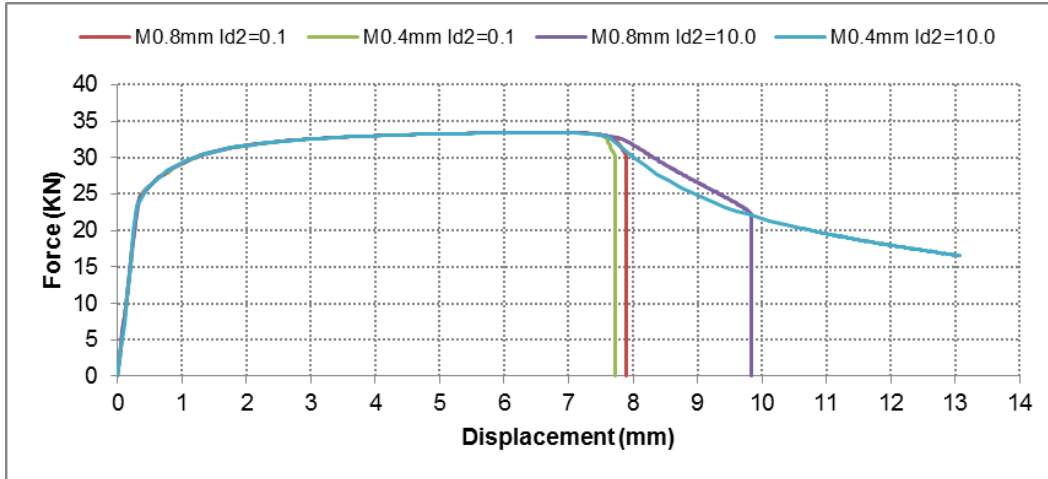


Fig. VIII-9 Force-Displacement curves of different values of internal length l_d

3). Different micromorphic density scalar ζ_d

Fig. VIII-10 shows the force-displacement responses for three different values of the micromorphic density scalar: 0.01, 1 and 100. It is worth noting that the significant shrinkage of the density scalar yields very small influence on the system responses (about 8.0mm in displacement), while higher values of the micromorphic density result in latter final fracture displacements (around 9.2mm). That can be explained from the reason of that the higher values of micromorphic mass enhances the dynamic effect which results in the relative smaller acceleration of the micromorphic damage and consequently the slower evolution of the damage. For the sake of simplicity, in the next analysis, the micromorphic density scalar is taken as 1.0.

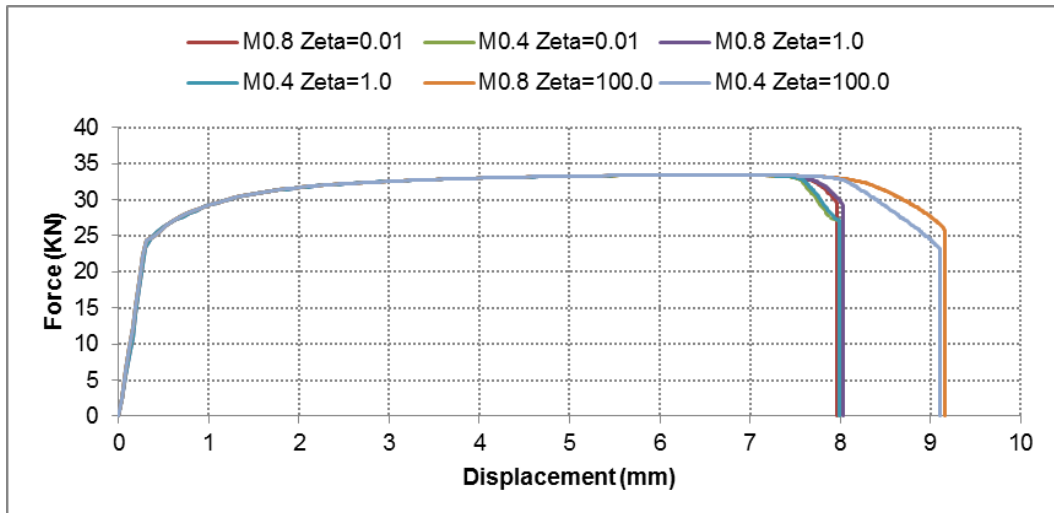


Fig. VIII-10 Force-Displacement curves for different micromorphic damage density scalar

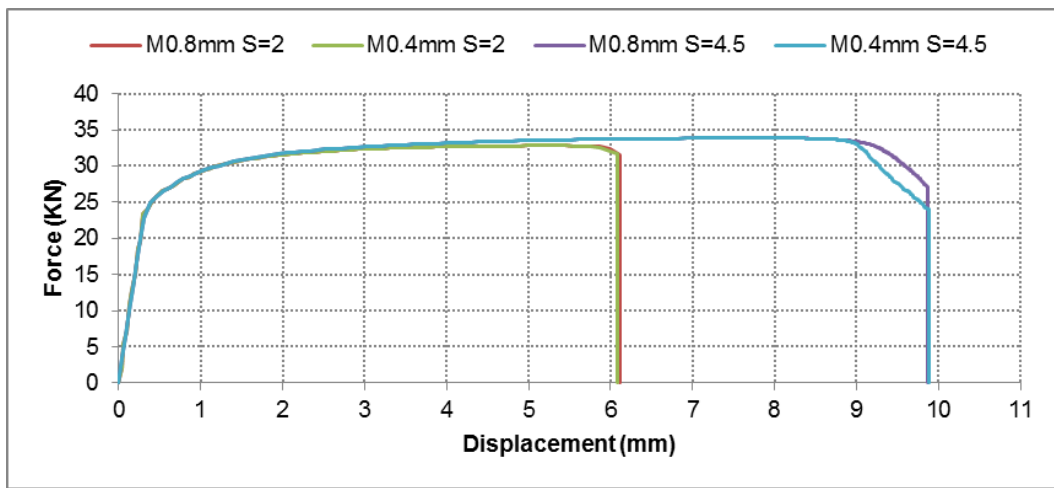


Fig. VIII-11 Force-Displacement curves of different values of local damage parameter S

4). Effects of the local damage parameters

In Fig. VIII-11, it presents the responses of force-displacement curves for two different values of the damage parameter S: 2.0 and 4.5. Clearly, the same tendency that higher value of S yields latter final fracture displacement is observed as in the local damage model. The consistency of the material response or final fracture displacements (around 6.1mm and 9.9mm) is preserved during the variation of the local damage parameter S. However, it should be noticed that the differences are captured in the necking region for high values of S, which is the consequence of the insufficient micromorphic variables to reflect the nonlocal behavior of the material.

Fig. VIII-12 illustrates the force-displacement curves for two different values of the local damage parameter s: 0.6 and 2.4. It is clear that smaller value of s yields earlier final fracture (about 7.5mm in displacement) and higher values of s provides latter final fracture displacement (around 9.1mm). More important is that the variation of the parameter s breaks the consistency property initially obtained with the specified group of local and micromorphic parameters: the smaller value of s

provides insufficient micromorphic effect and the higher value of s yields excessive effect of the micromorphic damage for smaller mesh sizes respectively.

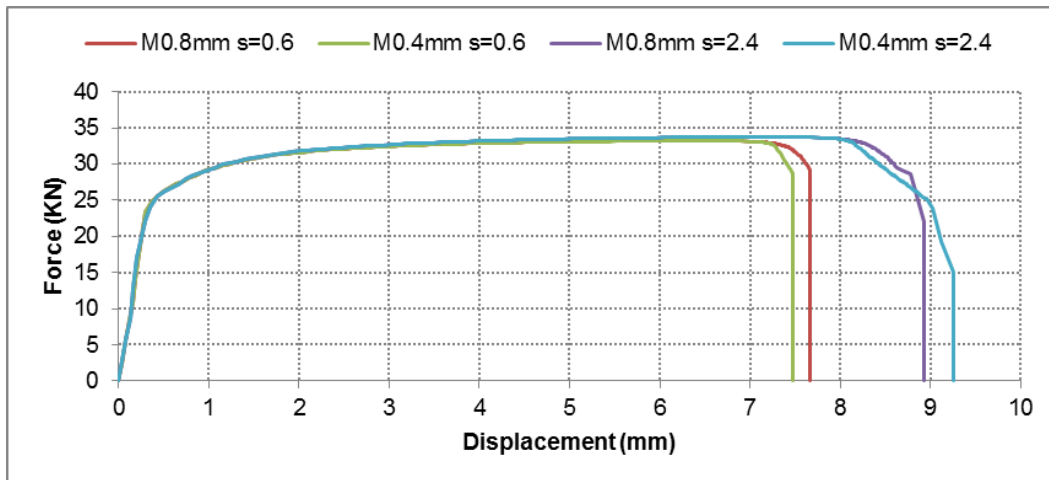


Fig. VIII-12 Force-Displacement curves of variations of local damage parameter s

In Fig. VIII-13, four different force-displacement curves are presented for two mesh sizes (0.4mm and 0.8mm) and two choices of the local damage parameter β : 1.0 and 4.0. As expected, the higher value of β accelerates the evolution of damage and yields earlier final fracture (about 7.5mm), the smaller value of β delays the final fracture displacement (around 8.5mm). Meanwhile, the consistency property loses gradually according to the increase of the parameter β .

It is worth noting that both the high values of the local damage parameter s and β result in smaller final fracture accumulated plastic strain for local damage model as shown in Fig. VIII-2 and Fig. VIII-3, however, in the analysis of the force-displacement curves for micromorphic damage model (in Fig. VIII-12 and Fig. VIII-13), the high value of s provides latter final fracture displacement. That is due to the high value of s suppresses the initial evolution of the damage, which needs more displacement to drive its initial evolution, although it accelerates the overall evolution of damage, as shown in Fig. VIII-2. For the damage parameter β , its high value yields both the faster initial and overall evolution of the damage, and consequently needs smaller displacement to final fracture.

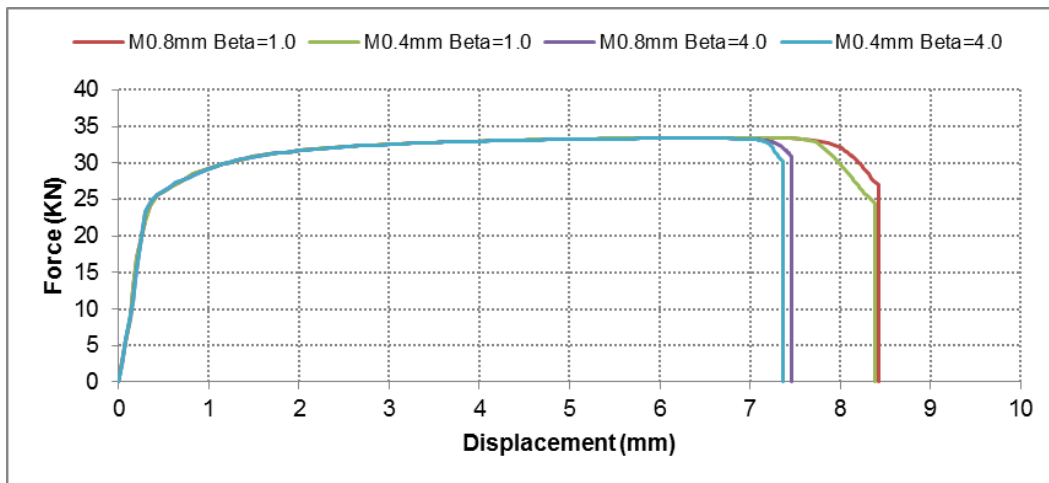


Fig. VIII-13 Force-Displacement curves of different values of local damage parameter β

Fig. VIII-14 represents different force-displacement curves for two mesh sizes (0.4mm and 0.8mm) and two choices of the initial damage energy release rate Y_0 : -0.5 and 0.5. Clearly, the negative value yields smaller final fracture displacement (about 7.1mm) and positive value delays the final fracture (around 9.2mm), meanwhile, both the increase and decrease in the initial damage energy release rate Y_0 lose the consistency of the material's response.

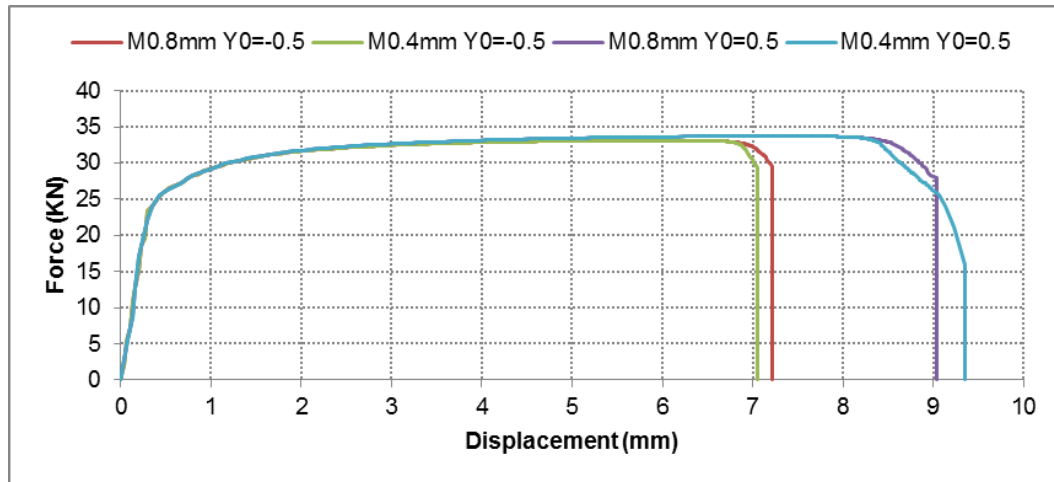


Fig. VIII-14 Force-Displacement curves of different values of the initial damage energy release rate Y_0

VIII.3.2 Effect of the micromorphic isotropic hardening moduli

In this section, the micromorphic isotropic hardening is introduced into the above micromorphic damage model taking the parameters: $\bar{H} = 37.5 \text{ N} \cdot \text{mm}^{-2}$, $\zeta_d = 1.0$, the internal length of micromorphic damage $l_d = 1.0 \text{ mm}$ and $S = 3.5$.

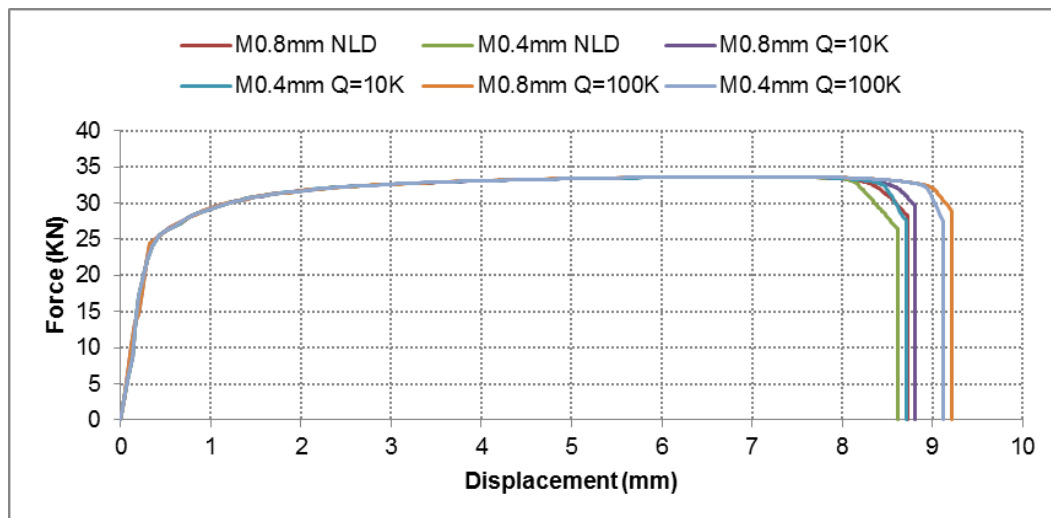


Fig. VIII-15 Force-Displacement curves of different values of the micromorphic isotropic hardening parameter \bar{Q}

In Fig. VIII-15, it presents three groups of force-displacement curves for the models of micromorphic damage, micromorphic isotropic hardening taking the parameters $\check{Q}=10KN\cdot mm^{-2}$ and $\check{Q}=100KN\cdot mm^{-2}$ while maintaining the internal length $l_r=1.0mm$ in two mesh sizes respectively. As expected, the introduction of the micromorphic isotropic hardening postpones the evolution of the damage and yields latter final fracture displacement. Clearly the system responses in the necking region are improved for small mesh size 0.4mm to approach the force-displacement curve of mesh size 0.8mm due to the introduction of the nonlocal effect of isotropic hardening. It should be noticed that the values of the parameter \check{Q} is much larger than the micromorphic damage parameter. That is because the relative small difference between the local and micromorphic isotropic hardening strain (around 2.87E-03 in maximum) which requires high values of the parameter \check{Q} to reflect the nonlocal effect of the isotropic hardening.

Fig. VIII-16 shows different force-displacement curves varying with the internal length of micromorphic isotropic hardening while the \check{Q} modulus remains $10KN\cdot mm^{-2}$. The same tendency that larger internal length of the micromorphic isotropic hardening provides bigger differences between the local and nonlocal isotropic hardening and delays the final fracture displacement (around 8.7mm and 8.9mm respectively), with the micromorphic damage model. The system response varying according to the internal length is less sensitive than that of the variation of the micromorphic parameter \check{Q} .

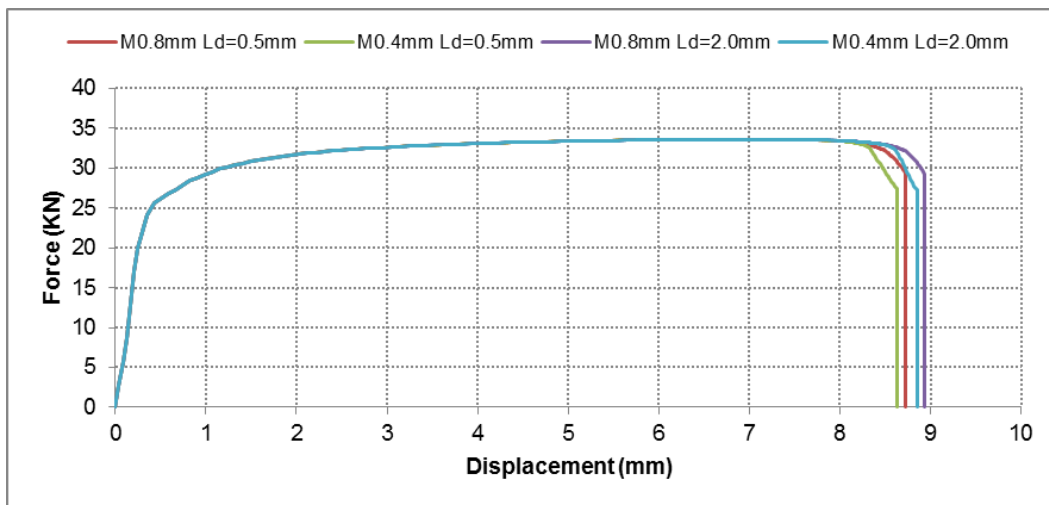


Fig. VIII-16 Force-Displacement curves of different values of internal length of micromorphic isotropic hardening

VIII.3.3 Summary

In summary, the local damage parameters and the micromorphic damage moduli together govern the nonlinear evolution of the damage in a rather complex methodology. The parametric study provides the following conclusions:

- 1). The system response behaves more sensitive to the modulus \check{H} than the internal length l_d (or the micromorphic gradient modulus \check{H}^g) for the ductile damage

It can be noticed from the equation of the damage energy release rate Eq.(II.43), in which the nonlocal effect directly reduces the damage-stress variable Y by scaling the difference between damage and micromorphic damage with the modulus \check{H} . On the other side, the internal length (or the micromorphic damage modulus \check{H}^g) only affects the difference between the local and micromorphic damage, which is clearly much smaller than 1, in the balance equation of the micromorphic damage;

- 2). The local damage parameters also affect the consistency of the material response

The variation of the parameter S remains the consistency while speeding or slowing the final fracture displacement; The increase in parameters s and Y_0 loses the consistency and yields latter the final fracture displacement, and vice versa; The influence from the parameter β in the consistency is relative small and gradually enhanced according to its increase which yields earlier final fracture;

- 3). The system response is also more sensitive to the modulus \check{Q} than the internal length l_r (or the micromorphic gradient modulus \check{Q}^g) for the isotropic hardening

VIII.4 Anisothermal micromorphic damage model

In this section, the parametric study of the anisothermal micromorphic damage model, which considering the elasto-visco-plasticity coupling with thermal, local and micromorphic damage and hardening, is performed. The material property under the reference temperature (20°C) is given in the below table.

E (GPa)	ν	σ_y (MPa)	Q (MPa)	b	C (MPa)	a
205.0	0.3	792.0	320.0	0.6	5000.0	20.0
S	s	β	Y_0	γ	K^ν (MPa)	m_ν
20.0	2.0	1.0	0.0	1.8	793.8	2.7

Table VIII-2 Material parameters under reference temperature

As usual the material moduli are temperature dependent, the following relations are assumed:

$$P(T) = P_0 [1 - G^\alpha(T)] \quad (\text{II.419})$$

where, $G(T) = \frac{T - T_0}{T_f - T_0} \geq 0$ and T_0 is the reference temperature. T_f is the fusion temperature of the specific material. α is a coefficient. For Young's modulus $\alpha = 4.0$; for capital S of damage factor $\alpha = 1.08$ and for other modules it equals to 1.03.

VIII.4.1 Anisothermal viscoplasticity with local damage for a material point

In this section, the parametrical studies of temperature, load velocity, micromorphic density and its moduli are performed in a material point to examine the response of the proposed anisothermal elasto-visco-plastic model coupled with local and micromorphic isotropic damage, local isotropic hardening and kinematic hardening.

Fig. VIII-17 illustrates the thermal effects on the evolutions of equivalent stress based on the proposed constitutive equations coupled with local damage and local mixed hardening. The accumulated plastic strain (max: 0.652; min: 0.592) increases and the tensile stress (max: 1108.72MPa; min: 416.91MPa) decreases steadily as temperature increases.

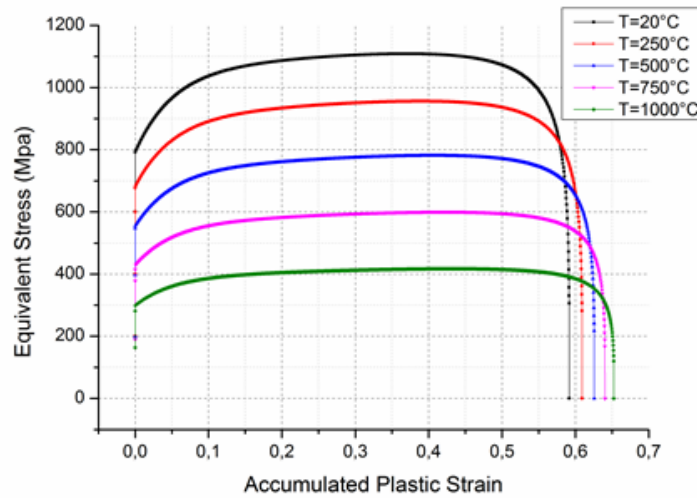


Fig. VIII-17 Stress-strain curves for different temperatures with the same strain rate $1.0E-04s^{-1}$

Fig. VIII-18 shows the four types of evolutions of local damage under different strain rates (velocity) (from $1.0E-04s^{-1}$ to $0.1s^{-1}$) under the initial temperature $1000^{\circ}C$. Clearly, the evolution of local damage is accelerated by the increasing strain rate. The fracture plastic strains are 0.652, 0.648, 0.636 and 0.605 respectively.

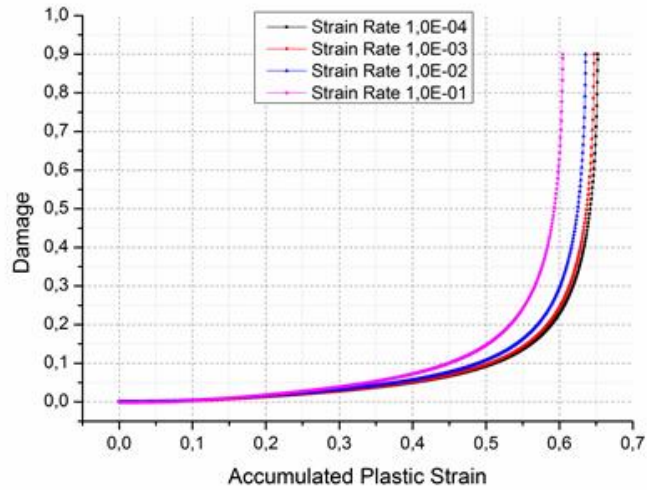


Fig. VIII-18 Evolution of damage for different loading velocity with the same temperature 1000°C

VIII.4.2 Biaxial tension for local damage with FE

The geometric size and boundary conditions of the sample are shown in Fig. VIII-19. For simplifications, three different initial temperatures (20°C, 500°C and 1000°C), and four velocities(2.0E-04mm/s, 2.0E-05mm/s, 2.0E-06mm/s and 2.0E-07mm/s) are performed on a single finite element in this example. The approximate strain rates are $1.0E-01\text{s}^{-1}$, $1.0E-02\text{s}^{-1}$, $1.0E-03\text{s}^{-1}$ and $1.0E-04\text{s}^{-1}$ respectively.

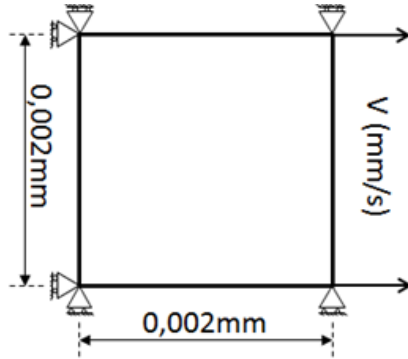


Fig. VIII-19 Scheme of biaxial tension test

Fig. VIII-20 summarizes the material responses of the local damage model, in terms of equivalent stress – accumulated plastic strain curves, for 7 cases including three temperatures and three velocities. From this figure the viscoeffects are very clear: when the temperature increases the ductile plasticity is extended and the final fracture plastic strain is also enlarged (0.591 in 20°C, 0.626 in 500°C and 0.653 in 1000°C with velocity 2.0E-07mm/s). However, both the initial yield stress (792.00MPa, 547.09MPa and 281.12MPa) and hardening effects are decreased. The opposite tendency of the fracture plastic strain is observed for the raise of loading velocity at each temperature, while the equivalent stress after yield point shows significant differences (31.24MPa for 500°C and 66.85MPa for 1000°C). In Fig. VIII-21, it illustrates the different evolutions of local damage for the same seven cases. It's clear that the evolution of damage is delayed by the raise of the temperature and the decelerated load velocity.

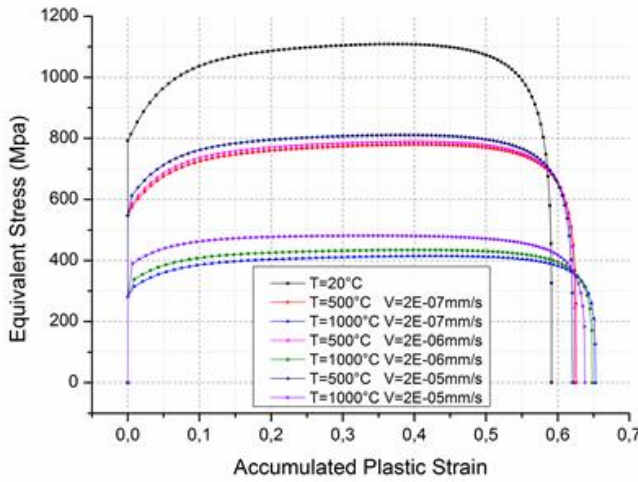


Fig. VIII-20 Stress-strain curves for different temperature and load velocity coupled with local damage

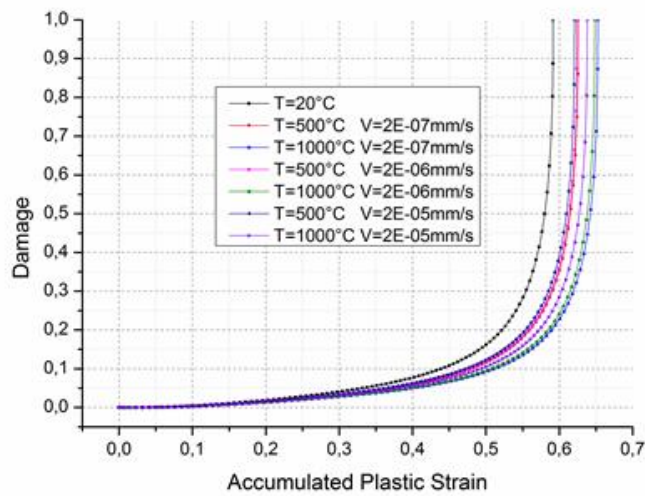


Fig. VIII-21 Evolution of local damage for different temperature and load velocity

VIII.4.3 Choices of micromorphic parameters with FE

Let us consider the choices of micromorphic parameters including micromorphic density, the H moduli for the coupled local damage and micromorphic damage and the gradient of micromorphic damage. In this section, all the simulations are performed under temperature 500°C and load velocity 2.0E-05mm/s.

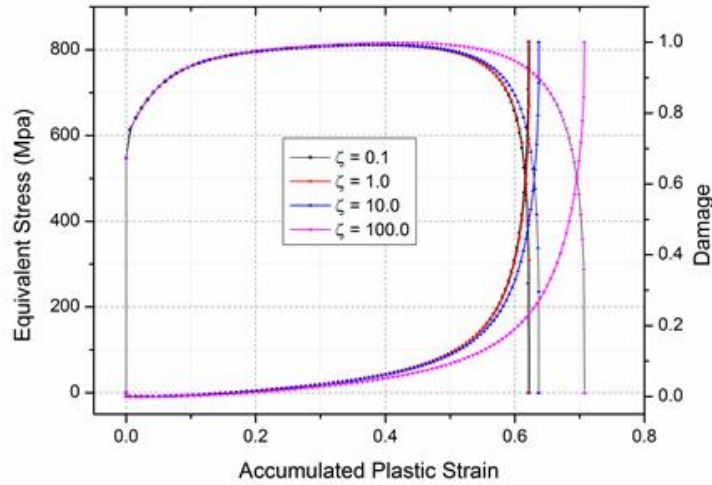


Fig. VIII-22 Stress-strain curves and evolution of damage for some values of micromorphic density

In Fig. VIII-22, it illustrates the stress-strain curves and the evolutions of damage for different micromorphic density (0.1~100 times of local density) with given H modules equal to 1000N. From the theoretical formula Eq.(II.111), we can see that the micromorphic density will be used to calculate the accelerate of micromorphic damage at each time step, which determines the incremental micromorphic damage and affects the local damage. In this figure, it clearly represents that the larger micromorphic density evidently slows the evolutions of local damage and enlarged the ductile plasticity of the material.

Fig. VIII-23 represents the effects of different choices of \tilde{H} modules (1.0~1000N) for the stress-strain curves and the evolution of local damage. From the state relations of stress-like variable with respect to local damage Eq.(II.43), we know that the evolution of the local damage is affected by the micromorphic damage through the H modules. In this figure, it describes that the larger H modules the slower evolution of local damage. We can also find this character from Eq.(II.37), the term of coupled local and micromorphic damage has a negative sign, which induces the reduction of the stress-like variable Y of local damage.

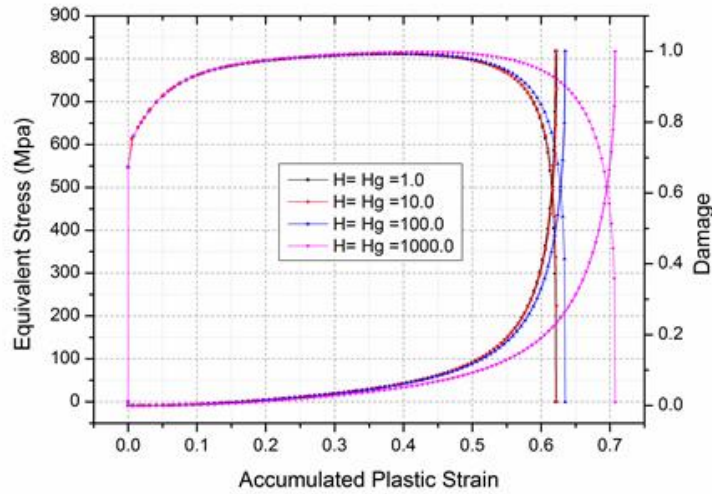


Fig. VIII-23 Stress-strain curves and evolution of damage for some values of micromorphic H modules

Compared with the curves for local damage, both of the figures imply that when the micromorphic density or the H modules approach to zero, the material response becomes closer and closer to the one from local damage.

VIII.4.4 Biaxial tension for micromorphic damage with FE

After the analysis of parameters, we have a conclusion that the smaller micromorphic density and H modules gives the more approximate result to the ones from the local damage formulas. In absence of any experimental indication, the micromorphic parameters: density 100 times, micromorphic modules 1000N, will be considered to perform the biaxial tension test in this section.

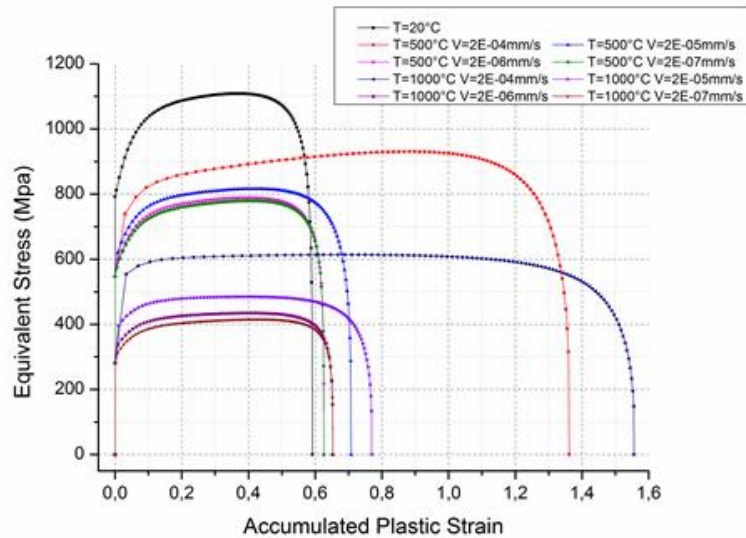


Fig. VIII-24 Stress-strain curves for different temperature and load velocity with micromorphic damage

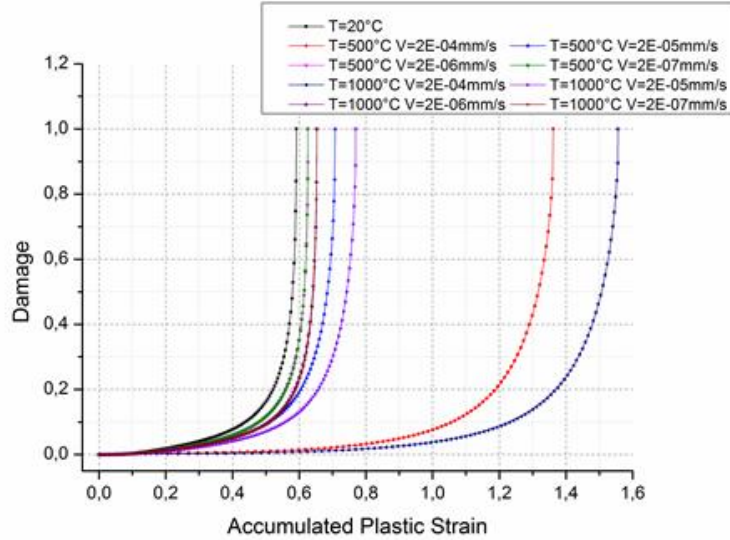


Fig. VIII-25 Evolution of damages for different temperature and load velocity with micromorphic damage

In Fig. VIII-24 and Fig. VIII-25, it gives the stress-strain curves and the evolutions of local damage of 9 cases (three temperatures and four velocities). It's clear that, in this choice of parameters, the fracture plastic strain is significantly improved and the evolution of local damage is apparently delayed. Compared with the curves from local damage formulas in Fig. VIII-20 and Fig. VIII-21, it's apparently that the maximum tensile stresses have very little differences for the four velocities on each temperature. However, the final fracture accumulated plastic strain grows larger significantly (maximum roughly 1.556 for temperature 1000°C and load velocity 2.0E-04mm/s).

Fig. VIII-26 shows the differences between the local and the micromorphic damage for different load velocity at 500°C. Clearly, it is observed that, for low velocities 2.0E-07mm/s and 2.0E-06mm/s, the differences remain close to 0 until the initiation of the damage criterion; however, for higher velocities 2.0E-05mm/s and 2.0E-04mm/s, the differences grow linearly up to around 0.04 and 0.15 respectively. The dynamic effect of the load velocity obviously enlarges the difference between the local and micromorphic damage, and yields latter final fracture accumulated plastic strain.

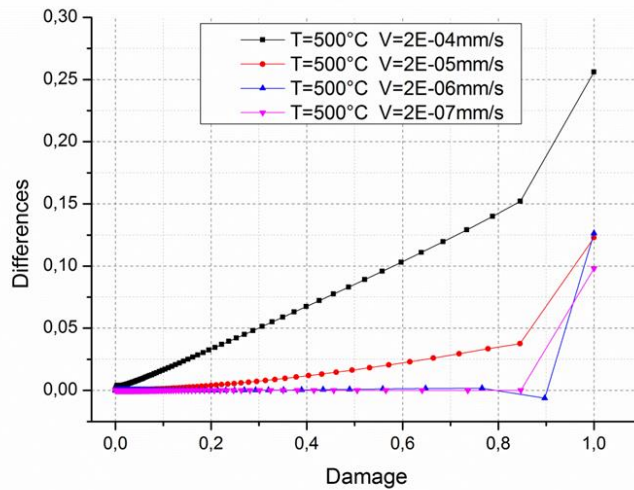


Fig. VIII-26 Evolution of the differences ($d - \check{d}$) between the local and the micromorphic damage for different velocity at 500°C

VIII.4.5 Summary

In this section, the constitutive models of elasto-visco-plasticity coupled with local damage and micromorphic damage is applied to a biaxial tensile test. The classical viscoeffects, the higher temperature the lower stresses and more ductility, the larger load velocity the higher stresses and less ductility, are observed by using the local damage model.

On the other hand, the elasto-visco-plastic model coupled with micromorphic damage, shows similar material responses of the local damage case when the micromorphic moduli approach to zero which yields the negligible nonlocal effect. However, the effect of the micromorphic damage becomes more significant and results in quite different material responses, the higher load velocity the more ductility, as the increase of the load velocity. From the comparisons of the biaxial tension between local and micromorphic damage model, we can make a conclusion that the micromorphic damage significantly delays the evolution of the local damage especially under cases of high temperature or high strain rate (dynamic effects).

IX. Applications

IX.1 Uniaxial tensile test of DP1000

In this section, the experimental results of uniaxial tensile tests of the dual phase steel DP1000 referenced in the work of Yue (2014), is chosen to perform new simulations with our micromorphic model. The uniaxial tensile test is conducted on Zwick 250 machine with velocity of 0.1 mm/s (quasi-static loading) and the geometry of the specimen is given in Fig. IX-1. The best set of material's local elastoplastic and damage parameters, found by the inverse procedure and discussed in the literature of Yue (2014), is given in the Table IX-1. Note that the damage parameters are determined with constant mesh size of 1.6mm. All the simulations in this section are performed under isothermal conditions (i.e. at room temperature) using the time-independent plasticity model with only micromorphic damage and micromorphic isotropic hardening under the plane stress assumption.

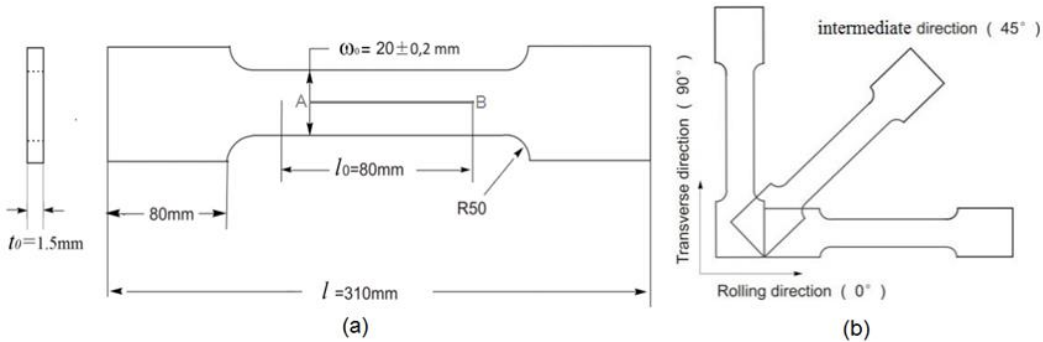


Fig. IX-1 Geometry of the uniaxial tension specimen

ρ (kg/m^3)	E (GPa)	ν	σ_y (MPa)	Q (MPa)	b	C (GPa)
7800.0	208.0	0.3	809.0	4000.0	13.0	32.0
a	F	G	H	L	M	N
150.0	0.525	0.546	0.455	1.5	1.5	1.6
S	s	β	γ	Y_0	h	
3.5	1.2	2.0	4.0	0.0	1.0	

Table IX-1 Damaged elastoplastic material parameters for DP1000 (local model)

IX.1.1 The local damage behavior

These results are obtained with fully local model (no micromorphic variables). Fig. IX-2, it gives the force-displacement curves of the tensile test with different constant mesh size: 1.6mm, 0.8mm, 0.4mm and 0.2mm, obtained from the simulations provided by Abaqus using the local damage model with the above material parameters and the quadrangular planar element, and compared with the experimental data. The mesh-dependency phenomenon is clearly observed: the final fracture displacements become smaller as the decrease of the constant mesh size.

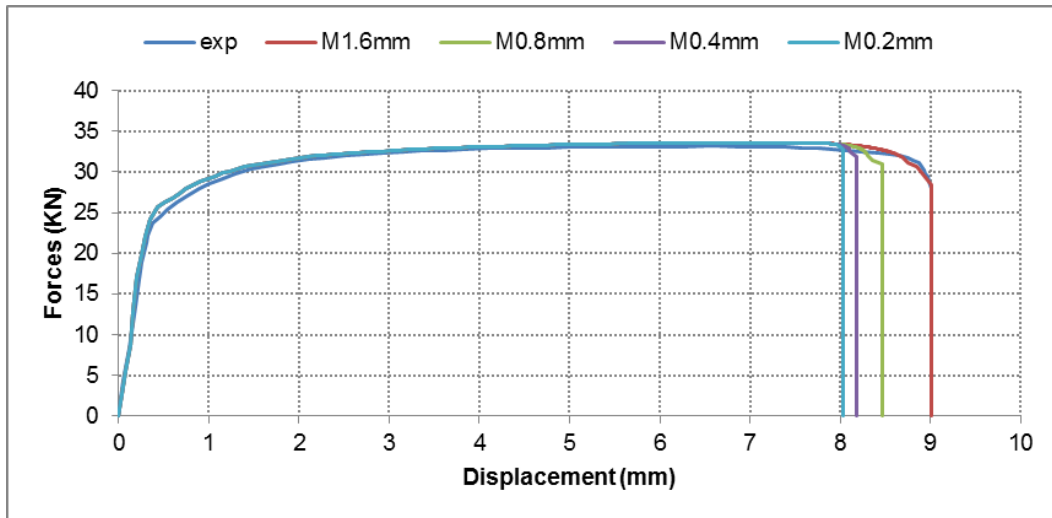


Fig. IX-2 Force-Displacement curves of the tensile test using the local damage model

If we plot the differences of the final fracture displacement from the adjacent mesh size in the ratio of 2.0, as shown in Fig. IX-3 and Fig. IX-4, the differences: 0.554mm ($u_{1.6}^f - u_{0.8}^f$), 0.296mm ($u_{0.8}^f - u_{0.4}^f$) and 0.149mm ($u_{0.4}^f - u_{0.2}^f$) are getting smaller and smaller substantially in the same ratio, in this tensile analysis.

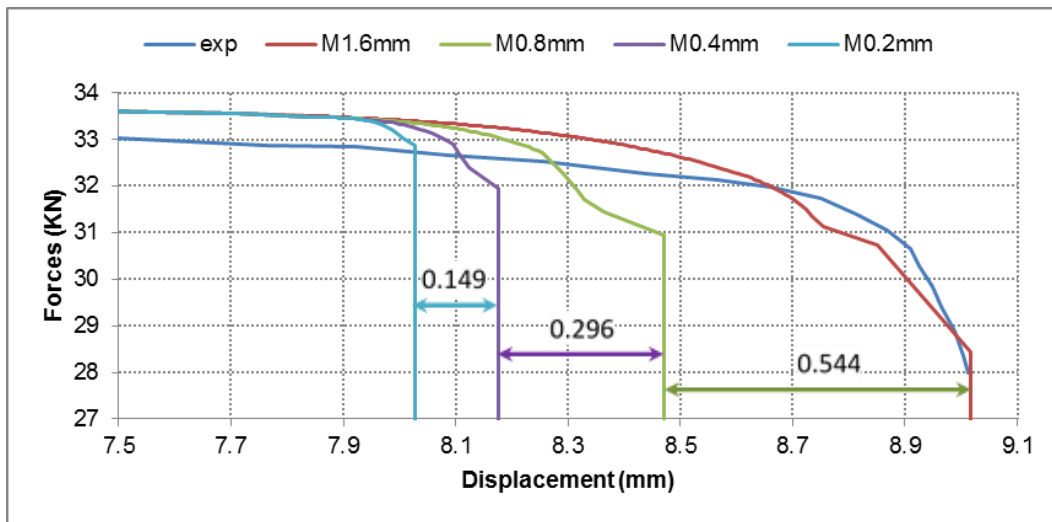


Fig. IX-3 Scaled force-displacement curves of the tensile test using the local damage model

Meanwhile, it should be mentioned that the local damage model yields the zero energy dissipation in the crack tip due to the finite-size region of strain softening tends to be zero. As shown in Fig. IX-7, the distributions of damage along the section AB as shown in Fig. IX-1, are predicted by the local damage model for three mesh sizes: 1.6mm, 0.8mm and 0.4mm. Clearly, it is observed that the damage highly localizes in one element's width and the damage values inside the adjacent elements remain low and don't exceed 0.2. Also the orientation of the macroscopic crack is orthogonal to the loading direction for the coarse mesh, while for two lower mesh sizes the macroscopic crack an orientation of approximately $\pm 45^\circ$.

$$Ms = 1.6\text{mm}, \quad U_{rupt} = 9.02\text{mm}$$

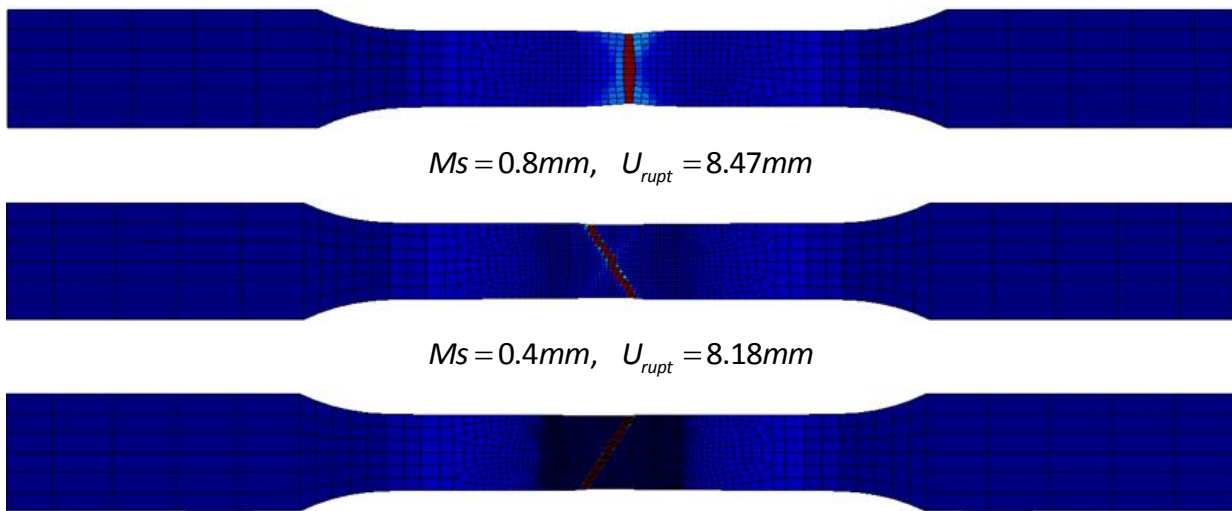


Fig. IX-4 Distributions of final fracture obtained from the local damage model for different mesh sizes

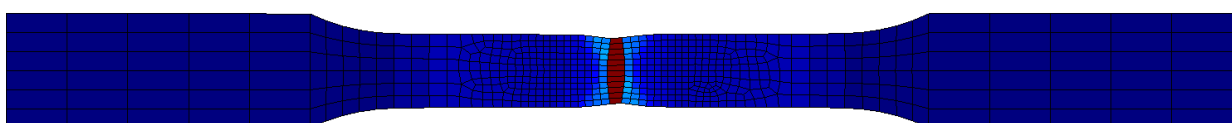
IX.1.2 The micromorphic damage behavior

In fact, for the model with micromorphic damage, there are three independent micromorphic damage parameters: the density scale ζ_d , the micromorphic modulus \check{H} and \check{H}^g which are related by the internal length scale $I_d = \sqrt{\check{H}^g / \check{H}}$.

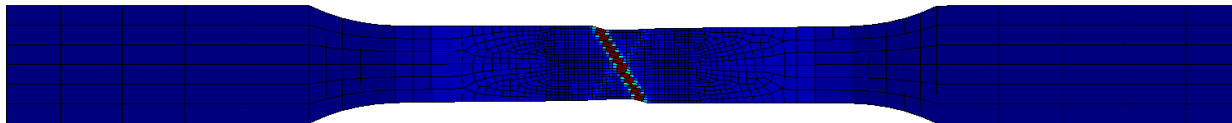


Fig. IX-5 Force-Displacement curves of the tensile test using the micromorphic damage model

$$Ms = 1.6\text{mm}, \quad U_{rupt} = 9.18\text{mm}$$



$$Ms = 0.8\text{mm}, \quad U_{rupt} = 9.15\text{mm}$$



$$Ms = 0.4\text{mm}, \quad U_{rupt} = 9.15\text{mm}$$

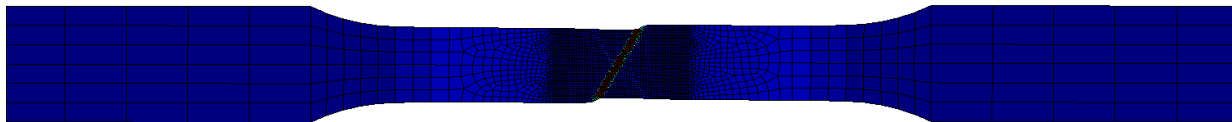


Fig. IX-6 Distributions of final fracture obtained from the micromorphic damage model for different mesh sizes

In Fig. IX-5, it shows three force-displacement curves predicted from the micromorphic damage model which taking the parameters: $S = 3.4$, $\zeta_d = 1.0$, $H = 43.75\text{N}\cdot\text{mm}^{-2}$ and $I_d = 1.0\text{mm}$, using different mesh sizes: 1.6mm, 0.8mm and 0.4mm, comparing with the experimental curve. Clearly, unlike the local damage model, the force-displacement curves give approximately the same final fracture displacement value around 9.15mm.

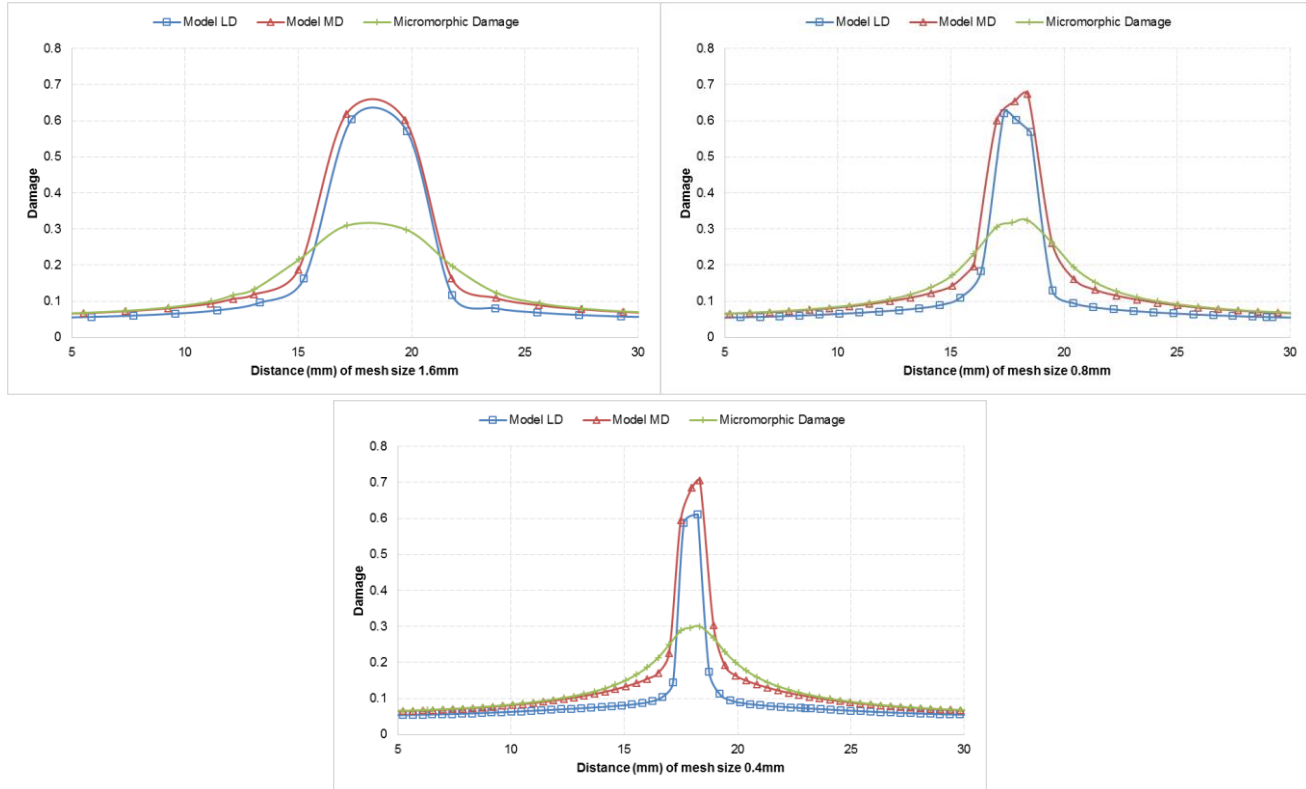


Fig. IX-7 Local and micromorphic damage distributions of line AB predicted by the local damage model (LD) and the micromorphic damage model (MD) for three mesh sizes: 1.6mm, 0.8mm and 0.4mm

Fig. IX-6 shows the distributions of local damage predicted with the micromorphic damage model in the tensile sample after the final fracture. Fig. IX-7 presents the distributions of local and micromorphic

damage along the central line AB which are obtained from the simulations of using local and micromorphic damage models. Clearly the distributions of the micromorphic damage are more smooth in the whole region (maximum value around 0.3), lower in the localized zone and higher at the outside of localization than the value of local damage. Considering the value of the micromorphic damage is governed by the equation Eq.(II.111), its maximum value (approximate 0.3) is mainly constrained to the internal length scale \bar{l}_d , the higher value of internal length the smaller maximum micromorphic damage. The local damage values of the adjacent elements in the diffusion regions are significantly elevated to about 0.3 compared with the values of 0.2 in local damage model, due to the nonlocal effects of the micromorphic damage.

It should be noticed that, in Fig. IX-5, the inconsistent force-displacement curves of different mesh sizes obtained from the micromorphic damage model present some deviations from each other in the range between 8.0mm to 9.15mm. These can be overcoming by introducing more micromorphic variables to fully represent the localization behavior of the material besides only the micromorphic damage as is shown here after.

IX.1.3 Solutions with micromorphic damage and micromorphic isotropic hardening

In order to enhance the micromorphic modeling of the material response, the micromorphic isotropic hardening associated with the nonlocal effect of the isotropic hardening is now taken into account together with the micromorphic damage.

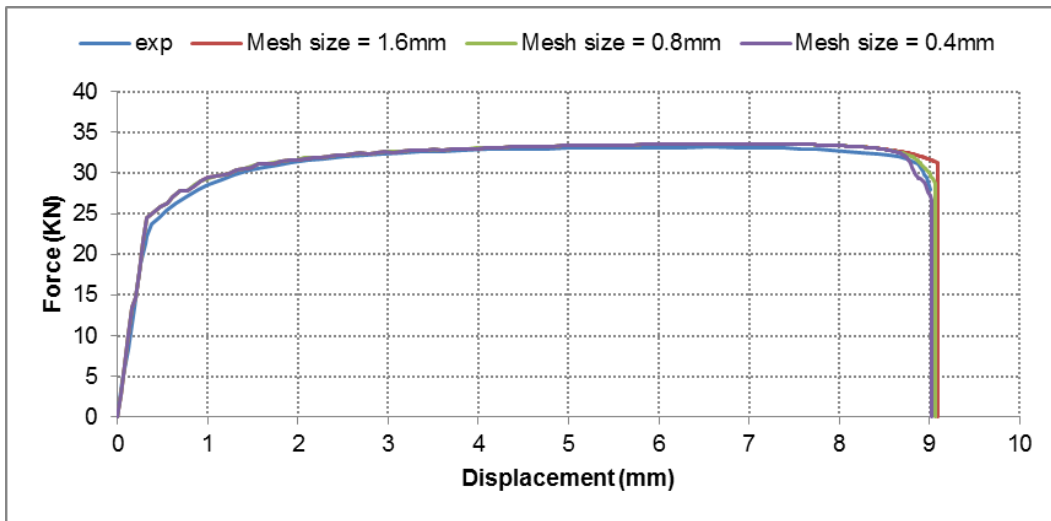


Fig. IX-8 Force-Displacement curves of the tensile test using the micromorphic damage and isotropic hardening model

Fig. IX-8 presents the predicted responses in terms of force-displacement curves of the same uniaxial tensile test, taking the parameters: $S=3.3$, $\zeta_d=1.0$, $\check{H}=43.75 N \cdot mm^{-2}$, $\bar{l}_d=1.0 mm$, $\zeta_f=1.0$, $\check{Q}=20 KN \cdot mm^{-2}$ and $\bar{l}_r=\sqrt{2} mm$, for the same three different mesh sizes of 0.4mm, 0.8mm and 1.6mm, as previously. As expected, this micromorphic model with two micromorphic phenomena (damage and isotropic hardening) predicts more consistently the force-displacement curves compared with the responses modeled by the sole micromorphic damage model shown in Fig. IX-5 especially in the beginning

of the softening stage (or diffuse necking region), where the final fracture displacements are approximately the same (9.03mm, 9.07mm and 9.10mm for mesh sizes 0.4mm, 0.8mm and 1.6mm respectively). This proves that combining the micromorphic damage with micromorphic isotropic hardening improves significantly the unicity of the force-displacement curves in the softening stage.

In Fig. IX-9, it presents the final macroscopic crack paths of the DP1000 tensile specimen as predicted by the three different mesh sizes. By comparing the macroscopic crack orientations in Fig. IX-4, Fig. IX-6 and Fig. IX-9, it is worth noting that the orientation of the final crack is not modified by the local or micromorphic character of the model but is the same for the same mesh sizes.

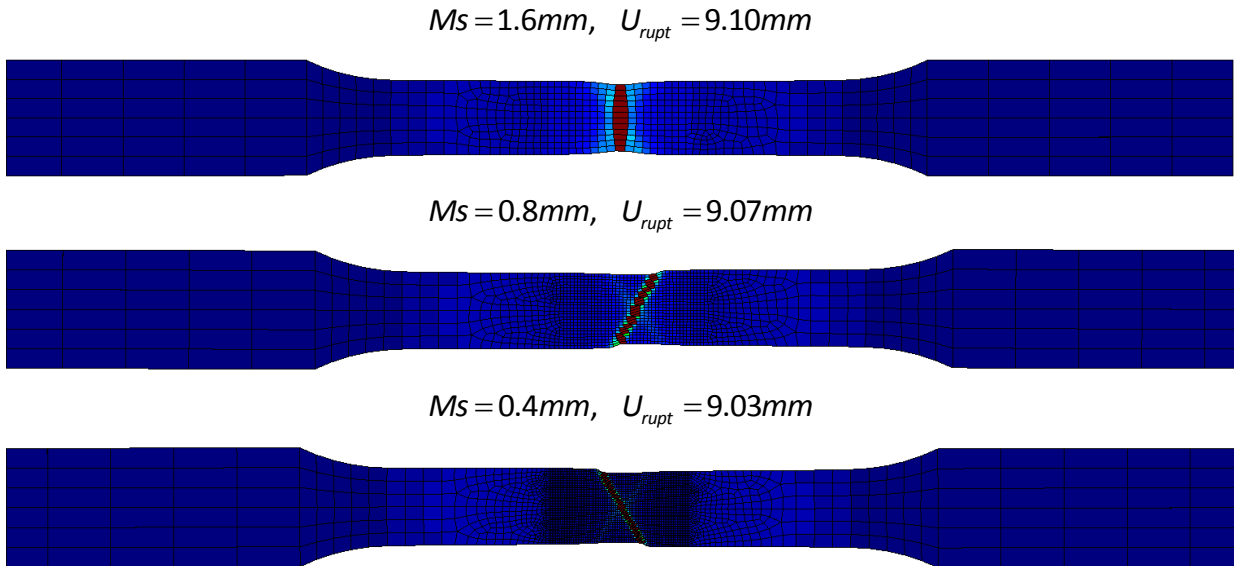


Fig. IX-9 Distributions of damage obtained from micromorphic damage and isotropic hardening model for different mesh sizes

Let's consider two stages: stage I, defined as when the maximum smoothed value of local damage is lower than 0.32 (i.e. far from the fracture of the first element); and stage II, defined as when the maximum value of smoothed local damage is higher than 0.7 (close to the final fracture of the first element). The distribution of the damage values inside the specimen around these two stages are predicted by the local damage model and by micromorphic damage and isotropic hardening model are now discussed.

In Fig. IX-11, the smooth distributions of the local damage, at stage I and stage II, obtained from the local damage model and the micromorphic damage and isotropic hardening model for three different mesh sizes respectively, are given. Clearly, and as expected the local damage model predicts the more localized damage values while the micromorphic model predicts wider damage zones. Also, the orientations of the localization bands (or the final crack paths) for the two fine meshes are inverted between the local and the micromorphic models.

Fig. IX-12 presents the distributions, at the two stages defined above, of the micromorphic damage as well as the difference between the local and micromorphic damage variables ($d - \bar{d}$), obtained from the micromorphic damage and isotropic hardening model for the three different mesh sizes. From this figure, we observe that the micromorphic damage distributes much smoother and wider than the local damage,

and the values of the local and micromorphic damage variables remain close to each other (the gap is strictly lower than 0.1) for the three mesh sizes when the local damage is relatively low (lower than 0.35). While, the gap between the local and micromorphic damage increases (higher than 0.3) when the local damage is high (higher than 0.7) and close the final fracture condition.

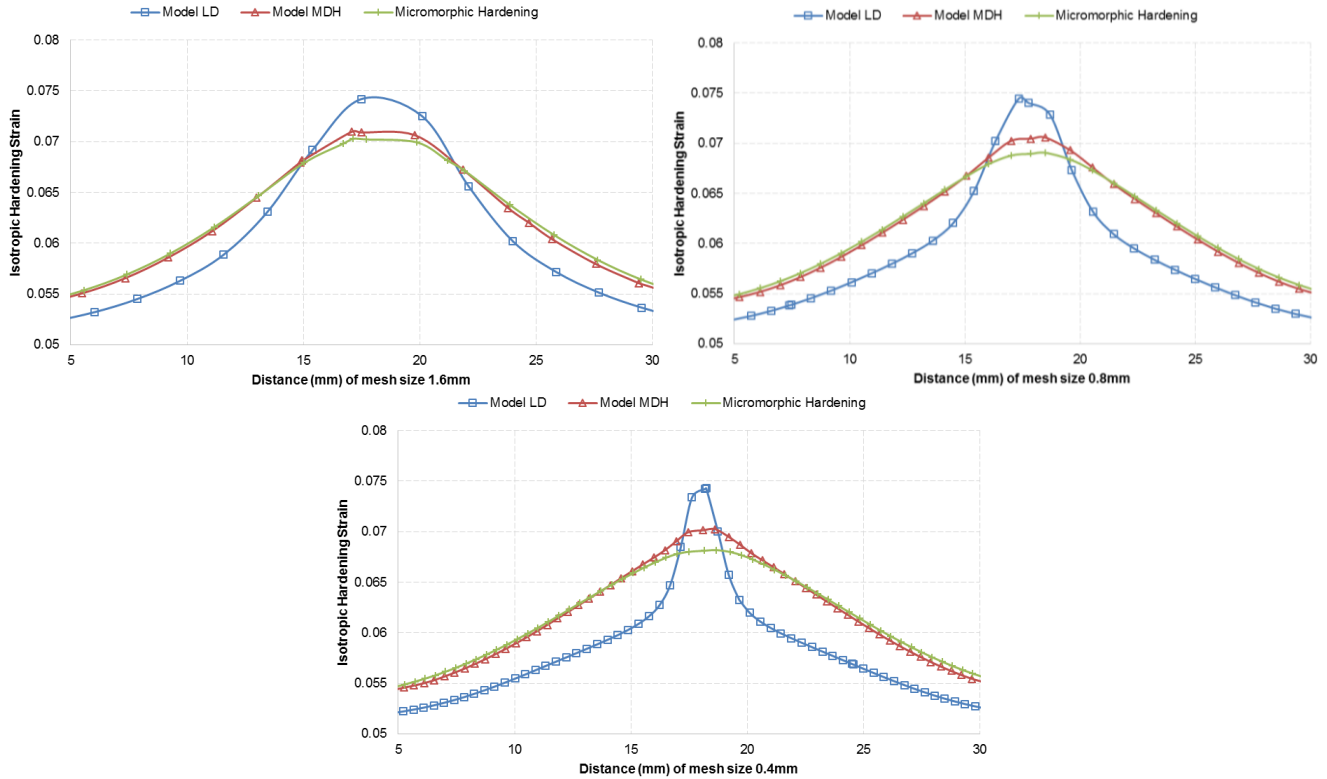


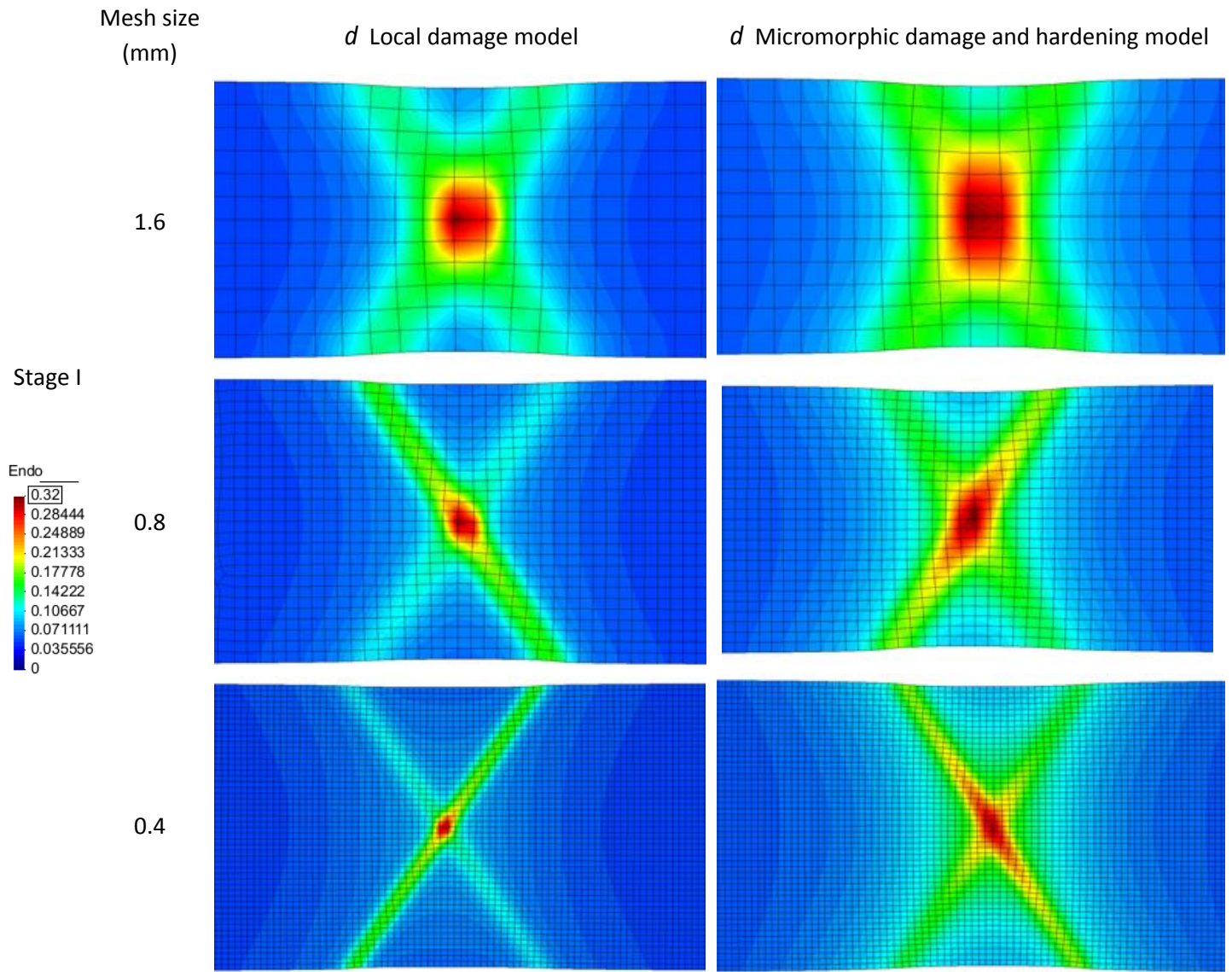
Fig. IX-10 Local and micromorphic isotropic hardening strain distributions of line AB predicted by the local damage model (LD) and micromorphic damage and isotropic hardening model (MDH) for three mesh sizes: 1.6mm, 0.8mm and 0.4mm

In Fig. IX-13, the distributions of the local isotropic hardening strains, predicted by both the local model and the micromorphic model for the three studied mesh sizes at both stage I and stage II, are plotted. Similar to the damage, the distributions of the isotropic hardening strains are wider for the micromorphic model than for the fully local model.

Recall the Fig. IX-10, which plots the distributions of local and micromorphic isotropic hardening strains, predicted by the local damage model and the micromorphic damage and isotropic hardening model respectively, along the central line AB. Clearly, it is observed that, similar to the damage, the isotropic hardening strain of local damage model is also localized in one element's width. However, the distributions of the isotropic hardening strain predicted by the micromorphic damage and isotropic hardening model is much more smooth than the results from local damage model. The differences between the local and micromorphic isotropic hardening strains predicted by the micromorphic model are getting larger as the refinement of the mesh size.

Finally, the Fig. IX-14 shows the distributions of the micromorphic isotropic hardening strains and the difference between the local and the micromorphic isotropic hardening strains ($r - \bar{r}$) for three different

mesh sizes and at both stages respectively. The same remarks as for the damage apply for the isotropic hardening: the micromorphic isotropic hardening is widely distributed of the specimen gauge length similar to the local hardening strains. However, the micromorphic isotropic hardening strains are closely equal to the the local isotropic hardening strains every where outside of the two shear bands. Consequently, we obtain a very small gap between both strains outside of the two shear bands, while the biggest gap is concentrated inside the two shear bands.



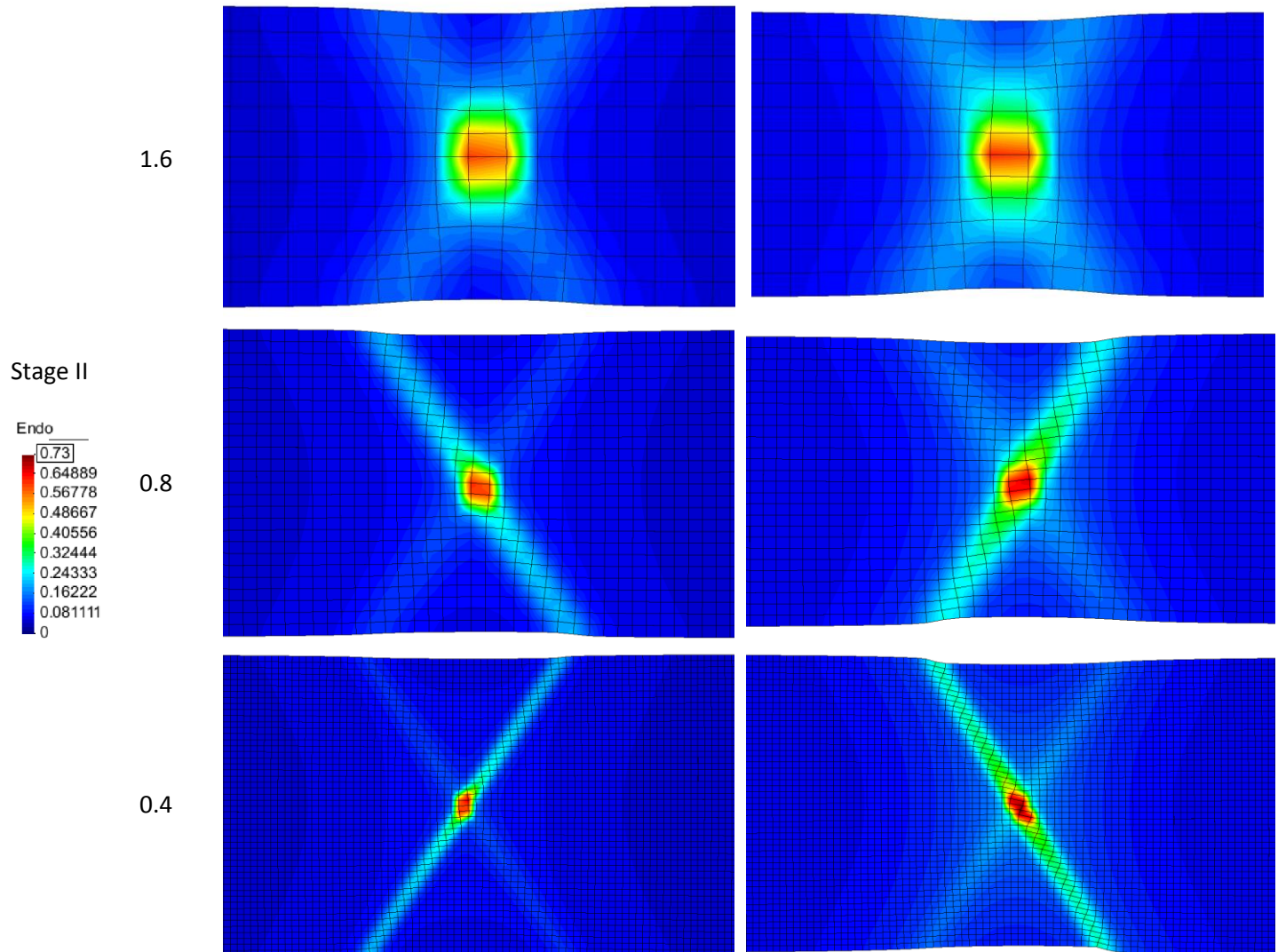
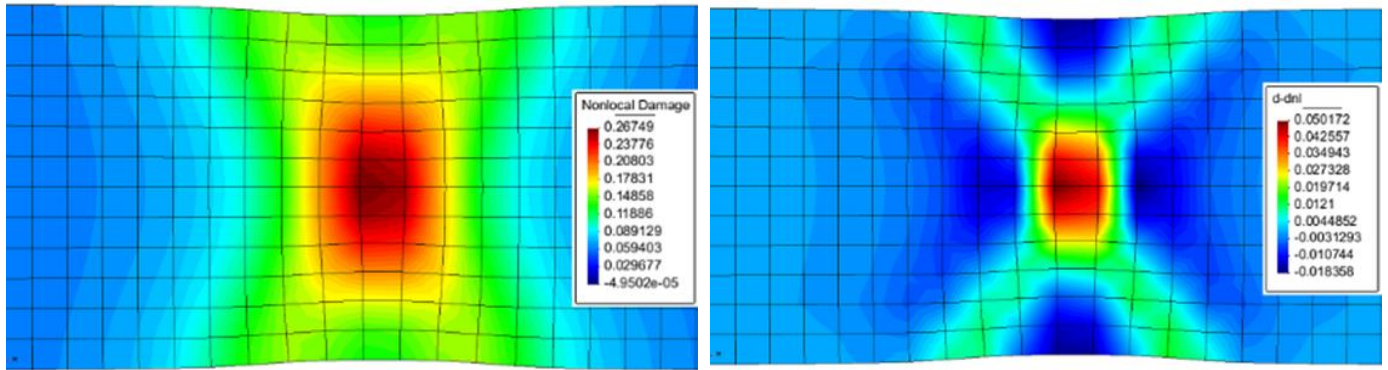


Fig. IX-11 Distributions of the local damage inside the tensile specimen as predicted by the local damage and the micromorphic damage and isotropic hardening model for three different mesh sizes

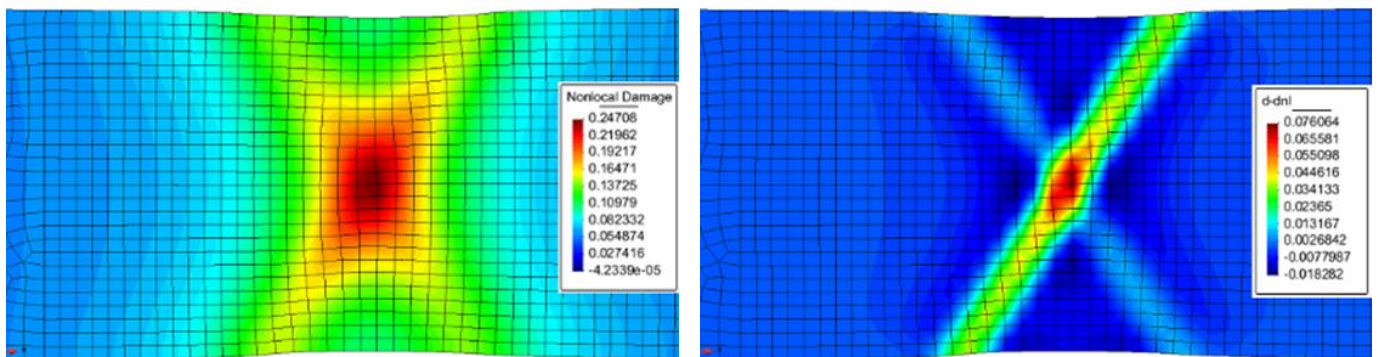
Micromorphic damage \bar{d}

The difference $(d - \bar{d})$

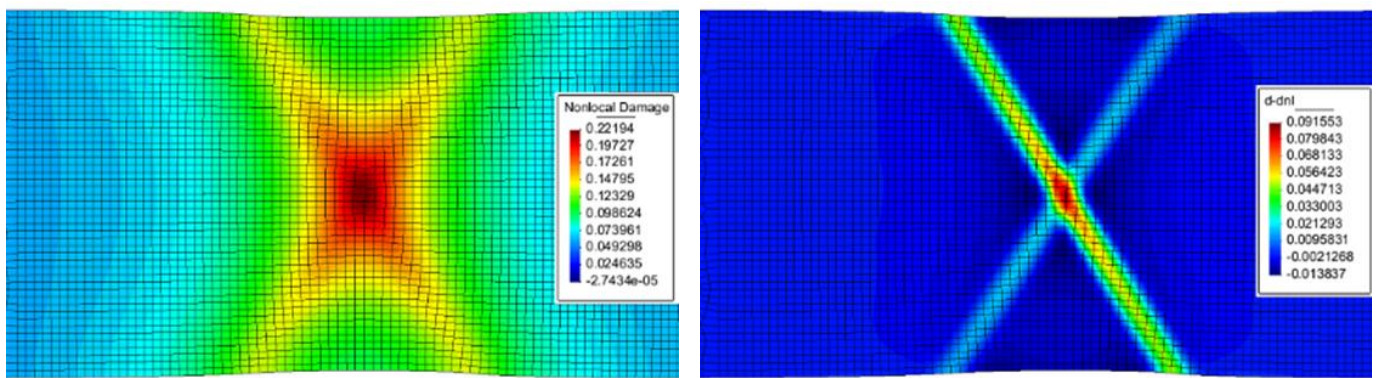
Stage I: mesh size 1.6mm



Stage I: mesh size 0.8mm



Stage I: mesh size 0.4mm



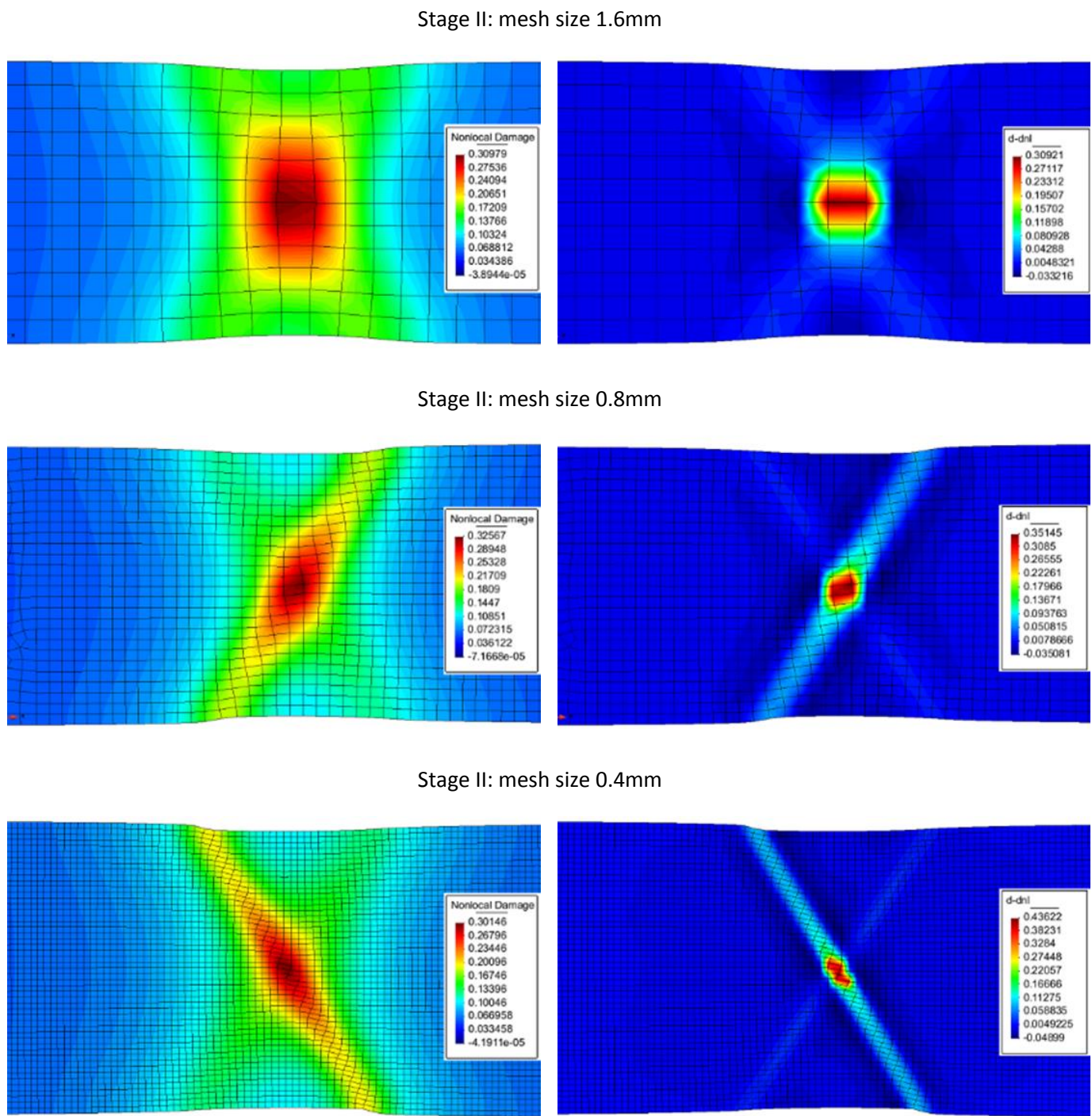
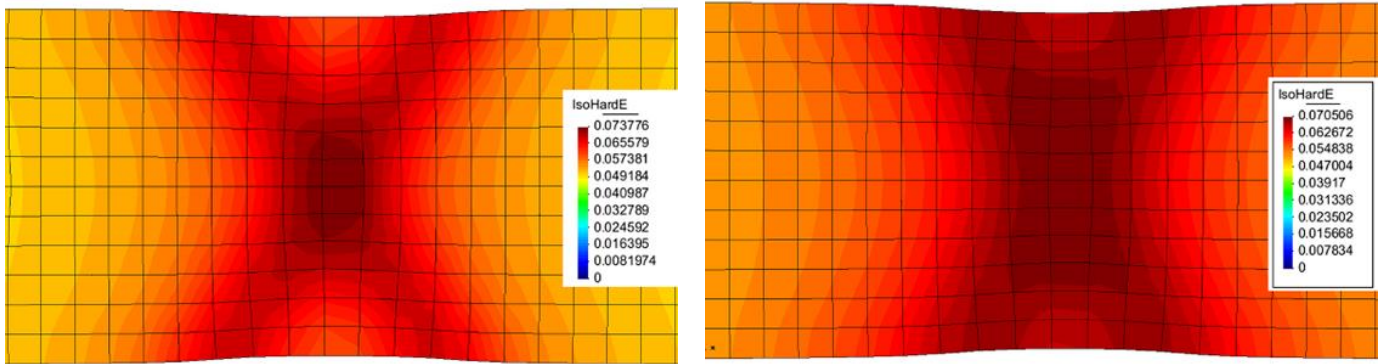


Fig. IX-12 Distributions of micromorphic damage and the difference between the local and micromorphic damage at stage I and stage II predicted by the micromorphic damage and isotropic hardening model for different mesh sizes

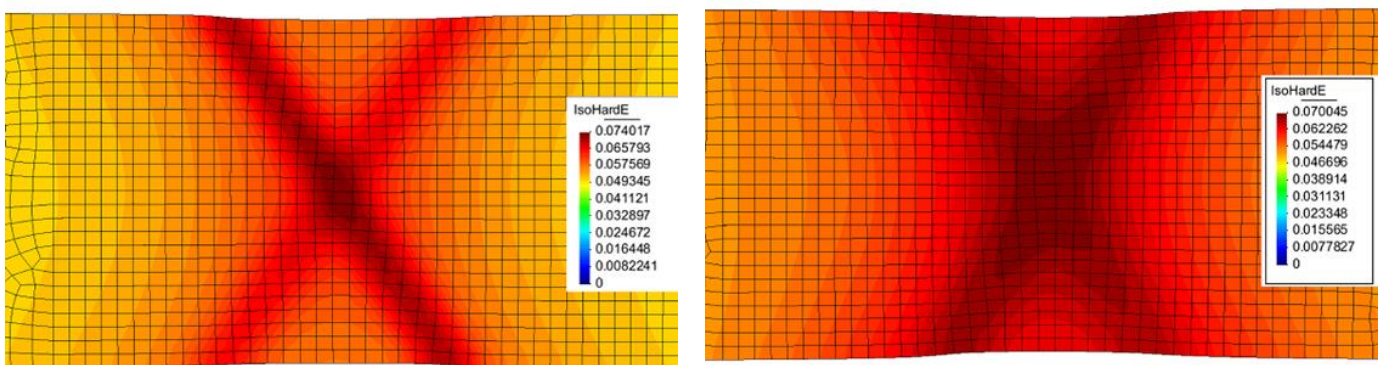
r Local damage model

r Micromorphic damage and hardening model

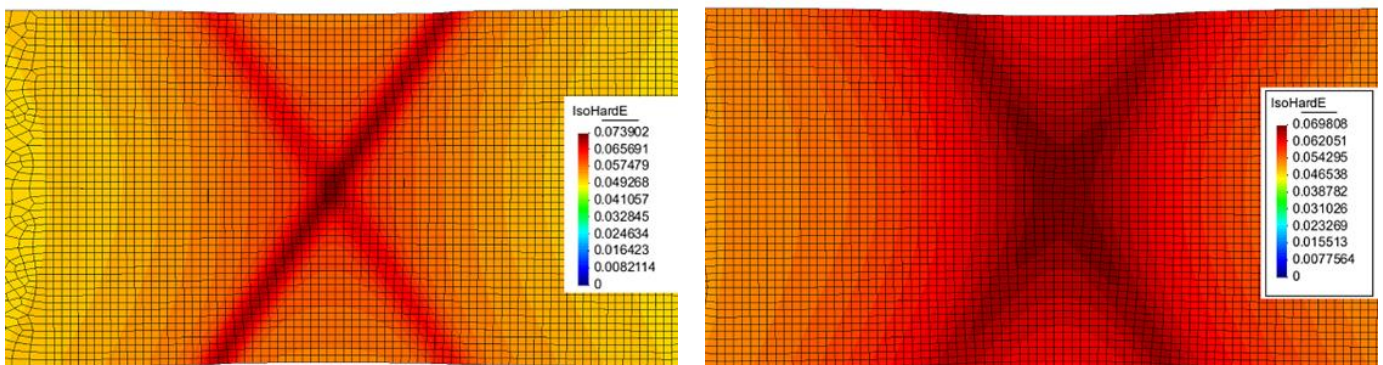
Stage I: mesh size 1.6mm



Stage I: mesh size 0.8mm



Stage I: mesh size 0.4mm



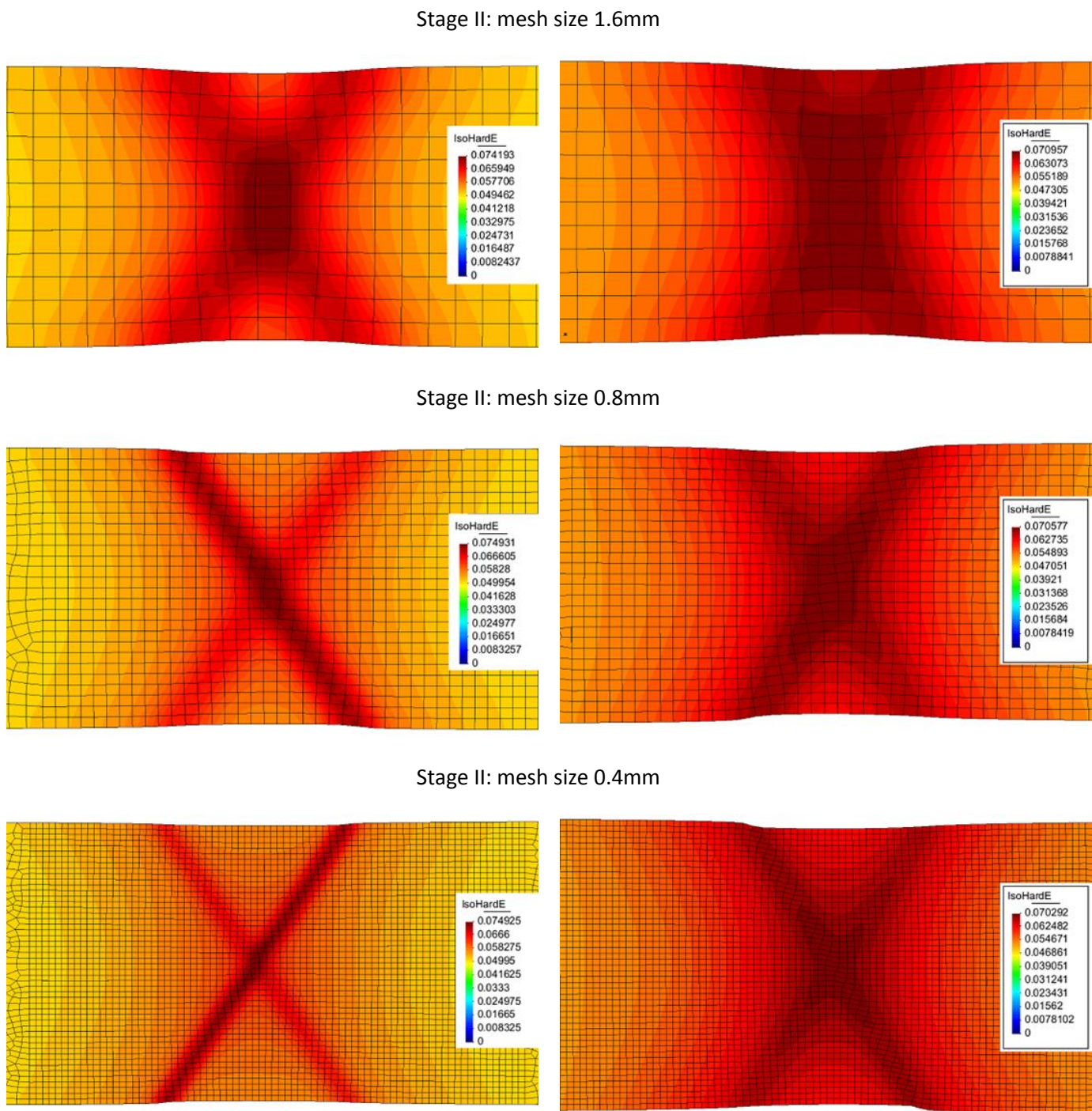
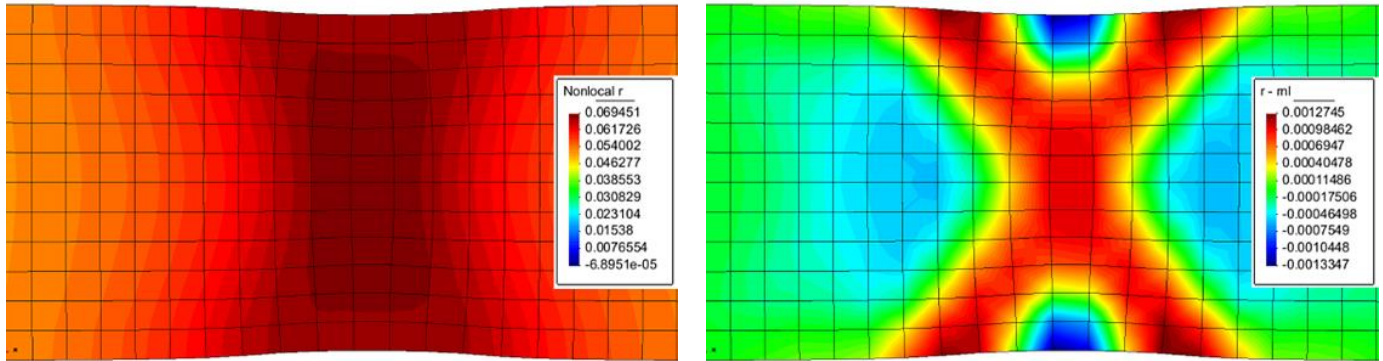


Fig. IX-13 Distributions of the isotropic hardening strain of the tensile test predicted by the local damage and micromorphic damage and isotropic hardening model for three different mesh sizes

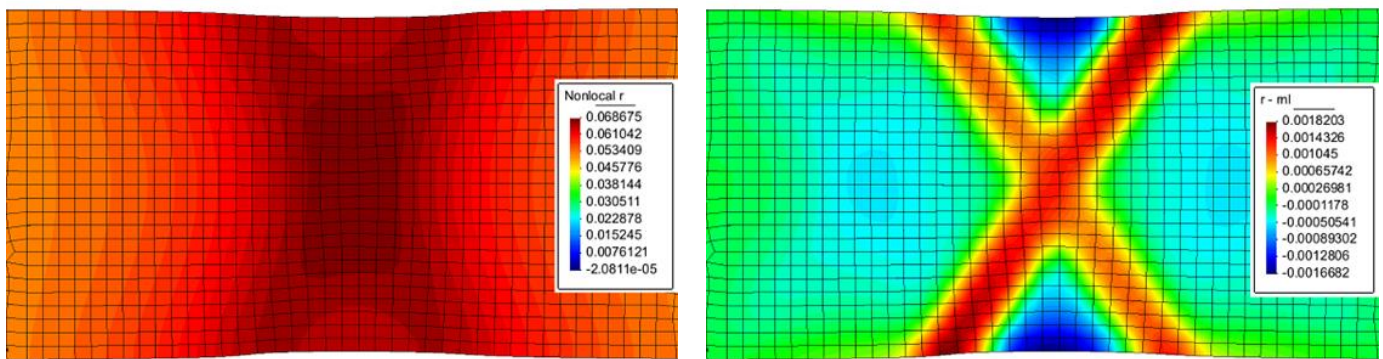
Micromorphic isotropic hardening strain \check{r}

The difference $(r - \check{r})$

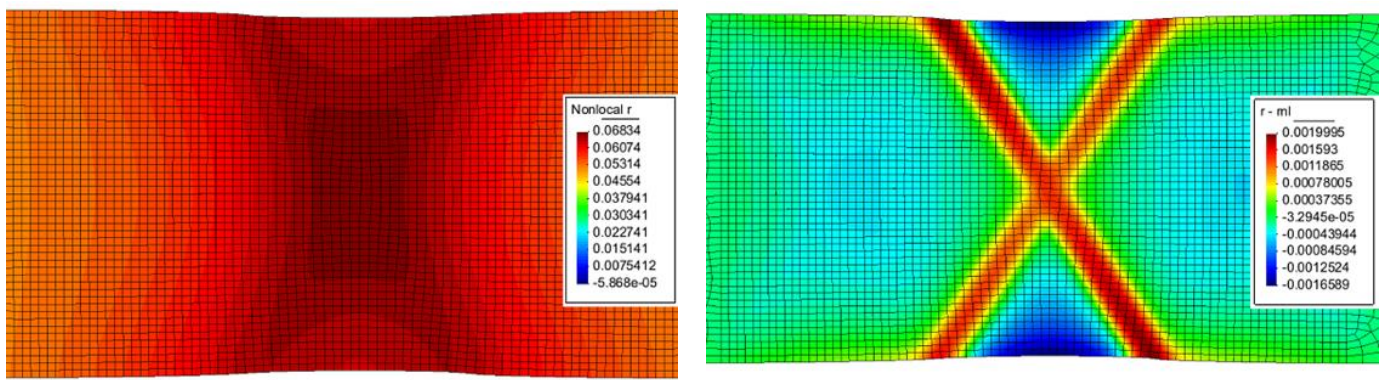
Stage I: mesh size 1.6mm



Stage I: mesh size 0.8mm



Stage I: mesh size 0.4mm



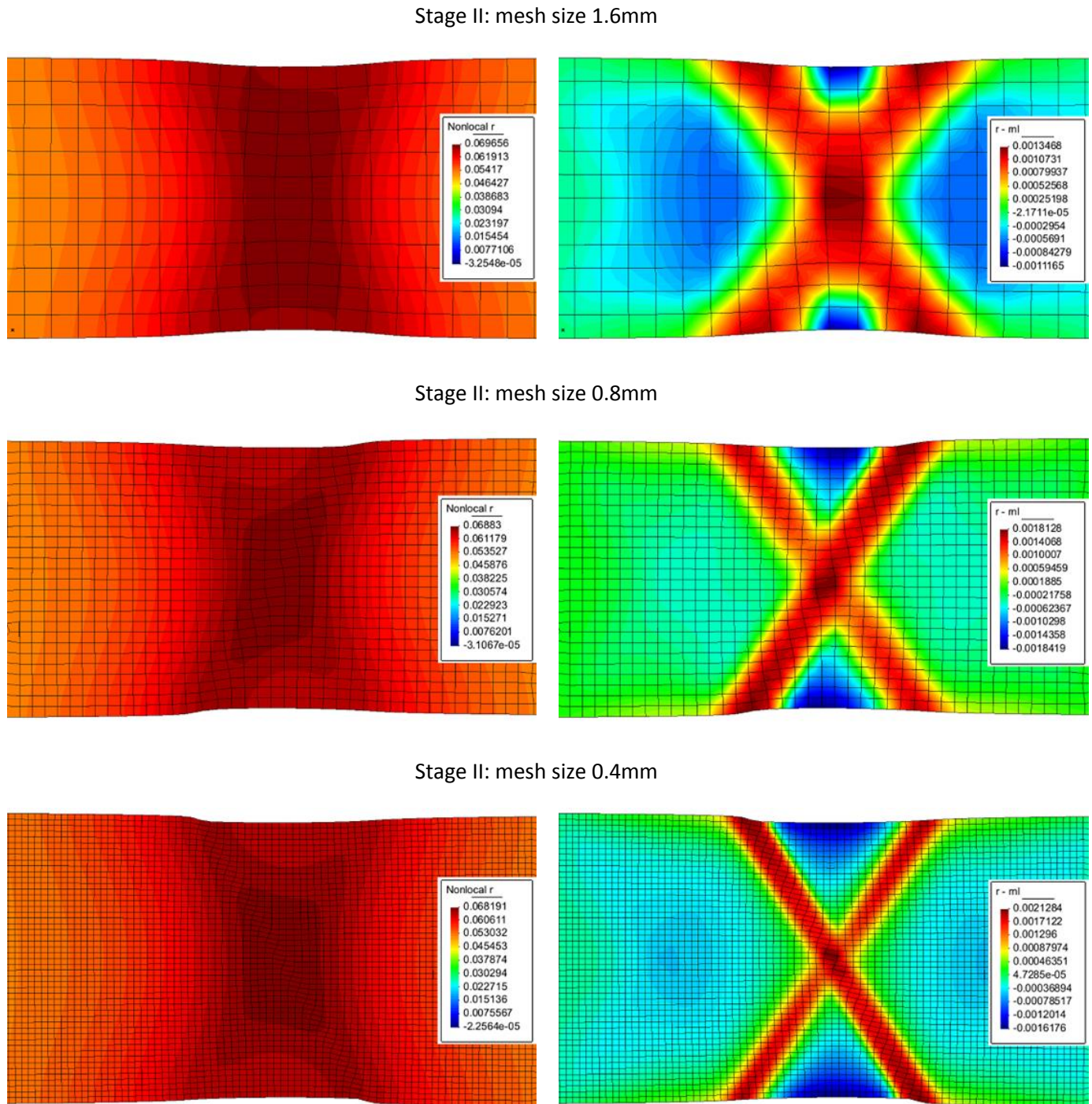


Fig. IX-14 Distributions of micromorphic isotropic hardening strain and the difference between the local and micromorphic isotropic hardening strain at stage I and stage II predicted by the micromorphic damage and isotropic hardening model for different mesh sizes

IX.2 Cross section deep drawing process

The cross section deep drawing (CSDD) tests are conducted by Yue (2014) in order to capture the initial fracture points and investigate the damage initiation and propagation under complex loading paths. The punch velocity is 0.5mm/s. A 0.1mm thickness CHF oil layer is used as the lubricant. Blank holder force is 400KN for the high strength steel DP1000. The geometric scheme of the tools are given in Fig. IX-15.

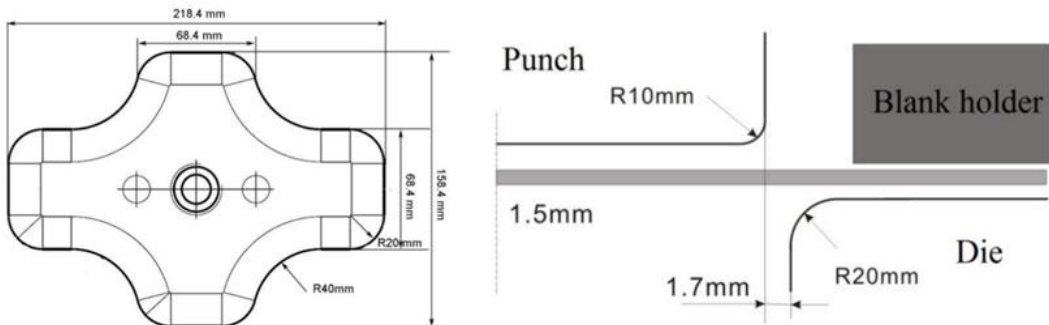


Fig. IX-15 Scheme of the cross section deep drawing (CSDD) process referenced Yue (2014)

The cross section deep drawing process is simulated using the subroutine VUEL of Abaqus/Explicit with the proposed strongly coupled local and micromorphic damage model assuming time-independent plasticity (no thermal effects). Only a quarter of the assembled geometry is given in Fig. IX-16 and the blank part is discretized with the unified mesh size 1.6mm, 2.0mm and 2.4mm respectively.

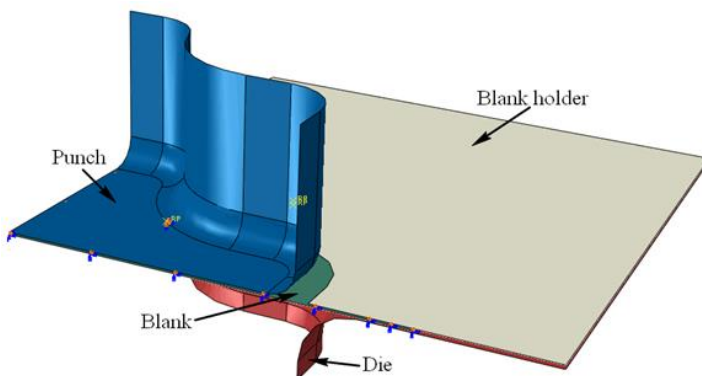


Fig. IX-16 Quarter part of the FEM model for the CSDD drawing process

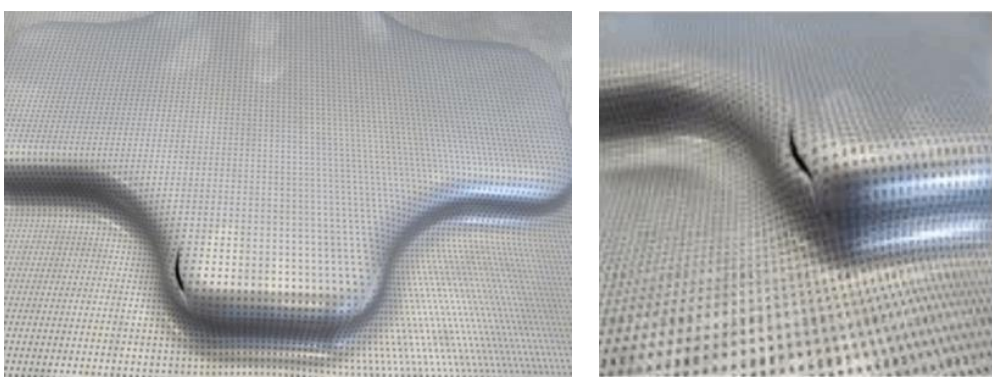


Fig. IX-17 Experimental failure observed in the sheet at the end of forming by CSDD

IX.2.1 CSDD processes using the local damage model

Considering the local damage model, the same elastoplastic material parameters of DP1000 steel are adopted as in Table IX-1, while the damage parameters S and coefficient h take the values of 8.5 and 0.25 respectively to take the microcracks closure effect into account.

In Fig. IX-18, the system responses in terms of punch force vs punch travel, as predicted by the local continuum damage model considering the micro-crack closure effects for different mesh sizes are presented. The clearly mesh-dependency is observed: the force-displacement curves drop from the approximate punch travel of 23.34mm, 26.14mm and 27.89mm for the analysis using mesh sizes 1.6mm, 2.0mm and 2.4mm respectively.

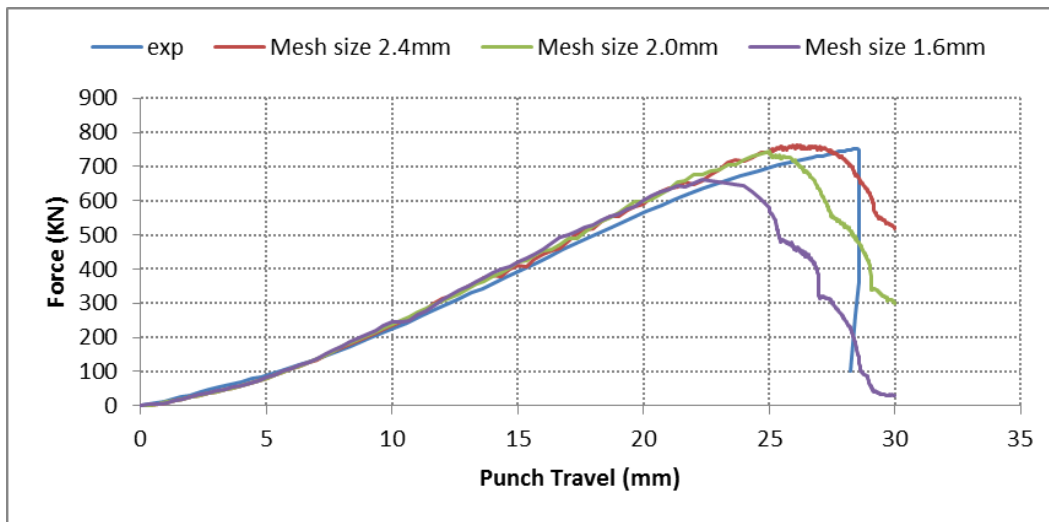


Fig. IX-18 Punch force-displacement curves predicted by the local damage model with microcracks closure effects for different mesh sizes of the CSDD process

Fig. IX-20 shows the distributions of local damage at stage I, when the finite element firstly reaches the failure criterion of the damage, for three mesh sizes using the local continuum damage model. We may notice: three different displacements of the initial crack appearing: 21.15mm, 24.12mm and 26.06mm; and different initial cracking positions are obtained for the mesh sizes: 1.6mm, 2.0mm and 2.4mm respectively.

In Fig. IX-21, the distributions of the accumulated plastic strains (PEEQ) and the equivalent stress for three mesh sizes at Stage I are illustrated. Clearly, the maximum values of PEEQ occur around the two corners and reach up to approximate 0.66 (or 66%) for all the three mesh sizes. Besides the two corners enduring large finite tensile deformation, the right side of the part appears seriously compressive deformations which may yield the wrinkle defects in the formability analysis. Considering the coefficient h takes 0.25 means that the evolution of damage under compression is much lower than its evolution in tension conditions. For that reason, we can image that if we let the coefficient h also takes 1.0, it seems probable that the initial crack would occur in this serious compression region, due to the same damage evolution similar under both tension and compression conditions. From the contour of equivalent stresses, the similar distributions and the consistent maximum values (around 1304.5MPa) are captured. The

equivalent stresses, for the compression zone are highly concentrated, and for the tensile localized zones vanishes due to the appearance of maximum damage values (initiation of cracks).

IX.2.2 CSDD processes using the micromorphic damage model

In order to overcome the above spurious numerical mesh-dependency of finite element results due to the damage-induced softening, the micromorphic damage model, taking the micromorphic density scale factor $\zeta_d = 1.0$, the micromorphic modulus $H = 110.0 \text{ N} \cdot \text{mm}^{-2}$ and the internal length $l_d = 1.0 \text{ mm}$ as well as the adjusted local damage parameter $S = 5.5$, is applied to the CSDD processes.

Fig. IX-19 represents the system responses in terms of force-displacement curves simulated using the micromorphic damage model for the three mesh sizes. Obviously, the mesh-independence is achieved and the system responses of different mesh sizes converge to a nearly unique consistent force-displacement curve.

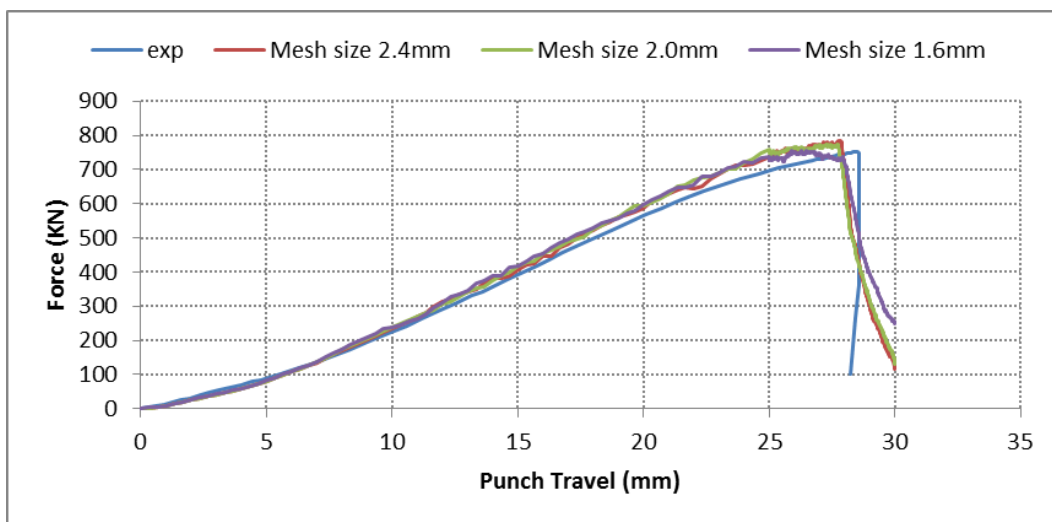


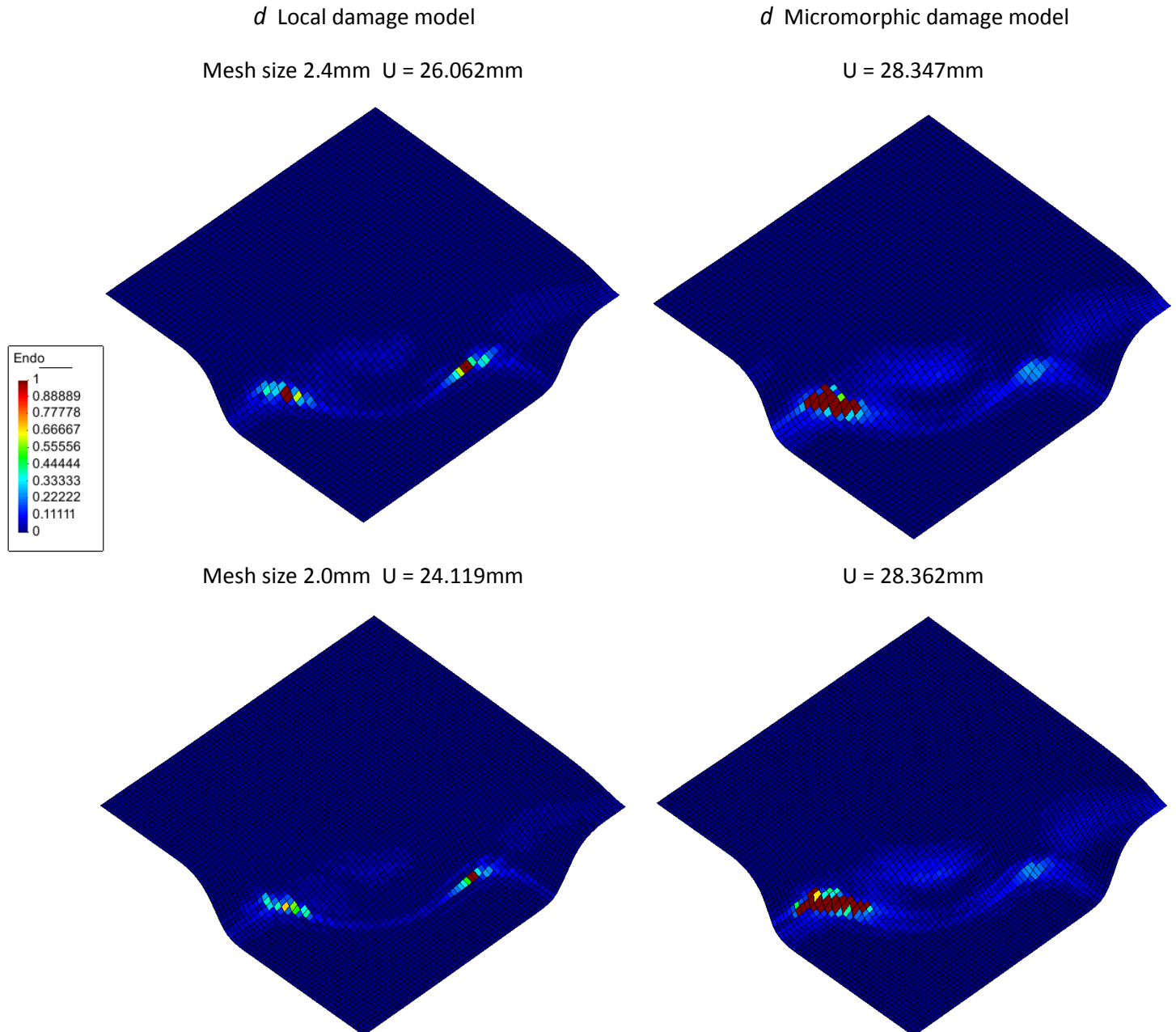
Fig. IX-19 Punch force-displacement curves predicted by the micromorphic damage model with closure effects for different mesh sizes of the CSDD process

From Fig. IX-20, we may clearly find that all the initial cracks appear approximately at punch travel 28.35mm as well as the consistent rupture positions on the left corner, obtained from the micromorphic damage model. In Fig. IX-21, the maximum values of equivalent plastic strain seem getting larger as the mesh refines: 1.02, 1.03 and 1.39 for mesh sizes 2.4mm, 2.0mm and 1.6mm respectively. The similar distributions of equivalent stress are observed with concentration in the compression region, the consistent maximum values (around 1291.0MPa) and the apparent zero stress inside the fully damaged zones, are also observed.

As shown in Fig. IX-22, the crack propagation, simulated by the micromorphic damage model, indicates that the crack initially appears at the left corner region at about the punch travel of 28.35mm in agreement with the experimental results as shown in Fig. IX-17 and Fig. IX-20, after the crack spreads forward from both sides of the initial crack frontlines and the consistent fractures at punch displacement around 29.50mm are predicted using the micromorphic damage model. However, it is worth noting that different positions and different punch travels of the initial crack are provided by the local damage model as shown in Fig. IX-20. We may find that the simulation from the local damage model gives macroscopic cracks

initiating in the two corners and evolves forward along their frontlines respectively. Considering the time of punch travel around 28.26mm, three different crack paths are observed from the simulations of the local damage model.

From this application of the deep drawing process, we may conclude that the micromorphic damage model taking the microcracks closure effects are capable of providing the converged numerical responses (force-displacement curves) close to experimental results as well as the consistent final fracture propagation.



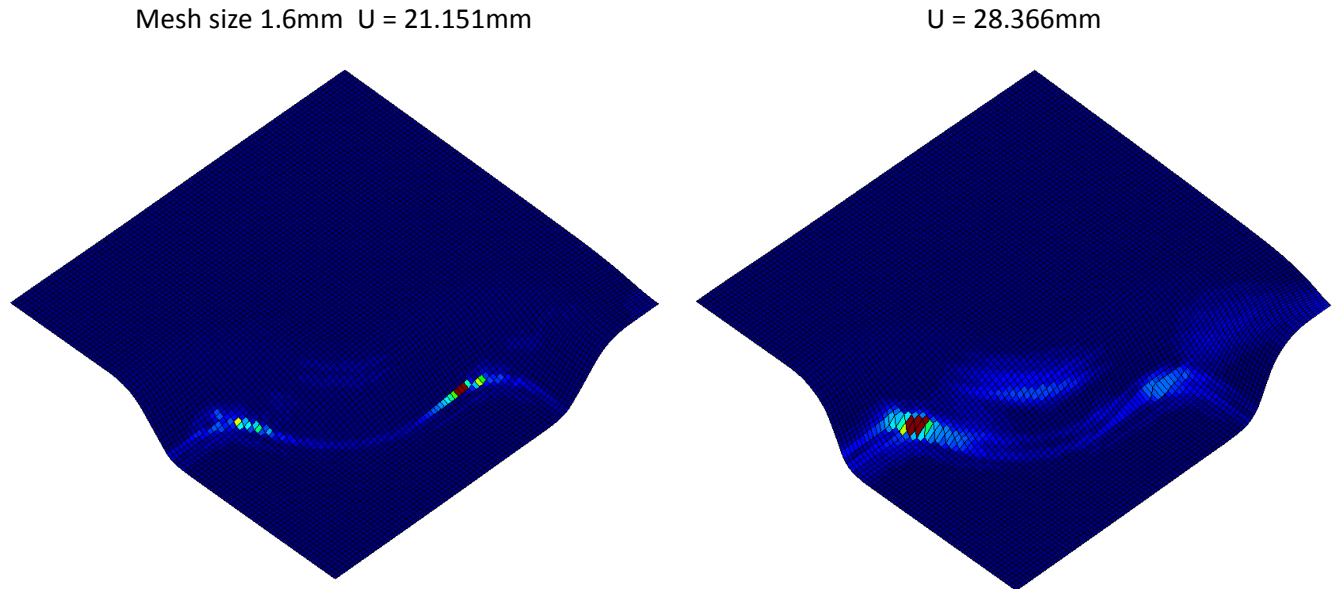
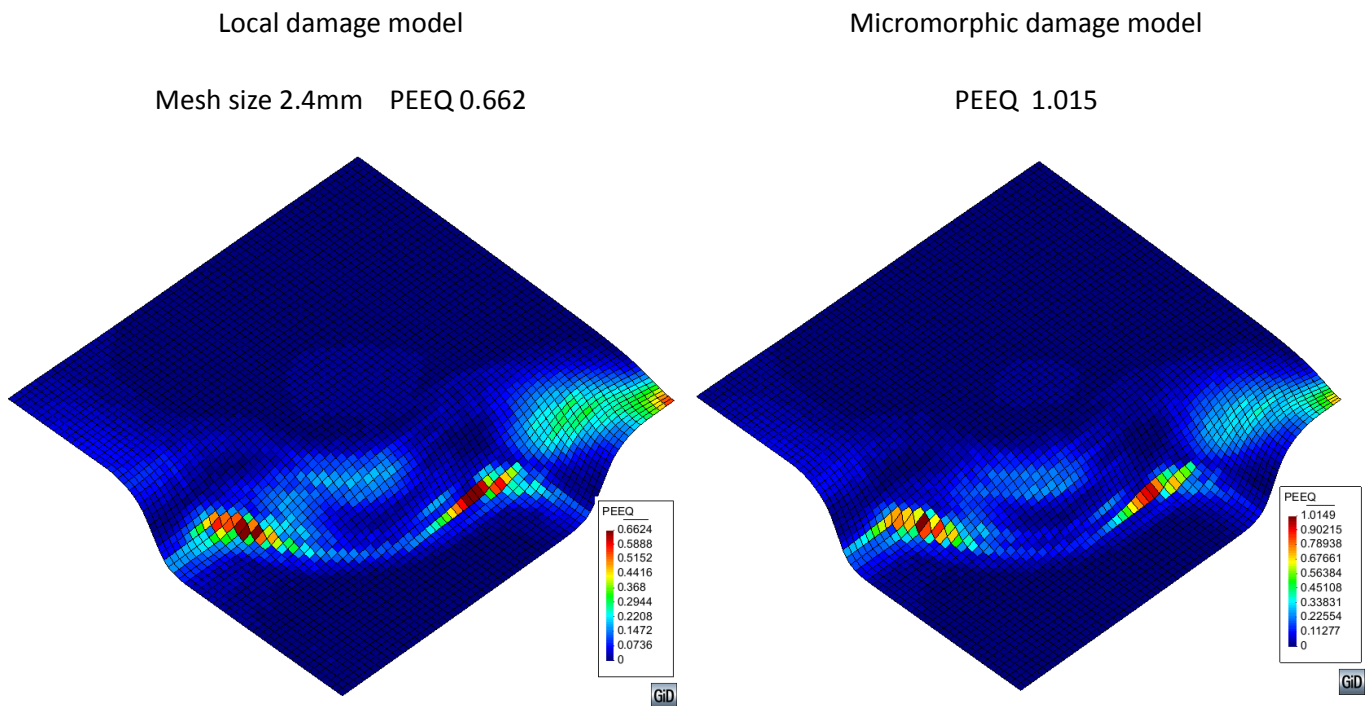
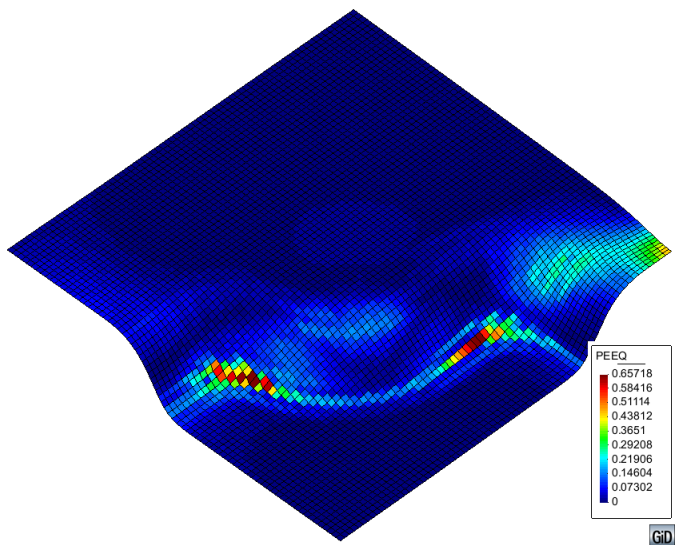


Fig. IX-20 Distributions of the local damage at stage I simulated by the local and micromorphic damage model for three different mesh sizes

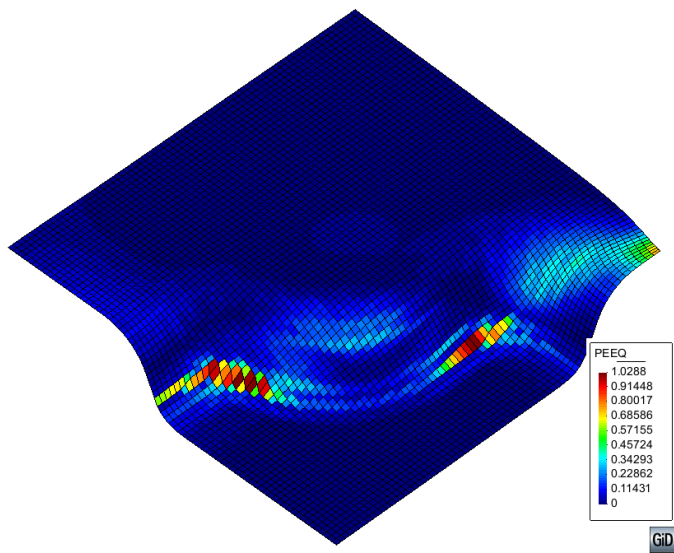


PART II CHAPTER IX APPLICATIONS

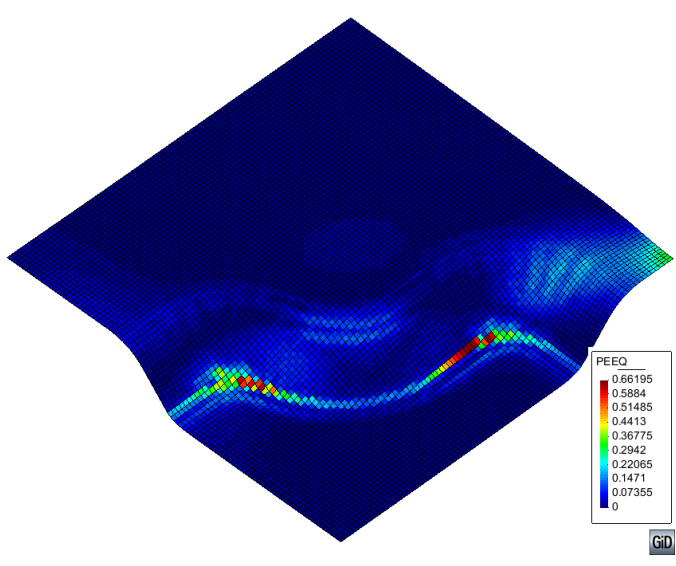
Mesh size 2.0mm PEEQ 0.657



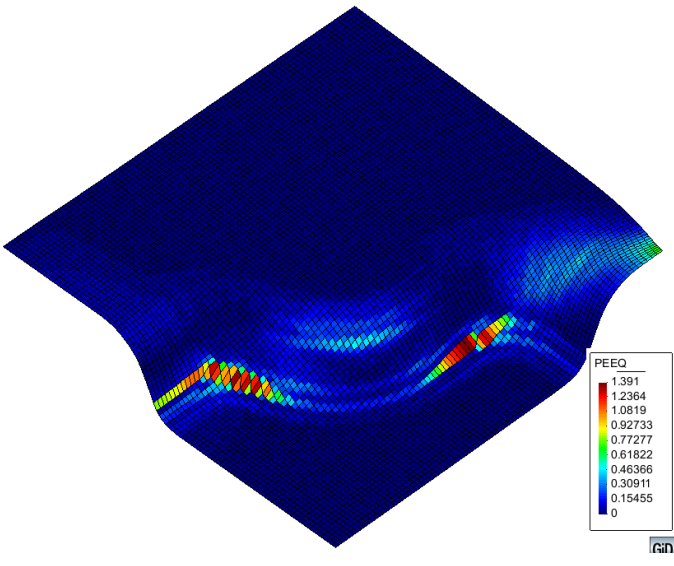
PEEQ 1.029



Mesh size 1.6mm PEEQ 0.662

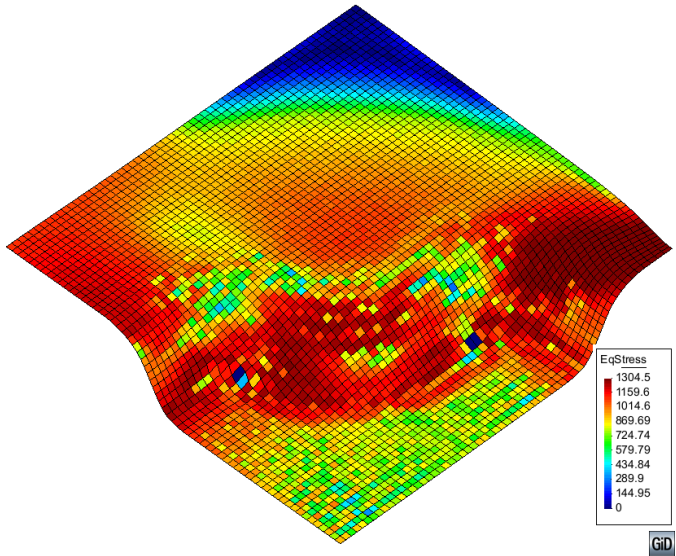


PEEQ 1.391

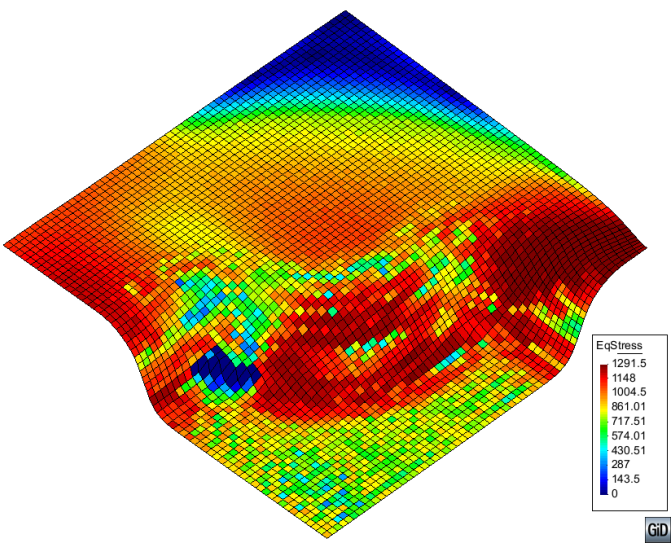


PART II CHAPTER IX APPLICATIONS

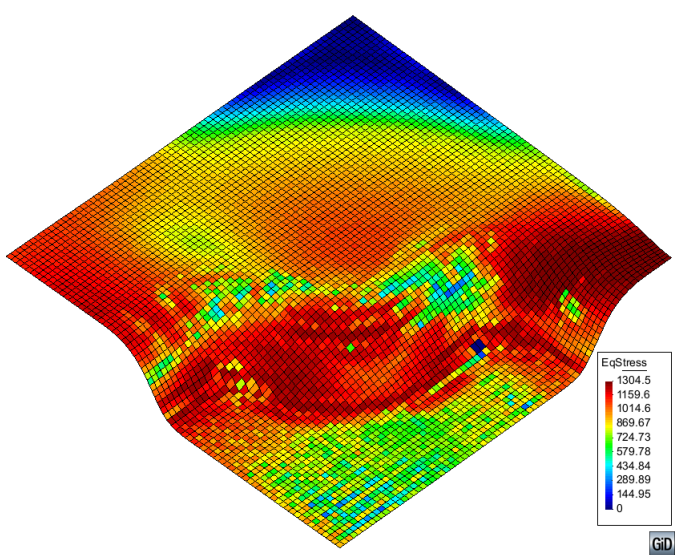
Mesh size 2.4mm EqStress 1304.5MPa



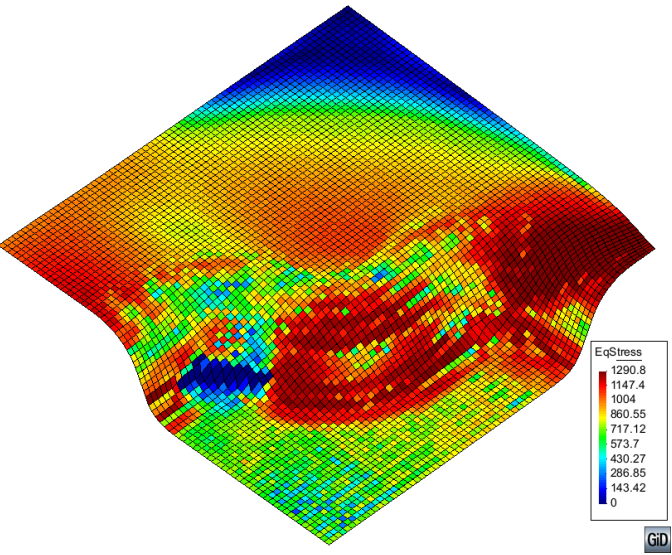
EqStress 1291.5MPa



Mesh size 2.0mm EqStress 1304.5MPa



EqStress 1290.8MPa



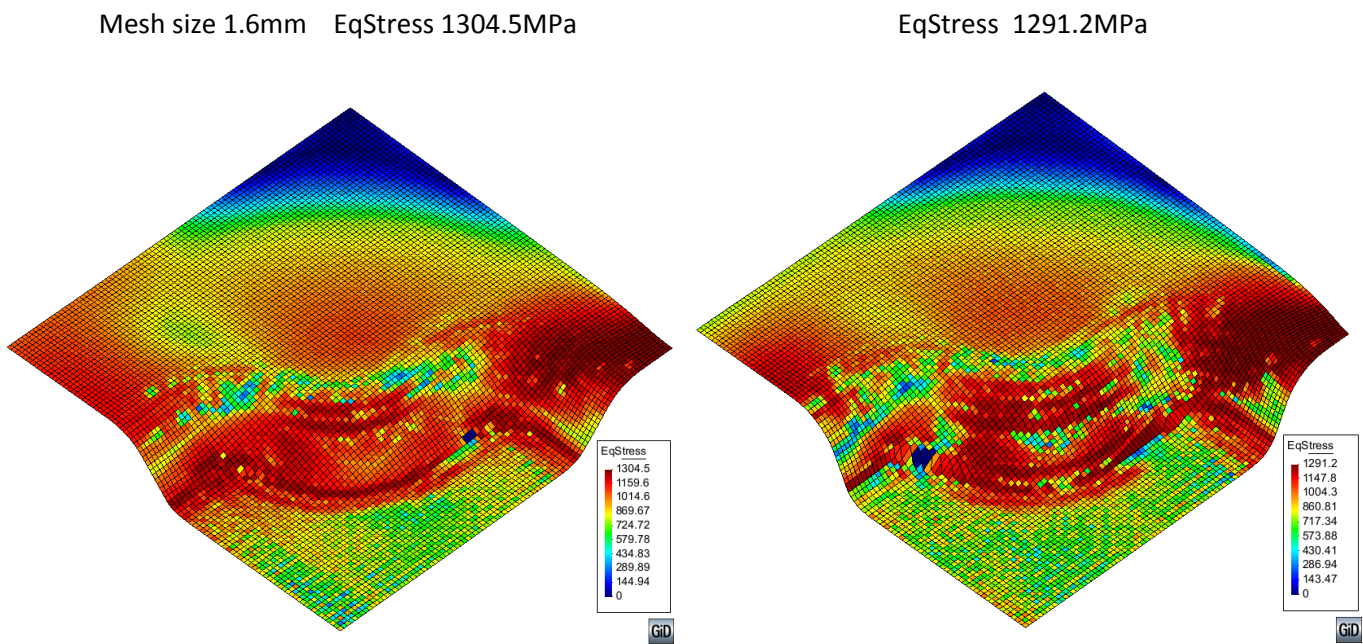
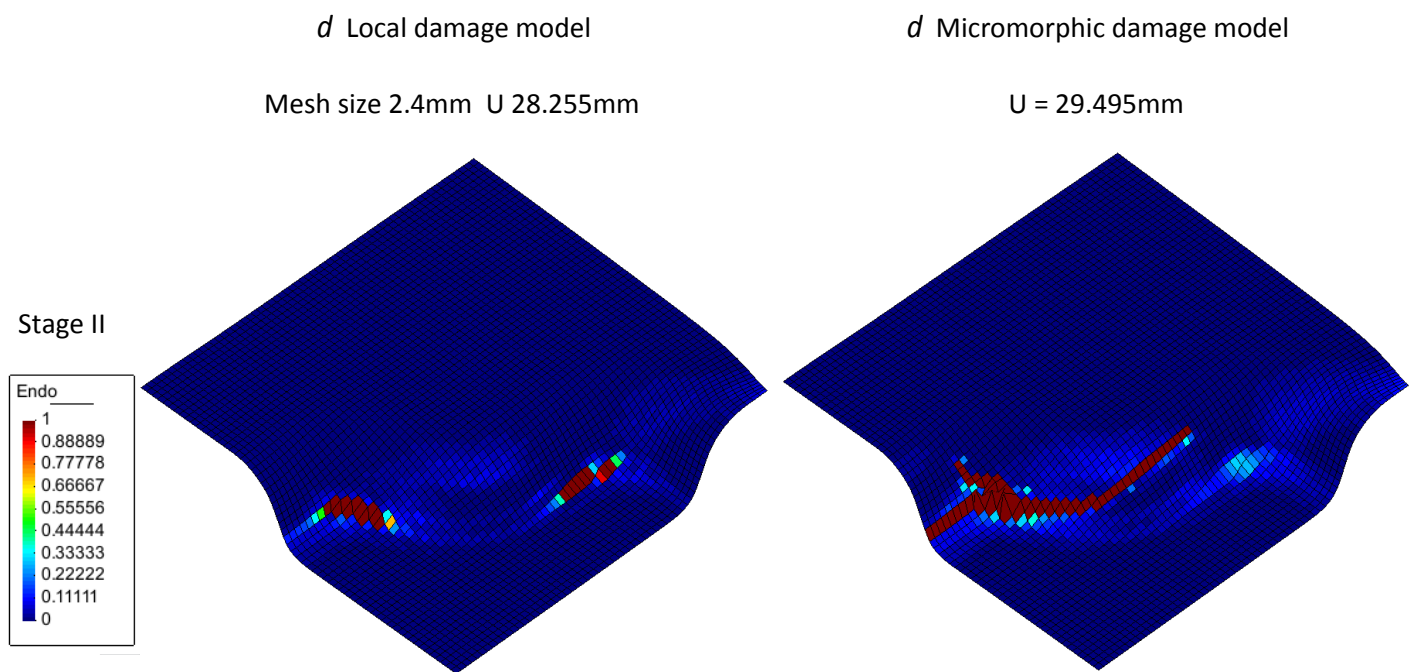


Fig. IX-21 Distributions of equivalent plastic strain and equivalent stresses at Stage I predicted by the local and micromorphic damage model for different mesh sizes



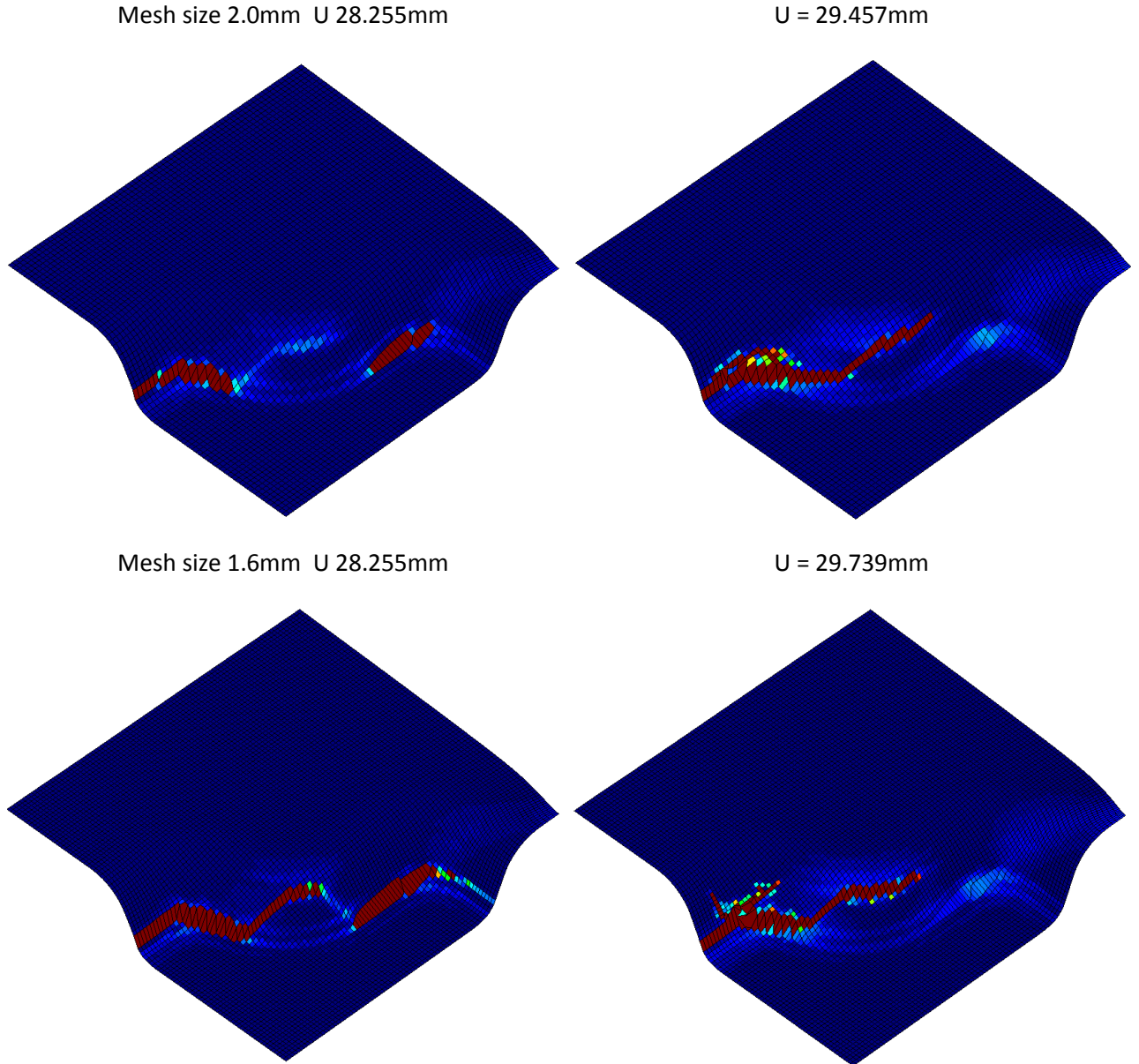


Fig. IX-22 Distributions of the local damage at stage II simulated by the local and micromorphic damage model for three different mesh sizes

IX.3 Pressure vessel

Considering the rupture process of a pressure vessel under high temperature, with given geometric informations and symmetric constraints of Y and Z axes depicted in Fig. IX-23. The inner thickness is 80mm. The material parameters of a typical common steel at room temperature is listed in Table IX-2. The simulation is performed by using the subroutine VUEL of Abaqus/Explicit under anisothermal conditions (i.e. elevated temperature around 600°C), using the time-dependent plasticity with strongly coupled local

damage, isotropic and kinematic hardening under the general three dimensional stress state assumption. Due to the limitation of time, only the local damage model is used in this simulation.

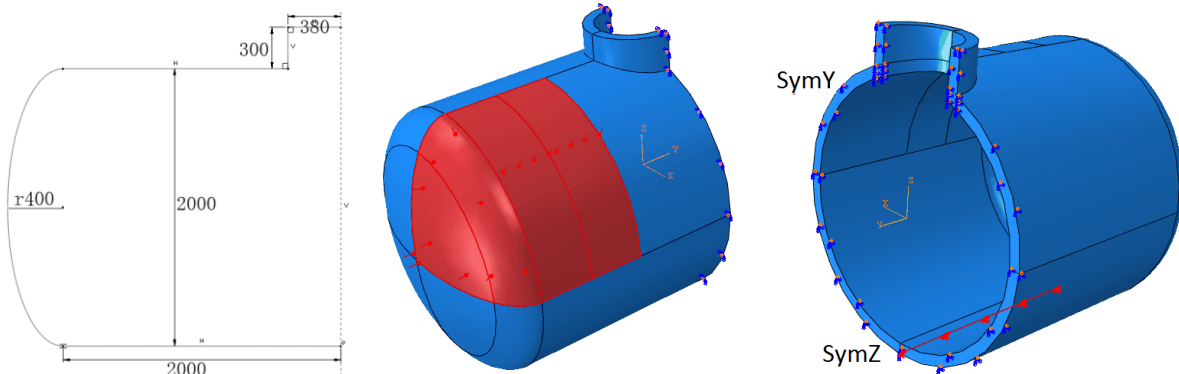


Fig. IX-23 Geometry and boundary conditions of the half of the pressure vessel

The stress-strain curves predicted by uncoupled and fully coupled models with local damage at strain rate of 1.0E-04/s at different temperatures lying from 20°C to 600°C are presented in Fig. IX-24 and Fig. IX-25, respectively. For the sake of simplicity, the thermal properties of the studied material are assumed to be temperature independent.

ρ (kg/m^3)	E (GPa)	ν	σ_y (MPa)	Q (MPa)	b	C (MPa)
7800.0	206.0	0.3	158.0	500.0	1.5	3000.0
a	S	s	β	γ	Y_0	h
26.0	3.0	1.2	2.0	4.0	0.0	1.0
κ ($W/m \cdot ^\circ C$)	C_e ($J/kg \cdot ^\circ C$)	α	K^{vp} (MPa)	m_{vp}		
60.0	450.0	1.2e-05	50.0	2.0		

Table IX-2 Material parameters of a type of common steel at room temperature

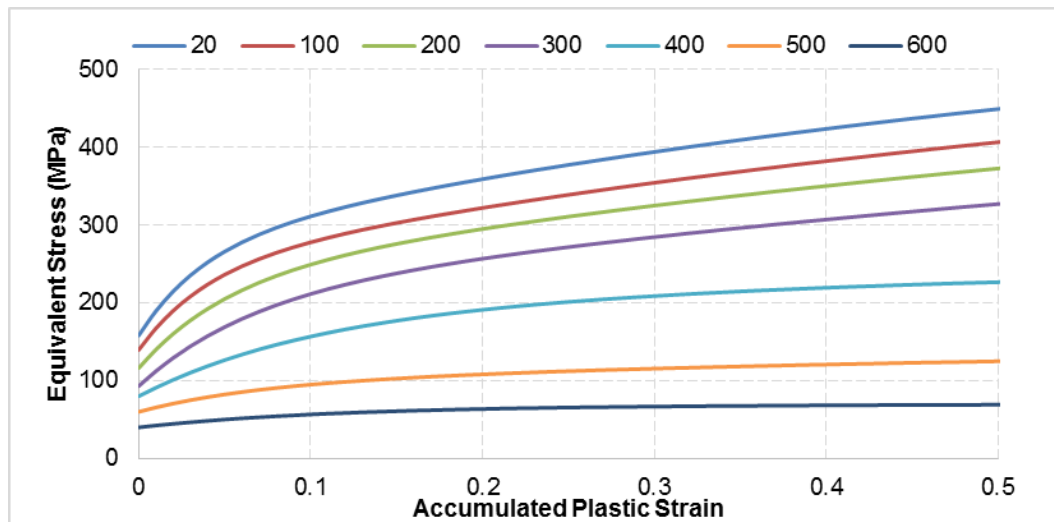


Fig. IX-24 Equivalent stress-strain curves for different temperatures

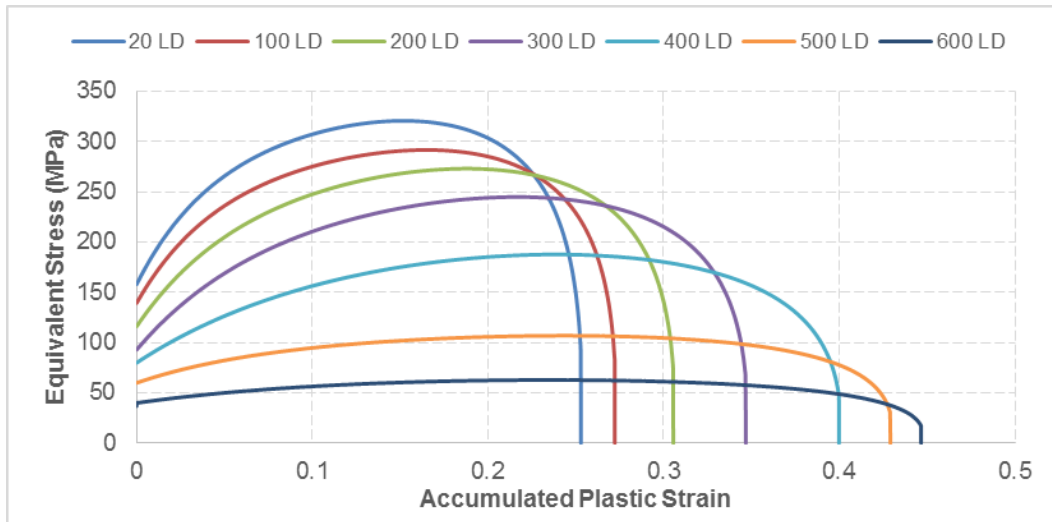


Fig. IX-25 Damaged equivalent stress-strain curves for different temperatures predicted by the fully local damage model (LD)

The pressure vessel is discretized with 9210 solid elements with two elements throughout the thickness. The scheme of the whole procedure works in the way: stage I, the temperature of the pressure vessel is homogeneously elevated up to around 600°C through the red external surface with an uniform heat flux; stage II, an uniform internal pressure of maximum 20MPa is linearly applied to the whole pressure vessel. Then, the red partition undergoes large deformation to final fracture mainly due to the material softening induced by the elevated temperature. Since the thermal diffusion process takes much longer in time than the process of mechanical deformation, here an artificial thermal conductivity ($6000W / m.^{\circ}C$) is used to shorten its computation time for the dynamic explicit solver, while ensuring the temperatures of outer and inner surface of the pressure vessel be elevated up to around 600°C in 2.1s.

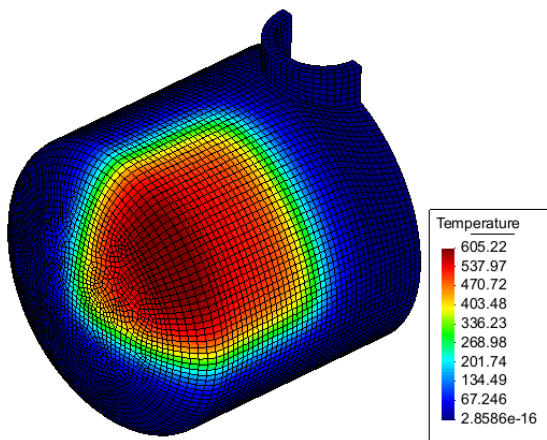


Fig. IX-26 Distributions of the elevated temperature at the end of stage I (2.1s)

The distributions of the temperature elevated by the uniform input heat flux at the end of stage I (2.1s) are illustrated in Fig. IX-26. The clear diffusion of the temperature is observed. The maximum values of the temperature of the outer and inner surfaces are about 605.2°C and 594.3°C, respectively.

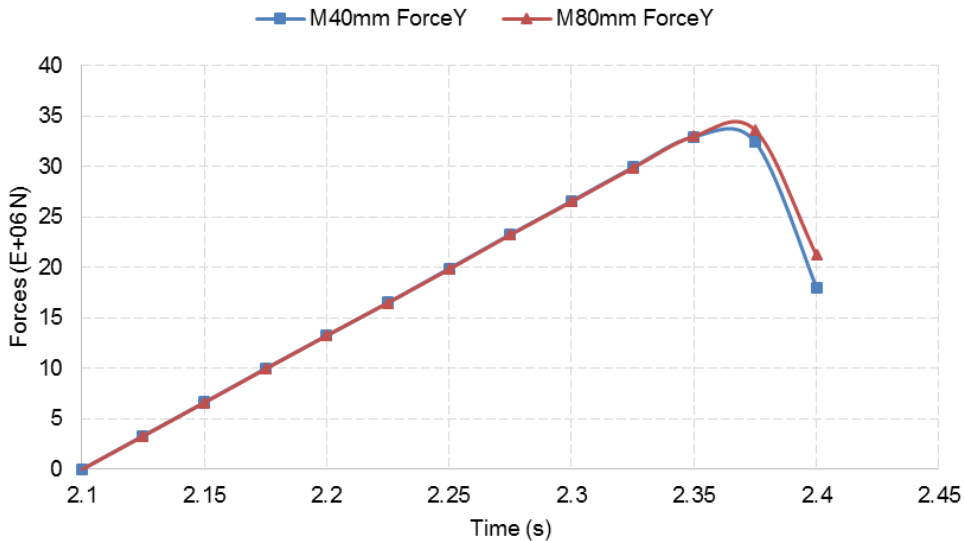


Fig. IX-27 The evolution of Forces along Y axis for different mesh sizes 40mm and 80mm

In Fig. IX-27 and Fig. IX-28, the curves of reaction forces the Y axial and Z axial for different mesh sizes 40mm and 80mm are plotted since the time 2.1s, when the uniform internal pressure is linearly applied. Clearly, in the period of before 2.35s (12.5MPa), the evolutions of reaction forces for the two mesh sizes behavior exactly the same. This is mainly due to the relative small value of the damage (around maximum values 0.078 for 80mm and 0.135 for 40mm), as shown in Fig. IX-29, which yields negligible damage effects on the material elasto-viscop-plastic behavior, in this period. Beyond that time, the numerical responses of reaction forces plot differences for the two mesh sizes. The mesh-dependency is clearly observed.

In Fig. IX-30, it illustrates the distributions of the accumulated plastic strain for different mesh sizes 40mm and 80mm under different inner pressures, with removed fully damaged elements. When the inner pressure is around 13.3MPa (time 2.366s), the first fracture of the element is observed for mesh size 80mm, while more fully damaged elements are removed for mesh size 40mm. The similar phenomenon is also captured for the sequential inner pressures 13.5MPa (time 2.370s) and 13.9MPa (time 2.378s). Clearly, this clear mesh-dependent phenomenon is similar to the behavior predicted by the local damage model with time-independent plasticity. As expected and shown in the literatures, the viscoplastic model may provide a cure of the pathological mesh-dependency problem, however, it is not able to fully remove the problems in strain-softening. Mainly due to the limitation of time, we didn't finish the simulations of this pressure vessel using the fully coupled micromorphic damage model, which is foreseen to overcome the mesh-dependency.

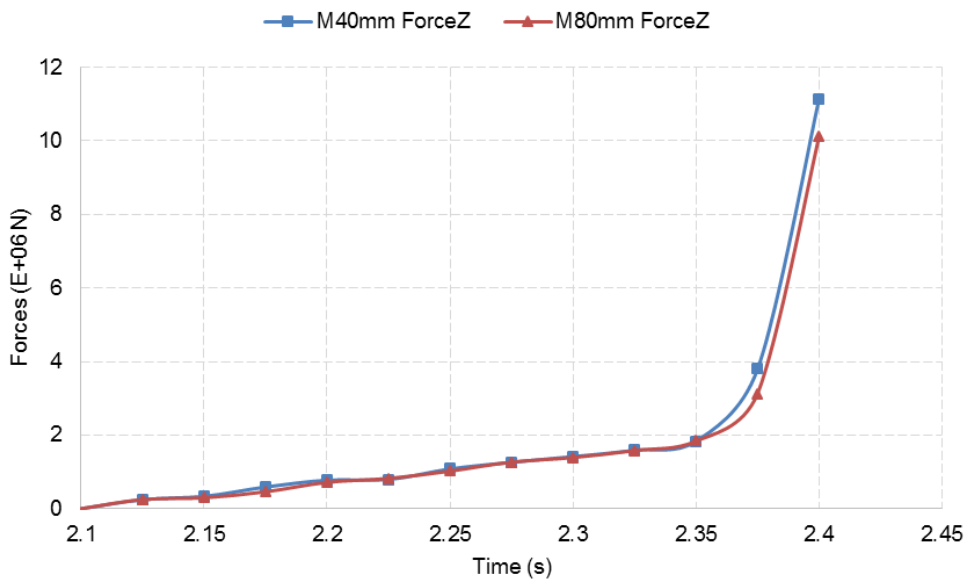


Fig. IX-28 The evolution of Forces along Z axis for different mesh sizes 40mm and 80mm

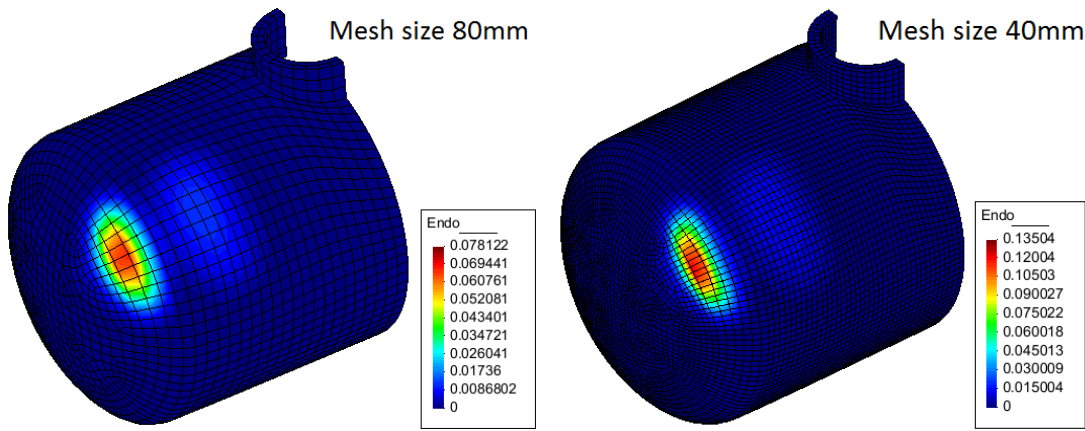


Fig. IX-29 Distributions of local damage of the pressure vessel at stage II (2.35s)

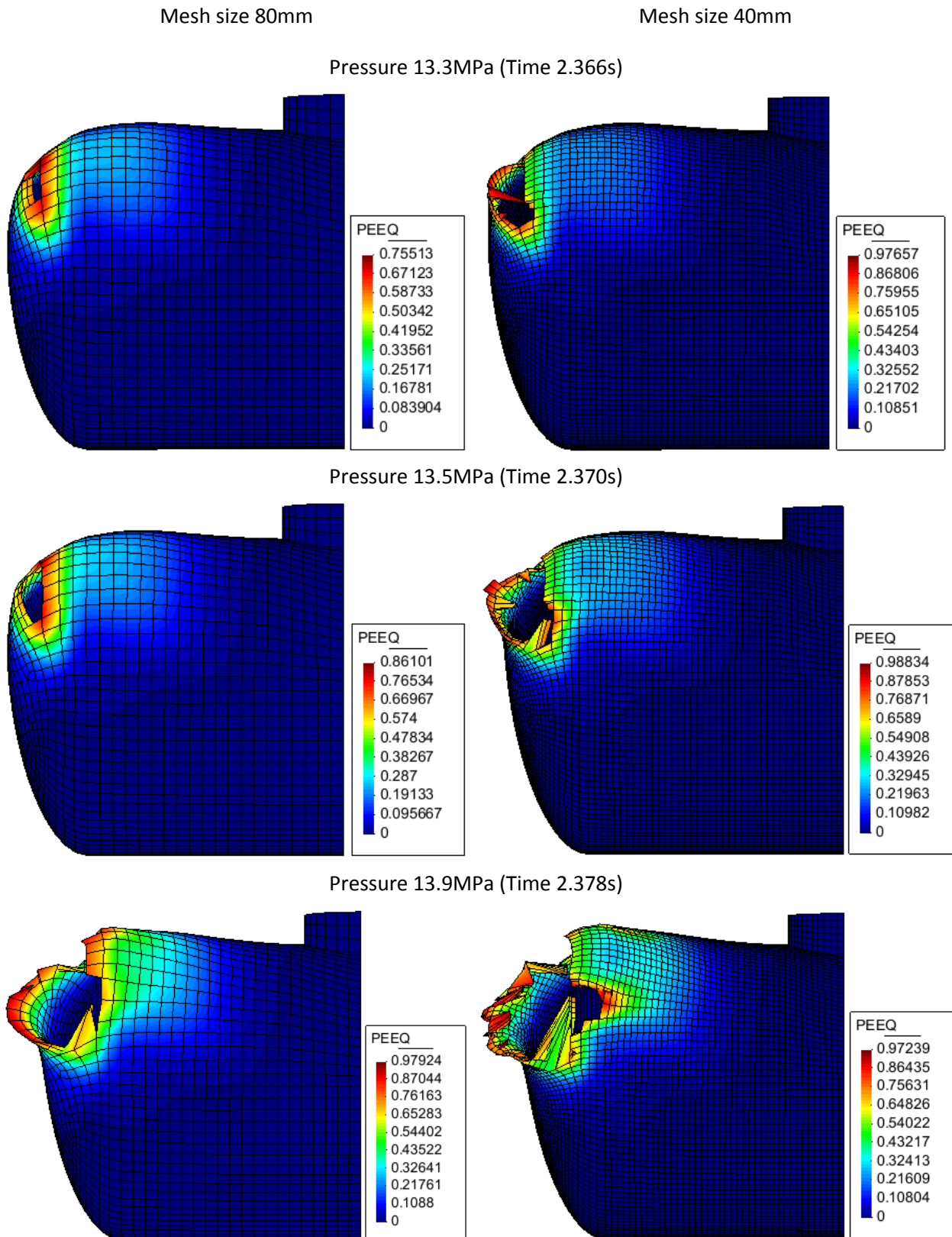


Fig. IX-30 Distributions of accumulated plastic strain of the damaged configurations of the pressure vessel for different mesh sizes at stage II

X. Conclusions

In part II, a complete set of nonlocal constitutive equations for anisotropic elasto-visco-plasticity solids, strongly coupled with thermal effects, isotropic ductile damage, isotropic and kinematic hardening, micromorphic temperature, micromorphic ductile damage, micromorphic isotropic hardening and micromorphic kinematic hardening, are derived from the state and dissipation potentials, under the framework of the extended irreversible thermodynamics, to represent the material strain-softening behaviour and avoid the ill-posed IBVP induced by the classical local damage model:

- 1). A group of additional balance equations associated with the new micromorphic variables are obtained by using the generalized principle of virtual power. The state relations including the classical and generalized stresses as well as the evolutions of the dissipative state variables are derived from the state potentials and dissipation potentials, respectively, according to the thermodynamically consistent formulations;
- 2). The introduction of the new micromorphic temperature and its first gradient to the free energy density, yields a pair of generalized micromorphic heat equations governing the evolution of temperature, which allows the introduction of nonlocal thermal effects and an internal length scale. Several extended heat equations, which are reviewed in detail, could be retrieved from the constrained generalized micromorphic heat equations;
- 3). The weak forms of the IBVP are obtained by using the Galerkin weighted residual methods, and discretized in time and space according to the standard finite element method, with new developed finite element possessing additional micromorphic dofs in the subroutine Vuel() of Abaqus. Parametric study of the damage parameters, the micromorphic moduli and viscoeffects is performed to well understand the predictive possibilities of the proposed micromorphic fully coupled constitutive equations;
- 4). Applications of the fully coupled micromorphic damage and isotropic hardening constitutive equations, are applied to the uniaxial tensile test and cross section deep drawing processes of the material of DP1000. The clear mesh-independency of the numerical responses and consistent final fracture propagations are obtained.

XI. Global conclusions and perspectives

In this work, we formulated a general micromorphic nonlocal elasto-visco-plastic constitutive model accounting for mixed nonlinear isotropic and kinematic hardenings strongly coupled with ductile damage in the context of thermodynamics of irreversible processes as well as generalized continuum mechanics, with applications to the numerical simulations of sheet metal forming processes.

Firstly, we developed a static-implicit multi-step FEM solver accounting for the classical elastoplasticity with isotropic hardening for efficient formability analysis (e.g. the prediction of defects, thickness variation, strain and stress fields) of the sheet metal forming component based on the inverse approach.

- 1). The multi-step solver improves the stress predictions by adopting several middle configurations representing deformation paths and simplified tools' actions (contact forces). The intermediate configurations of deformed sheet blank are efficiently constructed according to the procedures: solving an optimal quadratic program, generating initial solutions and balance equilibrium iterations;
- 2). Numerical applications validate the new derived finite strain measurement along thickness of the shell and examine the capability to improve the stress estimations during forming under complex loading paths.

Secondly, a general thermodynamically-consistent thermomechanical micromorphic nonlocal constitutive model has been derived and implemented in Abaqus/Explicit to capture the strongly nonlocal effects within the material strain-softening localization zones induced by thermal or ductile damage.

- 1). A complete set of micromorphic constitutive equations is formulated in the context of thermodynamics of irreversible processes.
 - i). The new additional balance equations associated with the new additional dofs carrying the micromorphic effects (e.g. the ductile damage, the isotropic hardening, the kinematic hardening and the temperature) are derived from the generalized principle of virtual power. Also, the state relations as well as the evolution equations related to the local and generalized (micromorphic) are derived in the framework of the thermodynamics of irreversible processes with state variables, derived from both the Helmholtz free energy, and the dissipation potentials. It is worth noting that all the constitutive equations (the state relationships as well as the evolution equations) are written under an additive form of classical local contribution and extra nonlocal contributions. The local constitutive equations are easily obtained as particular cases if the micromorphic material properties vanish;
 - ii). Numerical implementations related to the model, limited to micromorphic damage and micromorphic isotropic hardening for the sake of simplicity, have been carried out in Abaqus' subroutine Vuel using three types (membrane, shell and solid-shell) of assumed strain finite elements. The efficient and robust unconditionally stable local integration is performed thanks to the asymptotic scheme and the return-mapping algorithm;
 - iii). Parametric study concludes that:

CHAPTER XI GLOBAL CONCLUSIONS AND PERSPECTIVES

- a. only the local damage parameter S governs the more brittle or more ductile evolutions of damage;
 - b. the micromorphic moduli \check{H} and \check{Q} are more sensitive to the system responses than their micromorphic gradient moduli \check{H}^g and \check{Q}^g (or their associated internal lengths I_d and I_r) respectively;
 - c. the local damage parameters also significantly affect the obtained consistency of material responses except the parameter S which maintains the convergence while speeding or slowing the final fracture;
 - d. no differences are observed for case when the micromorphic density smaller than the local one;
 - e. the micromorphic damage effect becomes significantly under cases of high temperature or high strain rate due to the complex coupling between viscous effects and nonlocal damage effects.
- iv). The applications of the proposed micromorphic model, to both the uniaxial tensile test of DP1000 and the cross section deep drawing processes, predict physically sound solutions independent from the mesh refinement. The macroscopic crack initialization and propagation are also observed in the cross section deep drawing processes.
- 2). Concerning the thermal aspects, the micromorphic formulation is applied to the problem of heat transfer by means of a generalized principle of virtual power.
- i). The new microtemperature field is introduced as well as its first gradient and leads to a pair of thermodynamically-consistent coupled generalized heat equations. The constrained case for which the microtemperature coincides with the temperature itself is of particular interest because it can be compared to the various extensions of the heat equation available in the literature.
 - ii). The proposed heat equation is enhanced by essentially three new contributions which were illustrated in the linearized case. The three terms affect the transient thermal behavior of the material only. The first new term is related to the Laplacian of the temperature rate, a contribution which was proposed first by Cattaneo in an early version of his theory. A second contribution is proportional to the second time derivative of the temperature which changes the usual heat equation into a hyperbolic equation with a positive characteristic time. The last term associated with the third time derivative of temperature remains rather unexplored even though it is present in some generalized theories found in the literature.
 - iii). The proposed theory was shown to differ from existing thermomechanical extensions of Eringen's micromorphic model that rely on the introduction of a microtemperature vector akin to a relaxed temperature gradient. It has also been compared to the effective heat equation arising from the double temperature model involving two coupled heat equations and leading also to fourth order spatial derivatives:
 - a). The hyperbolic heat equation of Cattaneo II with relaxation time, can be obtained from the thermodynamically-consistent micromorphic heat equation by neglecting the nonlocal effects of the temperature;

- b). The classical, hyperbolic and generalized two-temperature models can be also retrieved from the micromorphic heat equations;
- c). Both the micro-temperature heat equation using Green's theory and the micromorphic heat equation provide a pair of governing equations for local and micro/micromorphic temperature. And the classical wave equation can be obtained from their constrained heat equations;
- iv). The proposed theory allows for a direct coupling with the mechanics of materials and is thought to be useful for the simulation of fast heat and mechanical treatments of materials including metal forming at high speeds, laser surface treatments of materials, etc. The nonlocality in the proposed theory resulting from the introduction of the gradient of micromorphic temperature could be an alternative to the analysis of heat transport based on enhanced heat fluxes.

Considering the conflict between the limitation in time and the complexity of coupling among the parameters in the sophisticated generalized micromorphic constitutive model, we have the following further developments to be continued in the future:

- 1). In general, all the variables that govern the strain-softening should be treated as nonlocal variables. For that purpose, an extension of the micromorphic kinematic hardening based on the present micromorphic model is necessary to fully capture the strain softening of materials' behavior;
- 2). Some more complete and systemic experiments are required to facilitate the identification of the large amount of temperature-dependent/independent material parameters entering the advanced nonlocal constitutive equations;
- 3). Generally, the ductile damage can be strongly anisotropic. An extension of the present micromorphic model to include the anisotropy of the ductile damage could be considered, referencing the work of anisotropic ductile damage accomplished in LASMIS (Badreddine, 2006; Saanouni, 2012) by representing the damage by a couple of second-rank tensors ($\underline{d}, \underline{Y}$) ;
- 4). Applications of the new generalized micromorphic heat equations are expected in Nano-structured media and Nanosystems, but also for fast material processing and surface treatments. The work performed by Saanouni and Hamed (2013) for finite time-independent plasticity could be extended to the thermomechanical processes (finite viscoplasticity) using the generalized heat equation based on the present microtemperatur model.

Résumé extensif en Français

Introduction

Afin de répondre aux nouvelles exigences mondiales de l'économie et de la protection de l'environnement dans l'industrie automobile, la sélection des matériaux pour la réduction de masse est un enjeu crucial. De nouvelles nuances d'acier à haute résistance permettent aux constructeurs automobiles de réduire la masse de leurs véhicules de 25 à 39% par rapport à l'acier conventionnel, permettant ainsi une économie de 3 à 4,5 tonnes de gaz à effet de serre sur toute la durée de vie du véhicule. Cependant, cette augmentation de la résistance de ces nouveaux matériaux se traduit souvent par une réduction significative de leur capacité d'étirage communément appelée la ductilité. Par ailleurs, pendant le processus de formage, le matériau métallique est soumis à une déformation irréversible importante non homogène qui finit par localiser dans des bandes de cisaillement où se forment souvent des micro défauts (microfissures, microcavités) qui croissent et coalescent pour former une fissure macroscopique dangereuses pour l'intégrité de la pièce.

La simulation numérique utilisant la méthode des éléments finis (MEF) est aujourd'hui un outil d'utilisation courante et d'intérêt considérable pour les industries mécaniques. Elle prend une place croissante et dominante dans de nombreux secteurs industriels comme dans l'industrie automobile. Pour simuler numériquement les procédés de formage, un modèle 3D décrivant les principaux phénomènes physiques (thermiques et mécaniques) et leurs diverses interactions (couplages) qui caractérisent le comportement du matériau est nécessaire. Cela peut être fait en utilisant deux types d'approche de modélisation, à savoir : l'approche mono échelle macroscopique phénoménologique et l'approche multi-échelle ou micro-macro.

Cependant, l'utilisation de ces modèles locaux avec adoucissement induit par les effets thermiques, d'endommagement ou autres, conduit à un problème d'évolution (problème aux valeurs initiales et aux limites PVIL) mal posé (perte d'ellipticité en statique ou d'hyperbolicité en dynamique) fournissant des solutions numériques non acceptables fortement dépendantes de la discrétisation en espace et en temps.. La façon naturelle d'éviter cet inconvénient est de recourir à une formulation non locale induisant des longueurs internes caractéristiques de la microstructure des matériaux. Ceci se fait relativement aisément dans le cadre de la mécanique des milieux continus généralisés.

Le but de ce travail est de développer des modèles de couplage thermomécanique avancés dans le cadre de la mécanique des milieux continus généralisés (milieux micromorphes) pour introduire le concept de longueurs internes représentatives des microstructures des matériaux tout en tenant compte de l'anisotropie initiale de l'écoulement inélastique en grandes déformations.

Tout d'abord, nous avons développé un solveur EF basé sur une approche inverse à étapes multiples, statique-implicite, qui tient compte de l'élastoplasticité classique avec écrouissage purement isotrope pour analyser la formabilité de tôles minces de sorte à éviter les défauts (fort amincissement, endommagement, plissement, ...).

Dans un deuxième temps, nous avons formulé un modèle thermomécanique non-local dans le cadre des milieux continus généralisés (milieux micromorphes), capable de tenir compte d'un effet d'échelle associé à chacun des phénomènes physiques micromorphes retenus dans la modélisation (endommagement ductile, température, écrouissages). Ces effets d'échelles se présentent sous la forme de longueurs internes caractéristiques de la microstructure du matériau étudié. L'enrichissement de l'espace des variables cinématiques par l'ajout de degrés de liberté (ddl) micromorphique, conduit via l'application du principe des puissances virtuelles étendues, à l'obtention d'autant d'équations de bilan supplémentaires. De même, l'extension de l'espace des variables d'état conduit à la généralisation des équations de comportement (équations d'état et équations d'évolution) par l'ajout d'une contribution non locale à chacune des équations de comportement. Concernant les phénomènes thermiques, l'approche micromorphe conduit à une nouvelle paire d'équations de régulation de la température faisant intervenir non seulement la température locale mais également une microtempérature ainsi que leurs dérivées successives jusqu'à un ordre donné. Le cas constraint pour lequel la microtempérature coïncide avec la température locale présente un intérêt particulier car il peut être comparé aux différentes extensions de l'équation de la chaleur proposées dans les littératures (Table 0-1).

Modèle	Auteurs	Equations de chaleur
Equation classique de chaleur avec le modèle de Fourier	Fourier, 1878	$\rho C_e \dot{T} = \kappa \Delta T$
Type hyperbolique avec temps de relaxation	Cattaneo I, 1948	$\rho C_e \dot{T} + \tau \kappa \Delta \dot{T} = \kappa \Delta T$
	Cattaneo II, 1948	$\rho C_e \dot{T} + \tau \rho C_e \ddot{T} = \kappa \Delta T$
	Coleman et al., 1982	$\begin{cases} \left(\rho C_e + \vec{q} \cdot \frac{dA}{dT} \cdot \vec{q} \right) \dot{T} + 2\vec{q} \cdot \underline{A} \cdot \dot{\underline{q}} = -\text{div}(\vec{q}) \\ \vec{q} + \underline{\tau} \cdot \dot{\underline{q}} = -\underline{\kappa} \cdot \vec{\nabla} T \end{cases}$
Modèle de gradient de température (ou d'entropie)	Nguyen, 2010	$\rho C_e \dot{T} + M \vec{\nabla} \dot{T} \cdot \vec{\nabla} T = \kappa \Delta T$
	Forest, 2008	$\rho C_e \dot{T} + T_0 A_T \Delta \dot{T} = \kappa \Delta T$
	Forest, 2008	$\rho C_e \dot{T} + T_0 A_T \Delta \dot{T} + \frac{A_s^2 C_e^2}{\rho T_0} \Delta^2 \dot{s} = \kappa \Delta T$
	Forest, 2010	$\rho C_e \dot{T} - \alpha T_0 \ddot{T} + M T_0 \Delta \dot{T} = \kappa \Delta T$
Modèle à double température	Aifantis, 1980	$\dot{T} + \alpha \ddot{T} - \beta \Delta \dot{T} + \gamma \Delta^2 T = \lambda \Delta T$
	Sobolev, 2016	$\dot{T}_i + (\tau + \tau_{12}) \ddot{T}_i + \tau \tau_{12} \ddot{\bar{T}}_i - l^2 \Delta \dot{T}_i = \bar{\kappa} \Delta T_i$
		$\dot{T}_i + (\tau + \tau_{12}) \ddot{T}_i + \tau \tau_{12} \ddot{\bar{T}}_i - (l^2 + l_e^2) \Delta \dot{T}_i - l_e^2 \tau_{12} \Delta^2 T_i = \bar{\kappa} \Delta T_i$

Modèle micro-température	lesan, 2002	$\begin{cases} c\dot{T} = k\Delta T + k_1 \operatorname{div}(\vec{T}) \\ b\ddot{\vec{T}} = k_6 \Delta \vec{T} + (k_4 + k_5) \vec{\nabla}(\operatorname{div}(\vec{T})) - k_2 \vec{T} - k_3 \vec{\nabla} T \end{cases}$
	lesan, 2005	$\begin{cases} a\ddot{T} + m\operatorname{div}(\dot{\vec{T}}) = k\Delta T \\ b\ddot{\vec{T}} = d_2 \Delta \vec{T} + (d_1 + d_3) \vec{\nabla}(\operatorname{div}(\vec{T})) - m\vec{\nabla}\dot{T} \end{cases}$
Modèle de température micromorphe	Type de microtempérature	$\rho T \left(\zeta_2 \ddot{\vec{T}} + \zeta_1 \ddot{\vec{T}} \right) - T \check{M}^g \Delta \dot{T}$ $-T \left[\frac{1}{2} \rho C_\varepsilon \left(\frac{\dot{\vec{T}}}{\check{\vec{T}}} - \frac{\dot{\vec{T}}}{\vec{T}} \right) + 2 \check{M} \left(\dot{\vec{T}} - \vec{T} \right) \right] = \kappa \Delta T$
	Type à deux températures	$\rho C_\varepsilon \dot{T} + \rho T \left(\zeta_2 \ddot{\vec{T}} + \zeta_1 \ddot{\vec{T}} \right) - 2T \check{M} \left(\dot{\vec{T}} - \vec{T} \right)$ $-T \check{M}^g \Delta \dot{\vec{T}} = \kappa \Delta T$ $\rho C_\varepsilon \dot{T} + \rho (\tau C_\varepsilon + T_0 \zeta_1) \ddot{\vec{T}} + \rho T_0 (\tau \zeta_1 + \zeta_2) \ddot{\vec{T}}$ $+ \tau \rho T_0 \zeta_2 \ddot{\vec{T}} - T_0 \check{M}^g \Delta \dot{\vec{T}} - T_0 \check{M}^g \Delta \dot{\vec{T}} = \kappa \Delta T$

Table 0-1 Différentes équations de chaleur généralisée

Partie I Approches inverses simplifiées pour les procédés de formage de tôles

L'approche inverse simplifiée a été initialement développée pour analyser rapidement et à moindre coût, la formabilité d'un composant mécanique de forme donné par les procédés de formage de tôles minces. L'idée de base est de résoudre un groupe d'équations non linéaires délibérément simplifiées pour trouver les positions initiales des points matériels de la tôle dans la configuration initiale (non déformée) en partant de la géométrie de la configuration finale (connue) sans tenir compte des processus incrémentaux de plasticité et de contact tôle/outils. Cette formulation repose sur les hypothèses simplificatrices suivantes: (i) état de contrainte plan dans la tôle; (ii) écoulement élastoplastique en grandes déformations avec incompressibilité totale; (iii) théorie de la déformation totale en plasticité; (iv) écrouissage purement isotrope; (V) actions simplifiées des forces de pression et de frottement entre la tôle et les outils d'emboutissage.

Afin de surmonter les mauvaises estimations de l'état de contrainte prédites par l'approche inverse en raison de l'absence de prise en compte de l'histoire de la déformation, l'approche en plusieurs pas est proposée en introduisant plusieurs configurations déformées moyennes intermédiaires pour mieux suivre le trajet de chargement. Les principales étapes de cette approche inverse multi-pas peuvent être résumées comme suit:

- 1). Construction des configurations intermédiaires de la tôle : elle nécessite deux étapes: la génération de la surface de glissement contraint et la résolution des équations initiales ;

- 2). Formulations cinématiques non linéaires pour tenir compte des grandes déformations et estimation de l'incrément de contrainte entre deux configurations successives
- 3). Intégration locale des équations constitutives décrivant l'écoulement plastique avec écrouissage.
En utilisant la méthode classique du retour radial pour mettre à jour l'état de contrainte.

I. Approche statique implicite en plusieurs étapes

I.1. Formulations cinématiques

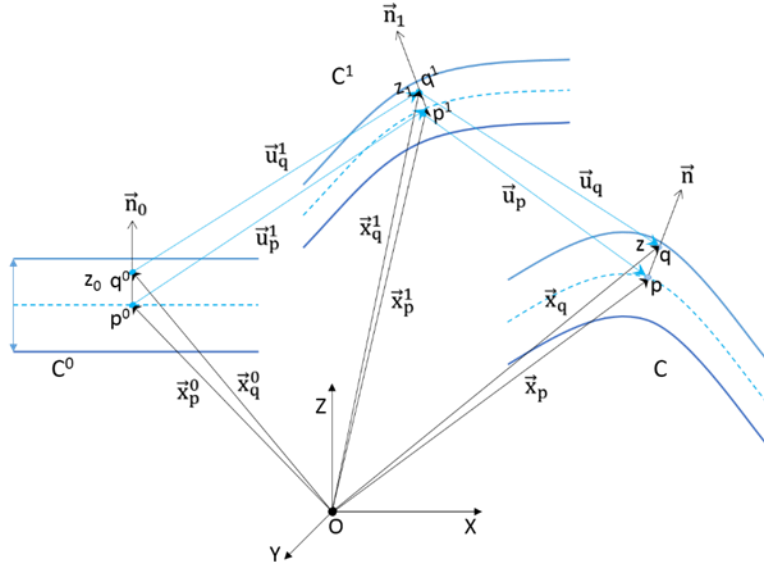


Fig. 0-1 Relations cinématiques de point matériel en trois configurations

En considérant les trois configurations de la Fig. 0-1, C^0 indique la configuration initiale, C est la configuration finale connue et C^1 est une configuration intermédiaire typique. Formulons la mesure de la déformation logarithmique du point matériel q sur les configurations C^1 et C .

Puisque la relation cinématique non linéaire entre la configuration C^0 et C^1 est exactement la même que celle de l'approche inverse à un seul pas, nous nous concentrerons sur le cas de la configuration de référence C^1 . L'inverse du tenseur des dilatations de Cauchy-Green gauche sur la configuration C^1 , est donné par :

$$[B]^{-1} = [F]^{-T} [F]^{-1} \approx \begin{bmatrix} a & b & 0 \\ b & c & 0 \\ 0 & 0 & (\lambda_3)^{-2} \end{bmatrix} \quad (1)$$

où,

$$\begin{aligned}
 a &= A_0(1+zs)^2 + 2B_0sz(1+zs) + C_0(sz)^2 \\
 b &= A_0(1+zs)sz + B_0(1+zs)(1+zt) + B_0(sz)^2 + C_0sz(1+zt) \\
 c &= A_0(sz)^2 + 2B_0sz(1+zt) + C_0(1+zt)^2
 \end{aligned} \tag{2}$$

et

$$\begin{aligned}
 A_0 &= a_0 - z_1 \vec{n}_{1,x} \left(2(\vec{o}_1 - \vec{u}_{p,x}) + z_1 (\vec{n}_{1,x}) \right) \\
 B_0 &= b_0 - z_1 \left((\vec{o}_2 - \vec{u}_{p,y}) \vec{n}_{1,x} + (\vec{o}_1 - \vec{u}_{p,x}) \vec{n}_{1,y} + z_1 \vec{n}_{1,x} \vec{n}_{1,y} \right) \\
 C_0 &= c_0 - z_1 \vec{n}_{1,y} \left(2(\vec{o}_2 - \vec{u}_{p,y}) + z_1 (\vec{n}_{1,y}) \right)
 \end{aligned} \tag{3}$$

Il est intéressant de noter que, si les points matériels ont été placés sur la surface médiane ($z=0$), l'équation Eq.(3) redonne les formules d'approche inverse, sinon la mesure de déformation du point matériel le long de l'épaisseur est sévère à cause des effets de flexion dus à la courbure de la configuration de référence.

I.2. Intégration locale élastoplastique

Avec la contrainte incrémentale obtenue, la méthode classique de prédition élastique et correction plastique avec retour radial est adoptée pour mettre à jour l'état des contraintes en élastoplasticité anisotrope avec écrouissage purement isotrope basée sur la théorie associée avec un critère d'écoulement quadratique de type Hill:

$$f(\sigma, q) = (\langle \sigma \rangle [P] \{\sigma\})^{1/2} - \bar{\sigma}_s(q) = (\langle \sigma \rangle [P] \{\sigma\})^{1/2} - \bar{\sigma}_s(\bar{\varepsilon}^p) \tag{4}$$

Le multiplicateur plastique de Lagrange est obtenu à partir de la condition de cohérence plastique pour obtenir:

$$\lambda = \frac{\left\langle \frac{\partial f}{\partial \{\sigma\}} \right\rangle [C] \{\dot{\varepsilon}\}}{\left\langle \frac{\partial f}{\partial \{\sigma\}} \right\rangle [C] \left\{ \frac{\partial f}{\partial \{\sigma\}} \right\} - \frac{\partial f}{\partial q}} \tag{5}$$

En conséquence, le taux des contraintes en fonction du taux des déformations totales s'exprime par :

$$\dot{\sigma} = [C^{ep}] \{\dot{\varepsilon}\} = \left[[C] - \frac{[C] \left\{ \frac{\partial f}{\partial \{\sigma\}} \right\} \left\langle \frac{\partial f}{\partial \{\sigma\}} \right\rangle [C]}{\left\langle \frac{\partial f}{\partial \{\sigma\}} \right\rangle [C] \left\{ \frac{\partial f}{\partial \{\sigma\}} \right\} - \frac{\partial f}{\partial q}} \right] \{\dot{\varepsilon}\} \tag{6}$$

Ensuite, l'algorithme classique du retour radial basé sur la prédition élastique et la correction plastique est effectué pour mettre à jour la contrainte. Nous avons remarqué que si la même anisotropie (isotropie planaire) pour le comportement élastique et plastique et qu'on considère l'incompressibilité pour la

déformation élastique, alors le coefficient de Poisson est lié au coefficient d'anisotropie moyenne de Lanckford r par :

$$\nu = \frac{r}{1+r} \quad (7)$$

Cela aboutit à une méthode de retour radial à un seul incrément ne nécessitant pas d'itérations pour assurer la condition d'admissibilité plastique en fin de l'incrément de charge.

I.3. Configurations moyennes

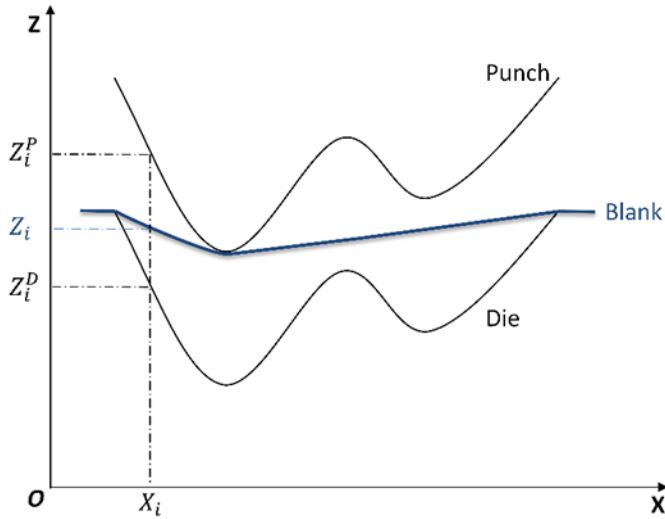


Fig. 0-2 Surface de glissement limitée par le poinçon et la matrice

Construction d'une surface de glissement

Dans le cas général 3D, la tôle vierge est censée être une membrane sollicitée en tension (dans son plan) par les outils (poinçon et matrice), comme montré à la Fig. 0-2. Ensuite, la forme de l'ébauche déformée peut être déterminée en minimisant la surface de la tôle sur la configuration actuelle :

$$\begin{aligned} \min: f(\xi) &= \sum_{e=1}^n A_e^2(\xi) \\ \text{s.t. } 0 \leq \xi_i &\leq 1 \quad (i=1,2,3..m) \end{aligned} \quad (8)$$

Considérant un élément fini triangulaire, le carré de la surface de l'élément est donné par :

$$A_e^2 = \frac{1}{4} \left(\frac{1}{2} \langle \xi_e \rangle [H_e] \{ \xi_e \} + \langle C_e \rangle \{ \xi_e \} + D_e \right) \quad (9)$$

Après assemblage de la matrice élémentaire, vectorielle et scalaire, on obtient la surface carrée de toute la structure :

$$f(\xi) = \sum_{e=1}^n A_e^2(\xi) = \frac{1}{4} \left(\frac{1}{2} \langle \xi \rangle [H] \{ \xi \} + \langle C \rangle \{ \xi \} + D \right) \quad (10)$$

qui est un modèle de programmation quadratique qui peut être résolu très efficacement en temps (par exemple le sous-programme quadprog de Matlab).

Solutions initiales de configuration

L'idée de base des solutions initiales de la configuration construite fonctionne de la manière suivante : la configuration centrale construite est un état de déformations globales possibles à un moment spécifique des processus de formage, alors les mailles vides par rapport à la configuration centrale et la configuration finale bien connue devraient être équivalentes. En gardant les deux mailles vierges équivalentes, nous sommes en mesure de trouver un groupe de distributions appropriées de points matériels globaux sur la configuration du milieu.

Avec les solutions initiales obtenues, un groupe d'équations d'équilibre non linéaires est résolu en utilisant la méthode itérative de Newton-Raphson ainsi que la fonction de pénalité pour équilibrer les configurations du milieu et pour contraindre le mouvement des points du matériau à rester sur les surfaces de glissement.

$$\{R(U^i)\} = \{F_{\text{ext}}(U^i) - F_{\text{int}}(U^i)\} = [K]\{\Delta U\} \neq 0 \quad (11)$$

II. Applications numériques

L'implémentation numérique est réalisée dans la plate-forme KMAS et comparée au logiciel d'éléments finis commercial LS-DYNA. Les nouvelles formulations cinématiques dérivées sont examinées en détail sur l'exemple du procédé de formage S-Rail. Les erreurs totales accumulées de différentes couches sont également présentées et analysées. L'exemple d'emboutissage profond en forme de boîte est sélectionné pour valider la construction des configurations intermédiaires de l'approche inverse multi-pas proposée. L'application de l'approche multi-pas à la composante B-Pillar montre clairement l'amélioration des estimations de l'état des contraintes en fonction de l'augmentation du nombre des configurations intermédiaires.

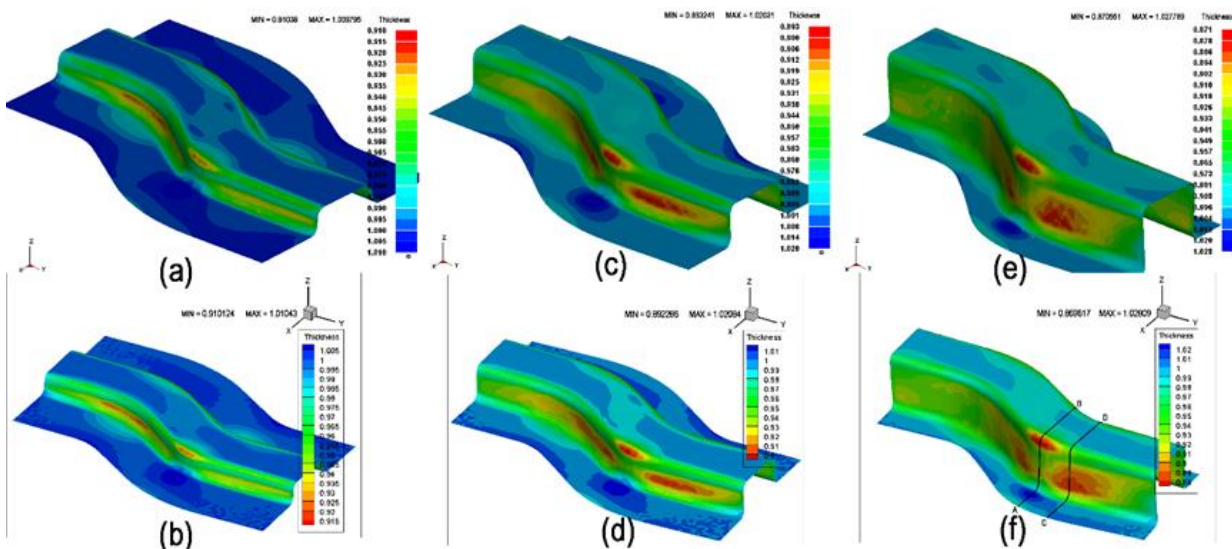


Fig. 0-3 Comparaisons des distributions d'épaisseur sur trois configurations intermédiaires simulées par LS-DYNA et Multi-pas

Partie II Modèle thermomécanique micromorphe avancé entièrement couplé à l'endommagement ductile

La rupture des composants techniques est souvent précédée de changements considérables dans la microstructure du matériau provoquant de fortes hétérogénéités locales à l'origine de divers types de défauts comme la microfissuration dans les bétons, la rupture des fibres ou le délamination fibres/matrice dans les composites ou la formation de microcavités et microfissures dans les métaux ductiles. On sait par ailleurs, que les modèles de comportement locaux (théorie de Cauchy ou du premier gradient) avec adoucissement induit par des phénomènes physiques violents comme l'endommagement (micro-discontinuités) où les variations de température à fortes vitesses (Laser), conduisent à un problème aux valeurs initiales et aux limites (PVIL) mal posé, i.e. conduisant à des solutions fortement sensibles aux paramètres de discrétisation sans possibilité de convergence. Ceci n'est pas acceptable et des efforts considérables ont été déployés par la communauté scientifique pour résoudre les problèmes de prévision des endommagements, aboutissant à l'amorçage de fissures macroscopiques et à leur propagation, d'une manière indépendante des aspects de discrétisation du temps (incrément de temps) et de l'espace (taille des éléments finis).

Afin de contribuer à cet objectif général, nous nous mettons dans le cadre des milieux continus généralisés (milieux micromorphes) pour formuler les équations non locales gouvernant le problème d'évolution de structures soumises à des grandes déformations inélastiques (plastiques ou viscoplastiques) et petites déformations élastiques. L'objectif étant d'aboutir à un PVIL conduisant à des solutions indépendantes (à convergence) des aspects de discrétisation de l'espace et du temps.

III. Formulations théoriques

Classiquement (voir Saanouni, 2012) l'état thermomécanique local d'un milieu continu est décrit par des couples de variables d'état "commandables" à savoir : $(\underline{\varepsilon}, \underline{\sigma})$ et (T, s) ; et des "internes" décrivant : l'écoulement inélastiques $(\underline{\varepsilon}, \underline{\sigma})$, les échanges thermiques $(\vec{g} = \text{grad}(T), \vec{q})$, l'écrouissage isotrope (r, R) , l'écrouissage cinématique $(\underline{\alpha}, \underline{X})$ et l'endommagement ductile isotrope (d, Y) . En plus de ces variables d'état locales, quatre nouvelles paires de variables micromorphes associées à leurs variables d'état local sont introduites : (\check{d}, \check{Y}) pour l'endommagement micromorphe, (\check{r}, \check{R}) pour l'écrouissage isotrope micromorphe, $(\check{\alpha}, \check{X})$ pour l'écrouissage cinématique micromorphe et (\check{T}, \check{s}) pour la température micromorphe.

III.1. Équations d'équilibre

En plus des champs des déplacements usuels nous introduisons $\check{d}, \check{r}, \check{\alpha}, \check{T}$ comme degrés de liberté additionnels pour décrire la cinématique du milieu. L'utilisation du principe généralisé des puissances virtuelles, qui stipule que la somme des puissances virtuelles des forces internes et externes équilibre la puissance des forces d'accélération pour toute vitesse virtuelle cinématiquement admissible (C.A.) :

$$\delta P_{\text{int}} + \delta P_{\text{ext}} = \delta P_a \quad \forall \dot{\delta u}, \dot{\delta d}, \dot{\delta r}, \dot{\delta \alpha}, \dot{\delta T} \text{ C.A.} \quad (12)$$

On obtient aisément l'équation d'équilibre classique et quatre équations d'équilibre additionnelles associées aux variables micromorphes ainsi que leurs conditions aux limites de Neumann :

$$\begin{aligned}
 & \left\{ \begin{array}{l} \vec{\nabla} \cdot \underline{\sigma} + \rho \vec{f}^u = \rho \ddot{u} \quad \text{in } \Omega \\ \underline{\sigma} \cdot \vec{n} = \vec{F}^u \quad \text{on } \Gamma \end{array} \right. \quad \left\{ \begin{array}{l} (\vec{\nabla} \cdot \vec{Y} - \vec{Y}) + \rho (f^d - \vec{\nabla} \cdot \vec{f}^{gd}) = \rho \zeta_d \ddot{d} \quad \text{in } \Omega \\ (\vec{Y} - \rho \vec{f}^{gd}) \cdot \vec{n} = F^d \quad \text{on } \Gamma \end{array} \right. \\
 & \left\{ \begin{array}{l} (\vec{\nabla} \cdot \vec{R} - \vec{R}) + \rho (f^r - \vec{\nabla} \cdot \vec{f}^{gr}) = \rho \zeta_r \ddot{r} \quad \text{in } \Omega \\ (\vec{R} - \rho \vec{f}^{gr}) \cdot \vec{n} = F^r \quad \text{on } \Gamma \end{array} \right. \quad \left\{ \begin{array}{l} (\vec{\nabla} \cdot \vec{X} - \vec{X}) + \rho (f^{\alpha} - \vec{\nabla} \cdot \vec{f}^{g\alpha}) = \rho \zeta_{\alpha} \ddot{\alpha} \quad \text{in } \Omega \\ (\vec{X} - \rho \vec{f}^{g\alpha}) \cdot \vec{n} = F^{\alpha} \quad \text{on } \Gamma \end{array} \right. \\
 & \left\{ \begin{array}{l} (\vec{\nabla} \cdot \vec{s} - \vec{s}) + \rho (f^{\bar{T}} - \vec{\nabla} \cdot \vec{f}^{g\bar{T}}) = \rho (\zeta_{\bar{T}_2} \ddot{\bar{T}} + \zeta_{\bar{T}_1} \dot{\bar{T}}) \quad \text{in } \Omega \\ (\vec{s} - \rho \vec{f}^{g\bar{T}}) \cdot \vec{n} = F^{\bar{T}} \quad \text{on } \Gamma \end{array} \right. \quad (13)
 \end{aligned}$$

III.2. Equations d'état

Considérant le premier principe de la thermodynamique postulant l'existence d'une fonction d'état appelée énergie interne E homogène à une quantité de travail, de sorte qu'en tout temps dans le domaine \mathcal{P}_t , la somme de la dérivée matérielle de l'énergie interne et de l'énergie cinétique K est égale à la somme de la puissance des forces externes appliquée à \mathcal{P}_t et de la quantité de chaleur Q reçue par \mathcal{P}_t :

$$\frac{d}{dt} (E + K) = P_{ext} + Q \quad (14)$$

À l'aide du théorème de l'énergie cinétique, la forme différentielle généralisée du premier principe de la thermodynamique est exprimée comme :

$$\rho \dot{e} = \left(\frac{\underline{\sigma} : \underline{D} + \vec{Y} \dot{d} + \vec{R} \dot{r} + \vec{X} : \dot{\underline{\alpha}} + \vec{s} \dot{\bar{T}}}{+ \vec{Y} \cdot \vec{\nabla} \dot{d} + \vec{R} \cdot \vec{\nabla} \dot{r} + \vec{X} : \vec{\nabla} \dot{\underline{\alpha}} + \vec{s} \cdot \vec{\nabla} \dot{\bar{T}}} \right) + \rho \zeta - \text{div}(\vec{q}) \quad (15)$$

De toute évidence, l'énergie interne spécifique est renforcée par de nouvelles contributions provenant des variables d'état micromorphe supplémentaires.

Le deuxième principe de la thermodynamique reste inchangé:

$$\frac{d}{dt} \int_{\mathcal{P}_t} (\rho s) dv - \int_{\mathcal{P}_t} \left(\rho \frac{\zeta}{T} \right) dv + \int_{\Gamma_t} \left(\frac{\vec{q}}{T} \cdot \vec{n} \right) ds \geq 0 \quad (16)$$

En utilisant l'énergie libre spécifique de Helmholtz, les première et deuxième lois de la thermodynamique, conduisent à l'inégalité de Clausius-Duhem, généralisée :

$$\begin{aligned}
 & \left(\underline{\sigma} - \rho \frac{\partial \psi}{\partial \underline{\varepsilon}^{re}} \right) : \dot{\underline{\varepsilon}}^{re} - \rho \left(s + \frac{\partial \psi}{\partial T} \right) \dot{T} \\
 & + \left(\bar{Y} - \rho \frac{\partial \psi}{\partial d} \right) \dot{\bar{d}} + \left(\bar{R} - \rho \frac{\partial \psi}{\partial r} \right) \dot{\bar{r}} + \left(\bar{X} - \rho \frac{\partial \psi}{\partial \underline{\alpha}} \right) : \dot{\underline{\alpha}} + \left(\bar{s} - \rho \frac{\partial \psi}{\partial \bar{T}} \right) \dot{\bar{T}} \\
 & + \left(\bar{\bar{Y}} - \rho \frac{\partial \psi}{\partial \bar{\nabla} \bar{d}} \right) \cdot \vec{\nabla} \dot{\bar{d}} + \left(\bar{\bar{R}} - \rho \frac{\partial \psi}{\partial \bar{\nabla} \bar{r}} \right) \cdot \vec{\nabla} \dot{\bar{r}} + \left(\bar{\bar{X}} - \rho \frac{\partial \psi}{\partial \bar{\nabla} \bar{\alpha}} \right) : \vec{\nabla} \dot{\underline{\alpha}} + \left(\bar{\bar{s}} - \rho \frac{\partial \psi}{\partial \bar{\nabla} \bar{T}} \right) \cdot \vec{\nabla} \dot{\bar{T}} \\
 & + \underline{\sigma} : \underline{D}^{ir} - \left(\rho \frac{\partial \psi}{\partial d} \dot{d} + \rho \frac{\partial \psi}{\partial r} \dot{r} + \rho \frac{\partial \psi}{\partial \underline{\alpha}} : \dot{\underline{\alpha}} \right) - \frac{\vec{q}}{T} \cdot \vec{\nabla} T \geq 0
 \end{aligned} \tag{17}$$

Sans perte de généralité, nous postulons que les quantités entre parenthèses de (17) ne dépendent pas de leurs taux respectivement, et que les variables micromorphes ne se dissipent pas. En suivant les arguments standard de Truesdell et Noll, les relations d'état suivantes peuvent être obtenues:

$$\begin{aligned}
 \underline{\sigma} &= \rho \frac{\partial \psi}{\partial \underline{\varepsilon}^{re}} & s &= -\frac{\partial \psi}{\partial T} \\
 Y &= -\rho \frac{\partial \psi}{\partial d} & R &= \rho \frac{\partial \psi}{\partial r} & X &= \rho \frac{\partial \psi}{\partial \underline{\alpha}} \\
 \bar{Y} &= \rho \frac{\partial \psi}{\partial \bar{d}} & \bar{R} &= \rho \frac{\partial \psi}{\partial \bar{r}} & \bar{X} &= \rho \frac{\partial \psi}{\partial \bar{\alpha}} \\
 \bar{\bar{Y}} &= \rho \frac{\partial \psi}{\partial \bar{\nabla} \bar{d}} & \bar{\bar{R}} &= \rho \frac{\partial \psi}{\partial \bar{\nabla} \bar{r}} & \bar{\bar{X}} &= \rho \frac{\partial \psi}{\partial \bar{\nabla} \bar{\alpha}} \\
 \bar{s} &= \rho \frac{\partial \psi}{\partial \bar{T}} & \bar{\bar{s}} &= \rho \frac{\partial \psi}{\partial \bar{\nabla} \bar{T}}
 \end{aligned} \tag{18}$$

et la dissipation totale locale classique comprenant la dissipation intrinsèque (mécanique) et la dissipation thermique est donnée par :

$$\phi = \phi_{in} + \phi_{th} = \underline{\sigma} : \underline{D}^{ir} + Y \dot{d} - R \dot{r} - X : \dot{\underline{\alpha}} - \frac{\vec{q}}{T} \cdot \vec{g} \geq 0 \tag{19}$$

Avec une sélection appropriée de l'énergie libre de Helmholtz, les expressions finales des relations d'état ci-dessus peuvent être obtenues.

III.3. Evolution equations

Outre l'analyse de la dissipation de la plasticité indépendante du temps, la viscoplasticité (plasticité dépendante du temps) est présentée dans cette section. Pour la plasticité dépendante du temps, l'état de contrainte n'est pas contraint de rester sur la surface d'écoulement $f_p(\underline{\sigma}, \bar{X}, \tilde{R}; T) = 0$. Cela se traduit par une sorte de généralisation de la théorie de la plasticité multi-surfaces de sorte que l'écoulement inélastique se produit même si $f_p(\underline{\sigma}, \bar{X}, \tilde{R}; T) > 0$. En effet, cette condition exprime la distance entre l'état actuel de contrainte en un point donné et la surface résultante définie par $f_p(\underline{\sigma}, \bar{X}, \tilde{R}; T) = 0$. Cette distance définit directement, dans l'espace des contraintes, la contrainte dite visqueuse σ^{vp} .

Le potentiel viscoplastique global est postulé pour être décomposé de façon additive en trois contributions : l'écoulement viscoplastique de type Norton-Hoff, la restauration par l'écrouissage cinématique et isotrope et le potentiel d'endommagement. En utilisant la règle de normalité généralisée, on obtient les équations d'évolution ci-dessous :

$$\begin{aligned}
 D^{vp} &= \frac{\partial \varphi}{\partial \underline{\sigma}} = \left\langle \frac{f_p}{K^{vp}} \right\rangle^{m_{vp}} \frac{1}{\sqrt{1-d}} \frac{\underline{H}_{\underline{\sigma}} : (\underline{\sigma} - \underline{X})}{\|\underline{\sigma} - \underline{X}\|} = \dot{\lambda}_{vp} \tilde{\eta}_f \\
 \dot{\underline{\alpha}} &= -\frac{\partial \varphi}{\partial \underline{X}} = \dot{\lambda}_{vp} \left[\tilde{\eta}_f - a \underline{1} : \underline{\alpha} - a (\underline{C}^{-1} : \underline{C}) : (\underline{\alpha} + \underline{\alpha}) \right] - \left\langle \frac{\|\tilde{\underline{X}}\|}{K^{rx}} \right\rangle^{m_{rx}} \frac{\underline{H}_{\underline{X}} : \underline{X}}{\|\tilde{\underline{X}}\|} \\
 \dot{r} &= -\frac{\partial \varphi}{\partial R} = \frac{\dot{\lambda}_{vp}}{\sqrt{1-d^\gamma}} \left[1 - \left(1 + \frac{\bar{Q}}{Q} \right) b(\tau) \tilde{r} + \frac{\bar{Q}}{Q} b \tilde{r} \right] - \left\langle \frac{\tilde{R}}{K^{rr}} \right\rangle^{m_{rr}} \\
 \dot{d} &= \frac{\partial \varphi}{\partial Y} = \frac{\dot{p}}{(1-d)^\beta} \left\langle \frac{Y - Y_0}{S} \right\rangle^s = \dot{p} \hat{Y}
 \end{aligned} \tag{20}$$

L'analyse de l'admissibilité thermodynamique montre que l'inégalité est satisfaite si $\sigma_{vp} \geq 0$, $\frac{b}{Q} \geq 0$, $K^{rx} \geq 0$, $K^{rr} \geq 0$ et $a \tilde{\underline{C}}^{-1}$ est défini semi-positif, en fonction de la positivité de toutes les autres grandeurs.

III.4. Expressions des équations de bilan micromorphique dans l'espace des déformations

Rappelons les équations de bilan généralisées ainsi que leurs conditions aux limites de Neumann dans l'équation Eq.(13), elles peuvent être transformées dans l'espace des déformations, à l'aide des relations d'état obtenues ci-dessous. Pour des raisons de simplicité, si les forces volumiques et de contact sont négligées, les équations d'équilibre généralisées prennent la forme :

$$\begin{cases} I_{\ddot{d}}^2 Lap(\ddot{d}) + \frac{\vec{\nabla} \check{H}^g(\tau)}{\check{H}(\tau)} \cdot \vec{\nabla} \ddot{d} \\ + (d - \ddot{d}) = \rho \frac{\zeta_{\ddot{d}} \ddot{d}}{\check{H}(\tau)} \\ \check{H}^g(\tau) \vec{\nabla} \ddot{d} \cdot \vec{n} = 0 \end{cases} \tag{21}$$

$$\begin{cases} (1-d^\gamma) \left[I_{\ddot{r}}^2 Lap(\ddot{r}) + \frac{\vec{\nabla} \check{Q}^g(\tau)}{\check{Q}(\tau)} \cdot \vec{\nabla} \ddot{r} + (r - \ddot{r}) \right] = \rho \frac{\zeta_{\ddot{r}} \ddot{r}}{\check{Q}(\tau)} \\ \left[(1-d^\gamma) \check{Q}^g(\tau) (\vec{\nabla} \ddot{r}) \right] \cdot \vec{n} = 0 \end{cases} \tag{22}$$

$$\begin{cases} (1-d) \left[I_{\ddot{\alpha}}^2 Lap(\ddot{\alpha}) + \frac{\vec{\nabla} \check{C}^g(\tau)}{\check{C}(\tau)} \cdot \vec{\nabla} \ddot{\alpha} + (\underline{\alpha} - \ddot{\alpha}) \right] = \rho \frac{\zeta_{\ddot{\alpha}} \ddot{\alpha}}{\check{C}(\tau)} \\ \left[(1-d) \check{C}^g(\tau) (\vec{\nabla} \ddot{\alpha}) \right] \cdot \vec{n} = 0 \end{cases} \tag{23}$$

$$\begin{cases} \left[I_{\bar{\tau}}^2 Lap(\bar{\tau}) + \frac{\vec{\nabla} \bar{M}^g(\bar{\tau})}{\bar{M}(\bar{\tau})} \cdot \vec{\nabla} \bar{\tau} \right] + \left[(\tau - \bar{\tau}) - \frac{\sqrt{1-d}}{\bar{M}(\bar{\tau})} \bar{P}(\bar{\tau}) : \underline{\varepsilon}^e \right] = \rho \left(\frac{\zeta_{\bar{\tau}_1}}{\bar{M}(\bar{\tau})} \dot{\bar{\tau}} + \frac{\zeta_{\bar{\tau}_2}}{\bar{M}(\bar{\tau})} \ddot{\bar{\tau}} \right) \\ (\bar{M}^g(\bar{\tau}) \vec{\nabla} \bar{\tau}) \cdot \vec{n} = 0 \end{cases} \quad (24)$$

où, $I_{\bar{\tau}}$, $I_{\bar{r}}$, $I_{\bar{\alpha}}$ et $I_{\bar{\tau}}$ sont les longueurs internes associées à chacun des phénomènes micromorphiques considérés.

III.5. Equations généralisées de la chaleur

Plusieurs équations étendues de la chaleur existantes sont revues et listées dans le Table 0-1 . Dans le but de se concentrer sur les équations de la chaleur, nous nous limitons à la thermo-élasticité dans cette section en négligeant l'écoulement inélastique avec écrouissage et endommagement afin de simplifier l'équation de la chaleur micromorphe généralisée complexe.

Considérant uniquement le champ de température micromorphe et son premier gradient comme variable non locale supplémentaire, à l'aide du principe des puissances virtuelles généralisées, des lois de la thermodynamique ainsi que de l'énergie libre de Helmholtz, une nouvelle paire d'équations de chaleur micromorphe généralisée est obtenue :

$$\begin{cases} \rho \dot{e} = \underline{\sigma} : \dot{\underline{\varepsilon}} + \left(\vec{s} \dot{\bar{T}} + \vec{s} \cdot \vec{\nabla} \dot{\bar{T}} \right) + \left(\rho \zeta - \text{div}(\vec{q}) \right) \\ \rho \dot{s} - \rho \frac{\zeta}{T} + \text{div} \left(\frac{\vec{q}}{T} \right) \geq 0 \end{cases} \quad (25)$$

Dans lequel, la température locale et micro sont couplées ensemble dans l'équation de chaleur locale et l'équation d'équilibre de température micro.

Supposons que l'énergie libre de Helmholtz soit définie comme :

$$\rho \psi(T, \bar{T}, \vec{\nabla} \bar{T}) = -\rho C T \left(\ln \frac{T}{T_0} - 1 \right) - \rho \bar{C} \bar{T} \left(\ln \frac{\bar{T}}{T_0} - 1 \right) - \frac{1}{2} \bar{M}(\bar{T} - T)^2 + \frac{1}{2} \bar{M}^g \vec{\nabla} \bar{T} \cdot \vec{\nabla} \bar{T} \quad (26)$$

Les équations de la chaleur micromorphe, considérant la contrainte interne qui consiste à forcer la différence entre température locale et température micromorphe à être voisine de 0, devient :

$$\rho T \left(\zeta_{\bar{\tau}_1} \ddot{\bar{\tau}} + \zeta_{\bar{\tau}_2} \ddot{\bar{\tau}} \right) + \rho (C - \bar{C}) \dot{T} - T \bar{M}^g \Delta \dot{T} = \kappa \Delta T \quad (27)$$

Il est intéressant de noter que :

- a) Si $\zeta_{\bar{\tau}_2} = 0$ (ce qui implique que l'inertie n'est proportionnelle qu'à la première dérivée de la température), la linéarisation de l'équation de la chaleur conduit à:

$$\rho T_0 \zeta_{\bar{\tau}_1} \ddot{\bar{\tau}} + \rho (C - \bar{C}) \dot{T} - T_0 \bar{M}^g \Delta \dot{T} = \kappa \Delta T \quad (28)$$

qui a la même forme que les équations thermiques généralisées dérivées du modèle à double températures (Forest et Aifantis (2010)), dans lequel si le terme d quatrième ordre était

suffisamment petit il pourra être négligé (par exemple, dans le métal pur, la conductivité thermique de la composante électronique est beaucoup plus grande que celle du réseau composant).

- b) Si les deux capacités calorifiques généralisées sont équivalentes $C = \check{C}$, l'équation de la chaleur devient:

$$\rho T_0 \zeta_{\bar{\tau}_1} \ddot{T} - T_0 \check{M}^g \Delta \dot{T} = \kappa \Delta T \quad (29)$$

Il est semblable à l'équation de la chaleur dérivée par Ieşan et Nappa (2005) en l'absence des dérivées du quatrième ordre, sur la base des milieux micromorphes.

- c) Dans l'équation Eq.(II.271), si $\check{M}^g = 0$ pour un milieu hypothétique ou si $\Delta \dot{T}$ est relativement petite par rapport aux deux autres termes, elle indique que la température satisfait à l'équation d'onde classique:

$$\ddot{T} = \frac{\kappa}{\rho T_0 \zeta_{\bar{\tau}_1}} \Delta T \quad (30)$$

avec une vitesse de propagation finie $\sqrt{\frac{\kappa}{\rho T_0 \zeta_{\bar{\tau}_1}}}$.

Avec des choix appropriés de l'énergie libre de Helmholtz et du flux thermique, l'équation de la chaleur hyperbolique avec temps de relaxation, l'équation de chaleur de type hyper-température, l'équation hyperbolique à double températures et le modèle à double températures généralisée peuvent être récupéré comme cas particuliers.

IV. Aspects numériques

IV.1. La discréétisation du temps et de l'espace

L'intervalle de temps total I_t est discréétisé en N_t sous-intervalles à intersections vides, de sorte que

l'approximation $I_t = [t_0, t_f] \cong \bigcup_{n=0}^{N_t} [t_n, t_{n+1} = t_n + \Delta t]$ est valable avec une précision suffisante. Pour chacun

de ces sous-intervalles de temps, nous résolvons donc un problème non linéaire pour déterminer toutes les inconnues du problème de valeurs initiales et aux limites.

La MEF standard basée sur le déplacement est utilisé pour discréétiser la configuration de référence Ω_{t_n} en un nombre fini de N_e sous-domaines ou d'éléments finis (EF) de forme géométrique simple appelée Ω_e , avec intersections vides. Trois éléments dits « en déformations supposées » basés sur le principe variationnel mixte de Hu-Washizu, sont développés dans le sous-programme Abaqus/Vuel.

Les six formes faibles discréétisées élémentaires, pour un élément typique (e), prennent la forme:

$$\left\{ \begin{array}{l} J_u(\delta \vec{v}) = \langle \delta \dot{u}_n^e \rangle \left([M_n^e] \{ \ddot{u}_n^e \} + \{ F_{int-u}^e \} - \{ F_{ext-u}^e \} \right) \\ J_{\bar{d}}(\delta \bar{d}) = - \langle \delta \bar{d}_n^e \rangle \left([M_{\bar{d}}^e] \{ \ddot{\bar{d}}_n^e \} + \{ F_{int-\bar{d}}^e \} - \{ F_{ext-\bar{d}}^e \} \right) \\ J_{\bar{r}}(\delta \bar{r}) = - \langle \delta \bar{r}_n^e \rangle \left([M_{\bar{r}}^e] \{ \ddot{\bar{r}}_n^e \} + \{ F_{int-\bar{r}}^e \} - \{ F_{ext-\bar{r}}^e \} \right) \\ J_{\bar{\alpha}}(\delta \bar{\alpha}) = - [\delta \bar{\alpha}_n^e]^T \left([M_{\bar{\alpha}}^e] [\bar{\alpha}_n^e] + [F_{int-\bar{\alpha}}^e] - [F_{ext-\bar{\alpha}}^e] \right) \\ J_{\bar{T}}(\delta \bar{T}) = - \langle \delta \bar{T}_n^e \rangle \left([M_{\bar{T}}^e] \{ \ddot{\bar{T}}_n^e \} + \{ F_{int-\bar{T}}^e \} - \{ F_{ext-\bar{T}}^e \} \right) \\ J_T(\delta T) = - \langle \delta T_n^e \rangle \left([M_T^e] \{ \dot{T}_n^e \} + \{ F_{int-T}^e \} - \{ F_{ext-T}^e \} \right) \end{array} \right. \quad (31)$$

Les expressions des matrices de masse et des vecteurs forces sont données dans le mémoire en anglais.

IV.2. Schéma de résolution globale

Les équations Eq. (31) après assemblage sur l'ensemble des éléments de la structure, forment le PVIL qu'il convient de résoudre sur chaque incrément de charge (ou de temps). Elles sont résolues par un schéma de résolution dynamique explicite disponible dans ABAQUS/Explicit (voir ABAQUS Theory Manual). Les équations de mouvement sont intégrées explicitement par le schéma d'intégration aux différences centrales appliqué à chacune des six équations après assemblage. Si on se limite à la première équation exprimant l'équilibre de la structure pour calculer le champ des déplacements, cela donne :

$$\begin{aligned} \{ \dot{u} \}^{(n+1/2)} &= \{ \dot{u} \}^{(n-1/2)} + \frac{\Delta t^{(n+1)} + \Delta t^{(n)}}{2} \{ \ddot{u} \}^{(n)} \\ \{ u \}^{(n+1)} &= \{ u \}^{(n)} + \Delta t^{(n+1)} \{ \dot{u} \}^{(n+1/2)} \end{aligned} \quad (32)$$

Les autres équations sont résolues, en même temps que l'équation d'équilibre, par le même schéma dynamique explicite. Notons que la procédure dynamique explicite ne nécessite aucune itération et n'a pas besoin de matrice tangente, cependant, elle est conditionnellement stable. L'incrément de temps stable avec amortissement est donné par :

$$\Delta t_u \leq \frac{2}{w_{\max}} \left(\sqrt{(1+\zeta^2)} - \zeta \right) \quad (33)$$

IV.3. Schéma d'intégration locale des équations de comportement

Le calcul des vecteurs forces internes présents dans les équations Eq.(31) nécessite la connaissance des variables d'état à l'instant t_{n+1} que sont : (i) le tenseur des contraintes σ_{n+1} , la variable endommagement local d_{n+1} , la variable d'écrouissage isotrope r_{n+1} , la variable d'écrouissage cinématique α_{n+1} et de la température locale T_{n+1} , à chaque point d'intégration de chaque élément à l'instant $(t_{n+1} = t_n + \Delta t)$. Cela se fait par intégration numérique des équations d'évolution de ces variables en supposant connues leurs valeurs à l'instant t_n , début de l'incrément de charge.

En combinant le schéma asymptotique avec l'algorithme du retour radial, tous deux purement implicites, conduit à un schéma d'intégration efficace et robuste inconditionnellement stable en présence de l'endommagement ductile qui induit un comportement fortement adoucissant.

Prévision élastique

Supposons que l'incrément de déformation totale ($\Delta\varepsilon$) imposé pendant l'incrément de temps soit purement élastique et n'indue aucun phénomène dissipatif (écoulement inélastique, écrouissages, endommagement...). Dans ce cas, la contrainte essai (trial stress) à t_{n+1} est donné par :

$$\underline{\sigma}_{n+1}^{trial} = (1 - d_n) \underline{\Delta}(\underline{T}_n) : \underline{\varepsilon}_{n+1}^{e,trial} - \sqrt{1-d_n} (\underline{T}_n - \underline{T}_0) \underline{P}(\underline{T}_n) - \sqrt{1-d_n} (\underline{T}_n - \bar{\underline{T}}_n) \bar{\underline{P}}(\underline{T}_n) \quad (34)$$

où $\underline{\varepsilon}_{n+1}^{e,trial} = \underline{\varepsilon}_n^e + \Delta\varepsilon = \underline{\varepsilon}_n - \underline{\varepsilon}_n^\rho + \Delta\varepsilon$ est la déformation essai supposée totalement élastique. Le critère d'écoulement correspondant à cette contrainte essai est donné par:

$$f_{n+1}^{vp,trial} = \frac{\|\underline{\sigma}_{n+1}^{trial} - \underline{X}_n\|}{\sqrt{1-d_n}} - \frac{R_n}{\sqrt{1-d_n^\gamma}} - \sigma_{yp}(\underline{T}_n) \quad (35)$$

Si $f_{n+1}^{vp,trial} \leq 0$, cela signifie que l'état de contrainte d'essai $\underline{\sigma}_{n+1}^{trial}$ est à l'intérieur de la surface d'écoulement (par exemple une décharge élastique), et la solution du problème à la fin du pas est bel et bien élastique définie par :

$$\begin{cases} \underline{\varepsilon}_{n+1}^{vp} = \underline{\varepsilon}_n^{vp} & \underline{\alpha}_{n+1} = \underline{\alpha}_n & \underline{r}_{n+1} = \underline{r}_n & \underline{d}_{n+1} = \underline{d}_n \\ \underline{\sigma}_{n+1} = \underline{\sigma}_{n+1}^{trial} & \underline{X}_{n+1} = \underline{X}_n & \underline{R}_{n+1} = \underline{R}_n & \underline{Y}_{n+1} = \underline{Y}_n \end{cases} \quad (36)$$

Correction plastique

Si $f_{n+1}^{vp,trial} > 0$, cela signifie que l'état de contrainte d'essai se situe à l'extérieur de la surface d'écoulement. Le pas de chargement est donc plastique et la solution essai doit être corrigée pour assurer les conditions d'admissibilité plastique ou viscoplastique suivantes :

$$\begin{aligned} f_{n+1}^p(\tilde{\underline{\sigma}}_{n+1}, \tilde{\underline{X}}_{n+1}, \tilde{\underline{R}}_{n+1}; \underline{T}_n) &= 0 && \text{plasticity} \\ f_{n+1}^{vp} = f_{n+1}^p(\tilde{\underline{\sigma}}_{n+1}, \tilde{\underline{X}}_{n+1}, \tilde{\underline{R}}_{n+1}; \underline{T}_n) - \sigma_{n+1}^{vp} &= 0 && \text{viscoplasticity} \end{aligned} \quad (37)$$

En considérant la viscoplasticité anisotrope, on obtient les trois équations non linéaires à trois variables indépendantes suivantes $\Delta\lambda_{vp}$, d et \underline{n}_f :

$$\begin{cases} f_{n+1}^{vp} = \frac{\|\underline{Z}_{n+1}\|}{\sqrt{1-d_{n+1}}} - \frac{R_{n+1}}{\sqrt{1-d_{n+1}^\gamma}} - \sigma_{n+1}^{vp} - \sigma_{yp}(\underline{T}_n) = 0 \\ g_{n+1} = d_{n+1} - d_n - \frac{\Delta\lambda_{vp}}{(1-d_{n+1})^{\beta(\underline{T}_n)}} \left\langle \frac{\underline{Y}_{n+1} - \underline{Y}_0(\underline{T}_n)}{S(\underline{T}_n)} \right\rangle^{s(\underline{T}_n)} = 0 \\ h_{n+1} = \underline{H}(\underline{T}_n) : \underline{Z}_{n+1} - \|\underline{Z}_{n+1}\| \underline{n}_{n+1}^f = 0 \end{cases} \quad (38)$$

En utilisant le schéma de Newton-Raphson pour linéariser et résoudre les équations non linéaires Eq.(.38) le système suivant est obtenu :

$$\begin{Bmatrix} f_{vp} \\ g \\ h \end{Bmatrix}_{n+1}^i + \begin{bmatrix} \frac{\partial f_{vp}}{\partial \Delta \lambda_{vp}} & \frac{\partial f_{vp}}{\partial d_{n+1}} & \frac{\partial f_{vp}}{\partial \underline{n}_{n+1}^f} \\ \frac{\partial g}{\partial \Delta \lambda_{vp}} & \frac{\partial g}{\partial d_{n+1}} & \frac{\partial g}{\partial \underline{n}_{n+1}^f} \\ \frac{\partial h}{\partial \Delta \lambda_{vp}} & \frac{\partial h}{\partial d_{n+1}} & \frac{\partial h}{\partial \underline{n}_{n+1}^f} \end{bmatrix}_{n+1}^i \cdot \begin{Bmatrix} \delta \Delta \lambda_{vp} \\ \delta d \\ \delta \underline{n}_f \end{Bmatrix}_{n+1} = \{0\} \quad (39)$$

A convergence la solution finale est obtenue en termes de $\Delta \lambda_{vp}, \underline{n}_{f,n+1}, d_{n+1}$. Cela permet de calculer toutes les variables de type contrainte par :

$$\begin{aligned} \underline{\sigma}_{n+1} &= (1 - d_{n+1}) \underline{\Delta} : \left(\underline{\varepsilon}_{n+1}^{e,trial} - \Delta \lambda_{vp} \frac{1}{\sqrt{1 - d_{n+1}}} \frac{H : (\underline{\sigma}_{n+1} - \underline{X}_{n+1})}{\|\underline{\sigma}_{n+1} - \underline{X}_{n+1}\|} \right) \\ &\quad - \sqrt{1 - d_{n+1}} (\underline{T}_n - \underline{T}_0) \underline{P} - \sqrt{1 - d_{n+1}} (\underline{T}_n - \check{\underline{T}}_n) \check{\underline{P}} \\ R_{n+1} &= (1 - d_{n+1}^\gamma) \left[(\underline{Q} + \check{\underline{Q}}) \left(r_n e^{-\Delta \lambda_{vp} b \left(1 + \frac{\check{\underline{Q}}}{\underline{Q}} \right)} + \left(1 - e^{-\Delta \lambda_{vp} b \left(1 + \frac{\check{\underline{Q}}}{\underline{Q}} \right)} \right) \frac{\underline{Q} + b \check{\underline{Q}} \check{\underline{r}}_{n+1}}{b \sqrt{1 - d_{n+1}^\gamma} (\underline{Q} + \check{\underline{Q}})} \right) \right. \\ &\quad \left. - \check{\underline{Q}} \check{\underline{r}}_{n+1} \right] \\ \underline{X}_{n+1} &= (1 - d_{n+1}) \left[(\underline{C} + \check{\underline{C}}) \left(\underline{\alpha}_n e^{-\Delta \lambda_{vp} a \left(1 + \frac{\check{\underline{C}}}{\underline{C}} \right)} + \left[1 - e^{-\Delta \lambda_{vp} a \left(1 + \frac{\check{\underline{C}}}{\underline{C}} \right)} \right] \left[\frac{\underline{C}}{a(\underline{C} + \check{\underline{C}})} \tilde{\underline{n}}_f + \frac{\check{\underline{C}}}{\underline{C} + \check{\underline{C}}} \check{\underline{\alpha}}_{n+1} \right] \right) \right. \\ &\quad \left. - \check{\underline{C}} \check{\underline{\alpha}}_{n+1} \right] \\ \sigma_{n+1}^{vp} &= K^{vp} \left(\frac{\Delta \lambda_{vp}}{\Delta t} \right)^{\frac{1}{m_{vp}}} \end{aligned} \quad (40)$$

V. Étude paramétrique et applications

V.1. Étude paramétrique

Avant d'effectuer les identifications, l'étude paramétrique du modèle micromorphe doit être soigneusement réalisée pour bien comprendre les équations constitutives proposées. Les effets des paramètres d'endommagement local (S, s, β, γ), les modules micromorphes ($\underline{H}, I_d, \zeta_d, \check{Q}, I_r$) et les effets thermiques (m, K_2) sont soigneusement étudiés. Un exemple de l'effet du paramètre d'endommagement local est donné en Fig.04.

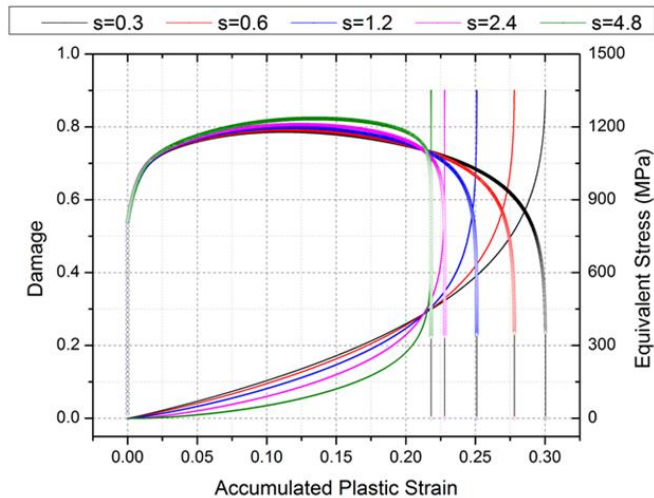


Fig. 0-4 Influence du paramètre s sur l'évolution de l'endommagement et de la contrainte équivalente

De cette étude paramétrique complète les conclusions suivantes sont tirées :

- 1). Les paramètres de l'endommagement local affectent significativement la réponse du modèle. La variation du paramètre S affecte la déformation à rupture (ductilité) en accélérant ou en ralentissant le déplacement final à rupture; les paramètres S et Y_0 affectent également le déplacement final à rupture ; alors que le paramètre β influence la nonlinéarité d'évolution de l'endommagement;
- 2). La réponse du modèle est plus sensible au module \check{H} qu'au module \check{H}^g
- 3). La réponse du modèle est également plus sensible au module \check{Q} qu'au module \check{Q}^g
- 4). L'endommagement micromorphe retardent significativement l'évolution de l'endommagement local surtout dans les cas des températures élevées ou des taux des déformations élevés.

V.2. Applications

Essai de traction uniaxial de DP1000

L'essai de traction uniaxial de l'acier biphasé DP1000 présenté dans le travail de Yue (2014) est simulé par le modèle micromorphe proposé. La géométrie de l'échantillon est donnée à la Fig. 0-5. Les paramètres élastoplastiques et d'endommagement matériels identifiés sont donnés dans le Table 0-2.

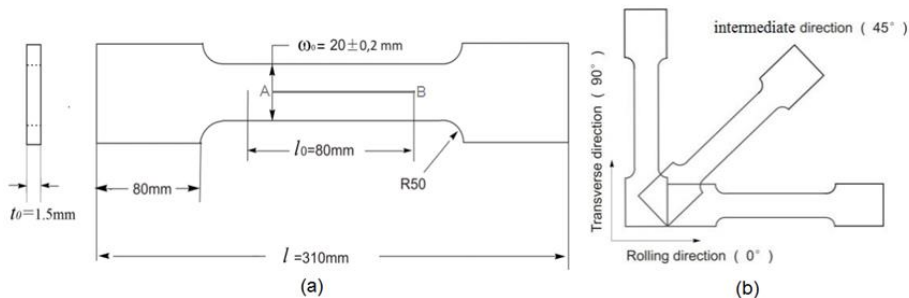


Fig. 0-5 Géométrie de l'éprouvette de tension uniaxiale

ρ (kg/m^3)	E (GPa)	ν	σ_y (MPa)	Q (MPa)	b	C (GPa)
7800.0	208.0	0.3	809.0	4000.0	13.0	32.0
a	F	G	H	L	M	N
150.0	0.525	0.546	0.455	1.5	1.5	1.6
S	s	β	γ	Y_0	h	
3.5	1.2	2.0	4.0	0.0	1.0	

Table 0-2 Paramètres de matériau élastoplastique endommagé de DP1000

Comme le montre la Fig. 0-6, le modèle donne différentes courbes force-déplacement en traction pour différentes tailles du maillage structuré de 1,6 mm, 0,8 mm, 0,4 mm et 0,2 mm. Les phénomènes de dépendance nette à la taille du maillage sont observés. La réponse postcritique du modèle est sensible au maillage et les déplacements à rupture sont d'autant plus faibles que la taille du maillage est faible.

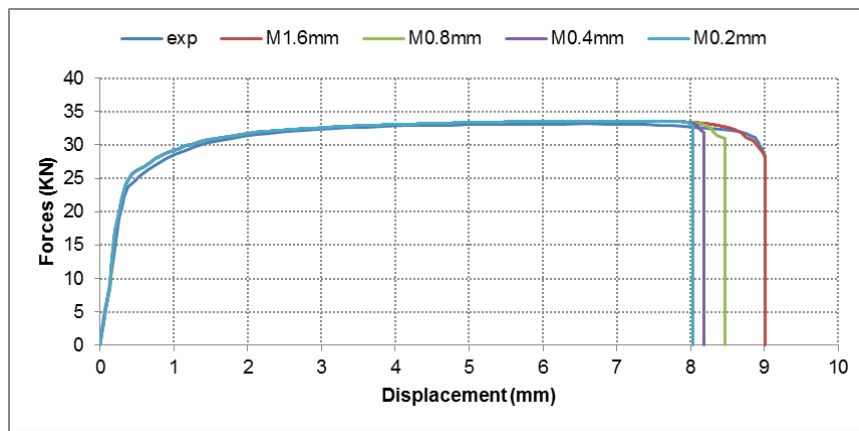


Fig. 0-6 Courbes force-déplacement de l'essai de traction en utilisant le modèle d'endommagement local

La Fig. 0-7 présente les réponses du modèle (courbes force-déplacement) du même essai de traction uniaxial, en prenant les paramètres: $S = 3.3$, $\zeta_d = 1.0$, $\check{H} = 43.75 N \cdot mm^{-2}$, $I_d = 1.0 mm$, $\zeta_r = 1.0$, $I_r = \sqrt{2} mm$ et $\check{Q} = 20 KN \cdot mm^{-2}$, pour trois maillage de différentes tailles de 0,4 mm, 0,8 mm et 1,6 mm respectivement. Comme prévu, le modèle prédit des courbes force-déplacement beaucoup moins sensibles à la taille du maillage. Les déplacements à rupture finale sont approximativement de 9,03 mm, 9,07 mm et 9,10 mm pour les mailles de 0,4 mm, 0,8 mm et 1,6 mm respectivement.



Fig. 0-7 Courbes de force-déplacement du test de traction à l'aide du modèle de endommagement micromorphe et de durcissement isotrope

Procédé d'emboutissage

Le procédé d'emboutissage profond d'une pièce cruciforme en DP1000, réalisé par Yue(2014), est simulé à l'aide du sous-programme VUEL d'Abaqus/Explicit avec respectivement le modèle de endommagement local et micromorphe fortement couplé. Seul un quart de la géométrie de la pièce est modélisée (Fig. 0-8) avec un maillage uniforme de 1,6 mm, 2,0 mm et 2,4 mm de taille.

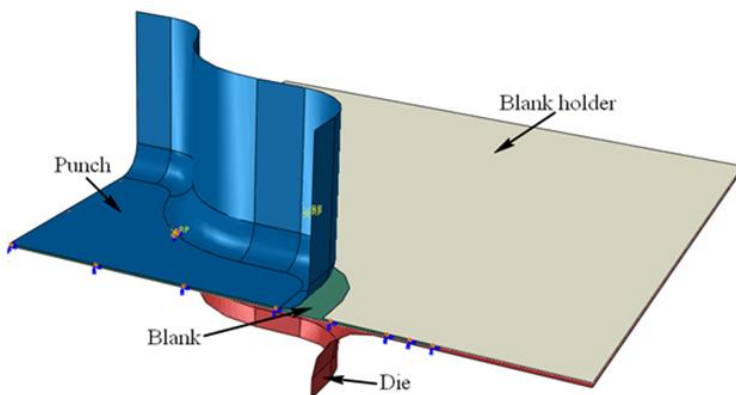


Fig. 0-8 Quatrième partie du modèle FEM pour le processus de CSD

La Fig. 0-9, montre les réponses numériques et expérimentale (force de poinçonnage en fonction du déplacement du poinçon) prédites par le modèle local en considérant les effets de fermeture de microfissures pour différentes tailles du maillage. On observe que les réponses du modèle local sont clairement dépendantes de la taille du maillage. Les courbes force-déplacement chutent plus rapidement pour les maillages de faible taille. En effet la force du poinçon amorce sa chute dès un déplacement de 23,34mm, 26,14mm et 27,89mm pour les maillage de taille de 1,6mm, 2,0mm et 2,4mm respectivement.

RESUME EXTENSIF EN FRANCAIS

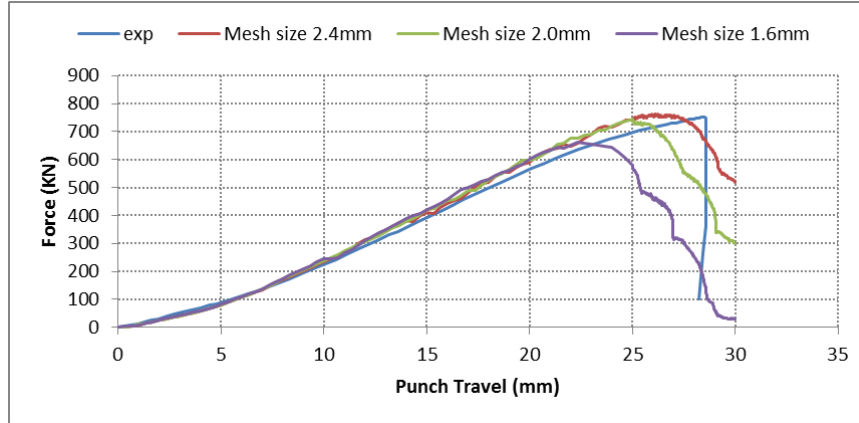


Fig. 0-9 Courbes de force-déplacement de perforation prédites par le modèle de endommagement local avec effets de fermeture pour différentes tailles de maille du processus de CSD

Nous avons également refait les mêmes simulations mais en utilisant le modèle de endommagement micromorphe, prenant le facteur d'échelle de densité micromorphe $\zeta_d = 1.0$, le module micromorphe $\check{H} = 110 N \cdot mm^{-2}$ et la longueur interne $l_d = 1.0 mm$ ainsi que le paramètre de endommagement local ajusté $S = 5.5$. La Fig. 0-10 représente les réponses prédites par le modèle non local où les courbes force-déplacement simulées sont quasiment indépendantes de la taille du maillage.

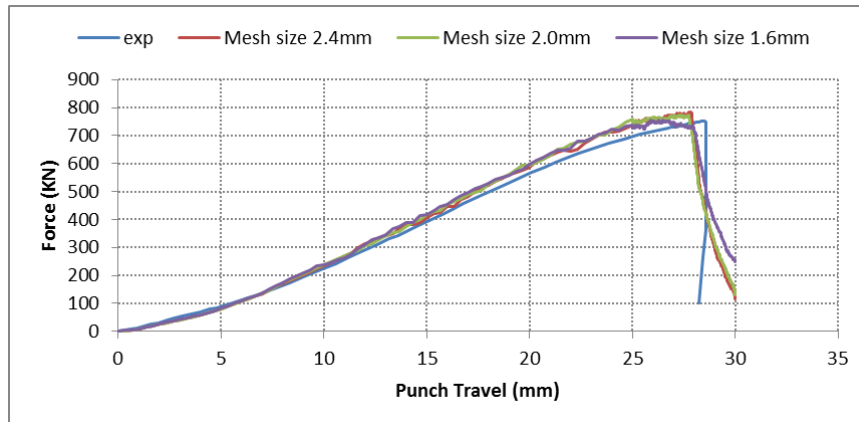


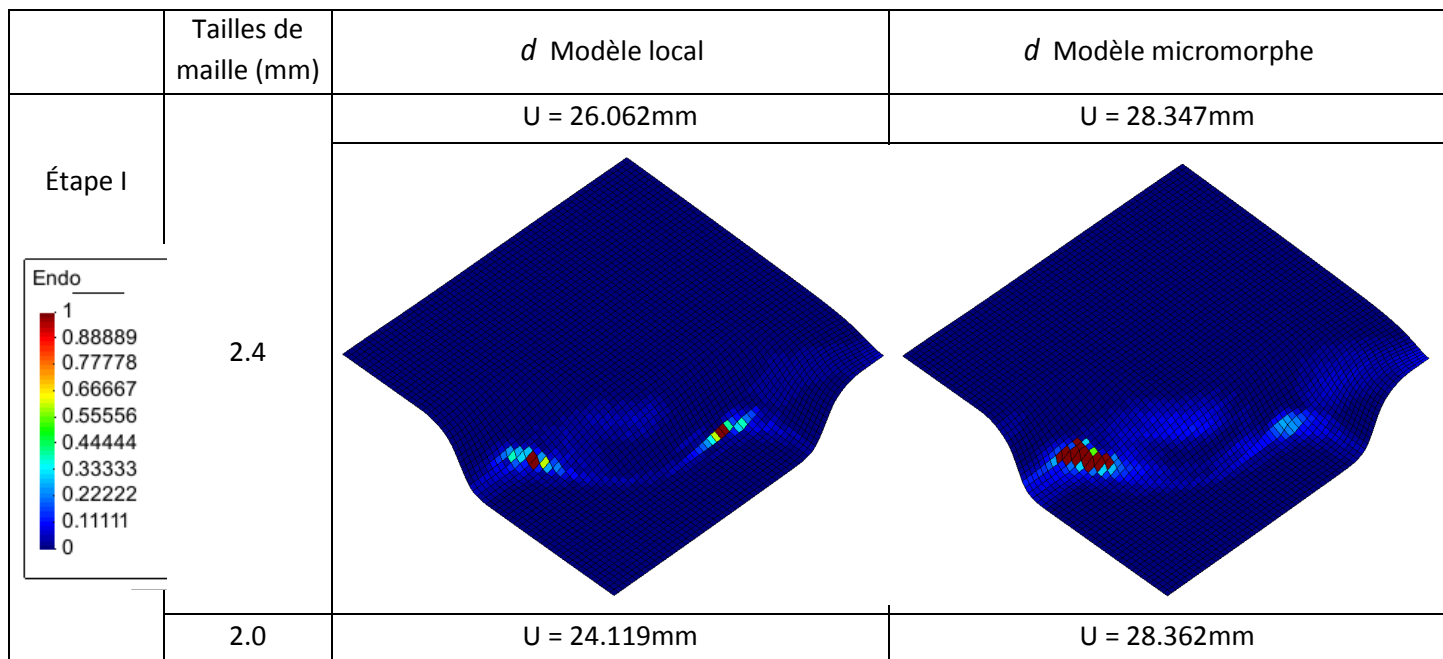
Fig. 0-10 Courbes de force-déplacement du poinçonnement prédites par le modèle de endommagement micromorphe avec effets de fermeture pour différentes tailles de maille du processus de CSD

La Fig. 0-12, montre les distributions des endommagements locaux au moment où le premier élément est complètement endommagé (amorçage d'une fissure macroscopique) pour les trois tailles du maillage. Nous pouvons remarquer que pour le modèle local, l'amorçage des fissures se produit en deux zones pour trois déplacements différents du poinçon de 21.15mm, 24.12mm et 26.06mm, pour les tailles de maille de 1.6mm, 2.0mm et 2.4 Mm respectivement. Pour le modèle micromorphe, toutes les fissures initiales apparaissent approximativement à la même place pour un même déplacement du poinçon de 28,35 mm et ce pour les trois maillages. Ceci confirme la régularité du PVIL micromorphe.



Fig. 0-11 Exemples de défaillance expérimentale de l'échantillon CSD

Comme le montre la Fig. 0-13, la propagation des fissures, simulée par le modèle micromorphe, indique que la fissure apparaît initialement dans la région du coin gauche pour un déplacement d' environ 28,35 mm du poinçon en accord avec le résultat expérimental tel qu'illustré à la Fig. 0-11 et Fig. 0-12, après que la fissure s'est propagée vers l'avant à partir des deux côtés de la ligne de front de la fissure initiale. Cependant, avec le modèle local, deux fissures s'amorcent et se propagent l'une vers l'autre mais pour différents déplacements du poinçon d'une manière dépendante de la tailles du maillage (Fig. 0-12). En conclusion, les résultats prédits par le modèle micromorphe sont indépendants du maillage et proches des résultats expérimentaux, ce qui n'est clairement pas le cas pour le modèle local.



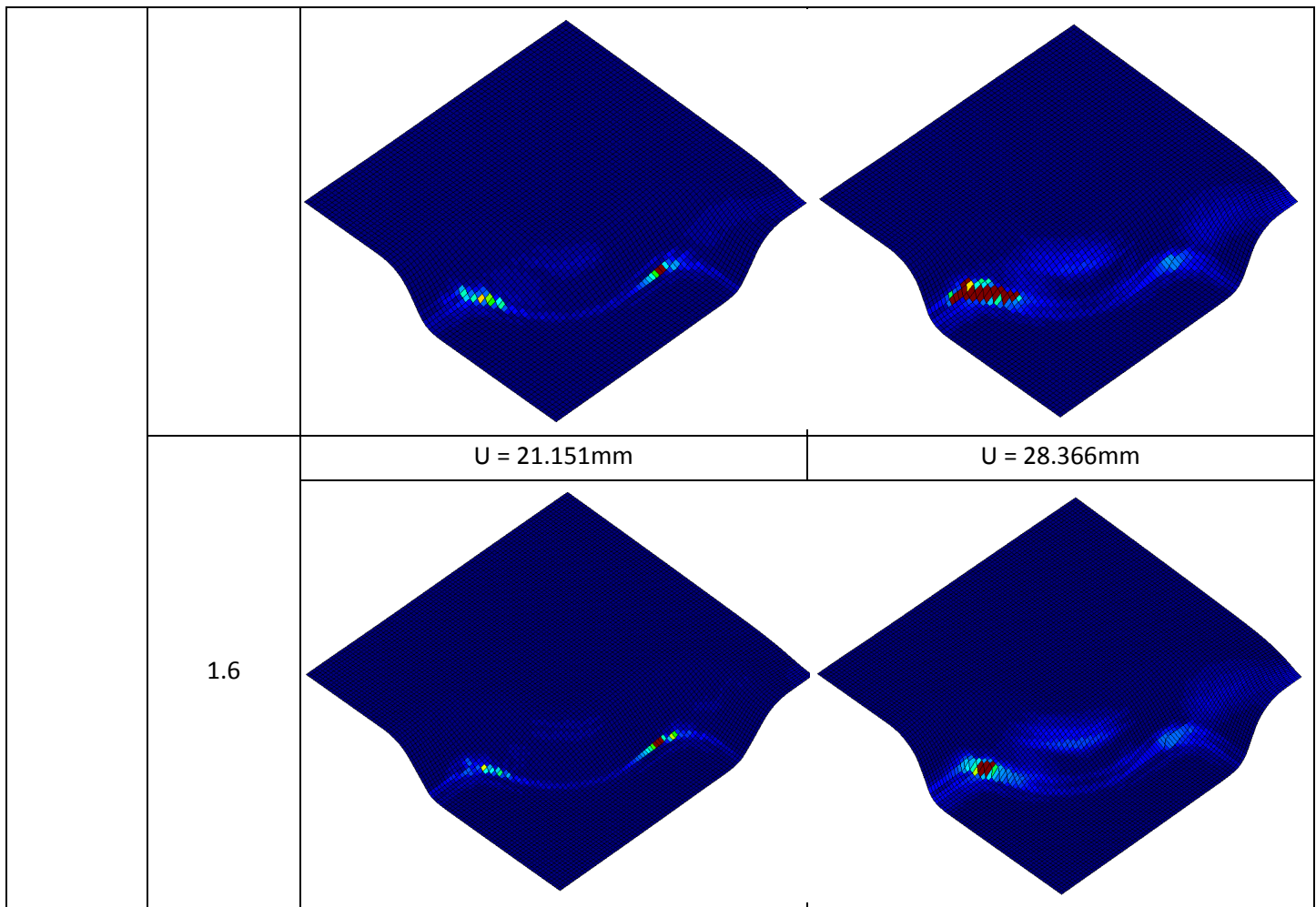
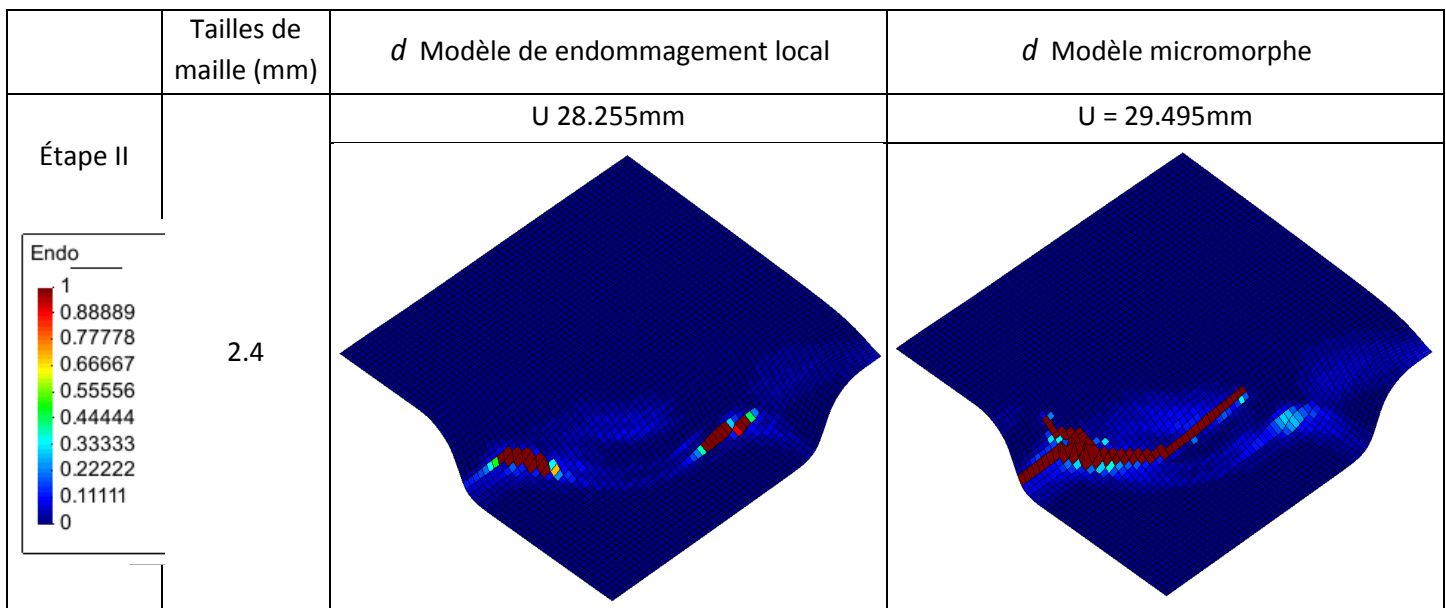


Fig. 0-12 Distributions des endommagement locaux au stade I simulées par le modèle de endommagement local et micromorphe pour trois mailles différentes



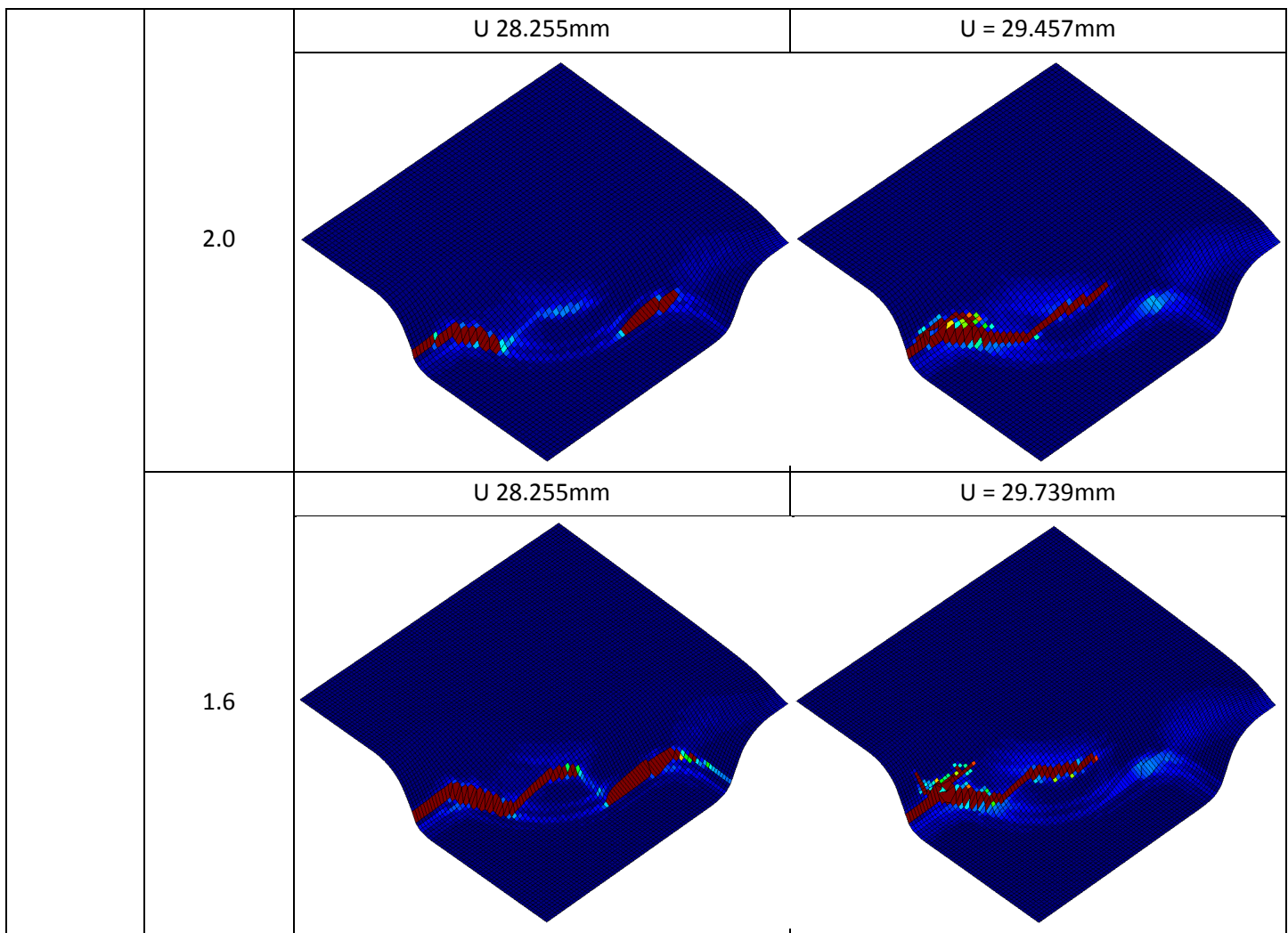


Fig. 0-13 Distributions des endommagements locaux au stade II simulés par le modèle de endommagement local et micromorphe pour trois mailles différentes

VI. Conclusions et perspectives

Dans ce travail, nous avons formulé un modèle constitutif élastoviscoplastique micromorphe, non local, qui tient compte de l'écrouissage mixte non linéaire isotropes et cinématiques fortement couplés aux endommagements ductiles dans le cadre de la thermodynamique des processus irréversibles étendue à la mécanique des milieux continus généralisés.

Dans un premier temps, nous avons développé un solveur EF basé sur la méthode inverse à plusieurs configurations intermédiaires, statique-implicite, qui tient compte de l'élastoplasticité classique avec écrouissage isotrope pour une analyse rapide et peu coûteuse de la formabilité des tôles minces :

- 1). Le solveur multi-pas améliore les estimations des contraintes en adoptant plusieurs configurations intermédiaires représentant les chemins de déformation et les actions simplifiées des outils (forces de contact). Les configurations intermédiaires d'ébauche de tôle déformée sont construites de manière efficace selon des procédures appropriées: résolution d'un programme quadratique optimal, génération de solutions initiales et équilibrage des itérations d'équilibre ;

2). Les applications numériques valident la nouvelle mesure des déformations finies dérivées le long de l'épaisseur de la coque et offrent la possibilité d'améliorer grandement les estimations des contraintes dans les chemins de déformation en comparaison avec l'approche inverse à un pas unique.

Deuxièmement, nous avons dérivé et mis en œuvre dans Abaqus/Explicit un modèle thermomécanique non-local, capable de capturer les effets non locaux dans les zones de forte localisation de la déformation induite par l'endommagement ductile ou par des échanges thermiques violents.

1). Un ensemble complet d'équations de bilan et d'équations constitutives micromorphes est formulé dans le contexte de la thermodynamique des processus irréversibles :

- i). Les nouvelles équations d'équilibre additionnelles associées aux ddls micromorphes (l'endommagement ductile, l'écrouissage isotrope, l'écrouissage cinématique et la température) sont obtenues à partir du principe des puissances virtuelles étendu. En utilisant la thermodynamique des processus irréversibles les relations d'état des variables locales et micromorphes sont déduites de l'énergie libre de Helmholtz. Les équations d'évolution des variables associées aux phénomènes dissipatifs sont obtenues à partir de critère d'écoulement et de potentiel des dissipations grâce à la règle de normalité. Il est remarquable de noter que les équations constitutives s'écrivent sous la forme additive d'une contribution locale (classique) et d'une contribution non locale (micromorphique). Le modèle de comportement local est retrouvé comme cas particulier quand on annule les paramètres micromorphes.
- ii). En se limitant, par manque de temps, à la version du modèle avec endommagement et écrouissage isotrope micromorphes, une implémentation a été réalisée dans les sous-programmes VUEL et VUMAT d'Abaqus/Explicit en utilisant trois types d'éléments finis (membrane, coque et coque solide) avec déformation assumée pour mieux contrôler la variation de volume. L'intégration numérique locale inconditionnellement stable des équations constitutives est réalisée grâce au schéma asymptotique combiné avec un schéma d'Euler avant basé sur la méthode de prédiction élastique correction plastique avec retour radial.
- iii). Une étude paramétrique assez exhaustive a été menée et qui conclut que: les paramètres d'endommagement local S, s, β, Y_0 influencent la réponse du matériau dans le stade postcritique (avec adoucissement induit). La réponse du modèle non local est plus sensibles aux modules micromorphes \check{H} et \check{Q} qu'aux modules de gradient micromorphe \check{H}^g et \check{Q}^g . Aucune différence n'est observée pour le cas de la densité micromorphe inférieure à la densité locale. L'effet régularisant de l'endommagement micromorphe est accentué dans les cas de température élevée ou de taux de déformation élevé en raison du couplage complexe entre effets de viscosité et effets de endommagements non locaux ;
- iv). Les applications du modèle micromorphe proposé, à un essai de traction uniaxiale et au procédé d'emboutissage profond d'une boîte cruciforme prédisent des solutions acceptables, indépendantes de la taille du maillage. Le modèle est capable non seulement

RESUME EXTENSIF EN FRANCAIS

de prédire la déformation, l'endommagement , l'amorçage de fissures macroscopiques mais également leur propagation jusqu'à la rupture finale d'une pièce.

2). Le modèle thermomécanique micromorphe a été formulé dans le même cadre et appliqué au problème discriminant de transfert de chaleur :

- i). Le nouveau champ de micro-température est introduit ainsi que son premier gradient et conduit à une paire d'équations thermiques couplées thermodynamiquement cohérentes. Le cas constraint pour lequel la microtempérature coïncide avec la température locale classique présente un intérêt particulier car il peut être comparé aux différentes équations de la chaleur disponibles dans la littérature ;
- ii). L'équation proposée est renforcée par essentiellement trois nouvelles contributions qui ont été illustrées dans le cas linéarisé. Les trois termes affectent le comportement thermique transitoire du matériau. Le premier nouveau terme est lié au Laplacien du taux de température, une contribution qui a été proposée d'abord par Cattaneo dans une première version de sa théorie. Une seconde contribution est proportionnelle à la deuxième dérivée de la température qui modifie l'équation thermique habituelle en une équation hyperbolique avec un temps caractéristique positif. Le dernier terme associé à la troisième dérivée de la température demeure plutôt inexploré même s'il est présent dans certaines théories généralisées trouvées dans la littérature ;
- iii). La théorie proposée diffère des extensions thermomécaniques existantes du modèle micromorphe d'Eringen qui reposent sur l'introduction d'un vecteur de micro-température apparenté à un gradient de température. Il a également été comparé à l'équation de la chaleur effective résultante du modèle à double température impliquant deux équations thermiques couplées et conduisant également à des dérivées spatiales du quatrième ordre :
 - a). L'équation de la chaleur hyperbolique de Cattaneo II avec temps de relaxation peut être obtenue à partir de l'équation de la chaleur micromorphe thermodynamiquement cohérente en négligeant les effets non locaux de la température ;
 - b). Les modèles à deux températures classiques hyperboliques peuvent être également extraits des équations de la chaleur micromorphe
 - c). L'équation de la chaleur avec micro-température, à l'aide de la théorie de Green et l'équation de la chaleur micromorphe, fournissent une paire d'équations gouvernant la température locale et micromorphe. Et l'équation d'onde classique peut être obtenue à partir de leurs équations de la chaleur contrainte.
- iv). La théorie proposée permet un couplage direct avec la mécanique des matériaux et est considérée comme utile pour la simulation des variations rapides de la chaleur comme les traitements de surface de matériaux au laser, etc. La théorie résultant de l'introduction du gradient de température micromorphe pourrait être une alternative à l'analyse du transport de chaleur basé sur des flux de chaleur améliorés.

Plusieurs aspects restent ouverts et nécessitent de continuer les efforts pour améliorer la modélisation proposée :

RESUME EXTENSIF EN FRANCAIS

- 1). En général, toutes les variables qui régissent le l'adoucissement induit doivent être traitées comme des variables non locales. A cet effet, il semble nécessaire d'implémenter l'écrouissage cinématique micromorphe et d'étudier sa contribution à la régularisation du PVIL.
- 2). Plus de données expérimentales (divers essais sous trajets de chargement thermomécanique variés) sont nécessaires pour faciliter l'identification de la grande quantité de paramètres de matériaux indépendants/dépendants de la température;
- 3). Généralement, l'endommagement ductile peut être fortement anisotropes. Une extension du modèle micromorphe actuel pour inclure l'anisotropie de l'endommagement ductile pourrait être utile, en référence au travail d'endommagement ductile anisotrope réalisé au LASMIS (Badreddine, 2006; Saanouni, 2012) où l'endommagement est représenté par un couple de tenseurs symétriques du second ordre ($\underline{d}, \underline{Y}$);
- 4). Il convient également d'implémenter les équations de la chaleur micromorphes. Les applications des nouvelles équations de la chaleur micromorphe généralisée sont attendues dans les nanomatériaux et les nano systèmes, mais aussi pour les procédés d'usinage à grandes vitesses ou de soudage ainsi que les traitements de surface. Le travail effectué par Saanouni and Hamed (2013) en plasticité indépendante du temps pourrait être étendu aux processus thermomécaniques (viscoplasticité finie) en utilisant l'équation de chaleur généralisée basée sur le modèle de micro-température.

中文扩展摘要

绪论

汽车行业中为满足迫切的经济增长和环境保护的需求，选用新材料降低车身自重的方法依然在汽车节能减排中发挥着重要作用。采用新一代的高强度钢板可以有效的减轻传统钢材车身约 25%-39% 的自重，相当于在整个汽车生命周期内减少了约 3 到 4.5 吨的温室气体排放。然而，一般而言，随着钢材强度的提升，工作硬化能力减弱，拉伸性能降低，从而增加了零件的成形困难。在冲压成形过程中，金属材料在外力的作用下产生较大的非均匀塑性变形而表现出应变软化或断裂现象，通常是由初始微孔洞或微裂纹等韧性缺陷随着变形不断的生长、联合而导致的。

利用基于有限元模拟的数值方法以辅助车身覆盖件成形制造过程，已广泛应用于汽车制造行业中。为准确的模拟金属冲压成形过程，需要建立复杂的热力耦合的三维本构模型以表征材料的力学行为。材料本构模型的建立主要通过两种方法：宏观唯象方法和微观多尺度方法。基于经典连续介质损伤力学模型的初始和边界值问题，在描述由高温或缺陷损伤等引起的材料软化行为时，会导致运动控制方程椭圆性的丧失，随着有限元网格的细化而收敛到没有物理意义的解，即成为数学上的病态提法问题，其数值上表现为数值响应病态的依赖于有限元网格尺寸。其根本原因在于基于经典连续体损伤的本构方程中没有考虑材料微观组织结构的影响，一种很自然的弥补措施是在本构模型中引入特征尺度范围内物质点间的相互作用，即广义连续体力学。

本文，旨在不可逆热力学和广义连续介质力学框架下，建立热力学一致性非局部弹粘塑性本构模型，以表征材料应变软化行为的非局部效应和克服经典损伤本构引起的初始和边界值病态提法问题。主要包括两部分研究内容：(1) 采用经典弹塑性本构模型，通过引入若干中间变形状态，建立了金属冲压成形分析高效的静力隐式多步有限元模拟方法，以克服一步法分析引起的应力估计不足的问题；(2) 建立了热力学一致性的，耦合各向同性损伤、混合硬化和温度场、及微态损伤、微态混合硬化和微态温度场的非局部弹粘塑性本构模型，引入了额外的表征材料微观组织的微态变量，利用广义虚功原理和自由能函数得到了除位移控制方程外的补充微态变量平衡方程，并于 ABAQUS 用户子程序中实现了该微态损伤模型。引入了新的微态温度变量，建立了一组热力学一致性的含材料内部特征长度的广义微态热传导方程，通过选取合适的自由能函数，该广义微态热传导方程在内部约束下可退化为若干对传统傅里叶热传导方程的扩展模型，如表 Table 0-1 所列。

模型	作者	热传导方程
经典傅里叶模型	Fourier, 1878	$\rho C_e \dot{T} = \kappa \Delta T$
带热松弛时间的双曲线形热传导方程	Cattaneo I, 1948	$\rho C_e \dot{T} + \tau \kappa \Delta \dot{T} = \kappa \Delta T$
	Cattaneo II, 1948	$\rho C_e \dot{T} + \tau \rho C_e \ddot{T} = \kappa \Delta T$

	Coleman et al., 1982	$\begin{cases} \left(\rho C_{\varepsilon} + \vec{q} \cdot \frac{dA}{dT} \cdot \vec{q} \right) \dot{T} + 2\vec{q} \cdot A \cdot \dot{\vec{q}} = -\text{div}(\vec{q}) \\ \vec{q} + \underline{\zeta} \cdot \dot{\vec{q}} = -\underline{\kappa} \cdot \vec{\nabla} T \end{cases}$
温度梯度和熵梯度模型	Nguyen, 2010	$\rho C_{\varepsilon} \dot{T} + M \vec{\nabla} \dot{T} \cdot \vec{\nabla} T = \kappa \Delta T$
	Forest, 2008	$\rho C_{\varepsilon} \dot{T} + T_0 A_r \Delta \dot{T} = \kappa \Delta T$
	Forest, 2008	$\rho C_{\varepsilon} \dot{T} + T_0 A_r \Delta \dot{T} + \frac{A_s^2 C_{\varepsilon}^2}{\rho T_0} \Delta^2 \dot{s} = \kappa \Delta T$
	Forest, 2010	$\rho C_{\varepsilon} \dot{T} - \alpha T_0 \ddot{T} + M T_0 \Delta \dot{T} = \kappa \Delta T$
双温度方程模型	Aifantis, 1980	$\dot{T} + \alpha \ddot{T} - \beta \Delta \dot{T} + \gamma \Delta^2 T = \lambda \Delta T$
	Sobolev, 2016	$\dot{T}_i + (\tau + \tau_{12}) \ddot{T}_i + \tau \tau_{12} \dddot{T}_i - l^2 \Delta \dot{T}_i = \bar{\kappa} \Delta T_i$
		$\dot{T}_i + (\tau + \tau_{12}) \ddot{T}_i + \tau \tau_{12} \dddot{T}_i - (l^2 + l_e^2) \Delta \dot{T}_i - l_e^2 \tau_{12} \Delta^2 T_i = \bar{\kappa} \Delta T_i$
微温度模型	Iesan, 2002	$\begin{cases} c \dot{T} = k \Delta T + k_1 \text{div}(\vec{T}) \\ b \dot{\vec{T}} = k_6 \Delta \vec{T} + (k_4 + k_5) \vec{\nabla} (\text{div}(\vec{T})) - k_2 \vec{T} - k_3 \vec{\nabla} T \end{cases}$
	Iesan, 2005	$\begin{cases} a \ddot{T} + m \text{div}(\dot{\vec{T}}) = k \Delta T \\ b \ddot{\vec{T}} = d_2 \Delta \vec{T} + (d_1 + d_3) \vec{\nabla} (\text{div}(\vec{T})) - m \vec{\nabla} \dot{T} \end{cases}$
微态温度模型	微态温度形式	$\begin{aligned} & \rho T \left(\varsigma_2 \ddot{\vec{T}} + \varsigma_1 \ddot{\vec{T}} \right) - T \check{M}^g \Delta \dot{\vec{T}} \\ & - T \left[\frac{1}{2} \rho C_{\varepsilon} \left(\frac{\dot{\vec{T}}}{\vec{T}} - \frac{\vec{T}}{T} \right) + 2 \check{M} \left(\frac{\dot{\vec{T}}}{\vec{T}} - \dot{\vec{T}} \right) \right] = \kappa \Delta T \end{aligned}$
	双温度模型形式	$\begin{aligned} & \rho C_{\varepsilon} \dot{T} + \rho T \left(\varsigma_2 \ddot{\vec{T}} + \varsigma_1 \ddot{\vec{T}} \right) - 2 T \check{M} \left(\frac{\dot{\vec{T}}}{\vec{T}} - \dot{\vec{T}} \right) \\ & - T \check{M}^g \Delta \dot{\vec{T}} = \kappa \Delta T \end{aligned}$
		$\begin{aligned} & \rho C_{\varepsilon} \dot{T} + \rho (\tau C_{\varepsilon} + T_0 \varsigma_1) \ddot{T} + \rho T_0 (\tau \varsigma_1 + \varsigma_2) \ddot{\vec{T}} \\ & + \tau \rho T_0 \varsigma_2 \ddot{\vec{T}} - T_0 \check{M}^g \Delta \dot{\vec{T}} - T_0 \check{M}^g \Delta \ddot{\vec{T}} = \kappa \Delta T \end{aligned}$

Table 0-1 广义热传导方程

第一部分 板金属冲压成形的简单逆方法

简单逆方法（也称为 Inverse Approach (IA) 或一步法(One-step)），是最初由 Guo 等人提出来的用于零件初始设计阶段以提供高效的成形性分析的方法，其基本原理是：通过不断调整平板构型上的物质点的坐标，以使得成形后的零件构型，在模具对板料的接触外力和由参考平板构型度量的应变和应力而得到的内力的作用下，达到力的平衡状态，即表现为数学上迭代求解一组非线性方程组的过程。为简化复杂的冲压成形过程，该逆方法采用了五个基本假设：(1) 平面应力状态、(2) 基于形变理论的全量弹塑性模型、(3) 塑性变形体积不可压缩、(4) 简单的各向同性硬化模型、(5) 简化的接触法向压力和切向摩擦力。诸多的数值验证表明：该简单逆方法，针对成形零件可以提供相对准确的应变估计，但是由于其采用的基于全量理论的本构模型忽略了变形历史，而导致其提供的应力估计偏差较大。

为克服简单逆成形法忽略了变形历史使得应力估计精度不足的问题，本文，提出了通过引入若干中间构型以反映变形历史的多步成形模拟方法。其主要步骤包括：

- 1). 构造中间构型：滑移约束曲面和初始解构型。滑移约束曲面可近似假设为在凸凹模约束下的张拉膜形状，则通过接触搜索判断或求解几何曲面面积最小的方法进而构造得到；采用基于全量理论的网格映射方法将物质点放置在滑移曲面合适的位置上，即得到了中间构型的初始场；
- 2). 非线性应变增量度量。由于引入了若干变形过程中的构型状态，则需要重新推导基于曲面构型的有限对数应变增量的几何关系式，以考虑参考构型的弯曲效应；
- 3). 本构积分过程。采用经典的图形返回算法实现对 2) 过程的有限应变增量对应的应力更新过程。

I. 多步成形有限元模拟方法

I.1. 运动几何关系

如图 Fig. 0-1 所示三个中间构型： C^0 是初始平板构型， C 是已知最终零件构型和 C^1 是中间构型。考虑沿厚度方向的一物质点 q 参考不同构型的对数应变度量。由于构型 C^0 和构型 C^1 之间的应变度量与一步法中的非线性几何关系一致，本节仅关注最终构型 C 上物质点参考变形后构型 C^1 的应变独立。经推导后，得到左柯西-格林变形张量的逆：

$$[B]^{-1} = [F]^{-T} [F]^{-1} \approx \begin{bmatrix} a & b & 0 \\ b & c & 0 \\ 0 & 0 & (\lambda_3)^{-2} \end{bmatrix} \quad (1)$$

其中，

$$\begin{aligned} a &= A_0(1+sr)^2 + 2B_0sz(1+sr) + C_0(sz)^2 \\ b &= A_0(1+sr)sz + B_0(1+sr)(1+st) + B_0(sz)^2 + C_0sz(1+st) \\ c &= A_0(sz)^2 + 2B_0sz(1+st) + C_0(1+st)^2 \end{aligned} \quad (2)$$

和

$$\begin{aligned} A_0 &= a_0 - z_1 \vec{n}_{1,x} \left(2(\vec{o}_1 - \vec{u}_{p,x}) + z_1 (\vec{n}_{1,x}) \right) \\ B_0 &= b_0 - z_1 \left((\vec{o}_2 - \vec{u}_{p,y}) \vec{n}_{1,x} + (\vec{o}_1 - \vec{u}_{p,x}) \vec{n}_{1,y} + z_1 \vec{n}_{1,x} \vec{n}_{1,y} \right) \\ C_0 &= c_0 - z_1 \vec{n}_{1,y} \left(2(\vec{o}_2 - \vec{u}_{p,y}) + z_1 (\vec{n}_{1,y}) \right) \end{aligned} \quad (3)$$

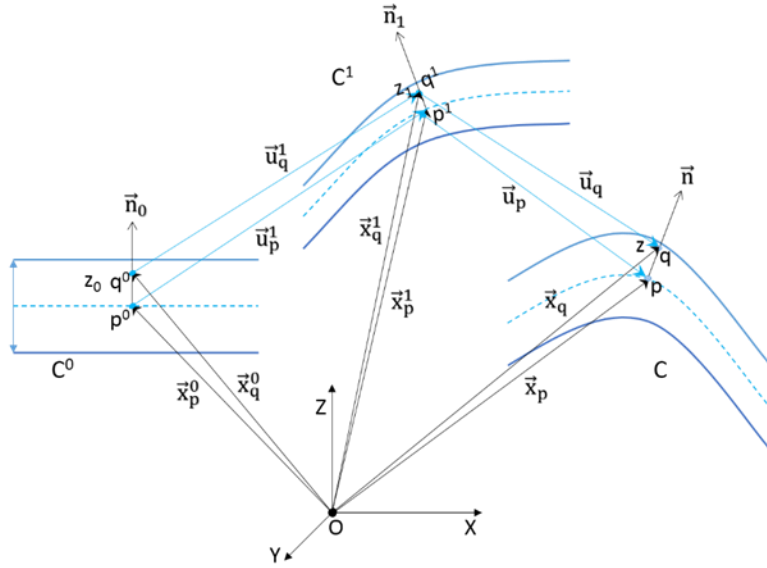


Fig. 0-1 中间构型间的运动几何关系

注意到，当物质点位于中性层上时($z=0$)，式子(3)退化为简单逆方法中的几何关系；当应变度量的物质点位于中性层外沿厚度方向时，由于参考构型的强烈的弯曲效应，应采用式子(3)建立对数应变增量的度量。

I.2. 经典弹塑性本构积分

采用了经典的各向异性弹塑性本构模型并耦合了幂指数形式的各向同性硬化，基于关联流动法则和 Hill48 的二次塑性势函数建立了塑性应变速率的演化方程，借助于 Simo 图形返回算法实现了该本构积分过程。Hill48 屈服准则可表示为：

$$f(\sigma, q) = (\langle \sigma \rangle [P] \{\sigma\})^{1/2} - \bar{\sigma}_s(q) = (\langle \sigma \rangle [P] \{\sigma\})^{1/2} - \bar{\sigma}_s(\bar{\varepsilon}^p) \quad (4)$$

拉格朗日塑性乘子，可由一致性条件求得：

$$\lambda = \frac{\left\langle \frac{\partial f}{\partial \{\sigma\}} \right\rangle [C] \{\dot{\varepsilon}\}}{\left\langle \frac{\partial f}{\partial \{\sigma\}} \right\rangle [C] \left\{ \frac{\partial f}{\partial \{\sigma\}} \right\} - \frac{\partial f}{\partial q}} \quad (5)$$

考虑应力率与弹性应变率之间的关系，可以得到：

$$\dot{\sigma} = [C^{ep}]\{\dot{\varepsilon}\} = \left[C - \frac{[C] \left\{ \frac{\partial f}{\partial \{\sigma\}} \right\} \left\langle \frac{\partial f}{\partial \{\sigma\}} \right\rangle [C]}{\left\langle \frac{\partial f}{\partial \{\sigma\}} \right\rangle [C] \left\{ \frac{\partial f}{\partial \{\sigma\}} \right\} - \frac{\partial f}{\partial q}} \right] \{\dot{\varepsilon}\} \quad (6)$$

采用经典的弹性预测和塑性返回的隐式图形返回算法以更新应力的状态。注意到，引入逆成形有限元方法中广泛采用的一个假设：弹性变形具有与塑性变形同样的各向异性特性，且弹性变形近似满足体积不可压缩条件，则可以得到泊松比 ν 和平均各向异性系数 r 之间存在如下的关系：

$$\nu = \frac{r}{1+r} \quad (7)$$

此时，该图形返回算法退化为 Guo 等提出的高效的直接标量返回算法。但还应当注意到，考虑到该逆成形有限元方法使用的较大的有限应变增量引起的收敛困难的现象，可以通过采用直接标量返回算法生成更优的图形返回算法的初始解，从而减轻收敛性问题。

I.3. 中间构型构造

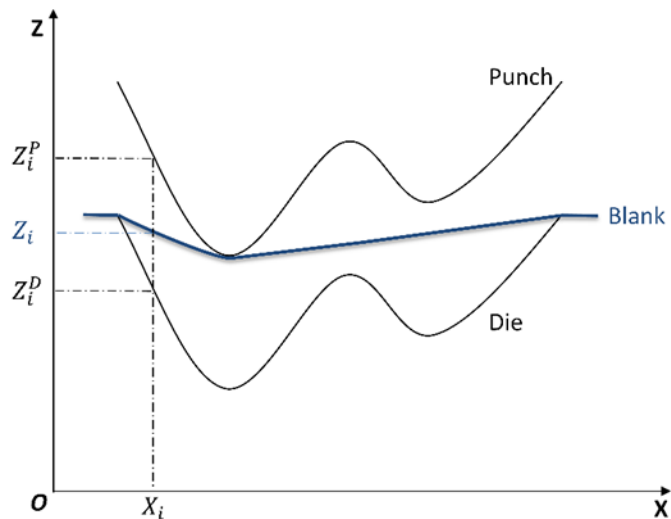


Fig. 0-2 冲压成形板料状态示意图

构造三维滑移约束曲面

如图 Fig. 0-2 所示，板料构型近似假设为在已知凸模和凹模的位置约束下的张拉膜，板料形状可近似为使板料的面积最小的曲面。考虑到有限元网格坐标与面积之间的非线性关系，该最小面积法对应为 NP 困难的序列二次规划模型，求解困难且效率低。本文通过拟最小面积法建立了一个多项式时间复杂度的二次规划模型，其目标函数和约束条件定义为：

$$\begin{aligned} \min: f(\xi) &= \sum_{e=1}^n A_e^2(\xi) \\ \text{s.t. } 0 \leq \xi_i &\leq 1 (i=1,2,3\dots,m) \end{aligned} \quad (8)$$

考虑三角形单元网格，则上式的单元面积的平方可写为如下形式：

$$A_e^2 = \frac{1}{4} \left(\frac{1}{2} \langle \xi_e \rangle [H_e] \{\xi_e\} + \langle C_e \rangle \{\xi_e\} + D_e \right) \quad (9)$$

遵循类似于组装单元刚度矩阵的方式整合结构面积矩阵，得到结构的优化模型：

$$f(\xi) = \sum_{e=1}^n A_e^2(\xi) = \frac{1}{4} \left(\frac{1}{2} \langle \xi \rangle [H] \{\xi\} + \langle C \rangle \{\xi\} + D \right) \quad (10)$$

注意到，上式为典型的二次规划模型，可以通过 Matlab/quadprog() 函数高效的求解，从而得到一般三维零件的滑移约束曲面。

生成中间构型

考虑到滑移约束曲面仅是一个几何形状曲面，本节则将板料的各物质点放置到该约束曲面合适位置上，以生成对应的中间构型的初始场。其基本思想为：由于中间构型状态为板料变形过程中的某一瞬时状态，其对应的初始板料与成形后零件对应的初始板料是完全一致的，则通过比较这两个不同构型对应的板料并使其一致，就可以得到更新后的约束曲面，即对应中间构型的初始解。

通过施加罚函数约束，使得中间构型上的物质点在平衡迭代过程中被限制在滑移曲面上移动。最终，经过组装结构的刚度矩阵、内力向量和外力向量，可以得到一组采用 Newton-Raphson 迭代求解的非线性方程组：

$$\{R(U^i)\} = \{F_{ext}(U^i) - F_{int}(U^i)\} = [K]\{\Delta U\} \neq 0 \quad (11)$$

II. 数值应用

本节对所提出的多步法的新的非线性几何关系和中间构型状态进行了比较分析，并应用到具体实例成形分析中。S 梁零件被用于验证新的有限应变度量，为便于比较起见，增量法对 S 梁零件的正向成形模拟结果和中间构型状态作为多步法分析的输入信息，并与多步法预示的厚度、应变和应力等进行比较；对 B 柱零件的分析验证了该多步成形方法的可行性。盒形支座零件的分析采用修正的拟最小面积法构造了若干中间构型，并应用到多步法分析过程中，其数值结果表明了该多步法的有效性。

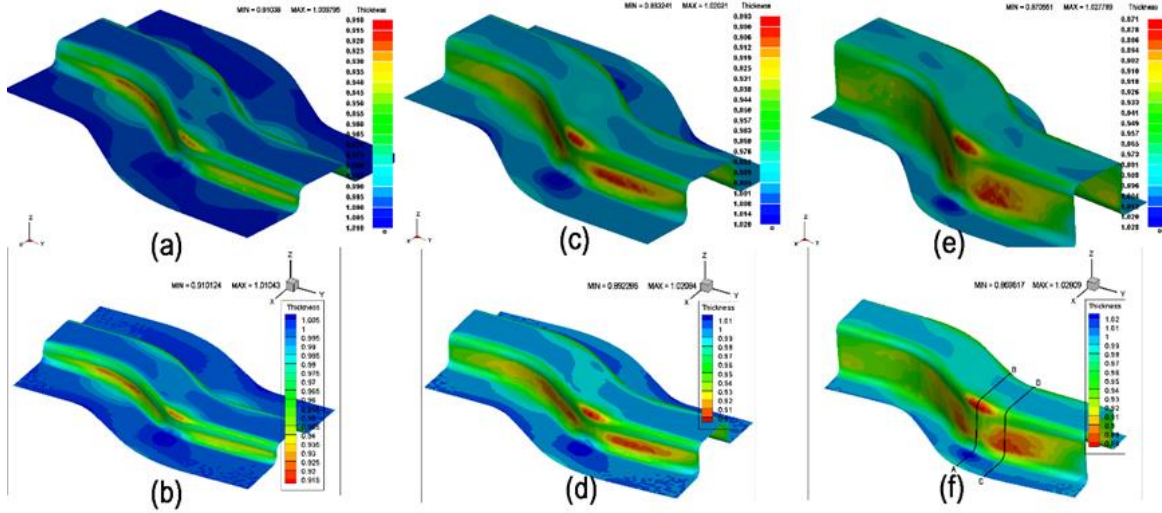


Fig. 0-3 LS-DYNA 和多步法分别模拟的三个构型状态的厚度分布图: (a) 增量法模拟 15mm 行程 (b) 多步法模拟 15mm 行程 (c) 增量法模拟 25mm 行程 (d) 多步法模拟 25mm 行程 (e) 增量法模拟 40mm 行程 (f) 多步法模拟 40mm 行程

第二部分 热力学一致性的微态本构模型

前章所述的为基于 Cauchy 介质的采用经典局部作用假设的简单连续体: 即占有空间区域的任一物质点的力学状态可由该点周围无限小范围内的状态变量的历史所确定。对于简单连续体而言, 变形梯度张量足以确定物质点的状态。

工程零件的宏观破裂往往是材料微观组织显著变化的结果, 比如混凝土中的微裂纹、纤维增强复合材料的脱层和纤维脱粘及韧性金属材料中的微空洞形成及发展。在混凝土等脆性材料的断裂分析中, 通常采用分离裂纹模型或弥散裂纹模型的无网格法、内聚单元有限元法或扩展有限元法等方法描述裂纹的扩展。当材料微观内部缺陷或温度等因素使得材料表现出强烈的应变软化行为时, 简单连续体损伤模型由于忽略了微观结构的影响, 而使得的控制方程丧失了椭圆性, 从而成为数学上的病态提法问题。其数值上表现为: 应变集中带的宽度和断裂耗散能随有限单元网格的细化趋于零, 且数值响应病态的依赖于网格尺寸, 而收敛到不正确的没有物理意义的有限元解。一个自然的弥补上述缺陷的方法是在本构模型中引入表征微观组织影响的状态变量, 即正则化机制。

本章采用基于热力学一致性的宏观唯象的广义连续体力学, 通过引入新的与局部变量相耦合的微态变量及扩展的亥姆霍兹自由能, 以克服简单连续体损伤模型导致的数学上的病态提法问题。

III. 理论推导

为考虑材料应变软化现象的非局部效应, 本章引入了新的微态各向同性损伤变量($\bar{d}, \bar{\gamma}$)、微态温度变量(\bar{T}, \bar{s})、微态各向同性硬化变量(\bar{r}, \bar{R})和微态随动硬化张量($\bar{\alpha}, \bar{X}$)及其一阶梯度以反映材料的非局部效应。

III.1. 平衡方程

通过广义虚功原理：对所有符合运动许可的虚位移和虚微态变量，内力和外力在系统上所做的虚功总和与惯性力虚功达到平衡。即：

$$\delta P_{int} + \delta P_{ext} = \delta P_a \quad \forall \delta \dot{u}, \delta \dot{d}, \delta \dot{r}, \delta \dot{\underline{\alpha}}, \delta \dot{\bar{T}} K.A. \quad (12)$$

可以得到以传统位移为自由度的控制方程和四个额外的与微态变量相关的平衡方程，及相应的纽曼边界条件：

$$\begin{aligned} & \left\{ \begin{array}{ll} \vec{\nabla} \cdot \underline{\sigma} + \rho \vec{f}^u = \rho \ddot{u} & \text{in } \Omega \\ \underline{\sigma} \cdot \vec{n} = \vec{F}^u & \text{on } \Gamma \end{array} \right. & \left\{ \begin{array}{ll} \left(\vec{\nabla} \cdot \vec{Y} - \vec{Y} \right) + \rho \left(f^d - \vec{\nabla} \cdot \vec{f}^{gd} \right) = \rho \zeta_d \ddot{d} & \text{in } \Omega \\ \left(\vec{Y} - \rho \vec{f}^{gd} \right) \cdot \vec{n} = F^d & \text{on } \Gamma \end{array} \right. \\ & \left\{ \begin{array}{ll} \left(\vec{\nabla} \cdot \vec{R} - \vec{R} \right) + \rho \left(f^r - \vec{\nabla} \cdot \vec{f}^{gr} \right) = \rho \zeta_r \ddot{r} & \text{in } \Omega \\ \left(\vec{R} - \rho \vec{f}^{gr} \right) \cdot \vec{n} = F^r & \text{on } \Gamma \end{array} \right. & \left\{ \begin{array}{ll} \left(\vec{\nabla} \cdot \vec{X} - \vec{X} \right) + \rho \left(f^{\alpha} - \vec{\nabla} \cdot \vec{f}^{g\alpha} \right) = \rho \zeta_{\alpha} \ddot{\alpha} & \text{in } \Omega \\ \left(\vec{X} - \rho \vec{f}^{g\alpha} \right) \cdot \vec{n} = F^{\alpha} & \text{on } \Gamma \end{array} \right. \\ & \left\{ \begin{array}{ll} \left(\vec{\nabla} \cdot \vec{s} - \vec{s} \right) + \rho \left(f^{\tau} - \vec{\nabla} \cdot \vec{f}^{g\tau} \right) = \rho \left(\zeta_{\tau_2} \ddot{\tau} + \zeta_{\tau_1} \dot{\bar{\tau}} \right) & \text{in } \Omega \\ \left(\vec{s} - \rho \vec{f}^{g\tau} \right) \cdot \vec{n} = F^{\tau} & \text{on } \Gamma \end{array} \right. \end{aligned} \quad (13)$$

III.2. 状态方程

根据热力学第一定律，体系的内能 E 和动能 K 之和的变化率等于体系吸收的热量 Q 和外力对体系作的功 P_{ext} 。用数学式表达为：

$$\frac{d}{dt} (E + K) = P_{ext} + Q \quad (14)$$

利用动能法则，考虑局部平衡假设，则可以得到如下微分形式的热力学第一定律的表达式：

$$\rho \dot{e} = \left(\frac{\underline{\sigma} : D + \vec{Y} \dot{d} + \vec{R} \dot{r} + \vec{X} : \dot{\underline{\alpha}} + \vec{s} \dot{\bar{T}}}{+ \vec{Y} \cdot \vec{\nabla} d + \vec{R} \cdot \vec{\nabla} r + \vec{X} : \vec{\nabla} \underline{\alpha} + \vec{s} \cdot \vec{\nabla} \bar{T}} \right) + \rho \zeta - \text{div}(\vec{q}) \quad (15)$$

注意到，内能密度函数引入了新的微态变量的贡献。

在当前构型下，熵不等式可以表示为如下的积分形式：

$$\frac{d}{dt} \int_{\Omega_t} (\rho s) dv - \int_{\Omega_t} \left(\rho \frac{\zeta}{T} \right) dv + \int_{\Gamma_t} \left(\frac{\vec{q}}{T} \cdot \vec{n} \right) ds \geq 0 \quad (16)$$

引入亥姆霍兹自由能、结合热力学第一和第二定律，可以得到广义的克劳修斯-迪昂不等式：

$$\begin{aligned}
& \left(\underline{\sigma} - \rho \frac{\partial \psi}{\partial \underline{\varepsilon}^{re}} \right) : \dot{\underline{\varepsilon}}^{re} - \rho \left(s + \frac{\partial \psi}{\partial T} \right) \dot{T} \\
& + \left(\bar{Y} - \rho \frac{\partial \psi}{\partial d} \right) \dot{\bar{d}} + \left(\bar{R} - \rho \frac{\partial \psi}{\partial r} \right) \dot{\bar{r}} + \left(\bar{X} - \rho \frac{\partial \psi}{\partial \underline{\alpha}} \right) : \dot{\underline{\alpha}} + \left(\bar{s} - \rho \frac{\partial \psi}{\partial \bar{T}} \right) \dot{\bar{T}} \\
& + \left(\bar{\bar{Y}} - \rho \frac{\partial \psi}{\partial \bar{\nabla} \bar{d}} \right) : \vec{\nabla} \dot{\bar{d}} + \left(\bar{\bar{R}} - \rho \frac{\partial \psi}{\partial \bar{\nabla} \bar{r}} \right) : \vec{\nabla} \dot{\bar{r}} + \left(\bar{\bar{X}} - \rho \frac{\partial \psi}{\partial \bar{\nabla} \bar{\underline{\alpha}}} \right) : \vec{\nabla} \dot{\underline{\alpha}} + \left(\bar{\bar{s}} - \rho \frac{\partial \psi}{\partial \bar{\nabla} \bar{T}} \right) : \vec{\nabla} \dot{\bar{T}} \\
& + \underline{\sigma} : \underline{D}^{ir} - \left(\rho \frac{\partial \psi}{\partial d} \dot{d} + \rho \frac{\partial \psi}{\partial r} \dot{r} + \rho \frac{\partial \psi}{\partial \underline{\alpha}} : \dot{\underline{\alpha}} \right) - \frac{\vec{q}}{T} \cdot \vec{\nabla} T \geq 0
\end{aligned} \tag{17}$$

不失一般性，假设微态变量不引起新的耗散，并且 $\left(\underline{\sigma} - \rho \frac{\partial \psi}{\partial \underline{\varepsilon}^{re}} \right)$, $\left(s + \frac{\partial \psi}{\partial T} \right)$, $\left(\bar{Y} - \rho \frac{\partial \psi}{\partial d} \right)$, $\left(\bar{R} - \rho \frac{\partial \psi}{\partial r} \right)$, $\left(\bar{X} - \rho \frac{\partial \psi}{\partial \underline{\alpha}} \right)$, $\left(\bar{s} - \rho \frac{\partial \psi}{\partial \bar{T}} \right)$, $\left(\bar{\bar{Y}} - \rho \frac{\partial \psi}{\partial \bar{\nabla} \bar{d}} \right)$, $\left(\bar{\bar{R}} - \rho \frac{\partial \psi}{\partial \bar{\nabla} \bar{r}} \right)$, $\left(\bar{\bar{X}} - \rho \frac{\partial \psi}{\partial \bar{\nabla} \bar{\underline{\alpha}}} \right)$ 和 $\left(\bar{\bar{s}} - \rho \frac{\partial \psi}{\partial \bar{\nabla} \bar{T}} \right)$ 不依赖于相应的应变速率，则可以得到如下形式的状态方程：

$$\begin{aligned}
\underline{\sigma} &= \rho \frac{\partial \psi}{\partial \underline{\varepsilon}^{re}} & s &= -\frac{\partial \psi}{\partial T} \\
Y &= -\rho \frac{\partial \psi}{\partial d} & R &= \rho \frac{\partial \psi}{\partial r} & X &= \rho \frac{\partial \psi}{\partial \underline{\alpha}} \\
\bar{Y} &= \rho \frac{\partial \psi}{\partial \bar{d}} & \bar{R} &= \rho \frac{\partial \psi}{\partial \bar{r}} & \bar{X} &= \rho \frac{\partial \psi}{\partial \bar{\underline{\alpha}}} \\
\bar{\bar{Y}} &= \rho \frac{\partial \psi}{\partial \bar{\nabla} \bar{d}} & \bar{\bar{R}} &= \rho \frac{\partial \psi}{\partial \bar{\nabla} \bar{r}} & \bar{\bar{X}} &= \rho \frac{\partial \psi}{\partial \bar{\nabla} \bar{\underline{\alpha}}} \\
\bar{\bar{s}} &= \rho \frac{\partial \psi}{\partial \bar{\nabla} \bar{T}} & \bar{\bar{s}} &= \rho \frac{\partial \psi}{\partial \bar{\nabla} \bar{\bar{T}}}
\end{aligned} \tag{18}$$

和与经典弹塑性损伤模型一致的耗散项：

$$\phi = \phi_{in} + \phi_{th} = \underline{\sigma} : \underline{D}^{ir} + Y \dot{d} - R \dot{r} - X : \dot{\underline{\alpha}} - \frac{\vec{q}}{T} \cdot \vec{g} \geq 0 \tag{19}$$

通过选取合适的亥姆霍兹自由能函数，可以得到以上状态变量的具体表达式。

III.3. 演化方程

鉴于率无关塑性材料可视为率相关塑性模型的粘性应力为 0 时一个特殊情况，本节仅考虑率相关塑性材料的耗散变量的演化方程。针对应力状态可位于屈服面之外 ($f_\rho(\underline{\sigma}, \bar{X}, \bar{R}; T) \geq 0$) 的粘塑性材料，采用诺顿-霍夫粘塑性势能 $\varphi(\underline{\sigma}, \bar{R}, \bar{X}, T)$ ，利用广义法向流动法则可得到如下的耗散变量的演化方程：

$$\begin{aligned}
 \underline{D}^{\nu p} &= \frac{\partial \varphi}{\partial \underline{\sigma}} = \left\langle \frac{f_p}{K^{\nu p}} \right\rangle^{m_{\nu p}} \frac{1}{\sqrt{1-d}} \frac{\underline{H}_{\underline{\sigma}} : (\underline{\sigma} - \underline{\chi})}{\|\underline{\sigma} - \underline{\chi}\|} = \dot{\lambda}_{\nu p} \tilde{\eta}_f \\
 \dot{\underline{\alpha}} &= -\frac{\partial \varphi}{\partial \underline{\chi}} = \dot{\lambda}_{\nu p} \left[\tilde{\eta}_f - a \underline{1} : \underline{\alpha} - a (\underline{C}^{-1} : \underline{C}) : (\underline{\alpha} + \underline{\alpha}) \right] - \left\langle \frac{\|\underline{\chi}\|}{K^{rx}} \right\rangle^{m_{rx}} \frac{\underline{\tilde{H}}_{\underline{\chi}} : \underline{\chi}}{\|\underline{\chi}\|} \\
 \dot{r} &= -\frac{\partial \varphi}{\partial R} = \frac{\dot{\lambda}_{\nu p}}{\sqrt{1-d^\gamma}} \left[1 - \left(1 + \frac{\bar{Q}}{Q} \right) b(T) \tilde{r} + \frac{\bar{Q}}{Q} b \tilde{r} \right] - \left\langle \frac{\tilde{R}}{K^{rr}} \right\rangle^{m_{rr}} \\
 \dot{d} &= \frac{\partial \varphi}{\partial Y} = \frac{\dot{p}}{(1-d)^\beta} \left\langle \frac{Y - Y_0}{S} \right\rangle^s = \dot{p} \hat{Y}
 \end{aligned} \tag{20}$$

通过热力学一致性分析可以发现，当 $\sigma_{\nu p} \geq 0$, $\frac{b}{Q} \geq 0$, $K^{rx} \geq 0$, $K^{rr} \geq 0$ 和 $a \underline{C}^{-1}$ 为半正定张量时，熵不等式可以得到满足。

III.4. 应变空间描述的平衡方程

回顾式子(13)中的广义平衡方程是在广义应力空间表示的，本节利用式(21)所示的状态变量方程，将其转换到广义应变空间，并忽略广义体力与接触力：

$$\begin{cases} \left[I_d^2 Lap(\underline{d}) + \frac{\vec{\nabla} \bar{H}^g(T)}{\bar{H}(T)} \cdot \vec{\nabla} \underline{d} \right] + (d - \underline{d}) = \rho \frac{\zeta_d \ddot{d}}{\bar{H}(T)} \\ \bar{H}^g(T) \vec{\nabla} \underline{d} \cdot \vec{n} = 0 \end{cases} \tag{22}$$

$$\begin{cases} (1-d^\gamma) \left[I_r^2 Lap(\underline{r}) + \frac{\vec{\nabla} \bar{Q}^g(T)}{\bar{Q}(T)} \cdot \vec{\nabla} \underline{r} + (r - \underline{r}) \right] = \rho \frac{\zeta_r \ddot{r}}{\bar{Q}(T)} \\ [(1-d^\gamma) \bar{Q}^g(T) (\vec{\nabla} \underline{r})] \cdot \vec{n} = 0 \end{cases} \tag{23}$$

$$\begin{cases} (1-d) \left[I_{\underline{\alpha}}^2 Lap(\underline{\alpha}) + \frac{\vec{\nabla} \bar{C}^g(T)}{\bar{C}(T)} \cdot \vec{\nabla} \underline{\alpha} + (\underline{\alpha} - \alpha) \right] = \rho \frac{\zeta_{\underline{\alpha}} \ddot{\alpha}}{\bar{C}(T)} \\ [(1-d) \bar{C}^g(T) (\vec{\nabla} \underline{\alpha})] \cdot \vec{n} = 0 \end{cases} \tag{24}$$

$$\begin{cases} \left[I_{\bar{T}}^2 Lap(\bar{T}) + \frac{\vec{\nabla} \bar{M}^g(T)}{\bar{M}(T)} \cdot \vec{\nabla} \bar{T} \right] + \left[(\tau - \bar{T}) - \frac{\sqrt{1-d}}{\bar{M}(T)} \bar{P}(T) : \varepsilon^e \right] = \rho \left(\frac{\zeta_{\bar{T}1}}{\bar{M}(T)} \dot{\bar{T}} + \frac{\zeta_{\bar{T}2}}{\bar{M}(T)} \ddot{\bar{T}} \right) \\ (\bar{M}^g(T) \vec{\nabla} \bar{T}) \cdot \vec{n} = 0 \end{cases} \tag{25}$$

式中， I_d , I_r , $I_{\underline{\alpha}}$ 和 $I_{\bar{T}}$ 是分别与微态损伤、微态各向同性硬化、微态随动硬化和微态温度相对应的材料内部特征尺度参数。

III.5. 微态热传导方程

表 Table 0-1 中列出了若干对传统傅里叶热传导方程的扩展研究模型，为简单起见，本节的推导均采用刚体材料的传热分析。考虑仅包含微态温度及其一阶梯度的情况，通过应用广义虚功原理、热力学一致性推导和亥姆霍兹自由能，可以得到如下的一组广义微态热传导方程组：

$$\begin{cases} \rho\dot{\epsilon} = \underline{\sigma} : \dot{\epsilon} + (\vec{s}\dot{T} + \vec{s} \cdot \vec{\nabla}\dot{T}) + (\rho\zeta - \text{div}(\vec{q})) \\ \rho\dot{s} - \rho\frac{\zeta}{T} + \text{div}\left(\frac{\vec{q}}{T}\right) \geq 0 \end{cases} \quad (26)$$

其中，局部与微态温度通过亥姆霍兹自由能相互耦合，并体现在该广义微态热传导方程组中。

假设亥姆霍兹自由能密度函数定义为：

$$\rho\psi(T, \bar{T}, \vec{\nabla}\bar{T}) = -\rho CT \left(\ln \frac{T}{T_0} - 1 \right) - \rho \bar{CT} \left(\ln \frac{\bar{T}}{T_0} - 1 \right) - \frac{1}{2} \bar{M}(T - \bar{T})^2 + \frac{1}{2} \bar{M}^g \vec{\nabla}\bar{T} \cdot \vec{\nabla}\bar{T} \quad (27)$$

引入内部约束使得局部温度与微态温度的差距趋于零，考虑傅里叶热流矢量模型并忽略内部热源，得到：

$$\rho T \left(\zeta_{\bar{T}_1} \ddot{\bar{T}} + \zeta_{\bar{T}_2} \ddot{\bar{T}} \right) + \rho(C - \bar{C}) \dot{T} - T \bar{M}^g \Delta \dot{T} = \kappa \Delta T \quad (28)$$

注意到：

- a) 若 $\zeta_{\bar{T}_2} = 0$ ，表明微态温度的惯性项仅依赖于其对时间的一阶导数，则线性化的热传导方程表示为：

$$\rho T_0 \zeta_{\bar{T}_1} \ddot{\bar{T}} + \rho(C - \bar{C}) \dot{T} - T_0 \bar{M}^g \Delta \dot{T} = \kappa \Delta T \quad (29)$$

上式与忽略四阶梯度效应（例如：纯金属材料或电子-晶格热传导过程）的双温度方程模型 (Forest et Aifantis (2010)) 的热传导方程具有相同的形式。

- b) 若两个广义比热容参数相等 $C = \bar{C}$ ，该方程简化为：

$$\rho T_0 \zeta_{\bar{T}_1} \ddot{\bar{T}} - T_0 \bar{M}^g \Delta \dot{T} = \kappa \Delta T \quad (30)$$

该热传导方程与 Ieşan et Nappa (2005) 等推导的微态介质下忽略四阶梯度项的热传导方程相一致，若满足 $\rho T_0 \zeta_{\bar{T}_1} = a$ 和 $\bar{M}^g = -m/T_0$

- c) 针对式子(II.271)，若假定某一介质的 $\bar{M}^g = 0$ 或 $\Delta \dot{T}$ 项相较于其它项较小，其退化为经典的波动方程形式：

$$\ddot{\bar{T}} = \frac{\kappa}{\rho T_0 \zeta_{\bar{T}_1}} \Delta T \quad (31)$$

波的传播速度为 $\sqrt{\frac{\kappa}{\rho T_0 \zeta_{\bar{T}_1}}}.$

通过选取合适的亥姆霍兹自由能密度函数和热流矢量模型，该广义微态热传导方程可退化为带松弛时间的双曲线形热传导方程、超温度模型、双曲线形双温度模型和包含非局部效应的广义双温度模型。

IV. 数值应用

IV.1. 时间与空间离散

有限元将总的时间长度 I_t 离散为 N_t 个子时间域 $I_t = [t_0, t_f] \equiv \bigcup_{n=0}^{N_t} [t_n, t_{n+1}] = t_n + \Delta t$ ， 并在每个子时间域内根据已知的 t_n 时刻的初始边界值问题，求解 $t_{n+1} = t_n + \Delta t$ 时刻的非线性方程组。

标准有限元将参考构型域 Ω_{t_n} 离散为 N_e 个无交集的有限子域 Ω_e 。位移场采用假设应变的方式插值，微态变量场采用标准的插值函数场进行插值。将单元的插值形式代入到初始和边界值问题的弱形式中，可以得到：

$$\begin{cases} J_u(\delta\bar{v}) = \langle \delta\dot{u}_n^e \rangle \left([M_u^e] \{ \ddot{u}_n^e \} + \{ F_{int-u}^e \} - \{ F_{ext-u}^e \} \right) \\ J_{\bar{d}}(\delta\bar{d}) = -\langle \delta\dot{d}_n^e \rangle \left([M_{\bar{d}}^e] \{ \ddot{d}_n^e \} + \{ F_{int-\bar{d}}^e \} - \{ F_{ext-\bar{d}}^e \} \right) \\ J_{\bar{r}}(\delta\bar{r}) = -\langle \delta\dot{r}_n^e \rangle \left([M_{\bar{r}}^e] \{ \ddot{r}_n^e \} + \{ F_{int-\bar{r}}^e \} - \{ F_{ext-\bar{r}}^e \} \right) \\ J_{\bar{\alpha}}(\delta\bar{\alpha}) = -[\delta\bar{\alpha}_n^e]^T \left([M_{\bar{\alpha}}^e] \{ \ddot{\alpha}_n^e \} + [F_{int-\bar{\alpha}}^e] - [F_{ext-\bar{\alpha}}^e] \right) \\ J_{\bar{T}}(\delta\bar{T}) = -\langle \delta\dot{T}_n^e \rangle \left([M_{\bar{T}}^e] \{ \ddot{T}_n^e \} + \{ F_{int-\bar{T}}^e \} - \{ F_{ext-\bar{T}}^e \} \right) \\ J_T(\delta T) = -\langle \delta\dot{T}_n^e \rangle \left([M_T^e] \{ \dot{T}_n^e \} + \{ F_{int-T}^e \} - \{ F_{ext-T}^e \} \right) \end{cases} \quad (32)$$

IV.2. 全局求解策略

本文采用基于动力显式的有限元求解器 Abaqus/Explicit 进行求解式子(31)中的非线性方程组。显式的中心差分格式的物体运动方程为：

$$\begin{aligned} \{\dot{u}\}^{(n+1/2)} &= \{\dot{u}\}^{(n-1/2)} + \frac{\Delta t^{(n+1)} + \Delta t^{(n)}}{2} \{\ddot{u}\}^{(n)} \\ \{u\}^{(n+1)} &= \{u\}^{(n)} + \Delta t^{(n+1)} \{\dot{u}\}^{(n+1/2)} \end{aligned} \quad (33)$$

由于动力显式算法是条件稳定的，即稳定的时间步长不大于弹性波穿过一最小网格单元特征长度的时间：

$$\Delta t_u \leq \frac{2}{w_{max}} \left(\sqrt{(1+\zeta^2)} - \zeta \right) \quad (34)$$

IV.3. 局部本构积分过程

为求解式子(31)的代数方程组，除计算对角化的质量阻尼矩阵与通过接触判断确定等效节点上的外力向量外，还需要计算等效节点上的内力向量，即根据 t_n 时刻的已知物理量，求解 t_{n+1} 时刻的应力张量 $\underline{\sigma}_{n+1}$ ，局部损伤 d_{n+1} ，各向同性硬化应变 r_{n+1} 和随动硬化应变 α_{n+1} 。由于Abaqus/Explicit热力耦合顺序求解的特点，在该本构积分过程中，各微态变量保持为 T_{n+1} 时刻的取值，而温度变量维持 t_n 时刻的取值。本文采用完全隐式的本构积分过程，通过返回算法的弹性预测和塑性修正过程使得更新后的广义应力等保持在屈服面上。

弹性预测

假设，由 t_n 时刻到时刻 T_{n+1} 产生的总的应变增量 $\Delta\varepsilon$ 为弹性的，即不引起新的塑性流动、硬化及损伤。则假设应变增量为弹性的弹性试应力为：

$$\underline{\sigma}_{n+1}^{trial} = (1-d_n)\underline{\Delta}(T_n):\underline{\varepsilon}_{n+1}^{e,trial} - \sqrt{1-d_n}(T_n-T_0)\underline{P}(T_n) - \sqrt{1-d_n}(T_n-\bar{T}_n)\bar{P}(T_n) \quad (35)$$

代入到率相关材料的屈服准则中，得到：

$$f_{n+1}^{vp,trial} = \frac{\|\underline{\sigma}_{n+1}^{trial} - \underline{X}_n\|}{\sqrt{1-d_n}} - \frac{R_n}{\sqrt{1-d_n^\gamma}} - \sigma_{vp}(T_n) \quad (36)$$

若 $f_{n+1}^{vp,trial} \leq 0$ ，表明弹性试应力位于屈服面内，该应变增量为全弹性并不产生新的塑性变形，则内变量更新为：

$$\begin{cases} \underline{\varepsilon}_{n+1}^{vp} = \underline{\varepsilon}_n^{vp} & \underline{\alpha}_{n+1} = \underline{\alpha}_n & \underline{r}_{n+1} = \underline{r}_n & d_{n+1} = d_n \\ \underline{\sigma}_{n+1} = \underline{\sigma}_{n+1}^{trial} & \underline{X}_{n+1} = \underline{X}_n & R_{n+1} = R_n & Y_{n+1} = Y_n \end{cases} \quad (37)$$

塑性修正

若 $f_{n+1}^{vp,trial} > 0$ ，表明弹性试应力位于屈服面外侧并产生新的塑性变形，则需通过塑性修正过程更新广义应力和内变量，使其满足屈服条件：

$$\begin{aligned} f_{n+1}^p(\tilde{\sigma}_{n+1}, \tilde{X}_{n+1}, \tilde{R}_{n+1}; T_n) &= 0 && \text{plasticity} \\ f_{n+1}^{vp} = f_{n+1}^p(\tilde{\sigma}_{n+1}, \tilde{X}_{n+1}, \tilde{R}_{n+1}; T_n) - \sigma_{n+1}^{vp} &= 0 && \text{viscoplasticity} \end{aligned} \quad (38)$$

鉴于粘塑性乘子与损伤的强耦合关系及考虑各向异性塑性材料，本文将 $\Delta\lambda_{vp}$ 、 d 和 n_f 分别视为三个独立的自变量，进而本构积分的塑性修正过程转化为求解下述非线性方程组的问题：

$$\begin{cases} f_{n+1}^{vp} = \frac{\|\underline{Z}_{n+1}\|}{\sqrt{1-d_{n+1}}} - \frac{R_{n+1}}{\sqrt{1-d_{n+1}^\gamma}} - \sigma_{n+1}^{vp} - \sigma_{vp}(T_n) = 0 \\ g_{n+1} = d_{n+1} - d_n - \frac{\Delta \lambda_{vp}}{(1-d_{n+1})^{\beta(T_n)}} \left\langle \frac{Y_{n+1} - Y_0(T_n)}{S(T_n)} \right\rangle^{s(T_n)} = 0 \\ h_{n+1} = H(T_n) : \underline{Z}_{n+1} - \|\underline{Z}_{n+1}\| \underline{n}_{n+1}^f = 0 \end{cases} \quad (39)$$

其中，广义应力变量的表达式可写为如下的形式：

$$\begin{aligned} \underline{\sigma}_{n+1} &= (1-d_{n+1}) \underline{\Delta} : \left(\underline{\varepsilon}_{n+1}^{e,trial} - \Delta \lambda^{vp} \frac{1}{\sqrt{1-d_{n+1}}} \frac{\underline{H} : (\underline{\sigma}_{n+1} - \underline{X}_{n+1})}{\|\underline{\sigma}_{n+1} - \underline{X}_{n+1}\|} \right) \\ &\quad - \sqrt{1-d_{n+1}} (T_n - T_0) \underline{P} - \sqrt{1-d_{n+1}} (T_n - \bar{T}_n) \bar{P} \\ R_{n+1} &= (1-d_{n+1}^\gamma) \left[\left(Q + \bar{Q} \right) \left(r_n e^{-\Delta \lambda_{vp} b \left(1 + \frac{\bar{Q}}{Q} \right)} + \left(1 - e^{-\Delta \lambda_{vp} b \left(1 + \frac{\bar{Q}}{Q} \right)} \right) \frac{Q + b \bar{Q} \tilde{r}_{n+1}}{b \sqrt{1-d_{n+1}^\gamma} (Q + \bar{Q})} \right) \right. \\ &\quad \left. - \bar{Q} \tilde{r}_{n+1} \right] \\ \underline{X}_{n+1} &= (1-d_{n+1}) \left[(C + \bar{C}) \left(\underline{\alpha}_n e^{-\Delta \lambda_{vp} a \left(1 + \frac{\bar{C}}{C} \right)} + \left[1 - e^{-\Delta \lambda_{vp} a \left(1 + \frac{\bar{C}}{C} \right)} \right] \left[\frac{C}{a(C+\bar{C})} \tilde{\eta}_f + \frac{\bar{C}}{C+\bar{C}} \underline{\alpha}_{n+1} \right] \right) \right. \\ &\quad \left. - \bar{C} \underline{\alpha}_{n+1} \right] \\ \sigma_{n+1}^{vp} &= K^{vp} \left(\frac{\Delta \lambda_{vp}}{\Delta t} \right)^{\frac{1}{m_{vp}}} \end{aligned} \quad (40)$$

采用牛顿-拉弗森方法线性化上式，得到：

$$\begin{cases} f_{vp} \\ g \\ h \end{cases}_{n+1}^i + \begin{bmatrix} \frac{\partial f_{vp}}{\partial \Delta \lambda_{vp}} & \frac{\partial f_{vp}}{\partial d_{n+1}} & \frac{\partial f_{vp}}{\partial \underline{n}_{n+1}^f} \\ \frac{\partial g}{\partial \Delta \lambda_{vp}} & \frac{\partial g}{\partial d_{n+1}} & \frac{\partial g}{\partial \underline{n}_{n+1}^f} \\ \frac{\partial h}{\partial \Delta \lambda_{vp}} & \frac{\partial h}{\partial d_{n+1}} & \frac{\partial h}{\partial \underline{n}_{n+1}^f} \end{bmatrix}_{n+1} \cdot \begin{cases} \delta \Delta \lambda_{vp} \\ \delta d \\ \delta \underline{n}_f \end{cases}_{n+1}^i = \{0\} \quad (41)$$

V. 参数敏感度分析及数值应用

V.1. 参数敏感度分析

由于上面章节所建立的微态本构模型，包含了需要通过实验数据确定的约 25 个局部材料参数和 12 个微态模量参数，为更好的理解和方便的使用所建立的微态模型，本节着重于局部损伤参数、微态参数和粘性效应参数的敏感度分析。

对微态本构模型的损伤参数、微态参数和粘性参数进行了敏感度分析，发现：

- 1). 系统的数值响应曲线对微态损伤模量 \bar{H} 和微态各向同性硬化模量 \bar{Q} 的敏感度明显高于其对应的内部特征尺度参数 I_d 和 I_r 及微态密度系数 ζ_d 和 ζ_r ；
- 2). 局部损伤参数的变化同样对数值响应的一致性产生影响：局部损伤参数 s 的变化并没有丧失数值响应曲线的一致性，仅增加或减小了最终断裂位移；损伤参数 s 、 β 和 γ_0 的变化均使得数值响应一致性丧失；
- 3). 当粘塑性模型与微态损伤耦合时，在高温或高应变速率下，微态损伤引起的正则化效应越发明显；

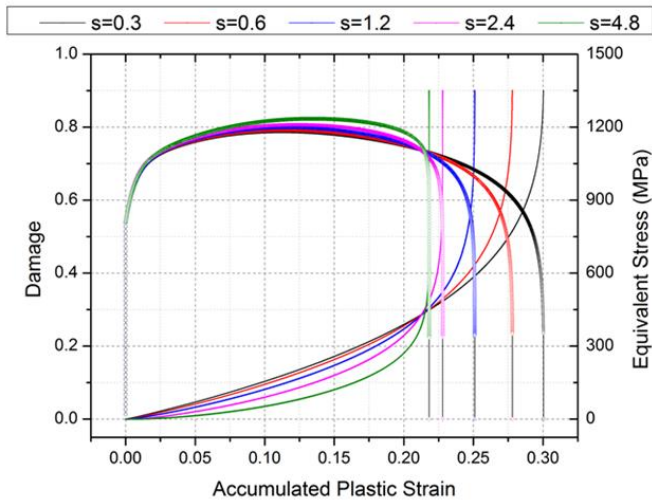


Fig. 0-4 材料参数 s 对损伤和等效应力演化的影响

V.2. 数值应用

DP1000 材料单向拉伸实验

本节针对 Yue(2014)展开的 DP1000 材料的单向拉伸实验进行模拟分析。拉伸实验样件的几何尺寸信息如图 Fig. 0-5 所示，表 Table 0-2 中列出的材料参数，是由 Yue(2014)通过单向拉伸实验和考虑包辛格效应的面内扭转试验，经逆向拟合过程所确定的。其中，考虑到局部损伤模型导致数值响应病态的依赖于网格尺寸，因此本文所采用的损伤参数 s 、 β 、 γ 、 γ_0 和 h ，是在统一网格尺寸 1.6mm 下通过逆向拟合确定的。

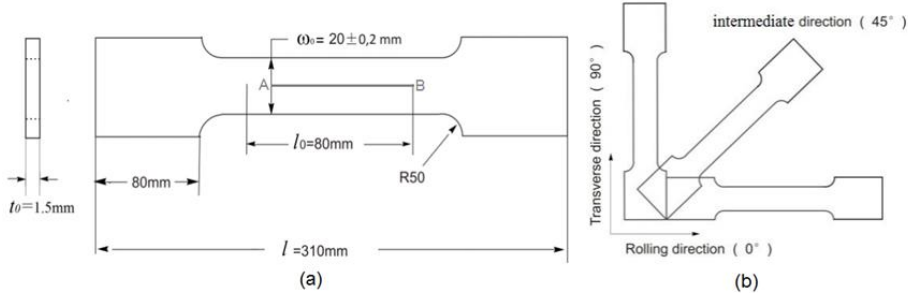


Fig. 0-5 DP1000 材料的拉伸样件几何尺寸

ρ (kg/m^3)	E (GPa)	ν	σ_y (MPa)	Q (MPa)	b	C (GPa)
7800.0	208.0	0.3	809.0	4000.0	13.0	32.0
a	F	G	H	L	M	N
150.0	0.525	0.546	0.455	1.5	1.5	1.6
S	s	β	γ	Y_0	h	
3.5	1.2	2.0	4.0	0.0	1.0	

Table 0-2 DP1000 材料的模型参数

考虑采用局部损伤模拟的分析，图 Fig. 0-6 给出了不同网格尺寸下（0.2mm、0.4mm、0.8mm 和 1.6mm）计算的单向拉伸过程的数值位移-载荷曲线。从图中可以看出，由于材料损伤参数是采用 1.6mm 网格尺寸逆向确定的，因此图中 1.6mm 网格尺寸下预测的数值响应与实验拉伸位移-载荷曲线吻合度最高，其断裂时位移约为 9.0mm；0.2mm 网格尺寸下计算的断裂时位移是最小的，约为 8.0mm；同时注意到，随着网格尺寸的减小，模拟的位移-载荷数值响应曲线下降的越早，断裂时位移越小，并且颈缩阶段的扩散区域越小，即表现出显著的网格依赖性。

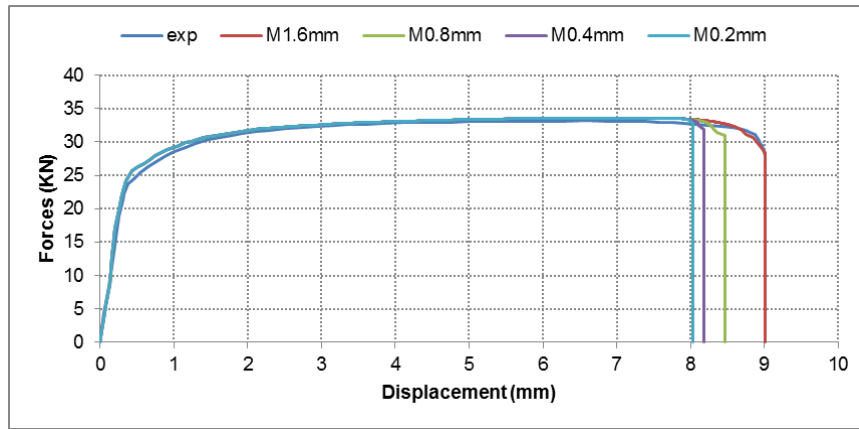


Fig. 0-6 局部损伤模型计算的单向拉伸实验的位移-载荷曲线

图 Fig. 0-7 展示了使用微态损伤及各向同性硬化模型计算的 DP1000 材料单向拉伸过程的位移-载荷曲线。其微态参数为： $S = 3.3$ 、 $\zeta_d = 1.0$ 、 $\bar{H} = 43.75 N \cdot mm^{-2}$ 、 $l_d = 1.0 mm$ 、 $\zeta_r = 1.0$ 、 $l_r = \sqrt{2} mm$ 和 $\bar{Q} = 20 KN \cdot mm^{-2}$ 。从图中可以看，与图 Fig. 0-6 的微态损伤模型呈现的应变软化区域

(约 8.0mm~9.0mm) 的不一致性相比, 引入各向同性硬化的非局部效应的模型极大的改善了应变软化区域的数值响应, 使得模拟的位移-载荷曲线均一致性的收敛于实验拉伸曲线, 不同网格尺寸的断裂时位移亦相差无几, 分别约为 9.03mm、9.07mm 和 9.10mm。注意到, 在位移约 8.8mm~9.0mm 之间的数值响应曲线存在着略微不同, 可以预见的是在引入随动硬化的非局部效应后会有进一步改善。



Fig. 0-7 微态损伤及各向同性硬化模型计算的单向拉伸实验的位移-载荷曲线

十字盒形零件冲压实验

考虑文献 Yue(2014)中的十字盒形零件的冲压实验, 冲压材料为 DP1000 对偶双相钢, 凸模冲压速度为 0.5mm/s, 模具与板料间有 0.1mm 厚的润滑油, 压边力为 400KN, 模具的几何尺寸和有限元分析的几何装配如图 Fig. 0-8 所示。本节使用 Abaqus/Explicit 求解器, 并结合本章建立的微态损伤本构模型对该零件的成形过程进行了有限元分析, 初始板料分别离散为 1.6mm、2.0mm 和 2.4mm 的有限元网格。

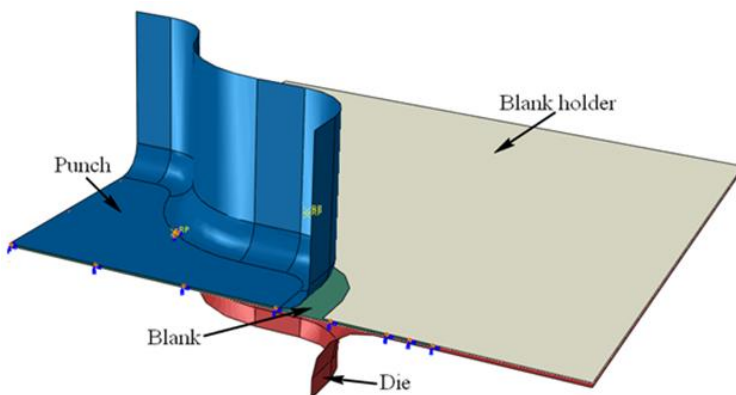


Fig. 0-8 十字盒形成形有限元分析的四分之一装配图

图 Fig. 0-9 比较了采用局部损伤模型计算的三个不同网格尺寸的冲头力-位移的响应曲线。可以观察到明显的网格依赖性, 对应 2.4mm、2.0mm 和 1.6mm 网格尺寸的初始宏观裂纹形成时的位移分别为 27.89mm、26.14mm 和 23.34mm, 即随着网格尺寸的细化, 局部损伤模型预测的数值响应曲线的下降位移越小。

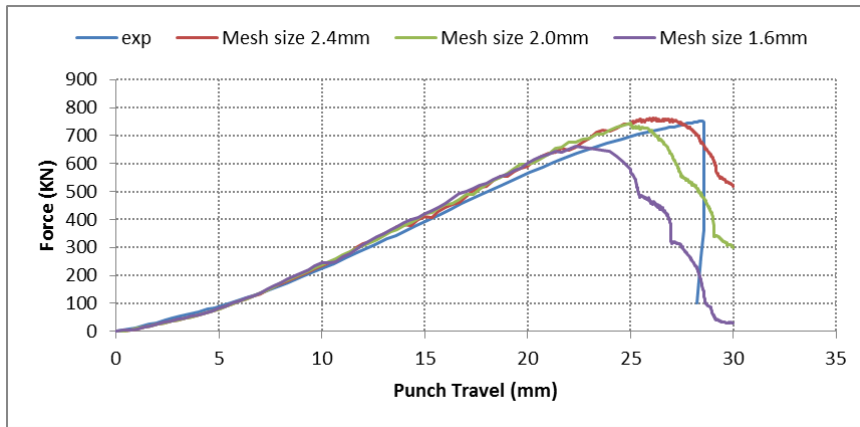


Fig. 0-9 局部损伤模型计算的十字盒形零件成形的不同网格尺寸的冲头力-位移曲线

为克服局部损伤模型描述材料应变软化现象时遇到的数值网格依赖性问题，考虑使用如下的微态参数的微态损伤本构模型： $\zeta_d = 1.0$ 、 $H = 110 N \cdot mm^{-2}$ 和 $I_d = 1.0 mm$ 模拟十字盒形零件的成形过程。Fig. 0-10 给出了微态损伤本构模型模拟的该零件成形过程的不同网格尺寸下的数值响应曲线。明显的，得到了一致性的收敛到实验曲线的冲头力-位移曲线。

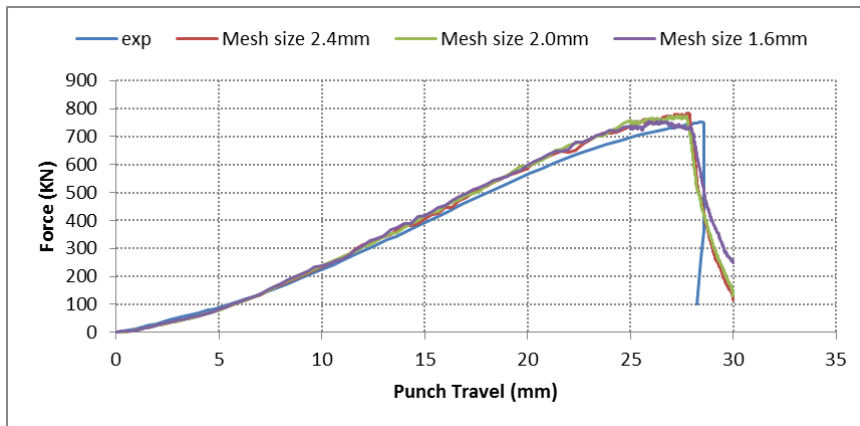


Fig. 0-10 微态损伤模型计算的十字盒形零件成形的不同网格尺寸的冲头力-位移曲线

图 Fig. 0-12 分别展示了局部和微态损伤模型预测的在 I 阶段（初始宏观裂纹形成时）的损伤分布图。可以看到，随着网格尺寸的细化，局部损伤模型给出了 3 个不同的冲头位移分别约为 26.06 mm、24.12 mm 和 21.15 mm，且初始宏观裂纹的位置各不相同：2.4mm 网格时短边和长边拐角处同时破裂、2.0mm 和 1.6mm 网格尺寸时长边拐角处破裂，均与图 Fig. 0-11 的实验样件的短边拐角处破裂不相符；而微态损伤模型预测了一致性的初始裂纹形成时的位移（约 28.35 mm），且初始裂纹形成在短边拐角处，与实验结果相符合。



Fig. 0-11 十字盒形成形实验的破裂样件

图 Fig. 0-13 所示为 II 阶段（约 28.3mm 和 29.5mm 时）局部和微态损伤模型模拟的裂纹扩展情况。注意到，微态损伤模型计算的裂纹初始形成于冲程约 28.4mm 时的零件短边拐角处，随后逐渐向两侧扩展至 29.5mm 时的裂纹形状；而局部损伤模型预测的裂纹初始位置虽然不同，见图 Fig. 0-12，但随后裂纹扩展均为自长边和短边拐角向中心和两边方向扩展。

对该十字盒形零件成形的分析表明，局部损伤模型表现出明显的网格依赖特性，及初始损伤极限的位置不一致且与实验不符；而微态损伤模型不仅提供了一致性的收敛到实验测量曲线的数值响应曲线，而且预测了与实验样件的破裂相吻合的初始损伤极限区域和一致性的最终裂纹扩展路径。

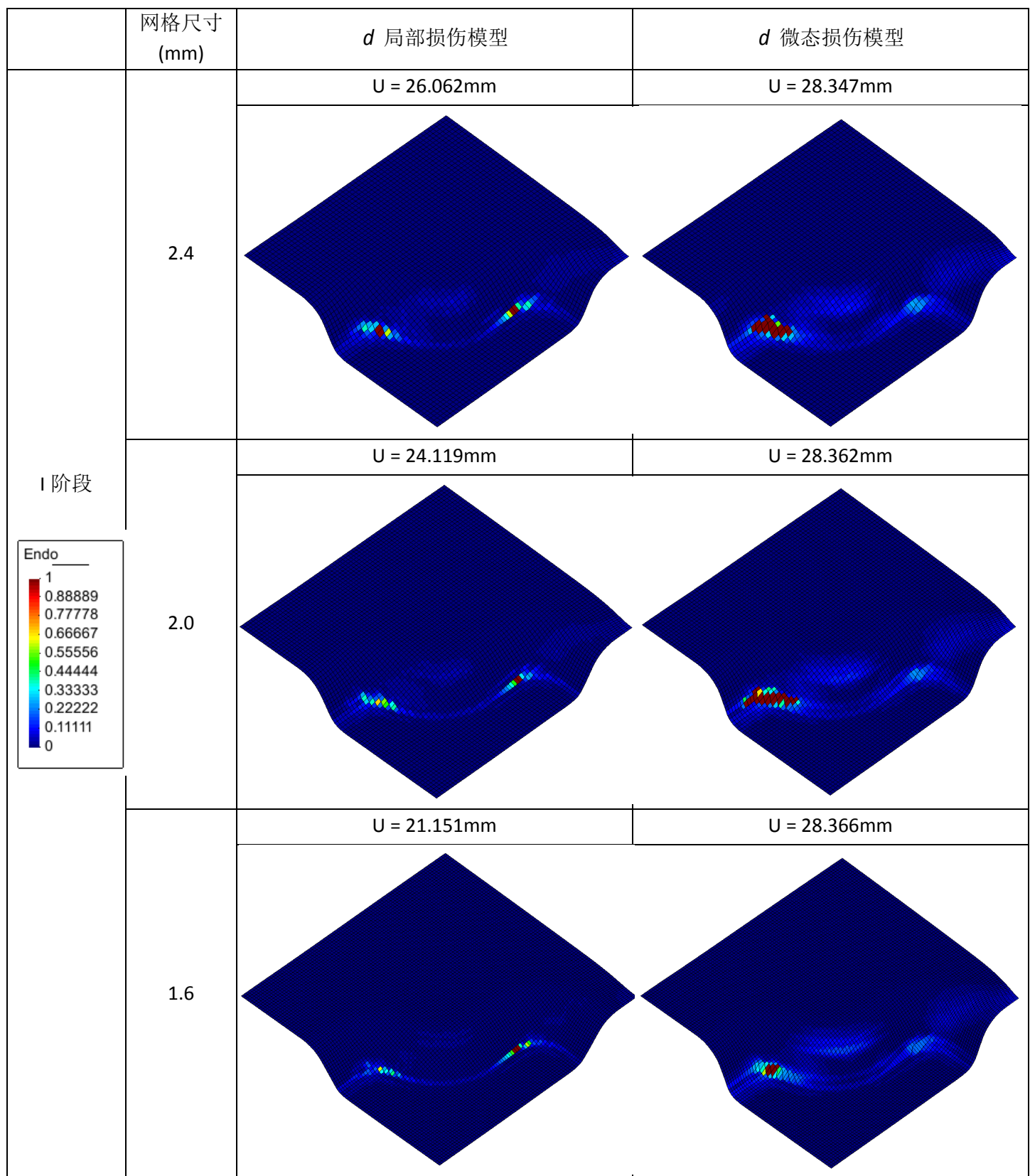


Fig. 0-12 局部和微态损伤模型预测的 I 阶段的不同网格尺寸的损伤分布

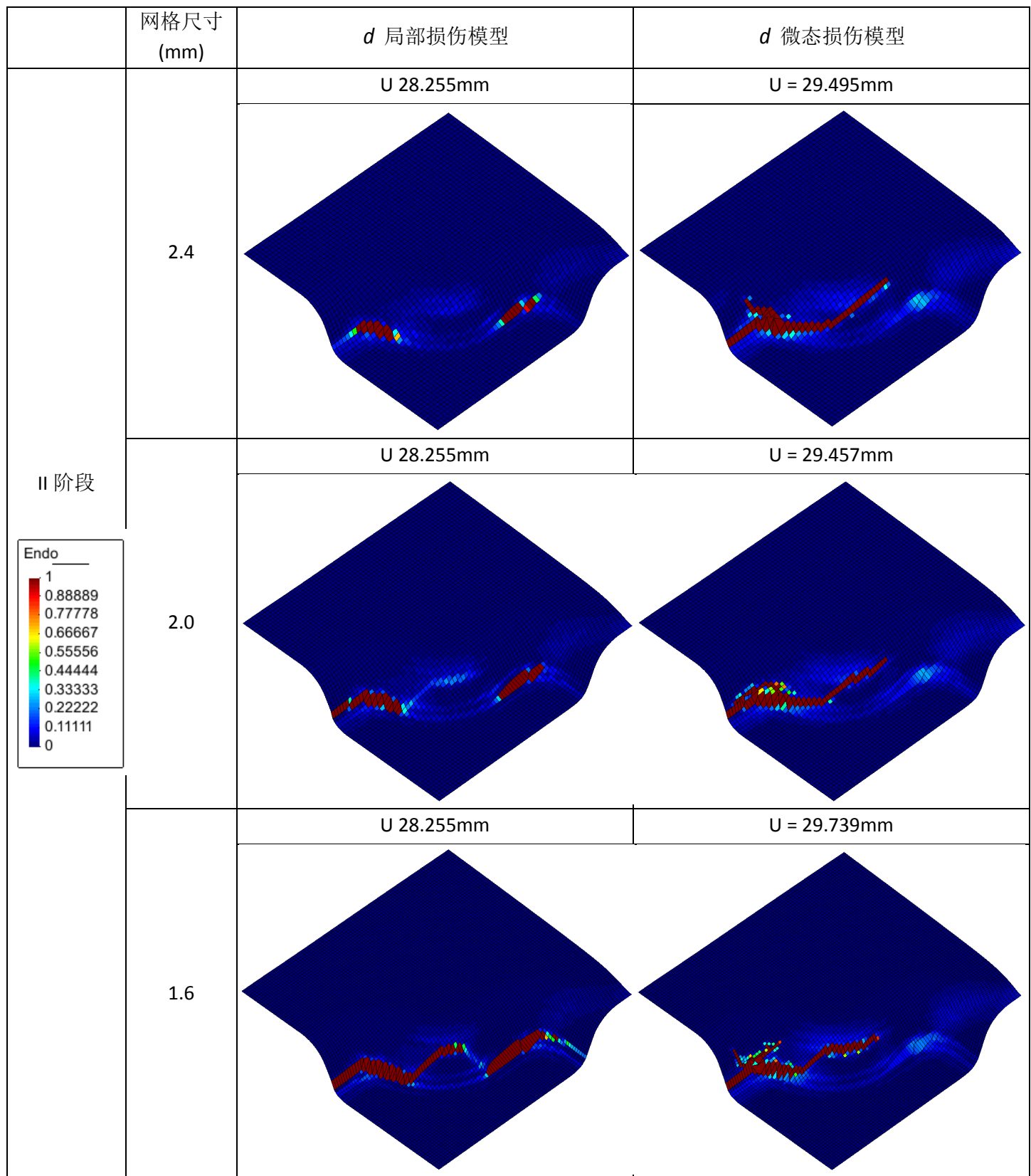


Fig. 0-13 局部和微态损伤模型预测的 II 阶段的不同网格尺寸的损伤分布

VI. 结论与展望

本文，基于广义连续介质力学，建立了热力学一致性的微态弹粘塑性损伤本构模型，以表征材料微结构的非局部效应和克服局部损伤模型的病态网格依赖性，通过数值实现了微态损伤和各向同性硬化模型，并应用到金属成形仿真分析中。

首先，本文在一步法的基础上通过引入若干表征板料变形历史的中间构型，建立了分析高效的静力隐式多步成形有限元模拟方法，以提高对金属成形零件的应力评估精度：

- 1). 提出了将构造一般三维滑移约束曲面问题转化为求解二次规划问题的拟最小面积法，建立了保面积坐标的物质点映射法以生成中间构型的初始解，通过施加罚函数约束使得平衡迭代过程中物质点保持在滑移面上移动，解决了多步法构造中间构型所面临的效率问题；建立了更新的拉格朗日式的有限对数应变增量度量；
- 2). 通过对 S 梁、B 柱和盒支座成形零件的数值分析表明：拟最小面积法可在多项式时间内高效地构造滑移约束曲面，通过物质点映射方法和平衡迭代过程构造的中间构型与增量法的构型相吻合，该多步成形有限元方法可显著改善最终零件的应力估计精度。

其次，在不可逆热力学框架下，推导建立了耦合各向同性韧性损伤、混合硬化和温度场，及微态变量（微态损伤、微态各向同性硬化、微态随动硬化和微态温度）的弹粘塑性本构模型，以表征由材料微缺陷、损伤或温度等引起的应变软化现象的非局部效应，并在 Abaqus 用户子函数中实现了该本构模型：

- 1). 在不可逆热力学框架下，建立了一组完整的微态本构模型。
 - i). 引入了新的微态变量以表征材料应变软化中的非局部效应，使用广义虚功原理和扩展的自由能得到了除传统位移控制方程外的，包含材料内部特征尺度的微态变量的补充平衡方程，在不可逆热力学框架下得到了与微态变量共轭的广义应力的状态方程，通过屈服函数、耗散势能以及非关联流动法则建立了描述耗散现象的内变量的演化方程，并得到了一致性的塑性乘子和切线刚度矩阵；
 - ii). 通过标准有限元方法，得到了位移和微态变量为自由度的弱形式的初始和边界值问题，经有限元的时间和空间离散，在 Abaqus 用户子程序 Vuel 中，开发了新的包含位移、微态损伤和微态各向同性硬化自由度的四边形平面和壳单元和实现了提出的微态模型的隐式本构积分过程；
 - iii). 对本构模型的损伤参数、微态参数和粘性参数进行了敏感度分析，并发现：局部损伤参数 s 控制着本构模型的韧性和脆性响应， γ 参数主导着各向同性硬化对损伤耗散释放率的贡献，系统的数值响应曲线对微态损伤模量 \bar{H} 和微态各向同性硬化模量 \bar{Q} 的敏感度高于其对应的内部特征尺度参数 I_d 和 I_r 及微态密度系数 ζ_d 和 ζ_r ；
 - iv). 应用微态损伤&各向同性硬化模型到对偶双相钢 DP1000 材料的单向拉伸实验中，得到了收敛到实验曲线的网格无关性的数值模拟响应；使用考虑损伤单边效应的微态损伤模型对十字盒形零件的成形实验的分析，得到了一致性的数值模拟响应曲线、初始损伤极限产生区域和最终裂纹扩展路径。
- 2). 引入微态温度及其一阶梯度到扩展的亥姆霍兹自由能函数中，得到了一组耦合的热力学一致性的广义的热传导方程：

- i). 引入了新的微态温度变量，得到了一组热力学一致性的包含内部特征尺度的广义热传导方程，通过施加内部温度约束和选取合适的自由能，其可退化为文献中若干对传统傅里叶热传导方程的扩展研究模型；
- ii). 对广义微态热传导方程的线性化分析发现，该方程引入了温度变化率的梯度的散度（拉普拉斯算子）项，引入了温度对时间二阶导数项，使得传统抛物线形的热传导方程变为了双曲线形，同时引入了温度对时间的三阶导数项；
- iii). 该广义微态热传导方程区别于已建立的在微态介质中引入微温度向量的热传导方程，通过该广义微态方程与双温度模型的等效热传导方程的分析可以发现：
 - a). Cattaneo II 模型的带热松弛时间的双曲线形热传导方程，可以视为建立的广义微态热传导方程在忽略了温度的非局部效应时的特殊情况；
 - b). 经典的、双曲线形的和广义的双温度模型的热传导方程可分别从该微态热传导方程中演绎得到；
 - c). 基于 Green 理论的微温度热传导方程与该微态方程均得到一组耦合的局部和微（态）温度的控制方程，并在约束条件下可退化为经典的波动方程；
- iv). 该热力学一致性的广义微态热传导方程，可方便地与材料的力学模型想耦合，并可以潜在地应用于金属高温高速成形、超短激光脉冲加热及纳米级介质或纳米结构中的传热分析，也可作为采用修正的热流矢量以考虑非局部热传导过程的一种选择。

由于时间所限，本论文工作并不完善，可进一步展开如下的研究工作：

- 1). 一般来讲，需要考虑控制材料应变软化行为的所有状态变量的非局部效应，本文仅实现了微态损伤和各向同性的本构模型，可进一步扩展引入随动硬化和塑性应变的非局部效应，以完善描述材料的应变软化行为
- 2). 由于本文仅对 DP1000 材料的单向拉伸实验进行了验证，尚需对复杂加载情况下的，如剪切、弯曲和多向加载等实验进行验证，并优化修正本文确定的材料参数组合
- 3). 一般来说，韧性损伤表现为强烈的各向异性，因此可进一步扩展为包含各向异性损伤张量 (d, Y) 的本构模型，以描述材料沿不同方向的损伤演化规律，参照在 LASMIS 已完成的工作 (Badreddine, 2006; Saanouni, 2013)。
- 4). 由于时间所限，本文尚未将提出的广义微态热传导方程应用到具体的热冲压成形实验分析中，后续可在已有工作(Saanouni and Hamed (2013))基础上扩展至有限变形率相关塑性材料中，并可潜在的应用于温度非局部效应明显的超短脉冲激光金属加热、激光金属表面处理以及纳米级半导体结构等的传热过程分析中。

References

- Abdul-Latif, A., Saanouni, K., 1994. Damaged anelastic behavior of FCC polycrystalline metals with micromechanical approach. *International Journal of Damage Mechanics* 3, 237-259.
- Abed-Meraim, F., Combescure, A., 2002. SHB8PS—a new adaptative, assumed-strain continuum mechanics shell element for impact analysis. *Computers & Structures* 80, 791-803.
- ABED-MERAIM, F., Combescure, A., 2007. A physically stabilized and locking-free formulation of the (SHB8PS) solid-shell element. *Revue Européenne de Mécanique Numérique/European Journal of Computational Mechanics* 16, 1037-1072.
- Abed-Meraim, F., Combescure, A., 2009. An improved assumed strain solid–shell element formulation with physical stabilization for geometric non-linear applications and elastic–plastic stability analysis. *International Journal for Numerical Methods in Engineering* 80, 1640-1686.
- Abed-Meraim, F., Trinh, V.-D., Combescure, A., 2013. New quadratic solid–shell elements and their evaluation on linear benchmark problems. *Computing* 95, 373-394.
- Abiri, O., Lindgren, L.-E., 2015. Non-local damage models in manufacturing simulations. *European Journal of Mechanics - A/Solids* 49, 548-560.
- Abu Al-Rub, R.K., Voyatzis, G.Z., 2006. A physically based gradient plasticity theory. *International Journal of Plasticity* 22, 654-684.
- Abu Al-Rub, R.K., Voyatzis, G.Z., Bammann, D.J., 2007. A thermodynamic based higher-order gradient theory for size dependent plasticity. *International Journal of Solids and Structures* 44, 2888-2923.
- Aifantis, E.C., 1980a. Further comments on the problem of heat extraction from hot dry rocks. *Mechanics Research Communications* 7, 219-226.
- Aifantis, E.C., 1980b. On the problem of diffusion in solids. *Acta Mechanica* 37, 265-296.
- Aifantis, E.C., 1984. On the Microstructural Origin of Certain Inelastic Models. *Journal of Engineering Materials and Technology* 106, 326-330.
- Aifantis, E.C., 1987. The physics of plastic deformation. *International Journal of Plasticity* 3, 211-247.
- Aifantis, E.C., 1992. On the role of gradients in the localization of deformation and fracture. *International Journal of Engineering Science* 30, 1279-1299.
- Aifantis, E.C., Serrin, J.B., 1983a. Equilibrium solutions in the mechanical theory of fluid microstructures. *Journal of Colloid and Interface Science* 96, 530-547.
- Aifantis, E.C., Serrin, J.B., 1983b. The mechanical theory of fluid interfaces and Maxwell's rule. *Journal of Colloid and Interface Science* 96, 517-529.
- Alam, S.Y., Kotronis, P., Loukili, A., 2013. Crack propagation and size effect in concrete using a non-local damage model. *Engineering Fracture Mechanics* 109, 246-261.
- Alvarez, F.X., Jou, D., 2007. Memory and nonlocal effects in heat transport: From diffusive to ballistic regimes. *Applied Physics Letters* 90, 083109.
- Andrade, F.X.C., CÉSAR DE SÁ, J.M.A., Andrade Pires, F.M., 2011. A Ductile Damage Nonlocal Model of Integral-type at Finite Strains: Formulation and Numerical Issues. *International Journal of Damage Mechanics*.
- Aravas, N., 1986. The analysis of void growth that leads to central bursts during extrusion. *Journal of the Mechanics and Physics of Solids* 34, 55-79.

REFERENCES

- Ari, N., Eringen, A.C., 1983. Nonlocal Stress Field at Griffith Crack. *Crystal Lattice Defects and Amorphous Materials* 10, 33-38.
- Aslan, O., Cordero, N.M., Gaubert, A., Forest, S., 2011. Micromorphic approach to single crystal plasticity and damage. *International Journal of Engineering Science* 49, 1311-1325.
- Badreddine, H., 2006. Elastoplastique anisotrope endommageable en transformations finies: Aspects théoriques, numériques et applications, ICD/LASMIS. Université de Technologie de Troyes.
- Badreddine, H., Labergère, C., Saanouni, K., 2016. Ductile damage prediction in sheet and bulk metal forming. *Comptes Rendus Mécanique* 344, 296-318.
- Badreddine, H., Saanouni, K., Dogui, A., 2010. On non-associative anisotropic finite plasticity fully coupled with isotropic ductile damage for metal forming. *International Journal of Plasticity* 26, 1541-1575.
- Badreddine, H., Saanouni, K., Nguyen, T.D., 2015. Damage anisotropy and its effect on the plastic anisotropy evolution under finite strains. *International Journal of Solids and Structures* 63, 11-31.
- Bai, C., Lavine, A.S., 1995. On Hyperbolic Heat Conduction and the Second Law of Thermodynamics. *Journal of Heat Transfer* 117, 256-263.
- Balieu, R., Lauro, F., Bennani, B., Matsumoto, T., Mottola, E., 2014. Non-associated viscoplasticity coupled with an integral-type nonlocal damage model for mineral filled semi-crystalline polymers. *Computers & Structures* 134, 18-31.
- Barenblatt, G.I., 1962. The mathematical theory of equilibrium cracks in brittle fracture. *Advances in applied mechanics* 7, 55-129.
- Barletta, A., Zanchini, E., 1997. Hyperbolic heat conduction and local equilibrium: a second law analysis. *International Journal of Heat and Mass Transfer* 40, 1007-1016.
- Bassa, B., 2011. Contribution à l'étude d'éléments finis de type coque sans degrés de liberté en rotation ou à formulation solide pour des simulations numériques de l'emboutissage et du retour élastique, Mécanique, Energétique, Génie Civil, Acoustique. L'institut national des sciences appliquées de Lyon.
- Batoz, J.L., Guo, Y.Q., Mercier, F., 1998. The inverse approach with simple triangular shell elements for large strain predictions of sheet metal forming parts. *Engineering Computations* 15, 864-892.
- Bažant, Z.k.P., Jirásek, M., 2002. Nonlocal Integral Formulations of Plasticity and Damage: Survey of Progress. *Journal of Engineering Mechanics* 128, 1199-1149.
- Bažant, Z.k.P., Pijaudier-Cabot, G., 1988. Nonlocal Continuum Damage, Localization Instability and Convergence. *Journal of Applied Mechanics* 55, 287-293.
- Bažant, Z.P., 1976. Instability, ductility, and size effect in strain-softening concrete. *Journal of the Engineering Mechanics Division* 102, 331-344.
- Bažant, Z.P., 1984. Imbricate Continuum and its Variational Derivation. *Journal of Engineering Mechanics* 110, 1693-1712.
- Bažant, Z.P., Belytschko, T.B., Chang, T.P., 1984. Continuum Theory for Strain - Softening. *Journal of Engineering Mechanics* 110, 1666-1692.
- Bažant, Z.P., Cedolin, L., 1983. Finite Element Modeling of Crack Band Propagation. *Journal of Structural Engineering* 109, 69-92.
- Bažant, Z.P., Oh, B.H., 1983. Crack band theory for fracture of concrete. *Matériaux et Construction* 16, 155-177.
- Beloune, J.P., Garnham, B., Bache, M., Korsunsky, A.M., 2010. The use of coupled nonlocal damage-plasticity to predict crack growth in ductile metal plates. *Engineering Fracture Mechanics* 77, 1721-1729.

REFERENCES

- Belnoue, J.P., Nguyen, G.D., Korsunsky, A.M., 2007. A One-Dimensional Nonlocal Damage-Plasticity Model for Ductile Materials. *International Journal of Fracture* 144, 53-60.
- Belytschko, T., Bažant, Z.P., Yul-Woong, H., Ta-Peng, C., 1986. Strain-softening materials and finite-element solutions. *Computers & Structures* 23, 163-180.
- Belytschko, T., Bindeman, L.P., 1993. Assumed strain stabilization of the eight node hexahedral element. *Computer Methods in Applied Mechanics and Engineering* 105, 225-260.
- Belytschko, T., Black, T., 1999. Elastic crack growth in finite elements with minimal remeshing. *International journal for numerical methods in engineering* 45, 601-620.
- Belytschko, T., Lu, Y.Y., Gu, L., 1994. Element - free Galerkin methods. *International journal for numerical methods in engineering* 37, 229-256.
- Bennani, B., Oudin, J., 1995. Backward can extrusion of steels: Effects of punch design on flow mode and void volume fraction. *International Journal of Machine Tools and Manufacture* 35, 903-911.
- Bennett, T., Rodríguez-Ferran, A., Askes, H., 2012. Damage regularisation with inertia gradients. *European Journal of Mechanics - A/Solids* 31, 131-138.
- Beran, M.J., McCoy, J.J., 1970. Mean field variations in a statistical sample of heterogeneous linearly elastic solids. *International Journal of Solids and Structures* 6, 1035-1054.
- Besson, J., Cailletaud, G., Chaboche, J.-L., Forest, S., 2001. Mécanique non linéaire des matériaux. Hermès Science Publ.
- Bezzina, S., Saanouni, K., 1996. Theoretical and numerical modeling of sheet metal shear cutting. *Mat-Tech* 96, 15-24.
- Bontcheva, N., Iankov, R., 1991. Numerical investigation of the damage process in metal forming. *Engineering Fracture Mechanics* 40, 387-393.
- Both, S., Czél, B., Fülöp, T., Gróf, G., Gyenis, Á., Kovács, R., Ván, P., Verhás, J., 2016. Deviation from the Fourier law in room-temperature heat pulse experiments. *Journal of Non-Equilibrium Thermodynamics* 41, 41-48.
- Boudeau, N., Gelin, J.C., 1994. Prediction of the localized necking in 3D sheet metal forming processes from FE simulations. *Journal of Materials Processing Technology* 45, 229-235.
- Boudifa, M., Saanouni, K., Chaboche, J.-L., 2009. A micromechanical model for inelastic ductile damage prediction in polycrystalline metals for metal forming. *International journal of mechanical sciences* 51, 453-464.
- Brunet, M., Sabourin, F., Mguil-Touchal, S., 1996. The Prediction of Necking and Failure in 3 D. Sheet Forming Analysis Using Damage Variable. *Journal de Physique IV Colloque* 06, C6-473-C476-482.
- Bubnov, V.A., 1976. Wave concepts in the theory of heat. *International Journal of Heat and Mass Transfer* 19, 175-184.
- Cahill, D.G., Braun, P.V., Chen, G., Clarke, D.R., Fan, S., Goodson, K.E., Keblinski, P., King, W.P., Mahan, G.D., Majumdar, A., Maris, H.J., Phillpot, S.R., Pop, E., Shi, L., 2014. Nanoscale thermal transport. II. 2003–2012. *Applied Physics Reviews* 1, 011305.
- Cahill, D.G., Ford, W.K., Goodson, K.E., Mahan, G.D., Majumdar, A., Maris, H.J., Merlin, R., Phillpot, S.R., 2003. Nanoscale thermal transport. *Journal of Applied Physics* 93, 793-818.
- Cahn, J.W., Hilliard, J.E., 1958. Free Energy of a Nonuniform System. I. Interfacial Free Energy. *The Journal of Chemical Physics* 28, 258-267.
- Cattaneo, C., 1948. Sulla conduzione del calore, in: Pignedoli, A. (Ed.), *Some Aspects of Diffusion Theory*. Springer-Verlag Berlin Heidelberg.

REFERENCES

- Cattaneo, C., 1958. Sur une forme de l'équation de la chaleur éliminant le paradoxe d'une propagation instantanée. Comptes Rendus Hebdomadaires Des Séances De L'Academie Des Sciences 247, 431-433.
- Chaboche, J., Boudifa, M., Saanouni, K., 2006. A CDM approach of ductile damage with plastic compressibility. International Journal of Fracture 137, 51-75.
- Chaboche, J.L., 1988a. Continuum Damage Mechanics: Part I—General Concepts. Journal of Applied Mechanics 55, 59-64.
- Chaboche, J.L., 1988b. Continuum Damage Mechanics: Part II—Damage Growth, Crack Initiation, and Crack Growth. Journal of Applied Mechanics 55, 65-72.
- Chen, G., 2001. Ballistic-Diffusive Heat-Conduction Equations. Physical Review Letters 86, 2297-2300.
- Chung, K., Richmond, O., 1993. A deformation theory of plasticity based on minimum work paths. International Journal of Plasticity 9, 907-920.
- Coleman, B.D., Fabrizio, M., Owen, D.R., 1982. On the thermodynamics of second sound in dielectric crystals. Arch. Rational Mech. Anal. 80, 135-158.
- Coleman, B.D., Fabrizio, M., Owen, D.R., 1985. Thermodynamics and the constitutive relations for second sound in crystals, in: Grioli, G. (Ed.), Thermodynamics and constitutive equations. Springer-Verlag Berlin Heidelberg, pp. 20-43.
- Cordero, N.M., Forest, S., Busso, E.P., 2013. Micromorphic modelling of grain size effects in metal polycrystals. GAMM-Mitteilungen 36, 186-202.
- Cosserat, E., Cosserat, F., 1896. Sur la Théorie de l'élasticité. Annales de la Faculté des Sciences de Toulouse, I.1–I.116.
- Cosserat, E., Cosserat, F., 1909. Notes sur la théorie des corps déformables. Traité de Physique t.2, 953–1173.
- Cosserat, E., Cosserat, F., 2009. Théorie des corps déformables (Librairie Scientifique A. Hermann et fils, Paris, 1909). Reprinted by Cornell University Library. English translation by DH Delphenich.
- Da Yu, T., 1989. Shock wave formation around a moving heat source in a solid with finite speed of heat propagation. International Journal of Heat and Mass Transfer 32, 1979-1987.
- De Borst, R., Mühlhaus, H.-B., 1992. Gradient-dependent plasticity: Formulation and algorithmic aspects. International Journal for Numerical Methods in Engineering 35, 521-539.
- De Borst, R., Pamin, J., 1996. Some novel developments in finite element procedures for gradient-dependent plasticity. International Journal for Numerical Methods in Engineering 39, 2477-2505.
- De Borst, R., Pamin, J., Geers, M.G.D., 1999. On coupled gradient-dependent plasticity and damage theories with a view to localization analysis. European Journal of Mechanics - A/Solids 18, 939-962.
- De Borst, R., Remmers, J.J.C., Needleman, A., Abellán, M.-A., 2004. Discrete vs smeared crack models for concrete fracture: bridging the gap. International Journal for Numerical and Analytical Methods in Geomechanics 28, 583-607.
- De Borst, R., SLUYS, L.J., MUHLHAUS, H.B., PAMIN, J., 1993. FUNDAMENTAL ISSUES IN FINITE ELEMENT ANALYSES OF LOCALIZATION OF DEFORMATION. Engineering Computations 10, 99-121.
- Diamantopoulou, E., Liu, W., Labergere, C., Badreddine, H., Saanouni, K., Hu, P., 2017. Micromorphic constitutive equations with damage applied to metal forming. International Journal of Damage Mechanics 0, 1056789516684650.
- Dillard, T., Forest, S., Lenny, P., 2006. Micromorphic continuum modelling of the deformation and fracture behaviour of nickel foams. European Journal of Mechanics - A/Solids 25, 526-549.
- Dolbow, J., Belytschko, T., 1999. A finite element method for crack growth without remeshing. International journal for numerical methods in engineering 46, 131-150.

REFERENCES

- Dubé, J.-F., Pijaudier-Cabot, G., Borderie, C.L., 1996. Rate Dependent Damage Model for Concrete in Dynamics. *Journal of Engineering Mechanics* 122, 939-947.
- Dugdale, D.S., 1960. Yielding of steel sheets containing slits. *Journal of the Mechanics and Physics of Solids* 8, 100-104.
- Engelen, R.A.B., Geers, M.G.D., Baaijens, F.P.T., 2003. Nonlocal implicit gradient-enhanced elasto-plasticity for the modelling of softening behaviour. *International Journal of Plasticity* 19, 403-433.
- Eringen, A.C., 1966a. Linear theory of micropolar elasticity. *Journal of Mathematics and Mechanics* 15, 909-923.
- Eringen, A.C., 1966b. Mechanics of micromorphic materials, in: Görtler, H. (Ed.), *Applied Mechanics: Proceedings of the Eleventh International Congress of Applied Mechanics Munich (Germany) 1964*. Springer Berlin Heidelberg, Berlin, Heidelberg, pp. 131-138.
- Eringen, A.C., 1966c. Theory of micropolar fluids. *Journal of Mathematics and Mechanics* 16, 1-18.
- Eringen, A.C., 1966d. A unified theory of thermomechanical materials. *International Journal of Engineering Science* 4, 179-202.
- Eringen, A.C., 1970. Balance laws of micromorphic mechanics. *International Journal of Engineering Science* 8, 819-828.
- Eringen, A.C., 1972. Nonlocal polar elastic continua. *International Journal of Engineering Science* 10, 1-16.
- Eringen, A.C., 1992. Balance laws of micromorphic continua revisited. *International Journal of Engineering Science* 30, 805-810.
- Eringen, A.C., 1999. *Microcontinuum field theories: I. Foundations and Solids*. Springer Verlag, New York.
- Eringen, A.C., 2002. *Nonlocal continuum field theories*. Springer Science & Business Media.
- Eringen, A.C., Edelen, D.G.B., 1972. On nonlocal elasticity. *International Journal of Engineering Science* 10, 233-248.
- Eringen, A.C., Suhubi, E.S., 1964. Nonlinear theory of simple micro-elastic solids—I. *International Journal of Engineering Science* 2, 189-203.
- Fish, J., Belytschko, T., 1988. Elements with embedded localization zones for large deformation problems. *Computers & Structures* 30, 247-256.
- Flanagan, D.P., Belytschko, T., 1981. A uniform strain hexahedron and quadrilateral with orthogonal hourglass control. *International Journal for Numerical Methods in Engineering* 17, 679-706.
- Forest, S., 2006. *Milieux continus généralisés et matériaux hétérogènes*. Presses des MINES.
- Forest, S., 2009. Micromorphic Approach for Gradient Elasticity, Viscoplasticity, and Damage. *Journal of Engineering Mechanics* 135, 117-131.
- Forest, S., 2016. Nonlinear regularization operators as derived from the micromorphic approach to gradient elasticity, viscoplasticity and damage. *Proceedings of the Royal Society of London A: Mathematical, Physical and Engineering Sciences* 472.
- Forest, S., Aifantis, E.C., 2010. Some links between recent gradient thermo-elasto-plasticity theories and the thermomechanics of generalized continua. *International Journal of Solids and Structures* 47, 3367-3376.
- Forest, S., Amestoy, M., 2008. Hypertemperature in thermoelastic solids. *Comptes Rendus Mécanique* 336, 347-353.
- Forest, S., Ammar, K., Appolaire, B., Cordero, N., Gaubert, A., 2014. Micromorphic approach to crystal plasticity and phase transformation, in: Schröder, J., Hackl, K. (Eds.), *Plasticity and Beyond*. Springer Vienna, pp. 131-198.

REFERENCES

- Forest, S., Cardona, J.-M., Sievert, R., 2000. Thermoelasticity of second-grade media, in: Maugin, G.A., Drouot, R., Sidoroff, F. (Eds.), *Continuum Thermomechanics*. Springer Netherlands, pp. 163-176.
- Forest, S., Sievert, R., 2003. Elastoviscoplastic constitutive frameworks for generalized continua. *Acta Mechanica* 160, 71-111.
- Forest, S., Sievert, R., 2006. Nonlinear microstrain theories. *International Journal of Solids and Structures* 43, 7224-7245.
- Forest, S., Sievert, R., Aifantis, E.C., 2002. Strain gradient crystal plasticity: Thermomechanical formulations and applications. *Journal of the mechanical behavior of materials* 13, 219-232.
- Fourier, J., 1822. *Theorie analytique de la chaleur*, par M. Fourier. Chez Firmin Didot, père et fils.
- Fourier, J., 1878. *The Analytical Theory of Heat*. Translated, with notes, by Alexander Freeman. Cambridge: University Press.
- Franciosi, P., Berveiller, M., Zaoui, A., 1980. Latent hardening in copper and aluminium single crystals. *Acta Metallurgica* 28, 273-283.
- Frémond, M., Nedjar, B., 1995. Damage in concrete: the unilateral phenomenon. *Nuclear Engineering and Design* 156, 323-335.
- Frémond, M., Nedjar, B., 1996. Damage, gradient of damage and principle of virtual power. *International Journal of Solids and Structures* 33, 1083-1103.
- Gelin, J.C., Moisan, A., 1990. Finite Element Analysis of Ductile Fracture and Defects Formation in Cold and Hot Forging. *CIRP Annals - Manufacturing Technology* 39, 215-218.
- Gelin, J.C., Oudin, J., Ravalard, Y., Moisan, A., 1985. An Improved Finite Element Method for the Analysis of Damage and Ductile Fracture in Cold Forming Processes. *CIRP Annals - Manufacturing Technology* 34, 209-213.
- Germain, P., 1973. The Method of Virtual Power in Continuum Mechanics. Part 2: Microstructure. *SIAM Journal on Applied Mathematics* 25, 556-575.
- Germain, P., Nguyen, Q.S., Suquet, P., 1983. Continuum Thermodynamics. *Journal of Applied Mechanics* 50, 1010-1020.
- Grassl, P., Jirásek, M., 2006. Plastic model with non-local damage applied to concrete. *International Journal for Numerical and Analytical Methods in Geomechanics* 30, 71-90.
- Green, A.E., Naghdi, P.M., 1977. On Thermodynamics and the Nature of the Second Law. *Proceedings of the Royal Society of London. Series A, Mathematical and Physical Sciences* 357, 253-270.
- Green, A.E., Naghdi, P.M., 1991. A Re-Examination of the Basic Postulates of Thermomechanics. *Proceedings of the Royal Society of London. Series A: Mathematical and Physical Sciences* 432, 171-194.
- Green, A.E., Naghdi, P.M., 1993. Thermoelasticity without energy dissipation. *Journal of Elasticity* 31, 189-208.
- Grot, R.A., 1969. Thermodynamics of a continuum with microstructure. *International Journal of Engineering Science* 7, 801-814.
- Guo, Y., Batoz, J., Detraux, J., Duroux, P., 1990. Finite element procedures for strain estimations of sheet metal forming parts. *International journal for numerical methods in engineering* 30, 1385-1401.
- Guo, Y., Gati, W., Naceur, H., Batoz, J., 2002. An efficient DKT rotation free shell element for springback simulation in sheet metal forming. *Computers & Structures* 80, 2299-2312.
- Guo, Y., Li, Y., Bogard, F., Debray, K., 2004. An efficient pseudo-inverse approach for damage modeling in the sheet forming process. *Journal of Materials Processing Technology* 151, 88-97.

REFERENCES

- Guo, Y., Naceur, H., Debray, K., Bogard, F., 2003. Initial solution estimation to speed up inverse approach in stamping modeling. *Engineering Computations* 20, 810-834.
- Guo, Y., Wang, M., 2015. Phonon hydrodynamics and its applications in nanoscale heat transport. *Physics Reports* 595, 1-44.
- Guo, Y.Q., Batoz, J.L., Naceur, H., Bouabdallah, S., Mercier, F., Barlet, O., 2000. Recent developments on the analysis and optimum design of sheet metal forming parts using a simplified inverse approach. *Computers & Structures* 78, 133-148.
- Gurson, A.L., 1977. Continuum Theory of Ductile Rupture by Void Nucleation and Growth: Part I—Yield Criteria and Flow Rules for Porous Ductile Media. *Journal of Engineering Materials and Technology* 99, 2-15.
- Gurtin, M.E., 1996. Generalized Ginzburg-Landau and Cahn-Hilliard equations based on a microforce balance. *Physica D: Nonlinear Phenomena* 92, 178-192.
- Guyer, R.A., Krumhansl, J.A., 1966. Solution of the Linearized Phonon Boltzmann Equation. *Physical Review* 148, 766-778.
- Hallquist, J.O., 1983. Theoretical manual for DYNA3D. ; Lawrence Livermore National Lab., CA (USA), p. Medium: X; Size: Pages: 81.
- Halouani, A., Li, Y., Abbès, B., Guo, Y.-Q., 2012. Simulation of axi-symmetrical cold forging process by efficient pseudo inverse approach and direct algorithm of plasticity. *Finite Elements in Analysis and Design* 61, 85-96.
- Hamed, M., 2012. Formulations micromorphiques en élastoplasticité non-locale avec endommagement en transformations finies. University of Technology of Troyes, p. 1 vol. (197 p.).
- Havlásek, P., Grassl, P., Jirásek, M., 2016. Analysis of size effect on strength of quasi-brittle materials using integral-type nonlocal models. *Engineering Fracture Mechanics* 157, 72-85.
- He, W., Wu, Y.-F., Xu, Y., Fu, T.-T., 2015. A thermodynamically consistent nonlocal damage model for concrete materials with unilateral effects. *Computer Methods in Applied Mechanics and Engineering* 297, 371-391.
- Hill, R., 1962. Acceleration waves in solids. *Journal of the Mechanics and Physics of Solids* 10, 1-16.
- Hillerborg, A., Modéer, M., Petersson, P.-E., 1976. Analysis of crack formation and crack growth in concrete by means of fracture mechanics and finite elements. *Cement and concrete research* 6, 773-781.
- Hirschberger, C.B., 2009. Classification of concepts in thermodynamically consistent generalized plasticity. *Journal of Engineering Mechanics* 135, 156.
- Holba, P., Šesták, J., 2015. Heat inertia and its role in thermal analysis. *J Therm Anal Calorim* 121, 303-307.
- Huang, Y., Chen, Y.-P., Du, R.-X., 2006. A new approach to solve key issues in multi-step inverse finite-element method in sheet metal stamping. *International Journal of Mechanical Sciences* 48, 591-600.
- Hutchinson, J., Evans, A., 2000. Mechanics of materials: top-down approaches to fracture. *Acta materialia* 48, 125-135.
- IEA, 2015. Key world energy statistics. International Energy Agency, Paris, France.
- İeşan, D., 2002. On the theory of heat conduction in micromorphic continua. *International Journal of Engineering Science* 40, 1859-1878.
- İeşan, D., 2007. Thermoelasticity of bodies with microstructure and microtemperatures. *International Journal of Solids and Structures* 44, 8648-8662.
- İeşan, D., Nappa, L., 2005. On the theory of heat for micromorphic bodies. *International Journal of Engineering Science* 43, 17-32.

REFERENCES

- leşan, D., Quintanilla, R., 2009. On thermoelastic bodies with inner structure and microtemperatures. *Journal of Mathematical Analysis and Applications* 354, 12-23.
- leşan, D., Scalia, A., 2010. Plane deformation of elastic bodies with microtemperatures. *Mechanics Research Communications* 37, 617-621.
- Iremanc, P., Nguyen, Q.-S., 2004. Using the gradients of temperature and internal parameters in Continuum Thermodynamics. *Comptes Rendus Mécanique* 332, 249-255.
- Issa, M., 2010. Modélisation et simulation numérique des procédés de fabrication sous conditions extrêmes. Université de Technologie de Troyes.
- Issa, M., Labergère, C., Saanouni, K., Rassineux, A., 2012. Numerical prediction of thermomechanical field localization in orthogonal cutting. *CIRP Journal of Manufacturing Science and Technology* 5, 175-195.
- Jackson, H.E., Walker, C.T., 1971. Thermal Conductivity, Second Sound, and Phonon-Phonon Interactions in NaF. *Physical Review B* 3, 1428-1439.
- Jinyan, W., Jun, C., Minghui, L.I., 2004. A URI 4-Node quadrilateral element by assumed strain method for nonlinear problems *Acta Mech Sinica* 20, 632-641.
- Jirásek, M., 1998. Nonlocal models for damage and fracture: Comparison of approaches. *International Journal of Solids and Structures* 35, 4133-4145.
- Jirásek, M., Rolshoven, S., 2003. Comparison of integral-type nonlocal plasticity models for strain-softening materials. *International Journal of Engineering Science* 41, 1553-1602.
- Jirásek, M., Rolshoven, S., 2009a. Localization properties of strain-softening gradient plasticity models. Part I: Strain-gradient theories. *International Journal of Solids and Structures* 46, 2225-2238.
- Jirásek, M., Rolshoven, S., 2009b. Localization properties of strain-softening gradient plasticity models. Part II: Theories with gradients of internal variables. *International Journal of Solids and Structures* 46, 2239-2254.
- Jou, D., Casas-Vazquez, J., Lebon, G., 1988. Extended irreversible thermodynamics. *Reports on Progress in Physics* 51, 1105-1179.
- Jou, D., Casas-Vázquez, J., Lebon, G., 2010. Extended Irreversible Thermodynamics. Springer Netherlands.
- Jou, D., Casse-Vasquez, N., Lebon, G., 1993. Extended Irreversible Thermodynamics. Springer, Berlin.
- Jou, D., Cimmelli Vito, A., 2016. Constitutive equations for heat conduction in nanosystems and nonequilibrium processes: an overview. *Communications in Applied and Industrial Mathematics* 7, 196-226.
- Jurgen, B.K., 1996. Finite element procedures. Prentice Hall India.
- Kachanov, L., 1958. Time of the rupture process under creep conditions. *Isv. Akad. Nauk. SSR. Otd Tekh. Nauk* 8, 26-31.
- Kachanov, L., 1986. Introduction to continuum damage mechanics. Springer Science & Business Media.
- Kaiser, J., Feng, T., Maassen, J., Wang, X., Ruan, X., Lundstrom, M., 2017. Thermal transport at the nanoscale: A Fourier's law vs. phonon Boltzmann equation study. *Journal of Applied Physics* 121, 044302.
- Kaminski, W., 1990. Hyperbolic Heat Conduction Equation for Materials With a Nonhomogeneous Inner Structure. *Journal of Heat Transfer* 112, 555-560.
- Kankarani Farahani, M., Bostan Shirin, M., Assempour, A., 2014. Development of an inverse finite element method with an initial guess of linear unfolding. *Finite Elements in Analysis and Design* 79, 1-8.
- Karbasian, H., Tekkaya, A.E., 2010. A review on hot stamping. *Journal of Materials Processing Technology* 210, 2103-2118.

REFERENCES

- Khelifa, M., Badreddine, H., Gahbiche, M., Saanouni, K., Cherouat, A., Dogui, A., 2005. Effect of anisotropic plastic flow on the ductile damage evolution in sheet metal forming. Application to the circular bulging test. *International Journal of Forming Processes* 8, 271-289.
- Kim, S.H., Huh, H., 2002. Construction of sliding constraint surfaces and initial guess shapes for intermediate steps in multi-step finite element inverse analysis. *Journal of Materials Processing Technology* 130–131, 482-489.
- Kirchner, N., Steinmann, P., 2005. A unifying treatise on variational principles for gradient and micromorphic continua. *Philosophical Magazine* 85, 3875-3895.
- Koh, S.L., 1973. Theory of a second-order microfluid. *Rheologica Acta* 12, 418-424.
- Körner, C., Bergmann, H.W., 1998. The physical defects of the hyperbolic heat conduction equation. *Applied Physics A* 67, 397-401.
- Krajcinovic, D., 1996. *Damage Mechanics*. Elsevier Science, Amsterdam.
- Kröner, E., 1967. Elasticity theory of materials with long range cohesive forces. *International Journal of Solids and Structures* 3, 731-742.
- Kröner, E., 1968. Interrelations between Various Branches of Continuum Mechanics, in: Kröner, E. (Ed.), *Mechanics of Generalized Continua: Proceedings of the IUTAM-Symposium on The Generalized Cosserat Continuum and the Continuum Theory of Dislocations with Applications*, Freudenstadt and Stuttgart (Germany) 1967. Springer Berlin Heidelberg, Berlin, Heidelberg, pp. 330-340.
- Krumhansl, J.A., 1968. Some Considerations of the Relation between Solid State Physics and Generalized Continuum Mechanics, in: Kröner, E. (Ed.), *Mechanics of Generalized Continua: Proceedings of the IUTAM-Symposium on The Generalized Cosserat Continuum and the Continuum Theory of Dislocations with Applications*, Freudenstadt and Stuttgart (Germany) 1967. Springer Berlin Heidelberg, Berlin, Heidelberg, pp. 298-311.
- Kunin, I.A., 1968. The Theory of Elastic Media with Microstructure and the Theory of Dislocations, in: Kröner, E. (Ed.), *Mechanics of Generalized Continua: Proceedings of the IUTAM-Symposium on The Generalized Cosserat Continuum and the Continuum Theory of Dislocations with Applications*, Freudenstadt and Stuttgart (Germany) 1967. Springer Berlin Heidelberg, Berlin, Heidelberg, pp. 321-329.
- Labergère, C., 2015. Activites de Recherche. Université de Technologie de Troyes.
- Labergere, C., Rassineux, A., Saanouni, K., 2014. Numerical simulation of continuous damage and fracture in metal-forming processes with 2D mesh adaptive methodology. *Finite Elements in Analysis and Design* 82, 46-61.
- Larson, B.C., Tischler, J.Z., Mills, D.M., 1986. Nanosecond resolution time-resolved x-ray study of silicon during pulsed-laser irradiation. *Journal of Materials Research* 1, 144-154.
- Lasry, D., Belytschko, T., 1988. Localization limiters in transient problems. *International Journal of Solids and Structures* 24, 581-597.
- Lebon, G., 2014. Heat conduction at micro and nanoscales: A review through the prism of Extended Irreversible Thermodynamics. *Journal of Non-Equilibrium Thermodynamics* 39, 35-59.
- Lee, C., Cao, J., 2001. Shell element formulation of multi-step inverse analysis for axisymmetric deep drawing process. *International Journal for Numerical Methods in Engineering* 50, 681-706.
- Lee, C.H., Huh, H., 1998. Three dimensional multi-step inverse analysis for the optimum blank design in sheet metal forming processes. *Journal of Materials Processing Technology* 80–81, 76-82.
- Lee, H., Peng, K., Wang, J., 1985. An anisotropic damage criterion for deformation instability and its application to forming limit analysis of metal plates. *Engineering Fracture Mechanics* 21, 1031-1054.
- Lemaitre, J., 1992. *A course on damage mechanics*. Springer Science & Business Media.

REFERENCES

- Lemaitre, J., Chaboche, J.-L., Benallal, A., Desmorat, J., 1985. Mécanique des matériaux solides. Dunod, Paris.
- Lemaitre, J., Chaboche, J.-L., Benallal, A., Desmorat, R., 2009. Mécanique des matériaux solides - 3ème édition. Dunod, Paris.
- Lemaitre, J., Desmorat, R., 2005. Engineering Damage Mechanics: Ductile, Creep, Fatigue and Brittle Failures. Springer-Verlag Berlin Heidelberg.
- Lestriez, P., Saanouni, K., Mariage, J.F., Cherouat, A., 2004. Numerical Prediction of Ductile Damage in Metal Forming Processes Including Thermal Effects. International Journal of Damage Mechanics 13, 59-80.
- Levin, V.M., 1971. The relation between mathematical expectations of stress and strain tensors in elastic microheterogeneous media. Journal of Applied Mathematics and Mechanics 35, 694-701.
- Li, Y., Abbes, B., Guo, Y., 2007. Two efficient algorithms of plastic integration for sheet forming modeling. Journal of manufacturing science and engineering 129, 698-704.
- Liu, W., Hu, P., Zhang, X., Zhou, P., 2013. A modified PMA method to generate sliding constraint surface in multi-step inverse approach. AIP Conference Proceedings 1567, 1052-1056.
- Luikov, A.V., Bubnov, V.A., Soloviev, I.A., 1976. On wave solutions of the heat-conduction equation. International Journal of Heat and Mass Transfer 19, 245-248.
- Majlessi, S.A., Lee, D., 1987. Further development of sheet metal forming analysis method. Journal of Engineering for Industry 109, 330-337.
- Majlessi, S.A., Lee, D., 1988. Development of multistage sheet metal forming analysis method. J. Materials Shaping Technology 6, 41-54.
- Mandl, F., 2008. Statistical Physics (2nd Edition). John Wiley & Sons.
- Mathur, K., Dawson, P., 1987. Damage evolution modeling in bulk forming processes. Computational methods for predicting material processing defects, 251-262.
- Maugin, G.A., 1990. Internal Variables and Dissipative Structures. Journal of Non-Equilibrium Thermodynamics 15, 173-192.
- Maugin, G.A., Muschik, W., 1994a. Thermodynamics with Internal Variables. Part I. General Concepts. Journal of Non-Equilibrium Thermodynamics 19, 217-249.
- Maugin, G.A., Muschik, W., 1994b. Thermodynamics with Internal Variables. Part II. Applications. Journal of Non-Equilibrium Thermodynamics 19, 250-289.
- Mediavilla, J., Peerlings, R.H.J., Geers, M.G.D., 2006a. Discrete crack modelling of ductile fracture driven by non-local softening plasticity. International Journal for Numerical Methods in Engineering 66, 661-688.
- Mediavilla, J., Peerlings, R.H.J., Geers, M.G.D., 2006b. An integrated continuous-discontinuous approach towards damage engineering in sheet metal forming processes. Engineering Fracture Mechanics 73, 895-916.
- Mindlin, R.D., 1964. Micro-structure in linear elasticity. Arch. Rational Mech. Anal. 16, 51-78.
- Mindlin, R.D., 1965. Second gradient of strain and surface-tension in linear elasticity. International Journal of Solids and Structures 1, 417-438.
- Mindlin, R.D., Eshel, N.N., 1968. On first strain-gradient theories in linear elasticity. International Journal of Solids and Structures 4, 109-124.
- Mindlin, R.D., Tiersten, H.F., 1962. Effects of couple-stresses in linear elasticity. Arch. Rational Mech. Anal. 11, 415-448.
- Müeller, I., 1966. Zur Ausbreitungsgeschwindigkeit von Störungen in kontinuierlichen Medien. Technische Hochschule, Aachen.

REFERENCES

- Mühlhaus, H.B., Alfantis, E.C., 1991. A variational principle for gradient plasticity. *International Journal of Solids and Structures* 28, 845-857.
- Muller, I., 1967. Zum Paradoxon der Wärmeleitungstheorie. *Z. Phys.* 198, 329-344.
- Müller, I., 2001. Thermodynamics of mixtures and phase field theory. *International Journal of Solids and Structures* 38, 1105-1113.
- Müller, I., Ruggeri, T., 1993. Extended thermodynamics. Springer-Verlag, New York.
- Murakami, S., 1988. Mechanical Modeling of Material Damage. *Journal of Applied Mechanics* 55, 280-286.
- Murakami, S., 2012. Continuum damage mechanics: a continuum mechanics approach to the analysis of damage and fracture. Springer Science & Business Media.
- Narayananmurti, V., Dynes, R.C., 1972. Observation of Second Sound in Bismuth. *Physical Review Letters* 28, 1461-1465.
- Nedjar, B., 2001. Elastoplastic-damage modelling including the gradient of damage: formulation and computational aspects. *International Journal of Solids and Structures* 38, 5421-5451.
- Needleman, A., 1987. A continuum model for void nucleation by inclusion debonding. *Journal of applied mechanics* 54, 525-531.
- Needleman, A., 1988. Material rate dependence and mesh sensitivity in localization problems. *Computer Methods in Applied Mechanics and Engineering* 67, 69-85.
- Needleman, A., 2015. The Effect of Rate Dependence on Localization of Deformation and Failure in Softening Solids. *Journal of Applied Mechanics* 82, 021002-021002.
- Ngo, D., Scordelis, A.C., 1967. Finite Element Analysis of Reinforced Concrete Beams. *Journal Proceedings* 64, 152-163.
- Nguyen, G.D., Korsunsky, A.M., Belnoue, J.P.H., 2015. A nonlocal coupled damage-plasticity model for the analysis of ductile failure. *International Journal of Plasticity* 64, 56-75.
- Nguyen, Q.-S., 2010. Gradient thermodynamics and heat equations. *Comptes Rendus Mécanique* 338, 321-326.
- Nguyen, Q.-S., 2011. Variational principles in the theory of gradient plasticity. *Comptes Rendus Mécanique* 339, 743-750.
- Nguyen, Q.-S., Andrieux, S., 2005. The non-local generalized standard approach: a consistent gradient theory. *Comptes Rendus Mécanique* 333, 139-145.
- Niazi, M.S., Wisselink, H.H., Meinders, T., 2013. Viscoplastic regularization of local damage models: revisited. *Computational Mechanics* 51, 203-216.
- Oñate, E., Kleiber, M., De Saracibar, C.A., 1988. Plastic and viscoplastic flow of void-containing metals. Applications to axisymmetric sheet forming problems. *International Journal for Numerical Methods in Engineering* 25, 227-251.
- Ortiz, M., Simo, J.C., 1986. An analysis of a new class of integration algorithms for elastoplastic constitutive relations. *International journal for numerical methods in engineering* 23, 353-366.
- Pardoen, T., Doghri, I., Delannay, F., 1998. Experimental and numerical comparison of void growth models and void coalescence criteria for the prediction of ductile fracture in copper bars. *Acta Materialia* 46, 541-552.
- Pardoen, T., Hachez, F., Marchionni, B., Blyth, P.H., Atkins, A.G., 2004. Mode I fracture of sheet metal. *Journal of the Mechanics and Physics of Solids* 52, 423-452.

REFERENCES

- Peerlings, R., De Borst, R., Brekelmans, W., De Vree, J., 1995. Computational modelling of gradient-enhanced damage for fracture and fatigue problems, Computational Plasticity, Fundamentals and Applications: Proceedings of the 4th International Conference. Pineridge Press: Swansea, pp. 975-986.
- Peerlings, R., De Borst, R., Brekelmans, W., DE VREE, J., 1996. Gradient enhanced damage for quasi-brittle materials. International Journal for numerical methods in engineering 39, 3391-3403.
- Peerlings, R.H.J., 1999. Enhanced damage modelling for fracture and fatigue. Technische Universiteit Eindhoven.
- Peerlings, R.H.J., Geers, M.G.D., de Borst, R., Brekelmans, W.A.M., 2001. A critical comparison of nonlocal and gradient-enhanced softening continua. International Journal of Solids and Structures 38, 7723-7746.
- Peerlings, R.H.J., Massart, T.J., Geers, M.G.D., 2004. A thermodynamically motivated implicit gradient damage framework and its application to brick masonry cracking. Computer Methods in Applied Mechanics and Engineering 193, 3403-3417.
- Peshkov, V., 1944. Second sound in helium II. Journal of Physics, USSR 8, 381-386.
- Peshkov, V., 1946. Determination of the velocity of propagation of the second sound in helium II. Journal of Physics, USSR 10, 389-398.
- Pietruszczak, S., Mróz, Z., 1981. Finite element analysis of deformation of strain-softening materials. International Journal for Numerical Methods in Engineering 17, 327-334.
- Pijaudier-Cabot, G., Bažant, Z.P., 1987. Nonlocal damage theory. Journal of engineering mechanics 113, 1512-1533.
- Pijaudier-Cabot, G., Bazant, Z.P., Tabbara, M., 1988. Comparison of various models for strain-softening. Engineering computations 5, 141-150.
- Rabotnov, I.U.r.N., 1969. Creep problems in structural members. North-Holland Pub. Co.
- Ramakrishnan, N., Singh, K.M., Suresh, R.K.V., Srinivasan, N., 1998. An algorithm based on total-elastic-incremental-plastic strain for large deformation plasticity. Journal of Materials Processing Technology 86, 190-199.
- Rashid, Y., 1968. Analysis of reinforced concrete pressure vessels. Nuclear Engineering and Design 7, 334-344.
- Rice, J.R., 1976. The localization of plastic deformation. North-Holland Publishing Company.
- Riha, P., 1977. Poiseuille flow of microthermopolar fluids. Acta Technica 22, 602-613.
- Říha, P., 1975. On the theory of heat-conducting micropolar fluids with microtemperatures. Acta Mechanica 23, 1-8.
- Říha, P., 1976. On the microcontinuum model of heat conduction in materials with inner structure. International Journal of Engineering Science 14, 529-535.
- Robert, C., Delamézière, A., Dal Santo, P., Batoz, J.L., 2012. Comparison between incremental deformation theory and flow rule to simulate sheet-metal forming processes. Journal of Materials Processing Technology 212, 1123-1131.
- Rodríguez-Ferran, A., Bennett, T., Askes, H., Tamayo-Mas, E., 2011. A general framework for softening regularisation based on gradient elasticity. International Journal of Solids and Structures 48, 1382-1394.
- SAANOUNI, #160, K., ABDUL-LATIF, #160, A., 1996. Micromechanical modeling of low cycle fatigue under complex loadings-Part I. Theoretical formulation. Elsevier, Kidlington, ROYAUME-UNI.
- Saanouni, K., 2008. On the numerical prediction of the ductile fracture in metal forming. Engineering Fracture Mechanics 75, 3545-3559.

REFERENCES

- Saanouni, K., 2012. Damage mechanics in metal forming: advanced modeling and numerical simulation. John Wiley & Sons.
- Saanouni, K., Belamri, N., Autesserre, P., 2010. Finite element simulation of 3D sheet metal guillotining using advanced fully coupled elastoplastic-damage constitutive equations. *Finite Elements in Analysis and Design* 46, 535-550.
- Saanouni, K., Chaboche, J., 2003a. Computational damage mechanics. Application to metal forming. Elsevier, Oxford.
- Saanouni, K., Chaboche, J.L., 2003b. Computational Damage Mechanics: Application to Metal Forming Simulation, in: Karihaloo, I.M.O.R. (Ed.), *Comprehensive Structural Integrity*. Pergamon, Oxford, pp. 321-376.
- Saanouni, K., Hamed, M., 2013. Micromorphic approach for finite gradient-elastoplasticity fully coupled with ductile damage: Formulation and computational aspects. *International Journal of Solids and Structures* 50, 2289-2309.
- Saouma, V., Ingraffea, A., 1981. Fracture mechanics analysis of discrete cracking, Proceedings of IABSE Colloquium on Advanced Mechanics of Reinforced Concrete, Delft, the Netherlands, pp. 413-436.
- Sellitto, A., Cimmelli, V.A., Jou, D., 2016. *Mesoscopic Theories of Heat Transport in Nanosystems*. Springer International Publishing, Switzerland.
- Sergei, L.S., 1997. Local non-equilibrium transport models. *Physics-Uspekhi* 40, 1043.
- Šesták, J., Holba, P., 2013. Heat inertia and temperature gradient in the treatment of DTA peaks. *J Therm Anal Calorim* 113, 1633-1643.
- Shewchuk, J.R., 2002. Delaunay refinement algorithms for triangular mesh generation. *Computational Geometry* 22, 21-74.
- Simo, J., Hughes, T., 1998. *Computational inelasticity*. Springer New York.
- Simo, J.C., Hughes, T.J.R., 1986. On the Variational Foundations of Assumed Strain Methods. *Journal of Applied Mechanics* 53, 51-54.
- Sluys, L.J., De Borst, R., 1992. Wave propagation and localization in a rate-dependent cracked medium—model formulation and one-dimensional examples. *International Journal of Solids and Structures* 29, 2945-2958.
- Sobolev, S.L., 1993. Two-temperature discrete model for nonlocal heat conduction. *J. Phys. III France* 3, 2261-2269.
- Sobolev, S.L., 1995. Two-temperature Stefan problem. *Physics Letters A* 197, 243-246.
- Sobolev, S.L., 2014. Nonlocal diffusion models: Application to rapid solidification of binary mixtures. *International Journal of Heat and Mass Transfer* 71, 295-302.
- Sobolev, S.L., 2016. Nonlocal two-temperature model: Application to heat transport in metals irradiated by ultrashort laser pulses. *International Journal of Heat and Mass Transfer* 94, 138-144.
- Suhubl, E.S., Eringen, A.C., 1964. Nonlinear theory of micro-elastic solids—II. *International Journal of Engineering Science* 2, 389-404.
- Suidan, M., Schnobrich, W.C., 1973. Finite Element Analysis of Reinforced Concrete. *Journal of the Structural Division* 99, 2109-2122.
- Sukumar, N., Moës, N., Moran, B., Belytschko, T., 2000. Extended finite element method for three-dimensional crack modelling. *International Journal for Numerical Methods in Engineering* 48, 1549-1570.
- Swendsen, R.H., 2006. Statistical mechanics of colloids and Boltzmann's definition of the entropy. *American Journal of Physics* 74, 187-190.

REFERENCES

- Swenson, R.J., 1978. Heat Conduction - Finite or Infinite Propagation. *Journal of Non-Equilibrium Thermodynamics* 3, 39-48.
- T J R, H., 1987. The finite element method: linear static and dynamic finite element analysis. Englewood Cliffs, NJ: Prentice-Hall.
- Tang, B., Li, Y., Lu, X., 2010. Developments of Multistep Inverse Finite Element Method and Its Application in Formability Prediction of Multistage Sheet Metal Forming. *Journal of Manufacturing Science and Engineering* 132, 041013-041019.
- Temizer, İ., Wriggers, P., 2010. A micromechanically motivated higher-order continuum formulation of linear thermal conduction. *ZAMM - Journal of Applied Mathematics and Mechanics / Zeitschrift für Angewandte Mathematik und Mechanik* 90, 768-782.
- Thomas, T.Y., 1961. Plastic Flow and Fracture in Solids. Elsevier.
- Titeux, I., Li, Y.M., Debray, K., Guo, Y.Q., 2004. Un algorithme efficace d'intégration plastique pour un matériau obéissant au critère anisotrope de Hill. *Comptes Rendus Mécanique* 332, 901-906.
- Toti, J., Gattulli, V., Sacco, E., 2015. Nonlocal damage propagation in the dynamics of masonry elements. *Computers & Structures* 152, 215-227.
- Toupin, R., A., 1964. Theories of elasticity with couple-stress. *Arch. Rational Mech. Anal.* 17, 85-112.
- Toupin, R.A., 1962. Elastic materials with couple-stresses. *Arch. Rational Mech. Anal.* 11, 385-414.
- Triantafyllidis, N., Aifantis, E.C., 1986. A gradient approach to localization of deformation. I. Hyperelastic materials. *Journal of Elasticity* 16, 225-237.
- Truesdell, C., Noll, W., 1965. The non-linear field theories of mechanics. Springer.
- Truesdell, C., Noll, W., 2004a. The Non-Linear Field Theories of Mechanics. Springer Berlin Heidelberg, Berlin, Heidelberg.
- Truesdell, C., Noll, W., 2004b. The non-linear field theories of mechanics. Springer.
- Tvergaard, V., 1982. Influence of void nucleation on ductile shear fracture at a free surface. *Journal of the Mechanics and Physics of Solids* 30, 399-425.
- Tvergaard, V., Needleman, A., Lo, K.K., 1981. Flow localization in the plane strain tensile test. *Journal of the Mechanics and Physics of Solids* 29, 115-142.
- Tzou, D.Y., 1995. A Unified Field Approach for Heat Conduction From Macro- to Micro-Scales. *Journal of Heat Transfer* 117, 8-16.
- Tzou, D.Y., 2014. Macro- to Microscale Heat Transfer: The Lagging Behavior, Second Edition. John Wiley & Sons.
- Ván, P., Fülöp, T., 2012. Universality in heat conduction theory: weakly nonlocal thermodynamics. *Annalen der Physik* 524, 470-478.
- Verma, P., Singh, D., Singh, K., 1979. Hagen-Poiseuille flow of microthermopolar fluids in a circular pipe. *Acta Technica* 24, 402-412.
- Vernotte, P., 1958. Les paradoxes de la théorie continue de l'équation de la chaleur. *Comptes Rendus Hebdomadaires Des Séances De L Académie Des Sciences* 246, 3154-3155.
- Voyiadjis, G.Z., Kattan, P.I., 1992a. Finite Strain Plasticity and Damage in Constitutive Modeling of Metals With Spin Tensors. *Applied Mechanics Reviews* 45, S95-S109.
- Voyiadjis, G.Z., Kattan, P.I., 1992b. A plasticity-damage theory for large deformation of solids—I. Theoretical formulation. *International Journal of Engineering Science* 30, 1089-1108.
- Voyiadjis, G.Z., Kattan, P.I., Voyiadjis, G.Z., Kattan, P.I., 1999. Advances in Damage Mechanics: Metals and Metal Matrix Composites. Elsevier, Oxford.

REFERENCES

- Wang, J., Wang, J.-S., 2006. Carbon nanotube thermal transport: Ballistic to diffusive. *Applied Physics Letters* 88, 111909.
- Wang, W.M., Sluys, L.J., Borst, R.d., 1996. Interaction between material length scale and imperfection size for localisation phenomena in viscoplastic media. *European Journal of Mechanics. A, Solids* 15, 447-464.
- WORLDAUTOSTEEL, 2014. Advanced High-Strength Steels Application Guidelines V5.
- Wozniak, C., 1967. Thermoelasticity of non-simple oriented materials. *International Journal of Engineering Science* 5, 605-612.
- Xenos, D., Grassl, P., 2016. Modelling the failure of reinforced concrete with nonlocal and crack band approaches using the damage-plasticity model CDPM2. *Finite Elements in Analysis and Design* 117–118, 11-20.
- Yue, Z., 2014. Ductile damage prediction in sheet metal forming processes. University of Technology of Troyes.
- Zanchini, E., 1999. Hyperbolic-heat-conduction theories and nondecreasing entropy. *Physical Review B* 60, 991-997.
- Zienkiewicz, O.C., Taylor, R.L., 2005. The finite element method for solid and structural mechanics. Butterworth-heinemann.

Weijie LIU

Doctorat : Matériaux, Mécanique, Optique et Nanotechnologie

Année 2017

Modélisation avancée pour la mise en forme des tôles à haute température

L'objectif de cette thèse est de proposer deux approches complémentaires de modélisation et de simulation numériques des procédés de mise en forme de structures minces.

La première est une approche inverse multi-pas, délibérément simplifiée, pour simuler et "optimiser" rapidement et à moindre coût des procédés d'emboutissage de tôles minces, tout en maintenant une bonne précision dans le calcul des contraintes. Un solveur statique implicite est développé en introduisant plusieurs configurations intermédiaires construites efficacement en utilisant une technique de programmation quadratique avec projection.

La deuxième approche, de nature incrémentale, repose sur (i) une formulation d'équations de bilan et d'équations de comportement multi-physics fortement couplés formulées dans le cadre des milieux micromorphes ; (ii) une discréttisation spatiale par EF et temporelle par DF avec un solveur global dynamique explicite et une intégration locale itérative implicite. Une attention particulière est accordée aux aspects thermiques avec l'introduction d'une microtempérature et ses premiers gradients conduisant à l'obtention de deux équations thermiques fortement couplées généralisant de nombreux modèles non locaux proposés dans la littérature.

L'approche inverse multi-pas a été implémentée dans le code maison KMAS et l'approche incrémentale non locale a été implémentée dans ABAQUS/Explicit. Des études paramétriques sont menées et des validations sur des exemples simples et sur des procédés d'emboutissage sont réalisées.

Mots clés : endommagement, mécanique de l' (milieu continu) - élastoviscoplasticité - éléments finis, méthode des - équation de la chaleur - simulation par ordinateur.

Advanced Modelling for Sheet Metal Forming under High Temperature

The aim of this thesis is to propose two complementary approaches for modeling and numerical simulations of thin sheet metal forming processes.

The first one is a deliberately simplified multi-step inverse approach to simulate and "optimize" rapidly and inexpensively thin-sheet stamping processes while maintaining good accuracy in the stress calculation. An implicit static solver is developed by introducing several efficiently constructed intermediate configurations using a quadratic programming technique with projection.

The second approach, which is of an incremental nature, is based on (i) a formulation of equilibrium equations and strongly coupled multiphysical behavior equations formulated in the context of micromorphic continua; (ii) spatial discretization by FEM and time discretization by FD with an explicit dynamic global solver and implicit iterative local integration scheme. Particular attention is paid to the nonlocal thermal aspects with the introduction of a micro-temperature and its first gradients leading to two strongly coupled thermal equations generalizing several thermal nonlocal models proposed in the literature.

The multi-step inverse approach was implemented in the KMAS in house code while the nonlocal incremental approach was implemented in ABAQUS/Explicit. Parametric studies are performed and validations are carried out on simple examples and on deep drawing processes.

Keywords: continuum damage mechanic - elasto-plasticity - finite element method - heat equation – computer simulation.

Thèse réalisée en partenariat entre :

